<center>

**METALS
AND SUPERCONDUCTORS**

</center>

Mobility and Diffusion of Oxygen Isotopes in $YBa_2Cu_3O_{6+x}$: Monte Carlo Simulation

M. Z. Uritsky and V. I. Tsidilkovski

*Institute of High-Temperature Electrochemistry, Ural Division, Russian Academy of Sciences,
ul. S. Kovalevskoĭ 20, Yekaterinburg, 620219 Russia*
*e-mail: umz@ihte.uran.ru*
Received September 17, 2002

Abstract—The self-diffusion (D_0) and isotope diffusion (D^*) coefficients of oxygen in $YBa_2Cu_3O_{6+x}$ are calculated as functions of the temperature (600–1200 K) and the oxygen content ($0 < x < 1$). The Monte Carlo simulation is performed with due regard for both the interaction of oxygen ions at lattice sites in the basal planes of $YBa_2Cu_3O_{6+x}$ and the interaction between a jumping ion at a saddle point and the environment. Equilibrium thermodynamic characteristics (including the phase diagram and the heat capacity) are calculated in terms of the Hamiltonian of interaction between oxygen ions at the lattice sites. It is found that an increase in the oxygen content leads to a decrease in the diffusion coefficients D_0 and D^*, an increase in the effective activation energies for diffusion by 0.3–0.5 eV, and a decrease in the Haven ratio from 1 to ~0.5. © *2003 MAIK "Nauka/Interperiodica".*

1. INTRODUCTION

A large number of theoretical and, especially, experimental works have been concerned with oxygen transport in $YBa_2Cu_3O_{6+x}$ compounds (see, for example, [1, 2] and references therein). The available data on the diffusion coefficients and the diffusion activation energies agree reasonably in order of magnitude [1, 2]. A somewhat poorer agreement is achieved in the case of concentration dependences of the oxygen transport coefficients, which are of our prime interest in the present work. However, if we disregard data on the diffusion coefficients determined in a methodically incorrect way (for example, data obtained for samples with a variable oxygen content without inclusion or with incorrect inclusion of the finite rate of oxygen exchange at the oxide–gas interface, etc.), the reliably established regularities in oxygen transport can be summarized as follows. (In this work, we will restrict our consideration to the temperature range 600–1200°C and will not touch on the diffusion anisotropy observed in the basal plane at lower temperatures [1].) (i) An increase in the oxygen content only slightly affects the isotope diffusion coefficients D^*. In particular, the diffusion coefficient D^* either remains constant to within the limits of the experimental error of secondary ion mass spectrometry [1] or, according to the results obtained by the isotopic exchange technique with analysis of the gas phase, somewhat decreases [3]. (ii) The chemical diffusion coefficient increases with an increase in the oxygen content x [2]. (iii) As follows from the internal friction data [4], an increase in the oxygen content x results in an increase in the diffusion activation energy, which jumpwise changes upon the transition from a tetragonal phase to an orthorhombic phase. These findings agree

with each other and can be explained theoretically when the correlations between mobile oxygen ions in the basal plane are taken into account. The above regularities can be interpreted in the framework of the dynamic cluster approach with consistent inclusion of the interionic interactions at lattice sites and the interaction between a jumping ion at a saddle point and the environment [5]. Earlier, analogous results were obtained by Choi *et al.* [6] with the use of the Kikuchi path probability method. In [6], the authors ignored the interaction at saddle points, which led to somewhat poorer agreement with the experimental data. (Note that the results obtained in [5] and [6] agree closely with each other when the interaction at saddle points is disregarded within the approach used in [5].)

Salomons and de Fontaine [7] carried out direct numerical Monte Carlo simulation of oxygen diffusion with allowance made for interionic interactions and obtained the results inconsistent with the available experimental data. As follows from the calculations performed in [7], an increase in the oxygen content x brings about an increase in the isotope diffusion coefficient by three to five orders of magnitude, a drastic increase in the diffusion activation energy, and a decrease in the chemical diffusion coefficient of oxygen. Note that, in the high-temperature range, the Hamiltonians used in [5–7] to describe the interaction of oxygen ions at lattice sites differ insignificantly; hence, their application for describing the thermodynamic properties at these temperatures offers similar results. Possibly, the strong dependence of the diffusion coefficient on the oxygen stoichiometry in [7] is caused by the use of the Metropolis scheme in the Monte Carlo calculation. For strong correlations between mobile
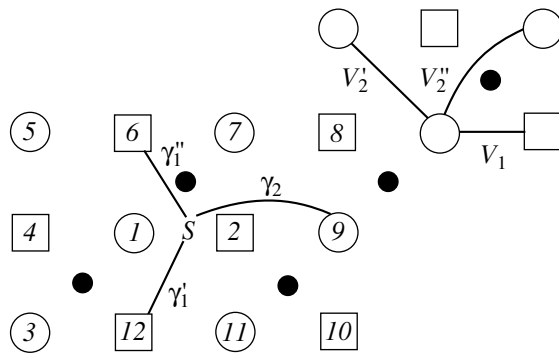
Fig. 1. A schematic drawing of the basal plane. Circles and squares correspond to the O_1 and O_5 oxygen sites, respectively. Points indicate the Cu_1 copper sites. The interaction of oxygen ions at the lattice sites according to the model proposed in [9] is illustrated at the top right. The interaction constant V_2 is equal to the half-sum of the constants V_2' and V_2'', which characterize the direct interaction and the interaction through an intermediate Cu ion. The interaction between the oxygen ion located at the saddle point S (jump from site 1 to site 2) and the environment is shown at the bottom left. The constant γ_1 in relationship (2) is defined as $\gamma_1 = (\gamma_1' + \gamma_1'')/2$.

particles, the Metropolis algorithm can lead to an incorrect description of migration processes (see below).

In this work, the mobility μ and the isotope diffusion coefficient D^* were calculated within the schemes allowing for the finite barrier to the jump with and without inclusion of the interaction between mobile ions. The calculations were performed with allowance made for both the interaction of oxygen ions at lattice sites in the basal planes of $YBa_2Cu_3O_{6+x}$ and the interaction between a jumping ion at a saddle point and the environment. The diffusion coefficient D^* was determined using a standard method of calculating the root-mean-square displacements of traced particles. In order to evaluate the mobility μ, we calculated the steady-state current induced in the system by an external dc electric field. The independent calculations of the quantities D^* and μ made it possible to determine the dependence of the Haven ratio H on the temperature and the oxygen content. The Haven ratio—an important characteristic of the correlated transport—is defined as $H = D^*/D_0$, where D_0 is the self-diffusion coefficient. In turn, the self-diffusion coefficient D_0 and the mobility μ are related by the standard expression $D_0 = \mu kT/q$, where T is the temperature and q is the carrier charge.

2. MODEL

It is known that, in YBaCuO, oxygen transport occurs in the basal planes involving the O_1 and O_5 oxygen sites and the Cu_1 copper sites and diffusion in the perpendicular direction (i.e., along the **c** axis) proceeds

at a considerably lower rate [1, 2]. The lattice formed by the O_1 and O_5 sites is similar to a square lattice. The interaction between oxygen ions in the basal plane is relatively strong and brings about ordering effects (see [6–8] and references therein). As was shown in [8], the tetragonal (space group $P4/mmm$) and orthorhombic (space group $Pmmm$) modifications of YBaCuO are stable at sufficiently high temperatures, which are actual for diffusion.[1] The transition from the tetragonal phase to the orthorhombic phase is accompanied by ordering of mobile oxygen ions in the basal plane with predominant occupation of the O_1 (or O_5) sites. As in [5], the interaction of oxygen ions at lattice sites in the basal plane will be described in the framework of a model similar to that proposed earlier in [9]. In [9], within the Bethe–Kikuchi approximation, the pair interaction of the O_1–O_5 nearest neighbors was properly taken into account and the interaction of the next-to-nearest neighbors (O_1–O_1 and O_5–O_5) was included in the mean-field approximation without regard for the interaction anisotropy (Fig. 1).

According to [5, 9], the energy U of interaction between the oxygen ions in the basal plane can be written in the form

$$U = V_1 \sum_{i,j}^{(1)} n_i n_j + V_2 \sum_{i,j}^{(2)} n_i n_j. \qquad (1)$$

Here, n_i is the occupancy of the ith site and $\sum_{(i,j)}^{(1)}$ and $\sum_{(i,j)}^{(2)}$ are the sums over the nearest and next-to-nearest site pairs (i, j), respectively. The interaction constants are as follows: $V_1 = 1200$ K is the energy of a nearest neighbor pair and $V_2 = -580$ K is the averaged energy of the next-to-nearest neighbor interaction, which is equal to the half-sum of the constants of the direct interaction and the interaction through an intermediate copper ion (Fig. 1). At the sufficiently high temperatures of interest, the approximation used is fairly adequate and allows one to describe not only the ordering effects but also the thermodynamics of oxidation of YBaCuO with a high accuracy (provided the contribution of the electronic subsystem in taken into account) [9].

As in [5], the energy of interaction between a jumping ion at a saddle point and the environment can be represented in the following form:

$$U^s = \gamma_1 \sum_{(i)}^{(1)} n_i + \gamma_2 \sum_{(i)}^{(2)} n_i, \qquad (2)$$

where $\sum_{(i)}^{(1)} n_i$ and $\sum_{(i)}^{(2)} n_i$ are the sums over the occupancies of lattice sites in the first and second coordination spheres, respectively. In this work, the oxygen

---

[1] At temperatures below room temperature, the $YBa_2Cu_3O_{6+x}$ crystals contain superstructures with a more complex ordering in the basal plane.

transport coefficients are calculated using different sets of interaction constants γ, namely, the set proposed in [5] (according to [5], the set of constants γ close to $\gamma_1 = V_1/2.5$ and $\gamma_2 = V_1/1.5$ permits one to describe the main features of diffusion), the set corresponding to the absence of interaction at the saddle point, and the set of intermediate interaction constants.

3. COMPUTATIONAL TECHNIQUE

The Monte Carlo simulation was performed using an $N \times N$ square lattice in the basal plane ($N = 16, 32, 64$) with periodic boundary conditions. The value of x was changed from 0.02 to 1 (this corresponds to a variation in the occupancy from 1% to half the number of lattice sites) with the step $\Delta x = 0.02$. The temperature was varied from 600 to 1200 K with a step of 25 K.

The simulation procedure involved the following three stages.

At the first stage, the empty sites were filled with particles to a specified concentration. For this purpose, each time, one of the empty sites was chosen in a random way and, then, a particle was placed at this site.

The generated state was not equilibrium at a nonzero temperature. At the second stage, in order to bring the system to the equilibrium state, we accomplished 1000–2000 initial Monte Carlo runs. Since we were not interested in the kinetics of relaxation of the system to the equilibrium state, the Metropolis algorithm (see the Appendix) was used for accelerating the convergence. The attainment of the required state can be judged from the relaxation of the corresponding parameters. In particular, the attainment of the equilibrium state can be judged from the behavior of the order parameter. For the system in the equilibrium state, we calculated a number of thermodynamic parameters, including the phase diagram and the heat capacity.

At the last stage, when the system reached the equilibrium state, the migration of oxygen ions was simulated by the Monte Carlo method. It was essential that the procedure allowed for the finite energy barrier to the jump both with and without inclusion of the interaction between mobile ions. In this case, we used a standard scheme of the Monte Carlo run (see the Appendix).

The isotope diffusion coefficient $D*$ was determined from the calculated root-mean-square displacement of an ensemble of traced particles. In the isotropic approximation for the basal plane (we consider the high-temperature range, see Section 2), the isotope diffusion coefficient can be written as

$$D* = \langle X^2 \rangle / 4N_t.$$

Here, $\langle X^2 \rangle$ is the sum of the displacements squared over all particles per particle and N_t is the number of Monte Carlo runs. The effective activation energy was calculated using a linear-regression procedure in which the

dependence $D(t)$ was approximated by an Arrhenius function in the vicinity of chosen temperatures.

The mobility μ was calculated from the steady-state current that arises in the system upon application of a weak dc electric field E. In order to determine the mobility, which is defined as the ratio of the total displacement of all the particles toward the chosen direction to the number of particles and the number of Monte Carlo runs, it is necessary to take into account the change in the probability p_{ij} of jumping between the adjacent sites i and j in the electric field; that is,

$$p_{ij}^E = p_{ij}(1 \pm qEa/2kT).$$

Here, p_{ij} is the probability of the jump $i \longrightarrow j$ in the absence of an electric field, a is the distance between the ith and jth sites, and the field direction is chosen to be parallel to the vector $(\mathbf{R}_j - \mathbf{R}_i)$.

The self-diffusion coefficient was calculated from the standard relationship $D_0 = \mu kT/q$.

The relationships for kinetic coefficients involve the root-mean-square displacement determined by the particle displacements associated with individual ion jumps occurring with different probabilities. The attainment of a steady-state contribution from all the jumping modes characterized by different probabilities requires a certain time. The calculated diffusion coefficients on this time interval depend on the number of Monte Carlo runs and, eventually, converge to their limiting values. With the aim of reliably excluding this dependence from our consideration and determining the time-independent transport coefficients, their values were calculated every 5000 Monte Carlo runs. In the model under consideration, the initial time it takes for the calculated quantities to converge corresponds to 15000–20000 Monte Carlo runs.

4. RESULTS AND DISCUSSION

For temperatures $T = 600$–1200 K and oxygen content $x = 0$–1, the calculated phase diagram is in agreement with the available experimental data. Figure 2 depicts the calculated curve indicating the boundary between the ordered orthorhombic phase and the tetragonal phase. The experimental data obtained by different authors are also presented in Fig. 2. The inset shows the temperature dependence of the heat capacity at $x = 0.7$ in the vicinity of the phase transition. It can be seen that the transition is rather smeared in temperature, which is associated with the finite sizes of the system. As a consequence, the order parameter upon transition to the ordered phase vanishes over a temperature range. On this basis, it was assumed that the boundary between the tetragonal phase and the orthorhombic phase corresponds to the order parameter in the range 0–0.03.

The dependences of the self-diffusion and isotope diffusion coefficients on the oxygen content at different temperatures are plotted in Figs. 3 and 4. With an
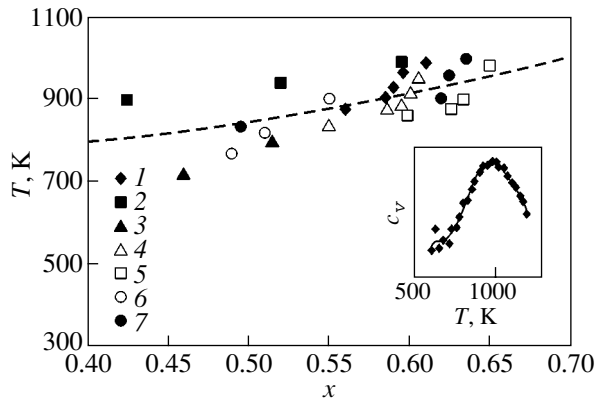
Fig. 2. Phase diagram of $YBa_2Cu_3O_{6+x}$ ($0 < x < 1$) in the temperature range 600–1200 K. Symbols are experimental data taken from (*1*) [10], (*2*) [11], (*3*) [12], (*4*) [13], (*5*) [14], (*6*) [15], and (*7*) [16]. The inset shows the calculated temperature dependence of the heat capacity c_v in the vicinity of the phase transition.
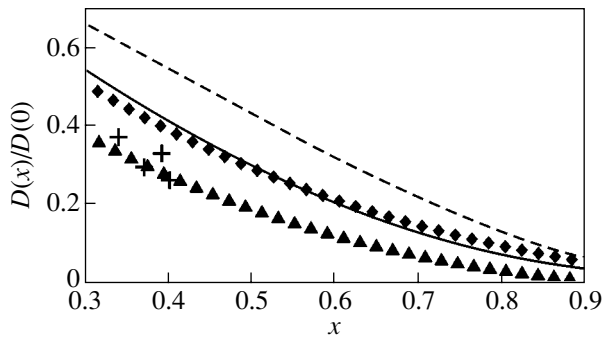
Fig. 3. Dependences of the isotope diffusion coefficient $D^*(x)$ [normalized to $D^*(x \longrightarrow 0)$] on the oxygen content at temperatures $T = 600°C$ (triangles) and $800°C$ (rhombuses). Triangles and rhombuses correspond to the calculated dependences $D^*(x)/D^*(x \longrightarrow 0)$ in the case when the interaction at the saddle point is characterized by the constants γ taken from [5]: $\gamma_1 = V_1/2.5$ and $\gamma_2 = V_1/1.5$ (where V_1 is the energy of the interaction between the nearest neighbors). The solid line shows the dependence $D^*(x)/D^*(x \longrightarrow 0)$ calculated for the halved constants γ at $T = 600°C$. The dashed line represents the same dependence calculated in the absence of the interaction at the saddle point ($T = 600°C$). Crosses are the experimental data obtained in [3] according to the isotopic exchange technique with analysis of the gas phase ($T = 600°C$).

increase in the oxygen content x, the coefficients D^* and D_0 decrease by less than one order of magnitude at high temperatures and within two orders of magnitude at low temperatures. The calculated diffusion coefficients agree well with the results obtained by the isotopic exchange technique with analysis of the gas phase [3] (Fig. 3). Agreement with the secondary ion mass spectrometric data is poorer (see [1, 2] and references therein). The diffusion coefficients D^* determined by the latter method for several values of x do not depend

on the oxygen content. However, the discrepancy between the experimental and theoretical data becomes insignificant in the case when not only the experimental error of the method itself but also the error in the determination of the diffusion coefficient D^* from the experimental data obtained by this method for a finite rate of oxygen exchange at the oxide–gas interface are taken into account.

Figure 5 shows the calculated dependences of the Haven ratio $H = D^*/D_0$ on the oxygen content at different temperatures. For low oxygen contents x, when the contribution of the correlations between mobile particles can be ignored, the diffusion coefficients D^* and D_0, as expected, coincide with each other. As the oxygen content x increases, the contribution of the correlations increases and the Haven ratio H decreases. An increase in the temperature leads to an increase in the mobility of the environment of a diffusing ion and an increase in the Haven ratio H.

The calculated dependences of the effective activation energies U_{eff} for diffusion and self-diffusion on the oxygen content in $YBa_2Cu_3O_{6+x}$ are shown in Figs. 6 and 7. The activation energies U_{eff} were determined from the diffusion coefficients $D^*(x)$ and $D_0(x)$ normalized to $D^*(0)$ and $D_0(0)$ (numerically calculated for diffusion of one particle), respectively. Therefore, the effective activation energy U_{eff} is reckoned from the activation energy in the absence of correlations, i.e., from the energy barrier for one particle in the lattice.

As can be seen from the theoretical dependences, an increase in the oxygen content x leads to an increase in the effective activation energy U_{eff}, which changes predominantly in the range of existence of the orthorhombic phase. The total change over the entire range of oxygen concentrations does not exceed ~0.5 eV. The dependences of the activation energy U_{eff} at the phase transition points do not exhibit features (which can occur and are revealed in terms of the analytical theory [5]). This can easily be explained by both the aforementioned smearing of the transition in the framework of the Monte Carlo method and the fact that the activation energy U_{eff} is determined from the derivative of the smoothed dependences of the diffusion coefficients.

The calculated gain in the effective activation energy U_{eff} is in agreement with the experimental data obtained by the internal friction method [4, 17, 18]. Indeed, according to Bonetti *et al.* [17], the difference between the activation energies U_{act} in the orthorhombic and tetragonal phases is approximately equal to 0.24 eV. Moreover, Schaller *et al.* [18] determined that the activation energy U_{act} changes by ~0.2 eV when the oxygen content x decreases from approximately unity to $x \sim 0.5–0.6$.

It seems likely that sufficiently reliable data were obtained by Xie *et al.* [4]. In [4], the experiments were carried using frozen samples (annealed at different temperatures) with a constant stoichiometry. According to

[4], the stoichiometry-independent portion of the activation energy for relaxation is equal to 1.03 eV, which virtually coincides with the universally accepted transfer activation energy [1, 2]. The experimental activation energies U_{act} determined in [4] are presented in Fig. 7. It can be seen that these energies agree well with the results of our calculations.

Finally, we dwell on the problem regarding the factors responsible for the physical-time interval equal to one time step of a stochastic procedure in different Monte Carlo schemes. This problem is of fundamental importance, because the time intervals involved in calculations of kinetic coefficients are measured in terms of Monte Carlo time steps. The physical-time interval can be related to the mean frequency of occurrence of a random event, i.e., a jump of a particle over a barrier at a given temperature. Within the Metropolis algorithm, the barrier heights determining the jump probability are specified in an artificial way (see the Appendix). In general, this should not lead to an adequate description of the dynamics in the presence of interaction; the same is also true for the model proposed in [7]. In this case, the Monte Carlo time step has no physical meaning. For example, all transitions proceeding with a decrease in the energy are characterized by the same probability and, correspondingly, by the same barrier height. It should be noted that the calculated kinetic coefficients depend on the interaction parameters and, hence, on the height of local interstitial barriers (Figs. 3, 4). In our algorithm, the jump probabilities are directly determined by the interaction parameters. Therefore, the Monte Carlo time step has a specific physical meaning. According to the proposed model, for a jumping ion at a specified temperature and specified interaction parameters there is a finite set of possible energy barriers. Let us now choose the time scale so that the mean frequency of occurrence of an event, namely, the jump of an ion over the lowest barrier, per unit time (or the probability of this event in a chosen unit time) is equal to unity; that is,

$$p_{ij}^{max} = \omega \exp(-E_{min}/kT)$$
$$= \nu \tau_{MC} \exp(-E_{min}/kT) = 1. \tag{3}$$

Here, ν is the preexponential factor (having the frequency dimension) in the activation jump probability and ω is the same preexponential factor expressed in terms of the Monte Carlo time steps τ_{MC}. In order to determine the relative probabilities of events required for generating the discrete step Monte Carlo run (see the Appendix), the probabilities of jumps over other barriers must be normalized to probability (3). Note that the relative frequencies of occurrence of events remain unchanged and the Monte Carlo time step is equal to the mean (and most probable) expectation time for the particle jump over the barrier E_{min} at the temperature T: $\tau_{MC} = 1/[\nu \exp(E_{min}/kT)]$.
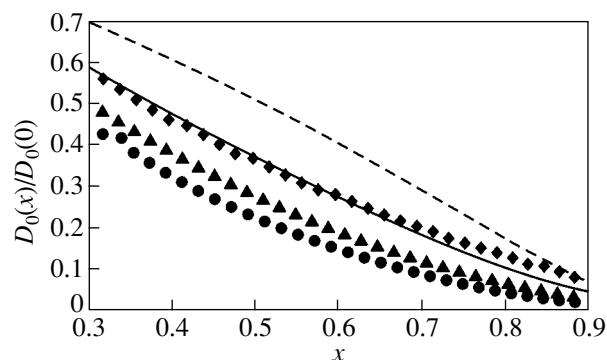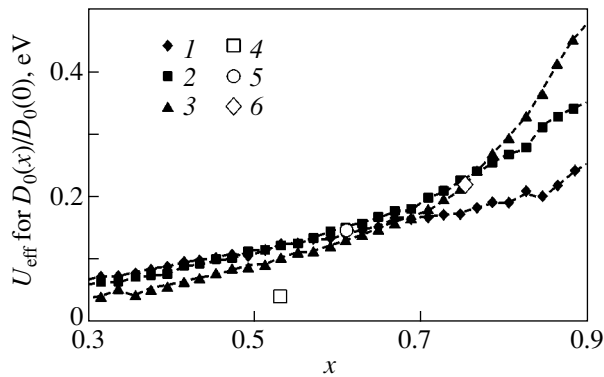
Fig. 4. Dependences of the diffusion coefficient $D_0(x)/D_0(x \longrightarrow 0)$ on the oxygen content at temperatures $T = 500°C$ (circles), $600°C$ (triangles), and $800°C$ (rhombuses). Symbols correspond to the calculated dependences $D_0(x)/D_0(x \longrightarrow 0)$ in the case when the interaction at the saddle point is characterized by the constants γ taken from [5]. The solid line shows the dependence $D_0(x)/D_0(x \longrightarrow 0)$ calculated for the halved constants γ at $T = 600°C$. The dashed line represents the same dependence calculated in the absence of the interaction at the saddle point ($T = 600°C$).
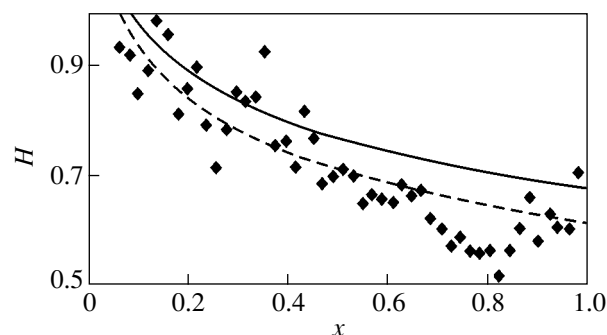
Fig. 5. Dependences of the Haven ratio on the oxygen content at temperatures $T = 500°C$ (dashed line and rhombuses) and $800°C$ (solid line).
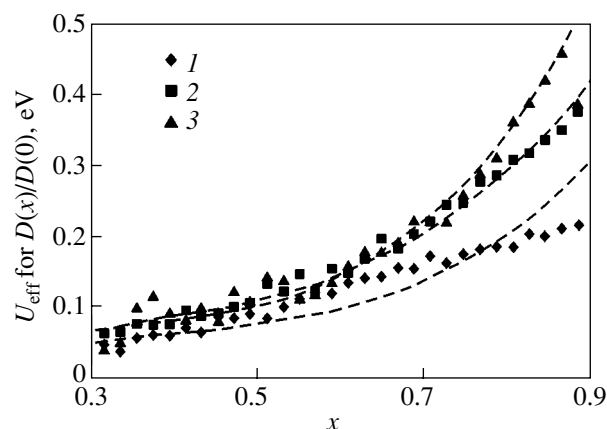
Fig. 6. Dependences of the effective activation energy for diffusion [determined from the isotope diffusion coefficients D^* normalized to $D^*(x \longrightarrow 0)$] on the oxygen content at temperatures $T = (1)$ 500, (2) 650, and (3) 800°C. Dashed lines indicate the smoothed dependences $U_{eff}(x)$ fitted to the calculated points.

Fig. 7. Dependences of the effective activation energy for self-diffusion [determined from the self-diffusion coefficients D_0 normalized to $D_0(x \longrightarrow 0)$] on the oxygen content at temperatures $T = $ (*1*) 500, (*2*) 650, and (*3*) 800°C. Open symbols are the experimental data obtained by the internal friction method in [4] at temperatures $T = $ (*4*) 650, (*5*) 600, and (*6*) 500°C.

The transition probabilities chosen above for the simulation of a random process in the framework of the Monte Carlo method correspond to the transition probabilities in the exact master equation, which describes the change in the distribution of particles over sites due to single jumps [5]. This choice seems to be reasonable. Furthermore, we believe that the displacement distribution function will be similar to the solution of the exact master equation, all other factors being the same.

5. CONCLUSIONS

Thus, the results obtained have demonstrated that consistent inclusion of the correlations between oxygen ions in the basal plane makes it possible to describe the thermodynamic properties in the framework of the Monte Carlo method and to achieve reasonable agreement with experimental data on the oxygen diffusion in YBaCuO. According to [5], correct description of the oxygen diffusion in this compound requires inclusion of both the interaction of mobile ions at the lattice sites and the interaction between the jumping ion at the saddle point and the environment. The proper choice of the computational scheme is essential for the Monte Carlo simulation of the correlated transport. In our opinion, the results of our theoretical calculations are in better agreement with the experimental and analytical data (as compared to the results obtained in [7]) owing to the choice of the more appropriate algorithm, which accounts for the finite barrier to jumps in the lattice without an interaction between mobile particles.

ACKNOWLEDGMENTS

The Monte Carlo algorithm used in this work is as follows.

(1) A particle is randomly chosen from the set of particles.

(2) One of the four directions of the possible ion jump into the nearest site is chosen in a random manner.

(3) The probability of a randomly chosen particle jumping from the *i*th site into the *j*th site chosen at the preceding step is represented as

$$p_{ij} = (1 - n_j)p_{ij}^0,$$

where n_j is the occupancy of the *j*th site and p_{ij}^0 depends on the procedure used for describing the dynamics in the Monte Carlo simulation.

In the Metropolis algorithm, we assume that

$$p_{ij}^0 = \omega \begin{cases} \exp((U_i - U_j)/kT), & \text{if} \quad U_i < U_j \\ 1, & \text{if} \quad U_i > U_j, \end{cases}$$

where ω is an arbitrary coefficient that does not affect the balance. As a rule, it is assumed that $\omega = 1$.

In the method allowing for the actual energy barrier at the saddle point, the probability p_{ij}^0 $(p_{ij}^0 \leq 1)$ is given by an appropriate relationship for describing the jump dynamics; that is,

$$p_{ij}^0 = \omega \exp(-(U_{ij}^s - U_i)/kT).$$

Here, ω has a specific physical meaning; more precisely, it is the frequency normalizing the Monte Carlo time step (see Section 4).

(4) Steps (1)–(3) are repeated N_p times, where N_p is the number of particles in the lattice. At this point, the Monte Carlo run is considered complete and the time is shifted by one Monte Carlo time step.

REFERENCES

1. J. L. Routbort and S. R. Rothman, J. Appl. Phys. **76**, 5615 (1994).
2. J. Claus, G. Borchardt, S. Weber, and S. Scherrer, Z. Phys. Chem. (Munich) **206**, 49 (1998).
3. É. Kh. Kurumchin, V. I. Tsidil'kovski, A. N. Ezin, *et al.*, Sverkhprovodimost: Fiz., Khim., Tekh. **7**, 1065 (1994).
4. X. M. Xie, T. G. Chen, and Z. L. Wu, Phys. Rev. B **40**, 4549 (1989).
5. V. I. Tsidilkovski, Ionics **4**, 316 (1998).
6. J. S. Choi, M. Sarikaya, I. A. Aksay, and R. Kikuchi, Phys. Rev. B **42**, 4244 (1990).
7. E. Salomons and D. de Fontaine, Phys. Rev. B **41**, 11 159 (1990).
8. N. M. Plakida, *High-Temperature Superconductivity* (Mezhdunarodnaya Programma Obrazovaniya, Moscow, 1996; Springer, Berlin, 1995).

9. V. I. Tsidilkovski, I. A. Leonidov, A. A. Lakhtin, and V. A. Mezrin, Phys. Status Solidi B **163**, 231 (1991).

10. P. Meuffels, R. Naeven, and H. Wenzl, Physica C (Amsterdam) **161**, 539 (1989).

11. J. D. Jorgensen, M. A. Beno, D. G. Hinks, *et al.*, Phys. Rev. B **36**, 3608 (1987).

12. J. D. Jorgensen, H. Shared, D. G. Hinks, *et al.*, Physica C (Amsterdam) **153/155**, 578 (1988).

13. P. Meuffels, B. Rupp, and E. Porschke, Physica C (Amsterdam) **156**, 441 (1988).

14. E. D. Specht, C. J. Sparks, A. G. Dhere, *et al.*, Phys. Rev. B **37**, 7426 (1988).

15. P. P. Freitas and T. S. Plaskett, Phys. Rev. B **36**, 5723 (1987).

16. Y. Kubo, Y. Nakabayashi, J. Tabuchi, *et al.*, Jpn. J. Appl. Phys. **26**, L1888 (1987).

17. E. Bonetti, E. G. Campari, and S. Mantovani, Physica C (Amsterdam) **196**, 7 (1992).

18. Y. Mi, R. Schaller, S. Sathish, and W. Benoit, Phys. Rev. B **44**, 12575 (1991).

Translated by O. Borovik-Romanova

METALS
AND SUPERCONDUCTORS

Magnetic Susceptibility and Superconductivity of $(Pb_{0.2}Sn_{0.8})_{1-x}In_xTe$ Alloys as a Function of In Content

M. Z. Tahar***, S. A. Nemov**, D. I. Popov***, and D. V. Shamshur*

*Ioffe Physicotechnical Institute, Russian Academy of Sciences, Politekhnicheskaya ul. 26, St. Petersburg, 194021 Russia
**St. Petersburg Polytechnical University, Politekhnicheskaya ul. 25, St. Petersburg, 195251 Russia
e-mail: nemov_s@mail.ru
***Physics Department, SUNY Brockport, Brockport, USA
Received October 15, 2002

Abstract—Experimental data on the superconductivity of In-doped $Pb_zSn_{1-z}Te$ alloys ($z = 0.2$) are discussed. The superconducting transition was detected from simultaneous measurements of the resistivity and magnetic susceptibility of a series of samples with different indium contents (2–12 mol % InTe). The superconducting transition detected by the magnetic susceptibility was observed at a temperature which was, on the average, 0.1 K below that determined from the resistivity. The increase in the superconducting transition temperature T_c with increasing indium content is of a threshold character, with T_c being proportional to the inverse electronic density of states at the Fermi level. The observed features in the experimental data are accounted for in terms of indium impurity resonance states in the material. © 2003 MAIK "Nauka/Interperiodica".

1. INTRODUCTION

The In-doped PbSnTe solid solutions studied in this work, as well as the nontraditional superconducting materials currently enjoying widespread interest, such as HTSC compounds [1], heavy-fermion superconductors [2], in which the effective carrier mass may be on the order of 100 free-electron masses, and MgB_2 intermetallic compounds [3], belong to a new class of superconducting materials. These materials are IV–VI semiconductors doped by Group III elements (In, Tl). They exhibit unusual physical properties due to the resonance states these impurities have in the valence band [4, 5].

The interest in In-doped IV–VI semiconductors is spurred by the unique properties of the In impurity, which include a high solubility (up to 20 at. %) and a small radius of electronic states. The indium impurity states are localized within one to two unit cells (6 Å [6]) and lie, in most solid solutions, in the allowed energy bands of electronic states because of the small band gap. In particular, the In energy level position in $Pb_zSn_{1-z}Te$: In solid solutions varies with matrix composition. In $Pb_zSn_{1-z}Te$: In alloys ($z < 0.72$), the In resonance level lies in the valence band. The existence of resonance states becomes most clearly manifest in the Fermi level pinning (stabilization) and resonance scattering of holes with energies falling in the impurity band. Fermi level pinning brings about a high spatial electric homogeneity of IV–VI compounds, a feature of particular practical importance for this class of materials, which are characterized by considerable deviations

from stoichiometry (the deviations may be as high as 0.1 at. % or greater).

Interest in these compounds additionally stems from their superconducting properties, with the critical temperature T_c (up to the helium temperatures [4, 5, 7]) being fairly high for semiconductors.

This communication reports on simultaneous measurements of the magnetic susceptibility and electrical conductivity of $(Pb_{0.2}Sn_{0.8})_{1-x}In_xTe$ with the indium content varied from 2 to 20 mol % InTe. The earlier studied [5, 8] $Pb_zSn_{1-z}Te$ system with 16 at. % indium and variable z showed a superconducting transition to occur in the resistivity, but no magnetic susceptibility measurements were carried out in support of this observation.

2. EXPERIMENT

All measurements were conducted on polycrystalline samples with an average grain size of the order of 200 μm. The samples were prepared by powder metallurgy and annealed at 650°C for 100 h. The samples were no more than 2 cm in length, with a cross section no greater than 5 mm² and a weight of ~1 g.

The ac magnetic susceptibility and resistivity measurements were performed simultaneously. The magnetic susceptibility was measured using inductance coils (of a geometry similar to that described by Maxwell [9]) along with a lock-in detector and a digital multifunctional generator. Digital control made it possible to maintain the excitation frequency at a level

from a few hertz to a few kilohertz. The magnetic susceptibility was measured at 208 Hz to avoid interference from the main carrier harmonics. The inductance coils were wound around a thin-walled glass Dewar flask immersed in liquid ^{4}He. The sample temperature was varied from 1.3 to 300 K and measured with a calibrated silicon diode or was determined from the ^{4}He vapor pressure.

To measure the electrical resistivity, four contacts were pasted on the samples with silver-loaded epoxy resin, which showed good characteristics under repeated cooling of the samples to helium temperatures. The ac and dc resistivity measurements were conducted at 100 μA and 10 mA, respectively. The ac measurements were performed at a frequency of 500 Hz. Thermoelectric effects at the contacts and the possible temperature gradient along the sample were disregarded, although measures were taken to reduce their influence to a minimum.

The sample housed in the thin-walled Dewar flask was cooled to a temperature $T \sim 80$ K, during which time the resistivity measurements were performed. The experimental data were recorded with a LabView 16-channel information retrieval package. Next, liquid helium was pumped into the cryostat to cool the solenoid coils. After the solenoid coils had been immersed fully in liquid helium, they were calibrated, without interrupting parallel resistivity measurements. This was followed by radiative cooling of the inner Dewar flask containing the sample to $T \sim 5$ K. Next, liquid helium was fed through a capillary into the flask containing the sample, from which it was subsequently pumped out to lower the temperature still further. To make an increase in temperature possible, a heater was double-wound on the boron nitride sample holder.

The superconducting transition was detected from a jump in resistivity under variation of the temperature and of the external magnetic field, as well as from magnetic measurements. The electronic density of states at the Fermi level $g(\varepsilon_F)$ was estimated from data on the second critical field H_{c2} measured near the superconducting transition temperature T_c. We have, for the two spin orientations [10],

$$g(\varepsilon_F) = 5.68 \times 10^{14} \frac{1}{\rho} \frac{\partial H_{c2}}{\partial T}\bigg|_{T \to T_c}, \qquad (1)$$

where ρ is the electrical resistivity in the normal state near the phase transition point to the superconducting state.

3. EXPERIMENTAL RESULTS

Figure 1 displays the temperature dependence of electrical resistivity normalized to its 300-K value (see table), which was measured for $(Pb_{0.2}Sn_{0.8})_{1-x}In_xTe$ samples with different indium contents. As the temperature is lowered, the resistivity $\rho(T)$ of all samples is seen to undergo a decrease followed by a rise. The tem-
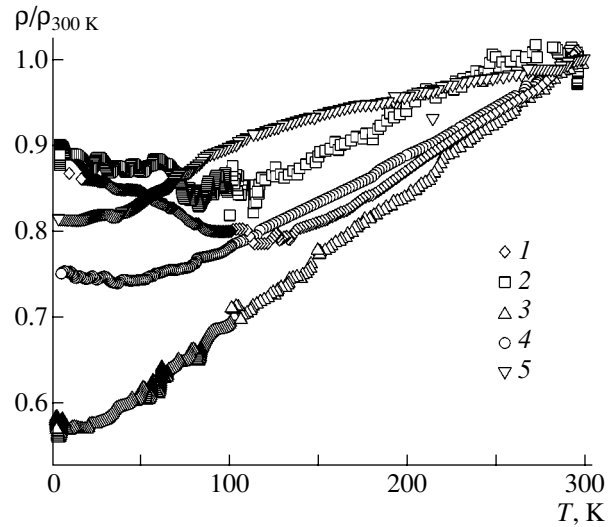
Fig. 1. Temperature dependences of the electrical resistivity of $(Pb_{0.2}Sn_{0.8})_{1-x}In_xTe$ ($x = 0.02–0.12$) normalized against its value at 300 K. The values of the electrical resistivity at 300 K are listed in the table. The values of x are (*1*) 2, (*2*) 3, (*3*) 5, (*4*) 8, and (*5*) 12.
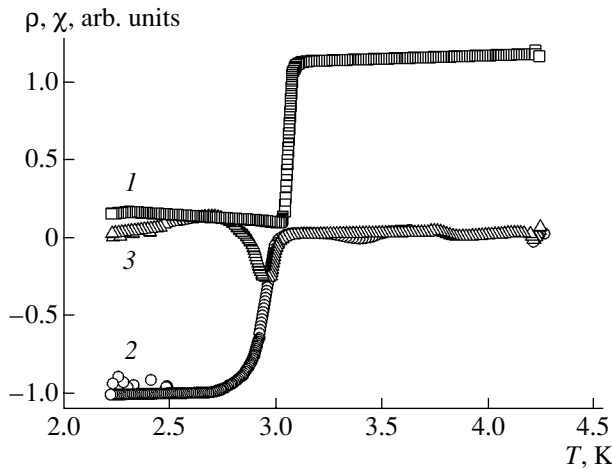
perature at which the resistivity reaches a minimum depends on the In content in the sample and reveals a general trend toward a decrease with increasing indium concentration N_{In}. Note the relatively high values of $\rho(T)$ of the samples, of the order of a few mΩ cm, which are in accord with the concept of resonance scattering of holes into the In impurity band [11].

Figure 2 shows the temperature behavior of the electrical resistivity and magnetic susceptibility of a sample with 8 at. % In in the neighborhood of the superconducting transition. The electrical resistivity is normalized against its value at 4.2 K and translated by an arbitrary constant to make it more revealing. The magnetic susceptibility was also normalized against the magnitude of its jump at the superconducting transition.
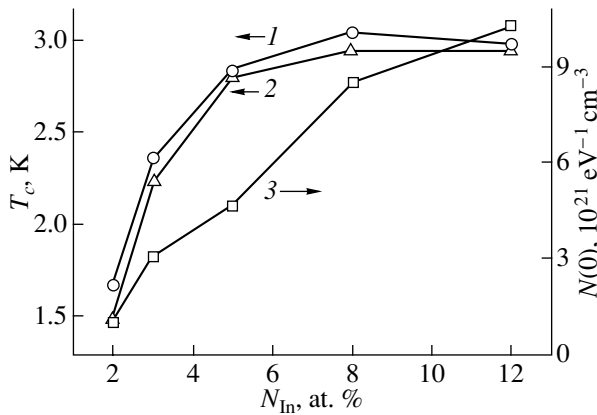
The superconducting transition is seen clearly in the resistance, with the resistivity dropping by approximately four orders of magnitude. The transition width

Superconducting transition temperature derived from data on the electrical resistivity ($T_c[\rho(T)]$) and magnetic susceptibility ($T_c[\chi(T)]$), electronic density of states at the Fermi level $g(\varepsilon_F)$, and electrical resistivity of samples with different indium contents (ρ_{300}, $T = 300$ K)

In, at. %	T_c, K $[\chi(T)]$	T_c, K $[\rho(T)]$	$g(\varepsilon_F)$, 10^{21} eV^{-1} cm^{-3}	ρ_{300}, mΩ cm
2	1.50	1.67	0.973	1.79
3	2.24	2.37	3.05	2.17
5	2.80	2.85	4.68	1.35
8	2.95	3.05	8.51	1.11
12	2.95	2.98	10.3	0.714

ρ, χ, arb. units

Fig. 2. (*1*) Electrical resistivity χ and (*2*) real χ' and (*3*) imaginary χ" magnetic susceptibilities plotted vs. temperature in the neighborhood of the superconducting transition in the $(Pb_{0.2}Sn_{0.8})_{0.92}In_{0.08}Te$ sample. The electrical resistivity is normalized against its value at $T = 4.2$ K and translated by an arbitrary constant to make the plot more revealing. The magnetic susceptibility is normalized to the magnitude of its jump at the superconducting transition.

Fig. 3. Dependence of the superconducting transition temperature in $(Pb_{0.2}Sn_{0.8})_{1-x}In_xTe$ derived from the temperature dependences of the (*1*) resistivity, (*2*) magnetic susceptibility, and (*3*) electronic density of states at the Fermi level on indium content *x*.

ΔT (measured between $0.9\rho_N$ and $0.1\rho_N$, where ρ_N is the normal-state resistivity near the superconducting transition) is less than 0.05 K.

The superconducting transition was detected simultaneously from the temperature dependence of the magnetic susceptibility $\chi(T)$; as is evident from Fig. 2, the $\rho(T)$ and $\chi(T)$ dependences obviously correlate in the vicinity of the superconducting transition. The transition seen in magnetic susceptibility is slightly more diffuse in temperature in all samples than the transition detected from $\rho(T)$, the width of the resistive transition varying from one sample to another. The superconduct-

ing transition temperature detected from the resistivity (at $0.5\rho_N$) is higher (by 0.1–0.2 K) than T_c derived from the magnetic susceptibility. Note that this difference in the values of T_c is of about the same order of magnitude as the width of the superconducting transition determined from $\rho(T)$ (see table).

Figure 3 displays the data on T_c derived from $\rho(T)$ and $\chi(T)$ and plotted vs. indium content, as well as the electronic density of states $g(\varepsilon_F)$. We readily see that the transition temperature first grows strongly with the indium content increasing to 5 at. % and then its growth becomes smoother. Thus, the observed $T_c(N_{In})$ relation is clearly of a threshold character. We also note that the value of T_c correlates with the density of states at the Fermi level in the normal state, $g(\varepsilon_F)$.

4. DISCUSSION OF THE RESULTS

First, we note that the superconducting transition (Fig. 2) was detected not only from the drop in resistivity (with conduction being possible over grain boundaries and polycrystal surfaces) but also from the sharp jump in the magnetic susceptibility, i.e., by the Meissner effect [12]). In addition to available data on the specific heat in similar systems [13]), these results indicate a volume character of the superconductivity in the class of materials under study. Note also that the superconducting transition temperature in $(Pb_{0.2}Sn_{0.8})_{1-x}In_xTe$ is higher by at least an order of magnitude than that in $Pb_zSn_{1-z}Te$ ($z = 0.2$) samples [14] because of the existence of In resonance states.

The position of the Fermi level relative to the energy bands and the impurity band plays an important part in these systems [4, 5]. Indium atoms produce a resonance impurity band in the $(Pb_zSn_{1-z})_{1-x}In_xTe$ solid solutions; this band is approximately 0.1–0.2 eV below the top of the valence *L* band [11] (the main conduction and valence band extrema of cubic IV–VI compounds are located at the *L* points of the Brillouin zone). The effect of the band structure and filling factor *k* (i.e., the ratio of the number of resonance states filled by electrons to their total number, assuming there to be two states per impurity atom [14]) on the superconducting parameters has been discussed on several occasions in the literature [4, 5]. We may add that superconductivity at temperatures $T > 0.4$ K was found to occur only in samples with the Fermi level lying within the resonance state band.

Figure 3 plots the dependence of the superconducting transition temperature T_c on indium content in the system under study. In contrast to the weak and practically linear growth of T_c (up to 0.3 K) with increasing hole concentration *p* in $Pb_zSn_{1-z}Te$ without indium (as described quantitatively by Cohen [10] in terms of the Bardeen–Cooper–Schrieffer theory), the In-doped material exhibits relatively high T_c temperatures at a lower hole concentration ($p \sim 10^{20}$ cm^{-3}) and, in addition, a distinct threshold character of the $T_c(N_{In})$ depen-
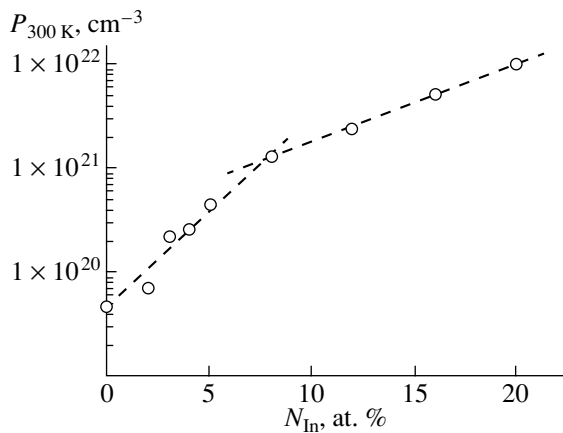
Fig. 4. Hole concentration at the Fermi level ($T = 300$ K) plotted vs. indium content in $(Pb_{0.2}Sn_{0.8})_{1-x}In_xTe$. The data for $x = 0.16$ and 0.20 were taken from [5].
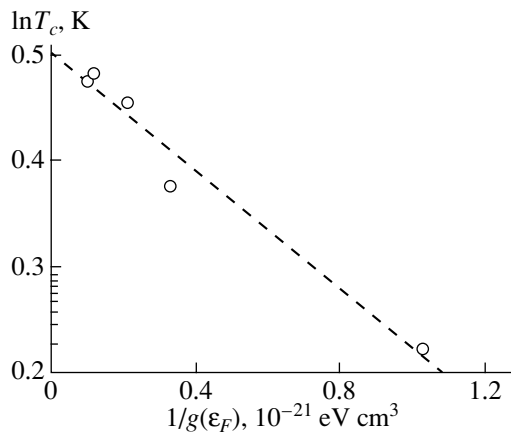
Fig. 5. Correlation between the logarithm of the superconducting transition temperature in the $(Pb_{0.2}Sn_{0.8})_{1-x}In_xTe$ samples and the reverse electronic density of states at the Fermi level $1/g(\varepsilon_F)$. Dashed line is the least squares fit to the experimental data.

dence. This $T_c(N_{In})$ dependence in $(Pb_zSn_{1-z})_{1-x}In_xTe$ finds natural explanation within the concept of In impurity resonance states and is due to the Fermi level entering the In band with an increase in hole concentration.

Indeed, as the indium content in the samples increases, the partly filled impurity states can accommodate more electrons from the higher lying electron states in the valence band (on the electron energy scale). This will bring about an increase in the density of In impurity states. As the indium content in the alloy continues to grow, the Fermi level is pinned and the increase in the hole concentration in the valence band slows down. The slight growth in the hole concentration and in T_c (Fig. 4) is associated, however, with the In band shifting into the valence band with increasing

N_{In} [5]. The impurity band filling factor k remains nearly constant (if one disregards the variation of point defect concentration in the matrix), and the $T_c(N_{In})$ dependence saturates.

Note also that the data on T_c and on the electronic density of states at the Fermi level $g(\varepsilon_F)$ are correlated (the straight line in Fig. 5 is the least squares fit to the experimental data), which should be expected from BCS theory. It is therefore possible that a modified BCS model (to include resonance states) would be applicable to describing the main features of the superconducting transition in the class of semiconductors–superconductors with deep resonance impurity states, to which the indium-doped $Pb_zSn_{1-z}Te$ belongs.

5. CONCLUSIONS

In summary, we have experimentally studied the superconducting transition in indium-doped $Pb_zSn_{1-z}Te$ by using both electrical resistivity and magnetic susceptibility. Both physical quantities undergo a jump at the superconducting transition, but at slightly different temperatures. The transition temperature increases with increasing indium content, and this dependence is of a threshold character. There is a correlation between the superconducting transition temperature and the electronic density of states at the Fermi level. The above-mentioned relations support the resonance character of the superconductivity and indicate that the key role is played by impurity states in physical phenomena observed to occur in the class of materials under study.

ACKNOWLEDGMENTS

REFERENCES

1. J. G. Bednorz and K. A. Muller, Z. Phys. B **64**, 189 (1986).

2. H. R. Ott, H. Rudinger, and J. L. Smith, Phys. Rev. Lett. **50** (20), 1595 (1983).

3. J. Nagamatsu, N. Nkagawa, T. Muranaka, *et al.*, Nature **410**, 63 (2001).

4. S. A. Nemov and Yu. I. Ravich, Usp. Fiz. Nauk **168** (8), 817 (1998) [Phys. Usp. **41**, 735 (1998)].

5. R. V. Parfen'ev, D. V. Shamshur, and S. A. Nemov, Fiz. Tverd. Tela (St. Petersburg) **43** (10), 1772 (2001) [Phys. Solid State **43**, 1845 (2001)].

6. Yu. I. Ravich, S. A. Nemov, and V. I. Proshin, Fiz. Tekh. Poluprovodn. (St. Petersburg) **29** (8), 1448 (1995) [Semiconductors **29**, 754 (1995)].

7. G. S. Bushmarina, D. V. Mashovets, R. V. Parfeniev, *et al.*, Physica B (Amsterdam) **169**, 687 (1991).

8. R. V. Parfeniev, D. V. Shamshur, and M. A. Shakhov, J. Alloys Compd. **219**, 313 (1995).

9. E. Maxwell, Rev. Sci. Instrum. **63**, 553 (1965).

10. V. I. Kaĭdanov, S. A. Nemov, R. V. Parfen'ev, and D. V. Shamshur, Pis'ma Zh. Éksp. Teor. Fiz. **35** (12), 517 (1982) [JETP Lett. **35**, 639 (1982)].

11. V. I. Kaĭdanov, S. A. Nemov, and Yu. I. Ravich, Fiz. Tekh. Poluprovodn. (St. Petersburg) **26** (2), 201 (1992) [Sov. Phys. Semicond. **26**, 113 (1992)].

12. W. Maissner and R. Ochsenfeld, Naturwissenschaften **21**, 787 (1933).

13. I. A. Chernik and S. N. Lykov, Fiz. Tverd. Tela (Leningrad) **23** (5), 1400 (1981) [Sov. Phys. Solid State **23**, 817 (1981)].

14. M. H. Cohen, in *Superconductivity*, Ed. by R. D. Parks (Marcel Dekker, New York, 1969).

Translated by G. Skrebtsov

METALS
AND SUPERCONDUCTORS

Spectral Density and Density of States in a Superconductor in an Exactly Solvable Model of a Pseudogap State

É. Z. Kuchinskiĭ

Institute of Electrophysics, Ural Division, Russian Academy of Sciences,
ul. Komsomol'skaya 34, Yekaterinburg, 620016 Russia
e-mail: kuchinsk@iep.uran.ru
Received October 21, 2002

Abstract—A simple, exactly solvable model of a pseudogap state induced by fluctuations of dielectric short-range order is used to study the peculiarities of the electronic spectral density and density of states of a superconductor in the model of the Fermi surface with hot patches. The problem is considered for arbitrary values of the short-range order correlation length ξ_{corr}. It is shown that the absence of self-averaging of the superconducting order parameter over the random field of dielectric fluctuations causes the spectral density and density of states to change significantly. The superconducting character of these quantities persists in a wide temperature range above the temperature T_c of the superconducting transition, which is uniform over the whole sample. © 2003 MAIK "Nauka/Interperiodica".

1. INTRODUCTION

The pseudogap state [1, 2] observed in a wide region of the phase diagram of HTSC cuprates gives rise to a number of anomalous properties of these materials in both the normal and superconducting states. There are two plausible explanations for these anomalies. One of them is based on the assumption that Cooper pairs form above the superconducting transition temperature [3]. The other explanation (more preferable, in our opinion) assumes that the pseudogap state is due to strong scattering of the charge carriers on well-developed fluctuations of short-range order of dielectric type (antiferromagnetic ordering or charge-density waves) [2]. This scattering leads to electronic-spectrum rearrangement of a "non-Fermi-liquid" type in certain regions of the momentum space in the vicinity of the Fermi surface, more specifically, near the so-called hot points or hot (flat) patches on this surface [2].

Most relevant theoretical papers have been focused on the influence of the pseudogap on the properties of the system in the normal state, whereas the superconductivity in the pseudogap state has been considered only in a few works [4–7]. In particular, superconductivity was studied in [5] in a simple, exactly solvable model of the pseudogap state based on the model of the Fermi surface of a two-dimensional system with hot patches [4]. In this case, the exact solution for the pseudogap, which had been obtained earlier [8] for the one-dimensional case, was used in the limit of very large values of the correlation length of fluctuations of dielectric short-range order. The use of the exactly solvable model of the pseudogap proposed by Bartosch and Kopietz [9] made it possible to generalize the results obtained in [5] to arbitrary values of the correlation

length [7]. It was shown in those papers that the superconducting gap averaged over short-range order fluctuations is generally nonzero even in a range of temperatures exceeding the mean-field superconducting transition temperature T_c, which corresponds to the appearance of the superconducting state that is uniform over the sample [5]. These results made it possible to conclude that superconducting droplets appear in the system at $T > T_c$ [5, 7]. In [5], this effect was attributed to the absence of self-averaging of the superconducting order parameter (gap width) in the case where the correlation length ξ_{corr} of fluctuations of short-range order is larger than the coherence length ξ_0 of superconductivity (the size of Cooper pairs). However, it was shown in [7] that total self-averaging of the superconducting gap is also absent in the case of $\xi_{corr} < \xi_0$ [7], which is inconsistent with the predictions of the standard approach [2, 6].

The absence of self-averaging, which brings about the appearance of strong fluctuations of the gap, can significantly change the physical properties of the superconducting material. In particular, the superconductivity can also manifest itself at temperatures above T_c, for example, in the spectral density and density of states in the limit of extremely large values of the correlation length of the dielectric short-range order [5]. Anomalies in the behavior of the spectral density and density of states in the superconducting phase have been observed experimentally [1, 2].

The aim of the present paper is to study the behavior of the spectral density and density of states of a superconductor with due regard for the absence of self-averaging of the superconducting gap in the framework of

the aforementioned simple model of the pseudogap state developed in [7] for describing superconductivity.

2. SIMPLE MODEL OF THE PSEUDOGAP STATE

Let us consider the one-dimensional motion of an electron in a periodic field:

$$V(x) = 2D\cos(Qx + \phi), \tag{1}$$

where $Q = 2p_F - k$, p_F is the Fermi momentum, and $k \ll p_F$ is a deviation from the selected scattering vector $2p_F$, implying incommensurability of the corresponding fluctuations. In the vicinity of the Fermi level, the electronic spectrum is chosen in the linearized form

$$\xi_1 \equiv \xi_p = v_F(|p| - p_F), \quad \xi_{p-2p_F} = -\xi_p \text{ (nesting)}, \\ \xi_2 \equiv \xi_{p-Q} = -\xi_p - v_F k \equiv -\xi_p - \eta, \tag{2}$$

where $\eta = v_F k$ (v_F is the Fermi velocity) is a variable, and this variable is widely used in what follows.

In the two-wave approximation of the ordinary band theory, the one-electron Green's functions (both diagonal ones corresponding to the transitions $p \longrightarrow p$ and $p - Q \longrightarrow p - Q$ and nondiagonal ones corresponding to the umklapp processes $p \longrightarrow p - Q$ and $p - Q \longrightarrow p$) actually form a matrix and have the following form in the Matsubara representation:

$$g_{11} = \frac{i\varepsilon_n - \xi_2}{(i\varepsilon_n - \xi_1)(i\varepsilon_n - \xi_2) - D^2},$$

$$g_{12} = \frac{De^{-i\phi}}{(i\varepsilon_n - \xi_1)(i\varepsilon_n - \xi_2) - D^2},$$

$$g_{21} = \frac{De^{i\phi}}{(i\varepsilon_n - \xi_1)(i\varepsilon_n - \xi_2) - D^2}, \tag{3}$$

$$g_{22} = \frac{i\varepsilon_n - \xi_1}{(i\varepsilon_n - \xi_1)(i\varepsilon_n - \xi_2) - D^2}.$$

In what follows, we consider a rather specific model of disorder [9] in which the deviation vector k is supposed to be a random variable, with the distribution function determined by the Lorentzian[1]

$$\mathscr{P}_k(k) = \frac{1}{\pi}\frac{\kappa}{k^2 + \kappa^2}, \tag{4}$$

the corresponding distribution for the variable η is

$$\mathscr{P}_\eta(\eta) = \frac{1}{\pi}\frac{v_F \kappa}{\eta^2 + (v_F \kappa)^2}, \tag{5}$$

---

[1] Actually, we consider a model of phase fluctuations of the field described by Eq. (1).

where $\kappa \equiv \xi_{corr}^{-1}$. The phase ϕ in Eq. (1) is also supposed to be randomly and uniformly distributed over the range from 0 to 2π:

$$\mathscr{P}_\phi(\phi) = \begin{cases} \dfrac{1}{2\pi}, & 0 \le \phi \le 2\pi \\ 0 & \text{for other values.} \end{cases} \tag{6}$$

Both the phase and the amplitude D of the field described by Eq. (1) can fluctuate. The amplitude is assumed to be distributed following a Rayleigh distribution [8–10]:

$$\mathscr{P}_D(D) = \frac{2D}{W^2}\exp\left(-\frac{D^2}{W^2}\right), \tag{7}$$

where W determines the width of the energy pseudogap.

If the field described by Eq. (1) is produced by fluctuations of a dielectric order parameter (for example, a parameter characterizing a charge-density wave or antiferromagnetic ordering), then the distribution given by Eq. (7) will describe Gaussian fluctuations of this parameter at sufficiently high temperatures [8, 11, 12]. When the temperature becomes smaller than some characteristic temperature, amplitude fluctuations are "frozen out" even before the onset of long-range order (see [3, 13]) and it can be supposed that $D = W$, whereas phase fluctuations exist down to extremely low temperatures. For this reason, we consider two regimes of dielectric fluctuations in what follows: the high-temperature regime, in which both the amplitude and phase fluctuate, and the low-temperature regime, in which amplitude fluctuations are frozen out.

In the low-temperature regime of fluctuations, the Fourier transform of the correlation function of fields (1) at different points $\langle V(x)V(x')\rangle$ is a Lorenzian determining the effective interaction of an electron with short-range order fluctuations [2]:

$$V_{eff}(q) = 2D^2\left\{\frac{\kappa}{(q - 2p_F)^2 + \kappa^2} + \frac{\kappa}{(q + 2p_F)^2 + \kappa^2}\right\}. \tag{8}$$

Inclusion of amplitude fluctuations in the high-temperature regime results in the substitution of W for D in Eq. (8). The random field with such a correlation function has been considered in a number of papers [8, 10–12, 14] focused on the dielectric pseudogap. However, this field was supposed to be Gaussian in those papers, whereas the random field $V(x)$ considered in this paper is, in general, non-Gaussian [9].

In this model [7, 9], the Green's function is determined by averaging g_{11} over distributions (4) and (6) in the low-temperature regime of fluctuations,

$$G(i\varepsilon_n, p) = \frac{i\varepsilon_n + \xi_p + i v_F \kappa}{(i\varepsilon_n - \xi_p)(i\varepsilon_n + \xi_P + i v_F \kappa) - D^2}, \quad (9)$$

and by additional averaging over the amplitude with distribution (7) in the high-temperature regime,

$$G(i\varepsilon_n, p) = \int_0^\infty dD \mathscr{P}_D(D)$$

$$\times \frac{i\varepsilon_n + \xi_p + i v_F \kappa}{(i\varepsilon_n - \xi_p)(i\varepsilon_n + \xi_P + i v_F \kappa) - D^2}. \quad (10)$$

In the limit of large values of the correlation length of fluctuations of the field in Eq. (1), i.e., for $\xi_{corr} \longrightarrow \infty$ ($\kappa \longrightarrow 0$), the solution given by Eq. (10) coincides with that found in [8] for a Gaussian random field. It has been shown [9, 12] that the density of states corresponding to the Green's function (10) contains a characteristic smeared pseudogap in the vicinity of the Fermi level and that the values of the density of states are close to those found in [10] (see [9, 12, 15]; for the incommensurate case, this is the case for virtually any energy), as well as to the results of exact numerical calculations for a Gaussian random field [16–18].

A generalization to the two-dimensional electron system typical of HTSC cuprates can be made in the model of the Fermi surface with hot patches proposed in [4–6]. In this case, it is assumed that there are two independent systems of fluctuations of type (1) in the system which are oriented along orthogonal axes x and y and strongly interact only with the electrons corresponding to the flat (hot) patches of the two-dimensional Fermi surface that are orthogonal to these axes. In addition, the two-dimensional potential in which the electrons move is supposed to be factorized with respect to these directions: $V(x, y) = V(x)V(y)$ [4–6]. In this model, different characteristics determined by integrals over the Fermi surface consist of additive contributions from the hot and cold parts. The pseudogap-type rearrangement of the electronic spectrum occurs only on the hot patches, whose relative fraction on the Fermi surface is α, whereas on the cold sections, whose relative fraction is $1 - \alpha$, the Fermi-liquid behavior persists [2].

This picture is in qualitative agreement with the results of numerous ARPES experiments on underdoped HTSC cuprates [1, 2], which indicate that pseudogap anomalies occur in the vicinity of the $(0, \pi)$ point of the Brillouin zone and vanish as we go to its diagonal. The presence of the flat parts on the Fermi surface of HTSC cuprates has also been reliably established in ARPES experiments by several independent groups of researchers [2].

3. SUPERCONDUCTIVITY IN THE PSEUDOGAP STATE

In the model of the pseudogap state, superconductivity was studied in [7]. Hereafter, we follow the approach used in that work. To consider superconductivity in the system with a pseudogap due to fluctuations of dielectric short-range order, we use the simplest BCS approximation. As usual, the BCS interaction is assumed to be characterized by the constant V in an energy interval $2\omega_c$ wide in the vicinity of the Fermi level (ω_c is the characteristic frequency of photons responsible for the attraction between the electrons). Following the approach used in [7], we consider the s-electron pairing only. There are no serious difficulties in the analysis of the d-electron pairing typical of HTSC cuprates; however, the angle dependence (anisotropy) of the superconducting gap [4, 5] results in additional integration, which significantly increases the time of numerical computation, leaving the basic qualitative results unchanged.

On the cold sections of the Fermi surface, superconductivity is described by the standard equations of the BCS theory. On the basis of the Green's functions for the normal state given by Eq. (3), a set of Gor'kov equations was found in [7] for the hot patches and the normal and anomalous Green's functions were derived for the specific random field of Eq. (1) (i.e., for certain values of η and D):

$$G(\varepsilon_n, p)$$
$$= -\frac{1}{\mathrm{Det}}\{(i\varepsilon_n + \xi_p)[\varepsilon_n^2 + (\xi_p + \eta)^2 + D^2 + \Delta^2] + D^2\eta\},$$
$$F^+(\varepsilon_n, p) = -\frac{1}{\mathrm{Det}}\Delta^*[\varepsilon_n^2 + (\xi_p + \eta)^2 + D^2 + \Delta^2],$$
(11)

where

$$\mathrm{Det} = (\varepsilon_n^2 + \xi_p^2 + D^2 + \Delta^2)$$
$$\times (\varepsilon_n^2 + (\xi_p + \eta)^2 + D^2 + \Delta^2) - \eta^2 D^2.$$

The superconducting gap is determined in the regular way as

$$\Delta^* = VT \sum_{np} F^+(\varepsilon_n, p). \quad (12)$$

From Eqs. (11) and (12), we obtain an equation for the superconducting gap $\Delta(\eta, D)$ at fixed values of η and D [7]:

$$1 = 2\pi\lambda T \sum_{n=0}^{\left[\frac{\omega_c}{2\pi T}\right]} \left\{ \alpha\mathscr{F} + \frac{1-\alpha}{\tilde{\varepsilon}_n} \right\}, \quad (13)$$

where the first term corresponds to the contribution from the hot patches, whose relative fraction is α:

$$\mathscr{F} = \frac{1}{\pi\Delta^*} \int\limits_{-\infty}^{\infty} d\xi_p F^+(\varepsilon_n, \xi_p)$$

$$= \frac{1}{\sqrt{2}} \left\{ \sqrt{\left(\tilde{\varepsilon}_n^2 + D^2 + \frac{\eta^2}{4}\right)^2 - \eta^2 D^2} + \tilde{\varepsilon}_n^2 + D^2 - \frac{\eta^2}{4} \right\}^{-1/2}$$

$$\times \left\{ 1 + \frac{\tilde{\varepsilon}_n^2 + D^2 + \frac{\eta^2}{4}}{\sqrt{\left(\tilde{\varepsilon}_n^2 + D^2 + \frac{\eta^2}{4}\right)^2 - \eta^2 D^2}} \right\}. \tag{14}$$

The second term in Eq. (13) gives the standard BCS contribution from the cold sections, whose fraction on the Fermi surface is $1 - \alpha$; $\lambda = N_0(0)V$ is the dimensionless constant of the pairing interaction ($N_0(0)$ is the free-electron density of states at the Fermi level); and

$$\tilde{\varepsilon}_n = \sqrt{\varepsilon_n^2 + \Delta^2}.$$

The numerical $\Delta(\eta, D)$ dependence, which was found in the explicit form [7], makes it possible to find the superconducting gap $\langle\Delta\rangle$ averaged over distributions (5) and, for high-temperature fluctuations, (7) without the standard assumption about self-averaging of the superconducting order parameter.

In most papers on superconductivity in disordered systems, the self-averaging of the superconducting order parameter is assumed; that is, the superconducting gap Δ is supposed to be virtually equal to the mean-field gap Δ_{mf}, which is independent of the random characteristics of the field (η and D in our model). In this case, Δ_{mf} is determined by the equation[2]

$$\Delta_{mf}^* = VT \sum_{np} \left\langle F_{\Delta = \Delta_{mf}}^+(\varepsilon_n, p) \right\rangle. \tag{15}$$

Here, the angle brackets denote averaging over η and D (in the high-temperature regime) with the distributions given by Eqs. (5) and (7), and the superconducting gap Δ in Eq. (11) for $F^+(\varepsilon_n, p)$ is considered equal to Δ_{mf}. The equations for Δ_{mf} are presented in [7] for both fluctuation regimes within the model of the pseudogap state in question. It is also shown in [7] that the superconducting gap $\langle\Delta\rangle$ averaged over short-range order fluctuations can significantly differ from the mean-field gap Δ_{mf}. In particular, $\langle\Delta\rangle$ is nonzero above the mean-field superconducting transition temperature T_c, correspond-

---

[2] It should be emphasized that we consider the mean-field approximation with respect to the averaging over fluctuations of the random field. The mean-field approximation in the ordinary thermodynamical sense is used in all equations, which is implied in the framework of the BCS theory.

ing (according to the assumption made in [5, 7]) to the onset of a superconducting state that is uniform over the whole sample. At temperatures $T > T_c$, the superconducting phase is likely to be in the form of isolated regions (droplets), which appear due to random fluctuations of the local electronic density of states.

As shown below, the absence of self-averaging of the superconducting order parameter significantly affects the electronic spectral density and the tunneling density of states in the superconducting phase [5].

4. SPECTRAL DENSITY AND DENSITY OF STATES

The spectral density is determined in the regular way as

$$A(E, \xi_p) = -\frac{1}{\pi} \text{Im}\, G^R(E, \xi_p). \tag{16}$$

In Eq. (11) for the normal Green's function, we substitute real frequencies for the Matsubara frequencies: $i\varepsilon_n \longrightarrow E + i\delta$. In this case, the spectral density in the vicinity of the hot parts of the Fermi surface corresponding to specific realizations of η and D is

$$A_{\eta D}(E, \xi_p) = -\text{sgn}(E)$$

$$\times \frac{(E + \xi_p)(-E^2 + (\xi_p + \eta)^2 + D^2 + \Delta^2) + D^2\eta}{2\eta\sqrt{(\xi_p + \eta/2)^2 + D^2}}$$

$$\times \left[\delta\left(\left(\sqrt{\left(\xi_p + \frac{\eta}{2}\right)^2 + D^2} + \frac{\eta}{2} \right)^2 + \Delta^2 - E^2 \right) \right.$$

$$\left. - \delta\left(\left(\sqrt{\left(\xi_p + \frac{\eta}{2}\right)^2 + D^2} - \frac{\eta}{2} \right)^2 + \Delta^2 - E^2 \right) \right]. \tag{17}$$

In the low-temperature regime of the dielectric fluctuations, the amplitude of the dielectric gap is frozen out and only the phase η fluctuates; averaging over these fluctuations should be performed using the distribution given by Eq. (5). The averaged spectral density on the Fermi surface ($\xi_p = 0$) is

$$A_D(E, 0) = -\int\limits_{-\infty}^{\infty} d\eta \mathscr{P}_\eta(\eta)|E| \frac{-E^2 + \eta^2 + D^2 + \Delta^2}{2\eta\sqrt{(\eta/2)^2 + D^2}} \tag{18}$$

$$\times [\delta(f_+^2 - E^2) - \delta(f_-^2 - E^2)],$$

$$f_\pm^2 = \left(\sqrt{\left(\frac{\eta}{2}\right)^2 + D^2} \pm \frac{\eta}{2} \right)^2 + \Delta^2. \tag{19}$$

It should be taken into account that the superconducting gap appearing in Eq. (18) also fluctuates; i.e., it depends on η and D. The $\Delta(\eta, D)$ dependence is determined from Eq. (13) numerically. It turns out that f_+ is minimal for $\eta = 0$ ($f_+ = \sqrt{D^2 + \Delta^2(0, D)}$) and increases

with $\eta > 0$. The value of f_- decreases with increasing η in both cases of $\eta \ll D$ and $\eta \gg D$, but it can have a local maximum $f_{\max}$ at a value of η close to $2D$ and corresponding to the maximum of $\Delta(\eta, D)$. The $f_-(\eta)$ function also has a minimum $f_{\min}$ in this case. Figure 1a shows the typical dependences of f_+, f_-, and Δ on η at fixed values of D, and Fig. 1b shows the dependences of $f_{\max}, f_{\min}$, and $\sqrt{D^2 + \Delta^2(0, D)}$ on D.

For $E > \sqrt{D^2 + \Delta^2(0, D)}$, only the first δ function in Eq. (18) makes a nonzero contribution (for $E > 0$, the argument of this δ function has a unique root η_0, $f_+(\eta_0) = E$; this root was found numerically):

$$A_D(E, 0) = -|E| \frac{-E^2 + \eta_0^2 + D^2 + \Delta^2(\eta_0, D)}{\eta_0 \sqrt{(\eta_0/2)^2 + D^2}}$$
$$\times \frac{\mathcal{P}_\eta(\eta_0)}{|df_+^2/d\eta|_{\eta = \eta_0}}. \qquad (20)$$

For $E < \sqrt{D^2 + \Delta^2(0, D)}$, only the second δ function contributes to Eq. (18). In the case of $f_{\min} < E < f_{\max}$, the argument of this function can have several roots; for $E < \min(f_{\min}; \Delta_0)$, where Δ_0 is the gap in the absence of dielectric fluctuations, the argument of the δ function can have no roots (the spectral density is equal to zero in this case). Thus, we have

$$A_D(E, 0) = -|E| \sum_i \frac{-E^2 + \eta_i^2 + D^2 + \Delta^2(\eta_i, D)}{\eta_0 \sqrt{(\eta_i/2)^2 + D^2}}$$
$$\times \frac{\mathcal{P}_\eta(\eta_i)}{|df_-^2/d\eta|_{\eta = \eta_i}}, \qquad (21)$$

where η_i are the roots of the equation $f_-(\eta) = E$.

It should be noted that if E is equal to $f_{\min}, f_{\max}$, or Δ_0, the spectral density diverges, because the derivative $df_-^2/d\eta$, appearing in the denominator of Eq. (21), vanishes at the points of the maximum and minimum of f_-, as well as at $\eta \longrightarrow \infty$, which corresponds to $E = \Delta_0$ (Fig. 1a).

Thus, there are three peaks in the spectral density in the low-temperature regime of the dielectric fluctuations at sufficiently small values of the amplitude D (in the case where $f_-(\eta)$ has a minimum and a minimum). These peaks correspond to $E = f_{\min}, f_{\max}$, and Δ_0; the behavior of the spectral density is shown in Fig. 2.[3] One of the peaks is at the edge of the gap in the spectral density, which is observed when $E < \min(f_{\min}; \Delta_0)$. At sufficiently large values of D, the minimum and maximum of $f_-(\eta)$ disappear (Fig. 1b) and the spectral density

---

[3] In what follows, calculations are performed for $\lambda = 0.2$ and $\alpha = 2/3$.
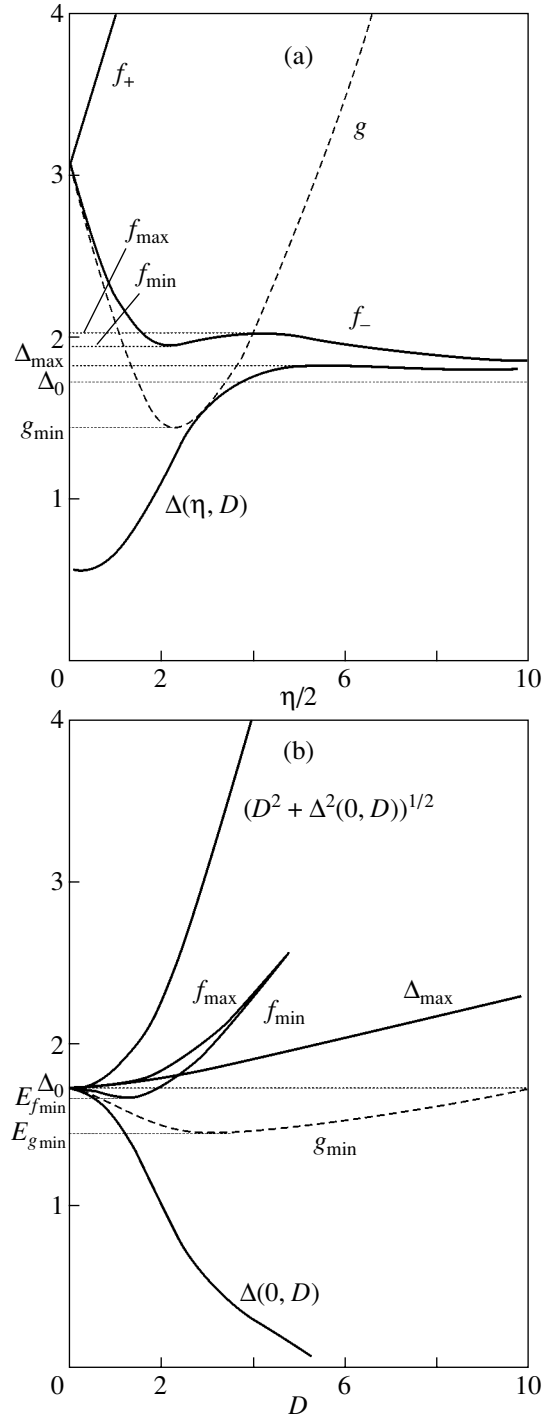
Fig. 1. Dependence of the calculated characteristic energy parameters on (a) the phase η and (b) amplitude D of the random field of dielectric fluctuations. All energy quantities are expressed in units of T_{c0}; $T/T_{c0} = 0.1$, $\lambda = 0.2$, and $\alpha = 2/3$.

diverges only in the vicinity of the edge of the gap at $E = \Delta_0$. Although the $f_-(\eta)$ curve has no peak, a significant decrease in $df_-/d\eta$ is observed near the value of η corresponding to the maximum of $\Delta(\eta, D)$; therefore,
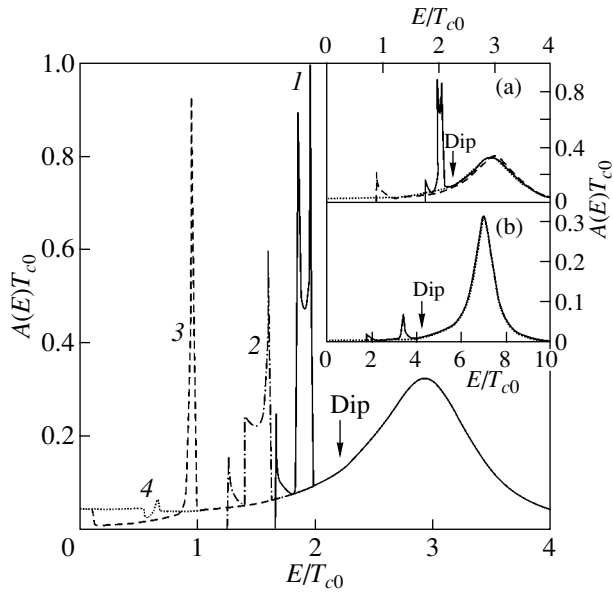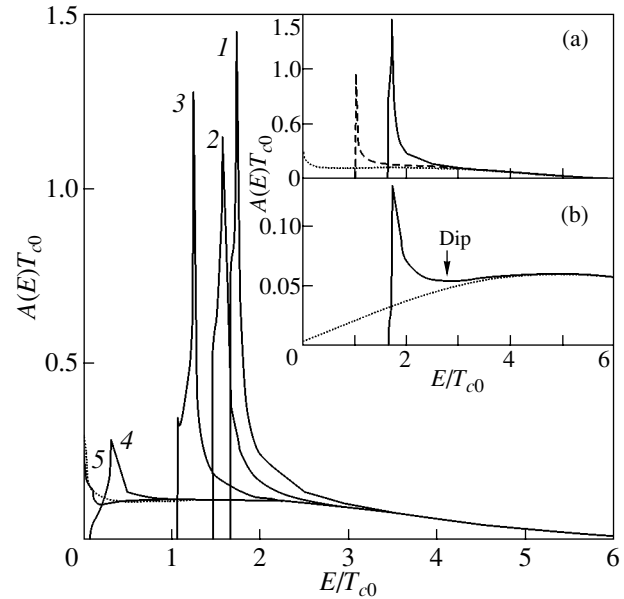
Fig. 2. Spectral density in the low-temperature regime of dielectric fluctuations. $D/T_{c0} = 3$, $v_F\kappa/T_{c0} = 1$, $T_c/T_{c0} = 0.52$, and T/T_{c0} is equal to (*1*) 0.52, (*2*) 0.8, (*3*) 1.01, and (*4*) 1.05. Inset a: $D/T_{c0} = 3$, $v_F\kappa/T_{c0} = 1$, and $T/T_{c0} = 0.1$; the dashed line corresponds to the approximation of self-averaging of the superconducting gap; here and in the other figures, the dotted line describes pure pseudogap behavior in the normal phase. Inset b: $D/T_{c0} = 7$, $v_F\kappa/T_{c0} = 1$, and $T/T_{c0} = 0.1$.

Fig. 3. Spectral density in the high-temperature regime of dielectric fluctuations. $W/T_{c0} = 3$, $\kappa/T_{c0} = 1$, $T_c/T_{c0} = 0.61$, and T_c/T_{c0} is equal to (*1*) 0.1, (*2*) 0.61, (*3*) 0.8, (*4*) 0.99, and (*5*) 1.01. Inset a: $W/T_{c0} = 3$, $v_F\kappa/T_{c0} = 1$, and $T/T_{c0} = 0.1$; the dashed line corresponds to the approximation of self-averaging of the superconducting gap. Inset b: $W/T_{c0} = 7$, $v_F\kappa/T_{c0} = 0.1$, and $T/T_{c0} = 0.1$.

an additional peak appears in the spectral density (see Fig. 2, inset b). When the temperature exceeds T_{c0}, the gap in the spectral density and the peak corresponding to $E = \Delta_0$ disappear but the peak at $E = f_{max}$ remains. In passing through the mean-field superconducting transition point T_c, the behavior of the spectral density remains qualitatively the same.

In the high-temperature regime, where fluctuations of the amplitude D of the dielectric gap are also significant, the averaging over the distribution given by Eq. (7) should also be carried out:

$$A(E, 0) = \int_0^\infty dD \mathscr{P}_D(D) A_D(E, 0). \tag{22}$$

The behavior of the spectral density in the high-temperature regime is shown in Fig. 3. The spectral density has a gap for $E < E_{fmin} < \Delta_0$, where $E_{fmin} = \min(f_{min}(D))$ (see Fig. 1b). At $E = \Delta_0$, the spectral density diverges, because $A_D(E, 0)$ diverges at any value of D at this point. As the temperature becomes larger than T_{c0}, both the gap and peak in the spectral density disappear, but negligible distinctions from the pure pseudogap behavior are observed even above T_{c0}. In the pseudogap-state model in question, a decrease in the correlation length ξ_{corr} (an increase in κ) results in a strong smearing of the

spectral-density pseudogap in the high-temperature regime of fluctuations; therefore, the pseudogap maximum is weakly pronounced at the values of the parameters chosen for the calculations ($W/T_{c0} = 3$, $\kappa/T_{c0} = 1$, and, hence, $T_c/T_{c0} = 0.61$) and the superconducting peak superimposes on it. As the width of the pseudogap and the correlation length increase, the superconducting peak and pseudogap maximum can be separated from each other[4] (Fig. 3, inset b). In this case, a characteristic dip appears after the main peak in the spectral density.[5] A similar dip has been observed in ARPES experiments [1, 2], and its interpretation is still in dispute.

On the assumption that the superconducting order parameter is self-averaging, the superconducting gap is independent of the random parameters η and D and is equal to the mean-field gap Δ_{mf}, which was determined in [7] from Eq. (15). Replacing the integration variable η by $-\eta$ for the second δ function in the integral over η in Eq. (18) yields an integral with one δ function,

---

[4] In this model, such behavior is observed at the parameters ($W/T_{c0} = 7$, $\kappa/T_{c0} = 0.1$) corresponding to unrealistically strong damping of the critical temperature ($T_c/T_{c0} \approx 0.1$).

[5] In the low-temperature regime of dielectric fluctuations, the corresponding dip in the spectral density (Fig. 2) is pronounced even more clearly; however, several peaks appearing in this case are not observed in ARPES experiments.

$\delta(f_+^2 - E^2)$. The unique root for the argument of this δ function is

$$\eta = \frac{E^2 - \Delta_{mf}^2 - D^2}{\sqrt{E^2 - \Delta_{mf}^2}}. \tag{23}$$

On the assumption of self-averaging of the superconducting order parameter in the low-temperature regime of fluctuations, the spectral density takes the form

$$A_{D,mf}(E, 0) = \frac{1}{\pi} \frac{\kappa}{(E^2 - \Delta_{mf}^2 - D^2)^2 + \kappa^2(E^2 - \Delta_{mf}^2)} \\ \times \frac{|E| D^2}{\sqrt{E^2 - \Delta_{mf}^2}}. \tag{24}$$

In the high-temperature regime, the spectral density should be averaged over the random amplitude D:

$$A_{mf}(E, 0) = \int_0^\infty dD \mathcal{P}_D(D) A_{D,mf}(E, 0). \tag{25}$$

The behavior of the spectral density in the low- and high-temperature regimes of fluctuations, provided that the superconducting gap is self-averaging, is shown in the insets to Figs. 2 and 3, respectively. Inclusion of fluctuations of the superconducting gap results in significant changes in the behavior of the spectral density in both regimes.

The density of states in this model consists of additive contributions from the cold and hot sections. The density of states for a specific realization of the random field (η, D) is

$$N_{\eta D}(E) = -\frac{1}{\pi} \sum_p \operatorname{Im} G^R \\ = \alpha N_0(0) \int_{-\infty}^\infty d\xi_p A_{\eta D}(E, \xi_p) + (1 - \alpha) N_{BCS}(E). \tag{26}$$

On the cold sections, whose fraction is $1 - \alpha$, there is no interaction with dielectric fluctuations. The normal Green's function and the contribution to the density of states $N_{BCS}(E)$ have the form typical of the BCS theory with a gap depending on η and D:

$$N_{BCS}(E) = N_0(0) \frac{|E|}{\sqrt{E^2 - \Delta^2(\eta, D)}} \\ \times \theta(E^2 - \Delta^2(\eta, D)). \tag{27}$$

On the hot sections, $A_D(E, \xi_p)$ is given by Eq. (18). The integration over ξ_p in Eq. (26) can be performed analyt-
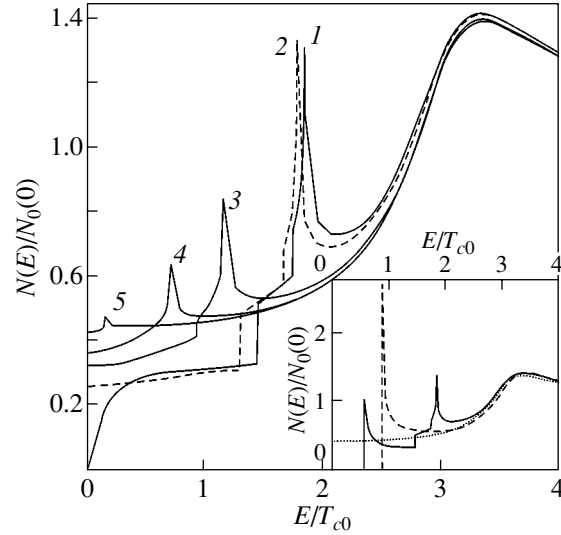
Fig. 4. Density of states in the low-temperature regime of dielectric fluctuations. $D/T_{c0} = 3$, $v_F\kappa/T_{c0} = 1$, $T_{cc}/T_{c0} = 0.33$, $T_c/T_{c0} = 0.52$, and T/T_{c0} is equal to (1) 0.33, (2) 0.52, (3) 0.9, (4) 1, and (5) 1.01. Inset: $D/T_{c0} = 3$, $v_F\kappa/T_{c0} = 1$, and $T/T_{c0} = 0.1$; the dashed line corresponds to the approximation of self-averaging of the superconducting gap.

ically, and the averaged density of states in the low-temperature regime of fluctuations is found to be

$$\frac{N_D(E)}{N_0(0)} = \int_{-\infty}^\infty d\eta \mathcal{P}_\eta(\eta) \frac{|E|}{\tilde{\varepsilon}} \theta(E^2 - \Delta^2(\eta, D)) \\ \times \left[\alpha \frac{|\tilde{\varepsilon} + \eta/2|}{\sqrt{(\tilde{\varepsilon} + \eta/2)^2 - D^2}} \theta(|\tilde{\varepsilon} + \eta/2| - D) + (1 - \alpha) \right], \tag{28}$$

where $\tilde{\varepsilon} = \sqrt{E^2 - \Delta^2(\eta, D)}$.

Assuming that the superconducting order parameter Δ is self-averaging, which means that this parameter is independent of η and D and equal to Δ_{mf}, one can rewrite Eq. (28) in the low-temperature regime as

$$\frac{N_{D,mf}(E)}{N_0(0)} = \frac{|E|}{\tilde{\varepsilon}} \theta(E^2 - \Delta_{mf}^2) \\ \times \left[\alpha \left(\int_{D - \tilde{\varepsilon}}^\infty d\eta \mathcal{P}_\eta(\eta) \frac{|\tilde{\varepsilon} + \eta/2|}{\sqrt{(\tilde{\varepsilon} + \eta/2)^2 - D^2}} \right. \right. \\ \left. \left. + \int_{-\infty}^{-D - \tilde{\varepsilon}} d\eta \mathcal{P}_\eta(\eta) \frac{|\tilde{\varepsilon} + \eta/2|}{\sqrt{(\tilde{\varepsilon} + \eta/2)^2 - D^2}} \right) + 1 - \alpha \right], \tag{29}$$

where $\tilde{\varepsilon} = \sqrt{E^2 - \Delta_{mf}^2}$.

The behavior of the density of states in the low-temperature regime of dielectric fluctuations is shown in Fig. 4. If there is no self-averaging of the superconducting order parameter, the behavior of the density of
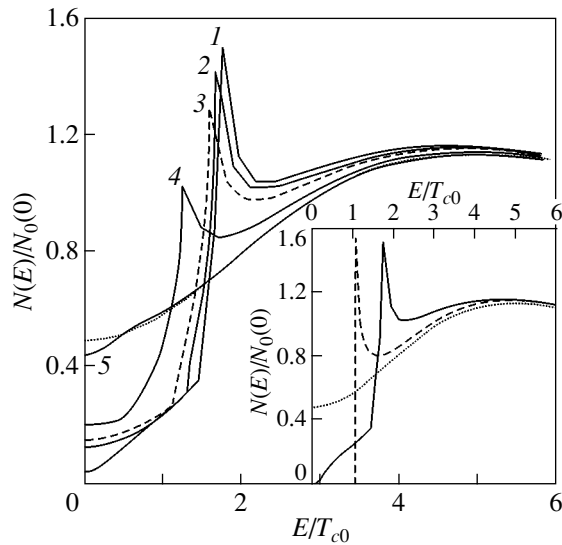
Fig. 5. Density of states in the high-temperature regime of dielectric fluctuations. $W/T_{c0} = 3$, $v_F \kappa/T_{c0} = 1$, $T_c/T_{c0} = 0.61$, and T/T_{c0} is equal to (*1*) 0.2, (*2*) 0.5, (*3*) 0.61, (*4*) 0.8, and (*5*) 1.01. Inset: $W/T_{c0} = 3$, $v_F \kappa/T_{c0} = 1$, and $T/T_{c0} = 0.1$; the dashed line corresponds to the approximation of self-averaging of the superconducting gap.

states changes qualitatively (see inset to Fig. 4). The gap in the density of states is observed for $E < \Delta(0, D) < \Delta_{mf}$. Let us introduce a characteristic temperature T_{cc} corresponding to the condition $\Delta(0, D) = 0$. As the temperature becomes higher than T_{cc}, the gap in the density of states disappears, while no qualitative changes occur in the density of states as one passes through the mean-field superconducting transition point T_c. Let us introduce the quantity $g(\eta) = \sqrt{(D - \eta/2)^2 + \Delta^2(\eta, D)}$, whose behavior is shown in Fig. 1a. This function has a minimum g_{min} at $\eta/2 \sim D$. For $\Delta(0, D) < E < \min(g_{min}; \Delta_0)$, only the cold section [the second term in Eq. (28)] make a contribution to the density of states. The density of states undergoes abrupt changes at $E = g_{min}$ and $E = \Delta_0$, which disappear at temperatures above T_{c0}. The density of states has a peak at $E = \Delta_{max} > (g_{min}; \Delta_0)$, where Δ_{max} is the maximum of $\Delta(\eta)$, which takes place at $\eta/2 \sim D$ (Fig. 1a). Thus, the superconducting gap determined by the peaks in the density of states corresponds to the condition $\Delta_{max} > \Delta_0 > \Delta_{mf}$ in the low-temperature regime of fluctuations and the peaks in the density of states remain even at $T > T_{c0}$.

In the high-temperature regime of dielectric fluctuations, averaging should also be performed over the amplitude of the dielectric gap D:

$$\frac{N(E)}{N_0(0)} = \int_0^\infty dD \mathscr{P}_D(D) \frac{N_D(E)}{N_0(0)}. \tag{30}$$

Assuming self-averaging of the superconducting order parameter, we have

$$\frac{N_{mf}(E)}{N_0(0)} = \frac{|E|}{\tilde{\varepsilon}} \theta(E^2 - \Delta_{mf}^2) \left[\alpha \int_{-\infty}^\infty d\eta \mathscr{P}_\eta(\eta) \right.$$

$$\left. \times \int_0^{|\tilde{\varepsilon} + \eta/2|} dD \mathscr{P}_D(D) \frac{|\tilde{\varepsilon} + \eta/2|}{\sqrt{(\tilde{\varepsilon} + \eta/2)^2 - D^2}} + 1 - \alpha \right]. \tag{31}$$

In the limit of the infinite correlation length ($\kappa \longrightarrow 0$), Eqs. (30) and (31) reduce to those derived in the model of the pseudogap state with a infinite correlation length of the dielectric fluctuations [5].

The behavior of the density of states in the high-temperature regime of dielectric fluctuations is shown in Fig. 5. The absence of self-averaging of the superconducting order parameter strongly affects the behavior of the density of states (see inset to Fig. 5). There is no gap in the density of states[6] despite the fact that we consider the case of *s*-electron pairing! For $E < E_{g, min} = \min(g_{min}(D))$ (see Fig. 1b), only the cold sections of the Fermi surface contribute to the density of states, and at $E = E_{min}$ (when the contribution from the hot sections becomes nonzero), the density of states shows a discontinuity in slope, which is associated with the peculiarity of the chosen model of the Fermi surface (separation into sharply defined hot and cold sections). The maximum in the density of states is observed at $E = \Delta_0$. Thus, the width of the superconducting gap determined as the distance between the peaks in the density of states corresponds to Δ_0 rather than to Δ_{mf}. The density of states does not change as one passes through the mean-field critical temperature T_c; the peaks in the density of states disappear only at $T = T_{c0} > T_c$, and nonsignificant distinctions from the pure pseudogap density of states in the normal phase are observed even at $T > T_{c0}$.

5. CONCLUSIONS

Thus, we have studied the spectral density and density of states of the superconductor in the framework of a very simplified model of the pseudogap state in a two-dimensional electron system that permits exact solution [7, 9]. The main advantage of the model is that it allows one to consider the case where there is no self-averaging of the superconducting order parameter (i.e., to include significant fluctuations of the superconducting gap observed in [5, 7] in the presence of strong fluctuations of dielectric short-range order) and the case of arbitrary values of the short-range order correlation length ξ_{corr} (in contrast to the case of $\xi_{corr} \longrightarrow \infty$ considered in [5]).

---

[6] The gap appears only at very low temperatures $T < T_{c\infty} = T_{c0}$ ($\tilde{\lambda} = \lambda(1 - \alpha)$), such that $\Delta(0, D \longrightarrow \infty)$ is nonzero [5].

The absence of self-averaging of the superconducting order parameter over the random field of dielectric fluctuations causes the spectral density and density of states to change significantly. The superconducting character of these quantities persists in a wide temperature range above the temperature T_c of the superconducting transition occurring uniformly over the sample; in this range, superconductivity appears to exist in separate regions (droplets) [5, 7], which arise due to random fluctuations of the local electronic density of states. The peculiarities found correlate with a number of anomalies observed in the superconducting state of underdoped HTSC cuprates.

REFERENCES

1. T. Timusk and B. Statt, Rep. Prog. Phys. **62** (1), 61 (1999).
2. M. V. Sadovskiĭ, Usp. Fiz. Nauk **171** (5), 539 (2001) [Phys. Usp. **44**, 515 (2001)].
3. V. M. Loktev, R. M. Quick, and S. G. Sharapov, Phys. Rep. **349** (1), 2 (2001).
4. A. I. Posazhennikova and M. V. Sadovskiĭ, Zh. Éksp. Teor. Fiz. **115** (2), 632 (1999) [JETP **88**, 347 (1999)].
5. É. Z. Kuchinskiĭ and M. V. Sadovskiĭ, Zh. Éksp. Teor. Fiz. **117** (3), 613 (2000) [JETP **90**, 535 (2000)]; Physica C (Amsterdam) **341–348**, 879 (2000).
6. É. Z. Kuchinskiĭ and M. V. Sadovskiĭ, Zh. Éksp. Teor. Fiz. **119** (3), 553 (2001) [JETP **92**, 480 (2001)].
7. É. Z. Kuchinskiĭ and M. V. Sadovskiĭ, Zh. Éksp. Teor. Fiz. **121** (3), 758 (2002) [JETP **94**, 654 (2002)].
8. M. V. Sadovskiĭ, Zh. Éksp. Teor. Fiz. **66** (5), 1720 (1974) [Sov. Phys. JETP **39**, 845 (1974)]; Fiz. Tverd. Tela (Leningrad) **16** (9), 2504 (1974) [Sov. Phys. Solid State **16**, 1632 (1974)].
9. L. Bartosch and P. Kopietz, Eur. Phys. J. B **17** (4), 555 (2000).
10. M. V. Sadovskiĭ, Zh. Éksp. Teor. Fiz. **77** (5), 2070 (1979) [Sov. Phys. JETP **50**, 989 (1979)].
11. J. Schmalian, D. Pines, and B. Stojkovic, Phys. Rev. Lett. **80**, 3839 (1998); Phys. Rev. B **60** (1), 667 (1999).
12. É. Z. Kuchinskiĭ and M. V. Sadovskiĭ, Zh. Éksp. Teor. Fiz. **115** (5), 1765 (1999) [JETP **88**, 968 (1999)].
13. S. A. Brazovskiĭ and I. E. Dzyaloshinskiĭ, Zh. Éksp. Teor. Fiz. **71** (6), 2338 (1976) [Sov. Phys. JETP **44**, 1233 (1976)].
14. P. A. Lee, T. M. Rice, and P. W. Anderson, Phys. Rev. Lett. **31** (7), 462 (1973).
15. M. V. Sadovskii, Physica C (Amsterdam) **341–348**, 811 (2000).
16. L. Bartosch and P. Kopietz, Phys. Rev. B **60** (23), 15488 (1999).
17. L. Bartosch, Ann. Phys. (N.Y.) **10** (3), 799 (2001).
18. A. J. Millis and H. Monien, Phys. Rev. B **61** (18), 12496 (2000).

Translated by A. Poushnov

SEMICONDUCTORS
AND DIELECTRICS

Thermal Stability of GaN Epilayers with Different Degrees of Mosaic Structure Order

G. V. Benemanskaya, A. I. Besyul'kin, M. S. Dunaevskiĭ, A. K. Kryzhanovskiĭ, and N. M. Shmidt

Ioffe Physicotechnical Institute, Russian Academy of Sciences, Politekhnicheskaya ul. 26, St. Petersburg, 194021 Russia
Received October 21, 2002

Abstract—Thermal stability of GaN epilayers grown through metal-organic compound vapor deposition on a (0001) sapphire substrate was studied using atomic-force spectroscopy. Samples differing in quality were thermally annealed in ultrahigh vacuum in the range 700–950°C. Mosaic spread in the epitaxial layers is shown to strongly affect their thermal stability. Epilayers with a well-ordered mosaic structure exhibit surface degradation at a temperature of ~950°C. The surface morphology of layers with a large mosaic spread starts to change at lower temperatures, ~780°C. © 2003 MAIK "Nauka/Interperiodica".

1. INTRODUCTION

Reviews dealing with the properties of nitrides [1, 2] stress the high thermal stability of gallium nitride as a characteristic feature. The few available studies of the thermal stability of GaN epilayers have shown that the surface morphology of hexagonal GaN epilayers grown through metal-organic compound vapor deposition (MOCVD) and annealed in a nitrogen environment undergo noticeable changes at temperatures above 1200°C [3]. Epilayers prepared following other techniques exhibit such changes at lower temperatures, 800–900°C. There is practically no information on the thermal stability of GaN epilayers annealed at a high temperature in vacuum. At the same time, such data are of both scientific and applied interest, because studies of the electronic properties of a surface, such as the work function, surface energy band bending, and the spectrum of surface states, are usually conducted after annealing directly in vacuum at various temperatures, up to ~800 [4], ~900 [5], and ~1000°C [6, 7]. Information on how annealing in vacuum modifies the GaN surface is also essential from the standpoint of its application potential (for instance, for use in photoemission devices).

We report here on an investigation of the thermal stability of GaN epilayers of hexagonal modification by using atomic-force microscopy (AFM); the layers were MOCVD grown and thermally annealed in a high vacuum. One of the goals of such investigations consists in establishing the extent to which the degree of order in the mosaic structure of an epitaxial layer affects the results of thermal treatment. The mosaic structure of epitaxial layers of hexagonal GaN is a fundamental property that is also characteristic of films of all nitrides employed in light-emitting diodes, photodetectors, and high-voltage devices based on these materials.

2. EXPERIMENTAL TECHNIQUE

The *n*-GaN epilayers studied were MOCVD grown on (0001) sapphire substrates at a pressure of 200 mbar. The layers had a carrier concentration of $(1–3) \times 10^{17}$ cm^{-3}, a thickness of ~3 μm, and a room-temperature carrier mobility of 300–600 cm^2 V^{-1} s^{-1}. The morphology of the GaN(0001) samples before and after thermal annealing in ultrahigh vacuum was studied using AFM. To quantify the mosaic spread in epitaxial layers, the structural data obtained by AFM were treated using multifractal analysis [8, 9].

The main results bearing on thermal treatments are presented for two GaN(0001) epilayers. Sample I is the most perfect from the standpoint of surface morphology and x-ray structural and electrical characteristics; the mosaic spread of its structure is –0.32, and the carrier mobility is 600 cm^2 V^{-1} s^{-1}. Sample II has a carrier mobility of 300 cm^2 V^{-1} s^{-1} and a mosaic spread of −0.335. Note that sample II, while being somewhat inferior to sample I in terms of its parameters, is in no way of poor quality. Poor-quality layers have typically low mobilities (~100 cm^2 V^{-1} s^{-1}) and a mosaic spread index of –0.36.

The thermal-stability limit of the above samples was deduced from a change in the layer surface morphology as revealed by AFM. We also employed the surface-sensitive method of threshold photoemission spectroscopy [10], which makes it possible to monitor the surface quality *in situ* from the change in the photoemission current of the GaN(0001) sample caused by the adsorption of Cs atoms. Adsorption was used in this case to probe the quality of the substrate. The results of these photoemission studies will be published in a separate communication.

A series of annealings, each 15 min long, were conducted in a high vacuum ($P \sim 10^{-10}$ Torr) at tempera-
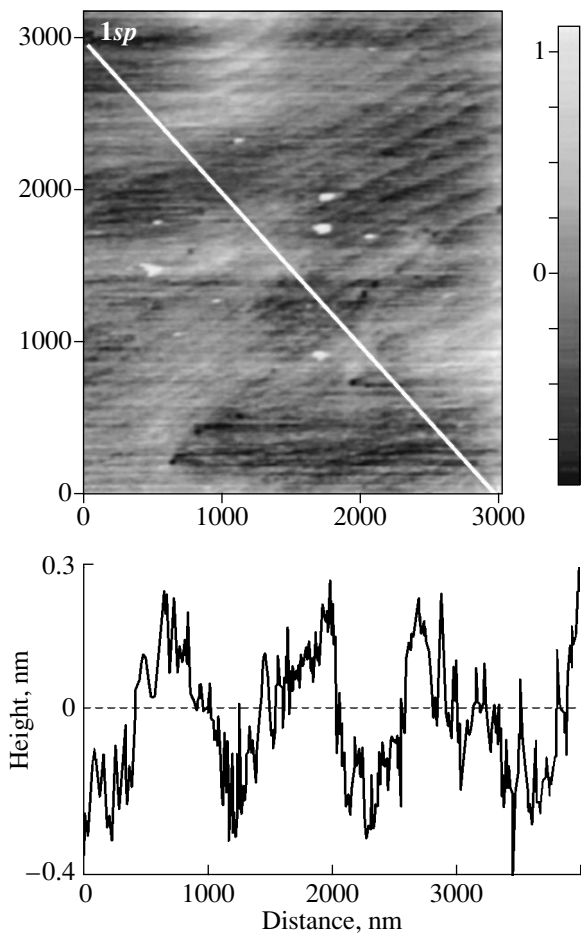
Fig. 1. AFM image of the surface (top) and the roughness profile (bottom) of an epitaxial GaN(0001) layer. Sample I, $\Delta = -0.32$.
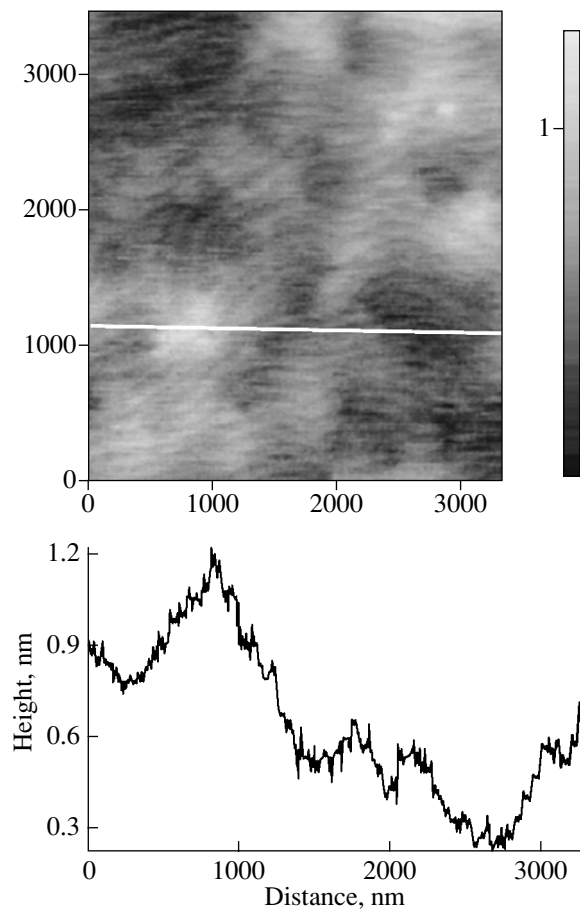
Fig. 2. AFM image of the surface (top) and the roughness profile (bottom) of an epitaxial GaN(0001) layer. Sample II, $\Delta = -0.335$.

tures of 700, 780, 850, 900, and 950°C. The annealing temperature was measured with a WRe5-WRe20 thermocouple and a PYRO optical pyrometer. The error in temperature determination did not exceed 20°C.

3. EXPERIMENTAL RESULTS

Figures 1 and 2 present AFM images of the surface morphology of GaN epilayers with different degrees of mosaic order in the initial stage before the annealing in vacuum. The mosaic spread of the samples studied was determined by applying multifractal analysis to the treatment of AFM images [9, 11]. The algorithm used reduces to the following operations.

1. The AFM images are transferred by modern methods of image acquisition and processing in BMP graphic files in the bitmap mode.

2. The image obtained is represented by a digital set by dividing the image under study into unit boxes containing dark and bright dots (pixels), to which the values "1" and "0" are assigned, respectively. Next, the image is divided into larger square grid boxes. Using the formalism developed for digital sets, one can construct a probability density function to describe the density distribution of the set in each box, with the measure chosen such that the measures of different boxes are self-similar. This approach permits numerical description of specific features of complex objects with a higher precision than if only one measure were selected for the total set. It should be stressed that the set of the correlation functions obtained in this approximation establishes the relations connecting different parts of a complex structure and their place in the total set through such multifractal parameters as the extent of breaking of the general and local symmetry and the degree of order of the structure as a whole.

The results obtained in the multifractal analysis of the more perfect sample I (Fig. 1) with a surface roughness amplitude less than 1 nm show that the mosaic spread of the sample is $\Delta = -0.32$, and those for sample II (Fig. 2) with a surface roughness of ~1 nm yield $\Delta = -0.335$. The smaller absolute value of Δ for sample I indicates that its mosaic structure is better ordered than that of sample II. Furthermore, as follows from the AFM

(a)   (b)
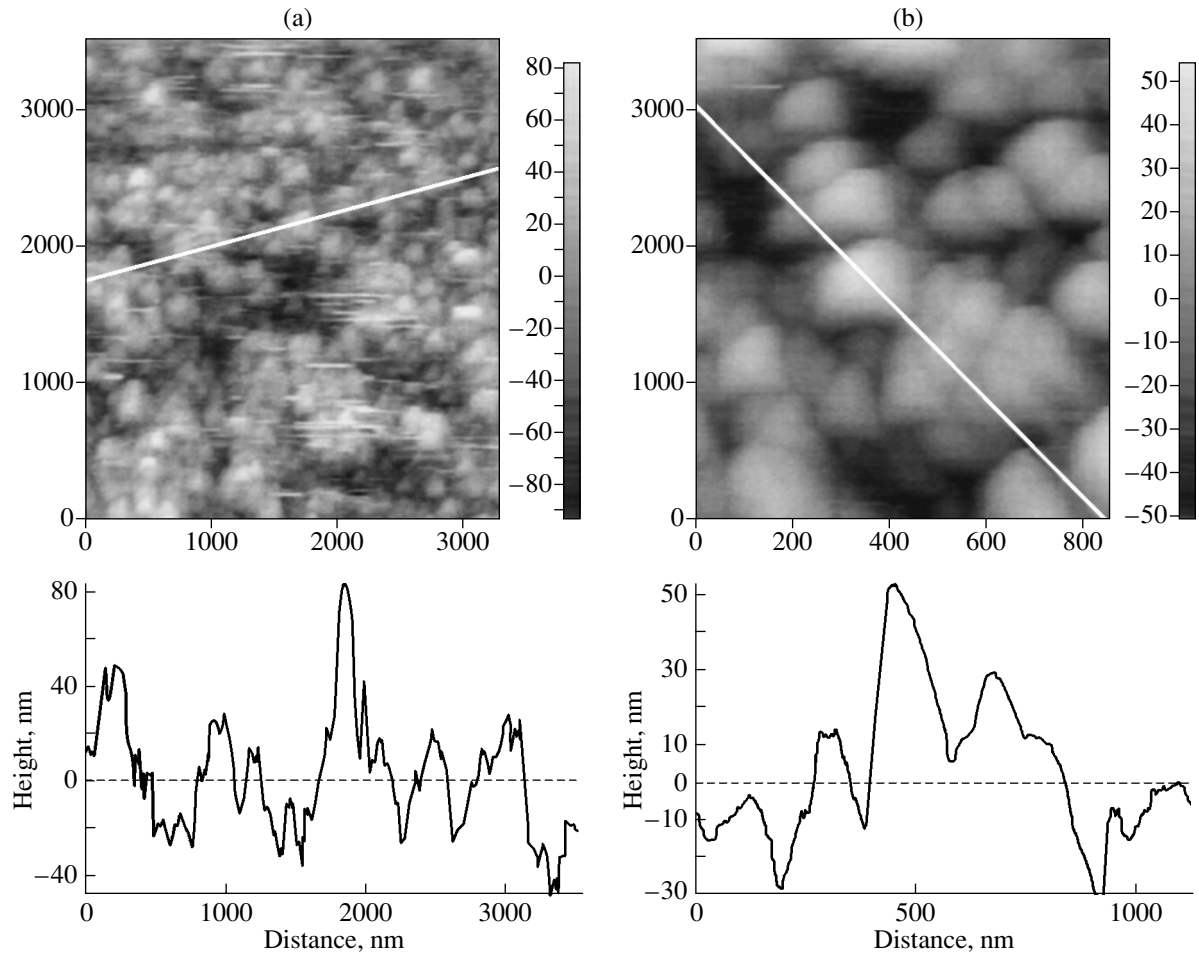
Fig. 3. AFM image of the surface (top) and the roughness profile (bottom) of an epitaxial GaN(0001) layer. Sample I after thermal annealing in vacuum at 950°C. Span size: (a) 3.5×3.5 μm and (b) 1×1 μm.

images (Figs. 1, 2), the pattern of growth in sample I is close to two-dimensional, with distinct growth steps seen. Sample II exhibits a growth pattern closer to three-dimensional, because one clearly sees large blocks with lateral dimensions of ~1000 nm that disrupt the stepped growth.

AFM studies conducted after thermal annealing in vacuum showed that noticeable changes in the surface morphology of these layers begin at different temperatures, namely, at 950°C for the more perfect sample I and at 780°C for the less perfect sample II. Note that both samples exhibit a similar trend in the character of modification of the surface morphology. Figure 3 displays the surface morphology of the more perfect sample I after thermal annealing performed at 950°C. One clearly sees a strong change in the degree of mosaic structure order and more distinct boundaries between large and small domains, which were only weakly pronounced before the annealing (compare Fig. 1 with Fig. 3). It was established that the average surface roughness amplitude increases by an order of magnitude, from 0.5–1.0 nm in the initial stage to 40–100 nm

after the annealing. The growth steps disappear. Annealing also brings about the emergence of Ga onto the surface, with its condensation observed to occur on the layer cleavage planes. Thus, the boundaries of the mosaic structure domains on which nonequilibrium defects aggregate turn out to be the least stable to thermal treatment.

The above results indicate a strong effect of mosaic spread on the thermal stability of GaN(0001) epilayers. The temperature of the onset of surface degradation under thermal treatment in vacuum for sample II with a less ordered mosaic structure was found to be 170°C lower than that for sample I with a smaller mosaic spread.

REFERENCES

1. M. Razeghi and A. Rogalski, J. Appl. Phys. **79**, 7433 (1996).

2. I. Akasaki and H. Amano, Jpn. J. Appl. Phys. **36** (9A), 5393 (1997).

3. M. A. Mastro, O. M. Kryliouk, M. D. Reed, *et al.*, Phys. Status Solidi A **188**, 467 (2001).

4. A. R. Smith and R. M. Feenstra, Appl. Phys. Lett. **72**, 2111 (1999).

5. L. S. Dhesi, C. B. Stagarescu, K. E. Smith, and T. D. Moustakas, Phys. Rev. B **56**, 10271 (1997).

6. V. M. Bermudez, Surf. Sci. **417**, 30 (1998).

7. R. Chierchia, T. Böttcher, S. Figge, *et al.*, Phys. Status Solidi B **228**, 403 (2001).

8. A. G. Kolmakov, V. V. Emtsev, W. V. Lundin, *et al.*, Physica B (Amsterdam) **308–310**, 1141 (2001).

9. N. M. Shmidt, V. V. Emtsev, A. G. Kolmakov, *et al.*, Nanotechnology **12**, 471 (2001).

10. G. V. Benemanskaya, D. V. Daĭneka, and G. É. Frank-Kamenskaya, Zh. Éksp. Teor. Fiz. **119**, 342 (2001) [JETP **92**, 297 (2001)].

11. G. V. Vstovskiĭ, A. G. Kolmakov, and I. Zh. Bunin, *Introduction to Multifractal Parametrization of Material Structures* (Regul. Khaot. Din., Izhevsk, 2001).

Translated by G. Skrebtsov

Electron Paramagnetic Resonance in Neutron-Transmutation-Doped Semiconductors with a Changed Isotopic Composition

P. G. Baranov, A. N. Ionov, I. V. Il'in, P. S. Kop'ev, E. N. Mokhov, and V. A. Khramtsov

Ioffe Physicotechnical Institute, Russian Academy of Sciences, Politekhnicheskaya ul. 26, St. Petersburg, 194021 Russia
*e-mail: Pavel.Baranov@mail.ioffe.ru*

Received October 21, 2002

Abstract—Potential applications of electron paramagnetic resonance (EPR) for investigating and controlling the process of neutron transmutation doping (NTD) of semiconducting germanium, silicon, and silicon carbide are discussed. It is shown that EPR enables one to control the process of annealing of radiation-induced defects in semiconductors subject to neutron irradiation and to detect the shallow donors restored in the process of annealing of donor-compensating defects by observing EPR signals from these donors. EPR can be used to separately detect isolated donors and clusters of two, three, and more exchange-bound donor atoms and thereby determine the degree of nonuniformity of the impurity distribution over the crystal. Neutron transmutation doping is demonstrated to produce a fairly uniform arsenic-donor distribution in a germanium crystal. It is argued that semiconductors enriched in the selected isotopes should be used for NTD. The results of an investigation of phosphorus donors in silicon carbide are presented. © 2003 MAIK "Nauka/Interperiodica".

1. INTRODUCTION

The problem that arises in doping semiconductors is how to obtain uniform distributions of donor and acceptor impurities and to control the content of these impurities over a wide concentration range. Neutron transmutation doping (NTD) is one of the promising methods for producing a uniform impurity distribution in a crystal [1–6]. The nuclei of stable isotopes can absorb slow (thermal) neutrons, and this process is characterized by a certain capture cross section. The neutron absorption is followed by nuclear reactions, because of which stable isotopes of new elements can arise. The impurity concentration N produced in the process of NTD is proportional to the thermal-neutron dose Φ_n (in units of cm^{-2}), the thermal-neutron cross section σ_i (in units of 10^{-24} cm^{-2}) for the ith isotope, and the content C_i of this isotope:

$$N = \Phi_n \sigma_i C_i. \qquad (1)$$

The NTD method is of considerable technological importance, because this method allows one to produce highly homogeneous *n*-type silicon films for high-power devices [7]. Natural silicon contains three stable isotopes: ^{28}Si (92.3%), ^{29}Si (4.7%), and ^{30}Si (3.1%) [8]. Silicon is doped with phosphorus donors through the process of slow-neutron capture by the silicon isotope ^{30}Si (capture cross section $\sigma(^{30}$Si) = 0.11 [8]) followed by its transmutation into phosphorus:

$$^{30}\text{Si} + n \longrightarrow {}^{31}\text{Si} \longrightarrow (\beta^- \text{ decay, } T_{1/2} = 2.62 \text{ h}) \,{}^{31}\text{P}, \quad (2)$$
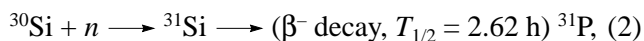
where $T_{1/2}$ is the half-life.

Due to the small ^{30}Si content and the secondary NTD process resulting in transmutation of ^{31}P into ^{32}S, the doping level is restricted to a value of the order of 10^{15} cm^{-3}. Obviously, the doping level will be increased considerably if the initial material is enriched in the isotope ^{30}Si. A similar scheme is used to dope silicon carbide with phosphorus; in this case, NTD was the only method that made it possible for the first time to introduce phosphorus donors into SiC [9–11]. According to recent investigations [12], doping of SiC with phosphorus is very promising, because SiC heavily doped with phosphorus through ion implantation exhibits a sharp increase in electrical resistivity in comparison with the resistivity of SiC doped with nitrogen to a similar concentration. It has been proposed that at high concentrations, nitrogen donors form clusters [12], which is a hindrance to the production of low-resistivity materials.

In principle, in addition to scheme (2), slow neutrons in SiC can be captured by the carbon isotope ^{13}C, which will then be transmuted into nitrogen according to the reaction $^{13}\text{C}(n, \gamma) \longrightarrow {}^{14}\text{C} \longrightarrow (\beta^- \text{ decay}) \,{}^{14}\text{N}$. However, this process is inefficient and, hence, is of no practical significance, because the thermal-neutron capture cross section is very small (9×10^{-24} [8]) and the half-life of the isotope ^{14}C is very long.

In studying NTD, germanium is of particular importance, because, first, this material can be of the highest purity grade and, second, there are five stable germanium isotopes, three of which are involved in the process of NTD. The nuclear reactions that were used to fabricate doped semiconducting germanium and that

Isotopic percentage composition of natural and enriched germanium

	^{70}Ge	^{72}Ge	^{73}Ge	^{74}Ge	^{76}Ge
Natural germanium [8]	20.5	27.4	7.8	36.5	7.8
Enriched germanium	1.7	2.4	1.0	93.9	1.0

involved slow-neutron capture by germanium isotopes ^{70}Ge, ^{74}Ge, and ^{76}Ge followed by their transmutation into gallium, arsenic, and selenium, respectively, are as follows [5, 6]:

$$^{70}\text{Ge} + n \longrightarrow \ ^{71}\text{Ge} \longrightarrow (\text{EC, } T_{1/2} = 11.2 \text{ d}) \ ^{71}\text{Ga,}$$

$$^{74}\text{Ge} + n \longrightarrow \ ^{75}\text{Ge}$$

$$\longrightarrow (\beta^- \text{ decay, } T_{1/2} = 82.8 \text{ min}) \ ^{75}\text{As,} \qquad (3)$$

$$^{76}\text{Ge} + n \longrightarrow \ ^{77}\text{Ge} \longrightarrow (\beta^- \text{ decay, } T_{1/2} = 11.3 \text{ h})$$

$$\longrightarrow \ ^{77}\text{As}(\beta^- \text{ decay, } T_{1/2} = 38.8 \text{ h}) \ ^{77}\text{Se.}$$
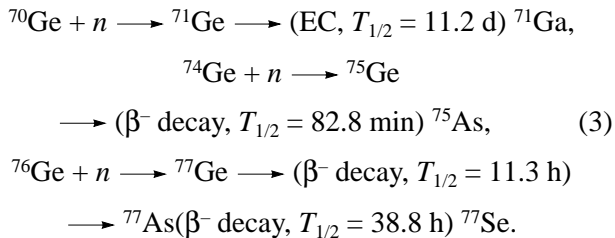
In this case, shallow Ga acceptors, shallow As donors, and deep double Se donors are created. In Eq. (3), EC stands for the K-electron capture. The other two germanium isotopes are transmuted into heavier stable germanium isotopes. Since the isotopes are uniformly distributed over the material and the slow-neutron capture cross sections for the Si and Ge isotopes are fairly small (for ^{70}Ge, ^{74}Ge, and ^{76}Ge, these cross sections are 3.25, 0.36, and 0.16, respectively [8]), one might expect a uniform distribution of the impurity produced in the process of NTD. The NTD method enables one to simultaneously incorporate donor and acceptor impurities into germanium; in this case, the relationship between their concentrations (the compensation ratio) is determined by the contents of different isotopes in the material. For example, neutron-transmutation-doped natural germanium is p type, with the compensation ratio being approximately 40% [3].

The materials mentioned above (Si, SiC, Ge) belong to Group IV of the periodic table and have qualitatively similar electronic band structures despite having many significant distinctions. Incorporation of Group-V impurities (such as nitrogen, phosphorus, arsenic) into these materials produces donor energy levels located near the bottom of the conduction band (shallow donor levels). Germanium, silicon, and silicon carbide are indirect-gap semiconductors; their conduction band consists of several valleys shifted from the center of the Brillouin zone. The character of this shift depends on the nature of the semiconductor. For example, in germanium, there are four equivalent valleys, shifted along the $\langle 111 \rangle$ directions, and in silicon, there are six valleys, shifted along the $\langle 100 \rangle$ directions. In silicon carbide, the character of the conduction band depends on the polytype. In the case of the multivalley conduction band, the shallow donor levels (which can be treated as those split off from the conduction band) are degenerate, with the degeneracy factor being equal to the number of valleys. For instance, the donor level in germanium is fourfold degenerate and split into a singlet and a triplet because of the interaction of the donor electron with the atomic core; in silicon, a sixfold degenerate donor level is split into a singlet, a doublet, and a triplet. In silicon carbide, the degeneracy and splitting depend on the polytype. For example, in the cubic polytype 3C-SiC, the situation is similar to that in silicon. In hexagonal polytypes, the situation is more complicated; in polytypes 4H- and 6H-SiC, the conduction bands are significantly different in character. The properties of electrons of shallow donors can be described in terms of the effective-mass theory developed in [13].

In this paper, we discuss the process of NTD of semiconducting germanium, silicon, and silicon carbide and potential applications of EPR for controlling this process. EPR is one of the most informative methods for detecting impurities (including nitrogen, phosphorus, and arsenic donor impurities) and intrinsic defects in semiconductors and for determining the electronic structure of these defects [14–19]. Therefore, EPR can be used to control impurity atoms created in the process of NTD. EPR also enables one to control radiation damage effects [14] which arise in the process of NTD, because a neutron flux contains not only thermal but also fast neutrons initiating various damage processes in the crystal. In order to optimize the process of NTD of semiconductors, it is important to monitor the defects and impurity centers and their transformation during annealing of the materials. The defects produced in a semiconductor under neutron irradiation shift the Fermi level to the middle of the band gap, with the consequence that the EPR spectra of donors cannot be observed. The type and concentration of radiation-induced defects depend on such parameters as the value of the neutron flux, the relationship between the fluxes of fast and slow neutrons, and the temperature of the semiconductor during neutron irradiation. The energy distribution of fast neutrons is also of importance. EPR can be very helpful in optimizing the process of NTD with the aim of minimizing the yield of radiation-induced defects that are characterized by high thermal stability and, hence, can be annealed only at high temperatures.

At sufficiently low temperatures, shallow donors are occupied by electrons; hence, EPR can be used to investigate such donors. The temperature at which a shallow donor can be detected depends on the ionization energy of the donor. For example, in crystalline germanium, the temperature must be less than 10 K; in silicon, less than 40 K; and in silicon carbide, less than

~40–100 K (depending on the polytype and the position of the donor center in the crystal).

According to the theory [13], only in a singlet state, the donor electron wave-function density at the donor nucleus site is isotropic; hence, only in this case exists isotropic hyperfine interaction between the unpaired electron and the magnetic moment of the donor impurity nucleus. EPR measurements showed that there is significant isotropic hyperfine interaction in shallow donors in germanium, silicon, and silicon carbide, and the conclusion has been drawn that the ground state in such donors is a singlet [15–17]. The experimentally observed hyperfine structure allowed one to unambiguously identify the type of donor impurities. It should be noted that in silicon carbide (except cubic 3*C*-SiC), the situation is more complicated than in germanium and silicon, because there are a few nonequivalent positions for donor centers in the crystal.

Using EPR spectra, one can obtain information on the degree of nonuniformity of the donor impurity distribution in the material, because the EPR spectra of isolated impurity atoms and of clusters consisting of two, three, or more atoms differ significantly. Since the NTD method is based on the presence of only one isotope ^{30}Si (in Si, SiC) or ^{74}Ge (in Ge), it is natural to use increased contents of the selected isotopes in order to increase the donor concentration. There is also another good reason to use crystals enriched in the ^{30}Si and ^{74}Ge isotopes for EPR measurements. The point is that, in such crystals, the EPR lines of shallow donors become significantly narrower; therefore, the intensity of the EPR signal increases in proportion to the ratio of the squares of the EPR line widths in the crystal with the natural isotopic composition and in the crystal enriched in the selected isotope. The increased intensity of EPR signals allows one to investigate very thin (e.g., ion-implanted) semiconductor layers.

The reason for the EPR lane narrowing is the decrease in the content of isotopes ^{29}Si (in Si, SiC) and ^{73}Ge (in Ge) with nonzero nuclear magnetic moments, because the EPR line widths of shallow donors in these crystals is determined chiefly by the superhyperfine interaction of the unpaired electron with the neighboring nuclei of odd isotopes ^{29}Si (in Si, SiC) and ^{73}Ge (in Ge). Let us discuss this issue in more detail. We assume that the EPR line width is determined by the unresolved superhyperfine structure, i.e., that the EPR line is inhomogeneously broadened, which is usually the case with shallow donors in germanium, silicon, and silicon carbide. Since the wave function of a shallow donor extends over a few coordination shells, a large number of the nuclei of isotopes ^{29}Si (in Si, SiC) and ^{73}Ge (in Ge) are involved in the hyperfine interaction. In SiC crystals, the ^{13}C nuclei should also be taken into account.

The probability P_m of finding m selected atoms (atoms of the selected isotope in the case under discussion) in a defect coordination shell consisting of n equivalent sites is given by

$$P_m = C_n^m f^m (1 - f)^{n-m}, \qquad (4)$$

where f is the relative concentration of the selected isotope. In natural germanium, silicon, and carbon, the contents of the ^{73}Ge, ^{29}Si, and ^{13}C isotopes are $f(^{73}\text{Ge}) = 0.078$, $f(^{29}\text{Si}) = 0.047$, and $f(^{13}\text{C}) = 0.011$, respectively.

The width ΔB of an EPR line with unresolved structure in the case where this width is determined by the superhyperfine interaction is given by

$$\Delta B = (8 \ln 2)^{1/2} \frac{1}{g \mu_\text{B}}$$

$$\times \left[\sum_i^R f(^N\text{X}) n_i(\text{X}) \frac{a_i^2(^N\text{X}) I(I+1)}{3} \right]^{1/2}, \qquad (5)$$

where ^{N}X stands for ^{73}Ge, ^{29}Si, or ^{13}C; n_i is the number of equivalent sites for atoms X in the ith coordination shell; a_i is the superhyperfine interaction constant for atoms ^{N}X located at equivalent sites in the ith coordination shell; g is the electronic g factor; μ_B is the Bohr magneton; and I is the nuclear spin for the ^{N}X isotope ($I = 9/2, 1/2, 1/2$ for isotopes ^{73}Ge, ^{29}Si, ^{13}C, respectively).

It follows from Eq. (5) that the concentration of an isotope with a nonzero nuclear spin significantly affects the EPR line width only if the superhyperfine interaction constant for this isotope is sufficiently large. Clearly, the superhyperfine interaction constants can be estimated only approximately from the EPR line width; the exact values of these constants have been found for a number of shallow donors in silicon [15, 18] and shallow nitrogen donors in silicon carbide [19] by using electron–nuclear double resonance.

Virtually any semiconductor can be doped using the NTD method. A nuclear reaction producing Ga can also be used for uniform donor doping of wide-band-gap semiconductors such as ZnO, which has attracted considerable recent attention because of its application potential in optoelectronics [20]; the corresponding reaction proceeds according to the equation ^{68}Zn $+ n \longrightarrow {}^{69}$Ge $\longrightarrow$ (β^- decay) ^{69}Ga.

In the ZnO crystal, gallium substitutes for zinc and is a donor impurity, whose EPR spectrum can easily be recorded.

All isotopes in semiconductors GaAs (^{68}Ga, ^{71}Ga, ^{75}As) and AlAs (^{27}Al) can be transmuted into shallow donors in the process of NTD; using the NTD method, one can fabricate isotopic superlattices consisting of layers with different properties.

It should be noted that the magnetic properties of nuclei and the corresponding atoms can differ radically

for the same element; for example, even and odd isotopes can have zero and nonzero nuclear spins and magnetic moments, respectively, or different nuclear spins, as in the case of hydrogen and deuterium. On the other hand, the nuclei and atoms of different elements, even those positioned in different corners of the periodic table, may have similar magnetic properties (e.g., hydrogen, fluorine, thallium). Thus, in specific cases, the EPR method offers significant advantages over the isotope mass spectroscopic methods, because the EPR spectra of different isotopes are determined by the superhyperfine interaction of the unpaired electrons with the nuclear magnetic moments and, hence, may be considerably different.

2. EXPERIMENTAL TECHNIQUE

Experiments were performed using a commercial Jeol EPR spectrometer operating at a frequency of 9.3 GHz (*X* band) with a custom-made helium gas flow cryostat, which enabled the temperature to be varied within the range 4–300 K. All EPR spectra presented in this paper are single scans (i.e., they were recorded without accumulation).

The germanium, silicon, and silicon carbide crystals investigated were cleaved or cut in the form of a plate with known crystallographic orientation. A sample mounted in the cavity of the EPR spectrometer could be rotated in certain planes. The crystals studied are characterized below.

3. EXPERIMENTAL RESULTS

3.1. Neutron Transmutation Doping of Germanium Enriched in Isotope ^{74}Ge

Germanium crystals were grown using the Czochralski method. Crystals enriched in the isotope ^{74}Ge were grown from a melt containing the selected isotope. Then, plates 1 mm thick were cut along the (111) plane. Samples were cut in the form of a rod with its length along the $\langle 110 \rangle$ direction. Mounted in the cavity of the EPR spectrometer, the samples could be rotated about the vertical $\langle 110 \rangle$ axis. The orientation of the samples was determined to within ~0.5° using x-ray diffraction. The isotopic composition of the samples and, for the sake of comparison, the isotopic composition of the natural germanium are listed in the table.

The germanium crystals were subjected to slow-neutron irradiation (the irradiation temperature was close to room temperature, the neutron flux was ~5×10^{16} cm^{-2}, the ratio between the thermal- and fast-neutron fluxes was equal to three) in order to transmute the ^{74}Ge isotopes into ^{75}As donors. The concentration of uncontrolled electrically active impurities before NTD was ~5×10^{13} cm^{-3}, which is much less than the concentration of donors and acceptors created in the process of NTD. In the natural germanium, only 9.8% of the captured slow neutrons bring about the creation of

^{75}As, whereas in the enriched germanium, this proportion was approximately 75%. Then, the samples were annealed in quartz ampoules at 460°C for 24 h in order to remove the radiation damage produced by fast neutrons. The concentration of arsenic donors was estimated from Hall effect measurements to be $N_D \cong 10^{16}$ cm^{-3} (the concentration of compensating shallow gallium acceptors was insignificant because of the low content of the isotope ^{70}Ge). Crystals from the same series were used previously for preliminary EPR measurements [21] and were fabricated by one of the authors of this paper (A.N.I.).

As indicated above, EPR of shallow donors in germanium should be studied at low temperatures. It is also of importance to minimize stresses in the crystal, which significantly broaden the EPR lines, with the result that EPR signals decrease and become less informative.

There are two dominant mechanisms of EPR line broadening of shallow donors in Ge. One of them is the spread of the electronic *g* factors caused by stresses in the crystal. This effect can be explained qualitatively as follows. The *g* factor of electrons occupying one of the four valleys of the conduction band of germanium is strongly anisotropic because of the anisotropy in the electronic effective mass. If the four valleys are filled by electrons to the same extent, the *g* factor will be isotropic and equal to $g = g_\parallel/3 + 2g_\perp/3 = 1.71$, where $g_\parallel = 0.98$ and $g_\perp = 2.07$ are theoretically calculated *g* factors for the magnetic field directed along the axis of the valley (the $\langle 111 \rangle$ direction) and perpendicular to this axis, respectively [16]. Due to stresses in the crystal, the valleys are filled differently, which causes a spread in the *g*-factor values and, hence, a broadening of the donor EPR lines. It was shown in [16] that this mechanism of EPR line broadening depends on the orientation of the crystal relative to the magnetic field and that the broadening vanishes to first order when the magnetic field is directed along the $\langle 100 \rangle$ axis; therefore, the axes of all four valleys make the same angle with the magnetic field direction. This effect is explained qualitatively by the fact that the relative fillings of the valleys are of no importance in this case, because the valleys are identically oriented relative to the magnetic field and, hence, are characterized by identical *g* factors. The second mechanism of EPR line broadening was already mentioned above and is associated with the hyperfine interaction of the unpaired electron with the nuclei of the germanium isotope ^{73}Ge. According to the effective-mass theory, the wave function of a donor in germanium is highly delocalized, because the binding energy is small, 9.2 meV (the Bohr radius is large, ~32 Å). Therefore, the donor electron will interact with a large number of germanium atoms whose nuclei have a nonzero magnetic moment. The interaction of the unpaired electron with the magnetic fields produced by these nuclei will be positive or negative depending on the ori-
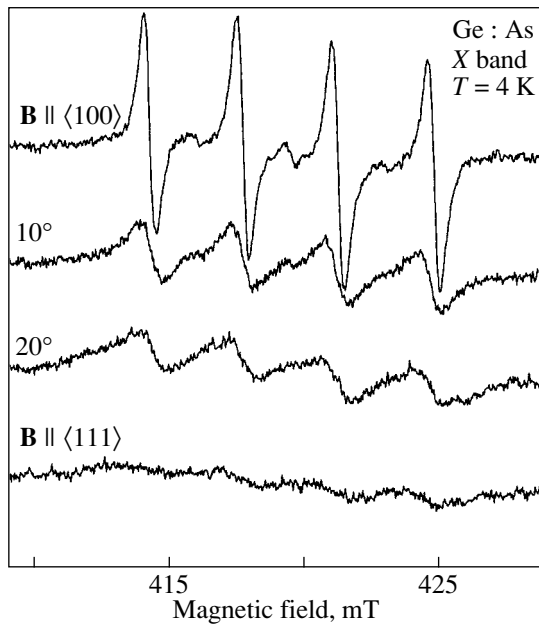
Fig. 1. EPR spectra of arsenic donors in a germanium crystal enriched in the isotope ^{74}Ge. The spectra were recorded at 4 K for four crystal orientations.

entation of the nuclear magnetic moment of ^{73}Ge (the number of possible orientations is equal to $2I + 1 = 10$ for each nucleus). Therefore, the EPR line will be broadened in accordance with Eq. (5). It follows from Eq. (5) that the EPR line can be made significantly narrower by decreasing the concentration of the germanium isotope ^{73}Ge. For example, for the ^{73}Ge content in the enriched germanium presented in the table, the EPR line becomes narrower by a factor of $(7.8/1)^{1/2} = 2.8$ according to Eq. (5); therefore, the EPR line intensity increases by almost an order of magnitude.

Figure 1 shows EPR spectra of arsenic donors in a germanium crystal enriched in the isotope ^{74}Ge; the spectra were recorded in the *X* band at 4 K for the following four crystal orientations: **B** ∥ $\langle 100 \rangle$, $\theta = 10°$, $20°$, and **B** ∥ $\langle 111 \rangle$, where θ is the angle between the magnetic-field direction and the $\langle 100 \rangle$ axis of the crystal, with the crystal being rotated in the {110} plane. The EPR lines are the narrowest for the orientation **B** ∥ $\langle 100 \rangle$ and become considerably broadened as the crystal deviates from this orientation. The EPR line width for arsenic donors in the germanium crystal enriched in the isotope ^{74}Ge is $\Delta B = 0.45$ mT, which is significantly smaller than that in the germanium crystal with natural isotopic composition ($\Delta B = 1.2$ mT). The experimental ratio between the EPR line widths of arsenic donors in the natural and enriched germanium crystals agrees with Eq. (5), which suggests that the inhomogeneous broadening of the EPR lines is due to the superhyperfine interaction with ^{73}Ge nuclei. Therefore, in this experiment, the EPR line broadening mechanism asso-

ciated with a spread of the *g* factors virtually does not operate in the case of the crystal orientation **B** ∥ $\langle 100 \rangle$.

The four strongest lines in the EPR spectrum can be described using the conventional spin Hamiltonian

$$\hat{H} = \mu_B \mathbf{B}\overset{\leftrightarrow}{\mathbf{g}}\mathbf{S} + \mathbf{S}\overset{\leftrightarrow}{\mathbf{A}}\mathbf{I} + \sum_{i=1}^{N} \mathbf{S}\overset{\leftrightarrow}{\mathbf{a}}_i\mathbf{I}_i, \qquad (6)$$

where the first term is the Zeeman energy of the impurity center (with spin $S = 1/2$ and the electronic *g* factor represented by the $\overset{\leftrightarrow}{\mathbf{g}}$ tensor) in a magnetic field **B**, the second term is the hyperfine interaction (described by the tensor $\overset{\leftrightarrow}{\mathbf{A}}$) between the unpaired electron of the shallow donor and a ^{75}As nucleus with spin $I = 3/2$, and the third term is the superhyperfine interaction (described by the tensor $\overset{\leftrightarrow}{\mathbf{a}}_i$) between the unpaired electron of the shallow donor and the nucleus of the *i*th atom of germanium ^{73}Ge. The hyperfine interaction constant and the *g* factor are isotropic to within the experimental error: $A = (26 \pm 0.5) \times 10^{-4}$ cm^{-1} (the average line splitting is 3.53 mT) and $g = 1.57$. The superhyperfine structure is not resolved and determines the EPR line widths. Thus, the EPR spectrum consisting of four lines of width 0.45 mT and of approximately the same intensity belongs to isolated arsenic donors. The experimental value of the *g* factor is close to its theoretical value indicated above.

In addition to the four EPR lines belonging to isolated arsenic donors, the EPR spectrum in Fig. 1 has a few weaker lines positioned between the four basic EPR lines and most clearly defined in the crystal orientation B ∥ $\langle 100 \rangle$, where the EPR line widths are minimum. These EPR signals belong to pairs and triplets of arsenic donors, whose formation is caused by the relatively strong isotropic exchange interaction arising between neighboring donors with overlapping wave functions. Earlier, this effect was observed for phosphorus [22–25] and arsenic [23, 26] shallow donors in silicon and arsenic donors in germanium [21], as well as for shallow nitrogen donors in silicon carbide [27–29]. A theoretical interpretation of the observed EPR spectra of exchange-coupled pairs was offered in [24].

The Hamiltonian of an exchange-coupled pair including the isotropic exchange interaction between two identical magnetic centers with spins $S_1 = S_2 = 1/2$ and the Zeeman interaction (without regard for the hyperfine and superhyperfine interactions) has the form

$$\hat{H} = J\mathbf{S}_1\mathbf{S}_2 + \mu_B \mathbf{B}\overset{\leftrightarrow}{\mathbf{g}}(\mathbf{S}_1 + \mathbf{S}_2), \qquad (7)$$

where J is the isotropic-exchange constant and $\overset{\leftrightarrow}{\mathbf{g}}$ is the *g* tensor of the dimer, which is equal to the *g* tensor of an isolated donor to within the experimental error. If $J \gg g\mu_B B$ (which is the case for pair centers in our experiments), the system can be conveniently described in terms of the total spin, equal to 0 or 1. For an isotro-

pic system with spin $S = 1$, the spin Hamiltonian is written as

$$\hat{H} = \mu_B \mathbf{B}\overset{\leftrightarrow}{\mathbf{g}}\mathbf{S} + \mathbf{S}\frac{\overset{\leftrightarrow}{\mathbf{A}}}{2}(\mathbf{I}_1 + \mathbf{I}_2) + \sum_{i=1}^{N} \mathbf{S}\frac{\overset{\leftrightarrow}{\mathbf{a}}_i}{2}\mathbf{I}_i, \qquad (8)$$

in this case, the hyperfine and superhyperfine constants become twice as small.

A similar Hamiltonian can be used for a cluster of three arsenic atoms with total electronic spin $S = 3/2$; the hyperfine and superhyperfine constants for isolated atoms will be three times as small in this case.

Figure 2a shows the EPR spectrum of arsenic donors in a germanium crystal enriched in the isotope [74]Ge; the spectrum was recorded in the X band at a frequency of approximately 9.3 GHz at 4 K. The crystal orientation corresponded to $\mathbf{B} \parallel \langle 100 \rangle$. An EPR spectrum calculated by means of the Win-EPR SimFonia computer code is presented at the bottom of Fig. 2a. In calculating the spectrum, it was assumed that the g factors and EPR line widths of isolated As donors, pair centers, and clusters of three atoms were identical and that the hyperfine interaction constants for pairs and triplets were smaller than that for isolated donors by a factor of two and three, respectively. The ratios of the total amplitudes of all EPR lines of isolated arsenic donors, pairs, and triplets were $1 : 0.12 : 0.04$. The same ratios will be observed for the integrated numbers of the corresponding impurity centers if one assumes that the EPR line widths of isolated donors and pairs are equal. The calculated EPR spectrum contains a noise component, which was added in order for this spectrum to resemble the experimental one more closely. Figure 2b shows EPR spectra calculated for isolated donors (1As), as well as for clusters of two (2As), three (3As), four (4As), and ten donor atoms (10As). The first three spectra with the corresponding intensity ratios were used to calculate the EPR spectrum presented in Fig. 2a.

In [21], EPR spectra were presented in which, in addition to the lines corresponding to pairs and triplets of arsenic atoms (whose percentages were approximately equal to those in our experiments), there was a relatively strong EPR line with an unresolved structure; the maximum and minimum of the derivative for that line corresponded approximately to the internal components of the EPR lines of isolated arsenic donors, and the integrated intensity of that line was equal to that of the EPR lines of isolated arsenic donors. The conclusion was made that the unresolved line belonged to weakly interacting donors, with the exchange interaction constant being of the order of the hyperfine interaction constant for isolated arsenic atoms, $J \sim A$. In our experiments, such a line was not observed. Furthermore, our calculations performed by means of the R-spectr computer code [30] for J ranging from 0 to ~100A showed that, in the case of $J \sim A$, the EPR spectrum is radically different and cannot be represented in
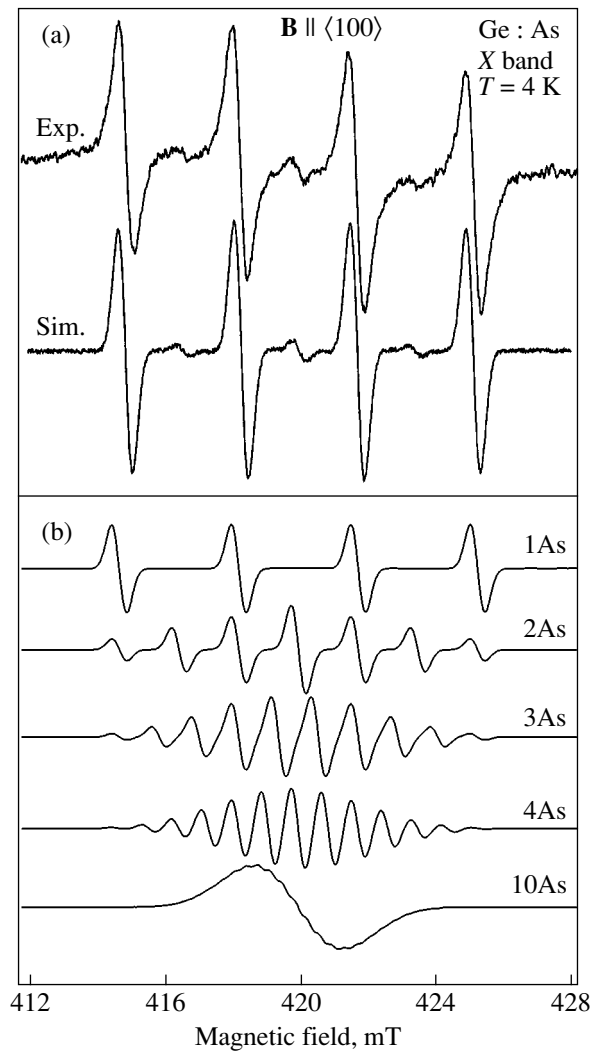
Fig. 2. (a) EPR spectrum of arsenic donors in a germanium crystal enriched in the isotope [74]Ge (see table); the spectrum was recorded at 4 K in the geometry $\mathbf{B} \parallel \langle 100 \rangle$. A calculated EPR spectrum is shown at the bottom. (b) Calculated EPR spectra of one As donor and of clusters of exchange-coupled two, three, four, and ten As donor atoms.

the form of the unresolved line presented in [21]. Such a line may belong to clusters n-As (with $n > 3$, Fig. 2b) of arsenic atoms strongly interacting via exchange interaction; therefore, we arrive at a conclusion opposite to that drawn in [21] as to the donor distribution in germanium. The EPR spectra consisting of seven lines with intensity ratios $1 : 2 : 3 : 4 : 3 : 2 : 1$ for donor pairs and the EPR spectra having ten lines with intensity ratios $1 : 3 : 6 : 9 : 12 : 12 : 9 : 6 : 3 : 1$ for donor triplets (Fig. 2b), which were used to calculate the EPR spectrum presented in Fig. 2a, appear only in the case of $J > $ ~50A. It is significant that as the exchange interaction is increased further, these spectra remain virtually unchanged and, therefore, have a well-defined structure. In the opposite case of $J < $ ~50A, the EPR spectrum changes radically with decreasing J down to val-

ues of $J < {\sim}0.1A$, which are less than the widths of separate EPR lines. As the value of J is decreased further, the EPR spectrum remains virtually unchanged and consists of four lines corresponding to isolated arsenic donors. Thus, EPR signals can be observed only in the cases of strong ($J > {\sim}50A$) and weak ($J < {\sim}0.1A$) exchange interactions. For intermediate values of J, the EPR spectrum depends on J and, when averaged over all possible values of J, represents a wide band with a complicated shape and low intensity that is difficult to detect; in addition, this band will blend into the wide background produced by stresses in the crystal. Thus, the only reliable data which should be used to characterize the actual donor distribution in germanium are the intensity ratios (presented above) of EPR signals from isolated donor centers, pairs, and triplets and the total donor concentration, determined, e.g., from electrical measurements.

The exchange interaction energy (J), causing the singlet and triplet energy levels to split, decreases exponentially with increasing separation between isolated impurity atoms. This energy can be estimated from the formula derived for the exchange interaction between two atoms in a hydrogen molecule. Of course, this formula should be modified with regard to the effective masses of identical hydrogen-like donor atoms in the ground state and to the dielectric constant of the semiconductor crystal. In [31], the exchange energy of two identical donor atoms in a semiconductor was found to be

$$ J = \left(\frac{m^*}{\varepsilon^2}\right) A_{\mathrm{H}} \exp\left[-B_{\mathrm{H}}\left(\frac{m}{\varepsilon}\right)^3 V\right], \tag{9} $$

where, for germanium, $m^* = 0.23 m_e$ is the average effective mass of a donor, $\varepsilon = 16$ is the dielectric constant of germanium, $A_{\mathrm{H}} = 9.66$ eV and $B_{\mathrm{H}} = 7.84 \times 10^{22}$ cm^{-3} are coefficients calculated for the hydrogen molecule, and $V = (4/3)\pi r^3$, with r being the separation between the interacting donor atoms. For germanium, we obtain $J = 0.0087 \exp(-2.33 \times 10^{17} V)$. For the exchange splittings $J = 50A = 1.62 \times 10^{-5}$ eV and $J = 0.1A = 0.324 \times 10^{-7}$ eV, the corresponding separations between the interacting donor atoms are found to be 185 and 235 Å, respectively.

Now, we estimate the concentrations of donors for which $r < 185$ Å and $r > 235$ Å in the case where the concentration of uncompensated donors is $N_D \cong 10^{16}$ cm^{-3} (this value was determined from the electrical measurements).

We assume that the impurity distribution is random and, following [31], use the Poisson distribution

$$ P(N) = (N!)^{-1} G^N \exp(-G), \tag{10} $$

where N is the number of events. The expected value G in this case is the number of donors $N_D V$ in the volume V. Let a donor atom be at the origin of coordinates.

Then, the probability that there will be no donors at distances less than r is found from Eq. (10) to be

$$ P(0, 0-r) = \exp\left[-\frac{4\pi N_D r^3}{3}\right]. \tag{11} $$

The probability of finding one donor atom in the shell of radius r and thickness dr (i.e., in the range from r to $r + dr$) is

$$ P(1, r-(r+dr)) = 4\pi r^2 N_D dr. \tag{12} $$

The product of the probabilities given by Eqs. (11) and (12) is the probability that there will be no donors at distances less than r and that there will be only one donor in the spherical shell of radius r and thickness dr; that is, this product is the probability that the separation between two donor atoms will be equal to r:

$$ dP = \exp\left[-\frac{4\pi r^3 N_D}{3}\right] 4\pi r^2 N_D dr. \tag{13} $$

Therefore, the concentration of donors separated by a distance less than a certain value R_0 (the case of strong exchange interaction between the members of a donor pair, $J > {\sim}50A$) is given by

$$ \begin{aligned} N(R_0) &= N_D \int_0^{R_0} \exp\left[-\frac{4\pi r^3 N_D}{3}\right] 4\pi r^2 N_D dr \\ &= N_D\left(1 - \exp\left[-\frac{4\pi R_0^3 N_D}{3}\right]\right). \end{aligned} \tag{14} $$

The concentration of donors separated by a distance larger than a certain value R_0 (the case of weak exchange interaction between virtually isolated donor atoms, $J < {\sim}0.1A$) can be found in the same way. In this case, integration is performed from R_0 to infinity.

The probability of finding three donor atoms in a sphere of radius r is equal to the probability that there will be one donor within the sphere of radius r and one donor within the spherical shell of radius r and thickness dr:

$$ dP(3) = \frac{4}{3}\pi N_D r^3 4\pi r^2 N_D dr \exp\left[-\frac{4\pi N_D r^3}{3}\right]. \tag{15} $$

It was shown in [31] that for a small volume $V < 1/N_D$, which is of interest for us in the case of strong exchange interactions, the ratio of the number of triplets to the number of pairs is approximately equal to $N_D V$, which corresponds to our experimental conditions, where $N_D \cong 10^{16}$ cm^{-3}. For this donor impurity concentration, the expressions derived above give the concentration ratios $1 : 0.3 : 0.08$ for isolated donors, pairs, and triplets, respectively. A comparison of these

ratios with the experimental data 1 : 0.12 : 0.04 presented above shows that, despite the crude model used, there is qualitative agreement. The results obtained indicate that the As donor distribution in a Ge crystal is fairly uniform. The agreement between the theoretical and experimental concentration ratios will become better if one assumes that the concentration of uncompensated donors is approximately 0.5×10^{16} cm^{-3}. This estimate is not unreasonable, because it is known [16] that for arsenic donor concentrations higher than approximately 10^{16} cm^{-3} (for phosphorus donors, this value is still lower) motion-induced EPR line narrowing occurs for arsenic donors and the hyperfine structure disappears. Since no motion effects on the EPR spectra were observed in our experiments, we can assume that the actual concentration N_D is lower than that estimated from the electrical measurements and is approximately 0.5×10^{16} cm^{-3}.

It should be noted that the observed EPR spectra can be associated not only with pairs and triplets formed by exchange-interacting donor atoms. Similar EPR spectra can arise when ionized arsenic donors are located near nonionized ones, for example, in the case where two or three closely spaced arsenic donors have a common, single, unpaired electron and form a cluster with spin $S = 1/2$. Such impurity centers are very likely to exist in partially compensated semiconductors, where a proportion of the donors is compensated, e.g., by radiation-induced defects or acceptor impurities.

We also note that EPR has been very rarely used to study defects in germanium, in contrast to those in silicon. This does not mean that the quantity of defects produced under irradiation is smaller in the former case; rather, the reason is that the EPR spectra in germanium are more difficult to interpret because of the large line widths, and therefore low temperatures should be used. Thus, it is not improbable that complex centers, such as a vacancy plus arsenic or phosphorus donor, which were studied comprehensively in silicon, can also form in germanium.

3.2. Neutron Transmutation Doping of Silicon

In the process of NTD, the isotope ^{30}Si (3.1%) is transmuted into phosphorus in accordance with Eq. (2). Figure 3 shows EPR spectra recorded in the X band for a silicon crystal irradiated with neutrons to a dose of 10^{18} cm^{-2}. Spectra 1 and 2 were recorded before annealing, and spectrum 3, after annealing at 800°C for 30 min. Spectra 1 and 2 were measured at 35 K in a magnetic field parallel to the $\langle 111 \rangle$ and $\langle 100 \rangle$ axes, respectively; spectrum 3 was measured at 15 K in a magnetic field parallel to the $\langle 111 \rangle$ axis. Before the NTD, the crystal was p type due to a small boron content (~10^{13} cm^{-3}); the oxygen content was less than $<5 \times 10^{16}$ cm^{-3}. The EPR spectrum of isolated phosphorus donors was observed only after annealing and consisted of two isotropic lines resulting from the hyper-
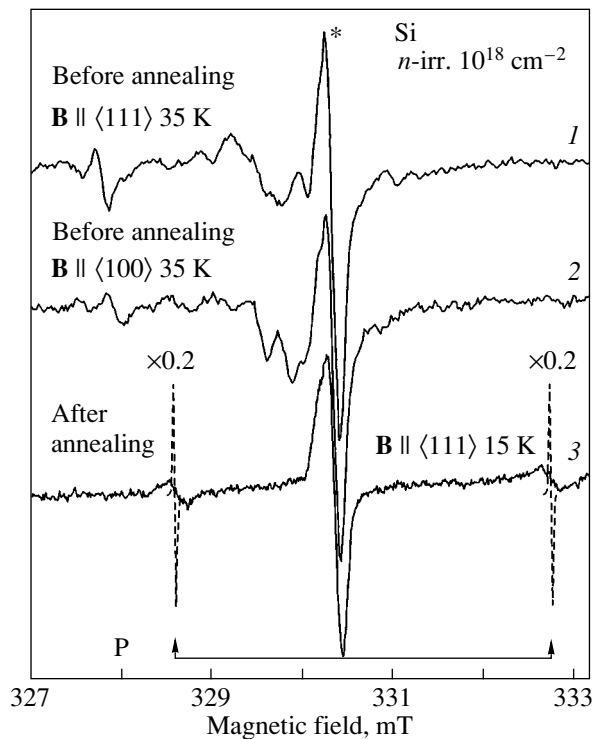
Fig. 3. EPR spectra for silicon crystals irradiated with neutrons to a dose of ~10^{18} cm^{-2}. Spectra 1 and 2 were recorded at 35 K before annealing for two different crystal orientations, and spectrum 3 was recorded at 15 K after annealing at 800°C for 30 min. The EPR line belonging to surface defects in silicon is marked by an asterisk. Dashed lines represent a calculated EPR spectrum of phosphorus donors in a silicon crystal enriched in the isotope ^{30}Si (the ^{29}Si content is ~0.1%).

fine interaction of the unpaired electron with the phosphorus nucleus ($I = 1/2$); therefore, in the process of NTD, the semiconductor changed to n type. The EPR spectra taken before annealing contain anisotropic bands of radiation-induced defects, whereas the lines of phosphorus are absent because the phosphorus donors were ionized. The EPR spectra of radiation-induced defects were not analyzed in this work; these spectra can be interpreted using the results of numerous studies [14]. The strong isotropic line at the center of the EPR spectra in Fig. 3 marked by an asterisk belongs to surface defects and will not be discussed in this paper, because this line does not overlap with the EPR signals of interest to us here. Dashed lines in Fig. 3 indicate the EPR signal from phosphorus donors in a silicon crystal depleted in the isotope ^{29}Si (0.1%) and possessing a nonzero nuclear magnetic moment. This signal in the case where the ^{29}Si content is equal to 0.1% is approximately seven times narrower, and, hence, the intensity of this EPR signal from the phosphorus donors is approximately 50 times higher (in proportion to the ratio of the line widths squared) than in the case of the natural silicon with the same phosphorus donor con-
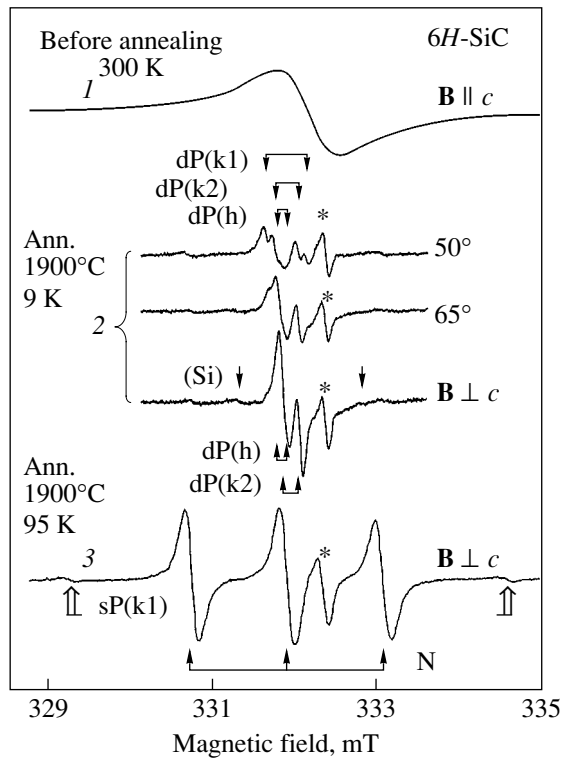
Fig. 4. EPR spectra of a *6H*-SiC crystal ($N_D \approx 5 \times 10^{16}$ cm^{-3}) irradiated with neutrons to a dose of ~10^{20} cm^{-2} at 90°C. Spectrum *1* was recorded at 300 K in the geometry **B** ‖ *c* before annealing, spectrum *2* was recorded at 9 K for three crystal orientations after annealing, and spectrum *3* was recorded at 95 K in the geometry **B** ⊥ *c* after crystal annealing. The triplet belonging to shallow nitrogen donors in the two quasi-cubic positions is indicated by arrows, and the EPR lines of shallow sP(k1) phosphorus donors are indicated by open arrows. Spectrum *1* was recorded with an effective amplification (including the decrease in the modulation amplitude) approximately 10^5 times lower than those for spectra *2* and *3*. The reference signals from quartz are marked by asterisks.

centration. The increase in the intensity of the EPR signal is of importance, because in the process of NTD of silicon the doping level increases considerably if the initial material is enriched in the ^{30}Si isotope and, hence, depleted in the ^{29}Si isotope. This increase in the EPR intensity can be helpful in studying thin silicon films enriched in the isotope ^{30}Si and doped with phosphorus by using NTD.

3.3. Neutron Transmutation Doping of Silicon Carbide

In contrast to crystals of germanium and silicon, in which shallow arsenic and phosphorus donors have been well studied using EPR, the situation with silicon carbide is less well understood. In 6*H*-SiC crystals irradiated with slow neutrons to a dose of 10^{20} cm^{-2} and then annealed at temperatures of the order of 2000°C, it has been found that there are two different types of EPR

spectra of phosphorus; these spectra were observed only at relatively high (77 K) [9] or low temperatures (4–10 K) [10]. The conclusion was made that these types of EPR spectra belong to different shallow phosphorus donors. Later, it was proposed [32] that the occupied energy levels of shallow phosphorus impurities are different at low and high temperatures (because of the multivalley character of the conduction band) and, hence, the EPR spectra are also different. In comparison with nitrogen donors, the sequential order of the energy levels is reversed in this case; that is, the singlet energy level of phosphorus donors corresponding to the EPR spectra observed in [9] is an excited level. Thus, until recently, there was no consensus on the EPR spectra of shallow phosphorus donors. In a recent work [33], it was shown that there are two types of phosphorus impurities, namely, shallow (sP) and deep (dP) P donors; both impurity types were observed experimentally at the same temperature (4.2 K). Therefore, it was proved in [33] that the EPR spectra under discussion belong to different impurity centers. For one of the two types of impurity centers, it was also shown that there is fairly strong superhyperfine interaction with ligand silicon atoms, which is characteristic of deep impurity centers. In addition, it was found that, for each of the two impurity types, three different EPR bands exist corresponding to three nonequivalent positions of the impurity in the crystal lattice of the polytype 6*H*-SiC: one with hexagonal symmetry [sP(h), dP(h) centers] and two with quasi-cubic symmetry [sP(k1), sP(k2), dP(k1), dP(k2) centers]. Two models were proposed in [33] for shallow and deep phosphorus impurities. According to those models, a shallow phosphorus impurity atom is positioned at a silicon site with a regular environment, whereas a deep phosphorus impurity is located at a silicon site adjacent to a carbon vacancy. In this paper, we assume that the shallow and deep phosphorus impurities substitute for carbon and silicon atoms, respectively, and that in the latter case, the phosphorus atom is displaced from the silicon site, much as the nitrogen atom is displaced in silicon, which brings about the formation of a deeper impurity center. Such an off-center displacement may also be responsible for the enhanced superhyperfine interaction with the nearest neighbor silicon atoms observed in [33].

Figure 4 presents the EPR spectrum of a 6*H*-SiC crystal irradiated with neutrons to a dose of ~10^{20} cm^{-2}. Before the irradiation, the crystal was *n* type with a nitrogen donor concentration of ~5×10^{16} cm^{-3}. Spectrum *1* was taken in the geometry **B** ‖ *c* at 300 K before annealing; this spectrum has a very strong isotropic line with an unresolved structure, which belongs to silicon vacancies of a high concentration. Here, we do not discuss these defects, even though their nature has been fairly well studied. After annealing at a temperature below 1800°C, the EPR spectra of numerous defects were observed, including multivacancy complexes. Spectra *2* and *3* were recorded after annealing of the crystals at 1900°C for 30 min. Spectra *2* were taken at

9 K for three values of the angle between the magnetic field and the *c* axis: 50°, 65°, and 90° (**B** ⊥ *c*). Spectrum *3* was recorded at 95 K for the annealed crystal in the geometry **B** ⊥ *c*. The triplet belonging to shallow nitrogen donors in the quasi-cubic positions is indicated in Fig. 4 by arrows, and the EPR lines of shallow sP(k1) phosphorus donors are indicated by open arrows.

Spectra *2* in Fig. 4, recorded at a low temperature, can be described using the spin Hamiltonian (6) and belong to the three different positions of the deep phosphorus centers characterized by the following parameters [33]: $g_\parallel = 2.0044$, $g_\perp = 2.0027$, $A_\parallel(P) = 1.0$ G, $A_\perp(P) < 1.0$ G, and $a(Si) = 11.2$ G for dP(h); $g_\parallel = 2.0037$, $g_\perp = 2.0025$, $A_\parallel(P) = 6.2$ G, $A_\perp(P) < 3.8$ G, and $a(Si) = 8.8$ G for dP(k1); and $g_\parallel = 2.0037$, $g_\perp = 2.0024$, $A_\parallel(P) = 4.8$ G, $A_\perp(P) < 1.9$ G, and $a(Si) = 7.6$ G for dP(k2). It should be noted that the relative intensities of the EPR spectra of the different dP centers depend significantly on the crystal orientation; for this reason, the relative contributions from these centers to spectra *2* in Fig. 4, recorded for three crystal orientations, are different. The superhyperfine structure resulting from the interaction with Si (presumably, with two Si atoms) is also indicated by arrows. The reference signals from quartz are marked by asterisks.

Signals from shallow phosphorus donors were not observed at low temperatures because of saturation (in [33], such signals were observed at 4.2 K under special rapid-sweep conditions). At 95 K, only EPR spectra of sP(k1) centers were observed (spectrum *3* in Fig. 4), because the other sP centers were ionized. The EPR spectra of shallow phosphorus donors occupying different positions are characterized by the following parameters [33]: $g_\parallel = 2.0041$, $g_\perp = 2.0022$, $A_\parallel(P) = 9.0$ G, and $A_\perp(P) = 7.2$ G for sP(h); $g_\parallel = 2.00375$, $g_\perp = 2.00276$, $A_\parallel(P) = 55.0$ G, and $A_\perp(P) = 54.2$ G for sP(k1); and $g_\parallel = 2.0038$, $g_\perp = 2.0025$, $A_\parallel(P) = 51.0$ G, and $A_\perp(P) = 51.0$ G for sP(k2).

The EPR spectra of phosphorus donors exhibit no effects from interaction between donors, because the donor concentrations are low and, in addition, the Bohr radius of shallow donors in silicon carbide is small in comparison with those in silicon and germanium crystals. However, at sufficiently high nitrogen donor concentrations, EPR spectra of pairs and triplets were observed in these crystals [27–29]. It is believed that the exchange interaction between donors gives rise to antiferromagnetic ordering, i.e., that the ground state is a nonparamagnetic singlet. This conclusion is supported by the temperature dependences of EPR spectra. The theory based on the hydrogen molecule model also predicts antiferromagnetic ordering. In this work, using numerous 6*H*-SiC samples (including commercial CREE *n*-type substrates and samples subjected to heavy neutron irradiation followed by annealing at temperatures up to 2400°C), the EPR intensity of nitrogen pair centers was observed to decrease and finally vanish with increasing temperature of observation, which is
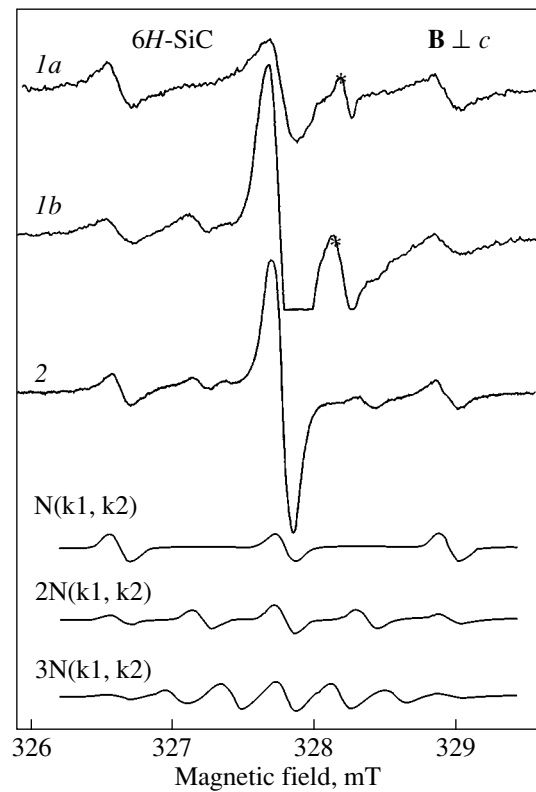
Fig. 5. EPR spectra of a CREE *n*-type 6*H*-SiC crystal recorded in the geometry **B** ⊥ *c* at (*1a*) 80 and (*1b*) 10 K and (*2*) an EPR spectrum (recorded in the geometry **B** ⊥ *c* at 10 K) of an *n*-type 6*H*-SiC crystal ($N_D \approx 5 \times 10^{17}$ cm^{-3}) subjected to neutron irradiation to a dose of ~10^{20} cm^{-2} followed by annealing at 2400°C. Calculated EPR spectra of one donor and clusters of exchange-coupled two and three N donors are shown at the bottom. Spectra *1a* and *1b* contain a reference signal from quartz marked by an asterisk.

inconsistent with antiferromagnetic spin ordering of interacting donors. [We note, however, that for small exchange splittings (less than 1 cm^{-1}) temperatures lower than 4.2 K should be used to detect changes in the population of the singlet and triplet levels.] The initial EPR intensity of nitrogen pairs was comparable to and even in excess of the EPR intensity of isolated nitrogen donors. Figure 5 shows EPR spectra recorded in the *X* band for a 6*H*-SiC crystal in the geometry **B** ⊥ *c*. Spectra *1a* and *1b* were measured on an *n*-type CREE crystal at 80 and 10 K, respectively; spectrum *2* was recorded at 10 K for an *n*-type 6*H*-SiC crystal ($N_D \approx 5 \times 10^{17}$ cm^{-3}) irradiated with neutrons to a dose of ~10^{20} cm^{-2} and then annealed at 2400°C. Calculated EPR spectra of one N donor and clusters of exchange-coupled two and three N donors are presented at the bottom of Fig. 5. In calculating these spectra, the hyperfine interaction constant averaged over the two nonequivalent quasi-cubic positions was used. As the temperature is increased, the EPR signals from pairs and triplets of N donors

decrease in intensity and finally vanish (at ~50 K), whereas the signals from isolated impurity centers are well pronounced. The EPR spectrum of nitrogen pairs consists of five lines with intensity ratios of 1 : 2 : 3 : 2 : 1. We note that the central (strongest) line of impurity pairs is superimposed on one of the three EPR lines of isolated nitrogen donors ($I = 1$); therefore, the EPR intensity of impurity pairs can be judged only from the intensity of the side lines, in contrast to the case of As donor pairs in Ge, where the central line of impurity pairs is located between EPR lines of isolated donors. Calculations of the EPR spectra for different values of the exchange interaction constant showed that the shape of side lines of impurity pairs ceases to vary with increasing J when $J > \sim 20A$ (the analogous condition for the central line of impurity pairs is more restrictive, $J > \sim 50A$). In the case of weak exchange interactions, the condition for the EPR spectra of isolated nitrogen donors being observable remains unchanged and is $J < \sim 0.1A$. It should be noted that the central lines of isolated N donors and their clusters coincide, with the consequence that the central line is the strongest. In spectra *1a* and *1b* in Fig. 5, the reference signals from quartz are marked by asterisks.

The relative intensities of the EPR signals from nitrogen donor pairs and isolated nitrogen donors in Fig. 5 are significantly different from those presented in [27, 29]. Furthermore, the intensities of the three EPR lines of isolated donors are approximately equal, which suggests, in accordance with the data from [27], that the concentration of isolated nitrogen donors is relatively low. Therefore, the strong signals from donor pairs cannot be explained in terms of the statistical distributions presented above. Thus, it is likely that the nitrogen impurity distribution in the SiC crystal is highly non-uniform and there is a mechanism (operative, probably, in the process of annealing) through which nitrogen clusters are created. Furthermore, antiferromagnetic ordering cannot arise in this case and the ground state is paramagnetic. Such a reversed sequential order of the energy levels may be due to the adjacent nitrogen atoms being close to the impurity, with the consequence that the spin state of the complex follows the Hund rules rather than being similar to the spin state of the hydrogen molecule. Another conceivable reason may be the presence of clusters of two or three nitrogen atoms having one common unpaired electron (ionized nitrogen molecules). In this case, the impurity state is paramagnetic and the temperature quenching of EPR signals is due to ionization.

In this work, we did not study SiC crystals with a changed isotopic composition. However, it is clear that crystals enriched in the isotope ^{30}Si should be used to increase the P donor doping level. Estimates show that in this case the intensity of EPR signals increases significantly because of the EPR line narrowing.

REFERENCES

1. J. W. Cleland, K. Lakr-Horovitz, and J. C. Pigg, Phys. Rev. **78** (6), 814 (1950).
2. H. Fritzsche and M. Cuevas, Phys. Rev. **119** (4), 1238 (1960).
3. *Neutron Transmutation Doping in Semiconductors*, Ed. by J. M. Meese (Plenum, New York, 1979).
4. A. A. Berezin, J. Phys. Chem. Solids **50**, 5 (1989).
5. E. E. Haller, Solid State Phenom. **32–33**, 11 (1993).
6. I. Shlimak, A. N. Ionov, R. Rentzsch, and J. M. Lazebnik, Semicond. Sci. Technol. **11**, 1826 (1996).
7. E. V. Haas and M. S. Schnoller, IEEE Trans. Electron Devices **23**, 803 (1976).
8. *Table of Isotopes*, 7th ed., Ed. by C. M. Lederer and V. S. Shirley (Wiley, New York, 1978).
9. A. I. Veĭnger, A. G. Zabrodskiĭ, G. A. Lomakina, and E. N. Mokhov, Fiz. Tverd. Tela (Leningrad) **28** (6), 1659 (1986) [Sov. Phys. Solid State **28**, 917 (1986)].
10. E. N. Kalabukhova, S. N. Lukin, and E. N. Mokhov, Fiz. Tverd. Tela (St. Petersburg) **35** (3), 703 (1993) [Phys. Solid State **35**, 361 (1993)].
11. H. Heissenstein, C. Peppermueller, and R. Helbig, J. Appl. Phys. **83** (12), 7542 (1998).
12. M. A. Capano, J. A. Cooper, Jr., M. R. Melloch, *et al.*, J. Appl. Phys. **87** (12), 8773 (2000).
13. W. Kohn and J. M. Luttinger, Phys. Rev. **98** (4), 915 (1955).
14. G. D. Watkins, in *Point Defects in Solids*, Ed. by J. H. Crowford and L. M. Slifkin (Plenum, New York, 1975), Vol. 2, pp. 333–392; G. D. Watkins, in *Deep Centers in Semiconductors*, Ed. by S. T. Pantelides (Gordon and Breach, New York, 1986), pp. 147–183.
15. G. Feher, Phys. Rev. **114** (5), 1219 (1959).
16. D. K. Wilson, Phys. Rev. A **134** (1), 265 (1964).
17. H. H. Woodbury and G. W. Ludwig, Phys. Rev. **124** (4), 1083 (1961).
18. J. L. Ivey and R. L. Mieher, Phys. Rev. B **11** (2), 849 (1975).
19. A. V. Duijn-Arnold, R. Zondervan, J. Schmidt, *et al.*, Phys. Rev. B **64**, 085206 (2001).
20. F. Leiter, H. Zhou, F. Henecker, *et al.*, Physica B (Amsterdam) **308–310**, 908 (2001).
21. V. S. Weiner, Mater. Sci. Forum **83–87**, 297 (1992).
22. R. C. Fletcher, W. A. Yager, G. L. Pearson, and F. R. Merritt, Phys. Rev. **95** (3), 844 (1954).
23. G. Feher, R. C. Fletcher, and E. A. Gere, Phys. Rev. **100** (6), 1784 (1955).
24. C. P. Slichter, Phys. Rev. **99** (2), 479 (1955).

25. D. Jerome and J. M. Winter, Phys. Rev. A **134** (4), 1001 (1964).

26. B. G. Zhurkin and N. A. Penin, Fiz. Tverd. Tela (Leningrad) **6** (4), 1141 (1964) [Sov. Phys. Solid State **6**, 879 (1964)].

27. A. I. Veĭnger, Fiz. Tekh. Poluprovodn. (Leningrad) **1** (1), 20 (1967) [Sov. Phys. Semicond. **1**, 14 (1967)].

28. I. M. Zaritskiĭ, L. A. Shul'man, and I. N. Geĭfman, Fiz. Tverd. Tela (Leningrad) **11** (1), 30 (1969) [Sov. Phys. Solid State **11**, 22 (1969)].

29. C. F. Young, K. Xie, E. H. Poindexter, *et al.*, Appl. Phys. Lett. **70** (14), 1858 (1997).

30. V. G. Grachev, Zh. Éksp. Teor. Fiz. **92** (5), 1834 (1987) [Sov. Phys. JETP **65**, 1029 (1987)].

31. E. Sonder and H. C. Schweinler, Phys. Rev. **117** (5), 1216 (1960).

32. S. Greulich-Weber, Phys. Status Solidi A **162** (1), 95 (1997).

33. P. G. Baranov, I. V. Ilyin, E. N. Mokhov, *et al.*, Phys. Rev. B **66**, 165 206 (2002).

Translated by Yu. Epifanov

Specific Features of Electron Transitions in Almost Ferromagnetic Semiconductors (with Reference to FeSi)

K. A. Shumikhina, A. G. Volkov, and A. A. Povzner

Ural State Technical University, ul. Mira 19, Yekaterinburg, 620002 Russia
e-mail: fka@kf.ustu.ru
Received October 24, 2002

Abstract—In the context of spin-fluctuation theory, the possibility of formation of Anderson localized states caused by a strong scattering of electrons by spin density fluctuations in almost ferromagnetic semiconductors is considered. The results are applied to FeSi. © *2003 MAIK "Nauka/Interperiodica".*

1. Magnetic semiconductors based on transition- and rare-earth-metal compounds undergo electron insulator–metal transitions which manifest themselves differently in various substances and are characterized by features whose nature remains unclear. The observed correlation between magnetic and electrical properties undoubtedly attracts interest of both experimentalists and theoreticians in such compounds. Nevertheless, despite the numerous approaches proposed to explain this phenomenon, there is still no adequate commonly accepted theory.

For example, in ferromagnetic semiconductors based on lanthanum manganites with the perovskite structure, the transition from the metallic to semiconducting state occurs as the temperature is increased. This phase transition takes place in a ferromagnetic phase, and its temperature virtually coincides with the Curie temperature T_C. Further, this transition is accompanied by an abrupt change in the transport and optical properties. In [1], it was shown that the relevant effects observed in lanthanum manganites cannot be associated with the specific features of these compounds (Jahn–Teller effect, double exchange), since in ferromagnetic semiconductors with similar properties, such as EuO, EuS, and $CdCr_2Se_4$, these features are absent. For the description of the properties of lanthanum manganites, a phase-separation model was suggested in [1, 2], from which it follows that an increase in temperature results in the creation of a magnetically nonuniform state, because the ferromagnetic order near impurity centers is destroyed to a lesser degree than in the remainder of the crystal. As a result, spatial fluctuations of magnetization occur and grow with temperature (only below the Curie temperature), which enhances the conduction electron scattering and, consequently, causes an abrupt nonmonotonic change in conductivity and in other electrical properties. In [3], it was suggested that, in compositionally homogeneous ferromagnetic semiconductors, strong scattering and even Anderson localization of the charge carriers can be caused by thermodynamic magnetic fluctuations growing with temperature. This idea is supported by the relationship between the squared magnetization and activation energy of charge carriers established from the temperature dependence of resistivity for these compounds. This relationship made it possible to quantitatively describe the metal–insulator transition in heavily doped ferromagnetic semiconductors based on lanthanum manganites [3].

Although the existing models of electron transitions [1–3] are applicable only to ferromagnetic semiconductors with localized magnetic moments (LMMs), similar transitions are also observed in almost ferromagnetic semiconductors, e.g., in FeSi [4] and $Fe_{1-x}Co_xSi$, $x \ll 0.05$. These compounds have low magnitudes of magnetization per site $M_0(0)$ near absolute zero. The characteristic feature of such compounds is an increase in the LMM amplitude with temperature and its subsequent saturation. As shown in [5], below the temperature of LMM saturation, transverse fluctuations of spin density (fluctuations of direction) are not dominant (as in ferromagnetic semiconductors based on transition- and rare-earth-metal compounds); in parallel with transverse fluctuations, there exist longitudinal fluctuations caused by the temperature variation of the modulus of LMMs. According to [6], the fluctuations cause renormalization of the electronic spectrum and its transformation with temperature. For example, it was shown in [7] that, in the almost ferromagnetic semiconductor FeSi, this renormalization results in the reduction of the band gap and its subsequent disappearance. In [5–7], it was admitted that in weak itinerant magnets there exist large, transverse and longitudinal, dynamic *d*-electron spin density fluctuations that grow with temperature and are not caused by the compositional inhomogeneity of magnetic semiconductors. However, the issue of the scattering of electrons by these fluctuations and the possibility of the Anderson localization was not considered in those papers.

2. To analyze the scattering of strongly correlated electrons by their spin and charge fluctuations, we invoke the Hubbard model with the Hamiltonian in the form

$$H = H_0 + H_U, \qquad (1)$$

where

$$H_0 = \sum_{\mathbf{k}, \sigma} \varepsilon_{\mathbf{k}} a^+_{\mathbf{k}, \sigma} a_{\mathbf{k}, \sigma} \qquad (2)$$

is the Hamiltonian of noninteracting d electrons;

$$H_U = U \sum_{\mathbf{v}} N_{\mathbf{v}, \uparrow} N_{\mathbf{v}, \downarrow} \qquad (3)$$

is the Hamiltonian of interatomic Habbard repulsion of d electrons, which can be expressed in terms of the Fourier transforms of the operators of charge and spin densities (see, e.g., [5])

$$H_U = U \sum_{\mathbf{q}} \left| S_{\mathbf{q}}^{(z)} \right|^2 - U \sum_{\mathbf{q}} \left| N_{\mathbf{q}}/2 \right|^2, \qquad (4)$$

$\varepsilon_{\mathbf{k}}$ are the one-electron band energies; $a^+_{\mathbf{k}, \sigma}$ ($a_{\mathbf{k}, \sigma}$) is the operator of creation (annihilation) of a d electron with a quasi-momentum $\mathbf{k}$ and spin σ; U is the parameter of interatomic Coulomb repulsion of d electrons; $N_{\mathbf{q}} = \sum_{\sigma} N_{\mathbf{q}, \sigma}$, $N_{\mathbf{q}, \sigma} = \sum_{\mathbf{k}} a^+_{\mathbf{k}, \sigma} a_{\mathbf{k} + \mathbf{q}, \sigma}$ is the Fuurier transform of the number density operator of d electrons at a site with spin σ; $\mathbf{q}$ is the quasi-momentum; and $S_{\mathbf{q}}^{(z)} = \sum_{\sigma} \sigma N_{\mathbf{q}, \sigma}$ is the Fourier transform of the operator of the spin-density vector projection of d electrons at a site on the quantization axis.

Calculation of the partition function of a system of strongly correlated electrons is a complicated many-body problem. One of possible methods of solving it is based on the use of the Stratonovich–Hubbard transformation [5]

$$\exp(a^2) = \pi^{-1/2} \int dx \exp(-x^2 + ax),$$

where a is an arbitrary real operator. The integration variable can be considered to be a random quantity, which fluctuates according to a Gaussian distribution. Thus, the Stratonovich–Hubbard transformation allows one to reduce the many-body problem of the motion of interacting electrons to the one-particle problem of the motion of a free electron in the field of a random potential.

Taking into consideration the well-known definition of the partition function

$$Z = \mathrm{Sp}\, T_\tau \exp\left\{ -\int_0^\beta H(\tau) d\tau \right\} \qquad (5)$$

[where $Y(\tau)$ is the Hamiltonian (1) in the Matsubara interaction representation, $\beta = 1/T$ and applying the Stratonovich–Hubbard transformation to the partition function (5), we obtain

$$Z = \iint \exp\left[-\sum_{\mathbf{v}} |V_{\mathbf{v}, \sigma}|^2 / UT \right] Z(V)(d\xi d\eta). \qquad (6)$$

Here, $Z(V) = \mathrm{Sp}\, T_\tau \{ \exp[-\beta H(V)] \}$ is the partition function describing the motion of electrons in the field of one of the configurations of a random potential with the effective Hamiltonian

$$H(V) = \sum_{k, \sigma} \varepsilon_k a^+_{k, \sigma} a_{k, \sigma} - \sum_{\mathbf{v}, \sigma} V_{\mathbf{v}, \sigma} N_{\mathbf{v}, \sigma}, \qquad (6a)$$

in which $V_{\mathbf{v}, \sigma}$ is the random interaction potential of an electron with inner exchange field ξ and charge field η,

$$V_{\mathbf{v}, \sigma} = \sum_q e^{iq\mathbf{v}} (C_q \xi_q^z \sigma + i C_q \eta_q/2), \qquad (7)$$

$\xi_q = \xi_q^{(1)} + i\xi_q^{(2)}(1 - \delta_{q, 0})$, $\eta_q = \eta_q^{(1)} + i\eta_q^{(2)}(1 - \delta_{q, 0})$, $q = (\mathbf{q}, \omega_{2n})$, ω_{2n} is the Matsubara boson frequency,

$$(d\xi d\eta) = (d\xi_0^{(1)} d\eta_0^{(1)}/\pi) \prod_{q \neq 0, j = 1, 2} (d\xi_q^{(j)} d\eta_q^{(j)}/\pi^{1/2}),$$

$$C_q = (UT)^{1/2}, \quad \mathbf{v} = (\mathbf{v}; \tau);$$

$$\sum_{\mathbf{v}} (...) = \sum_{\mathbf{v}} T \int_0^\beta (...) d\tau,$$

$$\sum_q (...) = \sum_{\mathbf{q}} \sum_{\omega_n} (...),$$

$a^+_{k, \sigma}$ and $a_{k, \sigma}$ are the Fourie transforms of the operators of creation ($a^+_{\mathbf{v}, \sigma}$) and annihilation ($a_{\mathbf{v}, \sigma}$) (in the Matsubara interaction representation) of d electrons with spin σ at site $\mathbf{v}$, $k = (\mathbf{k}, \omega_{2n+1})$, ω_{2n+1} is the Matsubara fermion frequency, and $N_{\mathbf{v}, \sigma} = a^+_{\mathbf{v}, \sigma} a_{\mathbf{v}, \sigma}$ is the particle number operator at site $\mathbf{v}$ in the Matsubara interaction representation.

The Hamiltonian (6a) is similar to the Hamiltonian of the random model alloy with "vertical" disorder considered by Anderson in [8] but differs from the latter in that the depth $V_{\mathbf{v}, \sigma}$ of periodically located potential wells varies randomly not only in space (as assumed in [8, 9]) but also in time. In addition, the random potential $V_{\mathbf{v}, \sigma}$ (in which field an electron is moving) depends on spin. However, these distinctions do not affect the key conclusion (following from the solution of the problem of the motion of an electron in potential wells

with vertical disorder) that the Anderson localization of electrons is possible.

As shown in [10], in the context of the present approach and in the uniform local field approximation [11], the one-electron Green function has the form

$$G_{k,\sigma} = \langle G_{k,\sigma}(V) \rangle, \quad (8)$$

where

$$\langle (\dots) \rangle = \frac{1}{Z} \iint \exp\left[-\sum_{\nu} |V_{\nu,\sigma}|^2/(UT)\right]$$

$$\times Z(V)(\dots\dots)(d\xi d\eta)$$

is the average over all possible configurations of random potential,

$$G_{k,\sigma}(V) = \sum_{\alpha} (1 + \alpha\sigma V^z_{\nu,\sigma}/|V_{\nu,\sigma}|)\frac{1}{\omega - \varepsilon_{\mathbf{k}} - \alpha\Sigma(V)}$$

is the Green function describing the motion of electrons in the random potential $V_{\nu,\sigma}$, $\Sigma(V) = \sqrt{|V_{\nu,\sigma}|^2 + \Gamma}$ is the self-energy, and

$$\Gamma(k,\omega) = G^{-1}_{k-\sigma}\sum_{q}(G_{k+q\sigma} - G_{k\sigma})V^2_{qz}$$

$$+ G^{-1}_{k-\sigma}\sum_{q}(G_{k+q,-\sigma} - G_{k,-\sigma})(V^2_{qx} + V^2_{qy})$$

characterizes the scattering of electrons by fluctuations of the random potential $V_{\nu,\sigma}$ and describes the damping of electron states.

In order to calculate the functional integrals determining the partition function (6) and to average the Green functions, we invoke a method of steepest descent. This procedure, as well as the results of estimating the most probable values of the potential-well depths and their fluctuations, is thoroughly described in [6]; however, only the energy spectrum of electron states with weak damping ($\Gamma \ll |\mu \pm Um|$, where the chemical potential μ is reckoned from the nearest band edge) was found in [6]. It was shown that the spin and charge fluctuations result in renormalization of the electron density of states while splitting it into two subbands corresponding to different spin projections onto the quantization axis (fluctuating in space and time) and thus changing the capacity of these subbands:

$$g_\sigma(\varepsilon) = \frac{1}{2}\sum_{\alpha = \pm 1} g_0(\varepsilon + \alpha U\sqrt{\langle |\xi_\nu|^2\rangle})$$

$$\times \left(1 + \alpha\sigma\frac{M_0 + H/U}{\sqrt{\langle |\xi_\nu|^2\rangle}}\right), \quad (9)$$

where M_0 is the uniform magnetization per site, H is an external magnetic field in units of the doubled Bohr magneton, $\langle |\xi_\nu|^2\rangle = 1/N_0\sum_{q\neq 0} m_q^2 + M_0^2 = \langle m^2\rangle + M_0^2 = m^2$ is the mean-square magnetic moment per site, $m_q = 1/\sqrt{2}(D^{-1} + X_q)$ is the saddle-point value of the variable r_q at $q \neq 0$, $g_0(\varepsilon)$ is the density of states of noninteracting electrons ($U = 0$), $\sigma = \pm 1$ is the spin quantum number,

$$D^{-1} = 1 - \frac{\langle m_\perp^2\rangle + M_0^2}{m^2}\frac{n_{ef}}{m} - \frac{\langle m_z^2\rangle}{m^2}U\tilde{g}(\mu, m)$$

is the exchange enhancement factor, and

$$\tilde{g}(\mu) = g_0(\mu + Um)g_0(\mu - Um)/g(\mu).$$

To estimate the damping, we take into account that the Gaussian fluctuation halfwidth at a site is

$$\sqrt{\langle(\xi_\nu - \langle\xi_\nu^2\rangle^{1/2})^2\rangle} = \sqrt{\langle m^2\rangle} \quad (10a)$$

for spin fluctuations and

$$\sqrt{\langle(\eta_\nu - \langle\eta_\nu\rangle)^2\rangle}$$
$$= \left(\sum_{\alpha=\pm 1} a g_0(\varepsilon + \alpha Um)/\sum_{\alpha=\pm 1} g_0(\varepsilon + \alpha Um)\right)\sqrt{\langle m^2\rangle} \quad (10b)$$

for charge fluctuations. Eventually, the amplitude (mean-square value) of fluctuations of the random-potential magnitude at a site becomes equal to

$$\langle(\delta V_{\nu,\sigma})^2\rangle = U^2(\langle\xi_\nu^2 - \langle\xi_\nu^2\rangle\rangle + \langle\eta_\nu^2 - \langle\eta_\nu^2\rangle\rangle)$$
$$= U^2(\tilde{g}(\mu)/g(\mu))\langle m^2\rangle, \quad (11)$$

where $g(\mu) = g_0(\mu + Um) + g_0(\mu - Um)$.

Next, we take into consideration that, according to Anderson, the localized states form within the energy width E_C (E_C is the mobility edge or the percolation threshold reckoned from the nearest band edge). The value of E_C can be calculated at this point only within simple models of electron density of states to within a constant factor, $E_C = \langle(\delta V_{\nu,\sigma})^2\rangle/\Delta$, where Δ is the effective band width. Then, following the chosen analogy and in the context of spin fluctuation theory, we have

$$E_C = \tilde{g}(\mu)U^2\langle m^2\rangle/g(\mu)\Delta. \quad (12)$$

In the particular case of $Um \ll \mu$ (the chemical potential is measured from the band edge), the magnetic moment m changes with temperature only slightly and

$$\langle(\delta V_{\nu,\sigma})^2\rangle = U^2(m^2 - M_0^2) = (Um)^2\left(1 - \frac{M_0^2}{m^2}\right).$$

Therefore, we have

$$E_C = \Delta(Um/\Delta)^2\left(1 - \frac{M_0^2}{m^2}\right).$$

A similar expression for the percolation threshold was obtained in [3] for magnets with LMMs.

From Eq. (12), it follows that if the spin fluctuations are strong (e.g., near the temperature of magnetic disorder or in strongly paramagnetic materials) and the $g_0(\varepsilon)$ dependence is weak [i.e., $g_0(\mu + Um) \approx g_0(\mu - Um)$], then the percolation threshold is markedly shifted with respect to the band edge and can become higher than the chemical potential. Therefore, for strong magnets (such as iron and nickel) with almost entirely filled d bands and with the amplitude of spin fluctuations so high that Um becomes larger or equal to the distance from the chemical potential to the bang edge [i.e., $g_0(\mu + Um) = 0$ and $\tilde{g}(\mu) = 0$], we have $E_C = 0$ and localized states in the band are absent.

Thus, spin density fluctuations result not only in a splitting of the electronic spectrum, but also in the creation of localized electronic states (rapidly decaying with distance) within the energy range between E_C and the nearest band edge. The temperature dependence of the mobility edge in this situation should be the strongest in almost ferromagnetic semiconductors, in which the energy gap in the electronic spectrum is small and the magnitude of spin fluctuations changes considerably with temperature and becomes comparable to the gap width.

The metal–insulator transition temperature T_{MI} can be determined from the condition $E_C(T_{MI}, H) = \mu(T_{MI}, H)$. For this purpose, we expand the equation of the magnetic state [7] into a power series in $\langle m^2(T)\rangle - \langle m^2(T_C)\rangle$,

$$M_0(D^{-1} + \gamma M_0^2) = h,$$

$$h = \frac{H}{U}, \quad D^{-1} = 1 - \frac{\langle m_\perp^2\rangle + M_0^2}{m^2}\frac{n_{ef}}{m} - \frac{\langle m_z^2\rangle}{m^2}U\tilde{g}(\mu, m),$$

$$\gamma = \frac{1}{m^2}\left(\frac{n_{ef}}{m} - U\tilde{g}(\mu, m)\right),$$

(13)

and, considering that according to [15] $\langle m^2\rangle = m^2 - M_0^2 = (T/T_C)^{4/3}m_C^2$ (m_C^2 is the magnetic moment near the Curie temperature; this moment is defined from the condition that the denominator of susceptibility tends to zero at $T \longrightarrow T_C$), finally obtain

$$T_{MI} = T_C\left(1 + \frac{H - \beta M_0^3}{\alpha M_0}\right)^{3/4},$$

(14)

where $\alpha = \gamma(T_C, B)m_C^2$, and $\beta = (5/2)\alpha$, $B = UM_0(H) + H$.
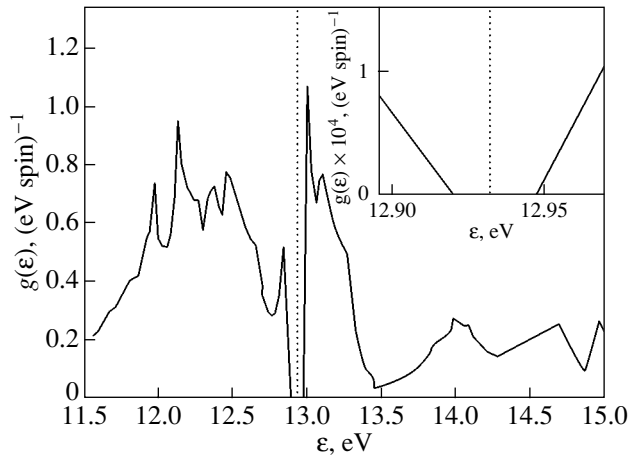
Fig. 1. Simulation curve of the electron density of states without renormalization due to spin fluctuations constructed using the data from [12]. Dotted vertical line corresponds to the position of the chemical potential.

Expression (14) differs from the corresponding formula derived in [3] in the exponent controlling the field dependence, which is the result of the inclusion of dynamic spin fluctuations. However, in the static limit ($\omega \ll T$), this distinction disappears. Furthermore, the coefficients α and β depend on the external magnetic field rather than being constant, as in the case considered in [3]. This dependence is determined by the band structure and can be different.

3. To discuss the possibility of electron phase transitions in almost ferromagnetic semiconductors caused by Anderson localization, we consider FeSi, whose band structure is known [12]. According to band calculations [12], the one-electron spectrum of this compound consists of two bands separated by an energy gap $E_g \approx 0.02$ eV (Fig. 1). Although the lower (valence) band in FeSi is entirely filled, and the upper (conduction) band is empty, experiments show [13] that the ground state of FeSi is metallic. Such a discrepancy between the results of band calculations and the experiment, as shown in [6], can be related to the fact that, at ultralow temperatures, there exist relatively high zero-point spin fluctuations in iron monosilicide. The estimation of the amplitudes of zero-point spin fluctuations made in [6] showed that, in accordance with Eq. (9), the energy gap between the valence and conduction bands is absent (Fig. 2a) and the chemical potential is located in the allowed energy range. However, the charge and longitudinal spin fluctuations were not considered in [6]; i.e., the possible strong spin-fluctuation scattering was ignored. The results obtained in this way described the variation of electron characteristics of FeSi only at $T < 5$ K and contradicted the experimental results in the range from 5 to 100 K. Furthermore, in order to explain the experimentally observed Curie–Weiss law for magnetic susceptibility, it was assumed in [6] that the density of states near the upper and lower edges of the

$g(\varepsilon)$, (eV spin)$^{-1}$
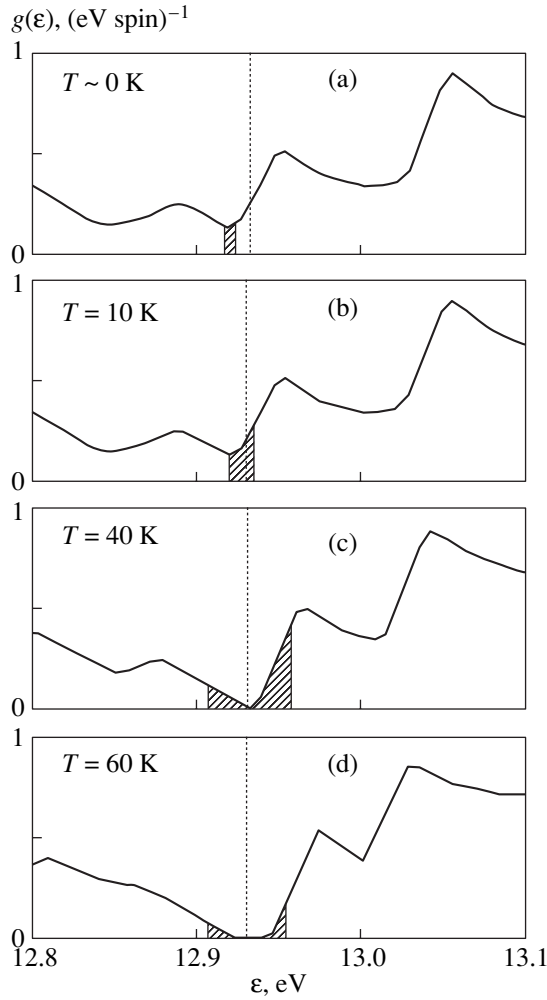
Fig. 2. Electron density of states in FeSi as a function of energy at various temperatures. Dotted line corresponds to the position of the chemical potential. Crosshatched regions correspond to localized states.

valence and conduction bands must have large values of the first derivative. This assumption is in contrast with the results of band calculations made in [14] (see inset to Fig. 1). Within our approach, the existence of spin fluctuations (zero-point ones in the case of FeSi) should lead to longitudinal spin and charge fluctuations and, as a consequence, to Anderson localization of the electronic states with energies falling within an interval of width E_C below the top of the valence band and above the bottom of the conduction band. If we assume that the effective widths of the valence band Δ_1 and of the conduction band Δ_2 are equal to each other, $\Delta_1 = \Delta_2 = 0.33$ (estimating them from the condition of equality of the densities of states at the mobility edges), then the electron states of the valence band at $T \longrightarrow 0$, according to Eq. (11), should be localized within the energy range $E_C^{(1)} > E^{(1)} - \varepsilon > 0$ and the conduction band states, within the range $E_C^{(2)} < \varepsilon - E^{(2)} < 0$; $E_C^{(1)}$ and $E_C^{(2)}$ are

the positions of the top and the bottom of the valence and conduction bands, respectively, and $E_C^{(1)}$ and $E_C^{(2)}$ are the mobility thresholds for the valence and conduction bands measured from $E^{(1)}$ and $E^{(2)}$, respectively (Fig. 2a). Because of spin-fluctuation splitting, the chemical potential lies in the range of delocalized electronic states (Fig. 2a) and the ground state of FeSi is metallic. Further, with increasing temperature, the amplitude of zero-point spin fluctuations reduces to a greater extent as compared with the increase in amplitude of thermal spin fluctuations [6]; therefore, the spin-fluctuation splitting of electronic spectrum reduces and the chemical potential at $5 < T < 50$ K becomes located within the range of the localized states (Figs. 2b, 2c). In this temperature range, the spin-fluctuation splitting of the electronic spectrum is so large that the energy gap is closed (Figs. 2b, 2c). In this temperature range, the hopping mechanism of conductance is operative and the resistivity ρ must obey the law $\ln\rho \sim T^{1/4}$, which is observed in the experiment [13, 15]. The magnetic susceptibility in this temperature range follows the Curie–Weiss law with the Curie constant $C = \mu_B^2 n_{\mathrm{loc}}$, where n_{loc} is the number of occupied localized states. The latter value can be found from Eqs. (9) and (11) to be

$$n_{\mathrm{loc}} = \int_{E^{(1)} - E_C^{(1)}}^{E^{(1)}} g(\varepsilon) f(\varepsilon - \mu) d\varepsilon + \int_{E^{(2)}}^{E_C^{(2)} + E^{(2)}} g(\varepsilon) f(\varepsilon - \mu) d\varepsilon.$$

The obtained magnitude of the Curie constant $C = 8.81 \times 10^{-5}$ emu K/mol coincides with that found experimentally [13]. A further increase in temperature makes the zero-point spin fluctuations disappear and results in the energy gap in the electronic spectrum opening (Fig. 2d). Since thermal fluctuations of spin density increase with T to a lesser extent than zero-point spin fluctuations decrease, the energy gap opens abruptly. Because of spin-fluctuation splitting, the gap width $E_g(T)$ is smaller than $E_g^{(0)}$ (found from one-electron band calculations) by the value $2Um$:

$$E_g(T) = E_g^{(0)} - 2Um. \qquad (15)$$

Because of this, FeSi undergoes a phase transitions to the semiconducting state at $T \sim 50$ K; its resistance, temperature dependence typical of hopping mechanism, abruptly changes to that typical of the activation type of conduction. The activation energy E_a is expected to differ from the energy gap because the energy range of width $E_C^{(1)}$ located below the energy gap and the energy range of width $E_C^{(2)}$ located above the energy gap correspond to localized electronic

states. Therefore, the activation energy of charge carriers is determined as

$$E_a = E_C^{(1)} + E_C^{(2)} + E_g^{(0)} - 2Um \qquad (16)$$

and decreases with increasing temperature. However, because of the linear increase in the amplitude of thermal spin fluctuations with temperature, a decrease in E_a with increasing T cannot be observed experimentally through measuring the resistivity [$\rho(T) \sim \exp(-E_a/T)$ and $m(T) \sim T$]. The activation energy found from the temperature dependence of resistivity is determined by the relation $\tilde{E}_a = E_C^{(1)} + E_C^{(2)} + E_g^{(0)}$ and, according to the estimation of the percolation threshold, should be equal to $\tilde{E}_a = 0.088$ eV. This explains the discrepancy between the activation energy found from the band calculations and the experimental results. A further increase in the amplitude of thermal spin fluctuations with increasing temperature T again results in the disappearance of the energy gap, in a shift of the percolation threshold in the valence (conduction) band upward (downward) with respect to the chemical potential and, as a consequence, in the activation energy vanishing at $T_{MI} \sim 81$ K [see Eq. (13)]. Thus, at $T_{MI} \sim 81$ K, FeSi once again displays an electron phase transition, but this time from a semiconductive to metallic state. Other features and mechanisms of the formation of electrical properties occurring in FeSi with a further increase in temperature were considered in [10]. It was established that the spin-fluctuation renormalization of the spectrum remains a deciding factor up to the temperature $T \sim 300$ K, above which the formation of the metallic state (particularly, an increase in the number of charge carriers) is completed. Above 300 K, the dominant processes regulating the temperature variation of electrical resistance become the scattering mechanisms and $\rho(T)$ in FeSi increases with increasing T. Investigation of FeSi in this temperature range was not the subject of this study as results on this were published in [10].

Thus, the generalization of spin-fluctuation theory given in this study has allowed us to describe the succession of electron transformations observed in almost ferromagnetic semiconductors. Based on the present analysis of the experimental data on FeSi, we may conclude that strong spin-fluctuation scattering can occur and may be responsible for the occurrence of localized electronic states. Taking account of this factor is important for further development of our insight into electron phase transitions in almost ferromagnetic semiconductors and semimetallic weak itinerant magnets. We may also predict that the considered mechanism of electron transitions will also take place in Kondo systems (e.g, in SmB_6), which behave similarly to FeSi [16].

REFERENCES

1. É. L. Nagaev, Usp. Fiz. Nauk **168** (8), 917 (1998) [Phys. Usp. **41**, 831 (1998)].

2. É. L. Nagaev, Usp. Fiz. Nauk **166** (8), 833 (1996) [Phys. Usp. **39**, 781 (1996)].

3. N. G. Bebenin and V. V. Ustinov, J. Phys.: Condens. Matter **10**, 6301 (1998).

4. P. Phodes and E. P. Wohlfarth, Proc. R. Soc. London, Ser. A **273** (1353), 247 (1963).

5. T. Moriya, *Spin Fluctuations in Itinerant Electron Magnetism* (Springer, Berlin, 1985; Mir, Moscow, 1988).

6. A. A. Povzner, A. G. Volkov, and P. V. Bayankin, Fiz. Tverd. Tela (St. Petersburg) **40** (8), 1437 (1998) [Phys. Solid State **40**, 1305 (1998)].

7. A. G. Volkov, A. A. Povzner, V. V. Kryuk, *et al.*, Zh. Éksp. Teor. Fiz. **116** (5), 1770 (1999) [JETP **89**, 960 (1999)].

8. P. W. Anderson, Phys. Rev. **109**, 1492 (1958).

9. N. F. Mott, *Metal–Insulator Transitions* (Taylor and Fransic, London, 1974; Nauka, Moscow, 1979).

10. A. G. Volkov, A. A. Povzner, V. V. Kryuk, and P. V. Bayankin, Fiz. Tverd. Tela (St. Petersburg) **41** (10), 1792 (1999) [Phys. Solid State **41**, 1644 (1999)].

11. J. A. Hertz and M. A. Klenin, Phys. Rev. B **10** (3), 1084 (1974).

12. L. I. Vinokurova, A. V. Vlasov, and É. T. Kulatov, Tr. Inst. Obshch. Fiz. Akad. Nauk SSSR **32** (4), 463 (1991).

13. M. B. Hunt, M. A. Chernikov, and E. Felder, Phys. Rev. B **50** (20), 14933 (1994).

14. H. Ohta, S. Kimura, E. Kulatov, *et al.*, J. Phys. Soc. Jpn. **63**, 4206 (1994).

15. Sh. Takagi, H. Yasuoka, and Sh. Ogawa, J. Phys. Soc. Jpn. **50** (8), 2539 (1981).

16. N. E. Sluchanko, V. V. Glushkov, S. V. Demishev, and M. V. Kondrin, Pis'ma Zh. Éksp. Teor. Fiz. **68** (10), 774 (1998) [JETP Lett. **68**, 817 (1998)].

Translated by A. Zalesskiĭ

SEMICONDUCTORS AND DIELECTRICS

Effect of Atomic Magnetic Moments on the Relative Intensity of the L_β and L_α Components in X-ray Emission Spectra of 3d Transition Metal Oxides

V. I. Grebennikov, V. R. Galakhov, L. D. Finkel'shteĭn, N. A. Ovechkina, and É. Z. Kurmaev

Institute of Metal Physics, Ural Division, Russian Academy of Sciences,
ul. S. Kovalevskoĭ 18, Yekaterinburg, 620219 Russia
e-mail: greben@imp.uran.ru
Received September 9, 2002

Abstract—The integrated-intensity ratio R of the L_β and L_α lines in x-ray emission spectra of 3d transition metal oxides was measured. The magnitude of the ratio was found to depend nonmonotonically on the atomic number of the 3d elements, with a sharp rise in the middle of the series. In terms of the theory of one-electron resonant x-ray scattering in a solid, a simple relation was derived connecting this ratio with the spin polarization of occupied and empty d states. The calculated values of R qualitatively reflect the behavior of the measured $I(L_\beta)/I(L_\alpha)$ ratio on the atomic number of 3d elements. Thus, the existence of a dependence of the integrated-intensity ratio of L_β and L_α lines on the atomic magnetic moment has been established. All calculated R curves lie above the $I(L_\beta)/I(L_\alpha)_{exp}$ data, because not all factors accompanying the x-ray emission process were included in the calculation. © 2003 MAIK "Nauka/Interperiodica".

1. INTRODUCTION

The x-ray emission spectra of transition metal compounds exhibit multiplet splitting into two lines, L_α and L_β (Fig. 1). The first line derives from the radiative electron transition from the 3d valence states to the inner $2p_{3/2}$ (L_3) level, while the L_β line is emitted in transition of the 3d electron to the $2p_{1/2}$ (L_2) level. The energy level splitting of states with a total angular momentum $j = l + s$ equal to 1/2 or 3/2 (l is the orbital angular momentum, and s is the 2p-hole spin) is caused by the spin–orbit coupling and varies from 5 eV for Sc to 17 eV for Ni. The number of states with different projections of the total angular momentum is given by the factor $2j + 1$; hence, the L_2 subshell contains two states and the L_3 subshell, four. Considered in terms of a simple diagram, the excitation probability of the L_2 level is one half that of the L_3 level; therefore, it follows that the intensity ratio of the L_β and L_α emission lines should be the same for all transition elements and equal the statistical value 1/2. Experiments, however, yield a completely different pattern: the integrated line intensity ratio depends on the atomic species, and its value varies over a broad range from 0.2 to 0.7.

A similar problem of the ratio between the L_2 and L_3 line intensities was studied in absorption spectra (see, e.g., [1]). The deviation of the magnitude of the ratio from its statistical value 1/2 is caused by the interaction of the core hole with the valence electrons, which partially destroys spin–orbit coupling or, in other words, mixes states with total angular momenta $j = 1/2$ and $3/2$, thus bringing about a redistribution of the intensity

between the two main lines. The intensities can be quantified only by way of complete numerical calculation for a free atom or an atom acted upon by a crystal field. Within this many-electron approach, it is fairly difficult to establish the main physical factors governing the magnitude of the intensity ratio.

The ratio between the L_β and L_α x-ray emission intensities in copper compounds was studied in [2]. This ratio is usually less than its statistical value because of the stronger absorption the L_β radiation suffers in matter compared to L_α (the self-absorption effect), as well as due to the shorter lifetime of the L_2 hole. The latter is determined by the additional decay channel associated with the L_2L_3V Koster–Kronig transition [3, 4]. This transition involves valence electrons and, hence, one may expect the transition probability to depend on the type of chemical bonding.

The main efforts of researchers have been focused on revealing fine differences in L_β and L_α emission between various compounds of the same transition element and on establishing an empirical correlation of the magnitude of the ratio with valence in chemical compounds. For the manganese oxides, the $I(L_\beta)/I(L_\alpha)$ ratio decreases in the order $MnO–Mn_3O_4–Mn_2O_3–MnO_2$, i.e., with increasing degree of manganese ion oxidation [5, 6]. In copper oxides, one observes the opposite situation, with the $I(L_\beta)/I(L_\alpha)$ ratio increasing as one crosses over from Cu_2O to CuO. This effect was employed to analyze the chemical state of copper [7–11]. It was shown that an increase in covalency of
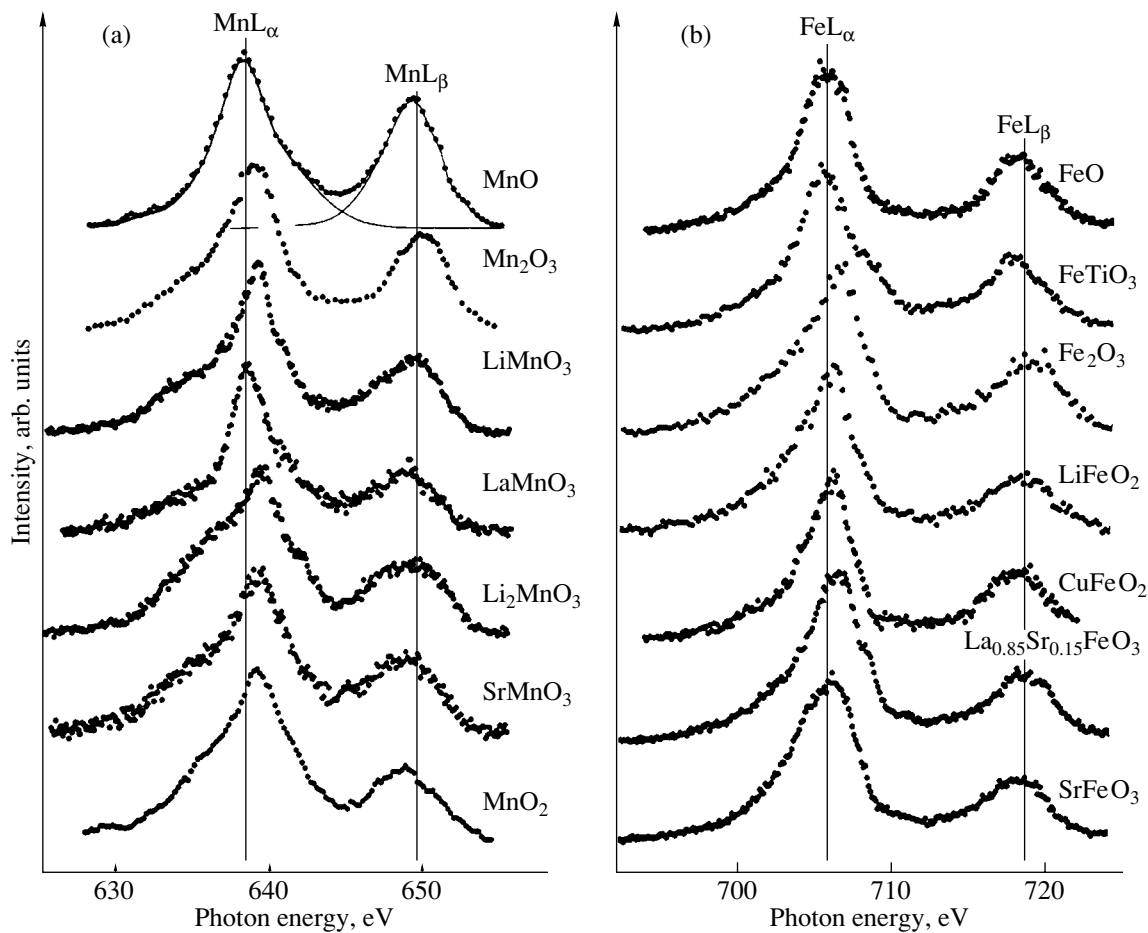
Fig. 1. (a) X-ray Mn $L_{\alpha,\beta}$ emission spectra of the manganese oxides MnO, Mn_2O_3, $LiMnO_2$, $LaMnO_3$, $SrMnO_3$, and MnO_2. MnO was chosen to illustrate isolation of the L_α and L_β components. (b) Fe $L_{\alpha,\beta}$ spectra of the iron oxides FeO, $FeTiO_3$, Fe_2O_3, $LiFeO_3$, $CuFeO_2$, $La_{0.85}Sr_{0.15}$, FeO_3, and $SrFeO_3$.

cuprates for the same formal copper ion valence results in a decrease in $I(L_\beta)/I(L_\alpha)$ [10].

This study was aimed at establishing the main relations governing the formation of the L_β and L_α emission lines; therefore, we investigated spectra of compounds of elements of the whole transition series. A comparison of experimental data obtained in emission with similar data for absorption [12, 13] demonstrates a clearly pronounced difference in behavior between the emission and absorption spectra. The L_2/L_3 absorption ratio is the largest at the beginning of the transition series, in atoms with a small number of $3d$ electrons, whereas the maximum of the L_β/L_α emission ratio falls on the manganese atom located in the middle of the series and possessing a large magnetic moment, with the ratio falling off as one proceeds to the extremes of the series. This apparently means that emission forms through an additional physical mechanism which does not operate in absorption. Note that this mechanism plays an active role: rather than reducing the magnitude of the $I(L_\beta)/I(L_\alpha)$ ratio, as is characteristic of the above

relaxation mechanisms (self-absorption, Koster–Kronig transition), this mechanism increases the ratio above its statistical value. This is the mechanism of atomic magnetic moments. The absorption intensity for each of the states of the subshell depends on the spin polarization $\overline{M}$ of the empty $3d$ states to which the electron transfers from the inner $2p_{j,\,m_j}$ state. Similarly, the emission cross section contains a contribution from the $3d$ electron spin polarization M. Summation over the states making up an energy level results, however, together with averaging over photon polarization, in a reduction of this M-odd contribution to the resultant signal, both in absorption and emission. This occurs if the emission transition is considered, as usual, separately from the core hole excitation process. In actual fact, photon emission is only a closing event in the process of resonant scattering of exciting primary photons or electrons with the participation of the inner-shell states. This approach sheds light on new features in emission spectra [14, 15] which defy explanation within the concept of independent absorption and emission events. In this particular case, it will be shown that

a second-order process gives rise to an explicit dependence of spectral emission intensity on atomic magnetic moment, because the emission cross section depends on the product $M\overline{M}$. This even contribution is preserved under subsequent summation over states with different angular-momentum projections m_j.

This communication provides a quantitative description of inelastic resonant x-ray scattering in a solid with allowance for the angular dependence of the cross section of this process and its dependence on the exciting radiation polarization. The theoretical results obtained can be used to devise new experiments on resonant scattering of synchrotron radiation and for extracting information from such experiments on the local characteristics of compounds. Next, we consider emission spectra averaged over the emergence angles and polarization and derive simple relations for the integrated-intensity ratio of the L_β and L_α lines. The results are employed in the interpretation of the experimental data obtained for the oxides of transition metals. The intensity ratio is shown to be related to the magnitude of the atomic magnetic moments.

2. MEASUREMENT OF X-RAY SPECTRA

All the compounds studied, with the exception of Co_2O_3 and Ni_2O_3, were single phase and close to stoichiometric in composition, except FeO, which is always deficient in metal. Co_2O_3 contains a Co_3O_4 impurity, and the so-called Ni_2O_3 reagent contains, when used in air, a certain amount of water [16]. Samples of binary oxides were prepared by solid-phase synthesis. The techniques employed in the preparation and characterization of these samples are described in considerable detail elsewhere [17–19]. The FeO and $CuFeO_2$ samples were single crystals [20, 21].

X-ray $L_{\alpha, \beta}$ emission spectra were obtained on an RSM-500 x-ray spectrometer under electron excitation. The x-ray radiation was decomposed with a grating of 600 lines/mm having a 6-m radius of curvature. The spectra were calibrated with the L_α lines of the corresponding metals, whose energies were taken from [22]. The x-ray tube was operated at 4 kV and a current of about 0.3 mA, which prevented the materials from decomposing under electron beam bombardment. The x-ray radiation was measured with a VÉU-6 open-aperture secondary electron multiplier with a CsI photocathode. The spectra were corrected for detector efficiency.

3. X-RAY *L* EMISSION SPECTRA OF TRANSITION METAL OXIDES

Figure 1a presents Mn $L_{\alpha, \beta}$ x-ray emission spectra of the manganese oxides MnO, Mn_2O_3, $LiMnO_2$, $LaMnO_3$, Li_2MnO_3, $SrMnO_3$, and MnO_2. The case with MnO exemplifies isolation of the L_α and L_β compo-

nents. In Fig. 1b, Fe $L_{\alpha, \beta}$ x-ray emission spectra of the oxides FeO, $FeTiO_3$, Fe_2O_3, $LiFeO_2$, $CuFeO_2$, $La_{0.85}Sr_{0.15}FeO_3$, and $SrFeO_3$ are displayed.

The $I(L_\beta)/I(L_\alpha)$ ratio for the manganese oxides decreases with increasing degree of oxidation of the manganese ions (in Fig. 1a, from top down). In iron oxides, this effect is less pronounced, although one also observes a falloff of the relative intensity $I(L_\beta)/I(L_\alpha)$ with increasing formal valence of iron ions in the oxides.

A comparison of the $I(L_\beta)/I(L_\alpha)$ values obtained on the same sample under different excitation conditions (by photons and electrons) did not reveal any systematic differences between these cases. The observed difference does not exceed the average error of either method of $\pm(0.03–0.04)$.

To find the $I(L_\beta)/I(L_\alpha)$ ratio for TiO and Ti_2O_3, we made use of the spectra from [23]; for V_2O_3, from [24]; and for Cr_2O_3, spectra measured by us and from [25].

4. THEORETICAL ANALYSIS

The cross section of scattering of monochromatic radiation accompanied by emission of a photon of energy $\hbar\omega'$ and polarization vector $\mathbf{u}'$ into a solid angle $d\Omega'$ in direction $\mathbf{k}'$, resulting from an electron transition from an occupied valence state m' of energy ε'_m to the inner-shell state c of energy E_c, can be written in the form

$$\frac{d\sigma_c(\mathbf{k'}, \mathbf{k})}{d\Omega' d(\hbar\omega')} = \alpha^2 \frac{\hbar^2 \omega'^3 \omega}{c^2} \sum_{m'm} \left| \frac{\langle c|\mathbf{u'r'}|m'\rangle \langle m|\mathbf{ur}|c\rangle}{E_c + \hbar\omega - \varepsilon_m - i\Gamma_c} \right|^2 \quad (1)$$
$$\times \delta(\varepsilon_{m'} + \hbar\omega - \varepsilon_m - \hbar\omega').$$

Here, $\alpha = e^2/\hbar c$ is the fine-structure constant, c is the velocity of light, $\hbar$ is Planck's constant, and e is the electronic charge. The process starts with excitation of an electron in an inner-shell state through a dipole transition to empty valence-band states with quantum numbers m and energies ε_m by absorption of a photon of energy $\hbar\omega$ and polarization vector $\mathbf{u}$ propagating in direction $\mathbf{k}$. The imaginary part of the energy Γ_c provides the decay rate of the core-level hole. The transition matrix elements are written in the dipole approximation.

Figure 2 sketches the energy diagram of the inelastic scattering process. As follows from Eq. (1), in the case of normal emission, the processes of the core-level hole excitation and of the emission itself are separable. Using the relation

$$\left| \frac{1}{E_c + \hbar\omega - \varepsilon_m - i\Gamma_c} \right|^2 \cong \frac{\pi}{\Gamma_c} \delta(E_c + \hbar\omega - \varepsilon_m), \quad (2)$$

one can present the resonant scattering cross section at the core level c as

$$\frac{d\sigma_c}{d\Omega'd\varepsilon'} = \sigma_c(\varepsilon)\frac{d\gamma_c(\varepsilon')}{\Gamma_c d\Omega'd\varepsilon'}. \qquad (3)$$

Here,

$$\sigma_c(\varepsilon) = \alpha 4\pi^2\hbar\omega\sum_m|\langle m|\mathbf{u}\mathbf{r}|c\rangle|^2\delta(\varepsilon_m-\varepsilon) \qquad (4)$$

is the cross section of the core-hole excitation through electron transition to empty valence states with an energy $\varepsilon = \hbar\omega - |E_c|$.

The quantity

$$\frac{d\gamma_c(\varepsilon')}{d\Omega'd\varepsilon'} = \frac{\alpha\hbar\omega'^3}{4\pi^2c^2}\sum_{m'}|\langle c|\mathbf{u}'\mathbf{r}'|m'\rangle|^2\delta(\varepsilon_{m'}-\varepsilon') \qquad (5)$$

describes the probability of radiative transitions of valence electrons from states with energy $\varepsilon' = \hbar\omega' - |E_c|$ to the core level. The photon energy in Eqs. (4) and (5) can be replaced by the binding energy of the core level $\hbar\omega \cong \hbar\omega' \cong |E_c|$.

The inner-shell $2p$ states in atoms of transition elements are split by spin–orbit coupling into two groups with a total angular momentum $j = l + s$, which can take on two values, $j = 1/2$ and $3/2$. Their angular and spin wave functions are given by well-known combinations of spherical harmonics and spin functions [15]. The valence states $|m\rangle = \Phi_{ik}^s$ (**k** is the wave vector, i is the band index, s is the spin) in a solid can also be expanded in spherical harmonics Y_{lm} centered on the excited atom

$$\Phi_{ik}^s(\mathbf{r}) = \sum_{lm}a_{lm,ik}^s R_{\varepsilon l,ik}(r)Y_{lm}^s(\mathbf{r}). \qquad (6)$$

Here, $R_{\varepsilon l,ik}(r)$ are the radial parts of the solution of the Schrödinger equation with an orbital angular momentum l and energy $\varepsilon = \varepsilon_{ik}^s$ inside an MT sphere. The expansion coefficients $a_{lm,ik}^s$ can be found from calculations of the band structure.

We express the scalar product of vectors in dipole matrix elements through spherical functions

$$\mathbf{u}\mathbf{r} = \sum_{q=\pm1,0}(-1)^q u_{-q}r_q, \qquad (7)$$

and cast the absorption amplitude squared

$$\sum_m|\langle m|\mathbf{u}\mathbf{r}|c\rangle|^2\delta(\varepsilon_m-\varepsilon') = f_q^c(\varepsilon)u_{-q}u_{-q}^* \qquad (8)$$
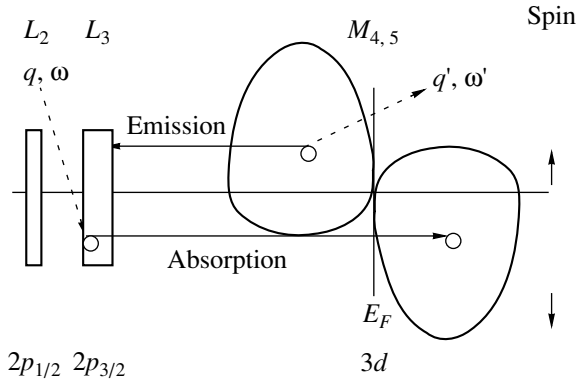
Fig. 2. Energy diagram of inelastic x-ray scattering (q, $\omega \longrightarrow q'$, ω') involving inner-shell $L_{2,3}$ and spin-polarized valence $M_{4,5}$ states.

in terms of the functions

$$f_q^c(\varepsilon) = \frac{1}{N}\sum_{iks}|\langle\Phi_{ik}^s|r_q|\Phi_c\rangle|^2\delta(\varepsilon_{ik}^s-\varepsilon). \qquad (9)$$

The integrals of the angular parts in Eq. (9) can be calculated in an explicit way. The coefficients $a_{lm,ik}^s$ squared are summed with the energy δ function to yield the partial electronic spin densities of states (DOSs):

$$g_{lm}^s(\varepsilon) = \frac{1}{N}\sum_{ik}|a_{bn,ik}^s|^2\delta(\varepsilon_{ik}^s-\varepsilon). \qquad (10)$$

According to the dipole selection rules, in the case of scattering at the $L_{2,3}$ level one can limit oneself to d states with an orbital angular momentum $l = 2$; therefore, we subsequently drop this index. The functions $f_q^c(\varepsilon)$ can be expressed through partial DOS of $3d$ states with orbital angular momentum projections m and spin orientations $s = \uparrow, \downarrow$. For instance, for an electron transition from state $c = 2p_{1/2,1/2}$ to the $3d$ band, we find

$$f_q^c(\varepsilon) = (R^2/15)\begin{cases} 4g_2^{\downarrow} + g_1^{\uparrow}, & q = 1 \\ (2/3)g_0^{\downarrow} + g_1^{\uparrow}, & q = -1 \\ 2g_1^{\downarrow} + (4/3)g_0^{\uparrow}, & q = 0. \end{cases} \qquad (11)$$

The quantum numbers $m = 0, \pm1, \pm2$ are determined by the dipole selection rules, and their weight, by the matrix elements of the angular parts (Clebsch–Gordan coefficients). The quantity R denotes the radial matrix element of the $2p$–$3d$ dipole transition, which we assume the same for all the six $2p$ states.

In what follows, we neglect the dependence of the partial DOSs on the quantum number m and retain only their dependence on the spin. This approximation

implies that the valence band is dominated by electron exchange interaction.

We finally obtain for the absorption cross section (at the core level c)

$$\sigma_c(\varepsilon) = \sigma_0[S + P_3 D \cos\theta$$
$$+ (Q/2)((1 + P_1)(3/2)\sin^2\theta - 1)],$$
(12)

where $\sigma_0 = 4\pi^2\alpha|E_c|$ is a constant and the DOS-dependent quantities

$$S = (1/3)(f_1 + f_{-1} + f_0), \quad D = (1/2)(f_1 - f_{-1}),$$
$$Q = (1/3)(2f_0 - f_1 - f_{-1})$$
(13)

relate to the contributions from the scalar, dipole, and quadrupole moments of the atom. The Stokes vector components

$$P_3 = |u_-|^2 - |u_+|^2, \quad P_1 = u_- u_+^* + u_+ u_-^*$$
(14)

characterize the degree of circular and linear polarization, respectively, of the incident electromagnetic wave.

The dependence on the angle θ between the spin polarization of the atom and the direction of propagation of exciting radiation characterizes the anisotropy of the absorption cross section. For unpolarized radiation (Stokes vector $\mathbf{P} = 0$), the angular dependence is determined by the small transition quadrupole moment Q:

$$\sigma_c(\varepsilon) = \sigma_0[S + (Q/2)((3/2)\sin^2\theta - 1)].$$
(15)

For the "magic" angle $\theta = 55°$ ($\sin^2\theta = 2/3$), cross section (12) is determined only by the scalar part, $\sigma_c(\varepsilon) = \sigma_0 S$. Averaging over all incidence angles θ produces the same result.

Similar expressions are obtained for the emission coefficient (5). Because the polarization of emitted photons is not detected in the experiments, one should sum over both their polarizations. Furthermore, observation is usually carried out at angles close to $\theta = 55°$, at which the quadrupole transition provides a negligible contribution, thus permitting one to write the emission probability in the form

$$\frac{d\gamma_c}{\Gamma_c d\Omega' d\varepsilon} = \frac{\alpha E_c^3}{\Gamma_c 2\pi\hbar^2 c^2} S_c'(\varepsilon'),$$
$$S_c'(\varepsilon') = (1/3)(f_1' + f_{-1}' + f_0').$$
(16)

The prime labels electron emission transitions from the filled part of the valence band.

4.1. Integrated Line Intensity

The normal-emission cross section (3) for one inner-shell state can be calculated as the product of the absorption and emission probabilities. In experiments, one determines the total signal due to two states ($m_j = \pm 1/2$) with total angular momentum $j = 1/2$ and to four

states ($m_j = \pm 1/2, \pm 3/2$) with $j = 3/2$. Because a sum of the products does not reduce to a product of the sums, the emission signal is in no way proportional to the absorption spectrum and is rather complex. In what follows, we consider integrated intensities of the emission lines L_β ($2p_{1/2} \rightleftharpoons 3d$ transition) and L_α ($2p_{3/2} \rightleftharpoons 3d$ transition), which are determined by energy integrals from a sum of expressions of the type of Eq. (3) over the corresponding inner-shell states $c = (j, m_j)$

$$I_j^e = \int d\varepsilon d\varepsilon' \sum_{m_j} \frac{d\sigma_{j, m_j}}{d\Omega' d\varepsilon'}.$$
(17)

Integrals (10) over the empty part ($\varepsilon > \varepsilon_F$) of the density of states of the $3d$ band (10), which enters functions $f_q^c(\varepsilon)$ of Eq. (9), yield the number of empty d states $\overline{N}_s$ (per atom), and integration over the filled part of the DOS ($\varepsilon' < \varepsilon_F$) gives the number of d electrons, N_s, with spin projections $s = \uparrow, \downarrow$. With the notation $N = N_\uparrow + N_\downarrow$, $M = N_\uparrow - N_\downarrow$, and, for the empty states, $\overline{N} = \overline{N}_\uparrow + \overline{N}_\downarrow$ and $\overline{M} = \overline{N}_\uparrow - \overline{N}_\downarrow$, we obtain (neglecting the difference in population between states with different quantum numbers m) the following expressions for the integrated cross sections for the L_β and L_α lines:

$$I_\beta^e = 2I_{1/2}^{0e}[(N\overline{N} + (1/9)M\overline{M})$$
$$- ((1/2)N\overline{M} + (1/6)M\overline{N})P_3 \cos\theta$$
(18)
$$- (1/45)M\overline{M}((1 + P_1)(3/2)\sin^2\theta - 1)],$$

$$I_\alpha^e = 4I_{3/2}^{0e}[(N\overline{N} + (5/9)M\overline{M})$$
$$+ ((1/4)N\overline{M} + (5/12)M\overline{N})P_3 \cos\theta$$
(19)
$$- (1/90)M\overline{M}((1 + P_1)(3/2)\sin^2\theta - 1)],$$

where

$$I_j^{0e} = \frac{a_0^2 E_{2p}^4}{m^2 c^4}\left(\frac{2}{90}\frac{R^2}{a_0^2}\right)^2 \frac{2\pi}{\Gamma_j},$$
(20)

a_0 is the Bohr radius, E_{2p} is the binding energy of the $2p$ level, R is the radial dipole-transition matrix element, Γ_j is the halfwidth of the level with $j = 1/2, 3/2$, and P_3 and P_1 are the degrees of circular and linear polarization of the exciting radiation, respectively.

The above relations can be compared with the expressions for integrated intensities of absorption lines obtained in the same approach

$$I_{1/2}^a = 2I_0^a[\overline{N} - (1/2)\overline{M}P_3 \cos\theta],$$
(21)

$$I_{3/2}^a = 4I_0^a[\overline{N} - (1/4)\overline{M}P_3 \cos\theta],$$
(22)

$$I_0^a = a_0^2 4\pi^2\alpha E_{2P}\left(\frac{2}{90}\frac{R^2}{a_0^2}\right).$$
(23)

Table 1. Integrated intensity ratio for the transition metal monoxides: experimental values of $I(L_\beta)/I(L_\alpha)$ and the ratio R calculated from Eq. (27); m^{exp} is the experimental value of the atomic magnetic moment

Compound	TiO	MnO	FeO	CoO	NiO	CuO	ZnO
$I(L_\beta)/I(L_\alpha)$	0.40	0.73	0.46	0.38	0.24	0.34	0.28
$M = m^{exp}$, μ_B	0.51 [29]	4.79 [30]	3.36 [31]	3.35* [32]	1.77 [33]	0.65 [34]	0
R	0.5	0.92	0.65	0.59	0.55	0.5	0.5

* With inclusion of the orbital contribution of $2.6\mu_B$ [35].

The integrated intensity of absorption lines is determined by the number of empty spin $3d$ states in the band. For unpolarized ($\mathbf{P} = 0$) and even linearly polarized exciting radiation, this intensity does not depend on the magnetic moment of the atom. The emission lines are determined as a sum of the products of the numbers of filled and empty states in the band. Even in the case of unpolarized excitation (or when averaged over all incidence angles), the emission intensity depends on the atomic magnetic moments

$$I_\beta^e = 2I_{1/2}^{0e}[N\overline{N} + (1/9)M\overline{M}], \qquad (24)$$

$$I_\alpha^e = 4I_{3/2}^{0e}[N\overline{N} + (5/9)M\overline{M}]. \qquad (25)$$

Using the above relations, we find the ratio of integrated intensities of the $2p_{1/2}$ (L_β) and $2p_{3/2}$ (L_α) lines:

$$\frac{I_\beta}{I_\alpha} = \frac{\Gamma_3}{2\Gamma_2}\frac{N\overline{N} + (1/9)M\overline{M}}{N\overline{N} + (5/9)M\overline{M}}, \qquad (26)$$

where Γ_2 and Γ_3 are the halfwidths (decay rates) of the corresponding levels, $N = N_\uparrow + N_\downarrow$ is the number of d electrons in the excited atom, $M = N_\uparrow - N_\downarrow$ is the magnetic moment of the atom (in Bohr magnetons), $\overline{N} = \overline{N}_\uparrow + \overline{N}_\downarrow$ is the number of empty states, and $\overline{M} = \overline{N}_\uparrow - \overline{N}_\downarrow$ is the difference between the numbers of spin-up and spin-down empty states.

Estimate (26) is also applicable to the case of x-ray emission induced by electron excitation, because the transition of a core $2p$ electron to valence $3d$ states rather than to higher lying nd states is also most probable here since the Coulomb excitation intensity is inversely proportional to the square of the energy transfer. In this case, the part of the polarization vector is played by the high-energy electron momentum transfer, which is also approximately perpendicular to the beam direction, as is the polarization vector of an electromagnetic wave.

In deriving Eq. (26), we neglected the effect of self-absorption on the L_β line intensity; calculation of Γ_2 requires knowledge of the mechanism of the Koster–Kronig transition in solids. These processes, considered in [26–28], remain presently open to question. Assuming these factors to vary little along the $3d$ period, we disregarded them, and, in our analysis of the dependence of the L_β-to-L_α line intensity ratio on the spin

polarization of the filled and empty d states, used Eq. (26) in a simplified form,

$$R = (1/2)\frac{N\overline{N} + (1/9)M\overline{M}}{N\overline{N} + (5/9)M\overline{M}}. \qquad (27)$$

While the R figures are, for the above reasons, *a priori* overestimates, the dependence of R on the atomic number of d elements is seen to mimic the experimental $I(L_\beta)/I(L_\alpha)$ relation well.

5. DISCUSSION OF EXPERIMENTAL RESULTS

Consider the monoxide series of transition elements. Table 1 lists measured values of the intensity ratio of the L_β and L_α lines, as well as the atomic magnetic moments derived from neutron diffraction measurements [29–35].

We take the iron monoxide FeO as an illustrative case to show how one can calculate the spectral-line intensity ratio. The iron atom donates two s electrons to an oxygen atom while retaining six d electrons; hence, $N = 6$ and the number of empty states is $\overline{N} = 10 - 6 = 4$. The experimental value of the magnetic moment is 3.36 Bohr magnetons. Thus, the difference between the numbers of empty spin-up and spin-down states is $\overline{M} = \overline{N}_\uparrow - \overline{N}_\downarrow = (5 - N_\uparrow) - (5 - N_\downarrow) = -M = -3.36$ and their product is $M\overline{M} = -M^2$. Substituting these values into Eq. (27) yields $R = 0.65$.

Results obtained in this way are presented in Fig. 3a together with the experimentally measured integrated line intensity ratios for the $3d$ metal monoxides and the FeTiO$_3$ compound. We readily see that estimate (27) correctly reflects the general pattern of variation of this quantity along the total series of divalent ions of the transition elements. The ratio is maximum for the MnO compound, which has the largest magnetic moment. The experimental curve in Fig. 3 passes below the theoretically predicted values for the reasons pointed out above.

A specific feature of the trivalent-metal compounds Me_2O_3 is the direct involvement of the d electron in chemical bonding. Table 2 presents measured values of the intensity ratio for the L_β and L_α lines, experimental values of the atomic magnetic moments [36, 37], the

Table 2. Integrated-intensity ratio for the trivalent transition metal oxides: experimental values of $I(L_\beta)/I(L_\alpha)$ and the ratio R calculated from Eq. (27); m^{exp} is the experimental value of the atomic magnetic moment; $N\uparrow N\downarrow$ are spin configurations of atomic electrons plus the d electron in the chemical bond at the times of absorption and emission

Compound	TiO	MnO	FeO	CoO	NiO	CuO	ZnO
$I(L_\beta)/I(L_\alpha)$	0.40		0.37	0.48	0.41	0.34	0.19
m^{exp}, μ$_B$		2.0* [36]	2.76* [36]	4.0* [36]	4.64 [37]	1.4* [36]	
$N\uparrow N\downarrow$ + bond							
Absorption	$1\uparrow + 1\uparrow$	$1.5\uparrow 0.5\downarrow + 1\uparrow$	$2.5\uparrow 0.5\downarrow + 1\uparrow$	$4\uparrow + 1\uparrow$	$4\uparrow 1\downarrow + 1\uparrow$	$4\uparrow 2\downarrow + 1\uparrow$	$4\uparrow 3\downarrow + 1\uparrow$
Emission	$2\uparrow$	$2.5\uparrow 0.5\downarrow$	$3.5\uparrow 0.5\downarrow$	$5\uparrow$	$5\uparrow 1\downarrow$	$5\uparrow 2\downarrow$	$5\uparrow 3\downarrow$
R	0.53	0.52	0.55	0.74	0.61	0.55	0.52

* Atomic moment derived from effective moment in the Curie–Weiss relation.

intensity ratio calculated from Eq. (27), and the electronic configurations of atoms at the instants of excitation and emission that were used in the calculation. The atomic magnetic moments M labeled by an asterisk were derived from the effective moments M_{eff} obtained in measurements of the temperature dependence of the paramagnetic susceptibility using the expression

$$M(M + 2) = M_{eff}^2 .$$

The magnetic moment in the Mn$_2$O$_3$ compound is four Bohr magnetons. The fifth d electron with spin up is involved in an oxygen bond. This result is indicated in the third line of Table 2 as the sum $4\uparrow + 1\uparrow$. Thus, we obtain $\overline{M} = -4$ and $\overline{N} = 10 - 4 = 6$ for the absorption stage. At the instant of emission, the d electron transfers from the bond to the metal atom by screening the x-ray hole to produce the $5\uparrow$ state with the values $M = 5$ and

Fig. 3. Integrated-intensity ratio $I(L_\beta)/I(L_\alpha)$ for (a) divalent transition-metal oxides and (b) trivalent-metal compounds Me_2O_3. Vertical bars specify experimental error.

$N = 5$. Substituting these figures into Eq. (27) yields $R = 0.74$.
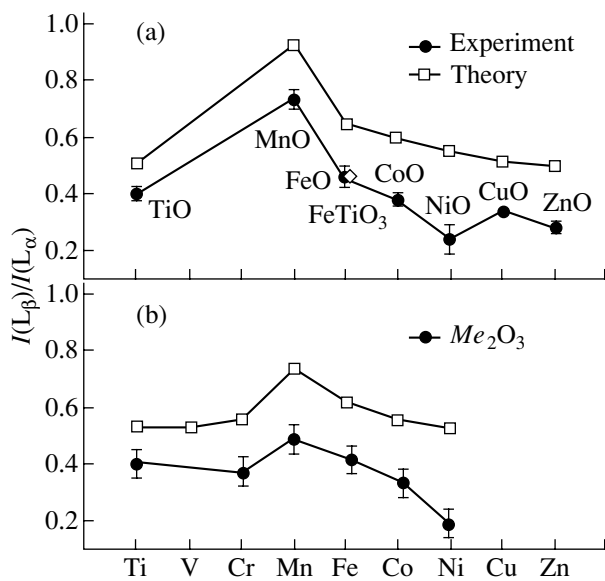
According to neutron diffraction data, the magnetic moment of the ground state in Fe$_2$O$_3$ is $m = 4.64\mu_B$. This state is not very stable; in any case, when a core hole forms, the atom can transfer to a state of type $4\uparrow 1\downarrow$ (plus one spin-up electron in the bond). In this case, we have $\overline{M} = -3$ and $\overline{N} = 5$. Similarly, for cobalt and nickel, we assumed the configurations $4\uparrow 2\downarrow$ and $4\uparrow 3\downarrow$ specified in Table 2.

The calculated and experimental values of the integrated line intensity ratio are shown in Fig. 3b. The L_β-to-L_α line intensity ratio is again the highest in the middle of the transition-metal series, for atoms with large magnetic moments. As follows from Eq. (27), the magnetic-moment influence becomes less significant for atoms with magnetic moments less than two Bohr magnetons. The relative line intensity in such substances is dominated by other mechanisms, which above all control the lifetime of the L_2-level hole [28].

Thus, an analysis of spectra based on the proposed approach suggests that, in compounds with the d electron involved in chemical bonding, the effects associated with the formation of a core hole begin to play a significant part in emission processes. These processes include both spin flip and d-electron transfer from a bond to the excited atom and, for heavy 3d elements, another spin flip.

6. CONCLUSIONS

To sum up, experimental and theoretical studies show that magnetic moments of atoms directly affect the intensities of the L_β and L_α lines. In atoms with large magnetic moments, the magnetic mechanism is dominant. It is this mechanism that accounts for the anomalously large L_β-to-L_α line intensity ratio in the series of transition-metal compounds. As follows from theoretical estimates, the influence of magnetic moments on the emission spectra should manifest itself most strongly in experimental dependences of the fluores-

cence on the angle of incidence and polarization of the exciting synchrotron radiation.

ACKNOWLEDGMENTS

REFERENCES

1. B. T. Thole and G. van der Laan, Phys. Rev. B **38** (5), 3158 (1988).
2. J. Kawai, K. Maeda, K. Nakajima, and Y. Goshi, Phys. Rev. B **52**, 6129 (1995).
3. E. J. McGuire, Phys. Rev. A **5**, 1043 (1972).
4. J. C. Fuggle and S. F. Alvarado, Phys. Rev. A **22**, 1615 (1980).
5. V. R. Galakhov, É. Z. Kurmaev, and V. M. Cherkashenko, Izv. Akad. Nauk SSSR, Ser. Fiz. **49**, 1513 (1985).
6. E. Z. Kurmaev, A. Moewes, V. R. Galakhov, *et al.*, Nucl. Instrum. Methods Phys. Res. B **168**, 395 (2000).
7. J. Ribble, Phys. Status Solidi A **6** (2), 473 (1971).
8. R. C. C. Perera, B. L. Henke, P. J. Batson, *et al.*, J. Phys. Colloq., No. C9, 1185 (1987).
9. M. Fujinami, H. Hamada, Y. Hashiguchi, and T. Ohtsubo, Jpn. J. Appl. Phys. **28** (11), L1959 (1989).
10. S. M. Butorin, V. R. Galakhov, E. Z. Kurmaev, and V. I. Glazyrina, Solid State Commun. **81** (12), 1003 (1992).
11. J. Kawai, J. Nakajima, and Y. Gohsji, Spectrochim. Acta B **48** (10), 1281 (1993).
12. R. D. Leapman, L. A. Grunes, and P. L. Fejes, Phys. Rev. B **26**, 614 (1982).
13. C. N. R. Rao, J. M. Thomas, B. G. Williams, and T. G. Sparrow, J. Phys. Chem. **88**, 57 (1984).
14. M. V. Yablonskikh, V. I. Grebennikov, Yu. M. Yarmoshenko, *et al.*, Solid State Commun. **117**, 79 (2001).
15. M. V. Yablonskikh, Yu. M. Yarmoshenko, V. I. Grebennikov, *et al.*, Phys. Rev. B **63** (23), 235117 (2001).
16. N. G. Klyuchnikov, *Manual on Inorganic Synthesis* (Khimiya, Moscow, 1965).
17. V. R. Galakhov, E. Z. Kurmaev, St. Uhlenbrock, *et al.*, Solid State Commun. **95** (6), 347 (1995).
18. V. R. Galakhov, E. Z. Kurmaev, St. Uhlenbrock, *et al.*, Solid State Commun. **99** (4), 221 (1996).
19. D. G. Kellerman, V. S. Gorshkov, V. G. Zubkov, *et al.*, Zh. Neorg. Khim. **42** (6), 1012 (1997).
20. T. R. Zhao, M. Hasegawa, M. Koike, and H. Takei, J. Crystal Growth **148**, 189 (1995).
21. V. R. Galakhov, A. I. Poteryaev, E. Z. Kurmaev, *et al.*, Phys. Rev. B **56** (8), 4584 (1997).
22. J. A. Bearden, Rev. Mod. Phys. **39**, 1 (1967).
23. D. W. Fischer and W. L. Baun, J. Appl. Phys. **39**, 4757 (1968).
24. D. W. Fischer and W. L. Baun, J. Appl. Phys. **40**, 4151 (1969).
25. D. W. Fischer and W. L. Baun, J. Phys. Chem. Solids **32**, 2455 (1971).
26. V. I. Grebennikov, Fiz. Met. Metalloved. **89** (5), 5 (2000).
27. M. O. Krause, J. Phys. Chem. Ref. Data **8** (2), 307 (1979).
28. J. Kawai, Rigaku J. **18** (1), 1 (2001).
29. P. K. Khowash and D. E. Ellis, J. Appl. Phys. **65**, 4815 (1989).
30. B. E. F. Fender, A. J. Jacobson, and F. A. Wegwood, J. Chem. Phys. **48**, 990 (1968).
31. P. Wei and Z. Q. Qi, Phys. Rev. B **49** (16), 10864 (1994).
32. D. C. Kahn and R. A. Ericson, Phys. Rev. B **1**, 2243 (1970).
33. O. K. Andersen and O. Jepsen, Phys. Rev. Lett. **53**, 2571 (1984).
34. J. B. Forsyth, P. J. Brown, and B. M. Wanklyn, J. Phys. C **21**, 2917 (1988).
35. I. V. Solivyev, A. I. Liechtenstein, and K. Terakura, Phys. Rev. Lett. **80**, 5758 (1998).
36. J. B. Goodenough, Prog. Solid State Chem. **5**, 145 (1971).
37. J. M. D. Coey and G. A. Sawatzky, J. Phys. C **4**, 2386 (1971).

Translated by G. Skrebtsov

Multiplication of Electronic Excitations in AgCl Crystals

**B. P. Aduev, É. D. Aluker, B. A. Sechkarev, E. V. Tupitsyn,
V. M. Fomchenko, and V. N. Shvayko**

Kemerovo State University, ul. Krasnaya 6, Kemerovo, 650043 Russia

e-mail: lira@kemsu.ru

Received September 19, 2002

Abstract—The kinetics of pulse conduction in silver chloride single crystals is investigated in the temperature range 12–300 K upon picosecond excitation with x-ray bremsstrahlung. It is found that the experimentally observed concentration of conduction electrons is nearly twice as high as the concentration of electron–hole pairs generated by an exciting pulse. This effect is associated with the chain multiplication of band charge carriers. © 2003 MAIK "Nauka/Interperiodica".

1. INTRODUCTION

In our earlier work [1], we investigated the kinetics of pulse conduction in AgBr single crystals in the temperature range 30–300 K upon excitation with x-ray bremsstrahlung pulses of an electron accelerator. As was shown in [1], the anomalous behavior revealed in pulse conduction of AgBr differs drastically from the behavior of pulse conduction in classical ionic crystals [2–4]. The anomalies observed are as follows:

(1) The conductivity of AgBr upon picosecond excitation increases for 3 ns after completion of the action of an exciting pulse.

(2) The conduction pulse amplitude of AgBr considerably exceeds (by at least two orders of magnitude) the amplitude of conduction pulses in classical ionic crystals under similar conditions.

(3) A comparison of the pulse conductivity upon picosecond excitation with dosimetric data demonstrated that the number of conduction electrons is almost one order of magnitude larger than the number of electrons generated by an exciting pulse in a sample.

An analysis of the observed anomalies revealed that electronic excitation occurring in AgBr crystals undergo a previously unknown multiplication with a characteristic time of $\sim 10^{-9}$ s.

In this work, we investigated the pulse conduction in single crystals of the AgCl compound (also used in photography) in order to elucidate whether the anomalies observed in [1] are the specific features of AgBr or if they are characteristic of silver halides.

2. SAMPLE PREPARATION AND EXPERIMENTAL TECHNIQUE

The experiments were performed with an AgCl crystal grown by the Stockbarger method from a high-purity initial material, which was preliminarily purified using zone melting (50 runs). Samples were cut from the single crystal and ground to a thickness of 100–130 μm. Electrodes were applied by the development technique, which made it possible to prepare a homogeneous silver film on the sample surface.

A GIN-540 needle-gap electron accelerator with an anode from an aluminum film 0.9 mm thick was used as an excitation source. This aluminum film completely absorbed the electron beam. The pulse duration was approximately equal to 50 ps, and the maximum energy of electrons was ~200 keV. The use of the aluminum foil as the anode was caused by the fact that we failed to prepare samples of thickness $d < 50$ μm, which is necessary for ensuring the uniformity of electron beam excitation. For this reason, the excitation was achieved by the bremsstrahlung generated upon complete absorption of electrons in the aluminum anode.

A conduction current pulse induced in the sample under x-ray bremsstrahlung was recorded using an S7-19 oscilloscope. The scheme of the measuring setup was described in detail in [1]. The time resolution of the measuring technique was equal to 150 ps. The measurements were performed in the temperature range 12–300 K. The radiation dose absorbed in the sample per exciting pulse was determined with TLD-K thermoluminescent dosimeters based on SiO_2. The calculation of the absorbed dose in the sample was carried out according to the procedure described in [1].

The error in measuring the amplitude of conduction current pulses was no more than ±10%, and the dosimetric measurements were performed accurate to within ±20%.

3. EXPERIMENTAL RESULTS

Figure 1 displays a typical oscillogram of a conduction current pulse at a temperature of 300 K. It is worth noting that the conduction current pulse in AgCl, as in AgBr [1], rises with a lag (~2 ns) that is more than one order of magnitude greater than the time resolution of

the recording channel (150 ps). This effect is observed over the entire temperature range 12–300 K. Under the same experimental conditions, the amplitude of the conduction current pulse in AgCl is five times smaller than that in AgBr but at least one order of magnitude larger than the amplitudes in alkali halide crystals and α-Al$_2$O$_3$ [1–4].

The current–voltage characteristics are linear and symmetric without any specific features. The resistance of the samples was calculated from the slope of the current–voltage characteristics. Then, the radiation-stimulated conductivity at the maximum of the conduction current pulse was determined with due regard for the geometric sizes of the samples.

The dependence of the maximum conductivity $\sigma(T)$ calculated by this method is depicted in Fig. 2. This dependence exhibits a nonmonotonic behavior with a maximum at $T = 70$ K.

The data presented in Fig. 2 were processed using the formula

$$\sigma = ne\mu_d, \qquad (1)$$

where n is the concentration of conduction electrons generated by an x-ray pulse, e is the elementary charge, and μ_d is the drift mobility. The behavior of the temperature dependence of the conductivity indicates the presence of electron attachment centers. In this case, the drift mobility and the Hall mobility μ_h differ from each other and are related by the expression [5]

$$\mu_d = \mu_h \frac{1}{1 + \dfrac{q_1}{q_2}\dfrac{N}{N_c}e^{E/kT}}, \qquad (2)$$

where E is the energy separation between the trap and the conduction band bottom; q_1 and q_2 are the statistical weights of filled and empty traps, respectively; and $N_c = 2(2\pi mkT/h^2)^{3/2}$ is the effective density of states in the vicinity of the conduction band bottom. The statistical weights q_1 and q_2 are related by the following formula [5]:

$$q_1/q_2 = 2. \qquad (3)$$

Since the effective electron mass is determined to be $m = 0.3m_0$ [5], the quantity N_c can be represented in the form

$$N_c = 7.9 \times 10^{14} T^{3/2}. \qquad (4)$$

The Hall mobility at temperatures $T > 40$ K was approximated by the expression [6]

$$\mu_h = 30(e^{280/T} - 1)\ \text{cm}^2/\text{V s}. \qquad (5)$$

The solid line in Fig. 2 corresponds to the results of calculations from formula (1) with allowance made for relationships (2)–(5) at the following parameters: $E = 0.02$ eV, $N = 6.9 \times 10^{16}$ cm^{-3}, and $n = 2.6 \times 10^{16}$ cm^{-3} (according to the scale factor). It can be seen from
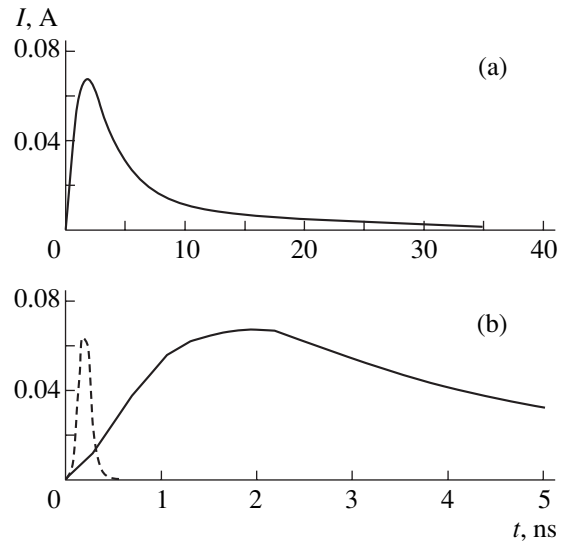

Fig. 1. Oscillograms of the conduction current pulses for the AgCl crystal. Time base: (a) 10 and (b) 2.5 ns/div. The dashed line shows the exciting pulse.
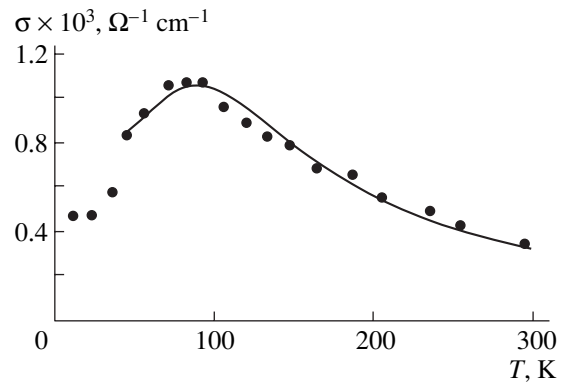

Fig. 2. Temperature dependence of the maximum conductivity for the AgCl crystal. Points are the experimental data. The solid line represents the results of calculations according to formula (1) with due regard for relationships (2)–(5).

Fig. 2 that the results of the calculations are in good agreement with the experimental data. The activation energy E for attachment centers coincides with that obtained by van Heyningen [5] in time-of-flight experiments on the determination of the drift mobility in AgCl. The nature of the attachment centers remains unclear. In [5], it was assumed that these centers are associated with mechanical defects formed upon treatment of the samples.

The next series of experiments was carried out at a fixed temperature $T = 300$ K by varying the excitation density. For this purpose, we changed the distance between the accelerator diode and the sample. The experiments were performed as follows. The conductivity of the crystal was measured at a fixed distance

$\sigma \times 10^3$, Ω^{-1} cm^{-1}
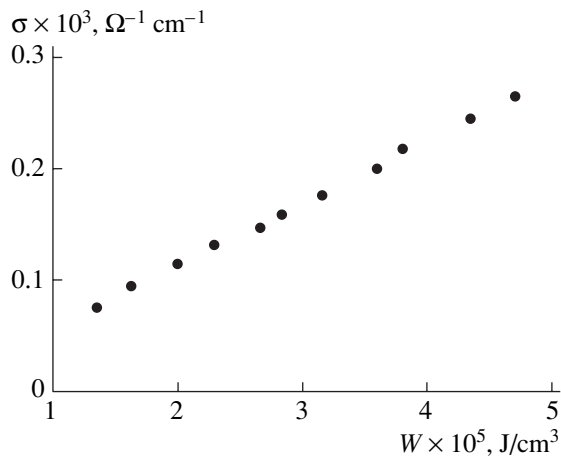
Fig. 3. Dependence of the maximum conductivity on the absorbed radiation dose density for the AgCl crystal.
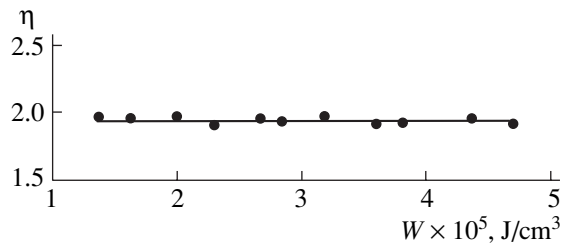
Fig. 4. Dependence of the multiplication factor for free charge carriers on the absorbed radiation dose density for the AgCl crystal.

between the diode and the sample. The results were averaged over ten pulses. Then, the dosimeters were mounted in place of the sample and the dose D absorbed in the sample was measured and calculated according to the procedure described in detail in our previous work [1]. In the calculations, we used the dose averaged over ten dosimeters. The absorbed radiation dose density in the sample was determined from the formula

$$W = D\rho, \tag{6}$$

where $\rho = 5.56$ g/cm^3 is the density of AgCl. The experimental dependence is depicted in Fig. 3.

4. DISCUSSION

From the above results, it is evident that anomalies similar to those revealed in AgBr [1] are also observed in AgCl. These anomalies are as follows: (i) a rise in conduction current pulses for ~2 ns after completion of the action of exciting pulses and (ii) anomalously large conduction pulse amplitudes (even though this effect is less pronounced than in AgBr [1]).

As was noted in [1] and Section 1 of the present work, these findings suggest that the multiplication of electronic excitations occurs after completion of the action of an x-ray pulse. The experimental data presented in Section 3 make it possible to calculate the multiplication factor η for free charge carriers. The multiplication factor η can be represented in the form

$$\eta = \frac{n}{n_g}. \tag{7}$$

Here, n is the concentration of electrons involved in the conduction [this concentration can be calculated from formulas (1)–(5) and the measured conductivity σ] and n_g is the concentration of electron–hole pairs generated by the exciting pulse. As a rule, the concentration n_g is described by the relationship

$$n_g = \frac{W}{\varepsilon}, \tag{8}$$

where W is the absorbed radiation dose density [see expression (6) and Fig. 3] and ε is the mean energy of generation of an electron–hole pair. The concentration n_g in AgCl was estimated from the experimental value $\varepsilon = 7.6$ eV/pair taken from [7].

The results of calculations with the use of the data presented in Fig. 3 are shown in Fig. 4. According to these calculations, we have $\eta = 1.93 \pm 0.08$. Therefore, as in the case of AgBr, we can draw the conclusion that the experimentally observed concentration of conduction electrons is approximately twice as high as the concentration of electrons generated by the exciting pulse. It is worth noting that this effect in AgCl is somewhat less pronounced than in AgBr [1].

5. CONCLUSIONS

Thus, the anomalies revealed in pulse conduction of silver halides indicate that electronic excitations occurring in these systems undergo multiplication.

The observed multiplication differs from the well-known collision ionization multiplication that is widely used for recording nuclear radiation (the time scale of the revealed process is approximately equal to 10^{-9} s, whereas the time scale of the processes associated with the collision ionization is shorter than 10^{-12} s). Possibly, the revealed multiplication is a chain process similar to that observed earlier in heavy metal azides [8, 9].

It should also be noted that the quantitative difference in the effect of electronic excitation multiplication in AgBr and AgCl correlates qualitatively with the different photosensitivities of these materials. This implies that the observed effect is associated with the high yield of centers of a latent image and the high photosensitivity of silver halides.

REFERENCES

1. B. P. Aduev, É. D. Aluker, N. L. Aluker, *et al.*, Zh. Nauchn. Prikl. Fotogr. **45** (3), 59 (2000).

2. B. P. Aduev and V. N. Shvayko, Fiz. Tverd. Tela (St. Petersburg) **41** (7), 1200 (1999) [Phys. Solid State **41**, 1093 (1999)].

3. B. P. Aduev, É. D. Aluker, V. M. Fomchenko, and V. N. Shvayko, Fiz. Tverd. Tela (St. Petersburg) **43** (7), 1185 (2001) [Phys. Solid State **43**, 1229 (2001)].

4. B. P. Aduev, É. D. Aluker, and V. N. Shvayko, Fiz. Tverd. Tela (St. Petersburg) **39** (11), 1995 (1997) [Phys. Solid State **39**, 1784 (1997)].

5. R. van Heyningen, Phys. Rev. **128** (5), 2112 (1962).

6. P. V. Meĭklyar, *Physical Processes in the Course of Formation of Latent Photographic Image* (Nauka, Moscow, 1972).

7. E. Fünfer and H. Neuert, *Zählrohre und Szintillationszähler*, 2nd ed. (Braun, Karlsruhe, 1959; Gos. Izd. Lit. Obl. At. Nauki Tekh., Moscow, 1961).

8. B. P. Aduev, É. D. Aluker, G. M. Belokurov, *et al.*, Zh. Éksp. Teor. Fiz. **116** (5), 1676 (1999) [JETP **89**, 906 (1999)].

9. B. P. Aduev, E. D. Aluker, V. I. Krasheninin, *et al.*, J. Appl. Phys. **89** (7), 4156 (2001).

Translated by O. Borovik-Romanova

Maxwell–Wagner Relaxation of Elastic Constants of Layered Polar Dielectrics

A. V. Turik and G. S. Radchenko

Rostov State University, ul. Zorge 5, Rostov-on-Don, 344007 Russia

e-mail: turik@phys.rsu.ru

Received November 6, 2002

Abstract—This paper reports on the results of investigations into the effective complex elastic compliances of a composite in the form of a multilayer piezoactive medium consisting of layers of polar dielectrics connected in series. Exact solutions for normal and inverse Maxwell–Wagner relaxations of elastic compliances are derived for the first time. The mechanical hysteresis loops corresponding to either a decrease or an increase in the elastic energy are analyzed. It is demonstrated that relaxation of elastic constants occurs only in piezoactive media. © 2003 MAIK "Nauka/Interperiodica".

1. INTRODUCTION

Interlayer polarization that is accompanied by dielectric dispersion and losses in ac electric fields, which are referred to as the Maxwell–Wagner relaxation, arises in inhomogeneous dielectrics due to the accumulation of free charges at interfaces between the components. This mechanism of polarization has been most thoroughly described by Maxwell and Wagner in their classical works (see, for example, [1, 2]). For a long time, all problems associated with the Maxwell–Wagner relaxation were regarded to be completely investigated and well understood and this subject did not attract research attention. Interest in the Maxwell–Wagner relaxation, especially in the Maxwell–Wagner relaxation occurring in piezoactive media [3, 4], was renewed only in the 1980s–2000s with a drastic increase in the number of research works and expansion of the commodities market for thin ferroelectric films, which are widely used in integrated memory devices, microprocessors, smart cards, actuators, sensors, etc.

However, theoretical investigations in this field have been started only in the very recent past; for the most part, they are based on substantial simplifications. For example, in their pioneering work on the Maxwell–Wagner piezoelectric relaxation in layered ferroelectric heterostructures, Damjanovic *et al.* [4] used a simplified model which was proposed earlier by Newnham *et al.* [5]. Within this model, the mechanical boundary conditions and the lateral piezoelectric response are ignored. It should be noted that, for layered composites with a connectivity of the 2–2 type [5], it is possible to obtain exact, but cumbersome, solutions. In our recent work [6], we analyzed an accurate model with primary emphasis on piezoelectric and dielectric relaxations, but formulas for elastic compliances were not given and

the relaxation of elastic constants was considered very briefly. Some indications of elastic Maxwell–Wagner relaxation were described by Ueda *et al.* [3]. The present work was devoted to the study of the elastic Maxwell–Wagner relaxation in a bilayer (multilayer) piezoactive system consisting of layers of polar dielectrics connected in series. A theoretical approach was proposed and computer programs were developed in order to investigate the normal and converse piezoelectric effects. These programs permitted simulation and analysis of the Maxwell–Wagner relaxation of the effective elastic constants. The formulas derived and the results of our calculations were compared with the model used in [4, 5].

2. MODEL

Let us consider a multilayer composite with a connectivity of the 2–2 type [5], which consists of two components with numbers $n = 1, 2$ and volume concentrations θ_1 and θ_2. It is assumed that the composite layers have an infinite length along the directions OX_1 and OX_2 in a rectangular coordinate system $(X_1X_2X_3)$. The vectors of the normal to the interface between the layers are parallel to the OX_3 direction. Both components are polarized along the OX_3 direction and are transversely isotropic in the X_1OX_2 plane. In what follows, we will use the symbols ξ_i, σ_j, E_k, and D_k for the components of the strains, stresses, electric field, and electric induction, respectively, and the matrix forms for all the elastic compliances s_{ij} (at $E = 0$) and piezoelectric coefficients d_{ki}.

If the homogeneous external harmonic stress σ_3^* with the frequency ω (quantities averaged over the composite layers are denoted by asterisks) is applied

along the polar axis OX_3 in the absence of other components of the external electric fields and mechanical stresses, the internal electric fields $E_3^{(n)}$ and mechanical stresses $\sigma_1^{(n)} = \sigma_2^{(n)}$ are induced in both layers. The appropriate piezoelectric equations and boundary conditions are as follows:

$$D_3^{(n)} = 2d_{31}^{(n)}\sigma_1^{(n)} + d_{33}^{(n)}\sigma_3 + \varepsilon_{33}^{(n)}E_3^{(n)},$$

$$\xi_1^{(n)} = \xi_2^{(n)} = (s_{11}^{E(n)} + s_{12}^{E(n)})\sigma_1^{(n)} + s_{13}^{E(n)}\sigma_3 + d_{31}^{(n)}E_3^{(n)},$$

$$\xi_3^{(n)} = 2s_{13}^{E(n)}\sigma_1^{(n)} + s_{33}^{E(n)}\sigma_3 + d_{33}^{(n)}E_3^{(n)}, \qquad (1)$$

$$\sigma_3^{(1)} = \sigma_3^{(2)} = \sigma_3^*, \quad D_3^{(1)} = D_3^{(2)}, \quad \xi_1^{(1)} = \xi_1^{(2)},$$

$$\sigma_1^{(2)} = -(\theta_1/\theta_2)\sigma_1^{(1)}, \quad E_3^{(2)} = -(\theta_1/\theta_2)E_3^{(1)},$$

where $\varepsilon_{33}^{(n)} = \varepsilon^{(n)} - i\gamma^{(n)}/\omega$ are the complex permittivities of the mechanically free ($\sigma = 0$) crystal. After averaging the strain components $\xi_3^{(n)}$ in Eqs. (1), we obtain

$$\xi_3^* = \theta_1\xi_3^{(1)} + \theta_2\xi_3^{(2)} = s_{33}^*\sigma_3^* = (\theta_1 s_{33}^{E(1)} + \theta_2 s_{33}^{E(2)})\sigma_3$$
$$+ 2\theta_1(s_{13}^{E(1)} - s_{13}^{E(2)})\sigma_1^{(1)} + \theta_1(d_{33}^{(1)} - d_{33}^{(2)})E_3^{(1)}. \qquad (2)$$

Next, we determine $\sigma_1^{(1)}$ and $E_3^{(1)}$ from Eqs. (1) and substitute these quantities into relationship (2). As a result, we obtain the general formula for the elastic compliance s_{33}^*:

$$s_{33}^* = \theta_1 s_{33}^{E(1)} + \theta_2 s_{33}^{E(2)} - \frac{2\theta_1\theta_2}{\Delta}(s_{13}^{E(1)} - s_{13}^{E(2)})$$

$$\times [(s_{13}^{E(1)} - s_{13}^{E(2)})(\theta_1\varepsilon_{33}^{(2)} + \theta_2\varepsilon_{33}^{(1)}) - (d_{33}^{(1)} - d_{33}^{(2)})$$

$$\times (\theta_1 d_{31}^{(2)} + \theta_2 d_{31}^{(1)})] - \frac{\theta_1\theta_2}{\Delta}(d_{33}^{(1)} - d_{33}^{(2)}) \qquad (3)$$

$$\times [(d_{33}^{(1)} - d_{33}^{(2)})(\theta_1(s_{11}^{(2)} + s_{12}^{(2)}) + \theta_2(s_{11}^{(1)} + s_{12}^{(1)})$$

$$- 2(s_{13}^{E(1)} - s_{13}^{E(2)})(\theta_1 d_{31}^{(2)} + \theta_2 d_{31}^{(1)})],$$

where

$$\Delta = (\theta_1(s_{11}^{(2)} + s_{12}^{(2)}) + \theta_2(s_{11}^{(1)} + s_{12}^{(1)}))$$
$$\times (\theta_1\varepsilon_{33}^{(2)} + \theta_2\varepsilon_{33}^{(1)}) - 2(\theta_1 d_{31}^{(2)} + \theta_2 d_{31}^{(1)})^2. \qquad (4)$$

A similar procedure of averaging the strain components $\xi_1^{(n)}$ makes it possible to derive the general formula for the elastic compliance s_{13}^*:

$$s_{13}^* = \theta_1 s_{13}^{E(1)} + \theta_2 s_{13}^{E(2)} - \frac{\theta_1\theta_2}{\Delta}(s_{11}^{(1)} + s_{12}^{(1)} - s_{11}^{(2)} - s_{12}^{(2)})$$

$$\times [(s_{13}^{E(1)} - s_{13}^{E(2)})(\theta_1\varepsilon_{33}^{(2)} + \theta_2\varepsilon_{33}^{(1)}) - (d_{33}^{(1)} - d_{33}^{(2)})$$

$$\times (\theta_1 d_{31}^{(2)} + \theta_2 d_{31}^{(1)})] - \frac{\theta_1\theta_2}{\Delta}(d_{31}^{(1)} - d_{31}^{(2)}) \qquad (5)$$

$$\times [(d_{33}^{(1)} - d_{33}^{(2)})(\theta_1(s_{11}^{(2)} + s_{12}^{(2)}) + \theta_2(s_{11}^{(1)} + s_{12}^{(1)})$$

$$- 2(s_{13}^{E(1)} - s_{13}^{E(2)})(\theta_1 d_{31}^{(2)} + \theta_2 d_{31}^{(1)})].$$

The terms proportional to $\theta_1\theta_2$ appear with the inclusion of the internal mechanical stresses $\sigma_1^{(n)} = \sigma_2^{(n)}$ and electric fields $E_3^{(n)}$, which are induced in both layers by the external stress σ_3^*. Formulas for s_{11}^* and s_{12}^* can be derived using the above procedure upon applying an external harmonic stress σ_1^* to the composite.

Since the permittivities $\varepsilon_{33}^{(n)}$ are complex quantities, all the permittivities, piezoelectric coefficients, and elastic compliances of the composite also prove to be complex and frequency dependent.

The frequency dependences of the elastic compliances s_{ij}^* of the composite are determined from the Debye formulas [2, 4]:

$$s_{ij}^* = s_{ij}'^* - i s_{ij}''^*,$$

$$s_{ij}'^* = s_{ij\infty}^* + \frac{\Delta s_{ij}'^*}{1 + \omega^2\tau^2}, \quad s_{ij}''^* = \frac{\Delta s_{ij}'^*\omega\tau}{1 + \omega^2\tau^2}, \qquad (6)$$

where $\Delta s_{ij}'^* = s_{ij0}^* - s_{ij\infty}^*$, s_{ij0}^*, and $s_{ij\infty}^*$ are the relaxation strength and the static ($\omega \longrightarrow 0$) and high-frequency ($\omega \longrightarrow \infty$) elastic compliances of the composite, respectively. The relaxation time τ, which was determined from the positions of the maxima of the imaginary parts of the elastic compliances for the composite, takes the form

$$\tau = \frac{\theta_1\varepsilon^{(2)} + \theta_2\varepsilon^{(1)}}{\theta_1\gamma_2 + \theta_2\gamma_1}$$

$$- \frac{2(\theta_1 d_{31}^{(2)} + \theta_2 d_{31}^{(1)})^2}{(\theta_1\gamma_2 + \theta_2\gamma_1)[\theta_1(s_{11}^{E(2)} + s_{12}^{E(2)}) + \theta_2(s_{11}^{E(1)} + s_{12}^{E(1)})]}. \qquad (7)$$

3. RESULTS AND DISCUSSION

In the case when $\omega\tau \ll 1$, the distribution of the internal electric fields $E_3^{(1)}$ and $E_3^{(2)}$ is determined by the imaginary parts of the complex permittivities; i.e.,
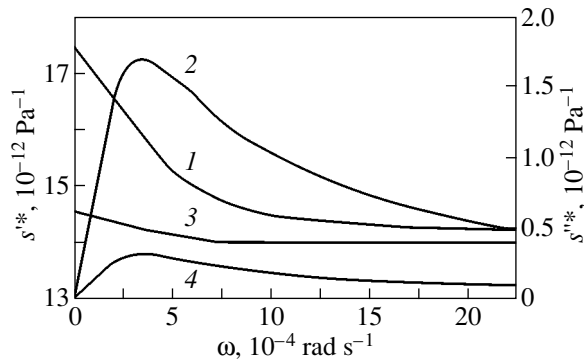
Fig. 1. Normal Maxwell–Wagner relaxation of the effective elastic compliances of a bilayer composite consisting of PKR-7M and PKR-1 ceramics: (1) $s_{33}^{'*}$, (2) $s_{33}^{''*}$, (3) $s_{11}^{'*}$, and (4) $s_{11}^{''*}$. Conditions: $\theta_1 = \theta_2 = 0.5$, $\gamma_1 = 10^{-13}\ \Omega^{-1}\ m^{-1}$, and $\gamma_2 = 10^{-11}\ \Omega^{-1}\ m^{-1}$.
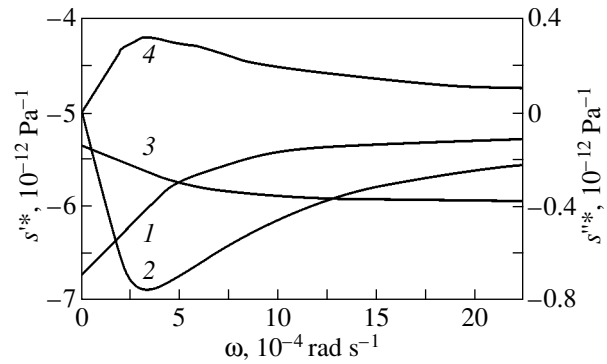
Fig. 2. Normal and inverse Maxwell–Wagner relaxations of the effective elastic compliances of a bilayer composite consisting of PKR-7M and PKR-1 ceramics: (1) $s_{13}^{'*}$, (2) $s_{13}^{''*}$, (3) $s_{12}^{'*}$, and (4) $s_{12}^{''*}$. Conditions: $\theta_1 = \theta_2 = 0.5$, $\gamma_1 = 10^{-13}\ \Omega^{-1}\ m^{-1}$, and $\gamma_2 = 10^{-11}\ \Omega^{-1}\ m^{-1}$.

$\gamma^{(n)}/\omega \longrightarrow \infty$. Hence, for the static elastic compliances, we can derive the following expressions:

$$s_{330}^* = \theta_1 s_{33}^{(1)} + \theta_2 s_{33}^{(2)} - \frac{2\theta_1\theta_2(s_{13}^{(1)} - s_{13}^{(2)})^2}{\theta_1(s_{11}^{(2)} + s_{12}^{(2)}) + \theta_2(s_{11}^{(1)} + s_{12}^{(1)})},$$

$$s_{130}^* = \theta_1 s_{13}^{(1)} + \theta_2 s_{13}^{(2)} \qquad (8)$$
$$- \frac{\theta_1\theta_2(s_{13}^{(1)} - s_{13}^{(2)})(s_{11}^{(1)} + s_{12}^{(1)} - s_{11}^{(2)} - s_{12}^{(2)})}{\theta_1(s_{11}^{(2)} + s_{12}^{(2)}) + \theta_2(s_{11}^{(1)} + s_{12}^{(1)})}.$$

From the boundary condition $D_3^{(1)} = D_3^{(2)}$, it follows that, at low frequencies (when $\omega \longrightarrow 0$), we have $E_3^{(1)} \longrightarrow 0$ and $E_3^{(2)} \longrightarrow 0$; i.e., the short-circuit mode is observed. As a result, the elastic compliances s^{*E} of the composite can be calculated from formulas (8). In the case when $\omega\tau \gg 1$, the distribution of the internal electric fields $E_3^{(1)}$ and $E_3^{(2)}$ is determined by the real parts of the complex permittivities $\varepsilon^{(n)}$. In this situation, the short-circuit mode is disturbed and the elastic compliances of the layers and the composite change and tend to the quantities $s^{(n)D}$ and s^{*D} but do not become equal to them. As can be seen from Eqs. (3)–(5) and the

corresponding equations for s_{11}^* and s_{12}^*, the real parts of s_{33}^*, s_{11}^*, and $-s_{13}^*$ decrease (normal relaxation) and only the real part of $-s_{12}^*$ increases with an increase in the frequency (inverse relaxation). The type of relaxation of the effective elastic compliances s_{ij}^* of the composite is determined by the magnitude and sign of the piezoelectric coefficients d_{ij}, which contribute to the quantities s_{ij} and s_{ij}^*. For all the elastic compliances, except s_{12}^*, it is possible to trace the hysteresis loop counterclockwise, which corresponds to energy losses. The inverse relaxation of s_{12}^* is in accordance with an uncommon relationship: $-s_{12}^{*D} = -[s_{12}^{*E} - (d_{31}^*)^2/\varepsilon_{33}^{*\sigma}] > -s_{12}^{*E}$, which is satisfied for both single-domain and polydomain ferroelectric crystals with different types of domain structure [7, 8]. It should be emphasized that the hysteresis loop of s_{12}^*, contrary to classical notions (see, for example, [4]), is traced clockwise, which corresponds to a partial gain in the elastic energy. However, as will be shown below, the total energy losses are always positive. The signs of the real and imaginary parts of all the elastic compliances, except for s_{12}^*,

Elastic compliances s_{ij}^E ($10^{-12}\ Pa^{-1}$), piezoelectric coefficients d_{ki} (pCN^{-1}), and permittivities $\varepsilon_{33}^\sigma/\varepsilon_0$ of ferroelectric ceramics in the PKR system at 25°C [10]

| Constants	s_{11}^E	s_{12}^E	s_{13}^E	s_{33}^E	d_{31}	d_{33}	$\varepsilon_{33}^\sigma/\varepsilon_0$
PKR-7M	17.5	−6.7	−7.9	19.6	−350	760	5000
PKR-1	12.5	−4.4	−5.8	15.9	−95	220	650

Note: PKR is the piezoelectric ceramics prepared in Rostov-on-Don.

coincide with each other. Thus, the mechanism of elastic Maxwell–Wagner relaxation involves redistribution of the electric fields with variations in the frequency of the mechanical stress applied and resembles the clamping effect [7–9]. The elastic Maxwell–Wagner relaxation occurs only in piezoactive media and is absent in composites with nonpolar components.

Figures 1–3 illustrate the elastic relaxation of a composite consisting of two piezoelectric ceramics with significantly different properties, namely, the PKR-7M ceramic used as the first layer and the PKR-1 ceramic used as the second layer (see [10] and table); both were prepared at the Rostov State University. Although the Maxwell–Wagner relaxation of the elastic constants was not analyzed in [4], the relaxation of the elastic compliance s_{33}^* can also be considered in the framework of the simplified model described in [4, 5]. The appropriate expressions can be obtained from relationships (3)–(7) under the assumption that $d_{31}^{(n)} = s_{31}^{(n)} = 0$. With this simplification, the contribution from the internal mechanical stresses $\sigma_1^{(n)} = \sigma_2^{(n)}$ to the elastic compliance s_{33}^* is disregarded and the curve $s_{33}^*(\omega)$ which was constructed from the data obtained within the model used in [4], passes above the curve calculated in terms of the precision model proposed in the present work. A comparison of these curves demonstrates that the inclusion of the additional internal mechanical stresses $\sigma_{1,2}^{(n)}$ [11], which develop upon applying an external mechanical stress σ_3^* to the layered composite, is of considerable importance.

Another interesting, qualitatively new result (as compared to the simplified model [4]) is the dependence of the elastic compliance s_{ij}^* and the relaxation time τ on $d_{31}^{(n)}$ and $s_{ij}^{*(n)}$ which is observed for normal and inverse relaxations. It should be noted that the curve $s_{11}^{"*}(\omega)$ coincides completely with the curve $s_{12}^{"*}(\omega)$ curve; i.e., we have $s_{11}^{"*}(\omega) = s_{12}^{"*}(\omega)$ at any frequency, as can be seen from Figs. 1 and 2. This coincidence results from the equality $s_{11}^{*E} - s_{11}^{*D} = s_{12}^{*E} - s_{12}^{*D} = (d_{31}^*)^2/\varepsilon_{33}^{*\sigma}$ due to the transverse isotropy of the composite under consideration (isotropy in the plane, ∞mm symmetry). Therefore, upon simultaneous application of the mechanical stresses σ_1^* and σ_2^* to the composite (biaxial stress), the total energy loss

$$W = 1/2 s_{11}^{"*}(\sigma_1^{*2} + \sigma_2^{*2}) + s_{12}^{"*}\sigma_1^*\sigma_2^*$$
$$= 1/2 s_{11}^{"*}(\sigma_1^* + \sigma_2^*)^2 \geq 0$$

(9)
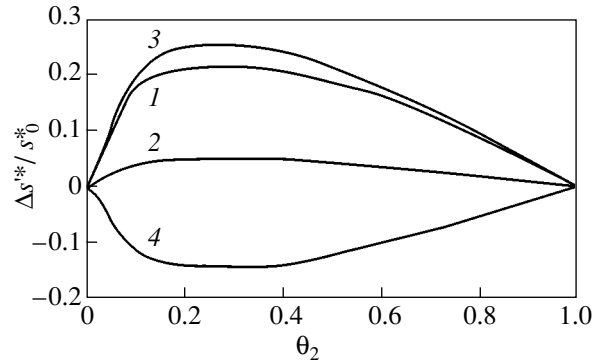
Fig. 3. Concentration dependences of the degree of Maxwell–Wagner relaxation of the effective elastic compliances of a bilayer composite consisting of PKR-7M and PKR-1 ceramics: (1) $\Delta s_{33}^{'*}/s_{330}^{'*}$, (2) $\Delta s_{11}^{'*}/s_{110}^{'*}$, (3) $\Delta s_{13}^{'*}/s_{130}^{'*}$, and (4) $\Delta s_{12}^{'*}/s_{120}^{'*}$. Conditions: $\gamma_1 = 10^{-13}\ \Omega^{-1}\ m^{-1}$ and $\gamma_2 = 10^{-11}\ \Omega^{-1}\ m^{-1}$.

is positive for any sign of σ_1^* and σ_2^*, even though the contribution $s_{12}^{"*}(\omega)\sigma_1^*\sigma_2^*$ to the energy loss can be negative, which, in turn, can lead to a partial increase in the elastic energy.

We focused main attention on the case of equal concentrations $\theta_1 = \theta_2 = 0.5$, when the degree of dispersion of the effective elastic constants $\Delta s_{ij}^{'*}/s_{ij0}^*$ is relatively large. For $\theta_1/\theta_2 \longrightarrow 0$ or $\theta_1/\theta_2 \longrightarrow \infty$, the degree of dispersion approaches zero. Consequently, the possibility exists of controlling the degree of elastic Maxwell–Wagner relaxation not only through the specific choice of the physical constants of the components but also by varying their relative volume concentrations (Fig. 3). It is interesting to note that, in the case under consideration, all the quantities $\Delta s_{ij}^{'*}/s_{ij0}^*$ have a maximum at the same concentration $\theta_2 = 0.27$.

4. CONCLUSION

It was demonstrated that, for a piezoactive composite consisting of two types of layers with complex permittivities, the majority of the effective elastic compliances undergo normal Maxwell–Wagner relaxation. However, for certain elastic constants, the Maxwell–Wagner relaxation can be inverse.

REFERENCES

1. W. F. Brown, *Dielectrics* (Springer, Berlin, 1956; Inostrannaya Literatura, Moscow, 1961).

2. A. R. von Hippel, *Dielectrics and Waves* (Wiley, New York, 1954; Inostrannaya Literatura, Moscow, 1960).

3. H. Ueda, E. Fukada, and F. E. Karasz, J. Appl. Phys. **60**, 2672 (1986).

4. D. Damjanovic, M. Demartin Maeder, P. Duran Martin, *et al.*, J. Appl. Phys. **90**, 5708 (2001).

5. R. E. Newnham, D. P. Skinner, and L. E. Cross, Mater. Res. Bull. **13**, 525 (1978).

6. A. V. Turik and G. S. Radchenko, J. Phys. D: Appl. Phys. **35**, 1188 (2002).

7. A. V. Turik, Fiz. Tverd. Tela (Leningrad) **12** (3), 892 (1970) [Sov. Phys. Solid State **12**, 688 (1970)].

8. A. V. Turik and E. I. Bondarenko, Ferroelectrics **7**, 303 (1974).

9. M. E. Drougard and D. R. Young, Phys. Rev. **94**, 1561 (1954).

10. A. Ya. Dantsiger, O. N. Razumovskaya, L. A. Reznitchenko, L. D. Grinyeva, R. U. Devlikanova, S. I. Dudkina, S. V. Gavrilyachenko, N. V. Dergunova, and A. N. Klevtsov, *Highly Effective Piezoceramic Materials: A Handbook* (Kniga, Rostov-on-Don, 1994).

11. A. V. Turik, Ferroelectrics **222**, 33 (1999).

Translated by N. Korovin

Anomalous Dispersion of Electromagnetic Eigenwaves in a Sandwich Structure with a Gap

V. I. Alshits and V. N. Lyubimov

Shubnikov Institute of Crystallography, Russian Academy of Sciences, Leninskiĭ pr. 59, Moscow, 119333 Russia
e-mail:alshits@ns.crys.ras.ru
Received November 14, 2002

Abstract—A system of two different isotropic dielectric plates aligned parallel to each other and separated by a gap is considered. For a sufficiently large gap, electromagnetic eigenwaves in the plates are virtually independent and dispersion curves for the studied system are characterized by an infinite set of intersections. A decrease in the gap thickness leads to coupling between the wave fields and the disappearance of the intersection points due to divergence of the dispersion curves. Each of the dispersion curves of the spectrum transformed under the action of coupling is formed by a set of adjacent portions of initially independent branches corresponding to different plates. A gradual change in the frequency along one of the new dispersion curves results in a periodic displacement of the localization zone of the wave field from one plate to the other. © 2003 MAIK "Nauka/Interperiodica".

1. INTRODUCTION

The purpose of this paper is to demonstrate that a sufficiently weak coupling between electromagnetic waves in a sandwich structure consisting of two isotropic plates separated by a gap leads to a radical transformation of the whole system of dispersion curves for eigenwaves in noninteracting plates. This transformation is characterized by a specific frequency dependence of the localization of the main zones of the wave field: a gradual change in the frequency is accompanied by a periodic displacement of these zones from one plate to the other. Let us describe this phenomenon in more detail.

2. FORMULATION OF THE PROBLEM

We consider a system of two isotropic plates that are aligned parallel to each other and have thicknesses $2d$ and $2\tilde{d}$ (Fig. 1). The plates are characterized by the permittivities ε and $\tilde{\varepsilon}$, respectively. They are located in a medium with the permittivity ε_0 and are separated by a gap of thickness h. In the case when the gap substantially exceeds the wavelength, the plates do not interact with each other. Based on the general electrodynamic principles (the Maxwell equations and standard boundary conditions for electric and magnetic fields [1, 2]), the unperturbed wave fields for the isolated lower plate can be represented in the following form:

$$\begin{bmatrix} \mathbf{E}(x, y, t) \\ \mathbf{H}(x, y, t) \end{bmatrix} = \begin{bmatrix} \mathbf{E}(y) \\ \mathbf{H}(y) \end{bmatrix} \exp\left[i\omega\left(\frac{1}{c}n_\parallel x - t\right) \right]. \quad (1)$$

Here, $\mathbf{E}$ and $\mathbf{H}$ are the vectors of the electric and magnetic fields, respectively; x and y are the coordinates of

the variable point; t is the time; ω is the frequency; c is the velocity of light in free space; $n_\parallel = kc/\omega$; and k is the wave number, which corresponds to the total projection of the wave vectors of all the partial waves onto the x axis parallel to the surfaces. In this case, the y projections of the wave vectors of the partial waves propagating in the plane and in adjacent media are defined as $k_y^+ = \pm\omega n_\perp/c$ and $k_{0y}^+ = \pm i\omega p/c$, respectively. Here,

$$n_\perp = \sqrt{\varepsilon - n^2}, \quad p = \sqrt{n_\parallel^2 - \varepsilon_0}. \quad (2)$$

These parameters are the components of the dimensionless wave vectors of the corresponding partial waves,

$$\mathbf{n}^\pm = (n_\parallel, \pm n_\perp, 0), \quad \mathbf{n}_0^\pm = (n_\parallel, \pm ip, 0). \quad (3)$$
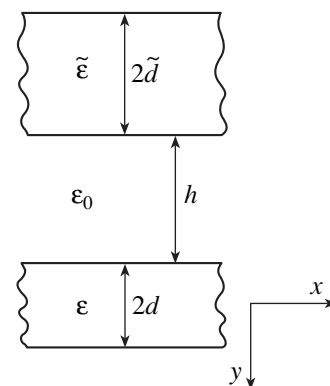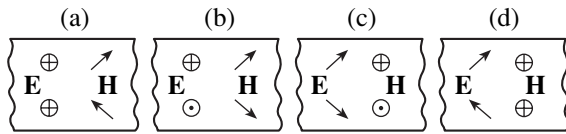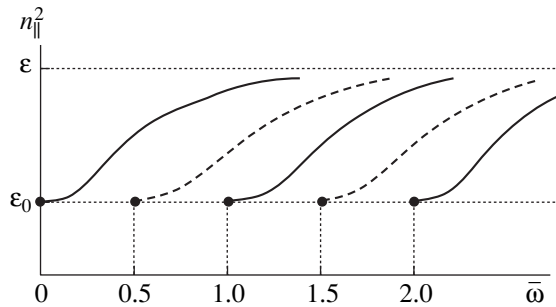

Fig. 1. System of two interacting plates.

Fig. 2. Four types of configurations of electric and magnetic fields for eigenwaves propagating in an isolated plate: (a) $(S_E A_H)_I$, (b) $(A_E S_H)_I$, (c) $(S_E A_H)_{II}$, and (d) $(A_E S_H)_{II}$.

Fig. 3. Dispersion curves for electromagnetic eigenwaves in an isolated plate. Solid and dashed lines are the dispersion curves for the configurations $(S_E A_H)_I$ and $(A_E S_H)_I$, respectively. $\bar{\omega} = \omega d \sqrt{\varepsilon - \varepsilon_0}/\pi c$.

In what follows, we will assume that the material parameters of the media and the wave number k are chosen in such a manner as to satisfy the condition

$$\varepsilon_0 \leq n_\parallel^2 \leq \varepsilon. \qquad (4)$$

Under condition (4), the parameters defined by relationships (2) are real quantities. This corresponds to the propagation of bulk waves in the plate and an exponential decay of the wave field outside the plate with the distance from the plate surfaces. This decay can be described by the following relationships:

$$\begin{bmatrix} \mathbf{E}(y) \\ \mathbf{H}(y) \end{bmatrix} \sim \begin{cases} \exp\left(-\omega \dfrac{1}{c} p y\right), & y \geq d, \qquad (5) \\[2mm] \exp\left(\omega \dfrac{1}{c} p y\right), & y \leq -d. \qquad (6) \end{cases}$$

This field provides a weak coupling with the second plate.

3. THEORETICAL ANALYSIS

Let us analyze the specific features of the wave fields generated in the lower plate in more detail. As usual, when the sagittal plane (xy) is the plane of symmetry, there should exist two independent families of eigenwaves, namely, families I and II. In family I, the electric field $\mathbf{E}$ is perpendicular to the sagittal plane,

whereas the magnetic field $\mathbf{H}$ related to it is parallel to this plane. Conversely, in family II, the magnetic field $\mathbf{H}$ is perpendicular to the sagittal plane and the electric field $\mathbf{E}$ is parallel to it. One more simplification emerges because of the symmetry of the problem with respect to the central plane of the plate ($y = 0$). By virtue of this symmetry, the waves belonging to families I and II are subdivided into symmetric and antisymmetric waves with respect to the plane $y = 0$. If the wave of the electric field is symmetric (S_E), the wave of the magnetic field is antisymmetric (A_H), and vice versa. In other words, four independent families of eigenwaves should propagate in the plate; these four families will be designated hereafter as $(S_E A_H)_I$, $(A_E S_H)_I$, $(S_E A_H)_{II}$, and $(A_E S_H)_{II}$ (Fig. 2). The amplitude factors corresponding to these families in formula (1) can be determined from the expressions

$$\begin{bmatrix} \mathbf{E}(y) \\ \mathbf{H}(y) \end{bmatrix}_I^{\pm} = A_I^{\pm} \left\{ \begin{bmatrix} (0, 0, 1) \\ (n_\perp, -n_\parallel, 0) \end{bmatrix} \exp\left(i\omega \frac{1}{c} n_\perp y\right) \right.$$

$$\left. \pm \begin{bmatrix} (0, 0, 1) \\ (-n_\perp, -n_\parallel, 0) \end{bmatrix} \exp\left(-i\omega \frac{1}{c} n_\perp y\right) \right\}, \qquad (7)$$

$$\begin{bmatrix} \mathbf{E}(y) \\ \mathbf{H}(y) \end{bmatrix}_{II}^{\mp} = A_{II} \left\{ \begin{bmatrix} (-n_\perp, n_\parallel, 0) \\ (0, 0, 1) \end{bmatrix} \exp\left(i\omega \frac{1}{c} n_\perp y\right) \right.$$

$$\left. \mp \begin{bmatrix} (n_\perp, n_\parallel, 0)/\varepsilon \\ (0, 0, 1) \end{bmatrix} \exp\left(-i\omega \frac{1}{c} n_\perp y\right) \right\}.$$

Here, $-d \leq y \leq d$ and A_I and A_{II} are the amplitude factors. In expressions (7) and (8), the upper and lower signs refer to the configurations $S_E A_H$ and $A_E S_H$, respectively.

Each of the families is characterized by its own dispersion curve $\omega(n_\parallel^2)$, which, in turn, is described by the appropriate relationship:

$$\omega(n_\parallel^2)$$

$$= \frac{c}{d} \begin{cases} [\arctan(p/n_\perp) + m_I \pi]/n_\perp, & (S_E A_H)_I, \qquad (9) \\[1mm] -[\arctan(n_\perp/p) + l_I \pi]/n_\perp, & (A_E S_H)_I, \qquad (10) \\[1mm] -[\arctan(\varepsilon_0 n_\perp/\varepsilon p) + m_{II} \pi]/n_\perp, & (S_E A_H)_{II}, \quad (11) \\[1mm] [\arctan(\varepsilon p/\varepsilon_0 n_\perp) + l_{II} \pi]/n_\perp, & (A_E S_H)_{II}. \quad (12) \end{cases}$$

Here, $m_{I, II}$ and $l_{I, II}$ are integers satisfying the condition $\omega(n_\parallel^2) > 0$. Figure 3 depicts the dispersion curves for wave fields of mode I [defined by expression (7)], which are described by relationships (9) and (10). The dispersion curves for mode II [defined by expression (8)], which are described by relationships (11) and (12), are qualitatively similar to the dependences shown in Fig. 3. Dispersion curves for modes I and II emerge from the

same points on the line $n_\parallel^2 = \varepsilon$ and have a common asymptote $n_\parallel^2 = \varepsilon_0$. However, the branches corresponding to symmetric and antisymmetric fields should exchange places for mode *II*. The run of the dispersion curves for mode *II* differs from that for mode *I* due to the distortion caused by the ratio $\varepsilon/\varepsilon_0$ appearing in formulas (11) and (12). It can be easily verified that, for all four families, the dispersion curves have no intersections at $n_\parallel^2 \neq \varepsilon_0$. It should be noted that, at any thickness *h* of the gap, dispersion curves for modes *I* and *II* also emerge from the same common points on the line $n_\parallel^2 = \varepsilon_0$ (when $p = 0$).

The isolated upper plate $(-h - d - 2d \leq y \leq -h - d)$ is described by similar relationships. At the same time, since $\varepsilon \neq \tilde{\varepsilon}$ and $d \neq \tilde{d}$, the configuration of the dispersion curves of the upper plate essentially differs from the corresponding configuration of the dispersion curves of the lower plate: the distances between the dispersion curves and the upper limiting value of $n_\parallel^2$ change.

Now, we consider a system of two plates. In the case when the gap thickness *h* is sufficiently large, wave fields induced in the plates are virtually independent and the dispersion curves determined by different parameters superpose onto one another and have a great number of intersections. A decrease in the gap thickness leads to coupling between the wave fields in the plates and a breaking of the symmetry of the fields with respect to the central planes of the plates. However, two families of wave fields persist because the sagittal plane remains the plane of symmetry as before. As a result, the points of intersection of the branches corresponding to the same family (*I* or *II*) disappear and the divergence of the dispersion curves is observed (Fig. 4). It follows from the calculations that the degree of divergence is determined by the quantity

$$D(n_\parallel^2) = 2|\Delta\omega|$$

$$= 4(c/\sqrt{d\tilde{d}})[\exp(-H)]\sqrt{\frac{n_\parallel^2 - \varepsilon_0}{(\varepsilon - \varepsilon_0)(\tilde{\varepsilon} - \varepsilon_0)}}. \tag{13}$$

Here, we assume that $\exp(-H) \ll 1$, where $H = h\omega\sqrt{n_\parallel^2 - \varepsilon_0}/c$ is the dimensionless thickness of the gap and the value of $n_\parallel^2$ should correspond to the relevant coordinate of the point of intersection. In this case, the points of intersection of branches belonging to different families are retained.

In this work, we considered the features of the dispersion spectrum for isotropic plates forming a sandwich structure. In our recent paper [3], we described
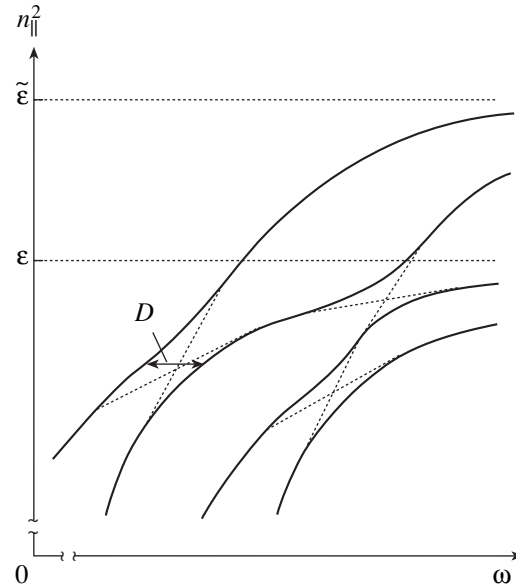
Fig. 4. Diagram illustrating the generation of mixed modes. Dashed lines are the dispersion curves in the absence of interaction between the plates.

similar features of the dispersion spectrum for a single anisotropic plate prepared from an optically uniaxial or biaxial crystal. The anomalous transformation of the spectrum of electromagnetic eigenwaves described in [3] was caused by a small deviation of the direction of propagation of the wave field from symmetric orientations. The dielectric anisotropy proved to be responsible for coupling between the wave fields. It was demonstrated that a gradual change in the frequency along the perturbed dispersion curve is accompanied by a sharp periodic change in the polarization of the wave field.

The situation described in the present work essentially differs from that analyzed in [3]. In the case studied here, the plates are isotropic and a change in the frequency along one of the dispersion curves corresponds to a periodic displacement of the zones of the intense wave field from one plate to the other.

REFERENCES

1. L. D. Landau and E. M. Lifshitz, *Course of Theoretical Physics*, Vol. 8: *Electrodynamics of Continuous Media*, 4th ed. (Nauka, Moscow, 1992; Pergamon, New York, 1984).

2. F. I. Fedorov and V. V. Filippov, *Reflection and Refraction of Light by Transparent Crystals* (Nauka i Tekhnika, Minsk, 1976).

3. V. I. Alshits and V. N. Lyubimov, Fiz. Tverd. Tela (St. Petersburg) **45** (2), 222 (2003) [Phys. Solid State **45**, 231 (2003)].

Translated by O. Moskalev

DEFECTS, DISLOCATIONS, AND PHYSICS OF STRENGTH

Model of Ideal Relaxation of Thermoelastic Stresses in the Course of Growth of Single Crystals

Sh. Kh. Khannanov*, S. P. Nikanorov**, and S. I. Bakholdin**

* Institute of Physics of Molecules and Crystals, Ufa Scientific Center,
Russian Academy of Sciences, Ufa, 450075 Bashkortostan, Russia
e-mail: imep@anrb.ru

** Ioffe Physicotechnical Institute, Russian Academy of Sciences, Politekhnicheskaya ul. 26, St. Petersburg, 194021 Russia
e-mail: nikanorov@pop.ioffe.rssi.ru
Received September 25, 2002

Abstract—A simple dislocation model is proposed for relaxation of thermoelastic stresses generated during the growth of single crystals from a melt. This model does not require a solution of the kinetic equations for dislocations involved in relaxation and makes it possible to obtain the lower estimate of the dislocation density in the bulk of a grown crystal. © *2003 MAIK "Nauka/Interperiodica".*

1. INTRODUCTION

The growth of perfect (dislocation-free) single crystals of different shapes is an important problem in solid-state physics [1, 2]. In the present paper, we will deal with melt-grown single crystals in which dislocations can be generated by thermoelastic stresses [1–3]. In this case, dislocations play the role of carriers of the plastic strain responsible for relaxation. In order to control the degree of perfection of single crystals, it is necessary to determine the dependence of the dislocation density ρ on the main physical factors, specifically on the temperature field $T(\mathbf{r})$. A rigorous treatment requires self-consistent solution of the problem including equations for determining the temperature field $T(\mathbf{r})$, thermoelastic stresses $\sigma_{ik}(\mathbf{r})$, and dislocation distribution functions $f^q(\mathbf{r}, t)$ in different slip systems q. This problem is rather complex and tedious and involves cumbersome calculations. The elastic–plastic problem remains complicated even within the macroscopic approach (see, for example, [4]).

In this respect, even in the first works on dislocation generation during the growth of single crystals, researches repeatedly attempted to obtain approximate estimates of the dislocation density from partial characteristics of the temperature field, such as the first and second derivatives in the growth direction (i.e., along the crystal axis) or in the radial direction. The theoretical models were constructed under the assumption that arising dislocations completely compensate for the temperature bending of the crystal, which is caused by a nonuniform temperature distribution along one of the axes [5–7]. In some cases, the obtained estimates have offered satisfactory results.

Moreover, in the majority of works, the above problem was solved using an approach based on an analysis of thermoelastic stresses rather than on an analysis of the crystal lattice bending. Since the uncompensated dislocations are responsible for both the lattice bending and thermoelastic stresses, in our opinion, it is possible to develop a model that combines the two aforementioned approaches. Such a model should be constructed with due regard for strick separation of different sorts of dislocations, depending on their effect on the characteristics of the crystal. Construction of this model was the main objective of the present work. We proposed the dislocation model of ideal relaxation of thermoelastic stresses. This model is valid under certain physical assumptions and allows one to obtain a lower estimate of the dislocation density ρ without solving kinetic equations for the dislocation distribution functions $f^q(\mathbf{r}, t)$

2. FORMULATION AND PHYSICAL JUSTIFICATION OF THE MODEL FOR IDEAL RELAXATION OF THERMOELASTIC STRESSES

Let us consider a single crystal of volume V with a nonuniform temperature distribution $T(\mathbf{r})$. It is assumed that a physical small-sized volume δV is cut from the volume V in such a way that the temperature $T(\mathbf{r})$ at the point $\mathbf{r}$ (the center of the volume δV) remains constant. In this case, the volume δV should undergo a free thermal expansion (distortion) $u_{ik}(\mathbf{r})$; that is,

$$u_{ik}(\mathbf{r}) = \chi T(\mathbf{r})\delta_{ik}, \qquad (1)$$

where δ_{ik} is the Kronecker symbol and χ is the thermal expansion coefficient. For simplicity, the thermal expansion is assumed to be isotropic. The distortions $u_{ik}(\mathbf{r})$ can be incompatible (we are interested precisely in this case) and induce thermoelastic stresses $\sigma_{ik}(\mathbf{r})$.

The internal stresses are also produced by dislocations. In the framework of the continuum theory, the stresses σ_{mn} are directly determined by the dislocation density tensor α_{pl} [8–10]. On this basis, the incompatible thermal distortions $u_{ik}(\mathbf{r})$ (1) can be replaced by the equivalent fictive-dislocation density tensor α_{pl}^{F} (responsible for the same elastic stresses):

$$\alpha_{pl}^{F} = -E_{pmk}u_{kl,m} = E_{pml}(\chi T_{,m}), \qquad (2)$$

where E_{pmk} is the unit antisymmetric tensor and the subscript after the comma indicates differentiation with respect to the corresponding coordinate. Here, expression (1) was used when changing over to equality (2). In the general case, the fictive-dislocation density α_{pl}^{F} includes the active part $\alpha_{pl}^{F(1)}$ and the nonactive part $\alpha_{pl}^{F(2)}$. Unlike the active part, the nonactive part does not produce internal elastic stresses σ_{mn} and can be rejected. For the present, we will assume that $\alpha_{pl}^{F(2)} = 0$ and $\alpha_{pl}^{F} = \alpha_{pl}^{F(1)}$; i.e., the tensor α_{pl}^{F} consists of the active part. The changes associated with the contribution of the nonactive part $\alpha_{pl}^{F(2)} \neq 0$ will be considered at the end of the paper.

Our subsequent reasoning is as follows. The thermoelastic stress relaxation due to the generation and motion of real (lattice) dislocations can be treated as relaxation of stresses that are induced by fictive dislocations with the density tensor α_{pl}^{F} defined by relationship (2). We believe that the relaxation proceeds to completion (this is one of the assumptions of the model of ideal thermoelastic-stress relaxation); i.e., the thermoelastic stresses $\sigma_{ik}(\mathbf{r})$ are eliminated completely. In this situation, the tensor α_{pl}^{R} of the density of real (lattice) dislocations should exactly compensate for the fictive-dislocation density tensor α_{pl}^{F}. To put it differently, at any point $\mathbf{r} \in V$, the following equality should be satisfied:

$$\alpha_{pl}^{F} + \alpha_{pl}^{R} = 0. \qquad (3)$$

Since the growth of crystals from a melt occurs very slowly even at premelting temperatures, the assumption regarding the complete relaxation of thermoelastic stresses [equality (3)] should hold under natural conditions. (In actual fact, equality (3) should be valid in the vicinity of the crystallization front, where the thermoelastic stresses and dislocation mobility are sufficiently high.)

Equality (3) enables us to determine the lattice dislocation density tensor

$$\alpha_{pl}^{R}(\mathbf{r}) = -\alpha_{pl}^{F}(\mathbf{r}). \qquad (4)$$

Substitution of expression (2) into equality (4) gives

$$\alpha_{pl}^{R} = -E_{pml}(\chi T_{,m}). \qquad (5)$$

Thus, we derived formula (5) for the tensor α_{pl}^{R} of the density of lattice dislocations that are required for ideal (complete) relaxation of the thermoelastic stresses associated with the specified temperature field $T(\mathbf{r})$ in the single crystal. Note that we obviated the need for solving the kinetic equations with respect to the distribution functions $f^{q}(\mathbf{r}, t)$ of lattice dislocations.

However, the density tensor α_{pl}^{R} does not contain detailed information on dislocations distributed in the volume V. Moreover, experimenters prefer to deal with the so-called scalar dislocation density ρ. In this respect, our next step consists in deducing the expression relating ρ and α_{pl}^{R}. This expression can be obtained for the known relative densities (contributions) of dislocations in different slip systems q.

The real-dislocation density tensor α_{pl}^{R} can be expressed through the distribution function $f^{q}(\mathbf{r}, t)$ according to the relationship [9]

$$\alpha_{pl}^{R} = \sum_{q} \tau_{p}^{q} b_{l}^{q} f^{q}, \qquad (6)$$

where $\boldsymbol{\tau}^{q}$ is the unit vector of the tangent to the dislocation line, $\mathbf{b}^{q}$ is the Burgers vector of the dislocation, and the summation is performed over all sorts q of dislocations. The scalar dislocation density ρ can be written in the form

$$\rho = \sum_{q} f^{q}. \qquad (7)$$

As can be seen from formulas (6) and (7), the quantities α_{pl}^{R} and ρ are not directly related, because they are expressed through different moments described by the unknown function $f^{q}(\mathbf{r}, t)$. The scalar dislocation density ρ can be approximately evaluated under reasonable assumptions regarding the form of the function $f^{q}(\mathbf{r}, t)$. In the general case, this function involves two terms f_{1}^{q} and f_{2}^{q}; that is,

$$f^{q}(\mathbf{r}, t) = f_{1}^{q} + f_{2}^{q}, \qquad (8)$$

where the terms f_{1}^{q} and f_{2}^{q} correspond to uncompensated and compensated dislocations, respectively. By definition, a set of compensated dislocations contains an equal number of dislocations with different signs and does not contribute to the tensor α_{pl}^{R}. Taking into

account this circumstance, from relationships (6) and (8), we have

$$\alpha_{pl}^{R} = \sum_{q} \tau_{p}^{q} b_{l}^{q} f_{1}^{q}. \tag{9}$$

The scalar dislocation density does not depend on the dislocation sign. Therefore, both terms f_{1}^{q} and f_{2}^{q} contribute to the density ρ. As a result, according to formulas (7) and (8), we obtain

$$\rho = \rho_1 + \rho_2 \equiv \sum_{q} f_{1}^{q} + \sum_{q} f_{2}^{q}. \tag{10}$$

In the framework of the proposed model of ideal thermoelastic-stress relaxation, we assume that $f_{2}^{q} = 0$. Consequently, we have

$$\rho = \rho_1 \equiv \sum_{q} f_{1}^{q}. \tag{11}$$

Relationships (9) and (11) can be closed under the simplifying assumption that dislocations of one sort make a contribution to each component of the tensor α_{pl}^{R} (9). The subscripts p and l refer to the sole sort $q(pl)$ of dislocations. Hence, from expression (9), we obtain

$$f_{1}^{q} = (\tau_{p}^{q} b_{l}^{q})^{-1} \alpha_{pl}^{R}. \tag{12}$$

Substitution of relationship (12) into formula (11) gives the expression for ρ_1 in the following form:

$$\rho_1 = \sum_{pl} (\tau_{p}^{q} b_{l}^{q})^{-1} \alpha_{pl}^{R}, \tag{13}$$

where $q = q(pl)$ is the dislocation sort specified by the subscripts p and l. It should be noted that the function f_{1}^{q} can also be derived in other ways, for example, with the use of experimental data on relative contributions of different slip systems to the tensor α_{pl}^{R}.

All the theoretical results obtained above hold true under the initial assumption that $\alpha_{pl}^{F} = \alpha_{pl}^{F(1)}$ and $\alpha_{pl}^{F(2)} = 0$ (see Section 2). When these conditions are not satisfied, the above scheme must be modified; specifically, α_{pl}^{F} in formulas (3) and (4) must be replaced by $\alpha_{pl}^{F(1)}$ and the temperature $T(\mathbf{r})$ in expression (5) must be replaced by $T^{(1)}(\mathbf{r})$. Here, $\alpha_{pl}^{F(1)}$, and $T^{(1)}(\mathbf{r})$ are defined by the relationships

$$\alpha_{pl}^{F(q)} = E_{pml}(\chi T_{,m}^{(1)}), \tag{14}$$

$$T^{(1)} = T - T^{(2)}, \tag{15}$$

where $T^{(2)}(\mathbf{r})$ is the temperature distribution that does not lead to elastic stresses σ_{mn} in the crystal. As a result, the solution of the problem is reduced to the determination of the temperature distribution $T^{(2)}(\mathbf{r})$ corresponding to the real situation.

In order to determine the function $T^{(2)}(\mathbf{r})$, we will use the strain compatibility conditions ($p, q = x, y, z$)

$$\eta_{pq} = 0, \tag{16}$$

where the symmetric incompatibility tensor η_{pq} for the thermal distortions (1) can be expressed through the derivatives of the temperature $T(\mathbf{r})$; that is,

$$\eta_{pq} = \eta_{pq}(T) = \chi(T_{,mm}\delta_{pq} - T_{,pq}). \tag{17}$$

By definition, we have $\eta_{pq}(T^{(2)}) = 0$. Making allowance for expression (17), this condition can be rewritten in the form

$$T_{,mm}^{(2)}\delta_{pq} - T_{,pq}^{(2)} = 0. \tag{18}$$

The solution to the set of second-order differential equations (18) is any linear function of the type

$$T^{(2)}(x, y, z) = ax + by + cz + d, \tag{19}$$

where a, b, c, and d are arbitrary coefficients. Consequently, the function $T^{(2)}$ cannot be uniquely determined from the compatibility conditions (18). Therefore, it is necessary to invoke additional physical conditions. In the framework of the proposed model of ideal thermoelastic-stress relaxation, it is reasonable to assume that the function $T^{(2)}(\mathbf{r})$ should satisfy the minimum condition for the integrated scalar dislocation density R; that is,

$$\frac{\delta R}{\delta T^{(2)}} = 0. \tag{20}$$

Here, the functional R of the function $T^{(2)}(\mathbf{r})$ can be represented in the form

$$R[T^{(2)}(\mathbf{r})] = \int_{V} \rho_1[T^{2}(\mathbf{r}')]d\mathbf{r}', \tag{21}$$

where $\delta R/\delta T^{(2)}$ is the variational derivative and V is the crystal volume.

Let us consider the one-dimensional problem when the temperature $T(z)$ depends on one variable z. It is approximately this situation that arises during the growth of single crystals from a melt. We assume that the crystal is located in the range $z_1 \leq z \leq z_2$ and the temperature $T(z)$ satisfies the boundary conditions $T(z_1) = T_1$ and $T(z_2) = T_2$. At $T = T(z)$, the set of equations (18) is reduced to one equation

$$T_{,zz}^{(2)} = 0 \tag{22}$$

and its general solution is represented by the linear function

$$T^{(2)} = kz + c, \qquad (23)$$

where k and c are arbitrary coefficients. Substitution of formula (23) into expression (15) permits us to determine the function $T^{(1)}$. By substituting $T^{(1)}$ for T in relationship (5), we obtain the nonzero components of the real-dislocation density tensor α_{kl}^{R}:

$$\alpha_{12}^{R} = -\alpha_{21}^{R} = \chi(\partial T/\partial z - k). \qquad (24)$$

A dislocation density tensor of the type given by relationship (24) allows us to represent edge dislocations in the form of a square network in the xy plane normal to the z axis. According to this representation and formulas (13) and (24), the density ρ_1 can be written as follows:

$$\rho_1 = 2/b\chi|\partial T/\partial z - k|, \qquad (25)$$

where b is the magnitude of the Burgers vector of edge dislocations. The appearance of the modulus sign in expression (25) is explained by the fact that the sign of the quantity $(\tau_p b_l)^{-1}$ in formula (13) is dependent on the sign of the term $(\partial T/\partial z - k)$. Note that formula (25) is invariant with respect to the inversion transformation of the coordinate system ($z' = -z$). Substitution of formula (25) into expression (21) gives the functional R of the integrated scalar dislocation density:

$$R = (2/b\chi S)\int_{z_1}^{z_2}|T_{,z}(z') - k|dz', \qquad (26)$$

where S is the cross-sectional area of the crystal. At a given temperature field $T(z)$, the functional R depends on the unknown constant k entering into the general expression (23) for the function $T^{(2)}(z)$. With due regard for this circumstance, the minimum condition (20) is reduced to the equation for the constant k; that is,

$$d/dk\left\{\int_{z_1}^{z_2}|T_{,z}(z') - k|dz'\right\} = 0. \qquad (27)$$

Now, we consider the linear temperature field

$$T(z) \equiv \tilde{T}(z) = T_1 + k_0(z - z_1),$$
$$k_0 = (T_2 - T_1)/(z_2 - z_1), \qquad (28)$$

which satisfies the boundary conditions $T(z_1) = T_1$ and $T(z_2) = T_2$. It is easy to see that the minimum of the functional R corresponds to the equality

$$k = k_0. \qquad (29)$$

In this situation, we obtain the integrated scalar dislocation density $R = 0$. Therefore, a linear temperature

field of the type represented by relationship (28) is ideal from the viewpoint of growth of dislocation-free crystals.

We now assume that $T(z)$ differs from $\tilde{T}(z)$ by a small quantity δT and has the form

$$T(z) = \tilde{T}(z) + \delta T(z). \qquad (30)$$

As follows from the foregoing, the constant k in this case only slightly differs from k_0, so that

$$k \approx k_0 \qquad (31)$$

and, taking into account relationship (25), we have

$$\rho_1 \approx (2/b\chi)|\partial T/\partial z - k_0|. \qquad (32)$$

3. DISCUSSION

The proposed model of ideal thermoelastic-stress relaxation can be used to obtain the lower estimate of the scalar density ρ of dislocations generated during the growth of single crystals from a melt. It seems likely that the assumption regarding the complete relaxation of thermoelastic stresses holds good. The conditions for the relaxation are especially favorable in the vicinity of the crystallization front, where crystals have a maximum temperature. This is supported by the exponential dependence of the dislocation velocity on the temperature for single crystals of silicon, germanium, and other similar materials (see, for example, [11, Chapter 5]). In this region, the temperature gradient ∇T can be approximately treated as directed along the z axis (perpendicular to the crystallization front) and, hence, formula (25) can be used for estimating the density ρ_1. According to expression (10), the scalar dislocation density ρ can also involve the component ρ_2 associated with the compensated dislocations. Therefore, by assuming that $\rho = \rho_1$ [see condition (11)], we can obtain the lower estimate for the scalar dislocation density ρ.

Let us now discuss the experimental data taken from [12, 13]. The growth of germanium ribbons with the use of an apparatus with passive shields is characterized by the temperature gradient $T_{,z} \approx -0.25$ K/m in the vicinity of the crystallization front (see Fig. 1 in [12]) and the constant $k_0 \approx -0.18$ K/m. On this basis, we found that $|T_z - k_0| \approx 0.07$ K/m in the vicinity of the crystallization front. Substituting this value into formula (32) and setting $\chi \approx 10^{-5}$ K^{-1} and $b = 2 \times 10^{-10}$ m, we obtain the estimate $\rho = \rho_1 \approx 0.7 \times 10^{8}$ m^{-2}. The scalar dislocation densities were experimentally determined to be $\rho \approx (10^{8}$–$10^{10})$ m^{-2} [12, p. 242]. As can be seen, the theoretical estimates based on the model of ideal thermoelastic-stress relaxation actually correlate with the lower bound of the scalar dislocation densities observed. Our theoretical estimates are also in agreement with the experimental data presented in [13].

Formulas (25) and (32) correspond to a general case. For example, the expression derived earlier in [6] can

be deduced (within an insignificant factor) as a case of these formulas. Therefore, our theoretical data also agree with the particular theoretical results available in the literature. The approach developed in the present work provides a way of analyzing three-dimensional problems when the temperature field depends on all three coordinates. In this case, the minimum of the functional R defined by relationship (21) can be sought using trial functions that are the solutions to the set of equations (18) [in particular, it is possible to use functions of the type represented by formula (9)].

Relationships (9) and (13) describe the dependence of the dislocation density on the orientation observed in the experiments. However, this problem calls for special consideration.

4. CONCLUSIONS

Thus, we proposed a model of ideal relaxation of thermoelastic stresses. This model adequately describes the effect of the temperature field on the density of dislocations generated during the growth of single crystals. Moreover, the model proposed makes it possible to predict the minimum dislocation density that can be attained under particular conditions.

REFERENCES

1. S. P. Nikanorov, Izv. Akad. Nauk, Ser. Fiz. **58** (9), 2 (1994).
2. R. Laudise and R. Parker, *The Growth of Single Crystal. Crystal Growth Mechanisms: Energetics, Kinematics, and Transport* (Prentice Hall, New York, 1970; Mir, Moscow, 1974).
3. J. Friedel, *Dislocations* (Pergamon, Oxford, 1964; Mir, Moscow, 1967).
4. F. Theodore, T. Duffar, J. L. Santailler, *et al.*, Izv. Akad. Nauk, Ser. Fiz. **63** (9), 1693 (1999).
5. E. Billig, J. Inst. Met. **83**, 53 (1954).
6. V. L. Indenbom, Kristallografiya **4**, 594 (1959) [Sov. Phys. Crystallogr. **4**, 555 (1960)].
7. S. V. Tsivinskiĭ, in *Proceedings of the 1st Conference on Semiconductor Materials Prepared by the Stepanov Method and Prospects for Their Applications in Instrument Making* (Fiz.–Tekh. Inst. Akad. Nauk SSSR, Leningrad, 1968), p. 173.
8. M. A. Kosevich, *Dislocations in the Theory of Elasticity* (Naukova Dumka, Kiev, 1978).
9. Sh. Kh. Khannanov, *Dislocation Arrangement* (BNTs Ural. Otd. Ross. Akad. Nauk, Ufa, 1992).
10. R. de Wit, in *Fundamental Aspects of Dislocation Theory*, Ed. by J. A. Simmons, R. de Wit, and R. Bullough (National Bureau of Standards, Washington, 1970; Mir, Moscow, 1977).
11. V. P. Alekhin, *Physics of Strength and Plasticity of Surface Layers in Materials* (Nauka, Moscow, 1983), Chap. 5.
12. P. I. Antonov and V. S. Yuferev, in *Problems in Strength and Plasticity of Solids*, Ed. by S. N. Zhurkov (Nauka, Leningrad, 1979), p. 236.
13. P. I. Antonov, S. I. Bakholdin, M. G. Vasil'ev, *et al.*, Izv. Akad. Nauk SSSR, Ser. Fiz. **52** (10), 1997 (1988).

Translated by O. Borovik-Romanova

==

DEFECTS, DISLOCATIONS,
AND PHYSICS OF STRENGTH

==

Low-Temperature Plasticity and Lattice Dynamics
of Solid Parahydrogen with an Isotopic Impurity

L. A. Alekseeva, E. S. Syrkin, and L. A. Vashchenko

Verkin Institute for Low Temperature Physics and Engineering, National Academy of Sciences of Ukraine,
Kharkov, 61103 Ukraine
e-mail: alekseeva@ilt.kharkov.ua
Received July 31, 2002; in final form, October 1, 2002

Abstract—The low-temperature plasticity of solid polycrystalline parahydrogen doped with an isotopic impurity (deuterium) is studied. The dependences of the rate of steady-state creep in p-H_2 on the impurity concentration and stress are obtained. The deformation of p-H_2 is described with inclusion of the zero-point mean-square displacements $\langle x^2 \rangle$ of particles making up a crystal. The calculated and experimental values of $\langle x^2 \rangle$ are compared for two possible isotope molecules (HD and D_2) at three stress levels. A correlation between the $\langle x^2 \rangle$ values and an increase in the force constants of a p-H_2 crystal doped with the isotopic impurity is established. An increase in the mean-square displacements of p-H_2 with the tensile load is discussed. Deformation-induced purification of a p-H_2 crystal from the isotopic impurity is suggested to occur. © 2003 MAIK "Nauka/Interperiodica".

1. INTRODUCTION

Solid parahydrogen is a unique crystalline material with a rather high degree of quantization [1], which can easily be controlled and suppressed [2–4]. The high zero-point energy of H_2 fully specifies its lattice dynamics and deformation kinetics, as well as the dynamics of the dislocation subsystem, over the whole range of existence of the crystal, since its solidification temperature is well below the Debye temperature Θ [1].

Quantum tunneling effects in the plasticity of solid parahydrogen are suppressed by, in particular, local lattice imperfections, e.g., even small proportions of orthohydrogen or deuterium impurity.

Quantum-mechanical features are most strongly suppressed by an isotopic impurity. Therefore, the influence of this impurity on the deformation kinetics of parahydrogen is one of the fundamental problems in the physics of quantum crystals. Progress in investigating the plastic and strength properties of p-H_2 depends on the amount of experimental data available on the effect of the isotopic impurity on deformation parameters.

In this work, we studied the effect of the isotopic impurity on the low-temperature plastic properties of solid parahydrogen. We measured the concentration dependences of the strain rate $\dot{\varepsilon}$ in the steady-state creep under a static stress σ at liquid-helium temperatures. In addition to the data from [5], where the effect of deuterium impurity on the steady-state strain rate $\dot{\varepsilon}$ of p-H_2 was investigated at only one level of stresses σ, we measured $\dot{\varepsilon}$ as a function of the content of the H_2 heavy isotope and the applied load. The results

obtained were analyzed using the calculated temperature dependences of the mean-square particle displacements. Based on this analysis, we drew inferences about the changes in the intermolecular interaction in solid p-H_2 doped with its stable isotopes.

2. EXPERIMENTAL

We studied polycrystalline p-H_2 specimens grown from liquid parahydrogen in a cryostat ampoule [6]. The concentration of orthohydrogen was reduced to ~0.2% by long-term holding of conventional hydrogen in a converter in the presence of the conversion catalyst $Fe(OH)_3$ at the boiling temperature. To remove impurities other than hydrogen, gaseous hydrogen bled in the converter was passed through activated carbon cooled to the boiling temperature of nitrogen and the extracted vapor over liquid p-H_2 was passed through a filter having high H_2 selectivity at a temperature of 20.4 K. Due to the high filter selectivity, the purity of the p-H_2 under study with respect to foreign impurities was significantly increased (to above 99.9999 mol % [5] with allowance made for the extremely low vapor pressure of nonhydrogenic impurities [7]).

Hydrogen is characterized by the maximum relative difference of its isotopic masses, and the saturated vapor pressures over the liquid fractions of its isotopes also considerably differ [7]. Therefore, hydrogen becomes depleted of the less volatile isotope and enriched in the more volatile basic component during the initial slow extraction of the gas for growing specimens due to the difference in the partial pressures of H_2 and the isotope [8]. Concentrating the less volatile iso-
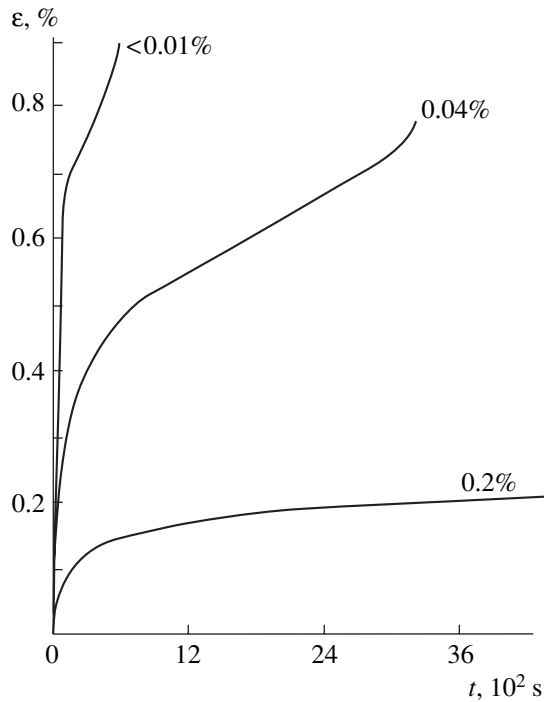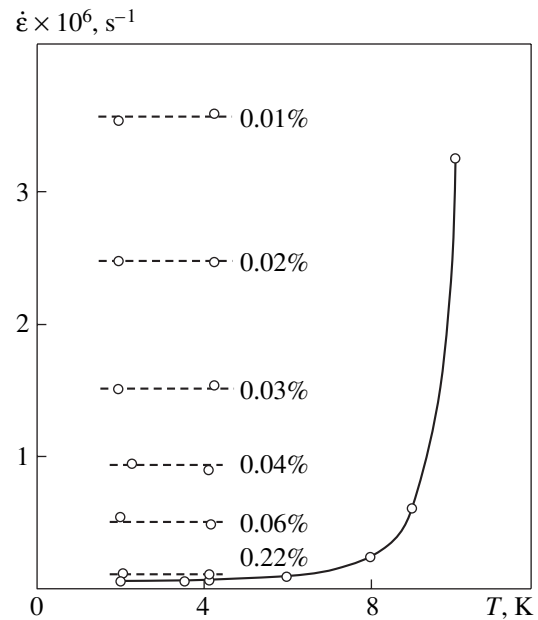
Fig. 1. Creep curves for p-H$_2$ specimens with the concentrations c shown on the curves ($\sigma = 53.9$ kPa, $T = 1.8$ K).

Fig. 2. Temperature dependences of the creep rate of p-H$_2$ obtained at the stress $\sigma = 53.9$ kPa and the concentrations c indicated on the curves. The solid line shows the data for n-H$_2$ polycrystals [6] (see text).

tope in the liquid phase and, accordingly, in the vapor of molecular p-H$_2$ led to an increase in the concentration of the isotopic impurity in each subsequently grown solid parahydrogen sample with respect to that in the previous sample. This increase was verified by isotopic analyses performed with an ROMS-1 and an MX-7304 mass spectrometer. The analyses revealed that the ratio of the number of D atoms to that of H atoms varied with the sample from $c = 0.01\% \pm 0.005$ at. % to $c = 0.2 \pm 0.002$ at. %.

Grown samples were released from the containers through evacuating the vapor over them, then annealed at $T = 11$ K, and slowly cooled to a given temperature. Then, they were loaded using a highly sensitive balance. The elongation of crystals was measured, using a variable-induction displacement pickup, with an accuracy of $\pm 10^{-4}$ cm, and the temperature was measured on semiconductor resistance thermometers with an accuracy of $\pm 2 \times 10^{-2}$ K. The variation of strain ε with time t was recorded with a KSP4 potentiometer. The polycrystalline nature of specimens (grain size of up to 1.5 mm) was verified by visual inspection using crossed polarizers. The temperature was varied in the range 1.8–4.2 K.

3. RESULTS AND DISCUSSION

Figure 1 shows the typical $\varepsilon(t)$ creep curves of the p-H$_2$ polycrystalline specimens recorded at a stress of 53.9 kPa for three different concentrations c (0.01,

0.04, 0.22%). The variation of the concentration is seen to substantially affect the $\varepsilon(t)$ curves and the plasticity parameters determined from them. It follows from Fig. 1 that a decrease in c leads to an increase in the strain of p-H$_2$ reached in the same time period at $\sigma = $ const and to a significant decrease in the time it takes for steady-state plastic flow (with a time-independent strain rate $d\varepsilon/dt$) to be established in the p-H$_2$ polycrystals. Figure 1 also shows that, as c decreases, the strain rate $\dot{\varepsilon}$ of the p-H$_2$ crystals in the stage of steady-state creep substantially increases and reaches its maximum value at $c = 0.01\%$ (the lower limit of the concentration range studied).

When studying specimens with the same isotope composition at different temperatures, we found that, although the strain rate $\dot{\varepsilon}$ depended strongly on the concentration of the isotopic impurity, the $\dot{\varepsilon}$ values measured at many different concentrations under the same load were independent of temperature throughout the σ, c, and T ranges studied. This behavior is illustrated in Fig. 2, which shows the strain rate $\dot{\varepsilon}$ measured for p-H$_2$ specimens with various [D]/[H] ratios under the same load ($\sigma = 53.9$ kPa). For comparison, Fig. 2 also demonstrates the temperature dependence $\varepsilon(t)$ of the creep rate (solid line) measured in n-H$_2$ (75% ortho-H$_2$) polycrystals at approximately the same value of σ (58.8 kPa) [6]. It is seen that an increase in the temperature from 1.8 to 4.2 K virtually does not change $\dot{\varepsilon}$;

therefore, we may neglect the effect of temperature on the low-temperature $\dot{\varepsilon}$ values as compared to the effect of impurity.

Thus, these experimental dependences indicate the decisive role of the heavy-hydrogen isotope impurity in developing the deformation in p-H$_2$ at a constant stress. Even low doping results in significant strengthening of p-H$_2$. When a relatively small amount of the isotopic impurity (the ratio of the numbers of atoms [D]/[H] ~ 0.2%) is introduced into parahydrogen, the values of strain rate $\dot{\varepsilon}$ in steady-state flow of polycrystalline p-H$_2$ specimens approach those for polycrystalline hydrogen with the conventional ortho–para composition (75% o-H$_2$). The effect of the isotopic impurity on the strain rate $\dot{\varepsilon}$ is similar to that on other physical quantities, in particular, the thermal conductivity of H$_2$ [9].

Our experiments showed that the rate of steady-state plastic flow of p-H$_2$ in the temperature range 1.8–4.2 K is a quantity that is very sensitive to the concentration of isotopes in the specimens. The sharp dependence of the creep rate $\dot{\varepsilon}$ on the concentration of the isotopic impurity in p-H$_2$ indicates that the low-temperature values of $\dot{\varepsilon}$ measured at σ = const are due to the interaction of dislocations with impurity molecules. The independence of $\dot{\varepsilon}$ from temperature against the background of the high sensitivity of $\dot{\varepsilon}$ to the content of the isotopic impurity shows that quantum rather than thermal fluctuations play the basic role in the dislocation breakaway from impurity centers in p-H$_2$ [10].

For cryocrystals (including p-H$_2$ [11]), the plastic strain rate as a function of temperature can be represented in the limit $T \longrightarrow 0$ K in the form of the law of corresponding states [12]:

$$\dot{\varepsilon} \sim f(\langle x_0^2 \rangle / \langle x_m^2 \rangle). \tag{1}$$

Here, the $\dot{\varepsilon}$ values are determined by the relative level of the zero-point mean-square displacements $\langle x_0^2 \rangle$ of particles making up a crystal. Using the law of corresponding states [12], we can write the creep rate of p-H$_2$-based solid solutions at low temperatures (to within a multiplicative constant approximately equal to unity) in the form of an Arrhenius-type expression:

$$\dot{\varepsilon} = \dot{\varepsilon}_0 \exp\left(-\frac{U - \gamma\sigma}{(\langle x_0^2 \rangle / \langle x_m^2 \rangle)kT_m}\right), \tag{2}$$

where $\langle x_0^2 \rangle$ and $\langle x_m^2 \rangle$ are the mean-square displacements of particles at 0 K and the melting temperature T_m, respectively. This expression implies that deformation proceeds via directed stress-induced dislocation flow through the saddle point of a barrier U caused by elastic stresses that appear in the p-H$_2$ lattice because of the size misfit between impurity and matrix molecules. The energy related to the stress σ is also specified by
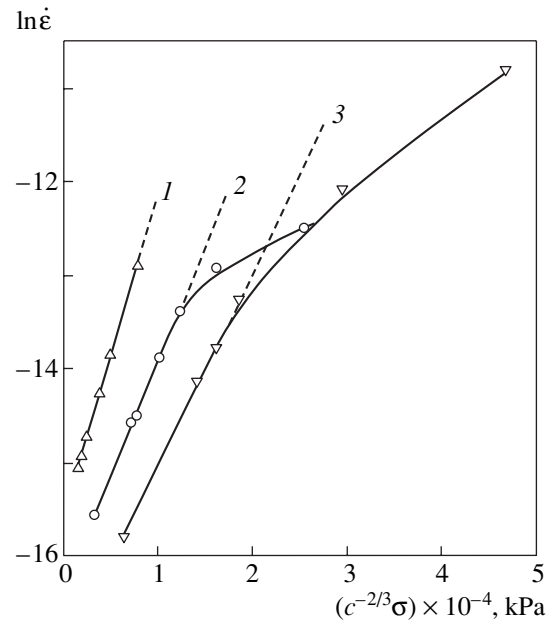

Fig. 3. Concentration dependences of the creep rate of p-H$_2$ in semilogarithmic coordinates obtained at various stresses: (*1*) 16.7, (*2*) 53.9 [5], and (*3*) 99.0 kPa.

the size γ of the activation volume in which an elementary act of deformation develops. The dependence of γ on the impurity concentration determines the behavior of $\dot{\varepsilon}$ as a function of the impurity concentration. In the presence of impurities in a crystal, rectilinear dislocations become unstable. Dislocations take a complex zigzag shape, which provides excess of the gain in the binding energy of a dislocation and impurity molecules over the loss in the energy of line tension due to an increase in the dislocation length [13]. Therefore, configurations with dislocation segments pinned by impurities begin to prevail even in the early stages of deformation in the p-H$_2$ crystals under study. In this case, when describing the behavior of plasticity parameters in classical (e.g., metallic) crystals, it is necessary to take into account the probability of passing dislocations through impurity-induced barriers because of the existence of the length distribution of dislocation segments [14–16].

Figure 3 shows the concentration dependences (on a semilogarithmic scale) of the rate of steady-state creep in the p-H$_2$ specimens for three different values of the applied stresses (16.7, 53.9, 99.0 kPa). Based on the theoretical results [16], we chose the product $c^{-2/3}\sigma$ as the abscissa. As is seen, all three dependences $\ln\dot{\varepsilon} = f(c^{-2/3}\sigma)$ obtained have extended straight-line segments, which indicates that the decisive role is played by impurity molecules existing in the bulk of the crystal in the deformation of p-H$_2$ [17]. Deviations from the straight lines at low values of c are due to retardation mechanisms associated with the residual o-H$_2$ impurity

Experimental values of normalized zero-point mean-square displacements $\overline{\delta_0^2}$ (exp) in p-H_2 at three values of tensile stress

Molecule	$(\Delta V/V)$	Quantity	σ, kPa		
			16.7	53.9	99.0
HD	-0.068	$\overline{\delta_0^2}$ (exp), HD	0.628	0.837	1.004
D_2	-0.138	$\overline{\delta_0^2}$ (exp), D_2	0.496	0.661	0.794

in the specimens and operating at high dislocation velocities. The effective mean free path of dislocations can be affected by both individual orthomolecules and their clusters [18] (mainly pair clusters for an orthohydrogen content of ~0.2% [19]). The character of the interaction of these molecules with dislocations differs only weakly from that of ordinary dilatation impurities. Dislocations can overcome such obstacles through both thermal and quantum fluctuations (for more detail, see [19]).

At $c \geq 0.03$–0.04%, energy barriers for dislocations in a p-H_2 specimen are mainly due to local breaking of the translational rather than rotational symmetry of the crystal caused by the isotope forms of the stable H_2 molecule. In this case, when analyzing the behavior of the function $\dot{\varepsilon}(T, c, \sigma)$, we have a unique opportunity to determine the relative mean-square displacements $\overline{\delta_0^2}$ (exp) $= \langle x_0^2 \rangle / \langle x_m^2 \rangle$ of hydrogen molecules in real p-H_2 specimens [even if it is only a qualitative estimation using Eq. (2)], which cannot be measured directly and are of great interest. To this end, we express the vol-

ume involved in a fluctuation through the known values $(\Delta V/V)$ of the dilatation of the p-H_2 lattice around HD and D_2 impurity molecules [20, 21] and use the slopes $\tan\alpha$ of the straight-line segments in the experimental $\ln\dot{\varepsilon} - c^{-2/3}$ curves obtained at $\sigma = $ const. Thus, the values of $\overline{\delta_0^2}$ (exp) are found from Eq. (2) to be

$$\overline{\delta_0^2}(\exp) = \frac{(\Delta V/3V)^{-1/3}\overline{\sigma}db^2}{k\tan\alpha T_m}, \qquad (3)$$

where $\tan\alpha = \Delta(\ln\dot{\varepsilon})/\Delta(c^{-2/3})$, $d = 2^{-1}\sqrt{8/3}a$ (a and d are the spacings between the nearest neighbors and the adjacent basal planes in the hcp p-H_2 crystal, respectively), $\overline{\sigma}$ is the average stress, $b = a$ is the magnitude of the Burgers vector, and k is the Boltzmann constant. The $\overline{\delta_0^2}$ (exp) values are calculated (see table) for the case where deuterium is present in p-H_2 as HD and D_2 molecules. The parameter a was taken to be equal to its extrapolated value at $T = 0$ K ($a = 0.37835$ nm [22]). The measured values $\tan\alpha$ were used to calculate the $\overline{\delta_0^2}$ (exp) values of the zero-point mean-square displacements of particles in p-H_2 from Eq. (3). These values are given in the table for both isotope forms in p-H_2 and for three values of tensile stress.

To analyze the results obtained, we estimate the $\overline{\delta_0^2}$ values for p-H_2, including for the specimens with impurity molecules represented by natural isotopes. To this end, we used the temperature dependence of the atomic root-mean-square displacements in pure and isotopically mixed fcc crystals [23]. The mean-square displacements in perfect structures are mainly specified by the number of nearest neighbors. Taking into account the ratio c/a for the perfect hcp p-H_2 structure [1] and the fact that the numbers of nearest neighbors in fcc and hcp lattices are the same, we may expect that the values of $\langle x^2 \rangle$ calculated using the Jacobian matrices in the fcc crystal model should be similar to those for the ideal hcp structure.

Figure 4 shows the temperature dependences of $\langle x^2 \rangle$ for the matrix p-H_2 molecules in the ideal crystal and for isotopic impurity molecules with $\Delta\mu$ equal to 0.5
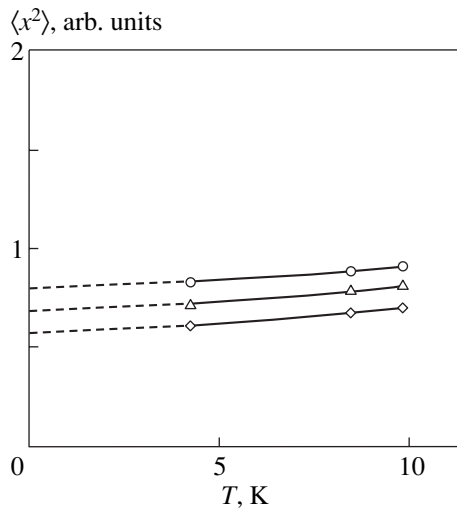
Fig. 4. Temperature dependences of the mean-square displacements of molecules in the ideal crystal (upper curve) and of impurity molecules with the mass defect equal to 0.5 (middle curve) and 1.0 (lower curve) in units of $\hbar^2/(km\Theta)$ with $\Theta = 118.5$ K [24].

and 1.0, where $\Delta\mu = (m_1 - m)/m$ is the mass defect, with m_1 being the mass of the impurity atom ($\Delta\mu = 0.5$ corresponds to the HD impurity, and $\Delta\mu = 1$, to the D_2 impurity). As is seen from Fig. 4, the mean-square displacements of impurity particles are significantly lower than the values of $\langle x^2 \rangle$ for the ideal lattice. Whence it follows that the isotopic impurity in p-H_2 should "freeze" molecular motion, including the zero-point oscillations of the matrix molecules in a crystal. This conclusion follows from the calculated values of $\overline{\delta_0^2}$ equal to 0.910, 0.878, and 0.836 for the H_2 matrix molecules and the D_2 and HD impurity molecules, respectively. A comparison of the calculated values of δ_0^2 with those given in the table shows that the molecular motion in the real specimens fabricated under laboratory conditions is less intense as compared to the hypothetic ideal infinite p-H_2 crystal with perfect structure. A decrease in the mean-square displacements of particles is equivalent to a significant increase in the intermolecular interaction (corresponding to a more rigid lattice) in the solid p-H_2 caused by impurity molecules. The degree of rigidity of the lattice and the decrease in the intensity of molecular motion in the solid p-H_2 are significantly different for the HD and D_2 impurity molecules present in the crystals. The features found are of purely quantum nature, since they are completely specified by the difference in the amplitudes of zero-point oscillations of isotopes. Interestingly, the $\overline{\delta_0^2}$ (exp) values obtained are closer to those calculated for the HD impurity than to those for D_2. This finding suggests that the majority of deuterium-containing molecules in the p-H_2 crystal studied are in the form of HD molecule rather than D_2, which agrees with the results of analysis of the specimens and with the fact that natural deuterium is present in hydrogen as deuterium–hydrogen (HD) molecules [8, p. 295].

The results obtained allow us to analyze the effect of the load applied to p-H_2 specimens on the mean-square displacements. It is seen from Fig. 3 that the slopes of the linear dependences $\ln\dot{\varepsilon} = f(c^{-2/3}\sigma)$ measured for p-H_2 at a constant load ($\sigma = $ const) decrease with increasing σ. It follows from the table that, as σ increases, the $\overline{\sigma_0^2}$ (exp) values significantly increase. The authors of [2–4] showed that point defects in quantum crystals can be considered as quasiparticles and can freely move to grain (block) boundaries or to the outer surface. The increase in the mean-square displacements in p-H_2 with increasing σ can indicate that deuterium impurities go out of the bulk of a parahydrogen crystal under a load (deformation-induced purification). The properties of this crystal become close to those of the ideal impurity-free crystal, in which the mean-square displacements of particles are noticeably higher than in the impurity crystal. The ability of solid p-H_2 to self-repair has been noted earlier [25–27].

REFERENCES

1. A. I. Prokhvatilov, *Plasticity and Elasticity of Cryocrystals* (Begell House, New York, 2001).
2. A. F. Andreev and I. M. Lifshits, Zh. Éksp. Teor. Fiz. **56**, 2057 (1969) [Sov. Phys. JETP **29**, 1107 (1969)].
3. A. F. Andreev, Zh. Éksp. Teor. Fiz. **68**, 2341 (1975) [Sov. Phys. JETP **41**, 1170 (1975)]; Usp. Fiz. Nauk **118**, 251 (1976) [Sov. Phys. Usp. **19**, 137 (1976)].
4. Yu. Kagan and L. A. Maksimov, Zh. Éksp. Teor. Fiz. **84**, 792 (1983) [Sov. Phys. JETP **57**, 459 (1983)].
5. I. N. Krupskiĭ, A. V. Leont'eva, L. A. Indan, and O. V. Evdokimova, Pis'ma Zh. Éksp. Teor. Fiz. **24**, 297 (1976) [JETP Lett. **24**, 266 (1976)].
6. I. N. Krupskiĭ, A. V. Leont'eva, L. A. Indan, and O. V. Evdokimova, Fiz. Nizk. Temp. **3**, 933 (1977) [Sov. J. Low Temp. Phys. **3**, 453 (1977)].
7. B. I. Verkin, V. G. Manzhelii, V. N. Grigoriev, V. A. Koval', V. V. Pashkov, V. G. Ivantsov, O. A. Tolkacheva, N. M. Zvyagina, and L. I. Pastur, *Handbook of Properties of Condensed Phases of Hydrogen and Oxygen* (Hemisphere, New York, 1991).
8. B. M. Andreev, Ya. D. Zel'venskiĭ, and S. G. Katal'nikov, *Heavy Hydrogen Isotopes in Nuclear Engineering* (Énergoatomizdat, Moscow, 1987).
9. O. A. Korolyuk, B. Ya. Gorodilov, A. I. Krivchikov, and V. G. Manzhelii, Fiz. Nizk. Temp. **25** (8/9), 944 (1999) [Low Temp. Phys. **25**, 708 (1999)]; B. Ya. Gorodilov, O. A. Korolyuk, A. I. Krivchikov, and V. G. Manzhelii, J. Low Temp. Phys. **119**, 497 (2000).
10. V. D. Natsik, A. I. Osetskij, V. P. Soldatov, and V. I. Startsev, Phys. Status Solidi B **54**, 99 (1972).
11. I. N. Krupskiĭ, A. V. Leont'eva, Yu. S. Stroilov, and L. A. Indan, Fiz. Nizk. Temp. **1**, 749 (1975) [Sov. J. Low Temp. Phys. **1**, 360 (1975)].
12. I. N. Krupskiĭ, A. V. Leont'eva, and Yu. S. Stroilov, Zh. Éksp. Teor. Fiz. **65**, 1917 (1973) [Sov. Phys. JETP **38**, 957 (1973)].
13. J. Friedel, *Dislocations* (Pergamon, Oxford, 1964; Mir, Moscow, 1967).
14. P. Haasen, *Physical Metallurgy*, Ed. by R. W. Cahn and P. Haasen (North-Holland, Amsterdam, 1983), Vol. 2, p. 1341.
15. V. N. Kovaleva, V. A. Moskalenko, and V. D. Natsik, Philos. Mag. A **70** (3), 423 (1994).

16. R. Labush, Phys. Status Solidi **41**, 659 (1970); Acta Metall. **20**, 917 (1972); N. F. Mott and F. R. N. Nabarro, in *Proceedings of Conference on Strength of Solids* (Phys. Soc., London, 1947), p. 1.

17. A. M. Kosevich, *Physical Mechanics of Real Crystals* (Naukova Dumka, Kiev, 1981), p. 290.

18. A. B. Harris, L. I. Amstutz, H. Meyer, and S. M. Myers, Phys. Rev. **175**, 603 (1968).

19. S. E. Kal'noĭ and M. A. Strzhemechnyĭ, Fiz. Nizk. Temp. **11**, 803 (1985) [Sov. J. Low Temp. Phys. **11**, 440 (1985)].

20. A. I. Prokhvatilov, M. A. Strzhemechnyĭ, and G. N. Shcherbakov, Fiz. Nizk. Temp. **19**, 622 (1993) [Low Temp. Phys. **19**, 445 (1993)].

21. M. A. Strzhemechny, A. I. Prokhvatilov, G. N. Shcherbakov, and N. N. Galtsov, J. Low Temp. Phys. **115** (3/4), 109 (1999).

22. I. N. Krupskiĭ, A. I. Prokhvatilov, and G. N. Shcherbakov, Fiz. Nizk. Temp. **9**, 83 (1983) [Sov. J. Low Temp. Phys. **9**, 42 (1983)].

23. V. I. Peresada, E. S. Syrkin, and V. P. Tolstoluzhskiĭ, Fiz. Kondens. Sostoyaniya, No. 33, 30 (1974).

24. *Physics of Cryocrystals*, Ed. by V. G. Manzhelii and Yu. A. Freiman (AIP Press, Woodbury, N.Y., 1996).

25. L. A. Alekseeva, Fiz. Nizk. Temp. **17**, 451 (1991) [Sov. J. Low Temp. Phys. **17**, 237 (1991)].

26. T. Oka, Fiz. Nizk. Temp. **22**, 134 (1996) [Low Temp. Phys. **22**, 96 (1996)].

27. T. Momose, J. Low Temp. Phys. **111** (3/4), 469 (1998).

Translated by K. Shakhlevich

The Influence of Breaking of Exchange Bonds on the Curie Temperature

V. I. Nikolaev* and A. M. Shipilin**

* Moscow State University, Vorob'evy gory, Moscow, 119899 Russia
e-mail: vnik@cs.msu.su
** Yaroslavl State Technical University, Moskovskiĭ pr. 88, Yaroslavl, 150023 Russia
e-mail: shipilin@polytech.yaroslavl.su
Received April 11, 2002

Abstract—The size effect of magnetically ordered nanoparticles on the Curie temperature is discussed. For a system of Fe_3O_4 nanoparticles with different dispersities, it is demonstrated that the smaller the size of the particles, the larger the thickness of their surface layer, which is characterized by considerable distortions of the regular structure. © 2003 MAIK "Nauka/Interperiodica".

1. INTRODUCTION

In recent years, great interest has been expressed by researchers in the structure and properties of ultrafine particles. This is caused not only by the unique physicochemical properties of nanoparticle systems but also by the wide possibilities of using these properties in practice [1, 2]. In particular, nanoparticles have an anomalously large coefficient of thermal expansion, which suggests that the anharmonicity of atomic vibrations plays a significant role in the surface layers of the nanoparticles [3]. The smaller the particle size, the more noticeable the influence of different factors on the surface layers and, consequently, on the properties of the particle as a whole [4].

One of the most important problems concerning the properties of ultrafine particles is associated with the elucidation of the interrelation between the specific features of the structure of the surface layers and the macroproperties of the particle as a whole. In this work, we would like to call attention to a relatively simple way of obtaining quantitative information on the structural features of the surface layer of nanoparticles from data on the Curie temperature. The proposed approach is based on the following obvious assertion. The larger the fraction of atoms in the surface layer of the particle, the greater the number of dangling exchange bonds between the atoms (as compared to the case of a large-sized particle).

2. THEORETICAL BACKGROUND

Let us first consider the situation where the surface layers of particles have a magnetic crystal structure similar to the structure of bulk particle regions. The particles are treated as identical sphere with radius r. If the particle size is not very small (for example, $r \geq 10$ nm), approximately half the exchange bonds between the magnetically active surface atoms are dangling. It is these bonds that are responsible for magnetic ordering inside the particle below the Curie temperature $T_C(r) \equiv T_C'$.

It is assumed that, for a large-sized particle, the number of exchange bonds per unit volume is equal to n. From the aforesaid it follows that, for the magnetically active surface atoms of a nanoparticle, this number amounts to $n/2$. In the case when the Curie temperature for a nanoparticle, as in our approximation, is proportional to the mean number of exchange bonds per unit volume, it is easy to show that the ratio between the Curie temperatures for ultrafine and large-sized particles can be expressed by a simple formula

$$\frac{T_C'}{T_C} = 1 - \frac{3\Delta r}{2r}, \tag{1}$$

where Δr is the thickness of the layer that is half-depleted of exchange bonds.

The quantity Δr is a convenient averaged parameter that characterizes the features of the defect structure of nanoparticles. If Δr is independent of the particle radius r, then, according to relationship (1), the relative correction to the Curie temperature, which is caused by the decrease in the particle size, changes with varying r in accordance with the hyperbolic law

$$\frac{\Delta T_C'}{T_C} = -\frac{3\Delta r}{2r}. \tag{2}$$

3. RESULTS AND DISCUSSION

The deviation from this law would unambiguously indicate that the quantity Δr is a parameter characterizing the influence of the surface layer on the Curie temperature rather than the thickness of the layer depleted
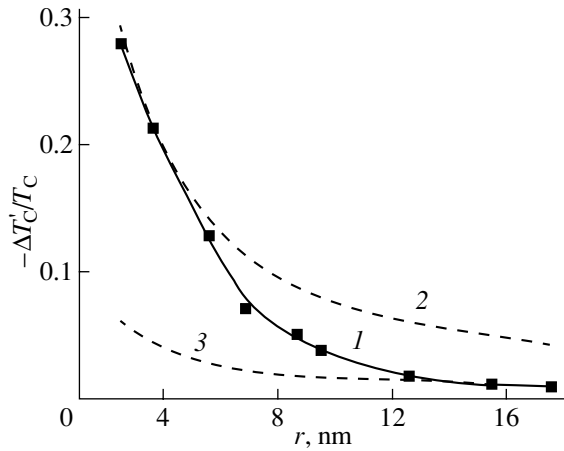
Fig. 1. Correction $\Delta T'_C / T_C$ applied to the Curie temperature (due to the decrease in the particle size) as a function of the radius r of Fe_3O_4 nanoparticles: (*1*) experimental data taken from [5] and (*2, 3*) variants of the fitting of the experimental data with the use of formula (2) for $\Delta r = 0.5$ and 0.1 nm, respectively.
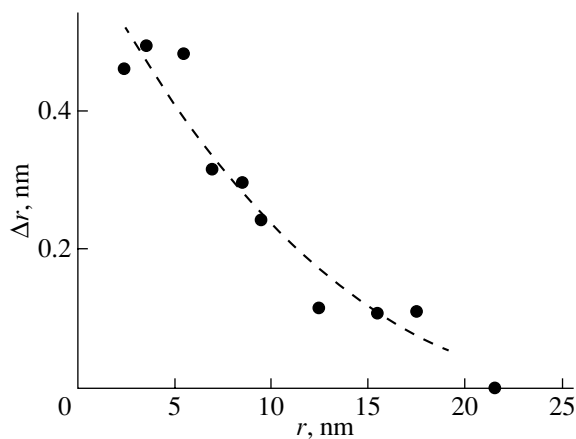
Fig. 2. Parameter of imperfection Δr for Fe_3O_4 nanoparticles as a function of the particle radius r.

of exchange bonds. In this case, an analysis of the dependence $\Delta r(r)$ for particular systems of magnetically ordered particles would permit us to trace the variation in this parameter with a decrease in the particle size.

As an example, we can use the experimental data obtained by Sadeh *et al.* [5], who measured and investigated the experimental dependence $T'_C(r)$ for nanoparticles of magnetite Fe_3O_4. As can be seen from Fig. 1, the attempts to fit theoretical curves calculated from relationship (2) at $\Delta r = $ const to the experimental data taken from [5] were unsuccessful. In other words, using the quantity Δr as the fitting parameter, we failed to achieve reasonable agreement between the calculated and experimental dependences.

For a system of Fe_3O_4 nanoparticles with different dispersities, it is possible to show that the quantities Δr and r, which are related to the correction to the Curie temperature $\Delta T'_C / T_C$ through relationship (2), characterize the interrelation between the degree of imperfection of the magnetic structure and the particle size. The dependence $\Delta r(r)$ for Fe_3O_4 nanoparticles (Fig. 2) is in agreement with relationship (2) and the results obtained in [5]. This dependence suggests a progressively increasing role of the surface layer with a decrease in the particle size. To put it differently, the smaller the size of the particles, the larger the effective thickness Δr of the layer characterized by considerable distortions of the regular structure. Therefore, the quantity Δr can be actually treated as the parameter of imperfection of the magnetic structure of the nanoparticles.

An analysis of the dependence $\Delta r(r)$ shown in Fig. 2 makes it possible to refine the size corresponding to the notion of large-sized particles. In the case of magnetite, particles with $r \geq 20$ nm can be considered to be large-sized. For these particles, the parameter of imperfection Δr is approximately equal to zero.

REFERENCES

1. J. L. Dormann and D. Fiorani, *Magnetic Properties of Fine Particles* (North-Holland, Amsterdam, 1992).
2. A. I. Gusev, Usp. Fiz. Nauk **168** (1), 55 (1998) [Phys. Usp. **45**, 49 (1998)].
3. V. I. Nikolaev and A. M. Shipilin, Fiz. Tverd. Tela (St. Petersburg) **42** (1), 109 (2000) [Phys. Solid State **42**, 112 (2000)].
4. V. I. Nikolaev, A. M. Shipilin, and I. N. Zakharova, Fiz. Tverd. Tela (St. Petersburg) **43** (8), 1455 (2001) [Phys. Solid State **43**, 1515 (2001)].
5. B. Sadeh, M. Doi, T. Shimizu, and M. J. Matsui, J. Magn. Soc. Jpn. **24** (4), 511 (2000).

Translated by N. Korovin

<div align="center">

MAGNETISM
AND FERROELECTRICITY

</div>

Formation and Evolution of Giant Dynamic Domains in an AC Magnetic Field

M. V. Logunov and M. V. Gerasimov

Mordovia State University, ul. Bol'shevistskaya 68, Saransk, 430000 Russia
e-mail: logunov@mrsu.ru
Received July 17, 2002

Abstract—Magnetization reversal in ferrite-garnet films placed in an ac magnetic field, bringing about the formation of metastable dynamic domains with sizes exceeding those of quasi-static domains by an order of magnitude or greater, was studied using a stroboscopic method. The formation of giant dynamic domains (GDDs) is due to the finite domain wall velocity and depends on the density of domain nucleation centers. It was shown that the GDD comblike boundary forms during the part of a field period near the moment of field polarity change. GDDs arise when the dynamic hysteresis loop shape changes from a triangle to an ellipse. © 2003 MAIK "Nauka/Interperiodica".

1. INTRODUCTION

When ferrite-garnet films are placed in an ac magnetic field at sound and ultrasonic frequencies, a great variety of dynamic domain structures appear in the process of magnetization reversal. In the phase diagram of dynamic systems of magnetic domains [1], there are more than ten regions corresponding to different kinds of domain structures. In general, these structures can be divided into two groups. The first group includes dynamic domain structures whose sizes are approximately equal to those of quasi-static stripe, dumb-bell, and bubble domains at the respective effective magnetic-field values. Such structures differ from quasi-static domains in the appearance of a new order in the domain arrangement, more specifically, in the formation of spiral and ring domains [1–5] and two-dimensional domain lattices [6–8]. Such structures are, as a rule, reflexive and retain their properties partly or fully after switching-off of the ac magnetic field or in the periods between pulses [3] (in the case of a pulse field).

The second group includes dynamic domain structures whose characteristic sizes exceed quasi-static-domain sizes by an order of magnitude or greater. These structures have the shape of concentric ring domains [2, 9], distorted bubble domains, etc. [1, 9, 10] and can either move along the film area [1] or be rigidly fixed to certain centers (defects) in the film [10]. The formation of giant dynamic domains (GDDs) takes place at a sufficiently large ac field amplitude, exceeding the static saturation field of a domain structure H_s [1, 2, 9, 10]. GDDs are relatively stable and retain their average shape almost unchanged over hundreds and thousands of field periods. When the field frequency is increased, the GDD maximal sizes decrease [1]. GDDs exist only under dynamic conditions; after switching-off of the ac field, these domains are transformed into a

network of labyrinth domains with sizes typical of equilibrium domains.

Because of the complex character of dynamic-domain phase diagrams and the variety of dynamic domain structures that appear, much in the origin of the phenomena under investigation remains unknown. Because of limitations of an experimental technique, the published GDD photographs represent average images of domains over tens of magnetic-field periods; the question of interconnection of GDD formation conditions and sample parameters remains open.

In order to find the mechanisms of GDD formation and evolution, we studied such domains using a stroboscopic method with a domain structure exposition time at least an order of magnitude shorter than the field period and with simultaneous measurement of the integral characteristics of magnetization reversal (dynamic hysteresis loops).

2. EXPERIMENTAL

The dynamic domains were observed using a magnetooptic method based on the Faraday effect; time resolution of the stroboscopic unit was 0.8 μs [5]. Information on the domain shape evolution was obtained by sweeping a light source pulse (helium–neon laser with microwave pumping) over a magnetic-field period. By changing the strobing ratio, the transition from the stroboscopic mode of domain observation to the high-speed photography mode was made; such a transition was necessary for investigating processes that were not repeated. Part of a magnetooptic signal was fed to a photoelectric multiplier with the help of a semitransparent mirror for recording of the hysteresis loop. A homogeneous ac magnetic field (field homogeneity ~1% over the sample region under investigation) was
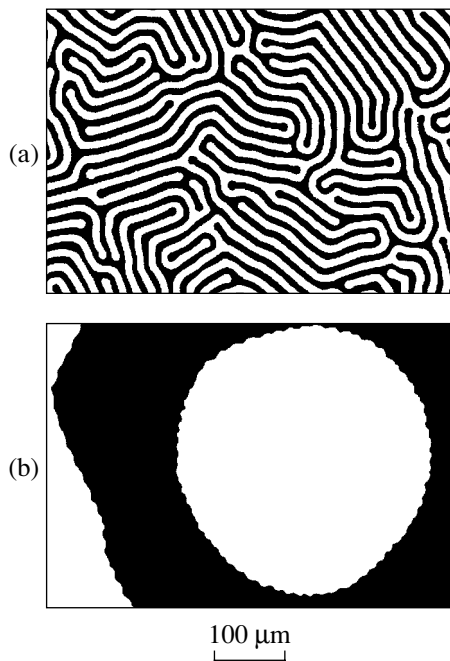
Fig. 1. (a) Equilibrium domain structure ($H_b = 0$) and (b) a giant dynamic domain in an ac magnetic field at field amplitude $H_m = 85$ Oe and field frequency $f = 40$ kHz.

produced using Helmholtz coils 2.5 mm in diameter. An ac field was applied along the easy magnetization axis of the film under investigation.

The results for a $(Bi, Tm)_3(Fe, Ga)_5O_{12}$ ferrite-garnet film with (111) orientation [5] are presented below. The film parameters are the following: thickness $h = 5.6$ μm, stripe-domain equilibrium width $w = 8.9$ μm, bubble domain collapse field $H_0 = 46$ Oe, and saturation magnetization $M_s = 9.9$ G. The sample possessed significant uniaxial anisotropy: the quality factor was $Q = K_u/2\pi M_s^2 = 20$ (K_u is the uniaxial anisotropy constant), with the easy axis being perpendicular to the film plane. In the absence of an external magnetic field, a labyrinth domain structure was observed in the film (Fig. 1a). In ac magnetic fields with frequency f in the range from 15 to 80 kHz and with amplitude H_M in the range from 70 to 160 Oe, GDDs were formed (Fig. 1b).

The choice of the sample was determined to a large extent by the simple dependence of the domain wall (DW) velocity V on the applied field H. Measurements of the DW velocity in a pulse magnetic field by using high-speed photography showed that, in a wide field range (from several oersteds to $H > 200$ Oe), the velocity V almost does not depend on field amplitude H and does not exceed 10 m/s. Such a $V(H)$ dependence for practically the entire range of instantaneous values of the ac field used in this work significantly facilitates interpretation of the experimental results.

3. EXPERIMENTAL RESULTS

We will consider the regularities of transition to GDD formation mechanisms, which become operative with increasing ac field amplitude, for field frequency $f = 40$ kHz (Fig. 2). At this frequency or near it, domain sizes can reach their maximum values. Microphotographs for the same field amplitudes but for different phases (Fig. 2) correspond to different field periods, which allows one to establish whether or not the magnetization reversal process is repeated.

If the field amplitude is $H_M < H_0$, then, as one goes from one field period to another, a rearrangement of the domain structure takes place, but the structure remains a labyrinth (Fig. 2a). It is easy to see that such a structure differs from a labyrinth structure formed quasistatically (Fig. 1a). The domain period becomes smaller and the disclination density in the domain structure increases. The last difference, as pointed out in [3, 6, 11], is an indirect but reliable sign of changes in the DW structure and of an increase in the Bloch line density in DWs. These changes can take place if DWs move with a velocity close to the saturation velocity. Thus, as the field frequency increases, obvious indications of transition from the quasi-static to the nonlinear dynamic regime of DW motion appear. The coercive force calculated from the half-width corresponding to a minor hysteresis loop somewhat increases (Fig. 3).

As the field amplitude increases, all the above-mentioned indications of the dynamic nature of DW motion (domain branching, an increase in disclination density, a decrease in the domain structure period at $H_b \sim 0$, a decrease in distortion period along the domain length) become more and more evident and are the most pronounced at $H_M \longrightarrow H_0$ (Fig. 2b). With an insufficient instrumental resolution, the dynamic domain structures shown in Figs. 2a and 2b may be perceived as a gray background [1] because of a significant change in the domain location as one goes from one field period to another.

When the ac field amplitude exceeds the static saturation field, part of the domains collapse during a field period, which results in the transition to a dynamic structure radically differing in shape and size from the equilibrium structures (Fig. 2c). As the field increases further, almost all domains collapse during a field period and only one or a few giant domains are left in the observable area (Fig. 2d). Their sizes exceed equilibrium domain sizes by an order of magnitude or greater.

As the period of a dynamic domain structure increases by several times in a magnetic field at an ultrasonic frequency, the hysteresis loop shape is modified. Figure 3 shows a dynamic hysteresis loop corresponding to the middle of the field amplitude and frequency ranges of GDD formation (Fig. 3e) and hysteresis loops outside these ranges (Figs. 3a–3d, 3f–3k). The following features are characteristic of GDD formation: (i) a hysteresis loop has the form of a distorted
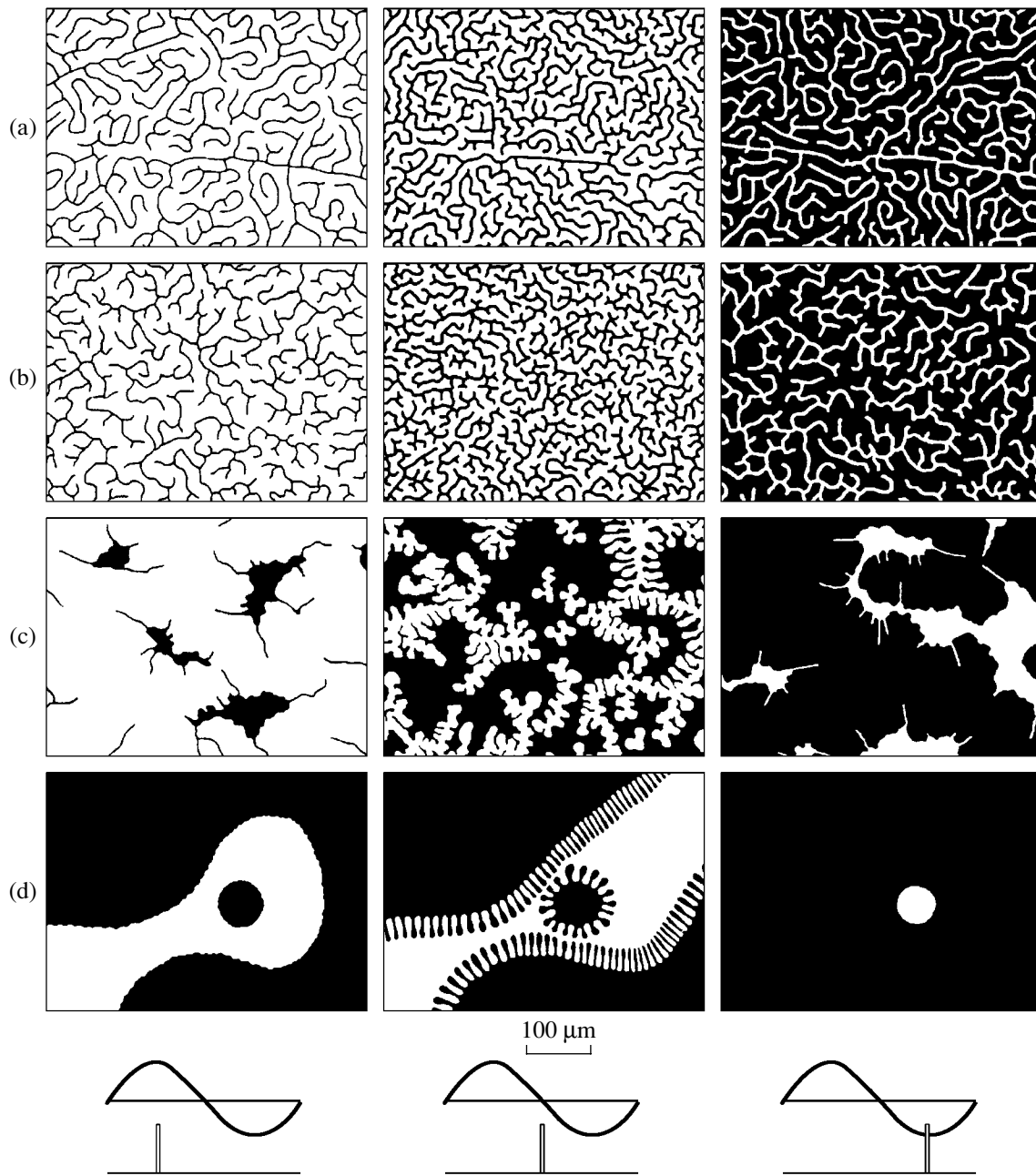
Fig. 2. Dynamic domain structures corresponding to phases $\varphi = 90°$, $180°$, and $270°$ of an applied ac magnetic field of frequency $f = 40$ kHz and amplitude $H_m =$ (a) 30, (b) 40, (c) 79, and (d) 98 Oe.

ellipse, (ii) the loop is shifted along the ordinate axis relative to the line corresponding to magnetization $M = 0$, and (iii) loop instability is possible.

In fields with amplitude $H_M \leq H_0$ (below the GDD formation region), the dynamic hysteresis loops are minor. The opening of loops (and the DW coercive force) increases with the field frequency because of a lag in DW motion (Figs. 3a, 3d, 3g). As the field amplitude increases, the maximal magnetization of the sample reached during a field period increases. Nevertheless, even at field amplitude $H_M > H_s$, the saturation is

not always reached during a field period because of the finite DW velocity (Figs. 3e, 3h, 3i). Above the frequency range of GDD formation, distortions of the elliptical shape of loops decrease.

An increase in amplitude or a decrease in frequency of the field (relative to the middle of the region of GDD formation) leads to a change in the domain nucleation field on a hysteresis loop and a decrease in the vertical size of the loop (Figs. 3b, 3c, 3f); during one of the field half-periods, the sample is magnetized to saturation and, during the other half-period, the sample does not
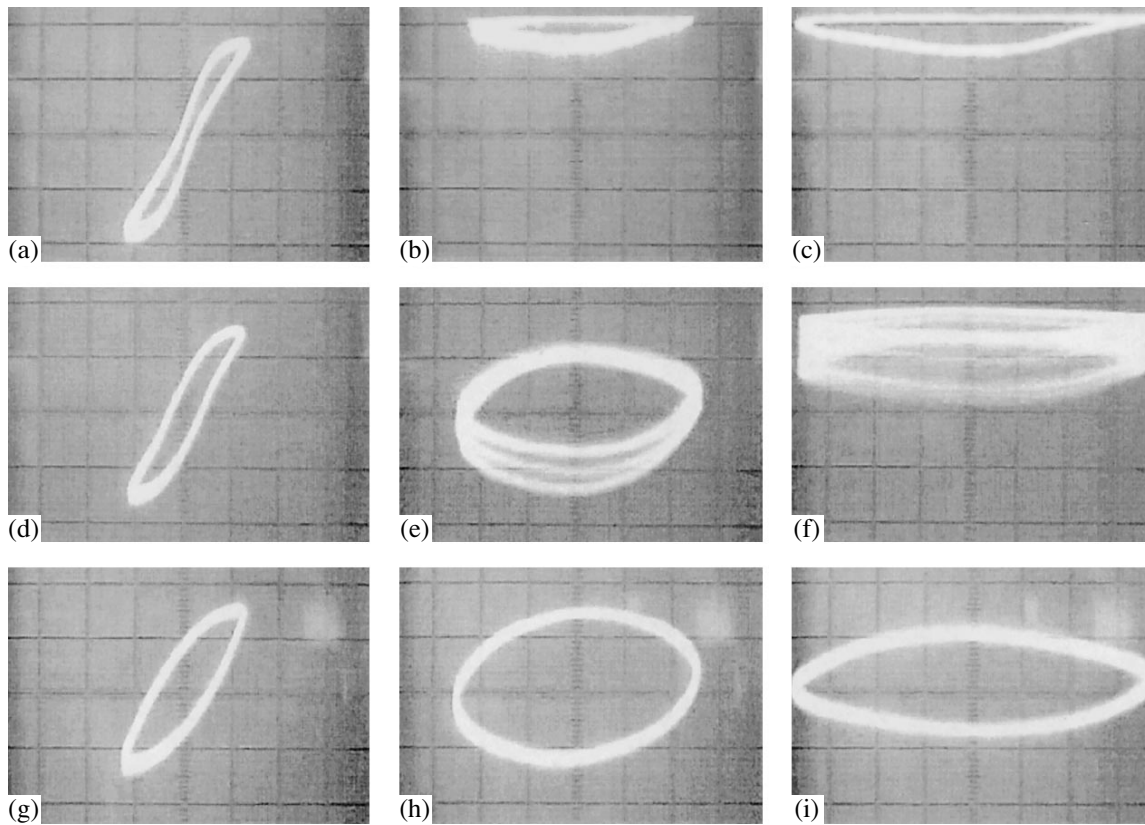
Fig. 3. Dynamic hysteresis loops in an ac magnetic field of frequency f = (a–c) 20, (d–f) 50, and (g–i) 100 kHz. For each frequency, the field amplitudes are (from left to right) H_m = 50, 100, and 150 Oe.

have time to demagnetize because of a delay in domain nucleation and growth and a limited number of nucleus formation centers. The hysteresis loop looses its symmetry about the origin of coordinates and shifts to a region of, say, positive magnetization (Figs. 3b, 3c, 3f). When the amplitude of the ac magnetic field increases, the tendency of the magnetization to be saturated along the preferred direction strengthens. The existence of the preferred direction may be due to insignificant asymmetry in the field sinusoid or in the sample parameters. It is easy to reverse this direction by applying a small static bias field $H_b \ll H_0$ along the easy axis of the film.

It is more convenient to analyze the GDD evolution during a field period in the case of a medium-sized (not the largest) domain (Fig. 4), which periodically nucleates in the same place on the film. The microphotographs, like those in Fig. 2, show domains in the same place on the sample but at different field periods. Small dynamic domains, upon expanding, have a cylindrical form (Figs. 4a, 4b). In the region of field polarity change (at phase $\varphi = 180° \pm 30°$), the decrease in the effective acting field leads to bending instability of the domain walls and an array of stripe domains (a "comb") forms (Fig. 2d; Fig. 4) instead of smooth DWs. The reason for the formation of the comb is analogous to that of petal distortions arising when a bubble domain

exhibits radial expansion [12, 13] due to its magnetostatic instability. It is likely that the presence of such a comb leads to blurring of GDD boundary images in the photographs presented in [1, 9].

The time dependences of domain sizes in Fig. 5 are found from data which are partly presented in Fig. 4. It is seen that the domain diameter d varies practically linearly with time both upon expansion (one half-period of the field) and upon compression (the other half-period); i.e., the DW moves with a constant velocity $V \sim 7$ m/s. This saturation velocity value agrees with both the calculated values obtained with the use of different models [14–16] and those measured by us experimentally in a pulse magnetic field.

4. DISCUSSION

The mechanism of GDD formation and time evolution in an ac magnetic field are determined by the peculiarities of domain nucleation and dynamic properties of the domain walls, primarily by the effect of saturation of the DW velocity. Since the DW saturation velocity is finite, the DW displacement during a time equal to a magnetic-field half-period $\tau/2$ (for the frequency range where the GDD formation occurs, $\tau/2 \sim 10$ μs) does not exceed a fraction of the GDD diameter. As a result, the saturation state is not reached during a field
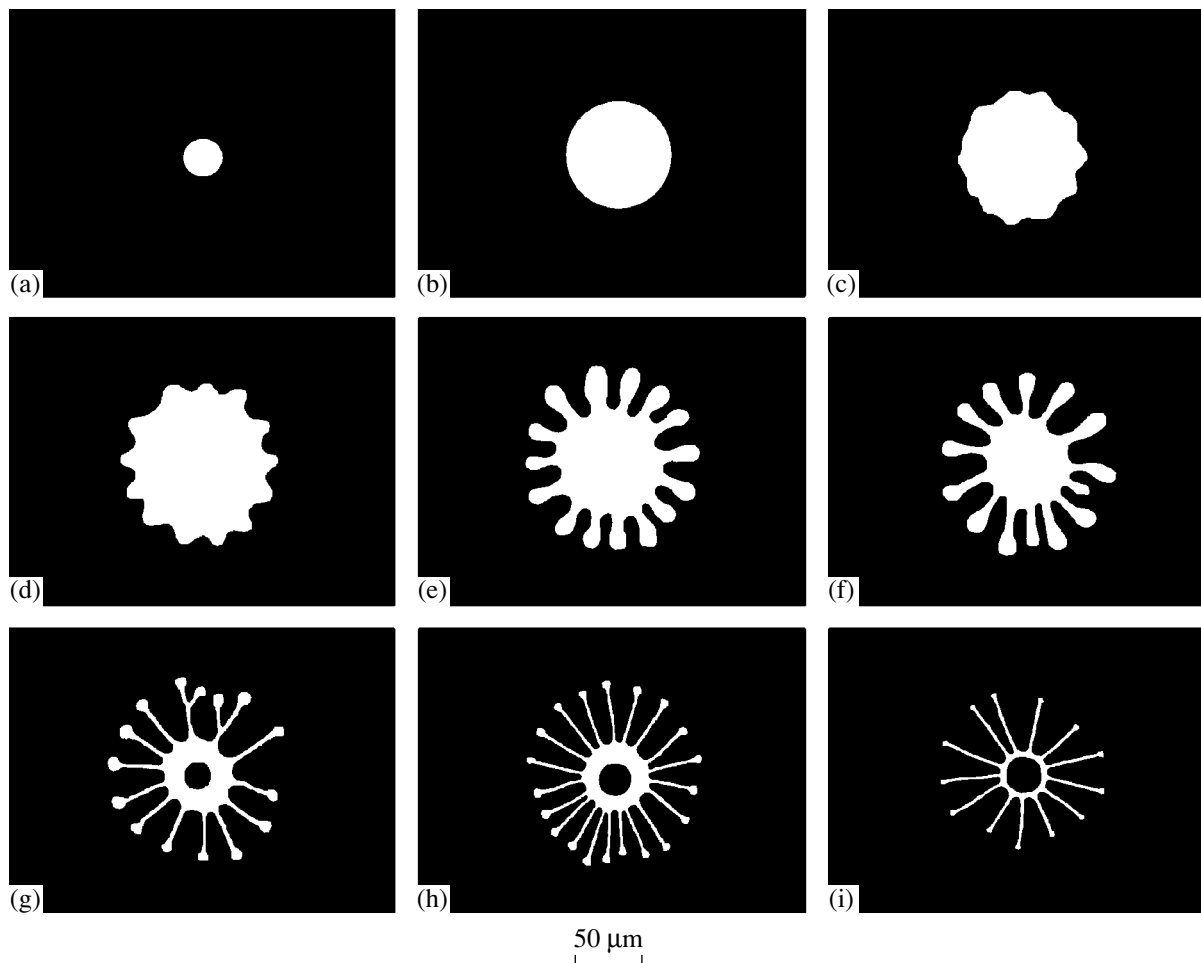
Fig. 4. GDD evolution in a field with frequency $f = 40$ kHz and amplitude $H_m = 98$ Oe. Moments of time relative to the change of field polarity t: (a) 0.8, (b) 6, (c) 7, (d) 9, (e) 11, (f) 12, (g) 13, (h) 14, and (i) 15 μs.

half-period. For this reason, such domain structures are relatively stable and significant changes take place only after 10^5–10^7 magnetic-field periods.

The changes in the GDD form and size, taking place as one goes from one field period to another, should lead to blurring of a hysteresis loop. It is seen from Fig. 3 that the blurring is small, but there is some instability of the loop shape. Therefore, the most significant changes in a GDD take place not continuously but in steps of 500–1000 magnetic-field periods (as in Fig. 3).

The transition to a triangular shape of a hysteresis loop is connected to the delay of the formation and growth of the reverse magnetic phase [17]. The saturation of a sample, reached during one field period, makes the existence of stable GDDs impossible during many subsequent field periods. An asymmetric hysteresis loop is characteristic of the region of GDD formation, as is the case with two-dimensional domain structures [8]. In the case of GDDs, the shape of the hysteresis loop is intermediate between those of triangular and elliptical loops (Fig. 3).

In a number of studies on the properties of ferrite-garnet films placed in an ac magnetic field, DW oscillations were investigated using integral methods [18–20] and, for the most part, at field amplitudes $H_M \ll H_s$. The dynamic mechanisms of magnetization reversal in strong ac fields with $H_M \geq H_s$ (nucleation of domains, DW motion) practically have not been studied; therefore, further investigation is required for determining the quantitative characteristics of the domain structure formation. The following peculiarities of magnetization reversal in an ac field, revealed in the course of this work, should be mentioned here (without elaboration of the reasons for doing so): domain nucleation may take place in a relatively long time (several microseconds) after field polarity change (for comparison, in a pulse field, $t \sim 0.1$ μs is sufficient for domain nucleation [21, 22]). Collapse of domain walls drawn close to the distance ~1 μm takes the time $t > 2$ μs (Figs. 4g–4i); the same time is required for the change in the comb motion direction when the field polarity changes (Fig. 5). The DW velocities have close values under different conditions: in the case of motion of relatively flat
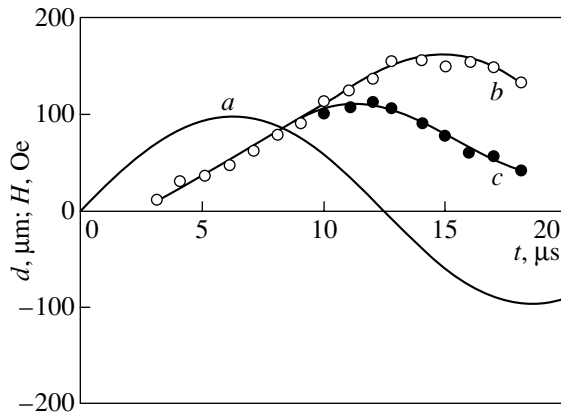
Fig. 5. (*a*) Magnetic field intensity *H* and (*b*, *c*) the change in GDD sizes during a field period: (*b*) GDD outer diameter and (*c*) GDD diameter without regard for the comb.

portions of the DW of an expanding domain and of the leading parts of a comb (DW rounding radii ~100 and ~5 μm, respectively) and in the case of domain expansion and compression.

5. CONCLUSIONS

Thus, the comparison of the results of direct investigation of dynamic domain structures using a stroboscopic method with the integrated characteristics of magnetization reversal (dynamic hysteresis loops) allows one to conclude that GDD formation in an ac magnetic field is possible under the following conditions.

(1) The field amplitude exceeds the static saturation field of the sample domain structure, but some of the domains do not have time to collapse because of the limited time of influence.

(2) The density of the surviving nuclei and domain pinning centers and the DW velocities are such that, during a field half-period, domain walls cover a distance not exceeding half the average distance between the domain centers.

(3) The existence of the lower limit of the field amplitude range and of the upper limit of the field frequency range of GDD formation is due to the impossibility of domains collapsing during a field period, in the former case because of a small field amplitude $H_M \leq H_s$ and in the latter case because of the lack of time for DWs to approach each other during half a field period.

(4) The upper limit of the field amplitude range and the lower limit of the field frequency range of GDD formation are determined by a practically complete suppression of domain nuclei during at least one field half-period, which, in turn, leads to a triangular form of a hysteresis loop and makes retention of the domain structure during many field periods impossible.

REFERENCES

1. G. S. Kandaurova and A. A. Rusinov, Dokl. Akad. Nauk **340** (5), 610 (1995) [Phys.–Dokl. **40**, 53 (1995)].
2. G. S. Kandaurova, Dokl. Akad. Nauk SSSR **308**, 1364 (1989) [Sov. Phys. Dokl. **34**, 918 (1989)].
3. I. E. Dikshteĭn, F. V. Lisovskiĭ, E. G. Mansvetova, and E. S. Chizhik, Zh. Éksp. Teor. Fiz. **100** (5), 1606 (1991) [Sov. Phys. JETP **73**, 888 (1991)].
4. M. V. Chetkin, A. I. Akhutkina, and T. B. Shabaeva, Mikroélektronika **27** (5), 396 (1998).
5. M. V. Logunov and M. V. Gerasimov, Fiz. Tverd. Tela (St. Petersburg) **44** (9), 1627 (2002) [Phys. Solid State **44**, 1703 (2002)].
6. F. V. Lisovskiĭ, E. G. Mansvetova, E. P. Nikolaeva, and A. V. Nikolaev, Zh. Éksp. Teor. Fiz. **103** (1), 213 (1993) [JETP **76**, 116 (1993)].
7. F. V. Lisovskiĭ, E. G. Mansvetova, and Ch. M. Pak, Zh. Éksp. Teor. Fiz. **108** (9), 1031 (1995) [JETP **81**, 567 (1995)].
8. M. V. Logunov and M. V. Gerasimov, Pis'ma Zh. Éksp. Teor. Fiz. **74** (10), 551 (2001) [JETP Lett. **74**, 491 (2001)].
9. G. S. Kandaurova and A. E. Sviderskiy, Physica B (Amsterdam) **176**, 213 (1992).
10. G. S. Kandaurova, Fiz. Met. Metalloved. **79** (1), 158 (1995).
11. D. J. Craik and G. Myers, Philos. Mag. **31**, 489 (1975).
12. G. J. Zimmer, T. M. Morris, and F. B. Humphrey, IEEE Trans. Magn. **10** (3), 651 (1974).
13. L. P. Ivanov, A. S. Logginov, G. A. Nepokoĭchitskiĭ, and V. V. Randoshkin, Fiz. Tverd. Tela (Leningrad) **22** (11), 3469 (1980) [Sov. Phys. Solid State **22**, 2034 (1980)].
14. F. H. de Leew, IEEE Trans. Magn. **14** (5), 596 (1978).
15. A. P. Malozemoff and J. C. Slonczewski, *Magnetic Domain Walls in Bubble Materials* (Academic, New York, 1979; Mir, Moscow, 1982).
16. V. A. Bokov, V. V. Volkov, and V. I. Karpovich, Fiz. Tverd. Tela (Leningrad) **24** (8), 2318 (1982) [Sov. Phys. Solid State **24**, 1315 (1982)].
17. G. S. Kandaurova and V. Kh. Osadchenko, Pis'ma Zh. Tekh. Fiz. **21** (20), 11 (1995) [Tech. Phys. Lett. **21**, 819 (1995)].
18. B. E. Argyle, J. C. Slonczewski, and M. H. Kryder, IEEE Trans. Magn. **18** (6), 1325 (1982).
19. L. V. Velikov, E. P. Lyashenko, and S. S. Markianov, Zh. Éksp. Teor. Fiz. **84** (2), 783 (1983) [Sov. Phys. JETP **57**, 453 (1983)].
20. A. F. Aleĭnikov and E. G. Rudashevskiĭ, Prib. Tekh. Éksp., No. 4, 149 (1988).
21. V. G. Kleparsky and I. Pinter, Phys. Status Solidi A **76** (1), K1 (1983).
22. V. G. Kleparsky, I. Pinter, and L. Bodis, IEEE Trans. Magn. **20** (5), 1156 (1984).

Translated by A. Titov

MAGNETISM
AND FERROELECTRICITY

Free Magnetization Oscillations in Garnet Ferrite Films with Quasi-Planar Anisotropy

E. N. Il'icheva, E. I. Il'yashenko, O. S. Kolotov, A. V. Matyunin, and V. V. Smirnov

Faculty of Physics, Moscow State University, Vorob'evy gory, Moscow, 119899 Russia
e-mail: PhysPhak@mail.ru
Received October 2, 2002

Abstract—Free magnetization oscillations in garnet ferrite films with quasi-planar anisotropy was studied. The oscillations were excited by a pulse of an in-plane magnetic field. An analytic expression relating the oscillation frequency to the film parameters and the external magnetic field was derived; the expression is in good agreement with the experimental data. The planar anisotropy is shown to increase the free-oscillation damping. © 2003 MAIK "Nauka/Interperiodica".

Investigation of the free oscillations of magnetization considerably broadens the possibilities for studying the spin–lattice interaction in transient processes occurring in magnets [1–6]. In particular, studies of free oscillations can yield important characteristics of magnetic materials, such as the Landau–Lifshitz damping and magnetic-anisotropy constants. Until recently, free oscillations had been investigated primarily in permalloy films [1–8]. It would be desirable to carry out such research on other magnetic materials differing in magnetic structure, magnetization, the nature of anisotropy, etc.

We report here on the observation of free magnetization oscillations in garnet ferrite films with quasi-planar anisotropy. These films are intended for the visualization of information stored on magnetic carriers [9, 10]. In their preparation, measures are taken to obtain easy-plane-type anisotropy. In real films, the influence of uncompensated cubic anisotropy is observed and manifests itself in the magnetization vector not being confined exactly to the film plane in the absence of an external magnetic field. Furthermore, noticeable anisotropy is observed to exist in the film plane itself. The easy magnetization axes (EMAs) are aligned along two mutually perpendicular directions [11]. We take into account the effect of planar anisotropy confining the magnetization to the film plane and characterized by a constant K_1 and the effect of biaxial anisotropy in the film plane (with a constant K_2).

The investigation was performed on an induction setup [12]. A removable longitudinal sense loop was employed to measure variations in the magnetization. The sample under study was saturated along one of the EMAs with the use of a bias magnetic field H_0. Oscillations were excited by applying a magnetic field pulse H_p perpendicular to the EMA. The pulse leading-edge duration was close to 0.3 ns. The pulse amplitude could be varied from 4 to 6 Oe.

The sample used had the following characteristics: $(Y, Lu, Bi)_{3.0}(FeGa)_{5.0}O_{12}$ composition, a thickness of 4 μm, technical saturation field along the EMA $H_{sat} \le$ 3 Oe, saturation magnetization M_S = 14 G, effective planar-anisotropy field H_{K1} = 1300 Oe, and an angle between the magnetization vector and the film plane with no external field applied of $\beta_0 \approx 5°$. The values of H_{K1} and β_0 and the EMA directions were determined with a magnetooptic setup [11, 13]. No technique for measuring the effective biaxial-anisotropy field in the material in question was available. The need to develop such a technique additionally motivated us to study free oscillations.

It was found that free magnetization oscillations are excited in the material under study and are fairly easily detected, provided the leading edge of the exciting pulse is substantially shorter than the oscillation period. Figure 1 illustrates an oscillographic trace of the magnetization oscillation signal. The signal was obtained at a bias field H_0 = 19 Oe. After the ≈1-ns-long peak, which identifies the initial rotation of the magnetization, one observes signal voltage oscillations associated with oscillations of the magnetization about a new equilibrium position. The oscillation frequency is close to 960 MHz for the field H_0 used. Similar to the case of permalloy films [1–3, 6, 7], the oscillation frequency squared was found to be proportional to the field H_0 (Fig. 2).

Interpretation of the above results can be facilitated by invoking the experience gained in studies of transient processes in permalloy films [1, 6, 14]. One has to bear in mind that the material under investigation differs from permalloy films in its substantially lower magnetization. Because of the planar anisotropy, however, the angle ψ the magnetization vector makes with the film plane in oscillations is small. As in permalloy films, this fact makes it possible to reduce the Landau–
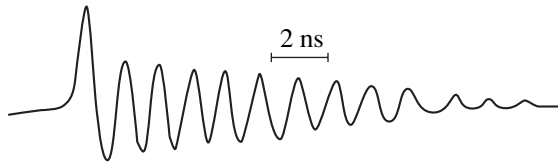
Fig. 1. Signal caused by free magnetization oscillations. $H_0 = 19$ Oe.
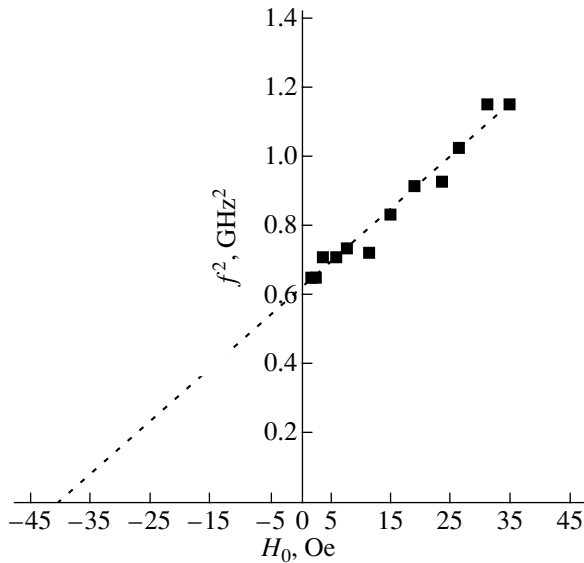
Fig. 2. Squared free oscillation frequency plotted vs. bias field H_0.

Lifshitz equation to a one-dimensional equation describing the variation of the angle φ between the instantaneous and initial directions of the projection of vector $\mathbf{M}_S$ on the film plane. For small values of ψ, the free-energy density can be written in the form

$$W = K_1\psi^2 - K_2\cos 2\varphi + 2\pi M_S^2\psi^2 \\ - H_p M_S\cos\varphi - H_0 M_S\sin\varphi, \tag{1}$$

where the first two terms describe the energy of the planar and biaxial anisotropy [15], the third term represents the demagnetizing-field energy, and, finally, the last two terms are the energy of magnetization in an external field. An analysis of Eq. (1) shows that the effective field of the planar anisotropy $H_{K1} = 2K_1/M_S$ greatly exceeds all other effective fields acting on the magnetization. As a result, the equation of motion acquires a simple form,

$$\ddot{\varphi} + a\lambda\dot{\varphi} + a\gamma^2\partial W/\partial\varphi = 0, \tag{2}$$

where

$$a = \frac{4\pi M_S + H_{K1}}{M_S}, \tag{2a}$$

λ is the Landau–Lifshitz damping constant, and γ is the gyromagnetic ratio. For small values of H_p, Eq. (2) reduces to a linear relation,

$$\ddot{\varphi} + a\lambda\dot{\varphi} + a\gamma^2 M_S(H_{K2} + H_0)\varphi = a\gamma^2 H_p M_S, \tag{3}$$

where $H_{K2} = 16K_2/M_S$ [15]. As seen from Eq. (3), the free-oscillation frequency is

$$f = (1/2\pi)\sqrt{a\gamma^2 M_S(H_{K2} + H_0) - \delta^2}, \tag{4}$$

and their amplitude falls off exponentially with the damping rate

$$\delta = a\lambda/2. \tag{4a}$$

An analysis of the signals reveals that the damping rate $\delta < 10^8$ Hz ($\lambda < 2 \times 10^6$ Hz). It follows that the oscillation frequency for characteristic values of M_S, H_{K1}, and H_{K2} is dominated by the first term under the square root sign of Eq. (4). Thus, we have

$$f^2 = b(H_{K2} + H_0), \tag{5}$$

where the coefficient of proportionality $b = (\gamma^2/4\pi^2)(4\pi M_S + H_{K1})$.

By extrapolating the straight line fitting the experimental dependence of the frequency squared on field H_0 to the intersection with the horizontal axis (Fig. 2), we find that for the sample under study $H_{K1} = 40 \pm 4$ Oe. Thus, investigation of free magnetization oscillations permitted us to estimate the effective field of biaxial anisotropy in the films under discussion.

The straight-line fit yields for the coefficient of proportionality $b = 1.3 \times 10^{16}$ Hz^2 Oe^{-1}. Using the above values of M_S and H_{K1} and accepting $|\gamma| = 1.76 \times 10^7$ Hz Oe^{-1}, we calculate this coefficient to be $b = 1.15 \times 10^{16}$ Hz^2 Oe^{-1}, which agrees with the experimental results.

As follows from Eqs. (2), (2a), (3), and (4), the existence of planar anisotropy should increase the damping and, accordingly, degrade the Q factor of the oscillation system under study. For small values of δ, the Q factor is approximately $Q \approx \pi f/\delta$. Thus, we have

$$Q = (\gamma/\lambda)\sqrt{\frac{M_S(H_{K2} + H_0)}{4\pi + H_{K1}/M_S}}. \tag{6}$$

The Q factor is seen to decrease with increasing ratio H_{K1}/M_S. This can be interpreted in the following way. It is known [6] that the demagnetizing field appearing when the magnetization vector leaves the film plane (to make an angle ψ with it) generates additional torque, which substantially enhances the magne-

tization variation rate. However, the magnitude of this effect decreases with increasing ratio H_{K1}/M_S.

Substituting the above-estimated value of δ into Eq. (4a), we find that the Landau–Lifshitz damping rate λ does not exceed 2×10^6 Hz, a figure two orders of magnitude smaller than that for permalloy. Thus, the decrease in the Q factor that may be caused by the increasing H_{K1}/M_S ratio should be more than compensated, in the material under study, by the small value of the damping rate, and this is what makes reliable observation of free oscillations possible.

REFERENCES

1. P. Wolf, Z. Phys. **160** (2), 310 (1960).

2. P. Wolf, J. Appl. Phys. **32** (3), 95S (1961).

3. B. R. Hearn, J. Electron. Control **16** (1), 33 (1964).

4. G. Matsumoto, T. Sato, and S. Iida, J. Phys. Soc. Jpn. **21** (2), 231 (1966).

5. Y. Suezava and F. B. Humphrey, IEEE Trans. Magn. **8** (2), 319 (1972).

6. O. S. Kolotov, V. A. Pogozhev, and R. V. Telesnin, Usp. Fiz. Nauk **113** (4), 569 (1974) [Sov. Phys. Usp. **17**, 875 (1974)].

7. W. K. Hiebert, A. Stankiewicz, and M. R. Freeman, Phys. Rev. Lett. **79** (6), 1134 (1997).

8. B. C. Choi, G. E. Ballentine, M. Belov, *et al.*, J. Appl. Phys. **89** (11), 7171 (2001).

9. A. V. Antonov, M. U. Gusev, E. I. Il'yashenko, and L. S. Lomov, in *Digests of International Symposium on Magnetooptics (ISMO'91), Kharkov, USSR* (1991), p. 70.

10. M. Yu. Gusev, R. M. Grechishkin, Yu. F. Kozlov, and N. S. Neustroev, Izv. Vyssh. Uchebn. Zaved., Mater. Élektr. Tekh., No. 1, 27 (2000).

11. E. N. Il'icheva, Yu. A. Durasova, O. S. Kolotov, and V. V. Randoshkin, in *Proceedings of XVIII International School–Seminar on New Magnetic Materials of Microelectronics, Moscow* (2002), p. 161.

12. O. S. Kolotov, V. A. Pogozhev, and R. V. Telesnin, *Methods and Equipment to Study Pulse Properties of Thin Magnetic Films* (Mosk. Gos. Univ., Moscow, 1970).

13. Yu. A. Durasova, E. N. Il'icheva, A. V. Klushina, *et al.*, Zavod. Lab. **67** (7), 27 (2001).

14. D. O. Smith, J. Appl. Phys. **29** (3), 264 (1958).

15. I. S. Édel'man, Izv. Akad. Nauk SSSR, Ser. Fiz. **30** (1), 88 (1966).

Translated by G. Skrebtsov

MAGNETISM
AND FERROELECTRICITY

Response of the Electrical Resistivity and Magnetoresistance of La$_{0.67}$Ca$_{0.33}$MnO$_3$ Epitaxial Films to Biaxial Compressive Mechanical (001) or (110) Strains

Yu. A. Boĭkov*, T. Claeson**, and A. Yu. Boĭkov***

*Ioffe Physicotechnical Institute, Russian Academy of Sciences, Politekhnicheskaya ul. 26, St. Petersburg, 194021 Russia
e-mail: yu.boikov@mail.ioffe.ru
**Chalmers Technical University, Göteborg, S-41296 Sweden
***Institute of Physics, St. Petersburg State University, ul. Pervogo Maya 100, Petrodvorets, St. Petersburg, 198904 Russia
Received October 4, 2002

Abstract—The behavior of the electrical resistivity and magnetoresistance of 40- to 120-nm-thick La$_{0.67}$Ca$_{0.33}$MnO$_3$ films grown on differently oriented lanthanum aluminate substrates was studied. The cell volume in thin (40 nm) La$_{0.67}$Ca$_{0.33}$MnO$_3$ films grown coherently on (001)LaAlO$_3$ was found to be substantially smaller. Mechanical stress relaxation in biaxially strained La$_{0.67}$Ca$_{0.33}$MnO$_3$ films is accompanied by an increase in the cell volume. The temperatures at which the electrical resistivity and magnetoresistance in biaxially strained La$_{0.67}$Ca$_{0.33}$MnO$_3$ films were maximum can differ by 60–70 K from those observed in bulk single crystals. © 2003 MAIK "Nauka/Interperiodica".

1. INTRODUCTION

Thin layers of the perovskite-like manganites La$_{1-x}$Ca$_x$MnO$_3$ have application potential for use in read and write heads in magnetic storage devices, IR radiation sensors, etc. [1, 2]. For proper use of them in microelectronics and measurement techniques, manganite films should be grown epitaxially on the corresponding substrates. The rigid bonding to the substrate, whose unit cell parameters and temperature coefficient of linear expansion may differ substantially from those of the grown layer, is one of the reasons for the generation of biaxial mechanical strains in the film.

The influence of mechanical strains on the parameters of perovskite-like manganites has been the subject of many publications [3–5]. Hydrostatic compression was shown to substantially increase the Curie temperature T_C in bulk La$_{1-x}$Ca$_x$MnO$_3$ samples [5]. According to [6], biaxial mechanical strains in heteroepitaxial manganite films should favor carrier localization and the values of T_C may differ by tens of kelvins from the corresponding values for bulk samples.

We report here on a study of the structure and electronic parameters of thin, biaxially stressed La$_{0.67}$Ca$_{0.33}$MnO$_3$ (LCMO) films grown on polished (001) and (110)LaAlO$_3$ (LAO) plates. Using substrates of different types is essential for establishing the dependence of the orientation, microstructure, and electronic properties of LCMO films on the symmetry and effective parameter of the plane ion array on the LAO surface.

2. EXPERIMENT

Laser ablation (COMPEX 100, KrF, $\lambda = 248$ nm, $\tau = 30$ ns) was employed to grow LCMO films on lanthanum aluminate substrates. The laser radiation density on the surface of the original LCMO target was 2 J/cm^2. The oxygen pressure in the growth chamber was maintained at 0.3 mbar. LCMO films of thickness $d = 40$, 60, 80, and 120 nm were grown under identical conditions on each of the above substrate types. The growth of epitaxial LCMO films is described in detail in [7, 8].

The orientation, phase composition, and unit cell parameters of the grown LCMO films were determined using x-ray diffraction (Philips X'pert MRD, Cu$K_{\alpha1}$, $\omega/2\theta$ and ϕ scans, rocking curves). The lattice parameters of the LCMO/(001)LAO films were derived from the values of 2θ for the (004) and (303)LCMO reflections, and those of the manganite films grown on (110)LAO were calculated from the values of 2θ for the (330) and (222)LCMO x-ray peaks measured with high-precision x-ray optics.

The morphology of the free surface of LCMO films was studied by atomic-force microscopy (AFM, Nanoscope-IIIa).

The resistance R of the LCMO films was measured under an ac current in the Van der Pauw configuration using an hp 4263A LCR meter, both with and without a magnetic field ($f = 100$ Hz). The electrical resistivity of the films was calculated from the relation $\rho = (\pi d/\ln 2)R$ [9]. A magnetic field $H = 0.4$ T was applied parallel to the substrate plane. Four silver contacts, located at the corners of a square, were deposited on the

manganite film surface through thermal evaporation from a tungsten boat.

3. THE STRUCTURE OF GROWN LCMO FILMS

The orientation of an LCMO film relative to the substrate is determined by the actual conditions of nucleation and subsequent growth. First to become stable are the LCMO nuclei with the lowest free energy of the free surface γ and the lowest elastic strain energy η in the nucleus–substrate system. In the absence of mechanical strain relaxation, it is these nuclei that govern the orientation of a heteroepitaxial LCMO layer with respect to the substrate.

The parameter of the LAO pseudocubic unit cell (~3.79 Å [4]) is smaller than that of the LCMO unit cell (~3.86 Å [10]), and the temperature coefficients of linear expansion of LAO and LCMO are similar [4, 11]. The lattice misfit m [$m = (a_L - a_S)/a_S$, where a_L and a_S are the layer and substrate unit cell parameters, respectively] for the LCMO and LAO is about 1.8%, with $m > 0$. This should give rise to the generation of in-plane compressive mechanical strains in the manganite layer. The elastic strain energy η per unit film–substrate interface area depends quadratically on m and grows linearly with layer thickness.

We could not find literature data on the magnitude and anisotropy γ for LCMO. Structural data available on LCMO films grown on substrate materials which are chemically unstable with respect to LCMO (Y–ZrO$_2$, $T_S \approx 750°C$) indicate, however, that the (110)LCMO plane has the smallest value of γ [12].

X-ray diffractograms of both (40–120 nm) LCMO/(001)LAO and (40–120 nm)LCMO/(110)LAO revealed reflections only from the manganite film and the substrate (Fig. 1), which implies the absence of microinclusions of secondary phases in the grown layers. As follows from the x-ray $\omega/2\theta$ and ϕ scans, the grown manganite layers coincided in orientation with the lanthanum aluminate substrates, which implies fully coherent growth.

### 3.1. Orientation and Lattice Parameters of LCMO Films Grown on (001)LAO

In manganite films (d = 40–120 nm) grown on (001)LAO, the (001) planes were parallel to the substrate plane and the [010]LCMO direction was parallel to [010]LAO (Figs. 1a, 2a). We did not succeed in revealing, in the x-ray diffractograms of (40 nm)LCMO films (even for $2\theta > 100°$), any complex x-ray (00n)LCMO peak structure (see inset to Fig. 1a) which could be assigned to mechanical strain relaxation. The cell parameter c in a (40 nm)LCMO/(001)LAO film measured along [001]LCMO (i.e., perpendicular to the substrate plane) was substantially larger than the parameter b determined along the [010]LCMO direction, parallel to the substrate plane ($b = a$, where a is the
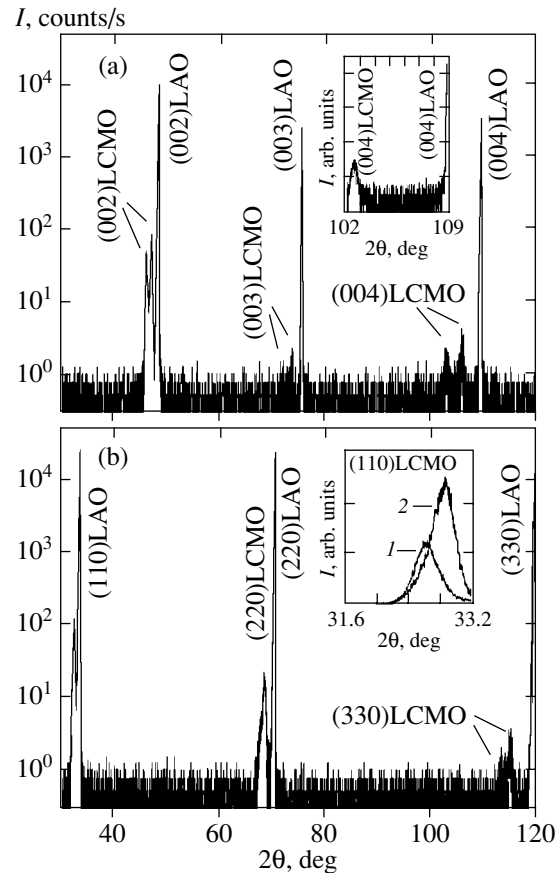
Fig. 1. (a) X-ray diffraction pattern (Cu$K_{\alpha1}$, $\omega/2\theta$) of an 80-nm-thick LCMO film grown on (001)LAO. The (00n) diffraction peaks from the manganite film are split in two. Inset shows a fragment of an x-ray scan made for a (40 nm)LCMO/(001)LAO film; the diffractogram does not exhibit any (00n) peak splitting. (b) X-ray diffraction pattern (Cu$K_{\alpha1}$, $\omega/2\theta$) of an 80-nm-thick LCMO film grown on (110)LAO. Inset shows (110) x-ray peaks measured on LCMO films of thickness (1) 60 and (2) 80; the (110) x-ray peak from the 80-nm-thick manganite film is distorted noticeably on the low-angle side.

cell parameter along [100]LCMO) (see Fig. 2a and table). The parameter b coincided with a high accuracy with the measured parameter of the lanthanum aluminate pseudocubic lattice, which implies that the manganite films (d = 40 nm) were grown coherently on the (001)LAO surface. The difference between the measured values of c and b for (40 nm)LCMO/(001)LAO indicates a substantial tetragonal unit cell distortion in thin (d = 40 nm) manganite films grown on (001)LAO. The cell volume $V_{eff} = (c \times b^2) \approx 56.7$ Å^3 in the (40 nm)LCMO/(001)LAO films was noticeably smaller than that in stoichiometric LCMO bulk samples [10].

The decrease in V_{eff} observed in 40-nm-thick LCMO/(001)LAO films suggests that the Mn^{4+} concentration in their volume is higher than 33%; this value follows from the chemical formula of the target mate-
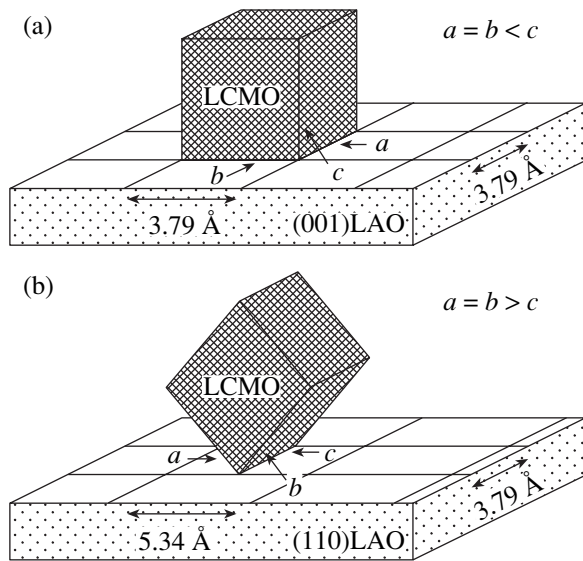
Fig. 2. (a) The lattice unit cell parameters *a* and *b* of a manganite film grown on (001)LAO are substantially smaller than the parameter *c* measured along the substrate plane normal ([001]LCMO direction). (b) The lattice cell parameters *a* and *b* of a manganite film grown on (110)LAO are larger than the parameter *c* measured along [001]LCMO.

rial. The ionic radius of Mn^{4+} is smaller than that of Mn^{3+}, and this is what accounts for the decrease in V_{eff} with increasing relative concentration of the Mn^{4+} ions. Using the data on the dependence of the effective lattice parameter on the concentration of quadrivalent manganese in bulk $La_{1-x}Ca_xMnO_3$ ceramic samples [11], we obtained 45% for the relative Mn^{4+} concentration in the (40 nm)LCMO/(001)LAO films. The main reason for the increase in concentration of quadrivalent manganese ions in 40-nm-thick manganite films is the compressive in-plane strains acting on LCMO nuclei. The increase in the Mn^{4+} concentration in (40 nm)LCMO/(001)LAO films is accompanied by the formation of vacancies on

the cation sublattice and enrichment of the films in calcium.

The (ω–2θ) rocking curve halfwidth of the (002) reflection obtained from a (40 nm)LCMO/(001)LAO film was 0.09°–0.1°, which implies a high quality of the microstructure in the bulk.

The (00*n*) reflections in the x-ray diffractograms of LCMO/(001)LAO films with $d \geq 60$ nm were actually doublets (Fig. 1a). This is the result of a film becoming stress-relieved after it has reached a critical thickness d_K (for (001)LCMO ∥ (001)LAO, $d_K \approx 45$–50 nm). A manganite film with only partially relieved mechanical strains consists of two parts, namely, (i) the substrate-adjoining layer, whose cell parameters are approximately equal to those in the (40 nm)LCMO/(001)LAO film, and (ii) the top part, whose parameter *c* is smaller and parameter *b* is larger than those of the (40 nm)LCMO/(001)LAO film (see table). A narrow interlayer with a high concentration of structural defects is sandwiched between the top and bottom parts of the LCMO/(001)LAO film ($d \geq 60$ nm) [13, 14]. The cell volume in the part of the LCMO film where the mechanical strains were partially relieved is larger than V_{eff} of a (40 nm)LCMO/(001)LAO film (see table) but is smaller than the value of V_{eff} for stoichiometric bulk samples, in which the Mn^{4+} concentration is 33%. Thus, the cell volume in an LCMO/(001)LAO film does not remain constant as its thickness decreases in the range 120–40 nm. The rocking curve width for the (002) x-ray peak from ($d \geq 60$ nm)LCMO/(001)LAO films was 50–80% larger than those for thin LCMO layers grown coherently on (001)LAO.

It is practically impossible to reduce the cell parameters in a (001)LCMO ∥ (001)LAO film along the [010]LCMO and [100]LCMO directions without changing the valence of the manganese ions, because the double sum ($\Sigma \approx 3.92$ Å) of the ionic radii of oxygen ($r(O^{2-}) = 1.32$ Å [15]) and manganese ($r(Mn^{3+}) = 0.66$ Å, $r(Mn^{4+}) = 0.60$ Å [15]) is in excess of the LCMO pseudocubic lattice parameter.

3.2. Orientation and Lattice Parameters of LCMO Films Grown on (110)LAO

The (110) plane in LCMO films ($d = 40$–120 nm) grown on (110)LAO was parallel to the substrate plane (Figs. 1b, 2b), and the [100] and [010]LCMO directions made an angle of 45° with this plane. The parameter *c* of ($d \leq 60$ nm)LCMO/(110)LAO films calculated using the x-ray data obtained was noticeably smaller than the *b* parameter (see table: *b* = *a*, as shown in Fig. 2b). The parameter *c* in LCMO films ($d \leq 60$ nm) grown on (1̄10)LAO practically coincided with the pseudocubic lattice parameter of lanthanum aluminate.

In contrast to manganite layers grown on (001)LAO, the doubling of the (110)LCMO peaks in x-ray ω/2θ scans was observed only for $d \geq 80$ nm; i.e., mechanical strain relaxation in (1̄10)LCMO ∥ (110)LAO films

Parameters of LCMO epitaxial films grown on (001) and (110)LAO

Substrate	d, nm	c, Å	b, Å	V_{eff}, Å^3	T_M, K
(001)LAO	40	3.948	3.789	56.7	179
		3.950*	3.789*	56.7	
	80	3.875**	3.833**	56.9	237
(110)LAO	60	3.788	3.893	57.4	234
		3.787*	3.894*	57.4	
	120	3.839**	3.872**	57.6	257

* Unit cell parameters of the LCMO buffer coherently grown on substrate.

** Unit cell parameters of the LCMO buffer after partial strain relaxation.

started at larger thicknesses than in the case of (001)LCMO ∥ (001)LAO films. The increase in d_K in (110)LCMO ∥ (110)LAO compared to (001)LCMO ∥ (001)LAO films is due to the value of η for a manganite film grown on (110)LAO being smaller than that for a film of the same thickness prepared on (100)LAO. This is due both to the difference between the effective elastic moduli and to the oxygen ion density on the (110)LAO substrate surface being about 40% lower than that on the (001)LAO surface. The width of the rocking curve for the (110)LCMO peak from manganite films grown on (110)LAO was within 0.19°–0.22°.

Similar to the manganite film grown on (001)LAO, the LCMO layer prepared on (110)LAO was acted upon by in-plane compressive mechanical strains. It is the mechanical strains that are responsible for the parameter c measured in the LCMO/(110)LAO film in the substrate plane being substantially smaller than unit cell parameters a and b (see table). However, the cell volume V_{eff} in the (40 nm)LCMO/(110)LAO film was larger than that of (40 nm)LCMO/(001)LAO while being slightly smaller than the corresponding value for bulk stoichiometric ceramic samples; i.e., the relative concentration of Mn^{4+} ions in LCMO/(110)LAO was slightly above 33%. Unlike LCMO/(001)LAO films, an increase in the thickness of manganite films grown on (110)LAO from 40 to 120 nm did not change the cell volume noticeably. The weak dependence of V_{eff} in manganite films grown on (110)LAO on thickness (d = 120–40 nm) suggests that mechanical stresses applied in the (110)LCMO plane initiate elastic deformation of the unit cell without a substantial change in the effective valence state of the manganese ion sitting at the center of the oxygen octahedron.

3.3. Surface Morphology of Grown LCMO Films

No systematic difference in surface morphology was observed between LCMO films of the same thickness grown on the (001)LAO and (110)LAO substrates. Figure 3a presents a micrograph of the surface of the (40 nm)LCMO/(110)LAO film obtained with an atomic force microscope. One clearly sees characteristic depressions which decorate crystal grains on the surface of the manganite film. The grains are 20–30 nm in size. The reasons for grain boundary formation in epitaxial films of perovskite-like oxides grown coherently on single-crystal substrates were analyzed in [16, 17]. The granular nature of LCMO films grown coherently on lanthanum aluminate plates is primarily due to distortions in the stoichiometry of the phase adsorbed on the surface of the growing layer. The density of grain boundaries on the surface of LCMO films decreases with increasing d (Fig. 3). For thicknesses $d > d_K$, the composition of the phase adsorbed on the surface of a growing layer approaches that of the starting LCMO target, a factor that favors an increase in the average grain size.
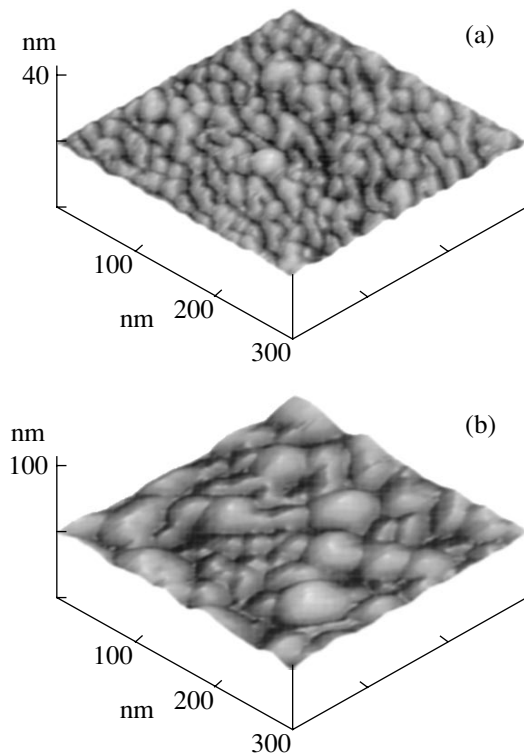
Fig. 3. (a) Surface micrograph of a (40 nm)LCMO film grown on a (110)LAO substrate. Grain boundaries in the film are decorated by characteristic depressions on the free film surface. (b) Surface micrograph of a (120 nm)LCMO film grown on a (110)LAO substrate. The density of grain boundaries in the top layer of the film with partially relieved mechanical strains was three to four times smaller than that in the thin LCMO layer grown coherently on a lanthanum aluminate substrate.

4. TEMPERATURE BEHAVIOR OF THE ELECTRICAL RESISTIVITY AND MAGNETORESISTANCE OF LCMO FILMS

The electrical resistivity of the grown LCMO films depended substantially on their thickness and the type of substrate used, with the highest values of ρ being obtained for (40 nm)LCMO/(001)LAO layers (Fig. 4a). The low conductivity of thin, coherently grown LCMO/(001)LAO films appears only natural, considering the estimates of the quadrivalent-manganese concentration in their volume derived from x-ray measurements. An analysis shows [18] that the conductivity in $(La,Ca)MnO_3$ solid solutions should be the highest for Mn^{4+} ion concentrations on the order of 32%. The high values of ρ in (40 nm)LCMO/(001)LAO films can also be partially accounted for by the formation of grains in their bulk with antiferromagnetically ordered spins; this has been observed in bulk ceramic $La_{0.6}Ca_{0.4}MnO_3$ samples [11] containing Mn^{4+} in relative concentrations of about 44%. The absolute values of ρ for the LCMO/(001)LAO and LCMO/(110)LAO films which underwent partial mechanical strain relaxation were similar in magnitude (Fig. 4).
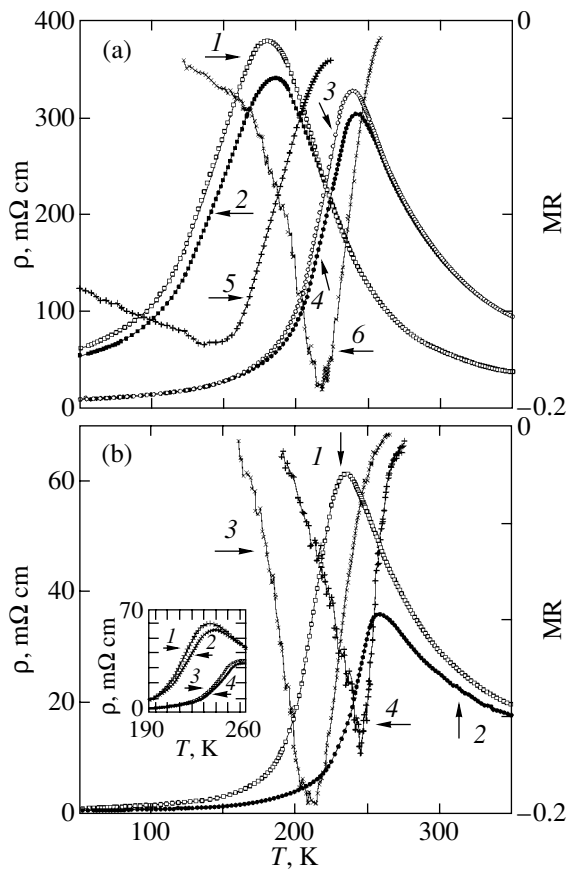
Fig. 4. (a) Temperature dependences of (*1–4*) the electrical resistivity ρ and (*5, 6*) magnetoresistance MR obtained for (001)LCMO ∥ (001)LAO films of thickness (*1, 2, 5*) $d = 40$ and (*3, 4, 6*) 80 nm (curves *3* and *4* for the film with $d = 80$ nm are scaled up by ten). (*1, 3*) $H = 0$ and (*2, 4*) $H = 0.4$ T. (b) Temperature dependences of (*1, 2*) the electrical resistivity ρ and (*3, 4*) magnetoresistance MR obtained for (110)LCMO ∥ (110)LAO films of thickness (*1, 3*) 60 and (*2, 4*) 120 nm. Inset shows ρ(*T*) relations at temperatures close to T_M measured on the same films (*2, 4*) in a magnetic field and (*1, 3*) without it. d (nm): (*1, 2*) 60 and (*3, 4*) 120.

As in the case of bulk LCMO single crystals, ferromagnetic spin ordering in the grown films was accompanied by a drop in their electrical resistivity, which accounted for the appearance of a clearly pronounced maximum in their ρ(*T*) relations. The temperature T_M at which ρ reached a maximum in LCMO/(001)LAO and LCMO/(110)LAO films with thicknesses $d < d_K$ was lower than that for manganite films with $d > d_K$ (Fig. 4). The higher temperatures T_M obtained for the LCMO films with partially relieved mechanical strains agree well with the data on the dependence of the Curie temperature in bulk (La,Ca)MnO$_3$ ceramic samples on the relative concentration of quadrivalent manganese ions quoted in [11]. According to [11], T_C in perovskite-like (La,Ca)MnO$_3$ manganites decreases by about 80 K as the Mn^{4+} concentration in their volume increases from 33 to 45%.

A magnetic field favors spin ordering in perovskite-like manganites, which was clearly pronounced in the decrease in the electrical resistivity of grown films. In the ($d \geq 60$ nm)LCMO/(001)LAO and ($d = 40$–120 nm)LCMO/(110)LAO films, the electrical resistivity was found to decrease substantially in a magnetic field in the interval $T_M - 60 < T < T_M + 10$ K. A noticeable decrease in ρ in (40 nm)LCMO/(001)LAO films was observed to occur as the temperature was lowered from $T_M + 20$ K to 50 K. The maximum in the ρ(*T*, $H = 0.4$ T) relations measured for grown LCMO films shifted by 3–5 K toward higher temperatures relative to its position on the ρ(*T*, $H = 0$) curves (see Fig. 4a, inset to Fig. 4b).

The temperature dependences of magnetoresistance MR = $[\rho(H = 0.4$ T$) - \rho(H = 0)]/\rho(H = 0)$ measured on the ($d \geq 60$ nm)LCMO/(001)LAO and ($d = 40$–120 nm)LCMO/(110)LAO films revealed a sharp peak at a temperature 10–20 K below T_M (Fig. 4). The maximum values of MR for the LCMO films with partially relieved mechanical strains agree well with the literature data reported for thick ($d > 100$ nm) epitaxial manganite layers and bulk ceramic samples [19].

The maximum in the MR(*T*) curves measured on ($d = 40$ nm)LCMO/(001)LAO films was not sharp (Fig. 4a), with large values of MR also observed at temperatures of about 50 K. The fairly large magnetoresistance obtained for strongly elastically strained ($d = 40$ nm)LCMO/(001)LAO films at low temperatures can be associated with the substantial manganese ion spin disorder occurring at temperatures below T_M.

5. CONCLUSIONS

Thus, lattice misfit accounts for the compressive biaxial mechanical strains in LCMO films grown epitaxially on (001)- or (110)-oriented lanthanum aluminate plates. The effective unit cell volume in an LCMO film grown coherently on a (001)LAO substrate is substantially smaller than V_{eff} in a manganite film of the same thickness grown on a (110)LAO substrate. The in-plane compressive biaxial mechanical strains favor the enrichment of LCMO films in quadrivalent manganese ions. The parameters of the (110)LCMO films are affected by mechanical strains induced by the film/substrate lattice misfit to a lesser extent than the parameters of the (001)LCMO films.

REFERENCES

1. Y. Tokura, in *Colossa Magnetoresistive Oxides*, Ed. by Y. Tokura (Gordon and Breach, Amsterdam, 2000), p. 2.
2. A. Goyal, M. Rajeswari, R. Shreekala, *et al.*, Appl. Phys. Lett. **71** (17), 2535 (1997).
3. E. Gommert, H. Cerva, J. Wecker, and K. Samwer, J. Appl. Phys. **85** (8), 5417 (1999).
4. R. A. Rao, D. Lavric, T. K. Nath, *et al.*, Appl. Phys. Lett. **73** (22), 3294 (1998).
5. H. Y. Hwang, T. T. Palstra, S.-W. Cheong, and B. Batlogg, Phys. Rev. B **52** (21), 15046 (1995).
6. A. J. Millis, T. Darling, and A. Migliory, J. Appl. Phys. **83** (3), 1588 (1998).
7. Yu. A. Boikov, D. Erts, and T. Claeson, Mater. Sci. Eng. B **79** (2), 133 (2001).
8. Yu. A. Boĭkov, D. Erts, and T. Claeson, Fiz. Tverd. Tela (St. Petersburg) **42** (11), 2042 (2000) [Phys. Solid State **42**, 2103 (2000)].
9. T. I. Kamins, J. Appl. Phys. **42** (11), 4357 (1971).
10. J. Aarts, S. Freisem, R. Hendrikx, and H. W. Zandbergen, Appl. Phys. Lett. **72** (23), 2975 (1998).
11. E. O. Wollan and W. C. Koehler, Phys. Rev. **100** (2), 545 (1955).
12. E. S. Vlakhov, R. A. Chakalov, R. I. Chakalova, *et al.*, J. Appl. Phys. **83** (4), 2152 (1998).
13. B. Wiedenhorst, C. Hofener, Y. Lu, *et al.*, Appl. Phys. Lett. **74** (24), 3636 (1999).
14. O. I. Lebedev, G. van Tendeloo, S. Amelinckx, *et al.*, Phys. Rev. B **58** (12), 8065 (1998).
15. R. C. Weast, *Handbook of Chemistry and Physics*, 55th ed. (CRC Press, Cleveland, 1974), p. F-198.
16. Yu. A. Boĭkov, T. Claeson, and A. Yu. Boĭkov, Zh. Tekh. Fiz. **71** (10), 54 (2001) [Tech. Phys. **46**, 1260 (2001)].
17. Yu. A. Boĭkov, V. A. Danilov, and A. Yu. Boĭkov, Fiz. Tverd. Tela (St. Petersburg) **45** (4), 649 (2003) [Phys. Solid State **45**, 681 (2003)].
18. J. B. Goodenough, Phys. Rev. **100** (2), 564 (1955).
19. H. Asano, J. Hayakawa, and M. Matsui, Phys. Rev. B **57** (2), 1052 (1998).

Translated by G. Skrebtsov

Microwave Magnetoabsorption in the CeAl₂ Magnetic Kondo Lattice at Low Temperatures

**N. E. Sluchanko*, A. V. Bogach*, I. B. Voskoboĭnikov*, V. V. Glushkov*, S. V. Demishev*,
N. A. Samarin*, G. S. Burkhanov**, and O. D. Chistyakov****

*General Physics Institute, Russian Academy of Sciences, ul. Vavilova 38, Moscow, 119991 Russia
e-mail: nes@lt.gpi.ru
**Institute of Metallurgy and Materials Sciences, Russian Academy of Sciences, Leninskiĭ pr. 49, Moscow, 117334 Russia
Received October 28, 2002

Abstract—The magnetic phase diagram of the CeAl₂ magnetic Kondo lattice was studied using microwave magnetoabsorption spectroscopy at frequencies of 37–118 GHz, temperatures of 1.8–4.6 K, and magnetic fields of up to 70 kOe. The observed anomalies in magnetoabsorption, when combined with the change in the carrier scattering pattern in (established in galvanomagnetic measurements) CeAl₂ near $H^* \approx 35$ kOe at liquid-helium temperatures, suggest that this compound undergoes a sequence of magnetic transitions accompanied by strong spin fluctuations. The nature of the magnetic phases and the mechanisms driving the phase transformations in CeAl₂ are discussed. © *2003 MAIK "Nauka/Interperiodica".*

1. The series of Ce-, Sm-, Eu-, Tm-, and Yb-based intermetallic compounds stands out among the rare-earth magnets [1]. The onset of a complex magnetic ground state in these compounds and, as a consequence, the realization of a complex magnetic phase diagram originate, as a rule, as a result of competition between indirect exchange interaction mediated by conduction electrons (the RKKY mechanism) and fast charge and spin fluctuations associated with localized magnetic moments (LMMs) of rare-earth ions (see, e.g., [2, 3]).

One of the best known compounds in this class of intermetallic compounds is cerium dialuminide, whose magnetic Kondo lattice undergoes a transition, at low temperatures $T \sim T_N \cong 3.85$ K, to an antiferromagnetic phase associated with cerium LMMs reduced through Kondo scattering of band carriers [4]. According to [4], the antiferromagnetic state in CeAl₂ has an incommensurate sine-modulated structure (K_I type); note also that, in addition to the negative Ce–Ce exchange interaction, this compound also revealed the existence of a ferromagnetic exchange component of comparable magnitude [4–6].

The conclusions drawn in [4] regarding the structure of the antiferromagnetic phase in CeAl₂ have been repeatedly discussed over the past decades. In particular, neutron diffraction studies of CeAl₂ single crystals [7] culminated in a description of the antiferromagnetic modulated (AFM) state in terms of a 3-component (characterized by a wave vector **k**) magnetic structure (K_{III} type) with a 24-component order parameter (see also [8]). Arguments were put forward [9, 10] for the formation in CeAl₂ of a magnetic structure in the form of a double elliptical helix with Ce magnetic moments

rotating in opposite directions in different fcc sublattices and with a slight change of the LMMs in magnitude along each of the helicoidal components (K_{II} type of magnetic structure). The mechanism responsible for the change in the magnitude of cerium localized magnetic moments along the helical axes (the so-called magnetic-structure modulation), which is about 30% of the amplitude value of the cerium LMM in the neighborhood of T_N [10], is apparently the Kondo compensation [9, 10].

The magnetic structure of CeAl₂ has also been a recent subject of intensive studies by μSR spectroscopy [11–13]; the results obtained in those studies and the conclusions drawn turned out, however, to be fairly contradictory. One of the factor that make investigation of the magnetic ground state of CeAl₂ difficult may be the dependence of the transition temperature T_N and of the specific features of establishment of long-range order on internal local strains and low-concentration impurities present in the samples studied [11, 14–16]. These factors that cause a spread of the Néel temperature within the interval $T_N = 3.4$–3.9 K [11], as well as the occurrence in CeAl₂ samples [14] of a sequence of two magnetic transitions with similar values of T_N, are apparently responsible for the above-mentioned difficulties encountered in attempts to interpret the magnetic structure and specific features in the H–T phase diagram of this compound. It should be stressed that despite the large number of studies and the obvious interest expressed in the investigation of the CeAl₂ magnetic Kondo lattice, the data available to date on the H–T magnetic phase diagram of this compound have been obtained primarily in measurements of the specific heat, thermal expansion, and magnetostriction [14,

15, 17, 18]. Recent high-precision measurements of the transport characteristics [19] showed CeAl$_2$ to indeed undergo two magnetic phase transitions at temperatures $T_N = 3.85$ K and $T_{N1} = 3.0$ K, with anomalies observed [19] in the Hall coefficient and magnetoresistance arguing for the existence of ferromagnetic correlations in the CeAl$_2$ matrix at low temperatures $T_N \le T \le 12$ K [4–6].

Microwave magnetoabsorption spectroscopy is an efficient experimental tool for studying magnetic phase diagrams of cerium-based heavy-fermion, mixed-valence (MV) systems. In particular, this technique was employed earlier to advantage in studying specific ground-state features of the CeB$_6$ magnetic Kondo lattice [20], as well as of the MV superconductor CeRu$_2$ [21]. In this connection, and with the aim to obtain additional information on the structure of the H–T magnetic phase diagram, we carried out a comprehensive investigation of microwave absorption at low temperatures $T < 5$ K both above the magnetic transition point $T_N \approx 3.85$ K and in the antiferromagnetic phase.

2. The measurements were carried out on polycrystalline CeAl$_2$ samples synthesized using arc melting in an argon environment from stoichiometric amounts of high-purity (4N–5N) components, with subsequent homogenization annealing of the intermetallic compound thus obtained. The polished plane-parallel CeAl$_2$ samples prepared for microwave studies typically measured $5 \times 5 \times 1$ mm; this permitted two-bolometer measurements in a bridge arrangement on a millimeter-range magnetooptic spectrometer, which is an upgraded version of the one used in [22, 23].

The scheme of the low-temperature part of the spectrometer is shown in Fig. 1. Ampoule *1* with a measuring unit evacuated and filled by exchange helium gas was placed in a superconducting solenoid *15* inside a helium cryostat. Microwave magnetoabsorption measurements were carried out in the range 1.8–4.6 K in magnetic fields of up to 70 kOe on the CeAl$_2$ samples employed earlier in galvanomagnetic studies [19]. The output of backward-wave tube generators (BWT) in the frequency range 37–118 GHz (output power of about 10 mW, stability of 10^{-4}) was propagated over waveguide line *14* and focused with an adjustable waveguide section and a Teflon lens *3* on a measuring unit consisting of two bolometers *13* and sample *4*, which was pasted directly onto one of the bolometers.

The measuring unit contained essentially a sapphire (*6*) and a brass (*8*) stage, which were insulated thermally from the body of the inner ampoule *2* by two Teflon washers *12*. Insertion of two carbon bolometers *13* into the measuring bridge, combined with the above-mentioned thermal insulation, substantially reduced the instabilities associated with temperature fluctuations and increased the instrument sensitivity by more than an order of magnitude as compared with the parameters obtained in [22, 23]. To reduce to a minimum the effect
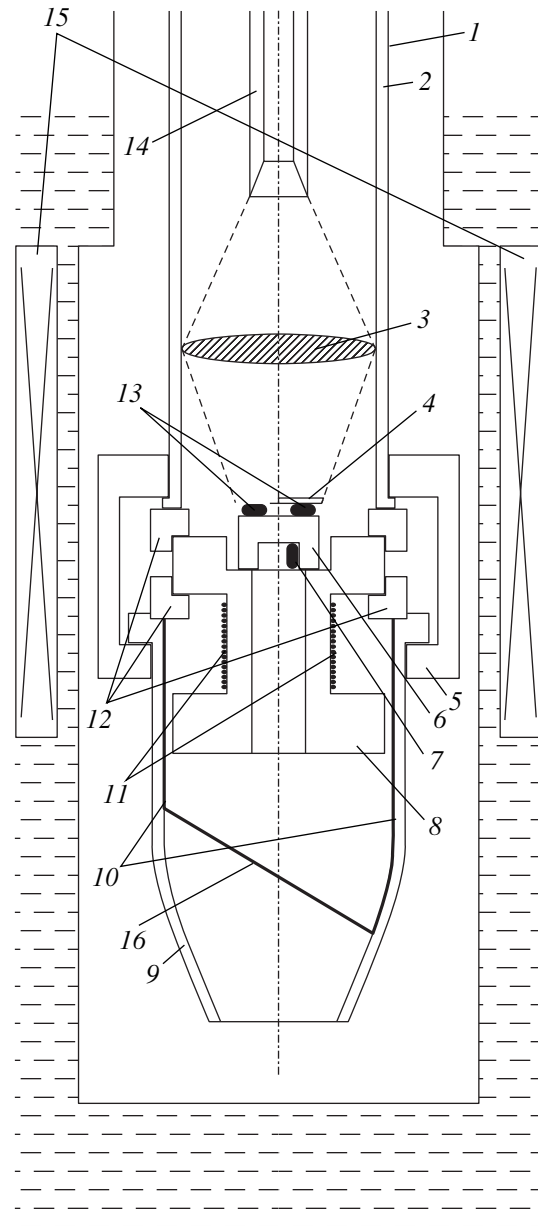
Fig. 1. Low-temperature part of the spectrometer. (*1*) External ampoule, (*2*) internal ampoule, (*3*) Teflon lens, (*4*) sample, (*5*) clamping nut, (*6*) sapphire stage, (*7*) carbon thermometer, (*8*) brass stage, (*9*) brass sensor cell body, (*10*) microwave absorber layer, (*11*) heater, (*12*) Teflon washers, (*13*) two bridge-connected bolometers, (*14*) waveguide, (*15*) superconducting solenoid, and (*16*) standing-wave damper.

of standing waves, the inner surface of the measuring-unit brass body *9* was coated by an absorbing layer (*10*) of activated carbon. A special standing-wave damper (*16*) of an isolating material mounted at an angle to the ampoule axis was also provided.

The temperature of the measuring unit containing the sample was measured with a carbon thermometer (*7*) screened from external radiation. A heater (*11*) was
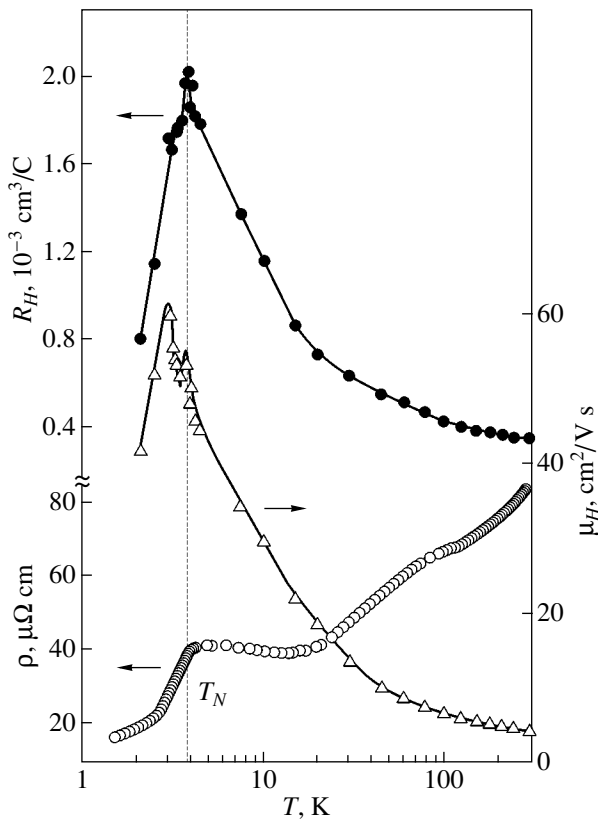
Fig. 2. Temperature dependence of the electrical resistivity, Hall coefficient, and μ_H parameter of CeAl$_2$.

used for measurements above the liquid-helium temperature. Measurements in the interval 1.8–4.2 K were carried out with the helium vapor pumped out of the cryostat with the loaded heater *11* circuit, and the temperature stabilization level needed for the measurements was reached by properly varying the exchange gas pressure in the ampoule.

3. Figure 2 displays the temperature dependences of the electrical resistivity ρ and of the Hall coefficient R_H obtained when testing CeAl$_2$ samples directly prior to microwave studies together with the temperature dependence of the parameter $\mu_H = R_H/\rho$. As is evident from Fig. 2, the temperature dependences of the electrical resistivity and of the Hall coefficient are essentially nonmonotonic and exhibit a broad maximum in ρ and R_H slightly below the Kondo temperature $T_K \approx 5$ K [6, 19], as well as a sharp kink in the $\rho(T)$ relation and a narrow peak in $R_H(T)$ in the vicinity of the transition to an antiferromagnetic state at $T_N \approx 3.85$ K [5, 6, 19]. The behavior of the $\mu_H = R_H/\rho$ parameter (Fig. 2) is also nonmonotonic, with the $\mu_H(T)$ relation having two narrow maxima in the neighborhood of $T_N \approx 3.85$ K and $T_{N1} \approx 3.0$ K, which argue in favor of a complex magnetic ground state in the CeAl$_2$ magnetic Kondo lattice.

Figures 3 and 4 display typical microwave absorption curves obtained on a CeAl$_2$ sample in the mag-

netic-field ranges $H \le 15$ kOe (I) and $25 \le H \le 70$ kOe (II), respectively. As seen from Fig. 3, the steplike feature in the $H_0^*-H_1^*$ interval is detected in the CeAl$_2$ microwave magnetoabsorption graphs in both the antiferromagnetic ($T < T_N$, Fig. 3a) and the paramagnetic ($T > T_N$, Fig. 3b) phases. The curve obtained at 3.05 K (Fig. 3a) also shows a noticeable hysteresis of magnetoabsorption for opposite directions of the magnetic field variation. Note that, as follows from the results reported in [17, 18] for CeAl$_2$, the anomalies in magnetostriction and thermal expansion observed to occur in fields $H \le 15$ kOe in the AFM phase ($T < T_N$) may be related to magnetization reorientation in the antiferromagnetic domains in this magnetic Kondo lattice, i.e., to the change from the random orientation of domains to their ordered, transverse orientation (with respect to the external magnetic field). The anomalous behavior of the physical characteristics of CeAl$_2$ in this range of temperatures and magnetic fields may be exemplified, in addition to the magnetoabsorption feature (Fig. 3a), by the formation of an anomalous Hall coefficient magnetic component in the antiferromagnetic phase, which peaks near 15 kOe [19]. The existence of strong antiferromagnetic fluctuations above T_N at temperatures up to 5.5 K in magnetic fields of up to 35 kOe is also believed [17, 18] to account for anomalies in the physical properties of CeAl$_2$. The boundary of the region of strong antiferromagnetic (AF) fluctuations (Fig. 5) was determined in [18] from measurements of the anomalies in thermal expansion in a magnetic field. Thus, following the arguments presented in [17, 18], the microwave magnetoabsorption anomalies observed in magnetic fields $H \le 15$ kOe at temperatures $T_N < T < 5$ K (Fig. 3b) should be considered to originate from strong antiferromagnetic fluctuations existing in the CeAl$_2$ matrix; therefore, the features seen in the $I(H, T_0)$ curves in Figs. 3 and 4 can be used to construct the H–T magnetic phase diagram of the CeAl$_2$ magnetic Kondo lattice (Fig. 5).

Let us dwell in more detail on the microwave magnetoabsorption measurements made in range II (25–70 kOe), in which the AFM state in CeAl$_2$ is, in accordance with [4–6, 14–18], suppressed by a magnetic field. The experimental data presented in Fig. 4 show a steplike anomaly in the $I(H, T_0)$ curves occurring in this region of H variation in the vicinity of the Néel temperature $T_N \approx 3.85$ K. As the temperature is lowered in the antiferromagnetic phase still further, down to 3.4 K, the amplitude of this feature grows noticeably, with an additional maximum in magnetoabsorption appearing on the $I(H, T_0)$ curves at temperatures $T < 3.4$ K (Fig. 4). As a result, the magnetoabsorption anomaly associated with destruction of the AF state in CeAl$_2$ by a magnetic field has a complex character and the beginning (H_2^*) and end (H_3^*) of the interval where this $I(H)$ feature is observed (Fig. 4) may be used to refine the
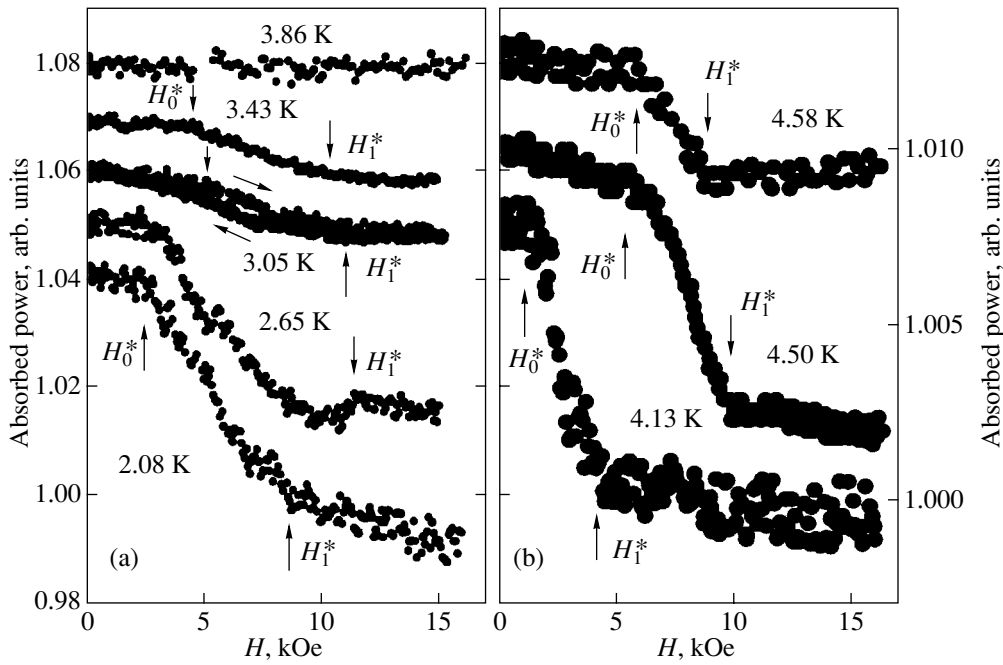
Fig. 3. Magnetoabsorption of CeAl$_2$ at low fields $H \leq 15$ kOe (range I).

magnetic phase diagram of CeAl$_2$. Figure 5 combines all the data related to the anomalies in the physical characteristics of CeAl$_2$ in the neighborhood of the magnetic phase transformations. The $H_0^*(T)$, $H_1^*(T)$, $H_2^*(T)$, and $H_3^*(T)$ curves, as well as the features corresponding to the critical behavior of the Hall coefficient and resistivity [19, 24], are displayed in Fig. 5 together with the results obtained in studies of the magnetostriction [17], thermal expansion [14, 15, 18], specific heat [25, 26], and elastic moduli [27, 28] of CeAl$_2$.

A comparison of the present measurements of microwave magnetoabsorption and galvanomagnetic characteristics of CeAl$_2$ with the magnetic and thermodynamic data used in [17, 18] to construct an H–T phase diagram suggests that the true magnetic phase diagram is substantially more complex than the one proposed in [17, 18]. For instance, the anomalous-magnetoabsorption region in the vicinity of the AFM state suppression by a magnetic field turns out to be substantially larger than the part of the phase boundary derived in [15, 17, 18] from studies of single-crystal and polycrystalline CeAl$_2$ samples. It should also be stressed that the beginning of the H_2^*–H_3^* interval of anomalous magnetoabsorption at $H_2^* \approx 35 \pm 4$ kOe is practically temperature-independent within a broad interval from 2 to 5 K and coincides with good accuracy both with the change in the carrier-scattering regime, which accounts for the appearance of anomalies in the magnetoresistance [24] and Hall coefficient [19], and with the onset of qualitative changes in the elastic properties of CeAl$_2$

(see symbols in the phase diagram of Fig. 5). It should also be pointed out that the upper boundary of the anomalous-magnetoabsorption region is located substantially above the critical-field curve of the AFM
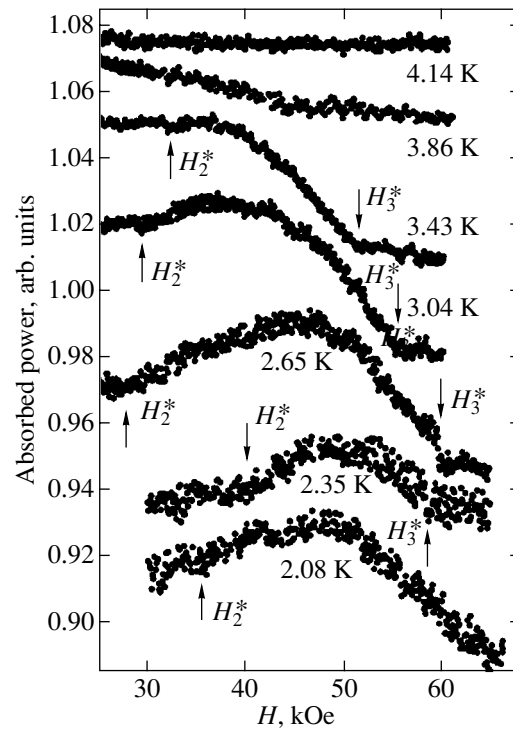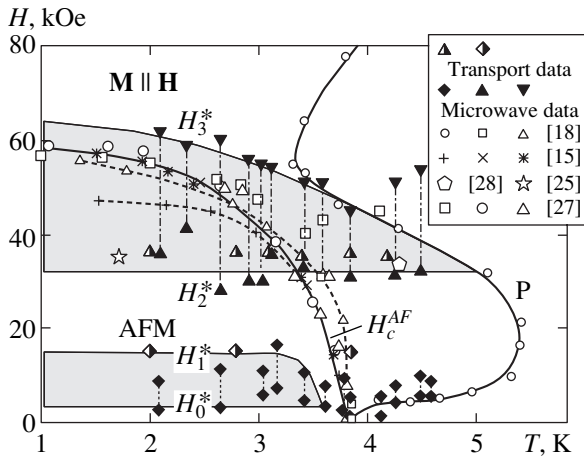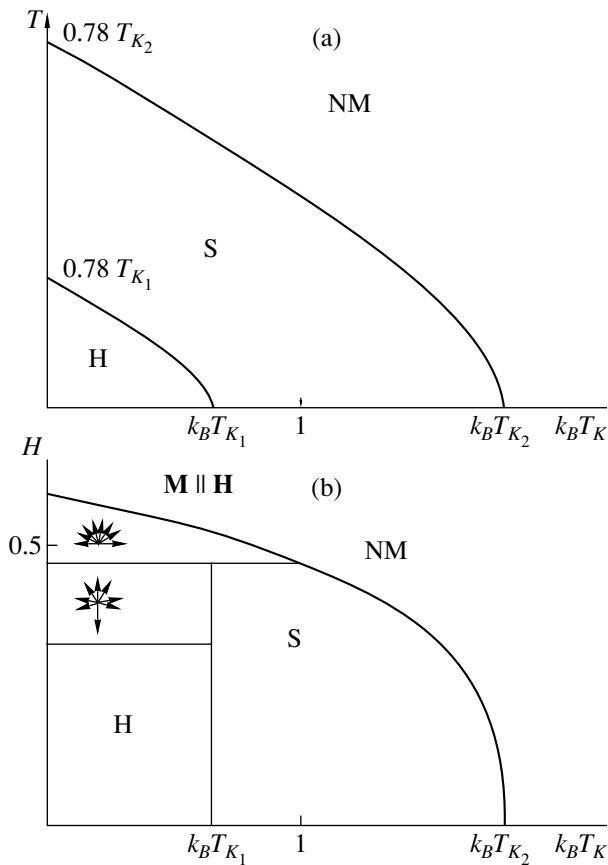

Fig. 4. Magnetoabsorption of CeAl$_2$ at high fields $H \geq 25$ kOe (range II).

Fig. 5. H–T phase diagram of CeAl$_2$. Transport Data are Hall coefficient and magnetoresistance measurements, Microwave Data are magnetooptic measurements, AFM is the antiferromagnetic modulated phase, and P is the paramagnetic phase (see text).

Fig. 6. (a) T–T_K phase diagram ($H = 0$) from [30], (b) H–T_K phase diagram ($T = 0$) from [30]; H is the helicoidal magnetic structure, S is the sinusoidal magnetic structure, and NM is the nonmagnetic phase.

phase obtained in [15, 17, 18] (H_c^{AF} in Fig. 5), which is particularly well defined in the temperature interval between T_{N1} and T_N. As a result, in the range 3.0–3.8 K, noticeable anomalous microwave magnetoabsorption is also observed above the critical curve H_c^{AF}, which suggests, in our opinion, a rearrangement of the magnetic structure occurring in both the paramagnetic and an unknown magnetic phase ([15, 17, 18] (**M** ∥ **H** in Fig. 5) in CeAl$_2$.

Because the change in the carrier-scattering regime and the appearance of anomalous magnetoabsorption in CeAl$_2$ at $H_2^* \approx 35$ kOe suggest, in our opinion, rearrangement of the magnetic state, the data obtained argue for the existence of a more complex magnetic phase diagram than the widely accepted one [17, 18]; considered in this vein, the additional plane boundary $H_2^* \approx$ const in the phase diagram of this compound, which was established experimentally by us, is new supportive evidence. This conclusion is also supported by the noticeable increase in the amplitude of the λ anomaly of specific heat, which was observed in [26] at 31 kOe and assigned to the proximity to the tricritical point in the CeAl$_2$ phase diagram.

4. Turning now to a discussion of the results obtained in this study (see Figs. 2–5), we note that all the trivalent rare-earth dialuminides in the series of Laves phases LnAl$_2$ (Ln stands for Ce, Nd, Tb, Dy, etc.), except CeAl$_2$, are ferromagnets. It is apparently the competition between the magnetic RKKY interaction and the mechanism of Kondo compensation of rare-earth LMMs (which dominates the formation of a nonmagnetic ground state and, thus, underlies the noticeable instability of the ferromagnetic structure) that accounts for the establishment of long-range AF order in the CeAl$_2$ magnetic Kondo lattice. At the same time, strong ferromagnetic fluctuations were observed in the CeAl$_2$ matrix both in strong magnetic fields $H > 60$ kOe at liquid-helium temperatures and at intermediate temperatures of 5–50 K [6, 15, 17, 18, 24]. In particular, measurements of quasi-elastic neutron scattering [6] revealed in CeAl$_2$ the coexistence of ferromagnetic correlations at intermediate temperatures with an AF-type short-range order; crude estimates of the lower bound on the ferromagnetic correlation length yield ξ ≥ 20 Å [6]. Similarly, diffuse neutron magnetic scattering experiments made on CeAl$_2$ at liquid-helium temperatures [29] revealed the existence of two characteristic spatial scales, ξ$_1$ and ξ$_2$, and, accordingly, of two critical exponents.

Because an external magnetic field $H \sim H_K \approx k_B T_K/\mu_B \approx 70$ kOe [(T_K(CeAl$_2$) ≈ 5 K] suppresses Kondo fluctuations of the Ce magnetic moment in this magnetic Kondo lattice, one may expect, in addition to destruction of long-range AF order, an enhancement of ferromagnetic correlations and, consequently, the

appearance of new phases in the magnetic H–T diagram of CeAl$_2$. In this connection, one may recall the calculations from [30] made within the model of a linear chain of Ce ions featuring ferromagnetic interaction J_1 between nearest neighbors and antiferromagnetic Ce–Ce interaction J_2 between second-to-nearest neighbors. Inclusion of the Kondo correlation term $k_B T_K$ results in a fairly complex magnetic phase diagram within this model [30] (Fig. 6). Assuming the AF exchange to be relatively strong, $J_2 > 1/4|J_1|$, and the values of T_K to be sufficiently low, the authors of [30] obtained for CeAl$_2$ a complex H–T–T_K phase diagram, according to which the AFM phase is replaced, with increasing external magnetic field, by a noncollinear magnetic structure (Fig. 6), with a subsequent metamagnetic transition to the **M ∥ H** state.

In our opinion, this sequence of transitions is the most probable scenario for the magnetic Kondo lattice and it is apparently this sequence that was detected in the present study in microwave magnetoabsorption experiments and in galvanomagnetic measurements performed on polycrystalline samples in the magnetically ordered state of the CeAl$_2$ concentrated Kondo system.

ACKNOWLEDGMENTS

REFERENCES

1. D. I. Khomskiĭ, Usp. Fiz. Nauk **129** (3), 443 (1979) [Sov. Phys. Usp. **22**, 879 (1979)].
2. J. M. Effantin, J. Rossat-Mignod, P. Burlet, *et al.*, J. Magn. Magn. Mater. **47–48**, 145 (1985).
3. P. Wachter, in *Handbook on the Physics and Chemistry of Rare Earths*, Ed. by K. A. Gschneidner, Jr., L. Eyring, G. H. Lander, and G. R. Choppin (North-Holland, Amsterdam, 1994), Vol. 19, Chap. 132, p. 177.
4. B. Barbara, J. X. Boucherle, J. L. Buevoz, *et al.*, Solid State Commun. **24** (7), 481 (1977).
5. M. C. Croft, R. P. Guertin, L. C. Kupferberg, and R. D. Parks, Phys. Rev. B **20** (5), 2073 (1979).
6. F. Steglich, C. D. Bredl, M. Loewenhaupt, and K. D. Schotte, J. Phys. Colloq. **40** (Suppl.), C5-301 (1979).
7. S. M. Schapiro, E. Gurewitz, R. D. Parks, and L. C. Kupferberg, Phys. Rev. Lett. **43** (23), 1748 (1979).
8. M. Ma and J. Solyom, Phys. Rev. B **21** (11), 5262 (1980).
9. E. M. Forgan, B. D. Rainford, S. L. Lee, *et al.*, J. Phys.: Condens. Matter **2** (6), 10211 (1990).
10. F. Giford, J. Schweizer, and F. Tasset, Physica B (Amsterdam) **234–236**, 685 (1997).
11. A. Amato, Rev. Mod. Phys. **69** (4), 1119 (1997).
12. A. Schenk, D. Andreica, M. Pinkpank, *et al.*, Physica B (Amsterdam) **259–261**, 14 (1999).
13. A. Schenk, D. Andreica, F. N. Gygax, and H. R. Ott, Phys. Rev. B **65** (2), 024 444 (2002).
14. R. Schefzyk, W. Lieke, and F. Steglich, Solid State Commun. **54** (6), 525 (1985).
15. E. Fawcett, V. Pluzhnikov, and H. Klimker, Phys. Rev. B **43** (10), 8531 (1991).
16. J. L. Gavilano, J. Hunziker, O. Hudak, *et al.*, Phys. Rev. B **47** (6), 3438 (1993).
17. M. Croft, I. Zoric, and R. D. Parks, Phys. Rev. B **18** (1), 345 (1978).
18. M. Croft, I. Zoric, and R. D. Parks, Phys. Rev. B **18** (9), 5065 (1978).
19. N. E. Sluchanko, A. V. Bogach, V. V. Glushkov, *et al.*, Pis'ma Zh. Éksp. Teor. Fiz. **76** (1), 31 (2002) [JETP Lett. **76**, 26 (2002)].
20. N. E. Sluchanko, S. V. Demishev, A. V. Semeno, *et al.*, Pis'ma Zh. Éksp. Teor. Fiz. **63** (6), 431 (1996) [JETP Lett. **63**, 453 (1996)].
21. N. E. Sluchanko, V. V. Glushkov, S. V. Demishev, *et al.*, Pis'ma Zh. Éksp. Teor. Fiz. **69** (10), 745 (1999) [JETP Lett. **69**, 798 (1999)].
22. S. V. Demishev, A. V. Semeno, N. E. Sluchanko, *et al.*, Zh. Éksp. Teor. Fiz. **111** (3), 979 (1997) [JETP **84**, 540 (1997)].
23. I. B. Voskoboĭnikov, S. V. Demishev, R. N. Lyubovskaya, *et al.*, Fiz. Tverd. Tela (St. Petersburg) **44** (2), 203 (2002) [Phys. Solid State **44**, 210 (2002)].
24. V. V. Moshchalkov, P. Coleridge, E. Fawcett, and A. Sachrajda, Solid State Commun. **60** (12), 893 (1986).
25. M. Croft, I. Zoric, J. Markovics, and R. Parks, in *Valence Instabilities and Related Narrow Band Phenomena*, Ed. by R. D. Parks (Plenum, New York, 1977), p. 475.
26. C. D. Bredl, F. Steglich, and K. D. Schotte, Z. Phys. B **29** (4), 327 (1978).
27. R. Schefzyk, W. Lieke, F. Steglich, *et al.*, J. Magn. Magn. Mater. **45** (2–3), 229 (1984).
28. B. Luthi and C. Lingner, Z. Phys. B **34** (2), 157 (1979).
29. T. Chattopadhyay and G. J. McIntyre, Physica B (Amsterdam) **234–236**, 682 (1997).
30. A. Benoit, J. Flouquet, and M. Ribault, J. Phys. Colloq. **40** (Suppl.), C5-328 (1979).

Translated by G. Skrebtsov

<center>

MAGNETISM
AND FERROELECTRICITY

</center>

Anisotropy and Phase States of Garnet Ferrite Films with Misoriented Surfaces

V. I. Butrim, S. V. Dubinko, and Yu. N. Mitsaĭ

Domain Design Office, Vernadsky National University, Simferopol, 95001 Ukraine
e-mail: domain@home.cris.net
Received July 15, 2002; in final form, November 4, 2002

Abstract—Anisotropy of garnet ferrite films is investigated in the framework of the two-parametric model. It is shown that a garnet ferrite film with an arbitrarily oriented surface is characterized by biaxial anisotropy. The directions of the easy, intermediate, and hard magnetization axes are determined as functions of the misorientation angle and weak cubic anisotropy. It is demonstrated that the region of existence of homogeneous states in a magnetic field is bounded by a slant astroid. The magnetic susceptibility tensor and the ferromagnetic resonance frequency are calculated, and the dispersion law of spin waves is determined. © *2003 MAIK "Nauka/Interperiodica".*

1. INTRODUCTION

In recent years, considerable interest has been expressed by researchers in epitaxial garnet ferrite films with a tilted easy magnetization axis (EMA). On the one hand, this is associated with the great variety of unique physical properties manifested by these systems as compared to conventional films with an easy magnetization axis perpendicular to the film surface. On the other hand, this interest stems from the fact that, as a rule, real films are characterized by anisotropies other than uniaxial. The tilted easy magnetization axes render these materials more promising for use in the design of magneto-optical data-processing devices and visualization of inhomogeneous magnetic fields whose period of inhomogeneity is comparable to the domain period of the epitaxial garnet ferrite films.

It is well known that one of the factors responsible for the physical properties of epitaxial garnet ferrite films is the crystallographic orientation of the substrate. This is caused primarily by the fact that the crystallographic orientation of the substrate determines the form of the anisotropy energy. In particular, films of the (111) type possess uniaxial anisotropy with an easy magnetization axis perpendicular to the film surface. Epitaxial garnet ferrite films with a small (no larger than 8°) deviation of the substrate orientation from the (111) plane were studied in [1–3]. It was demonstrated that these films are characterized by tilted easy magnetization axes and that the tilt of the easy magnetization axis with respect to the normal is determined by the misorientation angle of the substrate. A similar situation is observed for (112)-oriented films [4], in which the tilt of the easy magnetization axes can reach several tens of degrees.

However, no significance has hitherto been attached to the fact the inclination of an easy magnetization axis

is accompanied by the emergence of anisotropy in a plane perpendicular to this axis, i.e., in a plane other than basal. The biaxial anisotropy thus induced is responsible for the specific features of the magnetization reversal, determines the type of domain structure [4], and leads to variations in the spin- and elastic-wave spectra [5]. Films in which the magnetization vector in the ground state deviates only slightly from the basal plane also belong to this type. It should be noted that such films, i.e., films with a quasi-easy magnetic plane, offer a number of advantages over uniaxial films both for use in magneto-optical visualization of magnetic fields in the bulk of high-temperature superconductors [6, 7] and magnetic carriers [8] and for research into nanostructured magnetic materials [9].

Despite the broad spectrum of application of the aforementioned magnetic structures, the nature of their anisotropy has not been adequately investigated. From the practical standpoint, it is of interest to elucidate how the orientation of the substrate affects the magnetic properties of the film.

In this work, we investigated the anisotropy of epitaxial garnet ferrite films with arbitrarily oriented surfaces and a normal aligned with the ($\bar{1}10$) plane. For these films, we determined the stability boundaries of homogeneous states in a magnetic field, deduced the dispersion law of spin waves, and calculated the ferromagnetic resonance frequency and the magnetic susceptibility tensor.

2. ANISOTROPY AND THE GROUND STATE

For the studied system, the energy density of anisotropy can be represented in the form

$$W_a = W_a^G + W_a^K. \tag{1}$$

Here, W_a^G is the energy density of growth induced anisotropy, which is defined by the relationship

$$W_a^G = Am_i^2\gamma_i^2 + Bm_im_j\gamma_i\gamma_j, \quad i > j, \tag{2}$$

and W_a^K is the energy density of cubic crystalline anisotropy, which is expressed by the formula

$$W_a^K = K_1m_i^2m_j^2, \quad i > j. \tag{3}$$

In relationships (2) and (3), A and B are constants of the two-parametric model of growth induced anisotropy [10]; m_i and γ_i are the respective direction cosines of the magnetization vector and the growth direction of the film in a coordinate system specified by the unit vectors $\mathbf{e}_1$, $\mathbf{e}_2$, and $\mathbf{e}_3$, which are chosen parallel to the crystallographic directions [100], [010], and [001], respectively; and K_1 is the cubic anisotropy constant.

Let us now change over to a new coordinate system related to the film; that is,

$$\mathbf{e}_x = \frac{p}{\sqrt{2}}(\mathbf{e}_1 + \mathbf{e}_2) - q\mathbf{e}_3,$$

$$\mathbf{e}_y = \frac{1}{\sqrt{2}}(-\mathbf{e}_1 + \mathbf{e}_2), \tag{4}$$

$$\mathbf{e}_z = \frac{q}{\sqrt{2}}(\mathbf{e}_1 + \mathbf{e}_2) + p\mathbf{e}_3.$$

Here, the unit vector $\mathbf{e}_y$ is aligned parallel to the film plane and coincides with the $[\bar{1}10]$ direction; the unit vector $\mathbf{e}_z$ coincides with the normal to the film plane, whose orientation in the $(\bar{1}10)$ plane is specified by the misorientation angle δ measured from the [111] direction to the [112] direction; and

$$p = \cos\alpha = \frac{1}{\sqrt{3}}(\cos\delta + \sqrt{2}\sin\delta),$$

$$q = \sin\alpha = \frac{1}{\sqrt{3}}(\sqrt{2}\cos\delta - \sin\delta) \tag{5}$$

are the direction cosines of the unit vector $\mathbf{e}_x$ in the $(\bar{1}10)$ plane.

In the coordinate system ($\mathbf{e}_x$, $\mathbf{e}_y$, $\mathbf{e}_z$), the energy density of growth induced anisotropy W_a^G takes the form

$$W_a^G = K_u m_z^2 + K_{ort} m_x^2 + 2K_t m_x m_z, \tag{6}$$

where K_u, K_{ort}, and K_t are the uniaxial, orthorhombic, and tilted anisotropy constants, respectively:

$$K_u = \frac{1}{2}B - \frac{1}{2}\rho(1-3p^2)p^2, \quad K_{ort} = -\frac{1}{2}\rho(1-3p^2)q^2, \tag{7}$$

$$K_t = -K_{ort}\frac{p}{q}, \quad \rho = A - \frac{B}{2}.$$

The function W_a^G represents a quadratic form ($\mathbf{m}$, $\mathbf{Km}$) with the matrix

$$\mathbf{K} = \begin{pmatrix} K_{ort} & 0 & K_t \\ 0 & 0 & 0 \\ K_t & 0 & K_u \end{pmatrix}, \tag{8}$$

for which the eigenvalues are given by

$$2\lambda_\pm = I \pm \sqrt{I^2 - 4J}, \quad \lambda_0 = 0. \tag{9}$$

Here,

$$I = K_u + K_{ort}, \quad J = K_u K_{ort} - K_t^2 \tag{10}$$

are the spur and the determinant of the matrix $\mathbf{K}$, respectively. Their values are determined by the orientation of the substrate:

$$2I = B - \rho(1-3p^2), \quad 4J = -B\rho(1-3p^2)q^2. \tag{11}$$

The eigenvectors corresponding to the eigenvalues given by relationships (9) at $J \ne 0$ can be represented in the following general form:

$$\mathbf{n}_\xi = \begin{pmatrix} \cos\theta_0 \\ 0 \\ -\sin\theta_0 \end{pmatrix}, \quad \mathbf{n}_\zeta = \begin{pmatrix} \sin\theta_0 \\ 0 \\ \cos\theta_0 \end{pmatrix}, \quad \mathbf{n}_0 = \begin{pmatrix} 0 \\ 1 \\ 0 \end{pmatrix}, \tag{12}$$

where

$$\tan\theta_0 = -\frac{1}{\varepsilon}[\sigma + \sqrt{1+\varepsilon^2}],$$

$$\sigma = \mathrm{sgn}(K_u - K_{ort}), \quad \varepsilon = \frac{2K_t}{|K_u - K_{ort}|}. \tag{13}$$

For $\sigma = +1$, the in-plane anisotropy component dominates and the θ_0 angle falls in the range $\pi/4 \le |\theta_0| \le \pi/2$. For $\sigma = -1$, the $|\theta_0|$ angle lies in the range 0–$\pi/4$.

In the basis of eigenvectors of the matrix $\mathbf{K}$, the quadratic form (6) can be reduced to the sum of squares. In this case, the eigenvalues are the anisotropy constants and the eigenvectors are directed along the easy, intermediate, and hard magnetization axes. The eigenvector aligned with the easy magnetization axis corresponds to the smallest eigenvalue, whereas the eigenvector directed along the hard magnetization axis (HMA) is associated with the largest eigenvalue.

The nature of anisotropy substantially depends on the parameter J. For $J \ne 0$, all the eigenvalues differ from one another and the anisotropy is biaxial; that is,

$$W_a^G = \frac{1}{2}\beta_1(\mathbf{mn}_\zeta)^2 + \frac{1}{2}\beta_2(\mathbf{mn}_\xi)^2, \tag{14}$$

where $\beta_{2,1} = 2\lambda_\pm$.

The orientations of the magnetic axes are governed by the ratios between the eigenvalues λ_+, λ_-, and λ_0,

which have the following form for different values of I and J:

(i) $\lambda_- < \lambda_+ < \lambda_0 = 0, \quad J > 0, I < 0,$

(ii) $\lambda_0 = 0 < \lambda_- < \lambda_+, \quad J > 0, I > 0,$ (15)

(iii) $\lambda_- < \lambda_0 = 0 < \lambda_+, \quad J < 0, I$ is arbitrary.

Therefore, according to relationship (14), films of the given type are characterized by three phase states, namely, the Φ_1, Φ_2, and Φ_3 phases:

Φ_1: EMA $\parallel \mathbf{n}_\zeta$, IMA $\parallel \mathbf{n}_\xi$, HMA $\parallel [\bar{1}10]$,

Φ_2: EMA $\parallel [\bar{1}10]$, IMA $\parallel \mathbf{n}_\zeta$, HMA $\parallel \mathbf{n}_\xi$,   (16)

Φ_3: EMA $\parallel \mathbf{n}_\zeta$, IMA $\parallel [\bar{1}10]$, HMA $\parallel \mathbf{n}_\xi$.

Here, IMA is the intermediate magnetization axis. For $J = 0$, one of the eigenvalues (λ_+ or λ_-, depending on the sign of the spur I) goes to zero and the anisotropy becomes uniaxial with the preferred direction along the normal:

$$W_a^G = \frac{1}{2}\beta(\mathbf{m}\mathbf{n}_z)^2. \tag{17}$$

Here, $\beta = 2(K_u + K_{\text{ort}})$. It follows from relationships (11) that, at $B \neq 0$, the (001)- and (111)-oriented films should possess uniaxial anisotropy. At $B = 0$, the preferred direction coincides with the unit vector $\mathbf{e}_3$; in this case, we have $\beta = 2A$.

For slightly misoriented (111) films ($\delta \ll 1$), the θ_0 angle and the corrections to the anisotropy constants are linear in δ; that is,

$$\beta_{2,1} = \frac{1}{2}B + \sqrt{2}\rho\delta \pm \frac{1}{2}\left|B - \frac{2\sqrt{2}}{3}\rho\delta\right|,$$
$$\theta_0 = -\frac{4}{3}\frac{\rho}{B}\delta. \tag{18}$$

In the case where the substrate is oriented nearly parallel to the (001) plane, the α angle is small. Then,

$$\beta_{2,1} = A - \frac{3}{2}\rho\alpha^2 \pm \left|A - \frac{3A + 2B}{2A}\rho\alpha^2\right|,$$
$$\theta_0 = -\frac{\rho}{2A}\alpha. \tag{19}$$

The linear dependence of the θ_0 angle on α was confirmed experimentally in [1].

The energy density of cubic anisotropy can be conveniently represented in the form

$$W_a^K = -K_1(\mathbf{m}\mathbf{e}_+)^2 m_y^2 + \frac{1}{4}K_1(\mathbf{m}\mathbf{e}_3)^2[2 - 3(\mathbf{m}\mathbf{e}_3)^2]. \tag{20}$$

Here,

$$\mathbf{e}_+ \equiv \frac{1}{\sqrt{2}}(\mathbf{e}_1 + \mathbf{e}_2) = p\mathbf{e}_x + q\mathbf{e}_z.$$

The easy magnetization axes are the directions $R^{-1}\langle 111 \rangle$ at $K_1 < 0$ and $R^{-1}\mathbf{e}_1$, $R^{-1}\mathbf{e}_2$, and $R^{-1}\mathbf{e}_3$ at $K_1 > 0$. Here, R^{-1} is the matrix of the inverse transformation with respect to that described by expressions (4).

For the Φ_1 phase, the corrections to the θ_0 angle can be determined under the assumption that $m_y = 0$. In the approximation linear with respect to K_1/ρ, we obtain the following relationship for a weak cubic anisotropy ($K_1 \ll B, \rho$):

$$\tan\theta_0(K_1) = \tan\theta_0\left[1 + \frac{K_1}{\rho}\frac{f(\alpha + \theta_0)}{f(\alpha)}\right], \tag{21}$$

where $\theta_0(K_1)$ is the angle specifying the orientation of the vector $\mathbf{n}_\zeta$ at $K_1 \neq 0$ and

$$f(\alpha) = (1 - 3\cos^2\alpha)\sin 2\alpha. \tag{22}$$

The aforementioned misorientation effects manifest themselves only in samples with a finite size, because, for infinite crystals, these effects can be taken into account through a simple rotation of the coordinate system.

3. HOMOGENEOUS STATES IN A MAGNETIC FIELD

In the presence of an external magnetic field $\mathbf{H}$, the anisotropy energy should contain an additional term:

$$W_H = -M_0 H[\sin\theta\sin\theta_H\cos(\varphi - \varphi_H) + \cos\theta\cos\theta_H]. \tag{23}$$

Here, M_0 is the saturation magnetization, θ_H is the polar angle of the magnetic vector $\mathbf{H}$, φ_H is the azimuthal angle of the magnetic vector $\mathbf{H}$, θ is the polar angle of the magnetization vector $\mathbf{M}_0$ and φ is the azimuthal angle of the magnetization vector $\mathbf{M}_0$.

Our prime interest here is in the homogeneous state of the noncollinear phase Φ_1, for which the condition $\varphi = \varphi_H = 0, \pi$ is satisfied and the equation of the curve of regular rotation $\theta(H)$ takes the form

$$H\sqrt{1 + \varepsilon^2}\sin(\theta - \theta_H)$$
$$= H_A[\sigma\sin 2\theta - \varepsilon\cos 2\theta\cos\varphi_H]. \tag{24}$$

Here, H_A is the anisotropy field defined by the expression

$$H_A = 2\frac{|K_u - K_{\text{ort}}|}{M_0}\sqrt{1 + \varepsilon^2}. \tag{25}$$

The field region of existence of homogeneous states lies outside the astroid:

$$\sin^{2/3}(\theta_H - \theta_0) + \cos^{2/3}(\theta_H - \theta_0) = \left(\frac{H_A}{H}\right)^{2/3}, \tag{26}$$

where

$$\sin(\theta - \theta_H) = \frac{1}{\sqrt{3}}\sqrt{\left(\frac{H_A}{H}\right)^2 - 1}. \qquad (27)$$

The astroid contains two pairs of characteristic points specified by the relationship

$$\theta(H) = \begin{cases} 0, \pi, & \tan\theta_H = \pm\dfrac{\varepsilon}{2}, \\[2mm] \pm\dfrac{\pi}{2}, & \cot\theta_H = \mp\dfrac{\varepsilon}{2}. \end{cases} \qquad (28)$$

These states exist in the magnetic field satisfying the equation

$$H = H_A\sqrt{\frac{1 + \varepsilon^2/4}{1 + \varepsilon^2}}. \qquad (29)$$

The static susceptibility $\chi^0_{\alpha\beta} = \partial M_\alpha/\partial H_\beta$ of the Φ_1 phase can be represented in the form

$$\hat{\chi}^0 = \frac{1}{\Delta_0}\begin{pmatrix} \cos^2\theta & 0 & -\dfrac{1}{2}\sin 2\theta \\[2mm] 0 & 0 & 0 \\[2mm] -\dfrac{1}{2}\sin 2\theta & 0 & \sin^2\theta \end{pmatrix}, \qquad (30)$$

where

$$\Delta_0 = \frac{H}{M_0}\cos(\theta - \theta_H) - \frac{H_A}{M_0}\sigma\frac{\cos 2\theta + \varepsilon\sin 2\theta}{\sqrt{1 + \varepsilon^2}}. \qquad (31)$$

In this case, the static susceptibility $\hat{\chi}^0$ on the astroid exhibits a polar singularity characteristic of second-order phase transitions.

The inclusion of the magnetic dipole interaction for a film whose normal is aligned parallel to the z axis corresponds to the replacement $K_u \longrightarrow K_u^* = K_u + 2\pi M_0^2$.

4. HIGH-FREQUENCY PROPERTIES OF THIN FILMS

As is known, the dynamic properties of ferromagnetic materials can be described in terms of the high-frequency magnetic susceptibility tensor $\hat{\chi}(\mathbf{k}, \omega)$, which relates the oscillations of the internal field to the magnetization oscillations. (Here, $\mathbf{k}$ and ω are the wave vector and the oscillation frequency, respectively.) Within the phenomenological approach, the tensor $\hat{\chi}(\mathbf{k}, \omega)$ can be determined from the Landau–Lifshitz dynamic equations. In order to take into account the spatial dispersion, the exchange interaction energy must be allowed for in the total energy of the ferromagnet.

After linearization of the Landau–Lifshitz equations by analogy with the calculations performed in [11], we can determine the tensor $\hat{\chi}(\mathbf{k}, \omega)$ in the case when the $[\bar{1}10]$ direction coincides with the direction of hard magnetization and $\varphi = \varphi_H = 0$ (the Φ_1 phase):

$$\hat{\chi}(\mathbf{k}, \omega) = \frac{1}{\Delta}\begin{pmatrix} \Omega_1\cos^2\theta & i\dfrac{\omega}{\omega_0}\cos\theta & -\dfrac{1}{2}\Omega_1\sin 2\theta \\[3mm] -i\dfrac{\omega}{\omega_0}\cos\theta & \Omega_2 & i\dfrac{\omega}{\omega_0}\sin\theta \\[3mm] -\dfrac{1}{2}\Omega_1\sin 2\theta & -i\dfrac{\omega}{\omega_0}\sin\theta & \Omega_1\sin^2\theta \end{pmatrix}. \quad (32)$$

Here, $\omega_0 = gM_0$, g is the gyromagnetic ratio,

$$\Omega_1(\mathbf{k}) = ak^2 - 2\frac{K_u^*}{M_0^2}\cos^2\theta - 2\frac{K_{\mathrm{ort}}}{M_0^2}$$
$$- 2\frac{K_t}{M_0^2}\sin 2\theta + \frac{H}{M_0}\cos(\theta - \theta_H), \qquad (33)$$

$$\Omega_2(\mathbf{k}) = ak^2 - \Delta_0,$$

$$\Delta(\mathbf{k}, \omega) = \Omega_1(\mathbf{k})\Omega_2(\mathbf{k}) - \frac{\omega^2}{\omega_0^2},$$

a is the inhomogeneous exchange interaction constant, and $\theta = \theta(H)$ is determined from expression (24).

From the equations of magnetostatics and the definition of the tensor $\hat{\chi}(\mathbf{k}, \omega)$, we can easily derive the dispersion relation

$$k^2 + 4\pi k_\alpha k_\beta \chi_{\alpha\beta}(\mathbf{k}, \omega) = 0, \qquad (34)$$

which determines the dispersion law of spin waves $\omega_s(\mathbf{k})$, that is,

$$\omega_s^2(\mathbf{k}) = \omega_0^2[\Omega_1\Omega_2 \qquad (35)$$
$$+ 4\pi(\Omega_1(\tilde{\mathbf{k}}_x\cos\theta - \tilde{\mathbf{k}}_z\sin\theta)^2 + \tilde{\mathbf{k}}_y^2\Omega_2)].$$

Here, $\tilde{\mathbf{k}} = \mathbf{k}/|\mathbf{k}|$.

The frequency is the root of the equation

$$1 + 4\pi\chi_{zz}(0, \omega) = 0, \qquad (36)$$

from which we obtain the relationship

$$\omega^{(r)} = \omega_0\sqrt{\Omega_1(0)(\Omega_2(0) + 4\pi\sin^2\theta)}. \qquad (37)$$

For $\Delta_0 = 0$, the dispersion law for a spin wave propagating along the y axis becomes activationless. This suggests that a phase transition to an inhomogeneous state with a stripe domain structure oriented perpendicularly to the hard magnetization axis occurs on the astroid. For (112)-oriented films, similar domains were observed earlier in [4]. The orientation of the magneti-

zation inside the domains (in the vicinity of the astroid) can be determined from expression (27). Since the plane of the domain boundaries is perpendicular to the hard magnetization axis, they can be considered Bloch domain walls. The formation of a domain structure satisfying the condition $\theta = 0, \pi$ is accompanied by the ferromagnetic resonance frequency vanishing.

5. CONCLUSIONS

Thus, the misorientation of the substrate gives rise to a tilted anisotropy, which, in turn, affects both static and dynamic properties of the films. Specifically, the easy magnetization axis turns out to be tilted and orthorhombic anisotropy is observed in a plane perpendicular to this axis. The curve of lability is represented by an astroid whose axis coincides with the easy magnetization axis. The magnetization of the films along the normal or in the basal plane occurs in tilted fields. In the same fields, the ferromagnetic resonance frequency becomes zero. The astroid is characterized by a substantial change in the spectrum of spin waves, which is typical of phase transitions.

ACKNOWLEDGMENTS

REFERENCES

1. Yu. A. Burym, S. V. Dubinko, Yu. N. Mitsaĭ, *et al.*, Ukr. Fiz. Zh. **37** (5), 777 (1992).
2. V. A. Yatsenko, V. A. Bokov, M. V. Bystrov, *et al.*, Fiz. Tverd. Tela (Leningrad) **21** (9), 2656 (1979) [Sov. Phys. Solid State **21**, 1528 (1979)].
3. M. Marysko, Czech. J. Phys., Sect. B **33** (6), 686 (1983).
4. Yu. A. Burym, S. V. Dubinko, and Yu. N. Mitsaĭ, Preprint No. IMF-46-89 (Inst. of Metal Physics, Academy of Sciences of Ukraine, Kiev, 1989).
5. L. Ya. Arifov, Yu. A. Fridman, V. I. Butrim, and O. A. Kosmachev, Fiz. Nizk. Temp. **27** (8), 860 (2001) [Low Temp. Phys. **27**, 636 (2001)].
6. S. Gotoh and N. Koshizuka, Physica C (Amsterdam) **176** (1–3), 300 (1990).
7. M. Zamboni, M. Muralidhar, S. Koishikawa, and M. Murakami, Supercond. Sci. Technol. **13** (6), 811 (2000).
8. V. V. Randoshkin, M. Yu. Gusev, Yu. F. Kozlov, and N. S. Neustroev, Zh. Tekh. Fiz. **70** (8), 118 (2000) [Tech. Phys. **45**, 1075 (2000)].
9. M. J. Donahue, L. H. Bennet, R. D. McMichael, *et al.*, J. Appl. Phys. **79** (8), 5315 (1996).
10. E. M. Gyorgy, A. Rosencwaig, E. I. Blount, *et al.*, Appl. Phys. Lett. **18** (11), 479 (1971).
11. A. I. Akhiezer, V. G. Bar'yakhtar, and S. V. Peletminskiĭ, *Spin Waves* (Nauka, Moscow, 1967; North-Holland, Amsterdam, 1968).

Translated by O. Borovik-Romanova

MAGNETISM
AND FERROELECTRICITY

Nature of Physical Phenomena in Ferroelectric Relaxors

V. A. Isupov

Ioffe Physicotechnical Institute, Russian Academy of Sciences, Politekhnicheskaya ul. 26, St. Petersburg, 194021 Russia
Received August 16, 2002

Abstract—The nature of physical phenomena in ferroelectric relaxors, i.e., ferroelectrics undergoing smeared phase transitions, is discussed. These phenomena are closely related to the dynamics of polar regions (PRs), in which thermal fluctuations cause relaxation processes that control the crystal properties. The PRs interact with one another not only via electrical but also via mechanical interactions, and the deformed paraelectric interlayers between PRs play an important role in the transition to a macrodomain state. © 2003 MAIK "Nauka/Interperiodica".

1. INTRODUCTION

The ferroelectric relaxor (ferrorelaxor) is a crystal which undergoes a smeared ferroelectric phase transition (FEPT) and whose dielectric polarization in the vicinity of the smeared FEPT is relaxational in character. Currently, ferrorelaxors are the subject of numerous studies. The author of this paper dealt with ferrorelaxors in 1951 in studying FEPTs in $Ba(Ti_{1-x}Sn_x)O_3$ when doing graduate work under the supervision of G.A. Smolenskiĭ. It was detected that, at $x \geq 0.10$–0.15, the permittivity $\varepsilon'(T)$ exhibits a flat maximum instead of a classical distinct maximum at the FEPT point. Smolenskiĭ related this fact to internal stresses arising in the solid solution [1]. However, this phenomenon could also be caused by the incorporation of extraneous ions (Sn^{4+}) into the lattice, which could be nonuniformly distributed over the lattice sites (composition fluctuations). Due to the dependence of the Curie temperature on the concentration of the components, these fluctuations could result in different values of the local Curie temperature ($T_{C, loc}$) in crystal microvolumes and, hence, in the smeared phase transition (PT). (This concept was also considered in [1].) However, it would be inadequate to consider only composition fluctuations. A fluctuation is always associated with a certain volume and is significant only in a small volume. At the same time, the volumes under consideration must be sufficiently large when such macroscopic concepts as the component concentration and the Curie temperature are discussed. Thus, the question arises: what should the volume at which these macroscopic concepts are valid be? The answer was given in [2]: the volume of a region should allow the occurrence of spontaneous polarization $\mathbf{P}_s$ in it in the absence of $\mathbf{P}_s$ in the surroundings. It was shown that the smeared-FEPT temperature range is reasonable if the size of this polar region (PR) is of the order of 100 Å. Thus, the FEPT smearing is adequately explained by the presence of numerous PRs surrounded by the paraelectric (PE) phase. The number of PRs increases upon cooling; therefore, the amount of the ferroelectric (FE) phase increases.

The PR concept also allowed one to explain other phenomena associated with the smeared FEPT, since many properties of such ferroelectrics directly follow from the small PR sizes (e.g., relaxation electric polarization detected in $PbMg_{1/3}Nb_{2/3}O_3$ (PMN) and $PbNi_{1/3}Nb_{2/3}O_3$ (PNN), i.e., the first known ferrorelaxors [3]). The small PR sizes cause large temperature fluctuations ΔT in these PRs. If the crystal temperature T is approximately equal to $T_{C, loc}$, the local temperature alternately increases and decreases due to the PR temperature fluctuations. Therefore, the PRs will alternately lose and gain $\mathbf{P}_s$ (i.e., they will alternately disappear and appear again) [4]. In this case, the $\mathbf{P}_s$ direction in a revived PR can differ from the preceding one. Thus, the vector $\mathbf{P}_s$ can jump to another crystallographic direction through a state with zero polarization, which explains the relaxation behavior of the electric polarization in the vicinity of the smeared FEPT [4]. In [4], relaxation of unit cell groups at the PR boundary (in practice, PR boundary relaxation) is also allowed.

The PR concept also allowed explanation of the fact that the quadratic equation (see [5, 6])

$$1/\varepsilon' = A + B(T - T_m)^2. \qquad (1)$$

(rather than the Curie–Weiss law) is met for $1/\varepsilon'$ above the temperature T_m of the permittivity maximum. This fact was explained in [5, 6] by the specificity of the relaxation polarization in the vicinity of the smeared FEPT, differing from the ordinary relaxation in the temperature dependence (maximum) of the number of relaxing units. It was accepted that the number of PRs varies according to the Gaussian law upon cooling, while the PR activation energy (identical for all PRs and equal to a certain small value U_0 at $T_{C, loc}$) rapidly increases upon cooling, as does the ferroelectric coercive field. As a result, "old-living" PRs do not participate in the relaxation, and only "newborn" PRs relax,
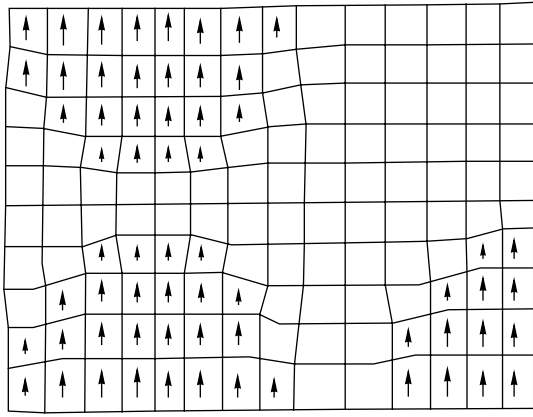
Schematic of atomic planes and unit cell distortions caused by the appearance of polar regions in a ferrorelaxor (in the case of the tetragonal FE phase).

whose $T_{C, \, loc}$ is approximately equal to the crystal temperature T and activation energy is a minimum (U_0). This results in a maximum number of PRs participating in polarization near the smeared FEPT:

$$n = C \exp \left[-\frac{(T - T_m)^2}{\sigma^2} \right], \qquad (2)$$

where σ is the PT smearing parameter. By expanding the exponent into a power series in $T - T_m$ and dropping the higher powers, one can obtain Eq. (1). Therefore, the maximum number of newborn PRs causes a quadratic dependence (1).

The significant role being played by the lattice atom ordering in ferroelectrics undergoing a smeared FEPT was indicated in [7]; complete or partial ordering improves the material homogeneity. These conclusions were experimentally confirmed in [8, 9], where it was detected that the long-range order of atoms B = Sc, Nb, and Ta in $PbSc_{1/2}Nb_{1/2}O_3$ (PSN) and $PbSc_{1/2}Ta_{1/2}O_3$ (PST) (varying in the course of annealing) has a significant effect on the FEPT: the relaxor properties arise in the case of disordering, and the PT becomes sharp in the case of ordering. Interest in ordering phenomena was significantly aroused after the detection of the phase transition referred to as the "spontaneous PT from the relaxor state to the normal FE state" and observed below T_m [10–12]. As a result, extensive experimental data on ferrorelaxors are now available, and a great number of theorists undertook to interpret these data. Nevertheless, a number of aspects of this problem have yet to be dealt with. This study is aimed at elucidating these aspects.

2. ENSEMBLE OF POLAR REGIONS

A ferrorelaxor is conventionally considered as a set of dipoles chaotically distributed over the crystal bulk.

Unfortunately, the dipole type is not always indicated, which sometimes oversimplifies the description of the phenomenon. Nevertheless, specific PRs of different sizes are considered in most of the papers rather than abstract dipoles.

The PR size should be considered in more detail. As indicated above, the PR size should somewhat exceed the critical size of an FE nucleus in the PE phase. We assumed in [2] that PRs formed at $T_{C, \, loc}$ have a size D_0 close to 100 Å. The question arises as to whether a smaller size PR can arise. We are of the opinion that this can take place but at a lower temperature T than $T_{C, \, loc}$. It is evident that the negative difference of the free energies of the FE and PE states, which affect the PR size, increases in absolute value upon cooling. Therefore, the PR formation becomes possible at a certain $T < T_{C, \, loc}$ in a sphere of size $D < D_0$, where PRs do not arise at $T_{C, \, loc}$. Thus, a size of 100 Å is not the smallest.

We note that the case in point in many relevant studies is polar clusters rather than PRs. However, the term cluster, as a rule, is not formulated, which creates uncertainty. It is the author's opinion that this term means the above-mentioned PR in most cases. If the polar cluster is understood as something else, this should be specified.

Thus, PRs are chaotically distributed over the crystal. They develop at various local Curie temperatures and have various sizes, shapes, dipole moments, spontaneous strains, and activation energies. In brief, there is an ensemble of PRs in the crystal in the vicinity of a smeared FEPT [13, 14]. The question arises as to whether the PE–FE spontaneous phase transition is possible in such an ensemble of PRs chaotically distributed over the crystal bulk. This problem has not yet been considered even in a simplified form (neglecting the PR various-parameter distribution). Meanwhile, this is of doubtless interest, since this problem is associated with the problem of spontaneous relaxor-to-normal FE phase transitions. The author a priori leaves room for the possibility of such an FEPT. However, it is probable that this process takes an infinite time in the absence of an external electric field, because there is mechanical interaction between PRs that prevents their coalescence [13, 14] (see below).

3. INTERACTION OF POLAR REGIONS

The electrostatic interaction between PRs and their PE surroundings is determined by the charges at the PR surfaces normal or inclined with respect to the vector $\mathbf{P}_s$. In this case, not only a PR influences its surroundings but the surroundings also affects the PR, decreasing its dipole moment. As for the mutual electrostatic influence of PRs, it may be considered as the interaction between elementary dipoles in the only case where PRs are widely spaced.

It is more intricate to calculate the deformational interaction. From the figure, one can see that PRs create a complicated pattern of normal and shear strains in the PE surroundings. The mechanical interaction between PRs depends not only on spacings between them but also on their mutual arrangement and the direction of $\mathbf{P}_s$ in them. In this case, a strongly deformed PE interlayer (see figure) arises between PRs that are close together, with their vectors $\mathbf{P}_s$ being parallel or antiparallel [13, 14]. This interlayer prevents coalescence of PRs with parallel spontaneous moments and the formation of FE macrodomains. In order that these PRs coalesce, the interlayer has to disappear. Hence, compression in the interlayer should give way to extension and vice versa. Furthermore, a spontaneous electric moment should arise in the interlayer; in other words, the PE–FE phase transition should take place in it.

It is worth noting the reverse process, when the macrodomain state is again split into PRs upon heating and the interlayer gives way to an indistinct FE phase layer. As this takes place, this layer should return into the PE state and deformations within the layer should reverse sign again.

As follows from the abovementioned, there is an energy barrier between adjacent PRs that prevents their coalescence and, vice versa, prevents large PR splitting into small ones. It is evident that the role of interlayers between PRs should be taken into account in the cases of an applied electric field and spontaneous PTs. Unfortunately, these interlayers and their important role in the ferrorelaxor dynamics are neglected in all the available papers, except for the author's articles [13, 14].

It is evident that the processes associated with the interlayer dynamics are relaxation in character and depend heavily on time. A prominent example of such time dependences was considered in [15]. A dc electric field (2.5 kV cm^{-1} or higher) applied to PMN at low temperatures caused a transition to a macrodomain state after a lapse of time rather than instantaneously. This time (the expectation time of a sufficient thermal fluctuation) increased as the field weakened.

Spontaneous relaxor-to-normal FE phase transitions should be considered within the same concepts as the phase transition to the macrodomain state caused by an electric field, with the difference that this field should be weakened to zero in order for the transition to be spontaneous. In [14], we cast doubt on the spontaneous and ferroelectric character of this PT. Indeed, it was not substantiated that macrodomains arising in this case feature a spontaneous electric moment until the crystal was exposed to an electric field. Mechanical stresses can also rearrange PRs; after this reorientation, all the major axes of unit cells (directions of $\mathbf{P}_s$) will be oriented along the extension axis. As a result, a ferroelastic macrodomain will form consisting of 180° microdomains (PRs) and its total electric moment (the sum of the PR moments) will be zero. The crystal state (before exposure to the field) will be macroferroelastic rather than macroferroelectric. Since internal mechanical strains always take place in crystals and ceramic grains, they can cause such a PT. It is evident that this PT will not be a spontaneous PT from the relaxor to the normal FE state. Meanwhile, as indicated above, the author leaves room for the possibility of the spontaneous transition from the relaxor to the normal FE state in a PR ensemble under zero field; however, the PT duration (the time required to overcome the energy barriers in interlayers between the PRs) must be infinite [14].

It seems that it will be difficult to distinguish between ferroelastic and ferroelectric macrodomains, in particular, if it is taken into account that the electric field applied to the crystal transforms ferroelastic macrodomains into ferroelectric ones and that it is difficult to determine their initial state (before exposure to the field).

4. DIPOLE-GLASS CONCEPTS

The dipole-glass concepts applied to ferrorelaxors allowed a number of achievements to be made in the study of these objects, since extension of the results obtained for spin glasses (see, e.g., [16, 17]) to ferrorelaxors was made possible. Abstraction from the actual nature of dipoles was efficient at the beginning and made it possible to closely relate the observed phenomena to dipole freezing at a certain temperature. In many studies, PRs are considered as dipoles. However, such important PR parameters as the volume and interaction are generally neglected.

Meanwhile, new differences between ferrorelaxors and spin glasses have become known. For example, it was shown in [18] that the Vogel–Fulcher relation in the case of PMN should be replaced by the formula

$$\omega = \omega_0 \exp[-(T/T_m)^p], \qquad (3)$$

where $p < 1$. According to [19], the Vogel–Fulcher relation can be derived as a direct consequence of gradual broadening of the relaxation time spectrum as the temperature decreases, rather than under the assumption of freezing in the system.

It seems that the conventional dipole-glass concepts neglecting the interaction between dipoles have been exhausted. Further steps require consideration of the actual nature of dipoles, i.e., PRs. However, the line of inquiry to be taken has not been determined.

5. SUPERPARAELECTRICITY IDEAS

In 1987, Cross [20] coined the term superparaelectricity for the PE phase of ferrorelaxors saturated with PRs. In fact, this is an extension of one of the ferromagnetism concepts to FE objects. Since that time, the term superparaelectricity has been used in scientific articles

on several occasions. However, this term is not quite adequate.

Let us consider the corresponding concept in magnetism. According to [21, 22], "superparamagnetism is a quasi-paramagnetic behavior of materials consisting of very small and weakly interacting ferro- or ferrimagnetic particles. Very small particles (10–100 Å) transfer to the ferro- or ferrimagnetic state. However, the magnetization direction of such particles chaotically varies due to thermal fluctuations…. Therefore, the system behaves similar to paramagnetic gas and obeys the Curie law in weak magnetic fields…. Typical representatives of superparamagnetism are fine Co particles precipitating in the course of Cu–Co (2% Co) solid-solution decomposition, fine Fe precipitate in β-brass (0.1% Fe), Cu precipitate in Mn, and Ni in Au, as well as some antiferromagnetic oxides."

As follows from this citation, there exists a certain nonmagnetic host in which the smallest ferromagnetic particles are distributed. These particles precipitate in the course of solid solution decomposition and almost do not interact.

In the case of ferrorelaxors, we have a PE crystal rather than a simple dielectric. This crystal contains already formed PRs surrounded by PE regions which have not yet become polar but are ready to do so. The regions that are already polar and the regions that are still nonpolar fill the whole crystal volume. It is obvious that the concept of paraelectric gas is invalid in this case.

Unfortunately, the term superparaelectricity is used even in [23], where the chemical inhomogeneity of material and the (Gaussian) distribution of PRs (30 Å in size) in local Curie temperatures were taken into account and, as a result, good agreement between the calculated and the experimental data was achieved. In this case, the interaction between PRs was neglected; thus, the model may be referred to as superparaelectric. However, the actual state of the material does not become superparaelectric, since PRs contact each other or are very narrowly spaced.

The theory of the phenomena in ferrorelaxors advanced by the author in [2, 4–7, 13, 14] and in this paper is adequate and, hence, intricate. However, the latter is not associated with the model; this property is an objective feature of the phenomena themselves, in which well-defined characteristics are almost absent and almost all the parameters obey a distribution: the PR coordinates, composition, local Curie temperature, PR shape, size, electric moment, and activation energy. Furthermore, there exist interlayers between PRs that can disappear and emerge again. It seems still impossible to take into account all these factors; therefore, reasonable simplifications are allowed and required.

As indicated above, one of the reasonable simplifications was the assumption that only PRs with a local Curie temperature close to the crystal temperature participate in relaxation [5, 6] (old-living PRs with an activation energy significantly increased upon cooling were omitted from the relaxation process). This simplification allowed us to explain not only the quadratic dependence of $1/\varepsilon'$ on T (see Eq.(1)) but also the drastic shift of the relaxation rate spectrum to lower frequencies upon cooling. It is worth mentioning the author's attempt to take into account relaxation of all PRs independently of their local Curie temperature [24] under the assumption that the PR activation energy increases linearly upon cooling. Unfortunately, this attempt did not yield an analytical expression for $\varepsilon'(T)$.

6. CONCLUSIONS

(i) Ferroelectric relaxors represent crystals with atomic disordering on one of their sublattices.

(ii) In the vicinity of a smeared FEPT, a ferrorelaxor represents an ensemble of PRs chaotically arranged in the crystal.

(iii) Below T_m, a ferrorelaxor represents a set of contacting regions that have already transformed into the FE state or are ready to do so.

(iv) Contacting PRs interact with surrounding PE regions and with each other not only through electric fields but also through mechanical strains.

(v) There are deformed PE interlayers between contacting PRs that prevent PR coalescence and play an important role in the transition into a macrodomain state.

REFERENCES

1. G. A. Smolenskiĭ and V. A. Isupov, Zh. Tekh. Fiz. **24** (8), 1375 (1954).

2. V. A. Isupov, Zh. Tekh. Fiz. **26** (9), 1912 (1956).

3. G. A. Smolenskiĭ, V. A. Isupov, A. I. Agranovskaya, and S. N. Popov, Fiz. Tverd. Tela (Leningrad) **2** (11), 2906 (1960) [Sov. Phys. Solid State **2**, 2584 (1960)].

4. V. A. Isupov, Fiz. Tverd. Tela (Leningrad) **5** (1), 187 (1963) [Sov. Phys. Solid State **5**, 136 (1963)].

5. V. V. Kirillov and V. A. Isupov, Izv. Akad. Nauk SSSR, Ser. Fiz. **35** (12), 2602 (1971).

6. V. V. Kirillov and V. A. Isupov, Ferroelectrics **5**, 3 (1973).

7. V. A. Isupov, Izv. Akad. Nauk SSSR, Ser. Fiz. **28** (4), 653 (1964).

8. C. G. F. Stenger, F. E. Sholten, and A. J. Burggraaf, Solid State Commun. **32** (11), 989 (1979).

9. C. G. F. Stenger and A. J. Burggraaf, Phys. Status Solidi A **61**, 275 (1980); Phys. Status Solidi A **61**, 653 (1980).

10. F. Chu, N. Setter, and A. K. Tagantsev, J. Appl. Phys. **74** (8), 5129 (1993).

11. F. Chu, I. M. Reaney, and N. Setter, J. Appl. Phys. **77** (4), 1671 (1995).

12. F. Chu, I. M. Reaney, and N. Setter, Ferroelectrics **151**, 343 (1994).

13. V. A. Isupov, Fiz. Tverd. Tela (St. Petersburg) **38** (5), 1326 (1996) [Phys. Solid State **38**, 734 (1996)].

14. V. A. Isupov, Phys. Status Solidi B **213**, 211 (1999).

15. E. V. Colla, E. Yu. Koroleva, N. M. Okuneva, and S. B. Vakhrushev, Phys. Rev. Lett. **74** (9), 1681 (1995).

16. S. B. Vakhrushev, B. E. Kvyatkovsky, A. A. Naberezhnov, *et al.*, Ferroelectrics **90**, 173 (1989).

17. D. Viehland, M. Wuttig, and L. E. Cross, Ferroelectrics **120**, 71 (1991).

18. Z.-Y. Cheng, L.-Y. Zhang, and Xi Yao, J. Appl. Phys. **79** (11), 8615 (1996).

19. A. K. Tagantsev, Phys. Rev. Lett. **72** (7), 1100 (1994).

20. L. E. Cross, Ferroelectrics **76** (3/4), 241 (1987).

21. A. S. Borovik-Romanov, Superparamagnetism, in *Great Soviet Encyclopedia* (BSE, Moscow, 1976), Vol. 25.

22. S. V. Vonsovskiĭ, *Magnetism* (Nauka, Moscow, 1971).

23. A. E. Glazunov, A. J. Bell, and A. K. Tagantsev, J. Phys.: Condens. Matter **7** (21), 4145 (1995).

24. V. A. Isupov, Izv. Akad. Nauk SSSR, Ser. Fiz. **39** (6), 1312 (1975).

Translated by A. Kazantsev

Evolution of the Optical Properties of $Pb_{0.94}Ba_{0.06}Sc_{0.5}Nb_{0.5}O_3$ (PBSN-6) Solid Solution Single Crystals Caused by a Static Electric Field

L. S. Kamzina*, I. P. Raevskiĭ**, V. V. Eremkin**, V. G. Smotrakov**, and E. V. Sakhkar**

*Ioffe Physicotechnical Institute, Russian Academy of Sciences, Politekhnicheskaya ul. 26, St. Petersburg, 194021 Russia
**Institute of Physics, Rostov State University, Rostov-on-Don, 344090 Russia
Received June 5, 2002; in final form, October 14, 2002

Abstract—The electric-field-induced variation of the optical properties (small-angle light scattering, birefringence) of PBSN-6 solid solutions was studied. It was found that in the absence of an electric field, the cubic nonpolar matrix contains, at temperatures below the dielectric permittivity maximum, spontaneously polarized regions of the ferroelectric phase not less than 10^4 Å in size. It was shown that a weak electric field (~0.4 kV/cm) is capable of inducing a kinetic phase transition to the ferroelectric state, with the temperature of this transformation depending on the sample heating rate. The destruction of the induced state was accompanied by a sharp peak in the temperature dependence of the small-angle light scattering intensity (indicating the percolation nature of the transition) and was independent of the sample heating rate. The boundaries of stability of the induced state in various modes of application of an external electric field were determined, and the *E–T* phase diagram was constructed. © 2003 MAIK "Nauka/Interperiodica".

1. INTRODUCTION

Compounds of the type $PbSc_{0.5}Nb_{0.5}O_3$ (PSN) and $PbSc_{0.5}Ta_{0.5}O_3$ (PST) occupy a particular place among a large number of disordered materials. By varying the amount of order *s* of Sc and Nb (Ta) ions through appropriate heat treatment of samples or by changing the temperature regime of growth [1, 2], one can modify the properties of these substances within a broad range without changing their chemical composition. Crystals featuring long-range order ($s \approx 1$) undergo a distinct ferroelectric phase transition. In a disordered state ($s \longrightarrow 0$), the ferroelectric transformation becomes diffuse and the compound exhibits characteristics typical of relaxors. In the PSN and PST compounds, however, one does not succeed in obtaining a stable relaxor behavior similar to the one observed in lead magnoniobate (PMN), a classical relaxor, even under complete Sc and Nb (Ta) site disorder; indeed, in practically disordered compounds, a spontaneous phase transition (PT) from the relaxor (microdomain) to the macrodomain ferroelectric state also takes place at temperatures below the maximum of the dielectric permittivity ε [3]. For a stable relaxor behavior to set in, the crystal lattice has to undergo additional lattice disordering. A stable relaxor state in such compounds is usually reached by producing additional disorder on the lead ion sublattice. A comparatively small PbO deficiency (~2.5–3%) or substitution of Ba (~6–7%) for the lead ions quenches the relaxor state in the PSN and PST compounds [3–5].

It has been shown [4, 5] that, in the absence of an electric field, crystals with a barium content ≤4 mol %

(PBSN-4) still retain features characteristic of both a normal ferroelectric and a relaxor. The spontaneous PT from the relaxor to macrodomain state which occurs in PBSN-4 crystals, as well as in PST and PSN, manifests itself in the form of a jump in ε below the temperature of the permittivity maximum and is accompanied by a sharp peak in the small-angle light scattering (SAS) intensity (or a minimum in the optical transmission, OT) [6–9]. The presence of the peak indicates the percolation nature of the transition and the formation of a large-scale structure in this transition. A theoretical description of anomalous light scattering in the neighborhood of first- and second-order phase transitions can be found in [10].

A further increase in Ba content to 6 mol % brought about disappearance of the spontaneous PT in these compounds and a manifestation of pure relaxor properties. At temperatures 40–50°C below the maximum in ε and with no electric field applied, already no anomalies accompanying the spontaneous PT were seen in the temperature dependences of ε and OT [6]; however, the macrodomain ferroelectric phase in these compounds can be nucleated by comparatively weak electric fields. Application of an electric field in excess of a threshold value to a zero-field-cooled sample induces a kinetic phase transition to the ferroelectric state a certain time after the field is turned on. This time depends strongly on both temperature and field amplitude [11].

The fairly scarce experimental studies, with the exception of [6], have focused primarily on the investigation of the dielectric properties of PBSN. The observed anomalies, however, were not always clearly

enough pronounced, which made their detection difficult. Optical methods of crystal studies (OT, SAS, birefringence Δn) are more sensitive, particularly for investigation of processes associated with variations of inhomogeneities in size. If the size of optical inhomogeneities changes at a phase transition, this will affect not only light scattering but also OT. Light scattering depends on the ratio of the scattering-particle size a to the light wavelength λ. If this ratio is small, then the scattered intensity is low, the sample is practically transparent, and there is no Δn in the cubic phase. Optical methods have been employed to advantage in studies of phase transitions in relaxors. The existence of polar nanoregions in the cubic nonpolar matrix is one of the reasons accounting for the relaxor behavior. If the size of these nanoregions changes slightly at the phase transition and remains smaller than λ, then Δn should not reveal any changes. For instance, the overall crystal structure of the classical relaxor PMN remained cubic with no electric field applied down to low temperatures and no Δn was observed. The absence of Δn within a broad temperature region correlates with the small dimensions of nanoregions in this crystal, which were found from x-ray and neutron measurements [12]. Application of an electric field to the PMN crystal initiated a kinetic, percolation-type ferroelectric phase transition to a macrodomain state [13]. This transition was accompanied by a sharp peak in the SAS intensity and a dramatic rise in scatterer size (from nanodomains in the relaxor phase to macrodomains in the ferroelectric state), and a nonzero Δn was observed [14].

The size of the inhomogeneities responsible for the relaxor behavior and their change at the phase transition in PBSN-6 crystals remain an open problem. This motivated the present comprehensive study of the heterophase state in the region of the diffuse phase transition, as well as of the conditions favoring the onset of a homogeneous ferroelectric state in these compounds, by using dielectric and optical methods.

2. GROWTH OF SINGLE CRYSTALS AND EXPERIMENTAL TECHNIQUES

PBSN-6 single crystals were grown from a melt solution. The technique of growth, as well as the x-ray and dielectric characterization of these crystals were described in [4, 5]. The crystals thus obtained were uniform in composition and shaped as {100}-faced plates. To avoid introducing additional strains, all measurements were performed on samples that were not mechanically treated. A dc electric field was applied in the [100] direction, and the light was propagated along [001]. The electric field was applied in various modes, namely, zero-field cooling (ZFC), zero-field heating (ZFH), field heating after ZFC (FHaZFC), field cooling (FC), field-heating after FC (FHaFC), and zero-field heating after FC (ZFHaFC). Prior to a measurement, the sample subjected previously to a field was heated at 150°C for 0.5 h. To obtain reproducible results and to
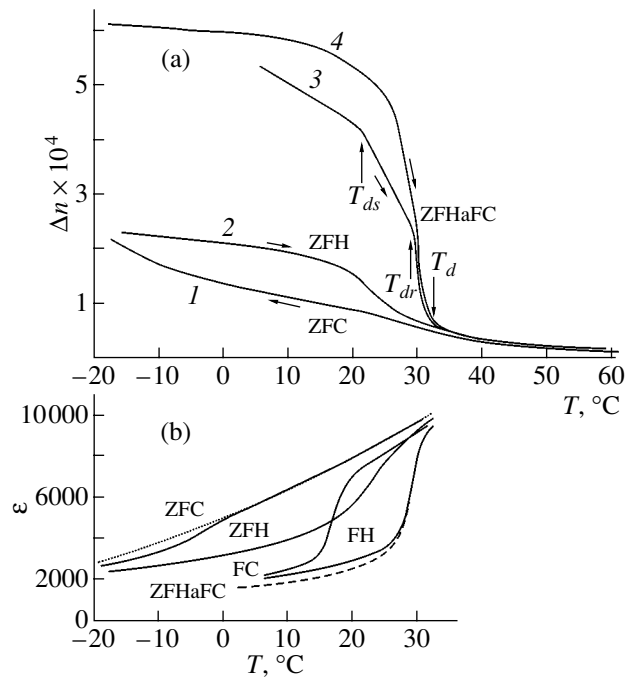
Fig. 1. Temperature dependences of (a) birefringence Δn and (b) dielectric permittivity ε measured in different electric field application modes for a PBSN-6 crystal. (*1*) ZFC, (*2*) ZFH, (*3*) ZFHaFC ($E = 1$ kV/cm, crystal field-cooled to +5°C), and (*4*) ZFHaFC ($E = 1$ kV/cm, crystal field-cooled to –20°C).

exclude dielectric ageing, an effect strongly pronounced in PBSN-6 crystals [5], the dielectric and optical measurements were carried out immediately after annealing of the sample. The sample temperature variation rate was adjusted from 2 to 10°C/min.

A He–Ne laser was employed in the optical measurements. We studied OT and SAS in the transmission geometry [12]. The sample birefringence Δn was derived from the relation $I = I_0 \sin^2 \pi \Delta n d/\lambda$, where I_0 is the incident light intensity; I is the light intensity transmitted through a sample placed between two crossed polarizers, with the optical axis of the sample making an angle of 45° to the incident polarization; and d is the sample thickness.

The dielectric measurements were conducted at 100 kHz.

3. EXPERIMENTAL RESULTS AND DISCUSSION

Figure 1a presents temperature dependences of the birefringence Δn measured in the ZFC (*1*) and ZFH (*2*) modes with no electric field applied and under ZFHaFC following sample cooling in a field of 1 kV/cm (curves *3*, *4*). Curve *3* was obtained after the sample had been cooled to +5°C, and curve *4*, to –20°C. When zero-field-cooled (curve *1*), the sample exhibits a smooth increase in Δn, which becomes steeper in the temperature range $\approx$–4 to –20°C. The monotonic

increase in Δn under cooling is due most likely to the polar nanoregions growing in size and to a transition of part of the regions to the macrodomain ferroelectric state. The scatterer size becomes comparable to the light wavelength ($\sim 10^4$ Å). This discriminates the crystal under study from the classical relaxor PMN, in which the dimensions of the nanoregions did not grow noticeably down to low temperatures. Since the number of regions undergoing a spontaneous PT is small, phase transition to the macrodomain state does not occur throughout the whole crystal and Δn does not change in a jump. When the sample is heated subsequently in a zero field (curve *2*), Δn is first only weakly temperature-dependent and then decreases substantially in the region 20–30°C, with the variation of Δn being the fastest in the interval $\sim$22–24°C. These temperatures coincide with those of the anomalous variation of ε (Fig. 1b). The difference in the behavior of Δn and ε between the heating and cooling runs made in a zero electric field can apparently be assigned to the existence of internal fields in the crystal. When heated to +150°C, the space charge and the internal fields in the crystal practically disappear; therefore, in the cooling run measurements (curve *1*), they are much lower than under heating. Furthermore, a sample may contain regions in which the critical field required to induce the ferroelectric state is very weak, so that even low internal electric fields are capable of driving the ferroelectric transition in these regions under cooling. Note that the temperature at which Δn decreases sharply (curve *2* in Fig. 1a) and ε increases (Fig. 1b) under heating is close, as follows from dielectric measurements [5, 11], to the Vogel–Fulcher temperature [3] and can be identified with the average temperature of spontaneous PT from the ferroelectric to the relaxor state. The fast variation of Δn observed to occur under sample heating is apparently due to collective processes of two types, namely, (i) a ferroelectric-to-relaxor phase transition in the crystal regions where the spontaneous PT takes place and (ii) depolarization of the macrodomain ferroelectric phase in the polar regions where the internal fields were strong enough to initiate the ferroelectric phase transition. These processes may be related; for instance, a spontaneous PT that has occurred in some regions stimulates a similar transition in neighboring regions. Since the number of polar nanoregions with a very low critical field is small, the Δn (T) dependence measured in the ZFH mode does not exhibit the anomaly corresponding to the depolarization temperature of these relaxor regions.

The conjecture of the existence of regions of the two types is supported by birefringence measurements made in the ZFHaFC mode following sample cooling in an electric field of 1 kV/cm (curve *3* in Fig. 1a). Indeed, the Δn (T) plot clearly shows two characteristic temperatures at which the slope undergoes a sharp change, namely, $T_{ds} \approx 22$°C and $T_{dr} \approx 29$–30°C. T_{ds} corresponds to the depolarization temperature of the spontaneous PT regions, and T_{dr}, to that of the nanoregions

in which cooling in an electric field induces formation of the ferroelectric phase. These temperatures are in good agreement with our dielectric measurements (Fig. 1b) and the data quoted in [11]. Note that when a sample is cooled to +5°C (which is above the average relaxor–ferroelectric spontaneous PT point [11]), the quantity $\Delta n(T)$ does not saturate, although it is considerably higher than in the ZFC case. This may be due to a ferroelectric phase transition being induced under field cooling in a larger number of polar regions. The absence of saturation of Δn in curve *3* indicates that not all of the crystal volume has transferred to the ferroelectric phase. After cooling the sample in the same field to a lower temperature (–20°C) and maintaining the sample at this temperature for $\sim$10 min, Δn did saturate, and after the field turnoff, the $\Delta n(T)$ relation measured in the subsequent heating run exhibited normal ferroelectric behavior (curve *4*). Δn starts to decrease sharply in the vicinity of $T_{ds} \sim 22$–25°C, and extrapolation $\Delta n \longrightarrow 0$ yields $T_d \sim 30$–32°C for the sample depolarization temperature. The $\Delta n(T)$ saturation implies that the crystal has transferred to the macrodomain state completely. Hence, the ferroelectric phase extends now not only through the spontaneous PT regions but also to all polar nanoregions. The depolarization temperature T_d being the same throughout the sample means that the destruction of this state has become a collective process. We attempted to at estimate the volume fraction of the ferroelectric phase regions in the paraelectric matrix from the relative magnitude of Δn measured in a zero electric field and in a field of 1 kV/cm (curves *2*, *4* in Fig. 1a). This volume fraction was found to be $\sim$30% already at –20°C.

Dielectric measurements performed on PBSN-6 crystals in an electric field [11] revealed a kinetic phase transition at a field-dependent temperature T_{ph} to the ferroelectric state, which was destroyed at $T_d \sim 30$–32°C. The ferroelectric phase formed in a threshold manner. Earlier [6], we reported that, in the same crystals acted upon by an electric field (FHaZFC mode) at the temperature of destruction of the ferroelectric state (T_d), which had been induced at a low temperature, a narrow SAS intensity peak was observed, implying that this destruction was of a percolation nature. We did not succeed in [6] in observing the SAS anomaly caused by the onset of the ferroelectric state.

We carried out more comprehensive studies of the temperature behavior of SAS intensity in the FHaZFC mode at different sample heating rates. Figure 2 displays the temperature dependences of the SAS intensity obtained in a field of 1 kV/cm. We see only a broad SAS intensity maximum at the temperature T_{ph} corresponding to the onset of electric polarization, whereas the SAS peak at the sample depolarization temperature T_d is narrow. The T_{ph} temperature increases with heating rate (see inset to Fig. 2), while T_d remains practically constant. The observed dependence of the temperature T_{ph} on the sample heating rate indicates that the elec-
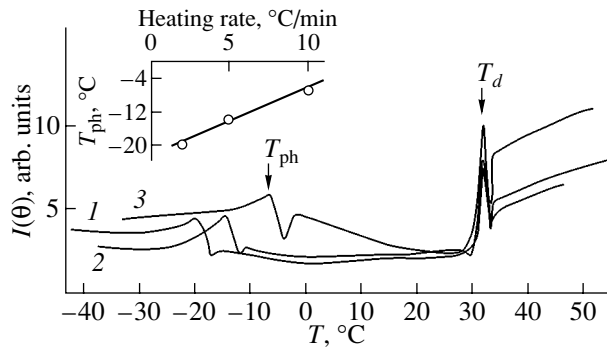
Fig. 2. (*1–3*) Temperature dependences of small-angle light scattering intensity measured on a PBSN-6 single crystal in the FHaZFC mode ($E = 1$ kV/cm) at different sample heating rates V: (*1*) 2, (*2*) 5, and (*3*) 10 °C/min. Inset plots the temperature of induced ferroelectric transition T_{ph} vs. heating rate. Scattering angle, 30°.

Fig. 3. Temperature dependences of birefringence measured in a field of 1 kV/cm. Field application mode sequence, ZFC–FHaZFC–FC–ZFHaFC.

tric-field-induced switching of polar nanoregions depends on time and that the induced ferroelectric transition is kinetic. It may be conjectured that the effect of heating rate on the position of the SAS intensity anomaly at the onset of induction of the ferroelectric state is related to the polarization orientation processes having long relaxation times in the glassy state. As a result, the formation of ferroelectric regions with dimensions large enough for the phase transition to occur requires a long time. This transition takes place over a wider temperature interval than does the destruction of the induced phase. The broad SAS intensity maximum observed in an electric field near T_{ph} is associated with the formation of fairly large macrodomain regions. The field does not, however, give rise to the formation of an infinite cluster nor, hence, to a percolation-type phase transition. Note that the induced phase transition in the PMN relaxor is of the percolative type and is accompanied by a narrow peak in the temperature dependence of SAS intensity [13]. The observed difference in the behavior of SAS intensity between the PBSN-6 and PMN crystals at the temperature T_{ph} correlates well with the time evolution of the dielectric permittivity of these crystals in an electric field. Indeed, the stepped decrease in ε at this transition observed in PBSN-6 crystals is not as sharp as that in PMN [11, 15].

The dielectric and optical properties of the PBSN-6 compounds were shown [5, 6] to depend strongly on the electric-field application regime employed. Figure 3 displays the temperature dependences of birefringence obtained on a PBSN-6 crystal with an electric field of 1 kV/cm applied in the following order: ZFC ⟶ FHaZFC ⟶ FC ⟶ ZFHaFC. Unlike the PMN and 0.9PMN–0.1PT crystals, in which Δn is practically zero in the absence of an electric field down to low temperatures [14], Δn in PBSN-6 cooled in the ZFC mode grows slightly with decreasing temperature because of the existence of regions of spontaneous PT (curve *1* in Fig. 1a; Fig. 3). When measured in the FHaZFC mode,
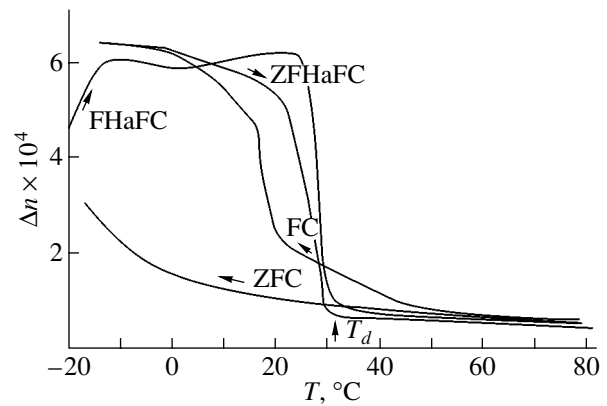
Δn grows substantially and passes through a broad maximum (with a width ~40°C). The variation of Δn in this process depends on the actual rate of sample temperature variation; more specifically, the higher this rate, the narrower the region of existence of the induced ferroelectric phase (Fig. 2) and, hence, the smaller the width of the $\Delta n\,(T)$ maximum. The difference observed in the temperature behavior of Δn measured in the ZFC and FHaZFC modes indicates the latter process to be metastable. On the other hand, the temperature dependence of $\Delta n\,(T)$ measured in the ZFHaFC mode reveals a normal ferroelectric behavior, with the extrapolation $\Delta n \longrightarrow 0$ yielding the depolarization temperature $T_d \approx$ 30–32°C (Fig. 3). This dependence is depicted graphically in Fig. 1a (curve *4*) and was discussed in detail above.

The above behavior of PBSN-6 suggests the conclusion that the presence of spontaneously polarized regions in a paraelectric matrix possessing relaxor properties is a fairly typical feature of solid solutions near the boundary of stability of the relaxor state. This domain of Ba ion concentrations is actually a morphotropic region separating the macroscopically cubic relaxor from the rhombohedral macrodomain ferroelectric phase. Since the structural differences between the cubic and rhombohedral phases are small, there is a fairly broad region of Ba ion concentrations where both phases coexist. Crystals of the PMN and 0.9PMN–0.1PT compositions are typical relaxors and are far from the boundary of stability of the relaxor state, and compositional fluctuations (~10 mol % PbTiO$_3$) affect their properties only insignificantly. It may be conjectured that as the PbTiO$_3$ content is increased still further (to ~20 mol %), with the composition approaching the stability boundary of the relaxor state, the optical properties of the corresponding compounds should approach those of PBSN-6.

We used the above data on the temperature dependences of Δn and ε to construct an E–T phase diagram
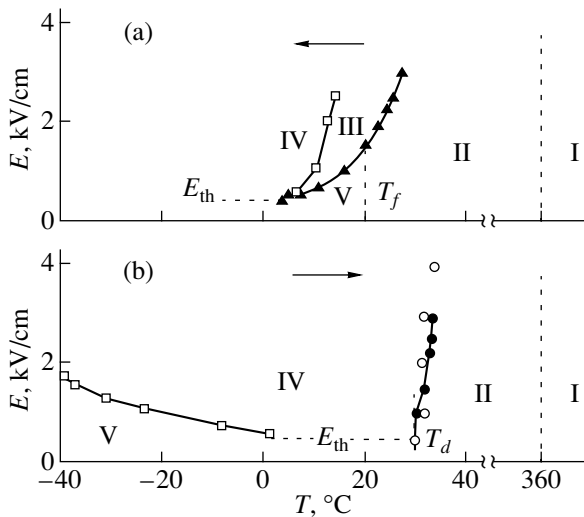
Fig. 4. *E–T* phase diagrams derived for a PBSN-6 crystal in (a) cooling and (b) heating runs from optical (open symbols) and dielectric (filled symbols) measurements. Sample temperature variation rate 2°C/min. I is the paraelectric phase; II is the ergodic relaxor phase; III is the inhomogeneous, macrodomain ferroelectric phase; IV is the homogeneous macrodomain ferroelectric phase; and V is the nonergodic relaxor phase. T_f is the Vogel–Fulcher temperature from [5]. Dashed line at T_f is the boundary separating the ergodic from nonergodic relaxor phase.

for PBSN-6. Figure 4 presents diagrams obtained in the cooling (Fig. 4a) and heating runs (Fig. 4b) for this crystal. Consider the cooling mode of the sample (Fig. 4a). By analogy with PSN and PST [16], the paraelectric phase (I) exists in PBSN-6 crystals apparently only above the Burns temperature $T \sim 400$°C. Below this temperature, the crystal placed in a field $E < E_{th}$ is first in the ergodic relaxor phase (II), and below the Vogel–Fulcher point T_f, in the nonergodic relaxor phase V. The temperature T_f was derived from the frequency dependence of ε [5]. The vertical dashed line at T_f in Fig. 4a is a boundary separating the ergodic from the nonergodic relaxor phases. As the temperature is lowered still further, the crystal transfers to phase III in electric fields above E_{th}. The boundary between phases II and III was determined as the point where a sharp decrease in ε was observed in the FC mode. At the II–III boundary, the induced phase transition has already occurred in most of the polar nanoregions. Phase III is an inhomogeneous macrodomain ferroelectric phase, in which not all of the polar nanoregions have transferred to the ferroelectric state. A further decrease in temperature initiates the transition of the remaining polar nanoregions to the ferroelectric phase (phase IV). As follows from [11], the spontaneous PT takes place under cooling in part of the sample volume in the temperature interval from –5 to +5°C, depending on the magnitude of the electric field; hence, region IV is a homogeneous macrodomain ferroelectric phase. The boundary

between phases III and IV is the temperature region within which birefringence saturates.

When heated from low temperatures up (Fig. 4b), the sample which resided initially in the nonergodic relaxor phase V transfers in fields $E > E_{th}$ to the macrodomain ferroelectric phase IV, which persists to the temperatures corresponding to the IV–II boundary. Note that the boundary position depends on the sample heating rate. The higher the rate, the narrower the temperature interval of existence of the ferroelectric phase. The boundary separating phases IV and II was derived both from the temperature of the narrow SAS intensity peak and from the depolarization temperature T_d corresponding to the jump in ε.

Thus, the phase diagram constructed provides a clue to understanding the reason for the observed differences in the phase transition inducing the ferroelectric state in PMN and PBSN-6. One of possible explanations lies in the low-temperature phase in these crystals being of different nature. At low temperatures, PMN in a zero electric field resides in a nonergodic glassy state, whereas in PBSN-6 at these temperatures, nanoregions coexist side by side with macrodomain ferroelectric regions in which the spontaneous PT has occurred. Therefore, the temperature interval of coexistence of the relaxor state and the electric-field-induced ferroelectric phase in PBSN-6 is considerably broader than that in PMN.

REFERENCES

1. N. Setter and L. E. Cross, J. Appl. Phys. **51** (8), 4356 (1980).

2. V. G. Smotrakov, I. P. Raevskiĭ, M. A. Malitskaya, *et al.*, Izv. Akad. Nauk SSSR, Neorg. Mater. **19** (1), 123 (1983).

3. F. Chu, I. M. Reaney, and N. Setter, Ferroelectrics **151** (1–4), 343 (1994).

4. I. P. Raevskii, V. G. Smotrakov, V. V. Eremkin, *et al.*, Ferroelectrics **247** (1–3), 27 (2000).

5. I. P. Raevskiĭ, V. V. Eremkin, V. G. Smotrakov, *et al.*, Fiz. Tverd. Tela (St. Petersburg) **42** (1), 154 (2000) [Phys. Solid State **42**, 161 (2000)].

6. L. S. Kamzina, I. P. Raevskiĭ, V. V. Eremkin, and V. G. Smotrakov, Fiz. Tverd. Tela (St. Petersburg) **44** (9), 1676 (2002) [Phys. Solid State **44**, 1754 (2002)].

7. L. S. Kamzina and A. L. Korzhenevskiĭ, Pis'ma Zh. Éksp. Teor. Fiz. **50** (3), 146 (1989) [JETP Lett. **50**, 163 (1989)].

8. L. S. Kamzina and A. L. Korzhenevskiĭ, Fiz. Tverd. Tela (St. Petersburg) **34** (6), 1795 (1992) [Sov. Phys. Solid State **34**, 957 (1992)].

9. L. S. Kamzina, A. L. Korzhenevskiĭ, N. N. Kraĭnik, and L. M. Sapozhnikova, Izv. Akad. Nauk SSSR, Ser. Fiz. **54** (4), 614 (1990).

10. A. L. Korzhenevskiĭ, Fiz. Tverd. Tela (Leningrad) **29** (9), 2754 (1987) [Sov. Phys. Solid State **29**, 1583 (1987)].

11. I. P. Raevskii, M. A. Malitskaya, E. S. Gagarina, *et al.*, in *Proceedings of II Rostov International Meeting on High Temperature Superconductivity (IMHTS-2R), Rostov-on-Don* (2000), p. 155.

12. M. Yoshida, S. Mori, N. Yamomoto, *et al.*, Ferroelectrics **217**, 327 (1998).

13. L. S. Kamzina and N. N. Krainik, Ferroelectrics **223**, 27 (1999).

14. K. Fujishiro, T. Iwase, Y. Uesu, *et al.*, J. Phys. Soc. Jpn. **69** (7), 2331 (2000).

15. E. V. Colla, E. Yu. Koroleva, N. M. Okuneva, and S. B. Vakhrushev, Phys. Rev. Lett. **74** (9), 1681 (1995).

16. L. S. Kamzina and N. N. Kraĭnik, Fiz. Tverd. Tela (St. Petersburg) **45** (1), 147 (2003) [Phys. Solid State **45**, 154 (2003)].

Translated by G. Skrebtsov

MAGNETISM
AND FERROELECTRICITY

Relaxor Properties of Fe-Doped TlInS$_2$

R. M. Sardarly*, O. A. Samedov*, I. Sh. Sadykhov*, and V. A. Aliev**

* Institute for Radiation Problems, Academy of Sciences of Azerbaijan, Baku, 370143 Azerbaijan
** Institute of Physics, Academy of Sciences of Azerbaijan, pr. Dzhavida 33, Baku, 370143 Azerbaijan
e-mail: sardarli@yahoo.com
Received October 28, 2002

Abstract—The relaxor properties of Fe-doped TlInS$_2$ crystals are investigated. It is shown that Fe-doped TlInS$_2$ compounds exhibit all features inherent in relaxor ferroelectric materials. The temperature range of existence of the microdomain (relaxor) state and the temperature of the transition from this state to a macrodomain state are determined. © *2003 MAIK "Nauka/Interperiodica".*

1. INTRODUCTION

Recent investigations into the temperature dependences of the permittivity $\varepsilon(T)$ of the TlInS$_2$ compound in the temperature range of phase transitions have revealed that the curves $\varepsilon(T)$ measured for TlInS$_2$ samples prepared from different batches differ significantly from one another. As was shown in our previous work [1], the differences in the shape of the curves $\varepsilon(T)$ for TlInS$_2$ crystal samples are associated with the fact that TlInS$_2$ belongs to the class of berthollides, i.e., compounds characterized by a composition redistribution during crystal growth. However, this feature does not lead to smearing of the phase transitions and the dependence $\varepsilon^{-1}(T)$ obeys the Curie–Weiss law with a constant of $\approx 10^{-3}$ beginning from the submillimeter range of the spectrum up to values of $\varepsilon(T)$ measured in the kilohertz range [2, 3]. According to neutron diffraction data, the TlInS$_2$ compound is an improper ferroelectric with an incommensurate phase [4].

It has been found that the temperature range of instability of the TlInS$_2$ crystal lattice is very sensitive to trivalent cation impurities with different ion radii and coordination numbers. It is worth noting that the phase transition temperatures can either increase or decrease depending on the impurity type (the results of these investigations have already been submitted for publication). In this respect, it is of interest to elucidate the origin and mechanisms of the phase transitions occurring in TlInS$_2$ crystals. Transition metals of the iron group represent multiply charged ion impurities and can form deep centers of strong localization that are capable of interacting with a highly polarized crystal lattice of TlInS$_2$.

This paper reports on the result of investigations into the dielectric polarization and pyroelectric properties of TlInS$_2\langle$Fe$\rangle$ crystals.

2. EXPERIMENTAL TECHNIQUE

Single crystals of TlInS$_2\langle$Fe$\rangle$ were grown using a modified Bridgman–Stockbarger method. No anisotropy of the dielectric properties in the plane of the layer was observed. The measurements were performed at crystal faces cut out perpendicular to the polar axis. The crystal faces were ground, polished, and coated with a silver paste. The permittivity ε and the dielectric loss tangent $\tan\delta$ were measured on E7-8 and E7-12 alternating-current bridges in the temperature range 150–250 K at frequencies of 1 kHz and 1 MHz, respectively. The rate of change in the temperature was equal to 0.1 K/min. The dielectric hysteresis loops were examined according to a modified Sawyer–Tower scheme at a frequency of 50 Hz. The pyroelectric effect was measured using the quasi-static method on a V7-30 universal voltmeter.

3. RESULTS AND DISCUSSION

Figure 1 shows the temperature dependences of the permittivity $\varepsilon(T)$ measured for TlInS$_2$ and TlInS$_2\langle$Fe$\rangle$ crystals during cooling and heating. As can be seen from Fig. 1, the TlInS$_2$ crystals (curves *1*, *2*) undergo a sequence of phase transitions [3] that begins with the phase transition from the paraelectric phase to the incommensurate phase at a temperature of 216 K. The origin of the two other phase transitions occurring at temperatures of 204 and 200 K was thoroughly discussed by Suleĭmanov *et al.* [5]. Most likely, these transitions are associated with a transformation of the modulated structure. The observed sequence of phase transitions ends with the transition to the polar phase at 196 K.

In the temperature range $T - T_1(216) \leq 50$ K, the dependence $\varepsilon(T)$ obeys the Curie–Weiss law with the Curie constant $C^+ = 5.3 \times 10^3$ K. An anomaly manifests itself at a temperature of 196 K upon cooling, and all the peaks are well pronounced without even insignificant indications of smearing. As is clearly seen from
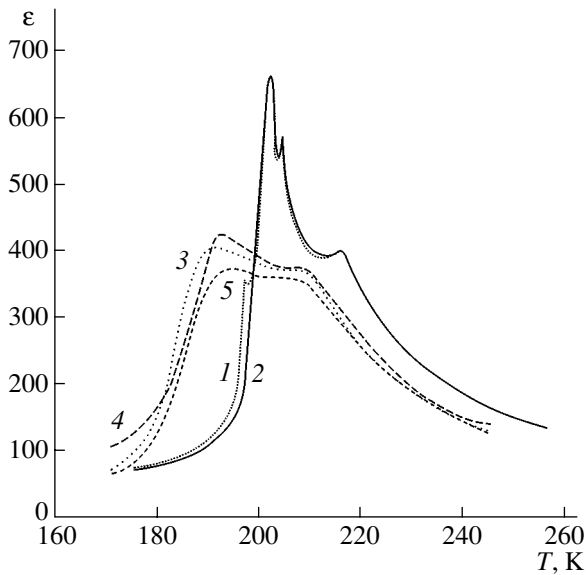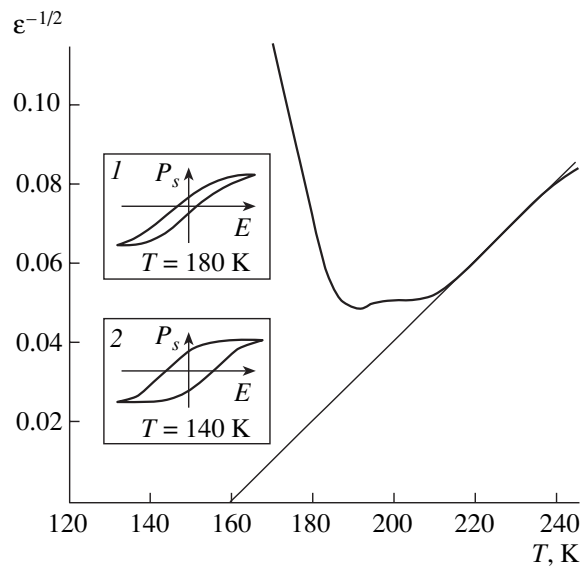
Fig. 1. Temperature dependences of the permittivity $\varepsilon(T)$ for (1, 2) TlInS$_2$ and (3, 4, 5) TlInS$_2\langle$Fe$\rangle$ crystals upon (1, 3, 5) cooling and (2, 4) heating. Frequency of measurements: (1–4) 1 kHz and (5) 1 MHz.

Fig. 2. Temperature dependence of $\varepsilon^{-1/2}$ for the TlInS$_2\langle$Fe$\rangle$ compound. The insets show the hysteresis loops for TlInS$_2\langle$Fe$\rangle$. The frequency of measurements is 1 MHz.

Fig. 1, the dielectric hysteresis for TlInS$_2$ is observed only in the vicinity of 196 K. For iron-doped samples, the dielectric hysteresis is revealed at temperatures close to T_m [the temperature at which the permittivity $\varepsilon(T)$ reaches a maximum] and amounts to approximately 2 K (Fig. 1; curves 3, 4).

At these temperatures, the dependence $\varepsilon(T)$ of (TlInS$_2$)$_{1-x}$(Fe)$_x$ crystals with $x = 0.001$ shows a different behavior: there is a wide spread of experimental points, the phase transition temperatures are shifted to the low-temperature range by 10 K, and the incommensurate phase is observed in a wider temperature range with two anomalies at 190 and 209 K. This raises the question as to why the introduction of 0.1 mol % Fe into the TlInS$_2$ compound leads to such a radical change in the dependence $\varepsilon(T)$.

As is known [6, 7], the smearing of phase transitions is caused primarily by the composition fluctuations. However, it does not always happen that an increase in the defect concentration brings about smearing of the phase transitions. According to Benguigai and Bethe [8], the phase transitions become smeared upon the formation of defects whose dipole moments induce local electric fields in the adjacent regions of the crystal. Moreover, as was shown by Mamin [9–11], upon doping of the TlInS$_2$ semiconductor compound, there arise centers of carrier localization that can generate local electric fields, which, in turn, induce polarization in the vicinity of the phase transition. An important feature of ferroelectric materials with smeared phase transitions is that the dielectric polarization above the temperature T_m changes with temperature in accordance with the

relationship $(\varepsilon')^{-1} = A + B(T - T_0)^2$ rather than with the Curie–Weiss law $(\varepsilon')^{-1} = C^{-1}(T - T_0)$.

The temperature dependence of the permittivity $\varepsilon^{-1/2}(T)$ for the TlInS$_2\langle$Fe$\rangle$ crystal is depicted in Fig. 2. In the case when the temperature decreases from the range of existence of the high-temperature phase, the curve $\varepsilon^{-1/2}(T)$ intersects the abscissa axis at $T = 164$ K, which coincides with the temperature of the maximum in the low-temperature pyroelectric coefficient (Fig. 3). Investigations into the polarization properties of the
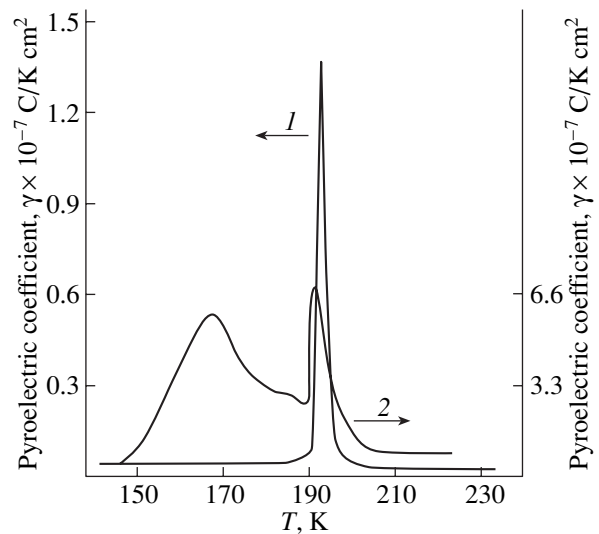
Fig. 3. Temperature dependences of the pyroelectric coefficient $\gamma(T)$ for (1) TlInS$_2$ and (2) TlInS$_2\langle$Fe$\rangle$ crystals.

TlInS$_2$⟨Fe⟩ crystal have revealed dielectric hysteresis loops at temperatures below 164 K. The maximum spontaneous polarization observed in this case reaches 7.5×10^{-8} C/cm^2. For undoped TlInS$_2$ crystals, we obtained the spontaneous polarization $P_S = 1.8 \times 10^{-7}$ C/cm^2. In the temperature range 164–190 K, the spontaneous polarization was determined to be $P_S = 1.5 \times 10^{-8}$ C/cm^2. The dielectric hysteresis loops for the TlInS$_2$⟨Fe⟩ crystal are displayed in the insets to Fig. 2. The upper inset shows the hysteresis loop observed in the temperature range 164–190 K. As is seen from this inset, the hysteresis loop is narrow and prolate in shape, which is characteristic of relaxor ferroelectrics. The lower inset shows the dielectric hysteresis loop at temperatures below 164 K. It is evident that, in this case, the hysteresis loop has a shape typical of conventional ferroelectrics.

The frequency dispersion was investigated at two frequencies of the measuring field: $f = 1$ kHz and 1 MHz. It turned out that an increase in the frequency f does not affect the location of the maxima observed at the temperature T_m in the curve $\varepsilon(T)$ for the TlInS$_2$ crystal, whereas the smeared maxima in the dependence $\varepsilon(T)$ for the TlInS$_2$⟨Fe⟩ crystal are shifted by 3 K (Fig. 1; curves *3*, *5*).

Figure 3 depicts the temperature dependences of the pyroelectric coefficient $\gamma(T)$ for pure TlInS$_2$ (curve *1*) and iron-doped TlInS$_2$ (curve *2*) crystals. The pyroelectric measurements were performed by the quasi-static method. The pyroelectric coefficient γ was calculated from the following relationship: $\gamma = J/A_0 dT/dt$, where J is the pyroelectric current intensity, A_0 is the surface area of the electrodes, and dT/dt is the heating rate. For these measurements, the samples were preliminarily polarized in an external electric field. It is clearly seen from Fig. 3 that, for the pure TlInS$_2$ crystal at a temperature of 196 K, the pyroelectric coefficient γ reaches a maximum value of 1.4×10^{-7} C/K cm^2. For iron-doped TlInS$_2$ samples, the dependence $\gamma(T)$ exhibits two anomalies at $T_m = 190$ K and $T_0 = 164$ K. Moreover, the behavior of $\gamma(T)$ at temperatures above 190 K (i.e., in the range of existence of the incommensurate phase) suggests that weak current flows through the sample.

An analysis of the curves shown in Figs. 1–3 demonstrates that the TlInS$_2$⟨Fe⟩ crystals exhibit all the features inherent in relaxor ferroelectrics: (i) doping of TlInS$_2$ with Fe^{3+} cations brings about the smearing of the phase transitions, (ii) the permittivity is characterized by the frequency dispersion, (iii) the dielectric hysteresis loop has a prolate shape in the temperature range of the smeared phase transition, and (iv) the temperature dependence of the permittivity in the range of existence of the high-temperature phase is described by the relationship $(\varepsilon')^{-1} = A + B(T - T_0)^2$ rather than by the Curie–Weiss law.

The smearing of phase transitions and the specific features observed in the ferroelectric properties of TlInS$_2$⟨Fe⟩ crystals are undeniably associated with the structural disordering, which, in turn, is responsible for local distortions of crystal symmetry and the generation of internal electric fields over a wide temperature range. Although the phase transitions have long since been studied, no satisfactory explanations have been offered for their mechanisms. In our opinion, this circumstance can be explained by the fact that all these investigations of the phase transitions in TlInS$_2$ compounds were performed without due regard for their semiconductor properties. This is especially true for TlInS$_2$ crystals doped with cation impurities that can form attachment levels (traps) in the vicinity of the conduction band bottom. Moreover, proper allowance must be made for both the localization of charge carriers at the impurity centers and their influence on the phase transitions. A detailed analysis of this problem was carried out by Mamin [9–11], who demonstrated that thermal filling of the traps gives rise to a branching sequence of phase transitions and can be responsible for the formation of an unstable intermediate state between the incommensurate and commensurate phases.

A comparison of the data presented in Figs. 1 and 3 shows that the maximum observed in the dependence $\gamma(T)$ at a temperature of 164 K does not manifest itself in the curve $\varepsilon(T)$. According to [11], this feature is inherent in relaxors and stems from the fact that the characteristic frequency of oscillations of the induced polarization is determined not only by the characteristic relaxation time of the lattice subsystem (as is the case with conventional ferroelectrics) but also by the relaxation times of the electronic subsystem. It is quite reasonable that the characteristic times of variations in the order parameter η and the electron concentration m in traps differ significantly ($\tau_\eta/\tau_m \ll 1$). On this basis, Mamin [11] investigated the above problem with due regard for the separation of the contributions from fast and slow processes. It was established that the effective temperature T_{cm} of the phase transition decreases as a result of thermal filling of the attachment levels. The phase transition to the state with spontaneous polarization is observed at the temperature T_{cm}. For TlInS$_2$⟨Fe⟩ crystals, this temperature is equal to 164 K (Fig. 2). As can be seen from Fig. 2, the hysteresis loop at temperatures below 164 K increases in size along the vertical axis. Note that the localized charges generate local electric fields. In this case, the spontaneous polarizations induced in separate microregions in weak external fields can be oriented along different directions due to the spatial distribution of localized charges. As a result, the hysteresis loop in the temperature range 164–190 K becomes narrow and prolate in shape. For this reason, the specific features associated with the phase transition occurring at the temperature T_{cm} are not observed in the dependence $\varepsilon(T)$.

4. CONCLUSIONS

Thus, it was demonstrated that, for TlInS$_2$ crystals doped with iron, there exists a temperature range in which Fe-doped TlInS$_2$ compounds exhibit all features inherent in relaxor ferroelectric materials. The phase transition from a microdomain (relaxor) state to a macrodomain ferroelectric state is observed at a temperature of 164 K. This transition is accompanied by a jump in the pyroelectric coefficient $\gamma(T)$.

REFERENCES

1. R. M. Sardarly, O. A. Samedov, I. Sh. Sadykhov, *et al.*, Izv. Nats. Akad. Nauk Azerb., Ser. Fiz.–Mat. Tekh. Nauk **22** (2), 31 (2002).

2. A. A. Volkov, Yu. G. Goncharov, G. V. Kozlov, *et al.*, Fiz. Tverd. Tela (Leningrad) **25** (12), 3583 (1983) [Sov. Phys. Solid State **25**, 2061 (1983)].

3. R. A. Aliev, K. R. Allakhverdiev, A. I. Baranov, *et al.*, Fiz. Tverd. Tela (Leningrad) **26** (5), 1271 (1984) [Sov. Phys. Solid State **26**, 775 (1984)].

4. S. B. Vakhrushev, V. V. Zhdanova, O. E. Kvyatkovskiĭ, *et al.*, Pis'ma Zh. Éksp. Teor. Fiz. **39** (6), 245 (1984) [JETP Lett. **39**, 291 (1984)].

5. R. A. Suleĭmanov, M. Yu. Seidov, F. I. Salaev, and F. A. Mikailov, Fiz. Tverd. Tela (St. Petersburg) **35** (2), 348 (1993) [Phys. Solid State **35**, 177 (1993)].

6. I. P. Raevskiĭ, V. V. Eremkin, V. G. Smotrakov, *et al.*, Fiz. Tverd. Tela (St. Petersburg) **42** (1), 154 (2000) [Phys. Solid State **42**, 161 (2000)].

7. M. D. Glinchuk, E. A. Eliseev, V. A. Stefanovich, and B. Hilczer, Fiz. Tverd. Tela (St. Petersburg) **43** (7), 1247 (2001) [Phys. Solid State **43**, 1299 (2001)].

8. L. Benguigai and K. Bethe, J. Appl. Phys. **47**, 2728 (1976).

9. R. F. Mamin, Fiz. Tverd. Tela (Leningrad) **33** (9), 2609 (1991) [Sov. Phys. Solid State **33**, 1473 (1991)].

10. R. F. Mamin, Pis'ma Zh. Éksp. Teor. Fiz. **58** (7), 534 (1993) [JETP Lett. **58**, 538 (1993)].

11. R. F. Mamin, Fiz. Tverd. Tela (St. Petersburg) **43** (7), 1262 (2001) [Phys. Solid State **43**, 1314 (2001)].

Translated by O. Borovik-Romanova

MAGNETISM
AND FERROELECTRICITY

Effect of Substrates on the Morphology of $Ba_xSr_{1-x}TiO_3$ Nanometer-Scale Films

V. V. Afrosimov*, R. N. Il'in*, S. F. Karmanenko**, V. I. Sakharov*, and I. T. Serenkov*

*Ioffe Physicotechnical Institute, Russian Academy of Sciences, Politekhnicheskaya ul. 26, St. Petersburg, 194021 Russia
e-mail: r.ilin@mail.ioffe.ru
**St. Petersburg State Electrotechnical University, ul. Prof. Popova 5, St. Petersburg, 197376 Russia
Received November 25, 2002

Abstract—The initial stages in the growth of $Ba_xSr_{1-x}TiO_3$ films on various dielectric substrates were studied using the middle-energy ion scattering spectroscopy, and the results obtained were used to analyze microdefects in the film. The character of film growth was found to depend on the shape, size, and electrostatic state of crystallographic unit cells of the substrate surface. The growth was epitaxial on an $SrTiO_3$ substrate. The film prepared on an $LaAlO_3$ substrate consists of slightly disordered crystallites. Films on MgO substrates demonstrated island-type growth up to a thickness of 20 nm, with foreign phases observed to form; as the film thickness increased, the growth acquired an epitaxial pattern. The film grown on the α-$Al_2O_3(1\bar{1}02)$ surface was polycrystalline and contained textured blocks. © *2003 MAIK "Nauka/Interperiodica".*

1. INTRODUCTION

An important step in the development of production technologies of thin-film structures for nanoelectronics devices consists in monitoring the initial stages in thin-film growth and determination of the effect these stages exert on the structure and electrical characteristics of the final product. One needs, in particular, information on the formation of transition layers at the interface and on the relative magnitude of the thickness of these layers and the transverse dimension of the layered structures themselves. It is important to know the extent to which the presence of transition layers affects further growth and properties of the film and its structural order, because the number and orientation of the blocks and crystallites making up a film dominate its electrical properties.

The electron and atomic force microscopy employed traditionally in studies of the initial stages of growth provide information on selected local areas only. X-ray and electron diffraction methods offer integrated data, with no depth resolution in the objects under study. The methods based on probing a sample with ion beams yield information on the composition and structure of thin films; this information, while being averaged over the surface, is differentiated in depth [1]. Thus, the middle-energy ion scattering method (MEIS), based on the analysis of the spectra of ions that were scattered through large angles or underwent channeling, represents a nondestructive way of determining the composition of a sample, the thickness of its various layers, and the perfection of the crystal structure both of the film as a whole and of its constituent blocks [2, 3]. MEIS may be considered a version of

the Rutherford backscattering (RBS) method, with the probing ion energy reduced by an order of magnitude, from 10^6 to 10^5 eV, which permits measurement of the ion energy with high-resolution electrostatic analyzers and, as a consequence, improvement of the resolution at depths down to 1 nm in the near-surface region. In addition, lowering the probing beam energy reduces the radiation load on the sample. As in RBS, channeling can be used in MEIS to estimate the quality of the film structure.

The energy spectra of backscattered ions are measured in RBS and MEIS in the channeling mode, with the beam aligned with one of the low-index single-crystal directions [the $Y_c(E)$ spectrum] or under a random beam orientation [the $Y_r(E)$ spectrum]. The channeling factor is defined by the normalized dependence of the yield of scattered ions on their energy, $\chi(E) = Y_c(E)/Y_r(E)$. The minimum relative yield χ_{min}, i.e., the value of the $\chi(E)$ function immediately after the surface peak on the $Y_c(E)$ curve, was accepted as a characteristic of the perfection of single crystals.

An analysis of the initial film growth stages should discriminate between such microdefects as foreign inclusions, misoriented crystallites in an epitaxial film, and the presence of a polycrystalline phase. The methods of determining the average angle of crystallite misorientation employed in the RBS and MEIS methods are based on measuring the angular dependences of the yield of backscattered ions at different incident energies and/or using various probing ions [4]. This study made use of two factors to analyze the structural features of a film, namely, the dependence of χ_{min} on the probe ion charge and the character of the dependence of

the minimum relative yield in MEIS spectra on depth t. If the probe ions have a nuclear charge Z_1 and initial energy E_0, then the minimum yield χ_{min} for a film with both crystallite misorientation (described by a normal distribution with a variance σ) and inclusions of a non-channeling polycrystalline fraction can be written as [4]

$$\chi_{min} = \delta + (1-\delta)[1 - (1 - \chi_0(Z_1, E_0)) \tag{1}$$
$$\times (1 + 2\sigma^2(\ln 2)\psi_c^{-2}(Z_1, E_0))^{-1}],$$

where δ is the volume fraction of polycrystalline inclusions, $\chi_0(Z_1, E_0)$ is the minimum yield for a perfect crystal, and $\psi_c(Z_1, E_0)$ is the characteristic channeling angle. Because all the measurements performed in this study were made at the same value of E_0, the dependences of the quantities χ_0, ψ_c, and, accordingly, of χ_{min} on this parameter will be subsequently disregarded. As follows from Eq. (1), if there is no crystallite misorientation ($\sigma = 0$), the $\chi_{min}(Z_1)$ relation is dominated by the $\chi_0(Z_1)$ function and is a rising curve [1]. Misorientation, even as small as $\sigma \sim 1°$, makes $\chi_{min}(Z_1)$ a decreasing function, because the quantity ψ_c^2 is proportional to the ion charge Z_1.

An analysis of films with thicknesses in excess of 100 nm should include detection of extended defects. The MEIS method enables one to detect such defects by using the $\chi(t)$ dependences, which can be found by combining the $\chi(E)$ relations with the known stopping cross sections. For backscattered ion energies $E < E_1$ (where E_1 is the energy corresponding to the minimum in the $Y_c(E)$ and $\chi(E)$ curves immediately beyond the surface peak), the quantity χ, as a rule, grows with decreasing energy. Assuming the increase in χ with depth t to be determined by dechanneling caused by extended defects with a constant concentration, this relation can be empirically presented in the form

$$\chi(t) = \chi_{min} + (1 - \chi_{min})[1 - \exp(-t/\lambda)], \tag{2}$$

where λ is the dechanneling length determined by the rate of dechanneling due to thermal vibrations of the perfect lattice and by the sum of dechanneling rates due to various extended defects (dislocations, grain boundaries, stacking faults, etc.). If additional information on the type of defects and the dechanneling cross sections is lacking, the value of λ can be used to judge the perfection of the prepared films (Fig. 1).

This communication reports on a MEIS study of the initial stages in the growth of ultrathin ferroelectric $Ba_xSr_{1-x}TiO_3$ (BSTO) films deposited on various dielectric substrates, including an analysis of defects in the films and of the influence the initial growth stages of films have on their quality in subsequent growth.

2. EXPERIMENT

The initial stages in BSTO film growth were studied on films deposited on single-crystal substrates of four
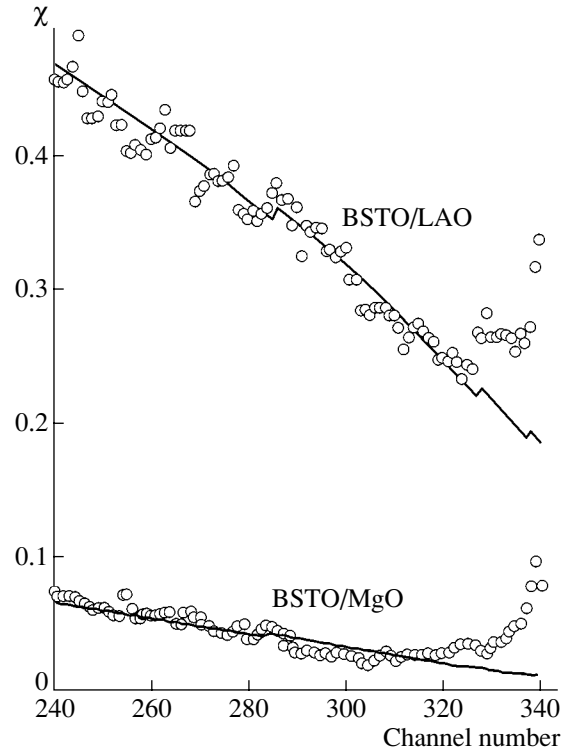
Fig. 1. Experimental (circles) and calculated (lines) $\chi(E)$ graphs for films BSTO/LAO (sample 7) and BSTO/MgO (sample 13). The lines are plots of Eq. (2) with λ as the fitting parameter. Channel numbers >320 relate to the surface peak. The measurements were performed with an H$^+$ beam and an SCD as a detector.

materials. The substrates used were the (100) surfaces of $SrTiO_3$ (STO), $LaAlO_3$ (LAO) and MgO single crystals and r cut ($1\bar{1}02$) from sapphire Al_2O_3 (AlO), which differ in their lattice structure and parameters. Of the 13 films with a thickness of up to 40 nm, three were deposited on STO, two on LAO, and four each on MgO and AlO. The films were rf magnetron sputtered at a substrate temperature of 700–800°C at a rate of about 100 nm/h in an oxygen environment at a pressure of 20 Pa, with subsequent cooling in O_2 for two hours [5]. In addition, to determine the film characteristics under steady-state deposition conditions, four BSTO films of thickness on the order of 100 nm or greater deposited on MgO and LAO were studied.

The experimental MEIS setup was described elsewhere [2]. The energies of the ions scattered through an angle 120° were determined using an electrostatic analyzer (ESA) with a resolution $\Delta E/E = 5 \times 10^{-3}$. The ion energy spectra for films of thickness 100 nm or greater were also measured in a channel consisting of a spectrometric semiconductor detector (SCD) and a pulse height analyzer.

The probe ions were H$^+$, He$^+$, and N$^+$ with an initial energy of 230 keV. We obtained for each sample the ion energy spectra $Y_c(E)$ and $Y_r(E)$ in the channeling and

Parameters of the films studied

Sample no.	Substrate	h, nm	σ_h, nm	C	$\tau = Ch$	$\chi_{min}(H^+)$	$\chi_{min}(He^+)$	$\chi_{min}(N^+)$
1	$SrTiO_3$	3.3	0.85	0.3	1.0	–	0.25	–
2	$SrTiO_3$	5.5	0.5	1.0	5.5	–	–	0.06
3	$SrTiO_3$	40.0	3.6	1.0	40.0	0.20	–	0.15
4	$LaAlO_3$	11.0	2.4	1.0	11.0	0.7	0.38	0.25
5	$LaAlO_3$	27.0	5.0	1.0	27.0	0.7	0.42	0.25
6	$LaAlO_3$	94	–	1.0	94	–	0.32	–
7	$LaAlO_3$	>400.0	–	1.0	>400.0	0.25	–	–
8	MgO*	8.1 (2.4)	9.9 (1)	0.11 (0.15)	0.9 (0.4)	0.95	0.80	–
9	MgO*	13.5 (12.9)	1.7 (8.6)	0.40 (0.25)	5.4 (3.2)	–	0.85 (0.7)	0.75
10	MgO	21.4	6.0	0.85	18.1	0.72	0.57	0.50
11	MgO	29.0	17.6	1.0	29.0	0.25	–	0.18
12	MgO	130	–	1.0	130	–	0.07	–
13	MgO	172	–	1.0	172	0.02	–	–
14	Al_2O_3	8.0	6.0	0.9	7.2	–	1	0.9
15	Al_2O_3	11.0	4.0	1.0	11.0	–	0.95	0.9
16	Al_2O_3	24.0	10.0	1.0	24.0	1.0	–	0.8
17	Al_2O_3	26.0	5.0	1.0	26.0	–	0.9	0.7

* The figures in parentheses are parameters of the TiO foreign-phase islands.

random-orientation modes, respectively, and measured the dependence of the normalized yield of scattered ions $\chi(E)$ on their energy. The $Y_r(E)$ relation thus obtained was used to deduce the composition of the films and their total thickness h, as well as the scatter in thickness σ_h and the substrate coverage C by the film, by following the method described in [6].

3. RESULTS AND DISCUSSION

The table lists the results obtained on the films studied. It specifies the substrate type, the average height of the islands or (in the case of complete coverage) the film thickness h, the spread of this quantity σ_h, the substrate coverage C, the average thickness of the deposited layer $\tau = hC$, and the values of the minimum yield χ_{min} for various probing ions. For films 8 and 9 which exhibit mosaic coating, the values of h, σ_h, and C are given separately for BSTO and TiO islands.

The parameter x for the $Ba_xSr_{1-x}TiO_3$ compound varied in the interval 0.35–0.5 for all films.

Using probing ions with different Z_1 offered the possibility of establishing the specific features of film growth during the course of deposition especially in the case of the MgO and LAO substrates. For the LAO substrates, the value of χ_{min} is determined by the ion species and is nearly independent of τ, which implies the presence of crystallite misorientation starting from the interface up. In the case of MgO, however, the dependence on the ion species is weak but χ_{min} falls off rap-

idly with increasing film thickness, which indicates improvement of the film crystal structure. The reasons for these phenomena will be dealt with in the corresponding sections below.

Let us consider the pattern of BSTO film growth on various substrates in more detail.

3.1. SrTiO₃ Substrate

This substrate is the closest in lattice constant and structure to the BSTO film. The substrate and the film have a perovskite cubic lattice in which the TiO_2 and SrO layers are not charged. The lattice misfit $\xi = 2|a_s - a_f|/(a_s + a_f)$ (where a_s and a_f are the lattice constants of the substrate and the film, respectively) is the smallest in this case: $\xi = 0.007$. Starting from a thickness of 5 nm, the substrate is completely covered by the film and the film thickness nonuniformity σ_h does not exceed the lattice constant (0.4 nm), which implies layer-by-layer growth. As the film thickness increases to 40 nm, the average nonuniformity σ_h grows but the layer-by-layer growth mode persists. The minimum yield depends only weakly on the probing ion species; in other words, there is no crystallite misorientation. As shown by measurements of the $\chi(E)$ dependence for a film 40 nm thick, the yield of scattered ions in the region of the film is $\chi_f = 0.15$ and in the region of the substrate, $\chi_s = 0.2$. The slight increase in χ observed as the interface is crossed may be assigned to dechanneling caused by misfit dislocations. No noticeable misori-

entation was observed in the film. The film starts to grow epitaxially from the interface up.

3.2. LaAlO₃ Substrate

Lanthanum aluminate crystals have perovskite structure with a slight rhombohedral distortion at room temperature ($\alpha = 90.4°$). A transition to the cubic phase occurs at 544°C. The lattice misfit between the film and the substrate is small ($\xi = 0.029$). As seen from the table, the minimum yield χ_{min} for BSTO films depends strongly on the probing ion species while being independent of the film thickness. This means that the main film defect is the crystallite misorientation. Estimates made using Eq. (1) suggest that the average misorientation of the crystallites making up the film is about 2°. Note that the columnar structure with numerous small-angle tilted grain boundaries was also detected using high-resolution electron microscopy in [7].

The crystallite misorientation in a film may be caused by twinning occurring at the phase transition in the LAO substrate as the sample is cooled. Specific features of the electrostatic interaction at the interface may be another cause of the misorientation. The crystal lattice of the LAO substrate can terminate either in LaO⁺ or (AlO₂)⁻ surfaces, whereas the outermost layers of a TiO₂ and BaO (SrO) film are neutral. As pointed out in [8], electrostatic misfit between the film and the substrate may give rise to the formation of a rough strained film or a transition defected layer.

The dechanneling length λ calculated from Eq. (2) for films thicker than 100 nm (Fig. 1) was found to be about 300 nm, which is an order of magnitude smaller than that for the best BSTO films. This quantity is practically independent of the actual deposition conditions; this may be due to the fact that dechanneling occurs primarily at grain boundaries and is determined by the grain transverse dimensions, which, in turn, are fixed by the distances between the misfit dislocations at the BSTO/LAO interface [7].

Thus, a BSTO film on an LAO substrate is characterized by epitaxial growth in the form of crystallites, for which the rms deviation of the [100] axes from the substrate surface normal is about 2°.

3.3. MgO Substrate

The MgO crystal has a cubic lattice with a constant $a = 0.4213$ nm, which is substantially larger than that of BSTO (the misfit $\xi = 0.067$). The strains caused by this misfit are relieved by misfit dislocations. It is these dislocations that are responsible for the probe ion dechanneling, and this makes it possible to estimate the dislocation density from the increase in the normalized yield at the energies corresponding to the interface depth [9]. Estimates of the dislocation density made for films 8–13 (see table) give a figure of 1.5×10^6 cm⁻¹.

An important difference between the deposition of a BSTO film on MgO and that on other substrates is the island growth pattern, which is characteristic of a weak interphase binding and brings about incomplete substrate coverage. This growth pattern persists up to a film thickness of 20 nm, whereas complete coverage by other films occurs at a thickness of no greater than 10 nm.

The interaction between different phases at the interface separating the MgO substrate from a BaTiO₃ film is discussed in [10]. The electrostatic interaction at the interface was found [10] to interfere with the deposition of a BaO (SrO) layer on a MgO substrate and give rise to the formation of three-dimensional misoriented nuclei. Epitaxial growth of BaTiO₃ (SrTiO₃) can also start with a TiO₂ layer; however, this layer can form only if titanium atoms do not attach to a part of the oxygen atoms. This suggests that, in our case, the deposition of BaO (SrO) layers in the initial stage of BSTO growth also nucleates three-dimensional misoriented islands, while the deposition of titanium oxides with the formation of a TiO₂ layer initiates growth of BSTO islands through the mechanism described in [10].

It follows from our results that, in addition to the above two mechanisms of nucleation in the deposition of BSTO on MgO, one can also conceive of epitaxial growth of islands of a foreign phase. An analysis of the composition of thin films 8 and 9 revealed an excess of titanium with respect to the level expected from the amounts of barium and strontium. Figure 2 displays MEIS spectra of these films. In the channel number interval 440–460 (excess titanium at the interface), film 9 (Fig. 2b) exhibits a decrease in the minimum yield compared to the energy region corresponding to the Ba and Sr signals (channel numbers >500), which is evidence that there is a higher degree of structural order in the phase containing excess titanium. Of all the appropriate titanium compounds, the structure of titanium monoxide TiO is closest to that of MgO. This compound has a cubic lattice and, in contrast to the other titanium oxides, its lattice constant a (0.424 nm) is very close to the MgO lattice constant (0.4213 nm). This gives us grounds to assume that the observed excess titanium signal is due to the growth of TiO islands. Figure 2 presents, side by side with experimental spectra, model spectra calculated under the assumption of the main film having the composition Ba₀.₄₂Sr₀.₅₈TiO₃ and of the presence of titanium monoxide TiO as a foreign phase. The peak due to titanium of the monoxide in the model spectrum starts at the same energy as the peak of titanium of the film, which means that this phase forms isolated islands with a free surface.

The differences between films 8 and 9 in the amount of deposited material and the surface coverage suggest that these films corresponding to different stages of growth; namely, film 8 corresponding to the stage of BSTO nucleation and film 9, to that of the beginning of coalescence. The variation in the shape of the parts of MEIS spectra related to BSTO islands indicates a
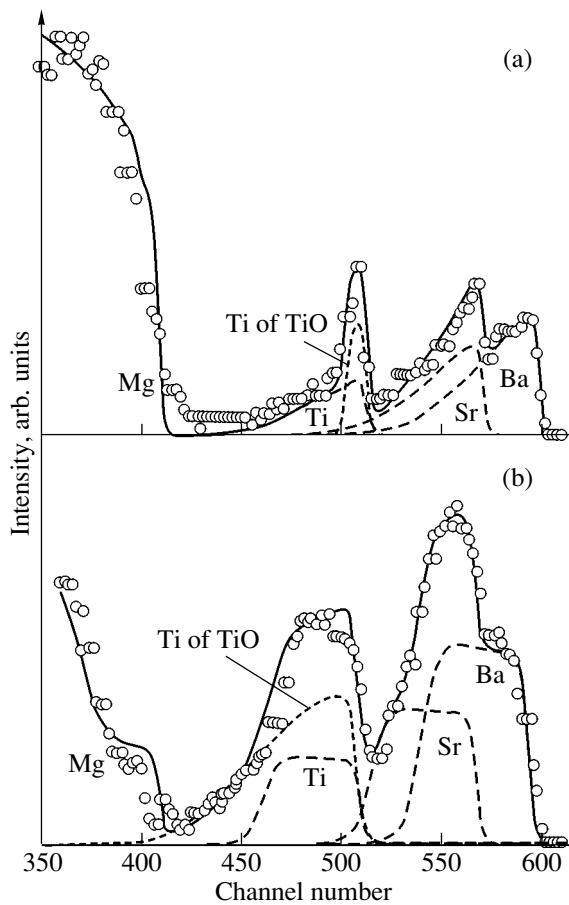
Fig. 2. Experimental and model MEIS spectra of samples (a) 8 and (b) 9. Circles are experimental data, dashed lines are model spectra of the BSTO film components, and dotted lines are model spectra for titanium monoxide. Solid lines are envelopes of the model spectra. The measurements were performed on a He$^+$ beam, with ESA used in the detection channel.

decrease in the island height spread with increasing amount of deposited material. Our earlier model calculations [11] show that this change in shape indicates a transition from island growth to layer-by-layer deposition. The increase in height of the BSTO islands is slower than the growth in their transverse size, which is proportional to the square root of the film-covered area. In contrast, the spread in the TiO island height increases, which may be assigned to a partial overlap of these islands by the laterally growing main film. Channeling is only weakly pronounced in these two films, but it depends on ion charge, which argues for a rise (in addition to the polycrystalline fraction) in misoriented BSTO crystallites.

The minimum yield χ_{min} of backscattered ions falls off rapidly as the film thickness increases even further. This suggests a transition from the island to layer-by-layer growth pattern. We succeeded in obtaining films with thicknesses on the order of 100 nm exhibiting $\chi_{min} = 0.02$ and a dechanneling length $\lambda \cong 2000$ nm

(Fig. 1), which is close to the figures quoted for single crystals.

Thus, the initial stage in BSTO film growth on a MgO substrate differs substantially from that on the other substrates studied by us. In the beginning, the film growth has an island character and is accompanied by the formation of foreign phases. The rate of film deposition in the island formation stage is lower than that on the other substrates, namely, 1.5 nm/min (for STO, 2 nm/min; for LAO, 3–4 nm/min; for AlO, 3 nm/min). As the thickness of the deposited layer increases, transition to the layer-by-layer growth occurs. The presence of a 10- to 20-nm thick defected layer, which shows a high χ_{min} and contains foreign phases, does not impede epitaxial growth of subsequent layers with a lower value of χ_{min}.

Interestingly, our earlier study of the growth of per-ovskite-like YBa$_2$Cu$_3$O$_{7-x}$ superconducting films on the same substrates revealed that complete surface coverage in the initial stage of deposition was attained latest of all for the MgO substrate. This process of YBa$_2$Cu$_3$O$_{7-x}$ film formation followed a clearly pronounced island character, and microcrystalline islands of the Cu$_2$O phase were detected on the interface [6].

3.4. Al$_2$O$_3$ Substrate

The *r*-cut ($1\bar{1}02$) sapphire surface has a rhombohedral lattice that does not match the BSTO lattice either in shape or dimension. These substrates are employed, however, to prepare BSTO films due to their high dielectric and mechanical properties and wide use in microelectronics. The film thickness at which complete coverage of an AlO substrate is reached is larger than that for the STO and LAO surfaces but is smaller than that for MgO. The minimum yield χ_{min} for the H$^+$ and He$^+$ ions is close to unity; i.e., channeling is practically absent. The decrease in the minimum yield observed to occur for N$^+$ probe ions with increasing film thickness suggests that the film contains a textured component whose volume fraction increases with film thickness. The fact that an epitaxial BaTiO$_3$ film cannot be obtained on the *r*-cut sapphire without coating the latter with a buffer layer was pointed out in [12].

4. CONCLUSIONS

To sum up, our MEIS study of the initial stages of growth of Ba$_x$Sr$_{1-x}$TiO$_3$ films on various substrates revealed specific features in this process that are determined both by the extent to which the substrate fits the film in lattice shape and in its dimensions and by the electrostatic interaction of the interface layers. The SrTiO$_3$ substrate supports layer-by-layer epitaxial growth. Films on LaAlO$_3$ grow epitaxially directly from the substrate up. Such films are made up of slightly misoriented crystallites growing in a direction

close to the surface normal. The film growth on MgO starts with the formation of $Ba_xSr_{1-x}TiO_3$ islands with a small volume fraction of the single-crystal phase, as well as of islands of a foreign phase; however, as the thickness of the film increases, its structure improves in quality, culminating in the onset of epitaxial growth, although a defected layer up to 20 nm in thickness persists. The film growing on α-Al_2O_3 is polycrystalline, and it may contain textured blocks.

ACKNOWLEDGMENTS

REFERENCES

1. L. C. Feldman, J. W. Mayer, and S. R. Picraux, *Materials Analysis by Ion Channeling* (Academic, New York, 1992).

2. V. V. Afrosimov, G. O. Dzyuba, R. N. Il'in, *et al.*, Zh. Tekh. Fiz. **66** (12), 76 (1996) [Tech. Phys. **41**, 1240 (1996)].

3. D. Huttner, O. Meyer, J. Reiner, and G. Linker, Nucl. Instrum. Methods Phys. Res. B **118**, 578 (1996).

4. H. Ishiwara and S. Furukawa, J. Appl. Phys. **47** (4), 1686 (1976).

5. S. F. Karmanenko, A. I. Dedyk, N. N. Isakov, *et al.*, Pis'ma Zh. Tekh. Fiz. **25** (19), 50 (1999) [Tech. Phys. Lett. **25**, 780 (1999)].

6. V. V. Afrosimov, R. N. Il'in, S. F. Karmanenko, *et al.*, Fiz. Tverd. Tela (St. Petersburg) **41** (4), 588 (1999) [Phys. Solid State **41**, 527 (1999)].

7. L. Ryen, E. Olsson, L. D. Madsen, *et al.*, J. Appl. Phys. **83** (9), 4884 (1998).

8. D.-W. Kim, D.-H. Kim, B.-S. Kang, *et al.*, Appl. Phys. Lett. **74** (15), 2176 (1999).

9. V. V. Afrosimov, R. N. Il'in, S. F. Karmanenko, *et al.*, Poverkhnost, No. 8, 71 (1997).

10. R. A. McKee, F. J. Walker, E. D. Specht, *et al.*, Phys. Rev. Lett. **72** (17), 2741 (1994).

11. V. V. Afrosimov, E. K. Gol'man, R. N. Il'in, *et al.*, Perspekt. Mater., No. 6, 10 (1998).

12. C. H. Lei, C. L. Lia, J. G. Lisoni, *et al.*, J. Cryst. Growth **219** (4), 397 (2000).

Translated by G. Skrebtsov

MAGNETISM
AND FERROELECTRICITY

Nonlinear Properties of Barium Titanate in the Electric Field Range $0 \leq E \leq 5.5 \times 10^7$ V/m

I. N. Leont'ev*, A. Leĭderman**, V. Yu. Topolov*, and O. E. Fesenko***

*Rostov State University, pr. Stachki 194, Rostov-on-Don, 344090 Russia
**University of Puerto Rico at Mayagues, PR, 00680 USA
***Institute of Physics, Rostov State University, pr. Stachki 194, Rostov-on-Don, 344090 Russia

Abstract—X-ray structural studies and dielectric measurements of $BaTiO_3$ single crystals were performed in the dc electric field range $0 \leq E \leq 5.5 \times 10^7$ V/m. The field dependence of the tetragonal cell parameter obtained was used to calculate the field dependence of the piezoelectric modulus d_{33}. The piezoelectric modulus d_{33} and the dielectric permittivity vary in magnitude by a factor of two with the field varied in the above range. The observed nonlinear behavior is shown to fit well to a relation connecting the dielectric with the electromechanical characteristics of the crystal. © 2003 MAIK "Nauka/Interperiodica".

The phase transitions induced by a strong electric field in ferroelectric crystals have been extensively studied to date [1–5]. However, there is apparently only one communication [6] that reports on the variation of structural parameters in single-phase states in electric fields far in excess of the coercive field. It was shown in [6] that the dependence of the piezoelectric modulus on electric field E calculated from the field dependence of the unit cell parameter for the $PbZr_{0.958}Ti_{0.042}O_3$ single crystal is strongly nonlinear and can saturate in a strong electric field [6]. It was conjectured [6] that this nonlinearity is a characteristic property of piezoelectric crystals, and this motivated our study of the lattice parameters and piezoelectric activity of other piezoelectric crystals in an electric field.

We chose for the next object barium titanate, whose $C4mm$ phase exhibits a broad region of stability in the E–T plane [7]. $BaTiO_3$ crystals were grown through spontaneous crystallization from a KF melt solution of $BaTiO_3$ [8]. The crystals selected for the study were c- and c–a-domain platelets 10 to 20 µm in thickness. Semitransparent graphite electrodes were deposited by sputtering on the larger sample sides, which were parallel to the (100) plane of the perovskite. After the electrode deposition, the crystal was attached to glass using glycerol, thereby minimizing accidental bending and displacement of the unclamped sample in measurements.

The parameters of the perovskite unit cell were measured with a DRON-2.0 diffractometer ($Cu_{K\alpha 1}$, $Cu_{K\alpha 2}$ radiation). The field dependence of the cell parameters was found by studying the $(00l)$ reflections. The positions of diffraction maxima were refined separately in the angles 2θ and φ. The error in measuring the parameter was $\Delta c = 5 \times 10^{-4}$ Å. When an electric field was applied along the [001] direction to the thin crystals,

they bent toward the positive electrode [9], which resulted in a slight crystal misalignment. Prior to each measurement, the crystal was adjusted, and after this, the positions of the diffraction maxima were refined. The (001) face under study, which was irradiated by x-rays, served as a positive electrode. However, no side maxima corresponding to the formation of a surface layer with anomalously large piezoelectric strains were revealed [10–12]. This is apparently due to the fact that, as the crystal thickness decreases, the electric field strength at which the side maxima were observed to appear increases considerably [13].

With no field applied, the $BaTiO_3$ samples studied have a perovskite tetragonal cell with parameters $c = 4.0345$ Å and $a = 3.9980$ Å at room temperature. The dependence of the cell parameter c on applied electric field (Fig. 1) fits well to a polynomial:

$$c(E) = c_0 + c_1 E + c_2 E^2 + c_3 E^3 + c_4 E^4 \quad (1)$$

with coefficients $c_0 = 4.0344$ Å, $c_1 = 5.3712 \times 10^{-10}$, $c_2 = -2.2865 \times 10^{-17}$, $c_3 = 5.7563 \times 10^{-25}$, and $c_4 = -4.7563 \times 10^{-33}$ Å m^4/V^4 and a correlation coefficient of 0.999.
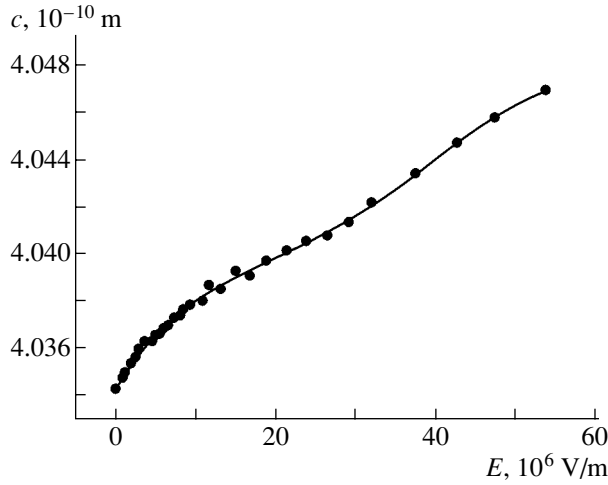
The differential coefficient of inverse piezoelectric effect d_{33} can be expressed through the parameter c of the tetragonal cell as

$$d_{33} = (1/c)(dc/dE). \quad (2)$$

Substituting Eq. (1) into Eq. (2) yields

$$d_{33}(E) = \frac{c_1 + 2c_2 E + 3c_3 E^2 + 4c_4 E^3}{c_0 + c_1 E + c_2 E^2 + c_3 E^3 + c_4 E^4} \quad (3)$$

(line *1* in Fig. 2).

c, 10^{-10} m

Fig. 1. Perovskite unit cell parameter c of single-crystal BaTiO$_3$ plotted vs. electric field.

In the alternative definition of the piezoelectric coefficient [6], the strain is reckoned from $c = c_0$:

$$d_{33}(E) = \frac{1}{c(0)} \frac{c(E) - c(0)}{E} \qquad (4)$$

(line *2* in Fig. 2). As seen from Fig. 2, lines *1* and *2* diverge noticeably in fields below 5×10^6 V/m.

In addition to x-ray structural studies, we conducted dielectric-permittivity measurements in electric fields $0 \le E \le 5.5 \times 10^7$ V/m; the results obtained were used to calculate the electric field dependence of induced polarization (line *1* in Fig. 3).

The relation of the piezoelectric modulus d_{33} to the dielectric permittivity and polarization is given by an expression similar to the one presented in [14, p. 163]:

$$d_{33} = \varepsilon_0 Q_{11}(2P_s + P_i)\chi_{33}, \qquad (5)$$

where Q_{11} is the electrostriction coefficient, which is equal, according to [14], to 1.23×10^{-2} m^4/C^2; χ_{33} is the unclamped-crystal dielectric permittivity; and P_s and P_i are the spontaneous and induced polarizations, respectively (line *3* in Fig. 2).

Equation (5) can be readily used to derive the function $\chi_{33}(E)$ satisfying the condition $d_{33} = \text{const}(E) = d_{33}(0)$:

$$\varepsilon_0 E\chi_{33}^2 + 2P_c\chi_{33} = \frac{d_{33}}{\varepsilon_0 Q_{11}}. \qquad (6)$$

Recalling that $\chi_{33}(E) > 0$ for any value of E, we obtain

$$\chi_{33}(E) = \frac{1}{\varepsilon_0} \frac{\sqrt{P_c^2 + Ed_{33}/Q_{11}} - P_c}{E} \qquad (7)$$

(line *3* in Fig. 3).

Figure 3 shows how strongly the $\chi_{33}(E)$ dependence calculated from Eq. (7) differs from the measurements.

d_{33}, 10^{-10} C/N
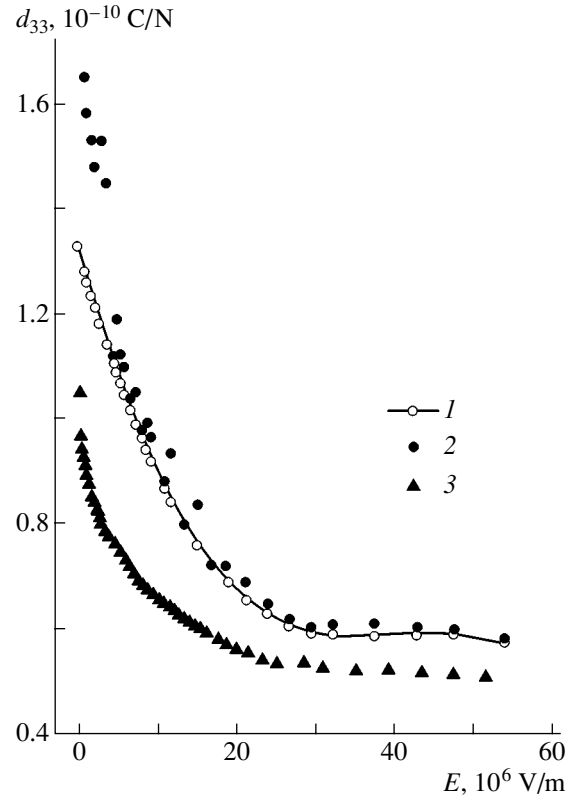
Fig. 2. Electric field dependences of the piezoelectric modulus d_{33} of single-crystal BaTiO$_3$. Curves *1*, *2*, and *3* are plots of Eqs. (2), (4), and (5), respectively.

(Note that, in the case of $\chi_{33}(E) = \text{const}$, d_{33} is a linear function of E.)

Thus, the experimentally observed $\chi_{33}(E)$ dependence brings about a nonlinear dependence of the piezoelectric modulus on electric field in the field range specified.
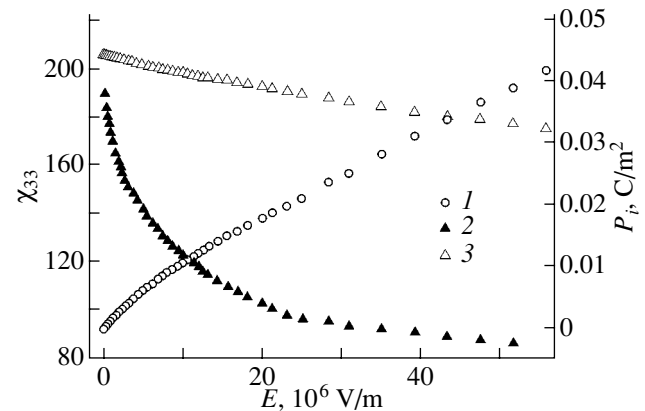
Fig. 3. Electric field dependences (*1*) of the induced polarization P_i of a BaTiO$_3$ single crystal and of the dielectric permittivity χ_{33} (*2*) derived from an experiment conducted at 1.5 kHz and (*3*) calculated from Eq. (7).

REFERENCES

1. E. A. Wood, R. C. Miller, and I. R. Remeika, Acta Crystallogr. **15** (12), 1273 (1962).
2. G. E. Shatalova and E. G. Fesenko, Kristallografiya **21**, 1207 (1976) [Sov. Phys. Crystallogr. **21**, 698 (1976)].
3. N. G. Leont'ev, R. V. Kolesova, O. E. Fesenko, and V. G. Smotrakov, Kristallografiya **29** (2), 398 (1984) [Sov. Phys. Crystallogr. **29**, 240 (1984)].
4. V. A. Shuvaeva, M. Yu. Antipin, S. V. Lindeman, *et al.*, Ferroelectrics **141**, 307 (1993).
5. A. V. Shuvaeva, M. Yu. Antipin, O. E. Fesenko, *et al.*, Kristallografiya **37** (4), 1033 (1992) [Sov. Phys. Crystallogr. **37**, 551 (1992)].
6. A. V. Leĭderman, I. N. Leont'ev, V. Yu. Topolov, and O. E. Fesenko, Fiz. Tverd. Tela (St. Petersburg) **40** (2), 327 (1998) [Phys. Solid State **40**, 299 (1998)].
7. O. E. Fesenko and V. S. Popov, Ferroelectrics **37**, 729 (1981).
8. J. P. Remeika, J. Am. Ceram. Soc. **76**, 940 (1954).
9. É. V. Bursian, *Barium Titanate Nonlinear Crystal* (Nauka, Moscow, 1974).
10. V. P. Dudkevich, I. N. Zakharchenko, V. S. Bondarenko, *et al.*, Kristallografiya **18** (5), 1095 (1973) [Sov. Phys. Crystallogr. **18**, 690 (1973)].
11. V. P. Dudkevich, I. N. Zakharchenko, A. N. Vas'kin, *et al.*, Kristallografiya **20** (1), 82 (1975) [Sov. Phys. Crystallogr. **20**, 45 (1975)].
12. V. P. Dudkevich, I. N. Zakharchenko, Yu. I. Golovko, *et al.*, Prace Fiz. (Polska) **8**, 70 (1980).
13. I. N. Zakharchenko, Candidate's Dissertation (Rostov-on-Don, 1978).
14. A. S. Sonin and B. A. Strukov, *Introduction to Ferroelectricity* (Vysshaya Shkola, Moscow, 1970).

Translated by G. Skrebtsov

Low-Temperature Raman Spectra of Hg$_2$(Br,I)$_2$ Mixed Crystals

Yu. F. Markov and E. M. Roginskiĭ

Ioffe Physicotechnical Institute, Russian Academy of Sciences, Politekhnicheskaya ul. 26, St. Petersburg, 194021 Russia
e-mail: Yu.Markov@pop.ioffe.rssi.ru
Received October 30, 2002

Abstract—Raman spectra of Hg$_2$(Br,I)$_2$ mixed crystals were studied. The spectra revealed multimode behavior of optical vibrations, which were assigned to the existence in these crystals of molecules of three types, namely, Hg$_2$Br$_2$, Hg$_2$I$_2$, and Hg$_2$BrI. The spectra exhibit a manifestation of phase transition effects associated with soft modes, the density of states of IR-active vibrational branches, and of nanoclusters, whose nucleation is induced by the Br–Hg–Hg–I dipole molecules. © *2003 MAIK "Nauka/Interperiodica".*

1. INTRODUCTION

The crystals of mercurous halides Hg$_2$*Hal*$_2$ (*Hal* = Cl, Br, I) have, at room temperature, a tetragonal body-centered D_{4h}^{17} structure with two linear molecules (formula units) per unit cell [1]. The molecules form linear chains along the $C_4(Z)$ axis in these crystals, which accounts for very strong anisotropy in their physical characteristics. They exhibit unique properties, among them record-high birefringence, a record-low sound velocity, and large acoustooptical constants [2]. For instance, Hg$_2$I$_2$ crystals are characterized by a record-low transverse sound (TA) velocity among solids, $V_{[110]}^{[1\bar{1}0]}$ = 254 m/s, a record-high birefringence, Δn = +1.5, and strong acoustooptical coupling (M_2 = 4284 × 10^{-18} CGSU for the TA wave) [2]. These crystals are widely used as principal components of polarizers, acoustic delay lines, acoustooptical filters, etc.

The interest aroused in these objects stems from their serving as model crystal systems in studies of general problems associated with structural phase transitions. The improper ferroelastic phase transitions $D_{4h}^{17} \longrightarrow D_{2h}^{17}$ (from the tetragonal to orthorhombic structure), which are driven by condensation of the slowest soft TA wave at the X point on the Brillouin zone edge and are accompanied by unit cell doubling and $X \longrightarrow \Gamma$ zone folding, were revealed in these crystals under cooling to T_c = 186 K (Hg$_2$Cl$_2$) and 144 K (Hg$_2$Br$_2$) [3]. We succeeded in achieving a phase transition in Hg$_2$I$_2$ crystals only at a high hydrostatic pressure (P_c = 9 kbar at T = 293 K) [4].

Recent years have witnessed an increased interest in lattice dynamics and phase transitions in mixed mercurous halides. In [5], Hg$_2$(Cl,Br)$_2$ was studied, and investigation of Hg$_2$(Cl,I)$_2$ [6] and Hg$_2$(Br,I)$_2$ [7] was begun. The present communication reports on a low-temperature (down to liquid-helium temperature) study of the

lattice dynamics and phase transition effects in mixed Hg$_2$(Br,I)$_2$ crystals by using Raman spectroscopy. The spectra were used to investigate the vibrational-mode behavior with concentration, phase transition effects, the influence of the anion sublattice disordering on the breaking of translational symmetry and selection rules in vibrational spectra, and the manifestation of symmetric (Hg$_2$Br$_2$, Hg$_2$I$_2$) and asymmetric (Hg$_2$BrI) mixed molecules in the vibration spectra and nanoclusters formed by them.

2. EXPERIMENTAL TECHNIQUE

Optical spectra were measured on a Dilor-Z24 triple Raman spectrometer with an argon (λ = 5145 Å) and a He–Ne (λ = 6328 Å) laser, whose power could be varied from a few tens to hundreds of milliwatts. The helium cryostats employed in low-temperature measurements were closed-cycle Cryogenics with good temperature stabilization (~0.1 K). The samples used in the measurements were 5 × 5 × 5-mm, (001)-cut Hg$_2$(Br,I)$_2$ single crystals cleaved along the (110) and ($1\bar{1}0$) planes and ground and polished properly.

3. EXPERIMENTAL RESULTS AND DISCUSSION

Figure 1 presents Raman spectra of pure starting Hg$_2$Br$_2$ and Hg$_2$I$_2$ single crystals of this solid solution. The spectra exhibit two lines (ν_1, ν_2) in the *XZ*(*YZ*) polarization (E_g symmetry) and two lines (ν_3, ν_4) in the *ZZ* polarization (A_{1g} symmetry), which is in agreement with group theory predictions. According to this theory, first-order Raman spectra of the Hg$_2$Br$_2$ and Hg$_2$I$_2$ crystals having tetragonal D_{4h}^{17} structure and one formula unit per primitive cell (four-atom linear molecule *Hal*–Hg–Hg–*Hal*) at room temperature involve four active vibrational modes, two of which are twofold-degenerate with E_g symmetry (*XZ,YZ*) and the other two are
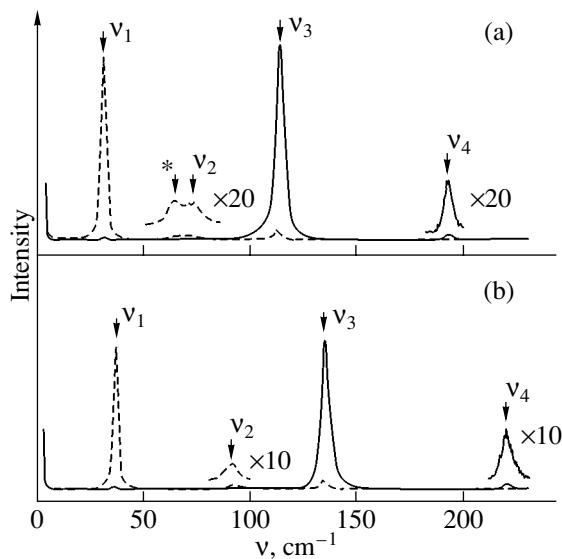
Fig. 1. Raman spectra of (a) Hg_2I_2 and (b) Hg_2Br_2 single crystals taken at room temperature. Dashed lines correspond to $XZ(YZ)$ polarization, and solid lines, to ZZ polarization. Star denotes the ν_1 overtone.
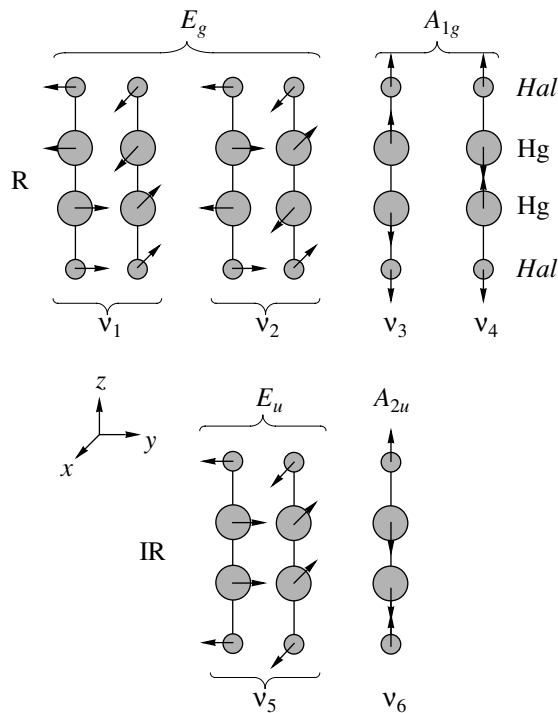
Fig. 2. Eigenvectors of vibrations in Hg_2Hal_2 crystals. R refers to Raman-active vibrations, and IR, to vibrations active in infrared absorption (reflection).

fully symmetric with A_{1g} symmetry ($XX + YY, ZZ$). (The parentheses enclose Raman-active polarizability components.) Figure 2 presents the eigenvectors of these vibrations. Note that the first vibration with E_g symme-

try is libration, i.e., rocking of the linear molecule as a whole about the horizontal axis X (or Y), denoted by ν_1. The second vibration with E_g symmetry is the bending zigzag vibration (ν_2). The fully symmetric A_{1g} stretch vibrational modes correspond primarily to Hg–Hg (ν_3) and Hal–Hg (ν_4) displacements. The odd vibrational modes with E_u (ν_5) and A_{2u} (ν_6) symmetry, corresponding to the halogen and mercury sublattices being displaced with respect to each other in the basal plane and along the Z axis, respectively, are allowed in IR spectra (Fig. 2).

X-ray structural measurements showed that, at room temperature, the $Hg_2(Br_{1-x}I_x)_2$ mixed crystals retain a tetragonal lattice similar to that of pure mercurous halides. They also retain cleavage along the {110} plane. Assuming the bromine and iodine atoms to be randomly distributed over the anion sublattice sites, the selection rules for the vibrational spectra of these mixed crystals should be the same as for pure starting crystals.

We studied Raman spectra of $Hg_2(Br_{1-x}I_x)_2$ mixed crystals of the following compositions: $x = 0$, 0.12, 0.18, 0.30, 0.50, 0.75, 0.90, and 1.0. The measurements were performed on these samples in different polarizations and low temperatures, from room to liquid-helium temperature, in steps of 50 K. Cooling was expected to considerably narrow the first-order lines in the spectra, quench second-order ones, and initiate the manifestation of phase transition effects.

Figure 3 displays low-frequency Raman spectra obtained at $T = 10$ K in the region of the librational mode ν_1 (E_g) and bending vibration ν_2 (E_g) in the allowed experimental geometries. Note that the librational lines are stronger and have a small halfwidth despite this vibration being intermolecular. The frequency of this vibration, ν_1, varies smoothly with concentration x and increases in going from Hg_2I_2 to Hg_2Br_2 ($x \longrightarrow 0$), while the halfwidth grows as one approaches medium concentrations. In this case, when only one line is present in the spectrum near ν_1 for all $Hg_2(Br_{1-x}I_x)_2$ mixed-crystal compositions ($0 \leq x \leq 1$), the spectra exhibit the so-called single-mode behavior. From the theoretical standpoint, the spectra of these molecular mixed crystals can be expected to behave in the single-, double-, and triple-mode manner, because these crystal systems allow the existence of molecules of three types: two types of symmetric pure molecules, Br–Hg–Hg–Br and I–Hg–Hg–I, and one type of asymmetric mixed molecules, Br–Hg–Hg–I and I–Hg–Hg–Br; the latter two cases are statistically not identical and should be counted twice by probability theory. The librational frequencies in pure starting crystals are similar (for instance, at $T = 10$ K, $\nu_1 = 32$ cm^{-1} for Hg_2I_2 and 38 cm^{-1} for Hg_2Br_2), and the dispersion of these lattice vibrations in the Brillouin zone is apparently sufficiently large. When the starting matrix Hg_2Br_2 (Hg_2I_2) is doped by the impurity component Hg_2I_2 (Hg_2Br_2),
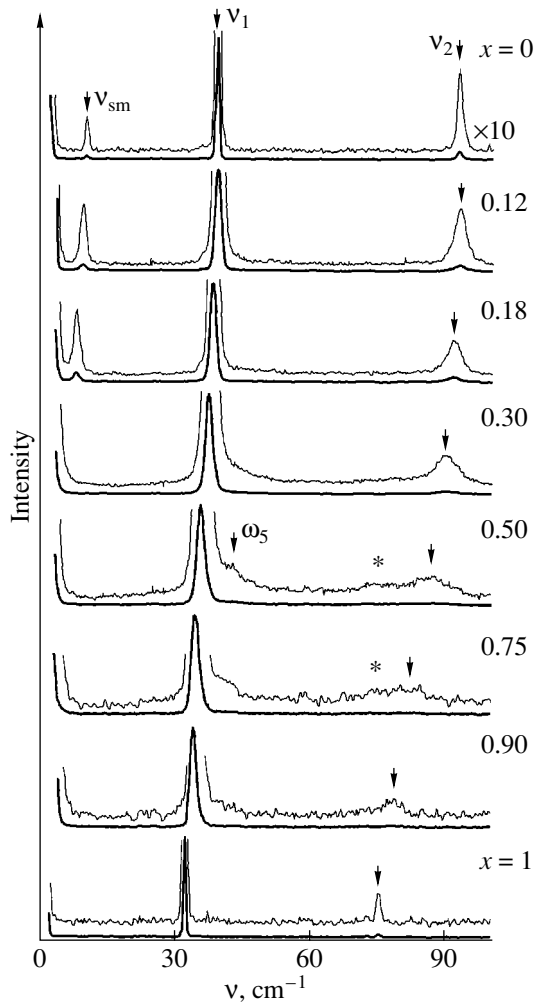
Fig. 3. Low-temperature (10 K), low-frequency Raman spectra of $Hg_2(Br_{1-x}I_x)_2$ mixed crystals in $XZ(YZ)$ polarization, the ν_2 vibrations are identified by an arrow, and the star refers to the overtone of the phonon branch corresponding to the ν_1 librational mode at the Brillouin zone center.
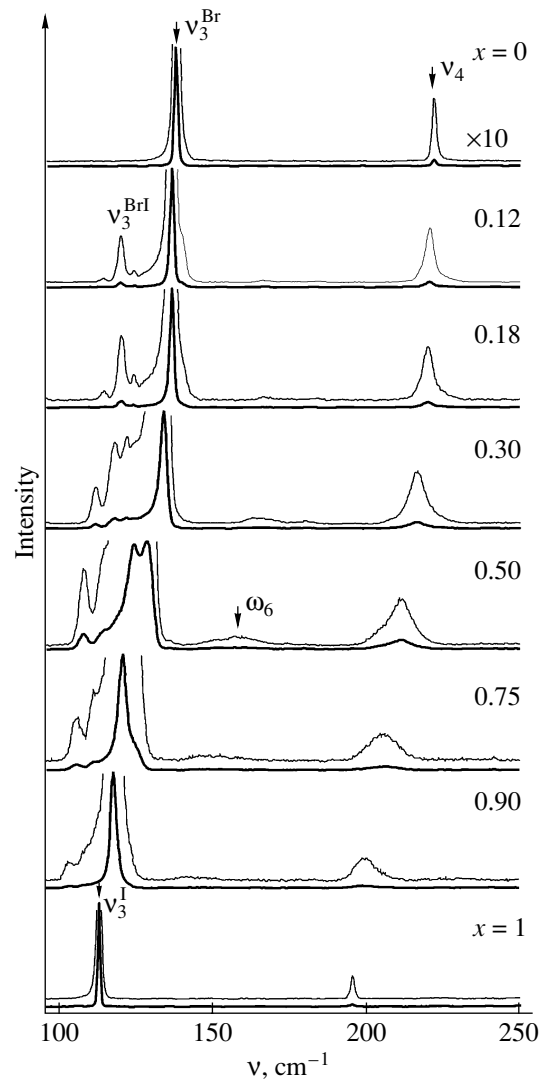

Fig. 4. High-frequency Raman spectra of $Hg_2(Br_{1-x}I_x)_2$ crystals taken in ZZ polarization at $T = 10$ K.

the frequencies of the impurity gap vibrations fall in the region of high density of librational and acoustic vibrational states and are no longer discernible. As a result, only vibrational modes of the starting matrix are observed experimentally. Thus, the single-mode behavior of the libration may be due to the frequencies ν_1 in pure starting crystal components being similar, to a noticeable dispersion of this vibration over the Brillouin zone, and to a high density of vibrational, including acoustic, states in this spectral region.

In the region of the bending vibration ν_2 in the $XZ(YZ)$ polarization, one observes a single weak broad line, whose frequency, halfwidth, and intensity depend strongly on concentration x. This line is also broadened somewhat in the pure starting components Hg_2Br_2 and Hg_2I_2, which should be attributed to the fairly strong anharmonicity of this vibration. Note that the halfwidth

of this line in pure components decreases by a few times under cooling from room to liquid-helium temperature, which supports the above interpretation. The frequency interval here is substantially larger than in the preceding case (at $T = 10$ K, we have $\nu_2 = 75$ and 92 cm^{-1} for the Hg_2I_2 and Hg_2Br_2 crystals, respectively), and the dispersion of this intramolecular vibrational branch in the Brillouin zone should be smaller than that of the intermolecular librational mode. However, as in the case of the ν_1 vibration, the ν_2 bend vibration exhibits a single-mode behavior in the spectra of $Hg_2(Br_{1-x}I_x)_2$ crystals.

Figure 4 presents Raman spectra obtained at a low temperature (10 K) in the region of fully symmetric A_{1g} stretch vibrations. The ν_4 vibration associated with the Hal–Hg displacement exhibits a strong concentration dependence on frequency and a considerable broaden-
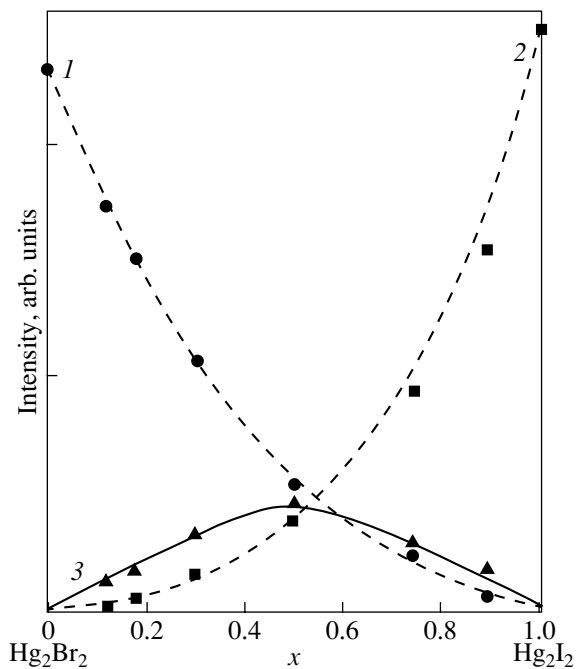
Fig. 5. Concentration dependences of integrated intensities of the Hg–Hg vibrations ν_3 in pure molecules (*1*) Hg_2Br_2, (*2*) Hg_2I_2, and (*3*) Hg_2BrI mixed molecules; the lines are drawn to guide the eye.

ing, including a slight asymmetry of this line at medium concentrations ($x = 0.5$). One observes here again only single-mode behavior, the reasons for which are apparently the same as in the two preceding cases.

The intramolecular stretch vibration ν_3, which is associated primarily with the Hg–Hg displacement, exhibits the most interesting and instructive behavior. At room temperature, a strong, asymmetric band appears in the spectra of the $Hg_2(Br_{1-x}I_x)_2$ mixed crystals in the ν_3 region; this band shifts gradually from $\nu_3 = 135$ cm^{-1} (Hg_2Br_2) to 113 cm^{-1} (Hg_2I_2), is broader than that of the pure starting compounds, particularly at medium concentrations, and has a complex structure [7]. At low temperatures (10 K, Fig. 4), in the Raman spectra of $Hg_2(Br_{1-x}I_x)_2$ mixed crystals close in composition to pure Hg_2Br_2, i.e., with x close to zero (for instance, $x = 0.12$ or 0.18), in the ν_3 region one can clearly see not only the above-mentioned strong ν_3^{Br} line, which shifts smoothly toward lower frequencies with increasing x and is associated with the Hg–Hg vibrations in the Br–Hg–Hg–Br molecules, but also a weak symmetric ν_3^{BrI} triplet on the low-frequency wing of this line, at about 120 cm^{-1}. This triplet is seen to consist of three narrow lines with halfwidths on the order of 3–4 cm^{-1}, its central component having an intensity nearly an order of magnitude higher than those of the side components. The intensity of the triplet grows with increasing x relative to that of the main

ν_3 line (see Figs. 4, 5), which appears reasonable if one assigns this triplet to Hg–Hg vibrations in Br–Hg–Hg–I mixed molecules. As one approaches medium concentrations of the $Hg_2(Br_{1-x}I_x)_2$ mixed crystals, for instance, compounds with $x = 0.3$ or 0.5, the intensities of the side components in this triplet grow anomalously fast, approaching that of the central component. In this process, all the lines of the triplet broaden noticeably and overlap partially to form a complex profile on the low-frequency wing of the main line ν_3. Note also that the ν_3 line in mixed crystals with $x = 0.5$ is already a clearly pronounced doublet with approximately equal component intensities; the high-frequency component originates from the Hg–Hg vibration in the Br–Hg–Hg–Br molecules (ν_3^{Br}), and the low-frequency one, from that in the I–Hg–Hg–I molecules (ν_3^{I}).

Figure 5 plots integrated intensities of the Hg–Hg stretch modes (ν_3) in pure Hg_2Br_2 (ν_3^{Br}) and Hg_2I_2 (ν_3^{I}) and in mixed molecules Hg_2BrI (ν_3^{BrI}) as functions of concentration. As x increases from zero to unity, the intensity of the ν_3^{Br} vibration drops sharply and the intensity of ν_3^{I} grows accordingly. The intensity of these vibrations in mixed molecules, ν_3^{BrI}, is a sum of the integrated triplet intensities and behaves differently by passing through a distinct maximum at medium concentrations near $x \approx 0.5$. Assuming the halogen atoms in $Hg_2(Br_{1-x}I_x)_2$ to be randomly distributed over the anion sublattices, the probability of formation of the Hg_2BrI molecules is proportional to $2x(1 - x)$; that of Hg_2I_2, to x^2; and that of Hg_2Br_2, to $(1 - x)^2$. The numerical values of the probability of formation of asymmetric Hg_2BrI molecules are 0.21 (for $x = 0.12$), 0.29 ($x = 0.18$), 0.42 ($x = 0.3$), 0.5 ($x = 0.5$), 0.37 ($x = 0.75$), and 0.18 ($x = 0.90$). The observed dependence of the total integrated intensity of this triplet on concentration correlates with the concentration dependence of the probability. The concentration dependences of the experimental integrated intensities for ν_3^{Br} and ν_3^{I}, which correspond to the Hg–Hg vibrations in the symmetric Br–Hg–Hg–Br and I–Hg–Hg–I molecules, behave as expected from theory. However, in order to quantitatively estimate the ratios of the integrated intensities of these vibrations in pure and mixed molecules, one has to assume slightly different oscillator strengths for the symmetric and asymmetric molecules.

The spectra of these mixed crystals also exhibited new weak lines which do not have counterparts in the Raman spectra of the pure starting components Hg_2Br_2 and Hg_2I_2. These broad lines, labeled in Figs. 3 and 4 by ω_5 and ω_6, lie in the high-frequency wing of the librational mode ν_1 and in the frequency interval 140–170 cm^{-1}, respectively. The frequencies of these lines are close to those of the IR-active modes ν_5 and ν_6,

which are forbidden in the Raman spectra of pure mercurous halides Hg_2Br_2 and Hg_2I_2. However, the random arrangement on the anion sublattice of mixed crystals and the corresponding violation of translational symmetry bring about a certain breakdown of the momentum selection rules, which entails the appearance of a density of states of IR-active vibrational branches in the Raman spectra, with the major contribution being due to vibrational states at the high-symmetry points on the Brillouin zone edge. Note also that the Raman spectra of asymmetric mixed molecules Br–Hg–Hg-I, which lack a center of symmetry, may exhibit the above-mentioned IR-active vibrations ν_5 and ν_6 (allowed on the molecular level).

Our earlier spectroscopic and x-ray studies of mixed $Hg_2(Br_{1-x}I_x)_2$ crystals [8], including a preliminary investigation of the phase transitions in them, showed that some of these crystals undergo ferroelastic transitions at real temperatures, while in others, only incipient transitions occur. In the first case, we have in mind the $Hg_2(Br_{1-x}I_x)_2$ mixed crystals with $x = 0$, 0.12, 0.18, and 0.30, whereas incipient transitions are expected to occur in the compounds with $x = 0.75$, 0.90, and 1.0. The phase transition in $Hg(Br_{0.5}I_{0.5})_2$ ($x = 0.5$) is strongly diffused and takes place within a limited temperature interval near 0 K. The Raman spectra of these mixed crystals in the vicinity of real phase transitions ($T < T_c$) should exhibit zone-edge-related odd vibrations (X point), more specifically, the acoustic and IR-active modes [3]. The most clearly pronounced is the rise in the intensity of the soft modes related generically to the slowest TA branches at the Brillouin zone X point, which is induced by unit-cell-content doubling and $X \longrightarrow \Gamma$ zone folding. Soft modes ν_{sm} of compounds with $x = 0$, 0.12, and 0.18 are seen to appear reliably in Raman spectra in the low-frequency region (a few cm^{-1}) (Fig. 3). Detection of the emergence of other odd vibrational branches at second-order phase transitions is an extremely difficult problem, even in the case of pure starting crystals, for instance, of Hg_2Br_2. In mixed crystals, this problem becomes still more complicated, because all spectral lines, including the emerging ones, are broadened and extend into the frequency region of density-of-states maxima of the vibrational modes (primarily at the zone-edge X point) that appear in the Raman spectra because of the breaking of translational symmetry.

Figure 6 shows concentration dependences of the vibration frequencies in these mixed crystals, some of which were obtained by simulating the spectral lines by oscillators. The vibrations ν_1, ν_2, and ν_4 are seen to follow single-mode behavior, in which the vibrations of one starting matrix transform smoothly into those of the other starting matrix, with the spectra having one line for each vibrational mode. The ν_3 vibration exhibits a complex multimode behavior, which is primarily due to its dispersion in the Brillouin zone being too small as compared to that of the other vibrational branches (see,
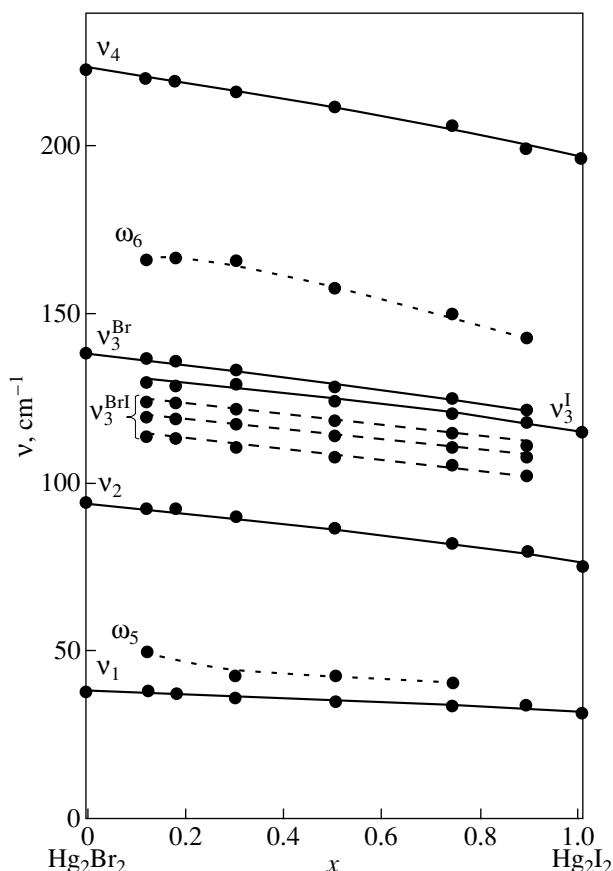
Fig. 6. Concentration dependences of vibration frequencies measured in $Hg_2(Br_{1-x}I_x)_2$ crystals at a low temperature (10 K). Circles are experiment; solid lines (drawn to guide the eye) relate to the ν_1, ν_2, ν_3^{Br}, ν_3^{I}, and ν_4 modes; and dashed and dotted lines (drawn to guide the eye) relate to concentration dependences of the ν_3^{BrI} triplet components and of the ω_5 and ω_6 frequencies related generically to the IR-active branches.

e.g., the case of Hg_2Cl_2 and Hg_2Br_2 in [9]). As already mentioned, the corresponding modes are denoted by ν_3^{Br} (Hg–Hg stretching vibration in the Hg_2Br_2 molecule), ν_3^{I} (Hg–Hg stretching vibration in the Hg_2I_2 molecule), and ν_3^{BrI} triplet (Hg–Hg vibrations in the Hg_2BrI mixed molecule). The concentration dependences of the Hg–Hg vibration frequencies (ν_3) in the symmetric molecules Hg_2Br_2 (ν_3^{Br}) and Hg_2I_2 (ν_3^{I}) are clearly pronounced. There is no ambiguity in the frequency behavior of the triplet as a function of concentration x, which originates from the Hg–Hg vibrations in asymmetric Hg_2BrI mixed molecules. The origin of the triplet is directly related to different nearest neighbor environments of the Hg_2BrI dipole molecule (along the linear chain):

Br–Hg–Hg–Br…**Br**–**Hg**–**Hg**–**I**…Br–Hg–Hg–Br, (1)

Br–Hg–Hg–Br…**Br**–**Hg**–**Hg**–**I**…Br–Hg–Hg–I, (2)

Br–Hg–Hg–Br…**Br**–**Hg**–**Hg**–**I**…I–Hg–Hg–Br. (3)

For low x, configuration (1) is the most probable, because the number of mixed molecules is still small, so that the nearest environment may consist only of pure symmetric (non-dipole) Hg_2Br_2 molecules. It is this configuration that accounts for the strongest central component of this triplet. The probabilities of the other two configurations, in which two neighboring asymmetric mixed molecules along the chain form a ferroelectric and an antiferroelectric local state (nanodomains), are considerably lower, and this is what accounts for the very weak intensity of the two satellites in this triplet. However, as x increases to approach the region of medium concentrations of these mixed crystals, the probability of formation of these nanodomains increases and approaches that of the first configuration, which manifests itself in the leveling off of all three triplet components in intensity (Fig. 4).

Figure 6 displays the concentration dependence of the frequencies of the maxima in the one-phonon density of states of IR-active vibrational branches (v_5 and v_6 at the center of the Brillouin zone) that appear in Raman spectra because of the breaking of translational symmetry and selection rules in momentum. The above IR-active vibrations, denoted in Figs. 3–5 by ω_5 and ω_6, exhibit single-mode behavior and a smooth dependence of the frequencies on concentration. In mixed crystals undergoing real phase transitions at $T < T_c$, these Raman lines should also become superposed by IR-active modes (at the Brillouin zone X point) that are induced by unit-cell-content doubling and $X \longrightarrow \Gamma$ zone folding; this effect can, however, be observed only in high-precision polarization measurements.

REFERENCES

1. R. J. Havighurst, J. Am. Chem. Soc. **48**, 2113 (1926).
2. *Proceedings of II International Symposium on Univalent Mercury Halides, Trutnov, CSSR* (1989).
3. Ch. Barta, A. A. Kaplyanskiĭ, V. V. Kulakov, *et al.*, Zh. Éksp. Teor. Fiz. **70** (4), 1429 (1976) [Sov. Phys. JETP **43**, 744 (1976)].
4. Ch. Barta, A. A. Kaplyanskiĭ, Yu. F. Markov, and V. Yu. Mirovitskiĭ, Fiz. Tverd. Tela (Leningrad) **27** (8), 2500 (1985) [Sov. Phys. Solid State **27**, 1497 (1985)].
5. Ch. Barta, G. F. Dobrzhanskiĭ, G. M. Zinger, *et al.*, Fiz. Tverd. Tela (Leningrad) **24** (10), 2952 (1982) [Sov. Phys. Solid State **24**, 1672 (1982)]; G. F. Dobrzhanskii, A. A. Kaplyanskii, M. F. Limonov, and Yu. F. Markov, Ferroelectrics **48**, 69 (1983).
6. G. M. Zinger, Yu. F. Markov, and V. V. Shabalin, Fiz. Tverd. Tela (Leningrad) **29** (12), 3620 (1987) [Sov. Phys. Solid State **29**, 2073 (1987)].
7. Yu. F. Markov and A. Sh. Turaev, Fiz. Tverd. Tela (St. Petersburg) **37** (7), 2133 (1995) [Phys. Solid State **37**, 1160 (1995)].
8. Yu. F. Markov, K. Knorr, and E. M. Roginskiĭ, Fiz. Tverd. Tela (St. Petersburg) **42** (5), 925 (2000) [Phys. Solid State **42**, 954 (2000)].
9. A. A. Kaplyanskiĭ, B. S. Zadokhin, M. F. Limonov, and Yu. F. Markov, Fiz. Tverd. Tela (Leningrad) **29** (1), 187 (1987) [Sov. Phys. Solid State **29**, 103 (1987)].

Translated by G. Skrebtsov

LATTICE DYNAMICS
AND PHASE TRANSITIONS

The Influence of Cation Impurities on Phase Transitions in the TlInS₂ Compound

R. M. Sardarly, O. A. Samedov, A. I. Nadzhafov, and I. Sh. Sadykhov

Institute for Radiation Problems, Academy of Sciences of Azerbaijan, Baku, 370143 Azerbaijan
e-mail: isadig@yahoo.com

Abstract—The temperature dependences of the permittivity of $TlInS_2$ crystals doped with 0.1 at. % Cr, Mn, Yb, Sm, Bi, or La are investigated, and the dependence of the phase transition temperature on the ion radius of the dopant impurity is determined. It is revealed that manganese and chromium substitute for indium in the $TlInS_2$ crystal lattice, whereas ytterbium, samarium, bismuth, and lanthanum ions occupy octahedral holes in an In_4S_{10} tetrahedral complex and, thus, produce an internal pressure responsible for the shift in the temperature of phase transitions toward the high-temperature range. © 2003 MAIK "Nauka/Interperiodica".

1. INTRODUCTION

As is known [1–4], $TlInS_2$ belongs to the small family of semiconductor compounds that undergo a sequence of phase transitions from an incommensurate phase to a ferroelectric phase. According to neutron diffraction and x-ray diffraction investigations [2, 5], the incommensurate phase observed in the temperature range $T_C = 201$ K $< T < T_i = 216$ K is characterized by the wave vector $k_i = (\delta, \delta, 0.25)$, where $\delta = 0.012$ is the incommensurability parameter. It should be noted that, in the temperature range of existence of the incommensurate phase, the dynamics of the phase transition is rather complex and very sensitive to structural defects.

The origin of the sequence of phase transitions occurring in the $TlInS_2$ compound with a layered structure has been the subject of many investigations. However, no unified concept has been offered for the mechanism of the phase transitions in this crystal. The situation is complicated by the fact that the temperature dependences of the permittivity $\varepsilon(T)$ measured for samples prepared from different batches differ significantly from one another. As was shown in our recent work [6], this feature is associated with the fact that $TlInS_2$ belongs to the class of berthollides, i.e., compounds characterized by a varying composition in the homogeneity region. Nonetheless, we can assert that the $TlInS_2$ compound of stoichiometric composition is an improper ferroelectric with an intermediate incommensurate phase. In particular, this means that, as the temperature decreases, the $TlInS_2$ compound undergoes the following sequence of phase transitions: (i) the transition from the initial paraelectric phase to the incommensurate phase at 216 K (according to Henkel *et al.* [7], the paraelectric phase has C_{2h}^6 symmetry); (ii) the transition from the incommensurate phase to the ferroelectric commensurate phase with the formation of a new incommensurability, which manifests itself as a specific feature in the dependence $\varepsilon(T)$ at 201 K; and (iii) the final phase transition to the commensurate phase upon further cooling [2].

The purpose of this work was to elucidate how cation impurities with different ion radii affect phase transitions that are incommensurate to the initial translation of the $TlInS_2$ lattice and to investigate the ferroelectric properties of doped $TlInS_2$ crystals.

2. EXPERIMENTAL TECHNIQUE

Single crystals of $TlInS_2$ doped with 0.1 at. % Cr, Mn, Yb, Sm, Bi, or La were grown using the Bridgman method.

The measurements were performed with samples $5 \times 2 \times 2$ mm in size. Since no anisotropy was observed in the (001) plane, the electrodes were applied to the surface of the crystals in the direction perpendicular to the layers. The contacts were prepared from a silver paste.
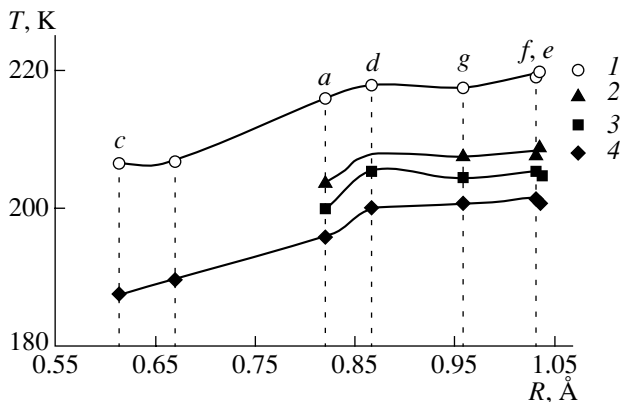
The temperature dependences of the permittivity were measured on an E7-12 alternating-current bridge at a frequency of 1 MHz with the use of a copper–constantan thermocouple at a rate of 0.1 K/min.

3. RESULTS

Figure 1 shows the temperature dependences of the permittivity $\varepsilon(T)$ measured for the studied samples during cooling in the temperature range 250–170 K. The anomalies observed in the temperature dependence $\varepsilon(T)$ for the $TlInS_2$ single crystal (curve *a*) indicate that this crystal undergoes a sequence of phase transitions at temperatures $T_{C1} = 196$ K, $T_{C2} = 200$ K, $T_{C3} = 204$ K, and $T_i = 216$ K. The dependences $\varepsilon(T)$ for $TlInS_2\langle Mn\rangle$ and $TlInS_2\langle Cr\rangle$ single crystals are represented by
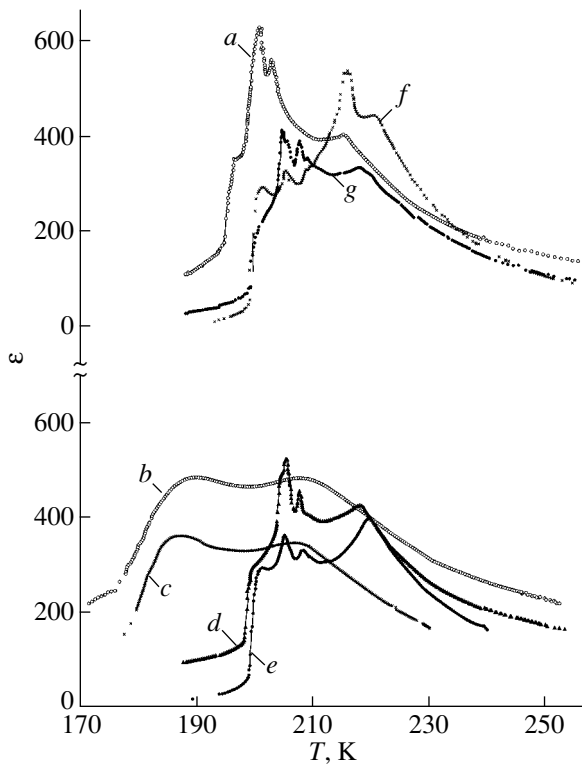
Fig. 1. Temperature dependences of the permittivity $\varepsilon(T)$ for different compositions: (*a*) $TlInS_2$, (*b*) $TlInS_2\langle Mn\rangle$, (*c*) $TlInS_2\langle Cr\rangle$, (*d*) $TlInS_2\langle Yb\rangle$, (*e*) $TlInS_2\langle Bi\rangle$, (*f*) $TlInS_2\langle La\rangle$, and (*g*) $TlInS_2\langle Sm\rangle$.

Fig. 2. Dependence of the temperature of the phase transition in the $TlInS_2$ crystal on the ion radius of the impurity: (*a*) In, (*b*) Mn, (*c*) Cr, (*d*) Yb, (*e*) Bi, (*f*) La, and (*g*) Sm. Curves *1–4* correspond to the shifts in the maxima of the temperature dependence of the permittivity $\varepsilon(T)$ on the impurity ion radius.

curves *b* and *c*, respectively. All the impurity ions used for doping of $TlInS_2$ are trivalent. The dependence of the temperature of the phase transition in the $TlInS_2$ compound on the ion radius of the dopant impurity is plotted in Fig. 2. The ion radii of manganese and chromium are smaller than the ion radius of indium ($R_{Cr} = $

0.615 Å, $R_{Mn} = 0.67$ Å, $R_{In} = 0.82$ Å). An examination of the dependences $\varepsilon(T)$ for these compositions (Fig. 1) revealed that the phase transitions are considerably smeared and shifted toward the low-temperature range. In both cases, the curves $\varepsilon(T)$ are characterized by two anomalies at temperatures $T_C = 189$ K and $T_i = 207.5$ K for the $TlInS_2\langle Cr\rangle$ single crystal and $T_C = 189.9$ K and $T_i = 207$ K for the $TlInS_2\langle Mn\rangle$ single crystal.

For $TlInS_2\langle Yb\rangle$, $TlInS_2\langle Bi\rangle$, $TlInS_2\langle La\rangle$, and $TlInS_2\langle Sm\rangle$ single crystals, the dependences $\varepsilon(T)$ are represented by curves *d*, *e*, *f*, and *g*, respectively (Fig. 1). In this case, the ion radii of ytterbium, samarium, bismuth, and lanthanum are larger than the ion radius of indium ($R_{Yb} = 0.868$ Å, $R_{Sm} = 0.958$ Å, $R_{Bi} = 1.03$ Å, $R_{La} = 1.032$ Å). It can be seen from Fig. 1 that these crystals undergo a sequence of phase transitions, as is the case with the initial compound $TlInS_2$. It is worth noting that the specific features in the curves $\varepsilon(T)$ and their shifts substantially depend on the ion radius of the relevant dopant. For convenience, the group of dopant impurities whose ion radii are smaller than the ion radius of indium will be designated by *A* (Cr, Mn) and the group of dopant impurities whose ion radii exceed the ion radius of indium will be denoted by *B* (Yb, Sm, La, Bi).

As can be seen from Fig. 2, an increase in the ion radius leads to an increase in the phase transition temperature. It should also be noted that, although the ion radii of bismuth and lanthanum are close in magnitude and the atomic weight of bismuth is approximately 1.5 times larger than that of lanthanum, the displacements ΔT of the phase transition temperatures for these impurities with respect to those for the $TlInS_2$ single crystal are nearly equal in magnitude (positions *e* and *f* in Fig. 2, respectively).

4. DISCUSSION

An analysis of the results presented in Fig. 2 demonstrates that the dopant impurities are not involved in thermal vibrations of atoms in the $TlInS_2$ crystal lattice, whose displacements are responsible for the occurrence of the phase transitions. The sole exception is the situation where the dopant impurities (in our case, lanthanum or bismuth ions) neither substitute for indium ions in lattice sites of the $TlInS_2$ crystal nor contribute to the soft mode. The curves $\varepsilon(T)$ for impurity atoms of group *B* are identical in shape. This suggests that ytterbium and samarium (like lanthanum and bismuth) do not substitute for indium in lattice sites of the $TlInS_2$ crystal structure.

In this respect, the question now arises as to where impurity atoms of group *B* can be located in the crystal lattice. As follows from the crystal chemical parameters, these atoms can occupy two types of possible positions in the $TlInS_2$ crystal structure (Fig. 3): (i) they can

substitute for In^{3+} cations in an InS_4 tetrahedron, and (ii) they can occupy interlayer cavities or octahedral holes between InS_4 tetrahedra inside an In_4S_{10} tetrahedral complex.

It is highly improbable that impurity ions of group *B* will substitute for indium ions in InS_4 tetrahedra. This stems from the fact that the radii of the former ions exceed the ion radius of indium. At the same time, impurity ions of group *B* could be located in interlayer cavities, because the spacing between layers in the $TlInS_2$ crystal structure is approximately equal to 3 Å. However, this situation is also unlikely; otherwise, impurity cations would not substantially affect the in-layer vibrations responsible for the observed dielectric dispersion.

Judging from the chemical bonding between impurity atoms of group *B*, the coordination numbers of these atoms in crystal structures of all known compounds should be equal to six or greater [8, 9]; i.e., impurities of this group can occupy octahedral holes inside an In_4S_{10} tetrahedral complex with a high probability (Fig. 3).

Moreover, Allakhverdiev *et al.* [10] investigated the effect of hydrostatic pressure on the behavior of the permittivity in the vicinity of the phase transitions occurring in $TlInS_2$ crystals. It was established that an increase in the pressure brings about an increase in the temperature of the phase transitions observed in the $TlInS_2$ compound. On this basis, it can be assumed that dopant impurities of group *B* occupy octahedral holes in the $TlInS_2$ crystal lattice and, owing to the large ion radii, produce an internal pressure, which leads to an increase in the temperature of the phase transitions, as is the case with hydrostatic pressure. It should be noted that an increase in the ion radius of dopant impurities of group *B* does not affect the curves $\varepsilon(T)$, which remain similar to the curve $\varepsilon(T)$ characteristic of pure $TlInS_2$ crystals and only shift toward the high-temperature range. Therefore, we can assert that impurity atoms of group *B* neither substitute for indium nor occupy lattice sites in the $TlInS_2$ crystal structure. Only in the case when the $TlInS_2$ crystal is doped with lanthanum does there appear an additional well-pronounced maximum at $T = 216$ K. However, the nature of this maximum is beyond the scope of the present work.

A different situation is observed upon doping of the $TlInS_2$ crystals with manganese and chromium (group *A*) (curves *b* and *c* in Fig. 1, respectively). For this group of dopant impurities, the temperature dependences of the permittivity $\varepsilon(T)$ of doped $TlInS_2$ exhibit a behavior typical of smeared phase transitions, whereas the phase transition temperatures decrease (positions *b* and *c* in curves *1, 4* in Fig. 2). These findings indicate that impurity atoms of group *A* substitute for indium in lattice sites of the $TlInS_2$ crystal structure (Fig. 3). This circumstance leads to a violation of the translational invariance and aperiodic damping of the soft mode.
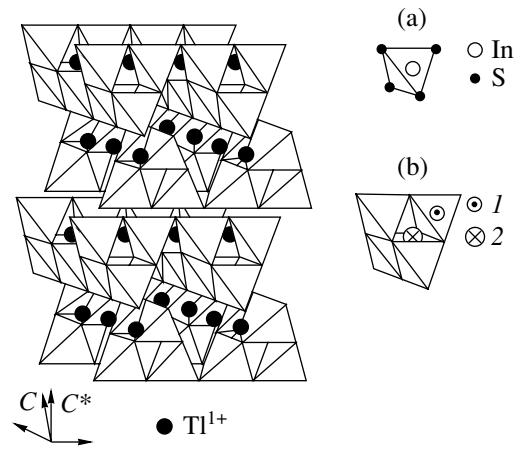
Fig. 3. Structure of the $TlInS_2$ crystal. (a) A fragment of the $TlInS_2$ crystal structure, namely, an InS_4 tetrahedron. (b) A fragment of the $TlInS_2$ crystal structure, namely, an In_4S_{10} tetrahedral complex (composed of four InS_4 tetrahedra) with impurities of groups (*1*) *A* and (*2*) *B* (octahedral holes). Designations: *C* is the crystallographic axis, and *C** is the pseudotetragonal axis of the crystal.

It is known that, during the growth of $TlInS_2$ crystals, even an insignificant deviation from the growth conditions results in a stoichiometry violation, which, as a rule, manifests itself in a metal deficit (Tl, In) [6, 8, 11]. The fluctuations of the vacancy density are nonuniformly distributed over the crystal bulk and can be considered intrinsic structural defects. There is no doubt that these fluctuations can lead to spontaneous dielectric dispersion and, consequently, a distortion of the phase diagram of the $TlInS_2$ compound with a layered structure. Earlier [6], we analyzed the influence of the aforementioned defects on the permittivity of the $TlInS_2$ crystal in the temperature range of the phase transitions. It turned out that, in this crystal, the intrinsic structural defects neither cause a shift in the phase transition temperatures nor affect the shape of the specific features observed in the curve $\varepsilon(T)$.

In our opinion, it is of interest that, irrespective of the ion radius of dopant impurities (Fig. 2), the temperature range of existence of the incommensurate phase does not change in magnitude and only shifts toward low and high temperatures for impurities of groups *A* and *B*, respectively. For clarity, the curves $\varepsilon(T)$ measured during heating are not shown in the figure. Investigations into the temperature dependences of the permittivity $\varepsilon(T)$ upon heating and cooling revealed that the hysteresis for $TlInS_2$ crystals doped with impurities of group *A* is more pronounced than that for $TlInS_2$ crystals doped with impurities of group *B*.

Lebedev *et al.* [12] determined the generalized susceptibility of the system in the incommensurate phase with point frozen defects interacting with the phase of the order parameter in the case when the phase at the defect site is governed primarily by the field of this defect (strong pinning). According to the authors' esti-

mates [12], strong pinning universally takes place at temperatures close to T_i in the presence of defects with a component of the random-field type. This range proved to be very large for systems with displacive phase transitions. A completely different situation occurs with defects that have no component of the random-field type due to their high symmetry. In this case, the defect is characterized only by a component of the random-anisotropy type and weak pinning should be observed.

The results of our investigations are in agreement with the inferences made by Lebedev *et al.* [12]. Atoms of group *A* substitute for indium in lattice sites of the TlInS$_2$ crystal structure and, thus, induce local random fields. According to [12], this should lead to strong pinning, which is observed in the experiments. Atoms of group *B* occupy octahedral holes (i.e., positions of higher symmetry) and can be treated as defects responsible for random anisotropy. This means that the condition of weak pinning is satisfied.

REFERENCES

1. A. A. Volkov, Yu. G. Goncharov, G. V. Kozlov, *et al.*, Fiz. Tverd. Tela (Leningrad) **25** (12), 3583 (1983) [Sov. Phys. Solid State **25**, 2061 (1983)].

2. S. B. Vakhrushev, V. V. Zhdanova, B. E. Kvyatkovskiĭ, *et al.*, Pis'ma Zh. Éksp. Teor. Fiz. **39** (6), 245 (1984) [JETP Lett. **39**, 291 (1984)].

3. R. A. Aliev, K. R. Allakhverdiev, A. I. Baranov, *et al.*, Fiz. Tverd. Tela (Leningrad) **26** (5), 1271 (1984) [Sov. Phys. Solid State **26**, 775 (1984)].

4. R. A. Suleĭmanov, M. Yu. Seidov, F. M. Salaev, and F. A. Mikailov, Fiz. Tverd. Tela (St. Petersburg) **35** (2), 348 (1993) [Phys. Solid State **35**, 177 (1993)].

5. A. U. Sheleg, O. B. Plyushch, and V. A. Aliev, Fiz. Tverd. Tela (St. Petersburg) **36** (1), 226 (1994) [Phys. Solid State **36**, 124 (1994)].

6. R. M. Sardarly, O. A. Samedov, I. Sh. Sadykhov, *et al.*, Izv. Nats. Akad. Nauk Azerb., Ser. Fiz.–Mat. Tekh. Nauk **22** (2), 31 (2002).

7. W. Henkel, H. V. Hochheimer, C. Carlone, *et al.*, Phys. Rev. B **26**, 3211 (1982).

8. S. G. Abdullaeva, S. S. Abdinbekov, and G. D. Guseĭnov, Dokl. Akad. Nauk AzSSR **36** (8), 34 (1980).

9. G. G. Guseĭnov, V. A. Gasymov, and T. S. Mamedov, Preprint No. 25, IF AN AzSSR (Inst. of Physics, Academy of Sciences of Azerbaijan, Baku, 1980).

10. K. R. Allakhverdiev, A. I. Baranov, T. G. Mamedov, *et al.*, Fiz. Tverd. Tela (Leningrad) **30** (6), 1751 (1988) [Sov. Phys. Solid State **30**, 1007 (1988)].

11. B. R. Gadzhiev, M. Yu. Seidov, and V. R. Abdurakhmanov, Fiz. Tverd. Tela (St. Petersburg) **38** (1), 3 (1996) [Phys. Solid State **38**, 1 (1996)].

12. N. I. Lebedev, A. P. Levanyuk, and A. S. Sigov, Zh. Éksp. Teor. Fiz. **92** (1), 248 (1987) [Sov. Phys. JETP **65**, 140 (1987)].

Translated by O. Borovik-Romanova

LOW-DIMENSIONAL SYSTEMS AND SURFACE PHYSICS

Localization of Nonlinear Waves between Interfaces

I. V. Gerasimchuk* and A. S. Kovalev**

* Institute of Theoretical Physics, Kharkov Physicotechnical Institute, National Scientific Center, Kharkov, 61108 Ukraine
e-mail: igera@ukr.net
** Verkin Institute for Low-Temperature Physics and Engineering, National Academy of Sciences of Ukraine,
pr. Lenina 47, Kharkov, 61103 Ukraine
e-mail: kovalev@ilt.kharkov.ua
Received June 18, 2002

Abstract—Stationary localized states of nonlinear waves propagating in a focusing medium along two plane-parallel interfaces repulsing the wave flux are investigated analytically. It is established that the nonlinear wave beam can be localized in the region between these interfaces. © 2003 MAIK "Nauka/Interperiodica".

1. INTRODUCTION

In recent years, particular emphasis has been placed on theoretical and experimental investigations into the spatial localization of high-power nonlinear waves in periodic (layered and modulated) systems in the direction perpendicular to the direction of their propagation [1–3]. In our previous work [4], we studied the spatial localization of nonlinear wave fluxes in layered media under the condition of propagation of a nonlinear wave beam in anharmonic medium along a system of two identical narrow plane-parallel layers playing the role of waveguides "attracting" the waves. For this purpose, we proposed a new analytical method of analyzing the problem, which was reduced to a model of coupled anharmonic oscillators. Under the assumption that the waveguides and the medium between them are nonlinear and differ in refractive indices, we derived discrete nonlinear dynamic equations describing the wave amplitudes in waveguides and demonstrated the possibility of localizing a nonlinear wave flux in one of the waveguides. The problem under consideration is closely related to nonlinear optics, because numerical and natural experiments on this problem have been intensively performed precisely in this field of the physics of real systems and systems of parallel optical waveguides have been used as optical switches in existing devices [5–8].

In this paper, we examine an opposite limiting case when a nonlinear wave flux is localized predominantly in the region between the defect planes repulsing the nonlinear wave and, thus, simulating the behavior of interfaces between optical media. However, in this case, the description of the system in terms of the field amplitudes at isolated interfaces becomes inconsistent and a theoretical treatment of the formulated problem does not lead to a system of coupled anharmonic oscillators. We demonstrated that, when a nonlinear wave propagates in a focusing medium along a system of two parallel thin layers repulsing the wave, the wave flux can be localized in the region between these plane-parallel interfaces.

2. ANALYTICAL TREATMENT OF THE FORMULATED PROBLEM

Let us consider a nonlinear focusing medium with two plane-parallel thin layers that exhibit linear properties differing from those of the surrounding matrix and are located perpendicularly to the z axis at a distance $2a$ from each other, which substantially exceeds their thickness (Fig. 1). We assume that, in this system, a nonlinear monochromatic wave propagates along the parallel defect layers (along the x axis) and the envelope $E(z, t)$ of this wave depends on the time and the transverse coordinate. An equation describing the envelope
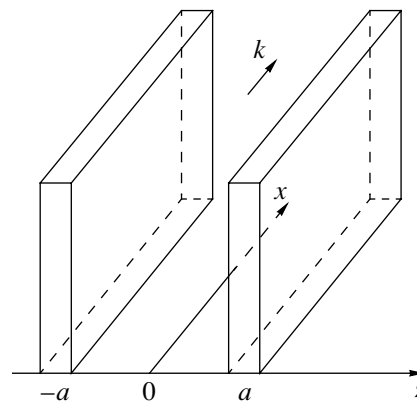
Fig. 1. System of two plane-parallel defect planes (interfaces).

$E(z, t)$ can be represented by a standard Schrödinger equation with two δ-function perturbations:

$$i\frac{\partial E}{\partial t} + \frac{\partial^2 E}{\partial z^2} + 2|E|^2 E = \lambda[\delta(z + a) + \delta(z - a)]E. \quad (1)$$

Here, it is assumed that the parameter λ is positive ($\lambda > 0$); i.e., the defect layers repulse the wave flux and play the role of interfaces between the optical media (see, for example, [9]).

The Lagrangian density corresponding to relationship (1) has the following form:

$$L = \frac{i}{2}\left(E^*\frac{\partial E}{\partial t} - E\frac{\partial E^*}{\partial t}\right) - \left|\frac{\partial E}{\partial z}\right|^2 + |E|^4 \quad (2)$$
$$- \lambda[\delta(z + a) + \delta(z - a)]|E|^2.$$

The problem is to solve the homogeneous equation (1) in the region outside the isolated layers with the boundary conditions (at $z = \mp a$)

$$E|_{\mp a - 0} = E|_{\mp a + 0}, \quad (3)$$

$$\left.\frac{\partial E}{\partial z}\right|_{\mp a + 0} - \left.\frac{\partial E}{\partial z}\right|_{\mp a - 0} = \lambda E|_{\mp a} \quad (4)$$

and zero asymptotics at infinity ($z \longrightarrow \pm\infty$). For this system, we will restrict our consideration to the special case of spatially localized stationary states described by the equation

$$E(z, t) = E(z)\exp(-i\omega t) \quad (5)$$

and will not analyze nonstationary phenomena.

It can easily be shown that, in this case, the function $E(z)$ for spatially localized states should be chosen to be real. Indeed, from Eq. (1) and boundary conditions (3) and (4) for the complex function $E(z) = A(z)\exp[i\varphi(z)]$, it follows that

$$\frac{d\varphi}{dz} = \frac{C}{A^2(z)},$$

where C is a constant and the phase φ and its derivative $d\varphi/dz$ are continuous at $z = \mp a$. It follows from the equation for the function $A(z)$ and the condition of its decrease when $z \longrightarrow \pm\infty$ that $C = 0$ outside the interfaces and, consequently (from the condition of continuity of the derivative $d\varphi/dz$ at $z = \mp a$), $C = 0$ between them, i.e., $\varphi = $ const.

The purpose of this work was to elucidate how the nonlinearity of the medium affects the localization of the wave beam in a system of two plane-parallel interfaces repulsing the wave. In this system, the wave flux can be localized between the interfaces. The symmetric solutions to the system of equations (1)–(5) in the

regions $z < -a$ (I), $z > a$ (II), and $-a < z < a$ (III) have the following form:

$$E_{I, II}(z) = \frac{\varepsilon}{\cosh[\varepsilon(z \mp z_0)]}, \quad (6)$$
$$E_{III}(z) = q\eta\, cn(\eta z, q).$$

Here, $\varepsilon = \sqrt{-\omega}$ is the parameter characterizing the wave amplitude, ω is the frequency, $cn(p, q)$ is the Jacobian elliptic function with the module $q(q' = \sqrt{1 - q^2})$, and $\eta = \varepsilon/\sqrt{2q^2 - 1}$. The elliptic module q varies in the range from $1/\sqrt{2}$ to 1, and the state localized between the interfaces corresponds to values of $z_0 > -a$. Solution (6) is one-parametric and is completely specified by the parameter ε. The parameters q and z_0 can be expressed in terms of ε through the boundary conditions at $z = \mp a$.

As in our recent paper [4], it is appropriate to introduce the field amplitude $U = E(z = \mp a)$ in defect planes, even though, in this case, it does not correspond to a maximum in the density of the wave flux. Then, from the boundary conditions (3) and (4) and the definition of the field amplitude U, we can deduce three relationships between the parameters ε, q, z_0, and U:

$$U = \varepsilon\, sech[\varepsilon(a + z_0)] = q\eta\, cn(\eta\alpha, q), \quad (7)$$

$$\sqrt{q^2 q'^2 \eta^4 + \varepsilon^2 U^2 - U^4} - U\sqrt{\varepsilon^2 - U^2} = \lambda U. \quad (8)$$

From these relationships in the limit $q \longrightarrow 1$ ($q' \ll 1$), it follows that the module q and the frequency of the solution (the parameter ε) are related by the expression

$$q'^2 \approx \frac{4\lambda(\lambda + 2\varepsilon)}{\varepsilon^2}\exp(-2\varepsilon a). \quad (9)$$

As a result, we obtain the inequality $\varepsilon a \gg 1$. In [4], this inequality corresponds to a weak coupling between the plane-parallel defect layers. Since the inequality $q' \ll 1$ holds in the case under consideration, the propagating flux has a typical soliton profile, that is,

$$E_{III}(z) \approx \frac{\varepsilon}{\cosh(\varepsilon z)} \quad (10)$$

and the width of the localized flux is considerably less than the distance between the interfaces: $\Delta \sim 1/\varepsilon \ll a$. The interaction of the localized wave with repulsing boundaries is exponentially small: $E(a)/E(0) \sim \exp(-\varepsilon a)$.

Using the definition of the total power of the wave flux

$$N = \int_{-\infty}^{+\infty} |E|^2 dz, \qquad (11)$$

we can obtain the dependence of the quantity N on the frequency ε, which is characteristic of solitons and has the following form:

$$N \approx 2\varepsilon. \qquad (12)$$

It should be noted that the relationships $q' \ll 1$ and $\Delta \ll a$, which correspond to a large distance from the localized flux to the interfaces, also hold for frequencies $\varepsilon \cong \lambda/2$ ($\varepsilon = \lambda/2$ corresponds to the frequency of the wave localized in the vicinity of the isolated defect plane in a linear medium [9]).

Another limiting case, namely, $z_0 = -a$ with frequencies ω close to the band edge of linear waves, corresponds to the module q somewhat exceeding $1/\sqrt{2}$:

$$q_c^2 \approx \frac{1}{2} + \frac{K^2(1/\sqrt{2})}{8\lambda^2 a^2}, \qquad (13)$$

where $K(q)$ is the complete elliptic integral of the first kind.

In this limit, the solution in the central region has the form

$$E_{III}(z) \approx \frac{K(1/\sqrt{2})}{\sqrt{2}a} \mathrm{cn}\left[\frac{K(1/\sqrt{2})z}{a}, 1/\sqrt{2}\right], \qquad (14)$$

and the frequency of the flux is determined by the critical parameter ε_c as follows:

$$\varepsilon_c \approx \frac{K^2(1/\sqrt{2})}{2\lambda} \frac{1}{a^2}. \qquad (15)$$

In the case when the distance between the defect planes is large ($2a \gg 1$), we have $\varepsilon_c \ll 1$; i.e., the critical frequency is close to the band edge of linear waves.

It follows from the form of solutions (14) and (15) that the flux, as before, is localized predominantly in the region between the planar repulsing interfaces, because the amplitude at the center of the flux $E(0) \sim 1/a$ is considerably larger than the field at the interfaces $E(a) \sim 1/a^2$. However, in this case, the characteristic width of the wave flux, according to relationship (14), has the same order of magnitude as the distance between the interfaces: $\Delta \sim a$.

At the critical point $\varepsilon = \varepsilon_c$, the solution changes: additional maxima of the amplitude appear in regions I and II; i.e., the wave flux escapes from the region
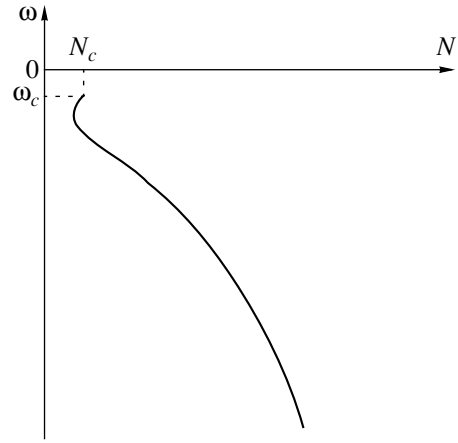

Fig. 2. Dependence $\omega(N)$ for a state localized between the interfaces in a nonlinear focusing medium.

between the defect planes repulsing the wave. Earlier [9], we proved that the solutions with two maxima on different sides of this interface are unstable. On this basis, we can assume that these states are unstable with respect to the escape of the wave flux from the system of the interfaces. Thus, we will not discuss these additional solutions.

The total power of the wave flux at the critical point can be determined from the relationship

$$N_c \approx \frac{K(1/\sqrt{2})}{\sqrt{2}a} \frac{dK(1/\sqrt{2})}{dq}, \qquad (16)$$

and the dependence $\varepsilon(N)$ in the vicinity of this point can be represented by the expression

$$\varepsilon - \varepsilon_c \approx -A\frac{N - N_c}{a^3} + B(N - N_c)^2 a^2, \qquad (17)$$

where

$$A \approx \frac{K^2(1/\sqrt{2})}{4\lambda^3}, \quad B \approx \frac{\lambda}{4K^2(1/\sqrt{2})}. \qquad (18)$$

An analysis of relationship (17) demonstrates that a rapid variation in the dependence $\varepsilon(N)$ occurs in a narrow region in the vicinity of the critical point $\Delta N \sim 1/a^5 \ll 1$. Figure 2 shows this dependence over the entire range of the variation in the frequency with due regard for asymptotics (12) and (17).

3. CONCLUSION

Thus, the analytical treatment performed in this work demonstrated that a nonlinear wave beam propagating in a focusing medium can be localized between the plane-parallel interfaces repulsing the nonlinear wave.

REFERENCES

1. A. B. Aceves, C. de Angelis, T. Peschel, *et al.*, Phys. Rev. E **53** (1), 1172 (1996).

2. H. S. Eisenberg, Y. Silberberg, R. Morandotti, *et al.*, Phys. Rev. Lett. **81** (16), 3383 (1998).

3. U. Peschel, R. Morandotti, J. S. Aitchison, *et al.*, Appl. Phys. Lett. **75** (10), 1348 (1999).

4. I. V. Gerasimchuk and A. S. Kovalev, Fiz. Nizk. Temp. **26** (8), 799 (2000) [Low Temp. Phys. **26**, 586 (2000)].

5. L. Thylen, E. M. Wright, G. I. Stegeman, and C. T. Seaton, Opt. Lett. **11** (11), 739 (1986).

6. S. Wabnitz, E. M. Wright, C. T. Seaton, and G. I. Stegeman, Appl. Phys. Lett. **49** (14), 838 (1986).

7. Y. Silberberg and G. I. Stegeman, Appl. Phys. Lett. **50** (13), 801 (1987).

8. D. R. Heatley, E. M. Wright, and G. I. Stegeman, Appl. Phys. Lett. **53** (3), 172 (1988).

9. M. M. Bogdan, I. V. Gerasimchuk, and A. S. Kovalev, Fiz. Nizk. Temp. **23** (2), 197 (1997) [Low Temp. Phys. **23**, 145 (1997)].

Translated by O. Moskalev

Exciton Polaritons and Their One-Dimensional Localization in Disordered Quantum-Well Structures

V. A. Kosobukin

Ioffe Physicotechnical Institute, Russian Academy of Sciences, Politekhnicheskaya ul. 26, St. Petersburg, 194021 Russia
e-mail: Vladimir.Kosobukin@mail.ioffe.ru
Received September 24, 2002

Abstract—A theory of the Anderson localization of light in randomly arranged ultrathin layers (quantum wells) uniform in lateral dimensions and possessing intrinsic optical resonances is put forward. To solve the multiple-scattering problem, a model of layers with a δ-function resonance dielectric polarization is proposed. The model is an electromagnetic counterpart of the electronic model of zero-radius potentials. Interlayer disorder is included under the assumption of a low average concentration of identical layers in order to calculate analytically the one- and two-photon characteristics of electromagnetic-radiation transport, in particular, the average energy density and the Anderson localization length of light. The analysis is carried out for a structure with randomly distributed quantum wells in which quasi-two-dimensional excitons of different quantum wells are in resonance while their wave functions do not overlap. It is shown that the average electromagnetic field propagates through this disordered structure in the form of polaritons but are produced in exciton reemission between quantum wells. The localization length of light in the polariton spectral region decreases substantially, because the scattering (reflection) of light by individual quantum wells grows near the excitonic resonance. © 2003 MAIK "Nauka/Interperiodica".

1. INTRODUCTION

Radiation energy transport, light localization phenomena, and the related spectroscopic effects have aroused considerable interest in the optics of disordered systems [1]. Of particular importance are the properties of dielectric media that are nonuniform in one dimension; in such media, a perturbation in uniformity can give rise either to the Anderson localization of light, if the perturbation is of a random nature [1], or to a photonic band gap, if the perturbation is strictly periodic [1, 2]. In both cases, electromagnetic waves of certain frequencies are attenuated exponentially and cannot propagate in the system, which becomes manifest in a strong reflection from the sample (disappearance of transmission) [1, 2].The similarity between the spectral features of these two phenomena reveals the importance of both independent and comparative studies of photon localization in one-dimensionally disordered systems [3] and of photonic band gaps in periodic structures (Bragg semiconductor [4] and dielectric [5] nanostructures, photonic crystals [2, 3]). The Anderson localization of photons also has considerable application potential; indeed, it underlies the development of multilayer broad-band optical reflectors, filters, etc. [6].

Theoretical studies of one-dimensional localization of light have been made primarily for nonabsorbing multilayer systems with random thicknesses of uniform layers and/or distances between them [7–12]. Those studies related to one-dimensionally disordered systems, which are, on the average, uniform [7–10] or periodic [5, 12]. In contrast to electron [13, 14], acoustic [15], and other scalar waves, electromagnetic waves are polarized, and their character changes substantially in interaction with resonance states of the medium. Both these factors are capable of affecting photon localization noticeably, which is important in controlling the localization process. Resonance light localization in the conditions of non-one-dimensional disorder was investigated in the spectral regions of excitons [16], bulk exciton polaritons [17], and surface plasmon polaritons [18]. No systematic study of resonance light localization has apparently been made in one-dimensionally disordered systems (see [11]).

In this paper, we report on a theoretical investigation of the spectral features of optical localization in systems made up of randomly arranged layers (quantum wells) which are laterally uniform and possess quasi-two-dimensional optical excitations. The main results are obtained using the model of δ-function exciton polarization of the layers. The results include prediction of the electromagnetic field in a disordered quantum-well system having a polariton structure and calculation of the length of the Anderson resonance polariton localization. The model of δ-function exciton polarization in one-dimensionally disordered quantum-well structures is described in Section 2. Section 3 formulates equations for the theory of multiple light scattering in terms of this model, and Section 4 discusses the propagation characteristics of mean-field polaritons. Section 5 puts forward a general theory of propagation and one-dimensional localization of exciton polaritons, and Section 6 deals with resonance features of the localization.

2. MODEL OF RESONANCE QUANTUM-WELL POLARIZATION

The model with a potential in the form of δ-function scatterers [13] is considered to be the most informative for electrons. In this section, we formulate a similar model of electromagnetic scatterers (quantum wells) with theirs dielectric polarization modeled by δ-function contributions. The possibility of describing multiple quantum wells in terms of such a model is supported by the following considerations: (i) the potential-well width under carrier confinement conditions is small compared to the light wavelength, (ii) the induced polarization fields of different quantum wells do not overlap, and (iii) the optically observable quantities (coefficients of reflection, transmission, etc.) are expressed in theory [4, 19–22] through parameters obtained by spatial averaging of the characteristics of a low-dimensional exciton. These parameters depend only weakly on fine features in the exciton polarization distribution and are usually assumed to be phenomenological in the treatment of experimental data.

Next, we study the propagation of light waves in a medium (with a background dielectric permittivity ε_b) containing a disordered quantum-well structure. The wells are perpendicular to the z axis and are stacked in a random manner along this axis. We consider waves with linear polarization s having only one electric-field component $\mathbf{E} = E \cdot \mathbf{e}_y$, where $\mathbf{e}_y$ is the unit vector of the Cartesian axis y. Following [19–21], we introduce a constitutive relation for the Fourier components of induced dielectric polarization $\mathbf{P} = P \cdot \mathbf{e}_y$ of laterally uniform quantum wells:

$$4\pi k_0^2 P(z; \kappa, \omega) = 2k \sum_{n=1}^{N} \chi_n^{(0)}(\omega)\delta(z - z_n)E(z; \kappa, \omega), \quad (1)$$

where $\chi_n^{(0)}(\omega)$ is the susceptibility tensor component of the nth quantum well, $k_0 = \omega/c$, ω is the frequency, c is the velocity of light in vacuum, $z = z_n$ is the median quantum-well plane, and N is the number of wells. In Eq. (1), $\kappa = \sqrt{\varepsilon_b} k_0 \sin\theta$ is the tangential component of the wave vector of a monochromatic wave of the form $E(\mathbf{r}, t) = E(z; \kappa, \omega)\exp(i\kappa x - i\omega t)$ and θ is the angle of incidence.

In view of Eq. (1), Maxwell's equations for the electric field $E(z)$ and the Green's function $G(z, z')$ for an s-polarized wave take the form

$$\left[\frac{d^2}{dz^2} + k^2 + 2k\sum_{n=1}^{N}\chi_n^{(0)}(\omega)\delta(z - z_n)\right] \quad (2)$$
$$\times \{E(z; \kappa, \omega), G(z, z'; \kappa, \omega)\} = \{0, -\delta(z - z')\},$$

where $k = \sqrt{\varepsilon_b k_0^2 - \kappa^2}$. For $z = z_n$, we use the boundary conditions

$$E(z_n^+) = E(z_n^-), \quad \frac{dE}{dz}\Big|_{z_n^+} - \frac{dE}{dz}\Big|_{z_n^-} = -2k\chi_n^{(0)}E(z_n) \quad (3)$$

for the field $E(z)$ and the same conditions in z for the Green's function $G(z, z')$, where $z_n^\pm = z_n \pm 0$ (here and in what follows, the parameter κ is not specified in an explicit form).

In the absence of quantum wells ($\chi_n^{(0)} = 0$), we obtain from Eq. (2) the equations

$$\left(\frac{d^2}{dz^2} + k^2\right)\{E^{(0)}(z), G^{(0)}(z - z')\} = \{0, -\delta(z - z')\}. \quad (4)$$

The second of Eqs. (4) can be solved to yield the one-photon Green's function $G^{(0)}(z - z') = i/(2k)\exp(ik|z - z'|)$ for a uniform medium. In view of Eq. (4), Eq. (2) can be recast in the equivalent forms

$$E(z) - E^{(0)}(z) = 2k\sum_{n=1}^{N} G^{(0)}(z - z_n)\chi_n^{(0)}E(z_n)$$
$$= 2k\sum_{n=1}^{N} G^{(0)}(z - z_n)\chi_n E^{(0)}(z_n), \quad (5)$$

where $\chi_n = \chi_n^{(0)}/(1 - i\chi_n^{(0)})$. As follows from Eq. (2) or (5), the field between the nth and $(n + 1)$th wells ($z_n < z < z_{n+1}$) can be written as

$$E(z) = A_n\exp[ik(z - \tilde{z}_n)] + B_n\exp[-ik(z - \tilde{z}_n)] \quad (6)$$

(the corresponding amplitudes on the left of the well with $n = 1$ are A_0 and B_0). The coordinate $\tilde{z}_n = (z_{n+1} + z_n)/2$ inside the structure defines the position of the right-hand boundary of the region in to which the nth Wigner–Seitz cell of the superlattice transforms when the latter becomes disordered.

The amplitudes of field (6) to the right and to the left of the nth well are related through the transfer matrix $\hat{\Lambda}(n)$ defined by

$$\begin{pmatrix} A_n \\ B_n \end{pmatrix} = \hat{\Lambda}(n)\begin{pmatrix} A_{n-1} \\ B_{n-1} \end{pmatrix}. \quad (7)$$

Equations (5) and (6) yield

$$\hat{\Lambda}(n) = \frac{1}{t_n}\begin{pmatrix} (t_n^2 - r_n^2)\exp(i\Theta_n) & r_n\exp(i\Psi_n) \\ -r_n\exp(-i\Psi_n) & \exp(-i\Theta_n) \end{pmatrix}, \quad (8)$$

where $\Theta_n = k(z_{n+1} - z_{n-1})/2$ and $\Psi_n = k(z_{n+1} - 2z_n + z_{n-1})/2$. The coefficients of reflection $r_n = i\chi_n$ and transmission $t_n = 1 + r_n = 1 + i\chi_n$ are derived from Eqs. (2)

and (3) for the single nth well centered in the $z = 0$ plane.

To reveal the physical meaning of the model introduced by phenomenological expression (1), we use the results of microscopic theory [19–21]. For a quasi-two-dimensional exciton of the nth quantum well with excitation frequency $\bar{\omega}_n$, we introduce in Eqs. (1) and (5) the exciton susceptibility component

$$\chi_n^{(0)}(\omega) = \frac{\Gamma_n/\cos\theta}{\bar{\omega}_n - \omega - i\gamma},$$

which manifests itself in s-polarized light. Going to the second equality in Eq. (5), we obtain

$$\chi_n(\omega) = \frac{\Gamma_n/\cos\theta}{\omega_n - \omega - i(\gamma + \Gamma_n/\cos\theta)}. \quad (9)$$

The frequency $\bar{\omega}_n$ takes into account size quantization of the carriers and their Coulomb interaction, and ω_n also includes the radiative shift; γ and $\Gamma_n/\cos\theta$ are the rates of nonradiative and radiative exciton decay, respectively, with Γ_n being independent of θ [20, 21]. Taking into account Eq. (9), the light reflection and transmission coefficients in the transfer matrix (8) can be written as

$$r_n(\omega) = \frac{i\Gamma_n/\cos\theta}{\omega_n - \omega - i(\gamma + \Gamma_n/\cos\theta)},$$

$$t_n(\omega) = \frac{\omega_n - \omega - i\gamma}{\omega_n - \omega - i(\gamma + \Gamma_n/\cos\theta)}. \quad (10)$$

If the quantum wells are identical, one can use Eqs. (9) and (10) with the notation

$$\chi_n = \chi, \quad r_n = r, \quad t_n = t, \quad \omega_n = \omega_0, \quad \Gamma_n = \Gamma_0. \quad (11)$$

If such wells make up a superlattice with a period d, then $z_n = dn$ and matrix (8) for an individual quantum well assumes the form

$$\hat{\Lambda} = \frac{1}{t}\begin{pmatrix} (t^2 - r^2)e^{ikd} & r \\ -r & e^{-ikd} \end{pmatrix}. \quad (12)$$

The quantities in Eqs. (10) and (12), derived from Eqs. (1) and (9), define the observable characteristics of electromagnetic-radiation transport. Expressions (10) and (12) are identical to the corresponding expressions from microscopic theory [21, 22] derived for quasi-two-dimensional excitons by using a nonlocal constitutive relation in place of Eq. (1) [19, 20]. This means that, from the standpoint of description of light propagation in multiple quantum wells, the above-formulated phenomenological theory is equivalent to the microscopic models proposed in [19–22]. Application of Eqs. (1)–(3) with a two-component susceptibility and boundary conditions differing from Eqs. (3) to the case of p-polarized waves leads one to the same conclusions;

the expressions for the quantities χ, r, and t thus obtained differ from Eqs. (9) and (10) in the presence of two excitonic resonances [21].

The electromagnetic equations (2) and (3) coincide formally with the Schrödinger equation for electrons in the one-dimensional model of δ-function potentials [13]. The properties of optical scatterers are, however, considerably more complicated than those of electron scatterers; indeed, the susceptibilities of Eq. (9) depend on frequency and are always complex, because the radiative-decay parameter Γ_n, which is a measure of exciton–photon coupling, cannot be arbitrarily small. The absence of electronic counterparts to the optical scatterers limits the applicability of the comparatively simple methods of the theory of one-dimensional electron scattering [13, 14], in particular, those that use time-reversal symmetry, to the optical problem. In developing an analytical theory of localization, we invoke a self-consistent diagrammatic technique [23] that has been applied to one-dimensional systems in some studies [10, 11, 15].

3. MULTIPLE-SCATTERING PROBLEM

The present theory of multiple scattering will be based on the one-photon Green's function $G(z, z')$, which is a solution to the second equation in (2). For a disordered quantum-well structure, an integral equation that is equivalent to this differential equation can be expressed in terms of the Green's functions

$$G(q, q') = \int_{-\infty}^{\infty}\int_{-\infty}^{\infty} dz\,dz'\, G(z, z')\exp(-iqz + iq'z') \quad (13)$$

in the wave-number (q, q') representation.

Following [10, 11, 15], we obtain from Eq. (4) [or Eq. (2) with $\chi_n^{(0)} = 0$] the following expression for the one-photon Green's function for a uniform medium:

$$G^{(0)}(q, q') = 2\pi\delta(q - q')G^{(0)}(q),$$
$$G^{(0)}(q) = (q^2 - k^2 - i0)^{-1}, \quad (14)$$

where $k = k(\omega)$. In the case of a single nth quantum well located at $z_n = 0$, the one-photon Green's function is found to be

$$G^{(n)}(q, q') = G^{(0)}(q)[2\pi\delta(q - q') - 2ikr_nG^{(0)}(q')]. \quad (15)$$

The elements of the T matrix defined by the integral relation [11, 15]

$$G^{(n)}(q, q')$$
$$= 2\pi\delta(q - q')G^{(0)}(q) + G^{(0)}(q)T_n(q, q')G^{(0)}(q') \quad (16)$$

can be found from Eq. (15) to be

$$T_n(q, q') = -2ikr_n = 2k\chi_n. \quad (17)$$

Significantly, the matrix elements of Eq. (17) do not depend on q and q', because each quantum-well provides a δ-function contribution to the polarization in Eq. (1).

Note that, with Eq. (17), the optical theorem for scattering from the nth quantum well can be written as

$$\operatorname{Im} T_n(k, k) = \frac{1}{4k}(|T_n(k, k)|^2 + |T_n(-k, k)|^2) + kA_n, \quad (18)$$

which formally coincides with that for the model of thick scattering layers [10, 11]. In Eq. (18), the quantity

$$A_n = 1 - |r_n|^2 - |t_n|^2 = -2(\operatorname{Re} r_n + |r_n|^2) \quad (19)$$

denotes the absorptivity of the quantum well.

In terms of the multiple-scattering theory [24], the one-photon Green's function for a quantum-well structure can be described by the integral equation

$$G(q, q') = G^{(0)}(q)\left[2\pi\delta(q - q') \right.$$
$$\left. + \sum_{n=1}^{N} \int \frac{dq''}{2\pi} T_n(q, q'') e^{-i(q - q'')z_n} G(q'', q') \right]. \quad (20)$$

This equation is valid for structures with an arbitrary one-dimensional (linear) quantum-well concentration $\nu = N/L$ ($N \gg 1$, L is the sample thickness); note that, in general, both the susceptibilities $\{\chi_n\}$ and the quantum-well positions $\{z_n\}$ can be random quantities. We restrict ourselves subsequently to the case of "dilute" structures with $\nu/k \ll 1$ ($2\pi/k$ is the light wavelength), which precede the formation of photonic crystals and short-period superlattices as ν is increased.

4. MEAN-FIELD POLARITON STRUCTURE

To address the problem of light propagation with Eq. (20), we simplify the model by assuming the quantum wells to be identical; in this case, in accordance with Eq. (11), the quantities T_n in Eqs. (17)–(20) are no longer dependent on the quantum-well index n. The quantum-well coordinates $\{z_n\}$ are randomly distributed along the z axis of the structure with a uniform average concentration ν (the average well separation is $1/\nu$). In an unlimited medium ($N \longrightarrow \infty$), the averaged one-photon Green's function $\langle G(z - z')\rangle$ is translation invariant (the angle brackets denote averaging over uncorrelated quantum-well positions $\{z_n\}$). The Fourier transform of $\langle G(z - z')\rangle$ satisfies the condition

$$\langle G(q, q')\rangle = 2\pi\delta(q - q')\langle G(q)\rangle. \quad (21)$$

In the lowest approximation in the concentration $\nu \ll k$, Eq. (20) yields

$$\langle G(q)\rangle = 1/(q^2 - k^2 - \Sigma(q)),$$
$$\Sigma(q) = \nu T(q, q) = -2ik\nu r. \quad (22)$$

Taking the inverse Fourier transform of the averaged one-photon function (21) and using Eq. (22), we obtain

$$\langle G(z - z')\rangle = \frac{i}{2\bar{k}} \exp(i\bar{k}|z - z'|), \quad (23)$$

which has the same form as the solution to Eq. (4) for a uniform medium. In Eq. (23),

$$\bar{k}(\omega) = \sqrt{k^2 - 2ik\nu r} \approx k - i\nu r \quad (24)$$

is a complex characteristic of propagation of the mean field (23) excited by an external polarization in the $z = z'$ plane. Substituting $r(\omega)$ given by Eq. (10) in to Eq. (24), we find

$$\operatorname{Re}\bar{k}(\omega) = k\left(1 + \frac{\nu}{k} \frac{(\omega_0 - \omega)\Gamma_0/\cos\theta}{(\omega - \omega_0)^2 + (\gamma + \Gamma_0/\cos\theta)^2} \right), \quad (25)$$

$$\operatorname{Im}\bar{k}(\omega) = \nu \frac{(\gamma + \Gamma_0/\cos\theta)\Gamma_0/\cos\theta}{(\omega - \omega_0)^2 + (\gamma + \Gamma_0/\cos\theta)^2}. \quad (26)$$

Equation (25) is the dispersion relation of the averaged s-polarized electromagnetic wave, and Eq. (26) is the effective attenuation of this wave in the disordered quantum-well structure. It is essential that wave (23) decays in space ($\operatorname{Im}\bar{k}(\omega) \neq 0$) even in the absence of dissipative exciton decay, i.e., for $\gamma \longrightarrow 0$. This property reflects attenuation (extinction) of the average light flux $|\langle G(z)\rangle|^2$ over the length scale $\sim 1/(2\operatorname{Im}\bar{k}(\omega))$, caused by light scattering from randomly arranged layers. Because of the low scatterer concentration ($\nu \ll k$), quantities (25) and (26) satisfy the weak-decay condition $\operatorname{Im}\bar{k}(\omega)/|\operatorname{Re}\bar{k}(\omega)| \sim \nu/k \ll 1$.

Figure 1 plots the values of $\operatorname{Re}\bar{k}(\omega)$ and $2\operatorname{Im}\bar{k}(\omega)$ calculated from Eqs. (25) and (26), respectively. Near the exciton frequency ω_0, the dispersion curves acquire a pattern typical of polaritons. As in superlattices [22], the polariton effect in our disordered structure, which is uniform on the average, originates from interaction of the electromagnetic wave with quasi-two-dimensional excitons of various wells having the same frequency ω_0. According to Eqs. (25) and (26), this effect is determined, for $\theta = 0$, by the exciton–photon coupling parameter $(\nu/k)\Gamma_0/(\gamma + \Gamma_0)$, where $\Gamma_0/(\gamma + \Gamma_0) < 1$ and $\nu/k \ll 1$. The polariton effect reaches the maximum value $\max_{\omega}[\operatorname{Re}\bar{k}(\omega)/k(\omega) - 1] = (\nu/k)\Gamma_0/[2(\gamma + \Gamma_0)] \leq (1/2)(\nu/k)$ at $\omega = \omega_0 \pm (\gamma + \Gamma_0)$.

5. CALCULATION OF THE ANDERSON LOCALIZATION LENGTH OF LIGHT

Now, we consider multiple electromagnetic-wave scattering in the above disordered quantum-well structure and calculate the Anderson localization length following [10, 11, 23]. Let the electromagnetic field be excited at the instant $t = 0^+$ by a source of current (polar-

ization) of the type $\sim \mathbf{e}_y \delta(z) \delta(t - 0^+)$. Each monochromatic field component of frequency ω undergoes one-dimensional multiple elastic scattering from the disordered chain of quantum wells (the frequency ω lies in the continuum in the absence of scatterers). We further follow wave propagation along the z axis, i.e., at an angle $\theta = 0$, conditions under which there is no difference between the s and p polarizations. The distribution of excitation energy in space and time

$$W(t, z) = \int \frac{d\omega}{2\pi} W_\omega(t, z)$$

$$= \int \frac{d\omega}{2\pi} \int \frac{d\Omega dQ}{(2\pi)^2} \exp(-i\Omega t + iQz) w_\omega(\Omega, Q) \tag{27}$$

is determined by the spectral density

$$w_\omega(\Omega, Q) = \int \frac{dq dq'}{(2\pi)^2} K_\omega(q, q')$$

$$= \iint \frac{dq dq'}{(2\pi)^2} \frac{1}{L} \langle G_{\omega_+}(q_+, q'_+) G^*_{\omega_-}(q_-, q'_-) \rangle. \tag{28}$$

Here, $G_\omega(q, q')$ is the one-photon Green's function (20), $K_\omega(q, q')$ is the two-photon Green's function averaged over the well positions $\{z_n\}$, and

$$\omega_\pm = \omega \pm \Omega/2, \quad q_\pm = q \pm Q/2. \tag{29}$$

The Anderson localization results from the constructive interference of waves passing, in propagating in opposite directions, through the same set of randomly arranged scatterers [1]. When excitation of frequency ω is localized, the energy density entering Eq. (27) satisfies the condition

$$\lim_{t \to \infty} W_\omega(t, z) \sim \exp\{-|z|/\xi(\omega)\}, \tag{30}$$

where $\xi(\omega)$ is the localization length. Whence follows one of the criteria of Anderson localization [13]: for $t \longrightarrow \infty$, the quantity $W_\omega(t, z = 0)$ in Eq. (30) should be finite, which is equivalent to the condition of finiteness of the Fourier transform $-i\Omega w_\omega(\Omega, z = 0)$ in the limit $\Omega \longrightarrow 0$ [25].

Let us now calculate the Anderson photon localization length in the quantum-well structure using the self-consistent diagrammatic technique [23]. Based on Eq. (20), we assume, as before, that the well concentration is low ($v/k \ll 1$) and that the system is, on the average, translation invariant. Since the general solution to a similar problem for layered media is given elsewhere [10, 11], we limit ourselves here to a brief formulation of the results obtained.
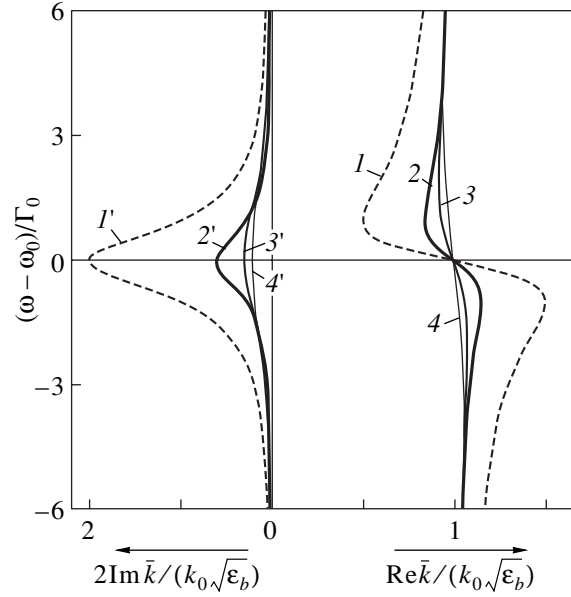
Fig. 1. Dimensionless dispersion relation $\mathrm{Re}\,\bar{k}\,(\omega)/(k_0\sqrt{\varepsilon_b})$ (curves *1–4*) and attenuation parameter $2\,\mathrm{Im}\,\bar{k}\,(\omega)/(k_0\sqrt{\varepsilon_b})$ (curves *1'–4'*) of electromagnetic waves plotted vs. $(\omega - \omega_0)/\Gamma_0$ for $\theta = 0$. The calculation was performed using Eqs. (25) and (26) for the following values of the parameters $\{v/(k_0\sqrt{\varepsilon_b}); \gamma/\Gamma_0\}$: (*1, 1'*) 1, 0; (*2, 2'*) 0.3, 0; (*3, 3'*) 0.3, 1; and (*4, 4'*) 0.3, 2.

The averaged two-photon Green's function $K_\omega(q, q')$ entering Eq. (28) satisfies the Bethe–Salpeter equation

$$K_\omega(q, q') = \langle G_{\omega_+}(q_+) \rangle \langle G^*_{\omega_-}(q_-) \rangle$$

$$\times \left[2\pi\delta(q - q') + \int \frac{dq''}{2\pi} U_\omega(q, q'') K_\omega(q'', q') \right], \tag{31}$$

where $U_\omega(q, q')$ is the irreducible vertex part. Equation (31) was formulated with due account of expressions (21) and (22). We define the quantities

$$F_m(\omega; \Omega, Q) = \int \frac{dq dq'}{(2\pi)^2} q^m K_\omega(q, q') \tag{32}$$

with $m = 0$ and 1, the first of which, $F_0(\omega; \Omega, Q) = w_\omega(\Omega, Q)$, is the Fourier transform of energy density, and the second, $F_1(\omega; \Omega, Q)$ is that of the energy flux. We use Eqs. (29), (31), and (32) to find coupled equations to the lowest orders in spatial, Q, and temporal, Ω, spectral variables:

$$\Omega F_0 - Q \frac{c^2}{\varepsilon_b \omega} F_1 = \frac{i}{2\bar{k}'} \frac{c^2}{\varepsilon_b \omega}, \tag{33}$$

$$Q F_0 - \frac{i}{2(\bar{k}')^3} (J[U] - I[\Sigma]) F_1 = 0. \tag{34}$$

To stress the polariton character of propagation, we specified here the variable $\bar{k}' \equiv \mathrm{Re}\,\bar{k}\,(\omega)$ with $\theta = 0$ from Eq. (25) in the explicit form and introduced the notation

$$I[\Sigma] = \int \frac{dq}{2\pi} q^2 \Delta\Sigma_\omega(q)\Delta\langle G_\omega(q)\rangle$$
$$\approx -2\nu\bar{k}'\,\mathrm{Im}\,T_\omega(\bar{k}', \bar{k}'), \tag{35}$$

$$J[U] = \int \frac{dq}{2\pi}\int \frac{dq'}{2\pi} q\Delta\langle G_\omega(q)\rangle U_\omega(q, q')\Delta\langle G_\omega(q')\rangle q', \tag{36}$$

where

$$\Delta\langle G_\omega(q)\rangle = \langle G_{\omega_+}(q_+)\rangle - \langle G_{\omega_-}^*(q_-)\rangle, \tag{37}$$

$$\Delta\Sigma(q) = \Sigma_{\omega_+}(q_+) - \Sigma_{\omega_-}^*(q_-) \approx 2i\,\mathrm{Im}\,\Sigma_\omega(q). \tag{38}$$

In deriving Eq. (34), we also used the identity

$$\int \frac{dq}{2\pi}\Delta\langle G_\omega(q)\rangle$$
$$\times \left[\Delta\Sigma_\omega(q) - \int \frac{dq'}{2\pi} U_\omega(q, q')\Delta\langle G_\omega(q')\rangle\right] = 0.$$

Equations (33) and (34) for function F_0 can be employed to find the expression

$$w_\omega(\Omega, Q) = \frac{1}{2\bar{k}'} \frac{c^2}{\varepsilon_b \omega}\left(\frac{1}{-i\Omega + DQ^2}\right), \tag{39}$$

which is the (Ω, Q) Fourier transform of the solution to the diffusion equation. The diffusion coefficient

$$D = 2(\bar{k}')^3 \frac{c^2}{\varepsilon_b \omega} \frac{1}{J[U] - I[\Sigma]} \tag{40}$$

is determined by functions Σ and U, with the first of them being defined by Eq. (22).

To lowest order $\nu/k \ll 1$, the irreducible vertex part in the case of identical quantum wells can be written as

$$U_\omega^B(q, q') = \nu T_{\omega_+}(q_+, q'_+) T_{\omega_-}^*(q_-, q'_-), \tag{41}$$

with the quantity $T_\omega(q, q')$ being given by Eq. (17) with the reflection coefficient $r_n = r(\omega)$. Expression (41) was obtained by summing the ladder diagrams, i.e., in the Boltzmann approximation, which takes into account incoherent scattering [11, 15, 23]. With Eqs. (35)–(38) and (41), Eq. (40) reduces to

$$D^B = \frac{1}{2\nu} \frac{c}{\sqrt{\varepsilon_b}} \frac{1}{|\mathrm{Re}\,r|} \tag{42}$$

(here and subsequently, we keep in mind that $\bar{k}' \approx k$). Function (39), with Eq. (42) substituted for D, possesses the property that $-i\Omega w_\omega(\Omega, Q) \longrightarrow 0$ for $\Omega \longrightarrow 0$. According to the localization criterion introduced above, there is no localization in the Boltzmann

approximation and an electromagnetic excitation spreads diffusively along the z axis of the structure, this process being characterized by coefficient (42).

In the case of Anderson localization, the wave propagation differs in character from the diffusive pattern because of constructive interference described by maximally crossed (fan) diagrams [11, 15, 23]. In the case of weak absorption (under the assumption of time reversal invariance), summation of these diagrams yields a correction,

$$\Delta U_\omega(q, q') = 8\frac{k^3 c^2}{\omega\varepsilon_b} \frac{\nu^2(\mathrm{Re}\,r)^2}{-i\Omega + D^B(q + q')^2}, \tag{43}$$

to the quantity U^B. Function (43) has a singularity for $\Omega \longrightarrow 0$ if $q \approx -q'$, which implies that backscattering is a preferred process. In these conditions, substituting $U^B + \Delta U$ for U in Eq. (40) yields the relation

$$\frac{1}{D} = \frac{1}{D^B} + \frac{1}{2\omega^2} \frac{c}{\sqrt{\varepsilon_b}} J[\Delta U]. \tag{44}$$

As in [11, 15, 23], we use a self-consistent approach to the problem, for which purpose we replace the diffusion coefficient D^B in Eq. (43) [and, therefore, in the integral $J[\Delta U]$ in Eq. (44)] by the exact value D. Setting the limit of integration over $P = q + q'$ in $J[\Delta U]$ to be equal to P_m, we obtain the following equation for the diffusion coefficient D:

$$D + \frac{2}{\pi} \frac{c}{\sqrt{\varepsilon_b}} \sqrt{\frac{iD}{\Omega}}\arctan\left(P_m \sqrt{\frac{iD}{\Omega}}\right) = D^B. \tag{45}$$

This equation can be solved to lowest order in Ω to yield

$$D(\omega) = -i\Omega\xi^2(\omega). \tag{46}$$

With Eq. (46), the Fourier transform $w_\omega(\Omega, z) \sim (-i\Omega\xi)^{-1}\exp(-|z|/\xi)$ of Eq. (39) over Q provides finiteness of the quantity $-i\Omega w_\omega(\Omega, z = 0)$ in the limit $\Omega \longrightarrow 0$. Hence, the localization criterion is now met and the quantity $\xi(\omega)$ is the Anderson photon localization length. The dimensionless localization length $X = \xi P_m$ satisfies the equation

$$X\arctan(X) = \frac{\pi}{2} \frac{\sqrt{\varepsilon_b}D^B}{c} P_m, \tag{47}$$

which follows from Eq. (45) under substitution of Eq. (46). It appears natural to assume that P_m is equal, in order of magnitude, to the inverse hydrodynamic length; i.e., $P_m = 1/l_D$, where

$$l_D = \frac{\sqrt{\varepsilon_b}D^B}{c} = \frac{1}{2\nu|\mathrm{Re}\,r|}. \tag{48}$$

Now, the solution to Eq. (47) takes on the form

$$\xi \approx 1.567 l_D \approx \frac{0.78}{\nu |\operatorname{Re} r|}. \tag{49}$$

In the next section, we discuss the frequency spectrum of the localization lengths (49).

6. SPECIFIC FEATURES OF RESONANCE LOCALIZATION OF LIGHT

The right-hand part of Eq. (49) can depend on frequency in a resonance manner through the reflectivity $r(\omega) = i\chi(\omega)$. The presence of random scatterers exhibiting resonance is an important feature of the electromagnetic model (1); one-electron δ-function potentials are energy-independent. Another essential feature of the photonic model consists in the finite rate of spontaneous decay of an optical excitation, as a result of which the response function $\chi(\omega)$ is complex and limited. We shall discuss the resonance photon localization effects for the $\chi(\omega)$ models corresponding to quasi-two-dimensional excitons and Lorentzian oscillators.

6.1. Exciton Polaritons

Using the exciton response function (9), Eq. (49) for the one-dimensional photon localization length in a disordered quantum-well sequence can be written as

$$\xi(\omega) = \frac{0.78}{\nu} \frac{(\omega - \omega_0)^2 + (\gamma + \Gamma_0)^2}{\Gamma_0(\gamma + \Gamma_0)}. \tag{50}$$

The localization length (50) is comparable to the extinction length $1/2\operatorname{Im}\bar{k}(\omega) = 1/2\nu|\operatorname{Re} r|$ in Eq. (26) and to the hydrodynamic length l_D in Eq. (48), with all the three lengths having the same frequency dependence (50).

We take the value of the radiative decay rate Γ_0 entering Eq. (9) as an energy scale (the vanishing of this parameter has no physical meaning, because this would entail disappearance of optical effects). To control the exciton resonance width in quantum-well structures, one can conveniently take the nonradiative exciton decay parameter γ, which, unlike Γ_0, varies within a broad range with variation of the sample temperature. Figure 2 shows the general behavior of the $1/|\operatorname{Re} r(\omega)|$ function for a quantum well (expressed in terms of dimensionless variables):

$$|\operatorname{Re} r|^{-1} = (1 + g)^{-1}[x^2 + (1 + g)^2], \tag{51}$$

where $x = (\omega - \omega_0)/\Gamma_0$ and $g = \gamma/\Gamma_0$. According to Eq. (50), far from the resonance, i.e., for $|\omega - \omega_0|/\Gamma_0 \gg 1$, the localization length $\xi(\omega) \approx (1/\nu)(\omega - \omega_0)^2/[\Gamma_0(\gamma + \Gamma_0)]$ substantially exceeds the average separation between the scatterers $1/\nu$. The function $\xi(\omega)$ reaches a minimum in the polariton region, to decrease at resonance ($\omega = \omega_0$) to $\xi(\omega_0) \approx (1/\nu)(1 + \gamma/\Gamma_0)$. As seen from
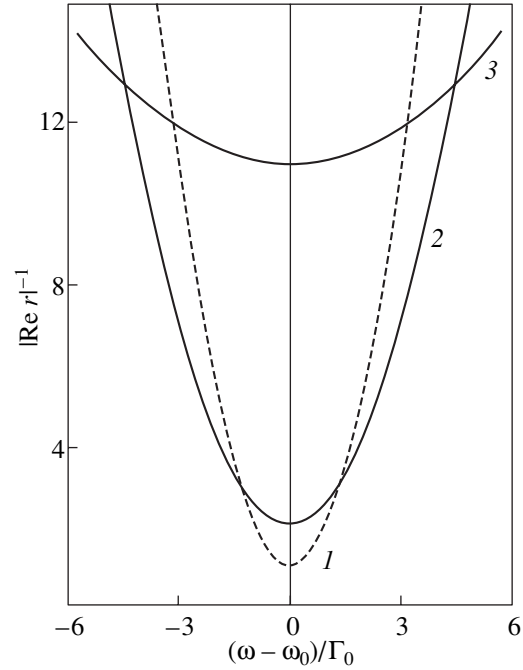
Fig. 2. The quantity $|\operatorname{Re} r|^{-1}$ (dimensionless localization length $\xi \nu / 0.78$) plotted vs. $x = (\omega - \omega_0)/\Gamma_0$ for structures with randomly distributed quantum wells containing quasi-two-dimensional excitons of frequency ω_0. The calculation was made using Eq. (51) for the following values of parameter $g = \gamma/\Gamma_0$: (1) 0, (2) 1, and (3) 10.

Eqs. (50) and (51) and Fig. 2, the resonance decrease in the localization length with $x = (\omega - \omega_0)/\Gamma_0$ depends noticeably on the ratio $g = \gamma/\Gamma_0$. The deepest minimum is reached in the dashed curve (Fig. 2), corresponding to the absence of dissipative decay ($\gamma \longrightarrow 0$). As the parameters γ and/or Γ_0 increase, the resonance dip in the $\xi(\omega)$ dependence broadens and the localization length at the minimum increases.

6.2. Lorentzian-Oscillator Model

For comparison, we consider a model assuming identical layers of thickness a randomly arranged along the z axis with a concentration $\nu \ll k$. The dielectric permittivity is ε_1 outside the layers and is equal to

$$\varepsilon_2(\omega) = \varepsilon_b + \frac{\Omega^2}{\omega_0^2 - \omega^2 - i\omega\gamma}. \tag{52}$$

inside them. This function relates to a model of Lorentzian oscillators for which ω_0 is the frequency, γ^{-1} is the relaxation time, and the quantity Ω^2 is proportional to the oscillator strength and is a measure of the oscillator coupling with light. The response function (52) can describe bulk excitons with weak spatial dispersion or polar optical phonons (in the $\theta = 0$ case, the interface phonons are insignificant).

The reflectivity of a thin layer ($a \ll c/\omega_0 \lesssim c/\Omega$) can be written as

$$\tilde{r} = \frac{i\sqrt{\varepsilon_1}\omega a}{2c}\left(\frac{\varepsilon_2 - \varepsilon_1}{\varepsilon_1}\right), \tag{53}$$

with the relation $\tilde{t} = 1 + \tilde{r}$. Following [11] and using Eqs. (52) and (53), we obtain, for $\varepsilon_1 = \varepsilon_b$, a relation for the localization length:

$$\tilde{\xi}(\omega) = \frac{\sqrt{\pi}}{\nu}\left(\frac{c}{\omega a}\right)^{3/2}\frac{(\omega^2 - \omega_0^2)^2 + (\omega\gamma)^2}{\Omega^3\sqrt{\omega\gamma}}. \tag{54}$$

At resonance, $\omega = \omega_0$, this quantity assumes a $\tilde{\xi}(\omega_0) = (\sqrt{\pi}/\nu)(\Omega a/c)^{-3/2}(\gamma/\Omega)^{3/2}$, where $\gamma/\Omega \ll 1$ and $\Omega \lesssim \omega_0$. Far from the resonance ($\gamma \ll |\omega - \omega_0| < \omega_0$), the localization length (54) obeys the same frequency dependence $\tilde{\xi}(\omega) \approx (4\sqrt{\pi}/\nu)(\Omega a/c)^{-3/2}(\gamma/\Omega)^{-1/2}(\omega - \omega_0)^2/\Omega^2$ as Eq. (50) but is substantially larger because of the conditions $\Omega a/c \ll 1$ and $\gamma/\Omega \ll 1$.

7. CONCLUSIONS

We note in conclusion that the above theory of frequency-dependent localization allows, in principle, generalization to two-dimensional plasmons in randomly arranged semiconductor quantum wells or atomically thin metal layers. The susceptibility of plasmons, which enters Eq. (1), is proportional to their spontaneous emission rate (the squared plasma frequency of two-dimensional electron gas $\omega_p^2 \sim \sin\theta$). As a consequence, for $\theta = 0$, light does not couple to two-dimensional plasmons. Therefore, to study the plasmon-induced localization of light, one has to generalize the theory put forward in Section 5 to arbitrary values of the angle of light incidence.

As follows from the above study, light propagation in low-dimensional quantum-well structures is adequately described in terms of a model of layers with a δ-function dielectric polarization. Despite the formal analogy to models involving electron zero-radius potentials, the electromagnetic model differs from them fundamentally. Indeed, the excitonic susceptibility (an analog of the potential for electrons) depends on frequency and includes the radiative and nonradiative exciton decay rates. As a consequence, the resonance excitonic susceptibility, responsible for the appearance of induced polarization and light-wave scattering, is a finite complex function of frequency.

We used structures with randomly distributed identical quantum wells containing quasi-two-dimensional excitons to show that, near the resonance frequency, the average field has a polariton character. The polariton scattering accounts for the disorder-induced frequency-dependent extinction, multiple scattering, and Anderson localization of light waves in a structure. The light localization length in the polariton region of the spectrum decreases substantially because of the resonantly increased light scattering (reflection) from individual quantum wells. We have considered localization under normal light incidence, but there are grounds to hope that the main conclusions will remain valid in the case of oblique incidence. Polarization effects expected to occur in one-dimensional localization of light in quantum-well structures, as in other layered systems [5–11], are of considerable interest, because *s*- and *p*-polarized waves may reveal essentially different characteristics in these structures. In particular, *p*-polarized light interacts with two excitonic resonances (rather than with one, as is the case for *s*-polarized light), which should give rise to a resonantly reduced localization length in the above two spectral regions. Finally, the strong dependence of the radiative decay rate of quasi-two-dimensional optical excitations on the angle of light incidence should manifest itself in an angular dependence of the localization length in the resonance region.

REFERENCES

1. *Confined Electrons and Photons. New Physics and Applications*, Ed. by E. Burstein and C. Weisbuch (Plenum, New York, 1995).

2. J. D. Joannopoulos, R. D. Meade, and J. N. Winn, *Photonic Crystals* (Princeton Univ. Press, Princeton, N.J., 1995).

3. Yu. A. Vlasov, M. A. Kaliteevski, and V. V. Nikolaev, Phys. Rev. B **60** (3), 1555 (1999).

4. E. L. Ivchenko, A. I. Nesvizhskiǐ, and S. Ǐorda, Fiz. Tverd. Tela (St. Petersburg) **36** (7), 2118 (1994) [Phys. Solid State **36**, 1156 (1994)].

5. X. Du, D. Zhang, X. Zhang, *et al.*, Phys. Rev. B **56** (1), 28 (1997).

6. D. Zhang, Z. Li, W. Hu, and B. Cheng, Appl. Phys. Lett. **67** (17), 2431 (1995).

7. J. E. Sipe, P. Cheng, B. S. White, and M. H. Cohen, Phys. Rev. Lett. **60** (2), 108 (1988).

8. K. M. Yoo and R. R. Alfano, Phys. Rev. B **39** (9), 5806 (1989).

9. A. G. Aronov and V. M. Gasparian, Solid State Commun. **73** (1), 61 (1990).

10. V. A. Kosobukin, Fiz. Tverd. Tela (Leningrad) **32** (1), 227 (1990) [Sov. Phys. Solid State **32**, 127 (1990)]; Fiz. Tverd. Tela (Leningrad) **32** (4), 1248 (1990) [Sov. Phys. Solid State **32**, 734 (1990)].

11. V. A. Kosobukin, Phys. Status Solidi B **161** (2), 405 (1990).

12. A. R. McGurn, K. T. Christensen, F. M. Mueller, and A. A. Maradudin, Phys. Rev. B **47** (20), 13 120 (1993).

13. I. M. Lifshits, S. A. Gredeskul, and L. A. Pastur, *Introduction to the Theory of Disordered Systems* (Nauka, Moscow, 1982; Wiley, New York, 1988).

14. Yu. N. Demkov and V. N. Ostrovskiĭ, *Zero-Range Potentials and Their Applications in Atomic Physics* (Leningr. Gos. Univ., Leningrad, 1975; Plenum, New York, 1988).

15. C. A. Condat and T. R. Kirkpatrick, Phys. Rev. B **33** (5), 3102 (1986).

16. V. M. Agranovich, V. E. Kravtsov, and I. V. Lerner, Phys. Lett. A **125** (8), 435 (1987).

17. Z. Cheng and S.-W. Gu, Phys. Rev. B **41** (5), 3128 (1990).

18. K. Arya, Z. B. Su, and J. L. Birman, Phys. Rev. Lett. **54** (14), 1559 (1985).

19. L. C. Andreani and F. Bassani, Phys. Rev. B **41** (11), 7536 (1990).

20. E. L. Ivchenko, Fiz. Tverd. Tela (Leningrad) **33** (8), 2388 (1991) [Sov. Phys. Solid State **33**, 1344 (1991)].

21. V. A. Kosobukin, Phys. Status Solidi B **208** (1), 271 (1998).

22. V. A. Kosobukin, Fiz. Tverd. Tela (St. Petersburg) **34** (10), 3107 (1992) [Sov. Phys. Solid State **34**, 1662 (1992)].

23. D. Vollhardt and P. Wolfle, Phys. Rev. B **22** (10), 4666 (1980).

24. M. L. Goldberger and K. M. Watson, *Collision Theory* (Wiley, New York, 1964; Mir, Moscow, 1967).

25. M. A. Lavrent'ev and B. V. Shabat, *Methods of the Theory of Functions of a Complex Variable*, 5th ed. (Nauka, Moscow, 1987; Wissenschaften, Berlin, 1967).

Translated by G. Skrebtsov

LOW-DIMENSIONAL SYSTEMS
AND SURFACE PHYSICS

Influence of Cluster Formation on Localization of Optical Phonons in Two-Dimensional Pseudobinary Substitutional Solid Solutions

M. I. Vasilevskiy*, O. V. Vikhrova**, and S. N. Ershov**

* Departamento de Fizika, Universidade do Minho, Campus de Gualtar, Braga 4710-057, Portugal
e-mail: Benushis@phys.unn.runnet.ru
** Nizhni Novgorod State University, pr. Gagarina 23, Nizhni Novgorod, 630950 Russia
Received September 26, 2002

Abstract—The influence of the composition and short-range order of the cluster formation type on optical phonon localization in two-dimensional pseudobinary substitutional solid solutions is studied. Direct numerical calculations of the so-called inverse participation ration (IPR) are carried out, and the scaling of this parameter is studied for the fundamental modes of the spectral density of states at the Brillouin zone center of the averaged crystal. It is shown that cluster formation promotes phonon delocalization, although the nature of this effect is different for resonant and local (in the low-concentration limit) modes. The influence of the ionicity of a solid solution on localization is considered. It is shown that the Coulomb interaction neutralizes the effect of cluster formation while simultaneously decreasing the observed IPR. Based on the form of the distribution of local site absorption of an external electromagnetic field, a new physical criterion is suggested, which allows one to analyze the localization degree of phonon modes in ionic alloys. © *2003 MAIK "Nauka/Interperiodica".*

1. INTRODUCTION

The localization of elementary excitations in solids, caused by atomic disorder, is one of the important problems in the theory of disordered systems. Studies of the localization of electronic and vibrational states in disordered alloys began close to forty years ago [1]. However, this problem has been solved only in part, mostly for simple models of low-dimensional systems. For example, in the case of two- and lower dimensional systems, it is generally believed that arbitrarily weak disorder causes localization of all the electron states. This conclusion was allowed by the one-parametric scaling theory [2]. However, in some recent papers dedicated to experimental studies of the metal–insulator transition in two-dimensional systems based on the metal–oxide–semiconductor structure (see, e.g., [3]), the validity of this statement was called into question for any two-dimensional system. The major factor, previously neglected when studying the localization, is the electron–electron interaction. A modified scaling theory was suggested that takes into account the influence of the electron–electron interaction, along with disorder, and allows the existence of delocalized states in disordered two-dimensional systems [4]. It is conceivable that not only the interaction between elementary excitations but also other factors can have a significant effect on their localization.

It is known that, although the distribution of impurities in actual disordered alloys is random, it is often characterized by spatial correlation extending over many interatomic spacings. For example, impurity

atom clusters are formed in alloys that have a tendency to decompose [5]. It is not inconceivable that the correlations of the random potential can significantly change the localization of elementary excitations in low-dimensional systems. For example, it is known that certain types of randomly correlated distribution of impurities in one-dimensional systems give rise to weakly localized states with wave functions that decrease with distance following a power law [6, 7]. This conclusion was made not only for electrons but also for other types of elementary excitations, e.g., magnons in randomly correlated linear chains [8].

Phonon localization in randomly correlated alloys has been studied theoretically [9] and using numerical simulation [10]. In [9], field-theoretic methods were applied to show that all acoustic phonon modes are also localized in two-dimensional systems with isotopic disorder even with correlations that can only have an effect on the localization radius. In [10], the acoustic-phonon localization was considered numerically in terms of the percolation problem. This allowed understanding of the mechanism of formation of localized and propagating phonon states in two- and three-dimensional model binary alloys. Furthermore, differences in the localization degree of phonon modes were detected. These differences depend on whether the modes are local or resonant in the limit of small impurity concentrations; however, the small size of the systems under study does not allow quantitative conclusions. It should also be noted that a continuum model (rather than a lattice one) with the simplest (elastic) interaction was considered in

[9]; the localization of optical phonons (OPs), to our knowledge, was not studied at all. Meanwhile, the degree of OP localization is important for mesoscopic systems in terms of the electron–phonon interaction and far-IR radiation absorption, even if the general conclusion on localization of any noninteracting elementary excitation in infinite two-dimensional systems with disorder also remains valid for OPs.

In this paper, we present numerical results on the influence of the correlation (short-range order) in the impurity atom arrangement on the localization of optical phonon modes in two-dimensional pseudobinary substitutional solid solutions (SSs). The calculations were carried out within a model that takes into account the Ising-type correlations in the arrangement of isovalent impurity atoms in one of the SS sublattices. The model is aimed at describing the properties of $Cd_xHg_{1-x}Te$ and $Al_xGa_{1-x}As$ semiconductor SSs of various compositions.

2. SHORT-RANGE ORDER MODELS AND LATTICE DYNAMICS

The thermodynamic–equilibrium short-range order (SRO) of substitutional atoms in one of the sublattices of the two-dimensional pseudobinary SS was simulated using the algorithm described in [11]. The algorithm is based on the Ising model of the static interaction between neighboring atoms in the sublattice. Random alloys with various SRO were constructed using the Monte Carlo method. The SRO was controlled by the given temperature of SS formation.

The influence of two SRO types that are feasible in the Ising model (cluster formation and superstructure formation due to ordering) on the total and spectral densities of SS phonon states without regard for the Coulomb interaction between ions was discussed in detail in [11]. We use a (more realistic) model of the lattice dynamics based on an analysis of published calculated data on the vibrational properties of Si, Ge, and III–V compounds [12, 13].

The equations of motion are written as

$$(\hat{F} - \omega^2 \hat{M})\mathbf{V} = 0, \qquad (1)$$

where $\hat{F}$ is the force constant matrix, $\hat{M}$ is the diagonal matrix of atomic masses, and $\mathbf{V}$ is the displacement vector. The interactions with the nearest and next-to-nearest neighbors were taken into account for each atom. Within the harmonic approximation, the potential energy is given by

$$U_0 = \frac{k}{2} \sum_{S=\{nn\}} (\mathbf{V}_0 - \mathbf{V}_S)^2, \qquad (2)$$

$$U_0 = \frac{k}{2a^2} \sum_{S=\{nnn\}} (\mathbf{a}_{0S}(\mathbf{V}_0 - \mathbf{V}_S))^2, \qquad (3)$$

for the nearest and next-to-nearest neighbors, respectively; here, k is the elastic constant, $\mathbf{a}_{0S}$ is the translational vector, and $\mathbf{V}_0$ and $\mathbf{V}_S$ are the displacement vectors of the corresponding atoms. As usual, the force constants $\hat{F}$ are equal to the second derivatives of the total potential energy.

To simulate the Coulomb interaction, we used the potential (for like-sign ions)

$$U = -A^2 \ln \frac{r}{r_0}, \qquad (4)$$

where $A^2 = \dfrac{\mu S_0}{2\pi}(\omega_{LO}^2 - \omega_{TO}^2)$; ω_{LO}^2 and ω_{TO}^2 are the frequencies (squared) of longitudinal and transverse long-wave-length OPs, respectively, in the binary compound without impurity; μ is the reduced mass of a positive and a negative ion; S_0 is the unit cell area; and r_0 is a constant. This "Coulomb" potential allows simulation of LO–TO splitting in a two-dimensional pseudobinary SS [14].

3. PARAMETERS OF PHONON MODE LOCALIZATION

The lattice dynamics of model SSs, constructed following the procedure outlined in Section 2, was studied by making direct numerical calculations using a software package developed by us. This package allows one to form a dynamic matrix of a square supercell of a pseudobinary SS on the basis of selected potentials with allowance for the periodic boundary conditions and to determine all its eigenvalues and eigenvectors using the QR algorithm [15]. The data obtained were used to calculate the parameters characterizing the localization of phonon modes.

In the calculations neglecting the Coulomb interaction (homopolar alloy), atomic displacements were considered to be scalar; the dynamic matrix was an $N \times N$ matrix (N is the number of atoms). To determine the localization degree of phonon modes, we calculated the spectral dependence of the parameter referred to as the inverse participation ration (IPR):

$$\mathrm{IPR}(\omega)$$

$$= \frac{1}{\sum_j \delta(\omega^2 - \omega_j^2)} \sum_j \frac{\sum_{j=1}^{N}(u_i^j)^4}{\left(\sum_{i=1}^{N}(u_i^j)^2\right)^2} \delta(\omega^2 - \omega_j^2), \qquad (5)$$

where u_i^j is the displacement (multiplied by the square root of the mass) of the ith atom for the jth eigenvalue. Formula (5) was derived by replacing the modulus of the electron wave function with the quantity u_i^j in the conventional IPR definition and by averaging over the

eigenmodes with close frequencies (the latter operation is convenient for analyzing the IPR variation in certain spectral regions). As is known [16], the parameter IPR is inversely proportional to the number of atoms participating in the formation of the eigenstate with frequency ω_j. Delocalized modes correspond to small values of IPR $\sim N^{-1}$, while localized modes correspond to IPRs of the order of unity. It should be mentioned that, as far as we know, it is not substantiated that the IPR parameter is a self-averaging quantity (in terms of [17]). A localization criterion based on the variations of the IPR is basically intuitive; nevertheless, this criterion is rather widely used.

If the Coulomb interaction is taken into account, displacements should be considered as vectors, which causes an increase in the dynamic matrix size. In this case, the parameter IPR was also calculated from formula (5) using the displacement magnitudes. The phonon state localization in the heteropolar alloy was studied not only by using the IPR spectral characteristics but also by using the distribution of the local intensity of forced vibrations excited by an external ac electric field. It turned out that the distribution of the local site absorption of an external field of frequency ω at various SS lattice sites is very sensitive to the localization degree of phonon modes of this frequency. This can readily be understood considering the following two extreme situations. In the case of a strongly localized mode, only a few neighboring atoms vibrate. In this small region ("hot zone"), the energy of the external field of resonant frequency is absorbed, while absorption is almost zero at lattice sites outside this region. In the case of a completely delocalized mode, however, the external-field absorption should be approximately identical at all crystallite sites. Thus, the distribution function of local absorption should significantly differ for localized and delocalized modes.

To formulate the suggested criterion quantitatively, we consider forced vibrations of a partially ionic pseudobinary $A_x B_{1-x} C$ solid solution in more detail. For simplicity, let the charges of isovalent A and B atoms be identical. It can be shown that the lattice susceptibility (to within the factor e_τ^2) is given by (see Appendix)

$$\chi = e_\tau^2 \frac{1}{N} \sum_{l,k} J_{lk}. \tag{6}$$

The energy absorption rate by the whole crystallite is written as

$$Q = -\frac{E_0^2 e_\tau^2}{2} \omega \, \mathrm{Im} \sum_{lk} J_{lk}.$$

Let us introduce the distribution function of the imaginary part of the quantities J_{lk},

$$f(t) = \frac{1}{N} \sum_{l,k} \delta\!\left(t - \frac{\mathrm{Im}\, J_{lk}}{\mathrm{Im} \langle J \rangle} \right),$$

$$Q \sim \sum_{lk} \mathrm{Im}\, J_{lk} = N \,\mathrm{Im} \langle J \rangle \int\limits_{-\infty}^{+\infty} f(t)t\,dt. \tag{7}$$

As shown in the next section, this function allows one to judge the character of optical phonon modes of the corresponding polarization with frequencies close to the frequencies of the external field.

4. RESULTS AND DISCUSSION

4.1. Homopolar Solid Solution

The spectral dependences of the IPR were calculated for pseudobinary SSs with atomic-mass disorder. There exist at least two semiconductor SSs that can be adequately described by the isotopic approximation [18], $Cd_xHg_{1-x}Te$ and $Al_xGa_{1-x}As$. The spectra of long-wavelength OPs of these SSs involve two modes; i.e., the spectral density of phonon states at the Brillouin zone center of such solid solutions contains two optical modes, e.g., the HgTe-like and CdTe-like modes in the case of $Cd_xHg_{1-x}Te$. The influence of clusters on the localization of specifically these modes is of primary interest. In calculations, we took the atomic masses equal to those of elements composing the SSs under study; the force constants and the charge A were selected such that accurate phonon frequencies were obtained at the Brillouin zone center. Hereafter, the model alloys under consideration are referred to as, e.g., $Cd_xHg_{1-x}Te$; however, the calculation results obtained should not be extended to actual SSs in the strict sense.

Figure 1 shows the dependences of the IPR of optical modes on the composition x for random and clusterized SSs. First, we discuss the behavior of the IPR for the CdTe-like mode as the Cd content increases. The IPR significantly decreases with x for random and clusterized SSs; in both cases, the dependence is almost linear. The IPR decrease observed indicates that the CdTe-like mode tends to delocalization with x. At $x = 0.9$, the IPR is proportional to $\sim N^{-1}$ for both random and clusterized SSs. This means that the localization radius becomes equal to the crystallite size.

The IPR(x) dependence in the case of the HgTe-like mode is significantly different. The values of IPR are much smaller than those of the CdTe-like mode virtually over the whole composition range (0.1–0.9). This is not unexpected since HgTe-like vibrations are resonant within the model we suggested, i.e., their frequencies fall within the CdTe optical-vibration range. In the case of a random SS, the IPR of the HgTe-like mode initially increases up to a maximum (at $x \sim 0.25$) in the
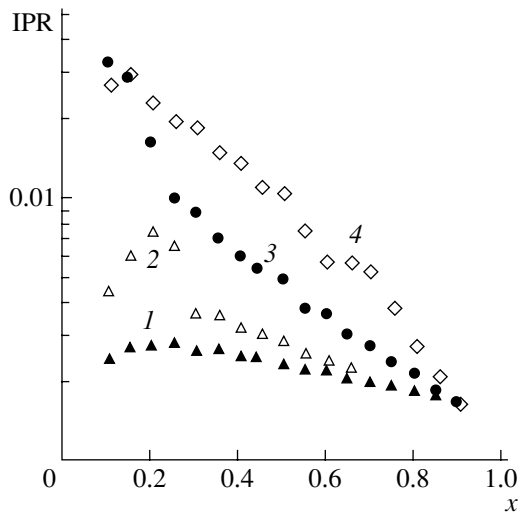
Fig. 1. Dependences of the IPR of OP fundamental modes on the composition of $Cd_xHg_{1-x}Te$ solid solutions (the crystallite size is 30×30): (1, 2) HgTe-like and (3, 4) CdTe-like modes of (1, 3) clusterized and (2, 4) random solid solutions.

Fig. 2. Same as in Fig. 1 but for $Al_xGa_{1-x}As$ solid solutions: (1, 2) GaAs-like and (3, 4) AlAs-like modes of (1, 3) clusterized and (2, 4) random solid solutions.

range of low Cd concentrations ($x < 0.3$) and then abruptly decreases; beginning from $x \sim 0.3$, this decrease is almost linear. It is worth noting that the IPR maximum in the IPR(x) dependences takes place for any crystallite size. In our opinion, this maximum is due to the fact that the Cd atoms in random SSs are, for the most part, arranged singly at low concentrations, which results in stronger scattering of HgTe-like vibrations. As the Cd concentration increases, the band of CdTe-like vibrations begins to form. Vibrations with frequencies close to that of the long-wavelength HgTe-like mode arise; however, these vibrations are not associated with vibrations of the Hg atoms. The density of states increases in the frequency range under consideration, and the IPR per state decreases. Thus, the behavior of the IPR, which seems unusual in the case of the HgTe-like mode, may be explained by the fact that this mode is quasilocal (i.e., resonant) in the limit of low Hg concentrations.

Similar calculations of the dependence of the IPR on the composition for optical modes in $Al_xGa_{1-x}As$ confirm this explanation. The case of $Al_xGa_{1-x}As$ differs from the preceding case in the fact that the GaAs-like mode is outside the AlAs band; i.e., it is local rather than resonant. We can see from Fig. 2 that the localization of the GaAs-like mode increases with the aluminum atomic fraction in the cation sublattice for both random and clusterized SSs. The shape of the AlAs-like mode curve virtually coincides with that of the CdTe-like mode in Fig. 1. However, the IPR(x) dependence for the HgTe-like mode is similar to that for the GaAs-like mode only in the range of small values of x. Thus, the local and resonant modes behave differently as the composition is varied (as indicated in [10]).
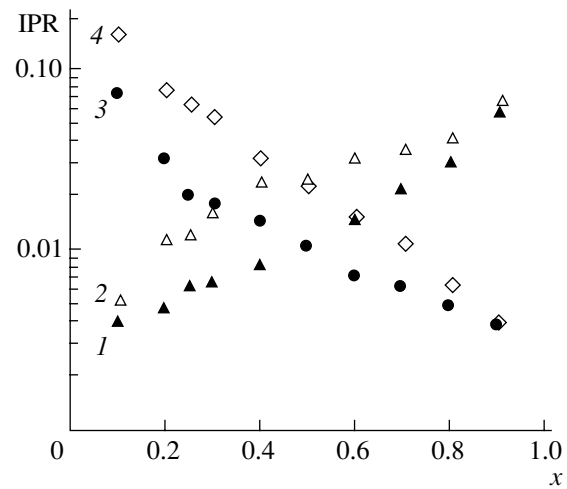
Let us enlarge on the influence of the SRO on the OP localization. We can see from Fig. 1 that cluster formation promotes a decrease in the IPR of the HgTe- and CdTe-like modes; i.e., it decreases their localization almost over the entire composition range. An analogous effect is also seen from Fig. 2 for $Al_xGa_{1-x}As$. To check this conclusion, we studied the "scaling" of the degree of phonon mode localization. The dependence of the IPR on the number of atoms in the $Cd_xHg_{1-x}Te$ crystallite with $x = 0.5$ is shown in Fig. 3 in the log–log scale. The localization is determined by the exponent in the dependence

$$IPR \sim N^{-\gamma}.$$
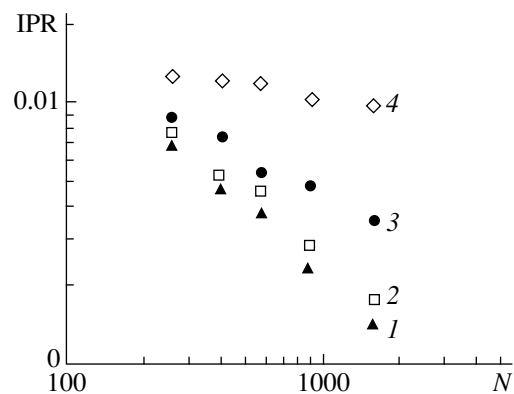
Fig. 3. Dependences of the IPR of fundamental phonon modes on the total number of atoms in the crystallite for clusterized and random $Cd_{0.5}Hg_{0.5}Te$ (the crystallite size varied from 16×16 to 40×40): (1, 2) the HgTe-like mode of clusterized ($\gamma \approx 0.897$) and random ($\gamma \approx 0.87$) solid solutions, respectively, and (3, 4) the CdTe-like mode of clusterized ($\gamma \approx 0.8$) and random ($\gamma \approx 0.71$) solid solutions, respectively.
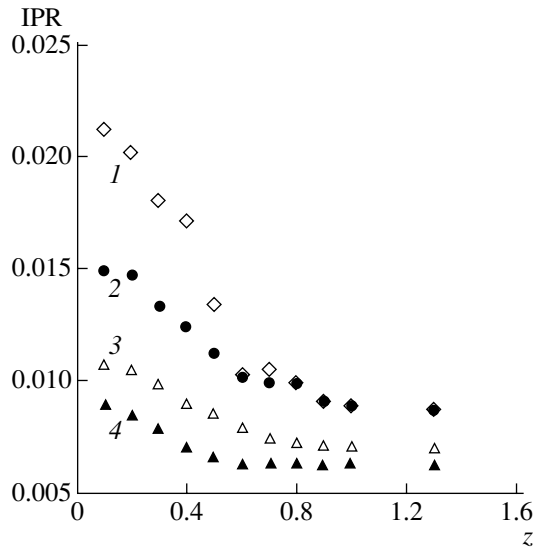
Fig. 4. Dependences of the IPR of the HgTe- and CdTe-like *LO* modes of random and clusterized $Cd_{0.5}Hg_{0.5}Te$ on the ion charge: (*1*, *2*) CdTe-like and (*3*, *4*) HgTe-like *LO* modes of (*1*, *3*) random and (*2*, *4*) clusterized solid solutions.
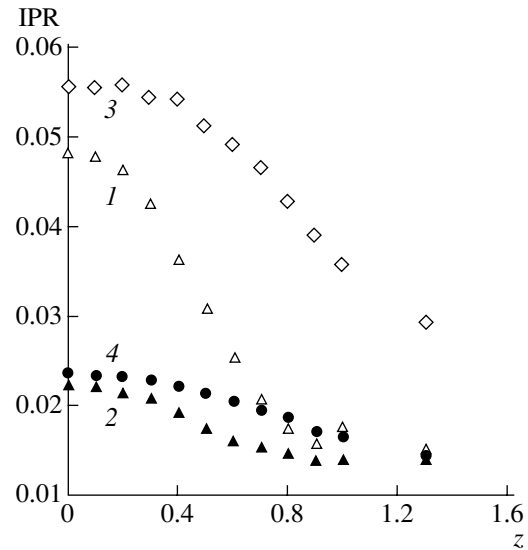
Fig. 5. Same as in Fig. 4 but for $Al_{0.5}Ga_{0.5}As$: (*1*, *2*) AlAs-like and (*3*, *4*) GaAs-like *LO* modes of (*1*, *3*) random and (*2*, *4*) clusterized solid solutions.

The data represented in Fig. 3 indicate that cluster formation appreciably decreases the localization of fundamental phonon modes (γ approaches unity). With cluster formation, the HgTe-like mode becomes almost delocalized (γ ≈ 1). The CdTe-like mode exhibits a fractal behavior with scaling where we have $0 < \gamma < 1$ and this parameter depends on the degree of cluster formation. In the case of strong cluster formation ($T = 0.95T_C$, T_C is the critical temperature in the two-dimensional model), we have γ ≈ 0.8. We will return to these values of the exponent γ below.

4.2. Heteropolar Solid Solution

In order to answer the question as to whether the influence of cluster formation on phonon mode localization is retained in the presence of the Coulomb interaction, we studied the dependences of the IPR on the "charge" A. These dependences for HgTe- and CdTe-like modes of clusterized and random $Cd_{0.5}Hg_{0.5}Te$ are shown in Fig. 4 ($z = A/A_0$, where A_0 corresponds to "proper," i.e., experimental, values of ω_{LO}^2 and ω_{TO}^2). We can see that an increase in the charge lowers the localization of phonon modes. This fact is explained by the range of the ion interaction being unlimited, which effectively increases the dimensionality of the system. We recall that this interaction does not involve disorder within the (isotopic) model we suggested.

At the same time, the influence of cluster formation on the IPR somewhat differs in the cases of the HgTe-like (low-frequency) and CdTe-like (high-frequency) modes. The localization of the high-frequency mode in the range of small charges ($z < 0.5$) significantly decreases due to cluster formation, as is the case in the

homopolar SS. At $z = 0.5$–1.3, the Coulomb interaction neutralizes the influence of the cluster formation. In this case, the IPR takes on virtually identical values for random and clusterized SSs. In the case of the low-frequency mode, the cluster formation causes a weak decrease in the degree of localization in the whole charge range. This mode is almost delocalized even in the homopolar SS with $x = 0.5$.

The IPR of AlAs- and GaAs-like *LO* modes in $Al_{0.5}Ga_{0.5}As$ depends on the charge and the degree of cluster formation in a similar way (Fig. 5). However, certain differences are observed. For example, the influence of cluster formation on the high-frequency mode localization at $z > 0.5$ is not compensated by the Coulomb interaction in full. Furthermore, the initial degree of the low-frequency mode localization and the range of its decrease due to cluster formation are much larger in this case. This mode remains localized even in the presence of strong Coulomb interaction, which is probably due to smaller effective values of the dynamic matrix elements corresponding to the interaction of Ga ions in comparison with those for Al ions (the ion mass is in the denominator). We also note that the same trends in the behavior of the IPR with composition are retained throughout the entire charge range, as is the case within the SS model without Coulomb interaction. It seems that the Coulomb interaction causes an increase in the scaling parameter, even though we were restricted to much smaller crystallite sizes in the calculations for the heteropolar SS.

We now discuss the results on the distribution function (DF) of the local intensity of absorption (see Eq. (7)), which is different for the low- and high-frequency modes. Figure 6 displays the DFs of the CdTe- and HgTe-like *LO* modes of $Cd_{0.5}Hg_{0.5}Te$. The DF of
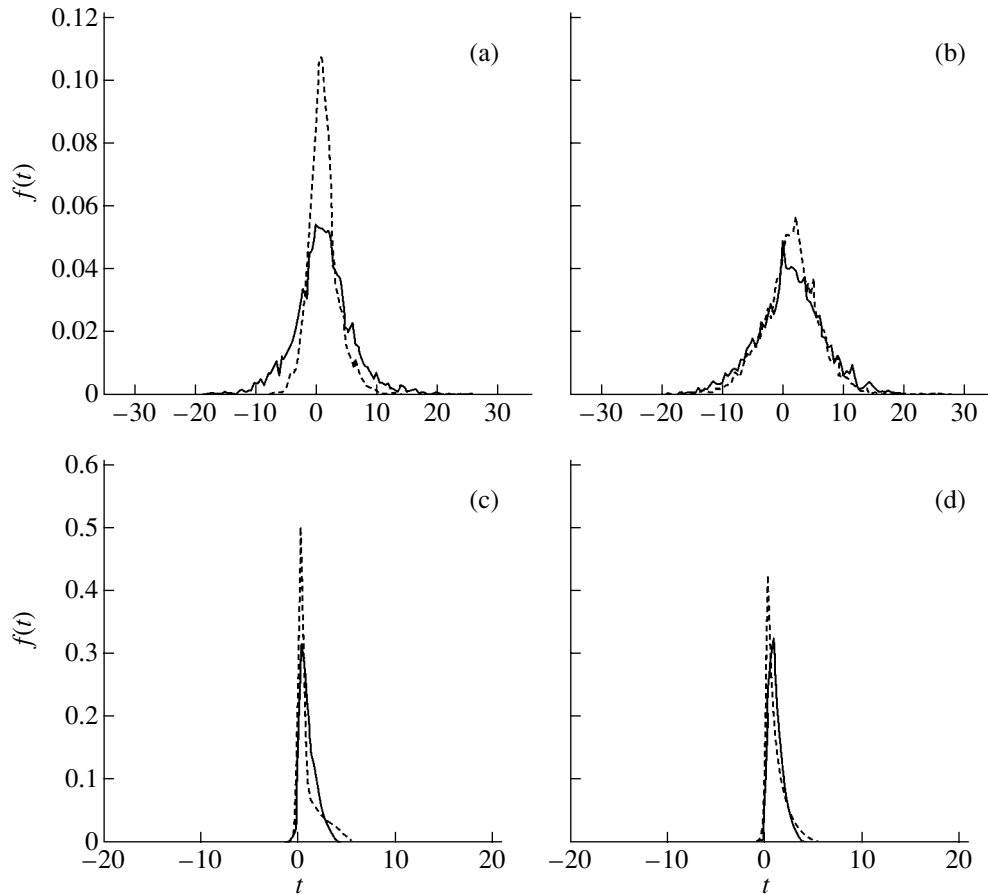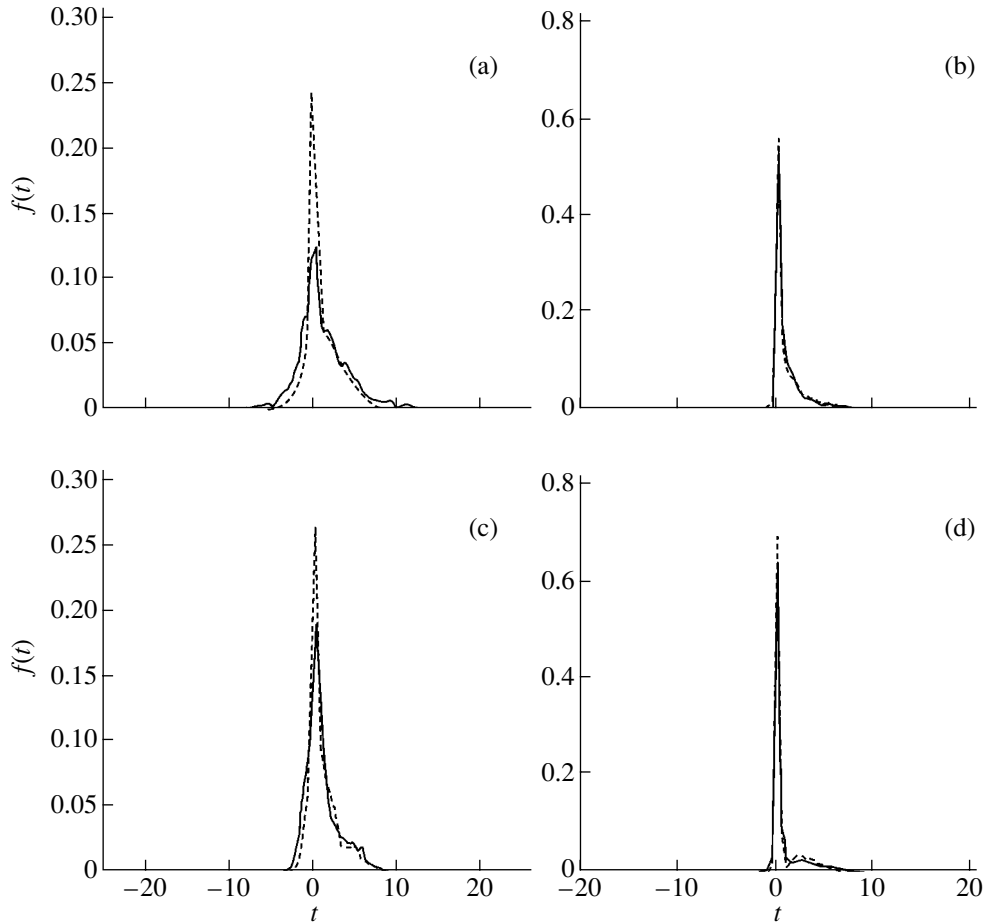
Fig. 6. Distribution functions of the intensity of local site absorption for fundamental phonon modes of $Cd_{0.5}Hg_{0.5}Te$: (a, b) HgTe-like and (c, d) CdTe-like *LO* modes. Solid and dashed lines correspond to random and clusterized solid solutions, respectively. The ion charge is (a, c) $z \approx 0$ and (b, d) 1.

the HgTe-like mode can be approximated by a Gaussian distribution with the average equal to unity, while the DF of the high-frequency CdTe-like mode is strongly asymmetric. In the case where the frequency of an external (longitudinal) field is in the range of the low-frequency *LO* mode, there exist lattice sites at which the local intensity of absorption is negative, i.e., where the energy is emitted rather than absorbed. Such sites correspond to Cd and Hg atoms which are not inside CdTe and HgTe clusters, respectively, and move in counterphase to the external field. As the SRO increases, the CdTe and HgTe clusters become larger and the number of anomalously moving atoms decreases. The oscillation of atoms at a frequency equal to the external field frequency in the range of the high-frequency (CdTe-like) mode is limited by CdTe clusters, and sites with negative absorption are virtually absent (see Figs. 6c, 6d). We emphasize that the effects under consideration are virtually independent of ion charge.

Similar calculations carried out for $Al_{0.5}Ga_{0.5}As$ and for a model SS whose anion mass m_C significantly exceeds the masses of two intersubstitutable cations

(m_A, m_B) confirm the above interpretation of the DF shape (Fig. 7). The amplitude of optical vibrations can be of the same order of magnitude (at different phases) almost at all lattice sites only in the case of a low-frequency resonant mode. Indeed, the DF of the GaAs-like *LO* mode is already appreciably asymmetric (Fig. 7a). In the case of the model SS, the DF of the low-frequency mode has the form characteristic of the high-frequency mode (Fig. 7c), which is approximately identical for all the alloys under study.

Thus, notwithstanding the fact that the values of the IPR of fundamental optical phonon modes are close in the SS with Coulomb interaction, especially in the case of intensive cluster formation, the localization of these modes can differ. The resonant low-frequency mode is delocalized in the sense that the amplitude of atomic displacements does not vanish for most of the crystallite ions. Disorder results in the possibility of the phase significantly differing for various sites. Cluster formation somewhat reduces variations in the atomic displacement phase, decreasing the variance of the DF of local site absorption.

Fig. 7. Distribution functions of the intensity of local site absorption in (a, b) $Al_{0.5}Ga_{0.5}As$ and (c, d) a model solid solution ($m_A = 69.72$, $m_B = 26.98$, $m_C = 174.92$) for (a, c) low- and (b, d) high-frequency *LO* modes. Solid and dashed lines correspond to random and clusterized solid solutions, respectively. The ion charge was taken to be the same and corresponded to $z = 1$ for $Al_{0.5}Ga_{0.5}As$ in all cases.

In contrast to the typical situation described for the HgTe-like mode in $Cd_xHg_{1-x}Te$, all high-frequency modes and those low-frequency modes that are local (rather than resonant) in the low-concentration limit are virtually localized inside the corresponding clusters, which are separated from each other. The typical size of clusters increases with the system size, causing scaling with an exponent γ close to unity (according to our numerical calculations). Electromagnetic energy absorption due to such vibrational modes takes place in the hot zones. Their existence is especially evident in the case of the model SS with specially selected masses (see Fig. 7d), where the majority of ions are immobile and do not interact with the external field. The absorption with the intensity variance near a certain typical value characterizes a cluster whose size corresponds to the external field frequency.

5. CONCLUSIONS

Thus, our direct numerical calculations have shown that the localization of the fundamental phonon modes in two-dimensional pseudobinary SSs depends heavily on the composition. The cluster-type SRO and the Coulomb interaction intensity (SS ionicity), promoting delocalization of optical phonon modes, also have a significant effect.

The delocalizing effect of the long-range Coulomb interaction can be explained by an effective increase in the dimensionality of the system (the initiation of additional channels for transferring the vibrational excitation between lattice sites). The analysis of the DF of local site absorption of an external electromagnetic field has shown that the high-frequency and nonresonant low-frequency optical modes are localized at clusters of a corresponding binary compound that are optimal in size. An electromagnetic field with a frequency corresponding to such modes is absorbed locally, which can be very important for the SS nonlinear properties. The tendency to delocalization in the course of cluster formation, manifesting itself in the IPR, is explained by an increase in the size of the clusters on which the excitation is localized. On the contrary, the resonant low-

frequency mode is characterized by appreciable amplitude throughout the crystal. The scaling ($\gamma \approx 1$) we detected for such a mode indicates its delocalization; however, this statement is of course valid at certain dimensions of the crystallites studied numerically.

ACKNOWLEDGMENTS

APPENDIX

In the case where an external electric field is applied, the equation of motion of ions composing the solid solution takes on the form

$$(\hat{B} - \omega^2 \hat{1})\mathbf{U} = \frac{e_k}{\sqrt{M_{lk}}}\mathbf{E}, \tag{A1}$$

where $\hat{B}$ is the dynamic matrix; $\mathbf{U}$ is the displacement vector multiplied by $\sqrt{M_{lk}}$; $e_k = (-1)^k e_\tau$ and M_{lk} are the ion charge and mass, respectively, in the lth unit cell of the kth sublattice; e_τ is the parameter referred to as the longitudinal charge; and $\mathbf{E}$ is the external spatially uniform ac electric field. The forced displacements defined by Eq. (A1) are given by

$$V_{lk}^{\alpha} \equiv \frac{U_{lk}^{\alpha}}{\sqrt{M_{lk}}} = -\frac{1}{\sqrt{M_{lk}}}\sum_{l', k', \beta} G^{\alpha\beta}(lk, l', k')\frac{e_{k'}E^{\beta}}{\sqrt{M_{l'k'}}}, \tag{A2}$$

where $\hat{G}$ is the phonon Green function,

$$G^{\alpha\beta}(lk, l'k') = \sum_{\nu}\frac{u_{\nu}^{\alpha}(l, k)u_{\nu}^{\beta}(l', k')}{\omega^2 - \omega_{\nu}^2 + i\delta}, \tag{A3}$$

$\mathbf{u}_{\nu}(l, k)$ are the eigenvectors corresponding to the νth eigenvalue of the dynamic matrix, and α and β are Cartesian superscripts.

The rate of local absorption of an electromagnetic field by the lattice at site (l, k) is given by

$$Q_{lk} = -\left\langle \frac{\partial}{\partial t}\int(e_k\mathbf{V}_{lk})d\mathbf{E}\right\rangle = -\frac{e_\tau^2 E_0^2}{2}\omega\,\mathrm{Im}\,J_{lk}(\omega), \tag{A4}$$

where E_0 is the field amplitude. In Eq. (A4), the angle brackets mean time averaging and

$$J_{lk}(\omega) = \frac{(-1)^k}{\sqrt{M_{lk}}}\sum_{\nu}\frac{D_{\nu}u_{\nu}(l, k)}{\omega_{\nu}^2 - \omega^2 - i\delta}, \tag{A5}$$

where

$$D_{\nu} = \sum_{l, k}\frac{(-1)^k}{\sqrt{M_{l, k}}}u_{\nu}(l, k).$$

In Eqs. (A4) and (A5), u_{ν} is the component of the νth eigenvector that is parallel to the external field.

REFERENCES

1. I. M. Lifshits, Usp. Fiz. Nauk **83**, 617 (1964) [Sov. Phys. Usp. **7**, 549 (1965)].
2. P. A. Lee and T. V. Ramakrishnan, Rev. Mod. Phys. **57**, 287 (1985).
3. S. V. Kravchenko, Phys. Rev. B **51**, 7038 (1995).
4. P. A. Lee, C. Castellani, and C. Di Castro, Phys. Rev. B **57**, R9381 (1998).
5. A. G. Khachaturyan, *The Theory of Phase Transformations and the Structure of Solids Solutions,* 2nd ed. (Nauka, Moscow, 1989).
6. S. M. Evangelou and A. Z. Wang, Phys. Rev. B **47**, 13 126 (1993).
7. A. Chakrabarti, S. N. Karmakar, and R. K. Moitra, Phys. Rev. Lett. **74**, 1403 (1995).
8. S. M. Evangelou and A. Z. Wang, J. Phys.: Condens. Matter **4**, L617 (1992).
9. S. John and M. J. Stephen, Phys. Rev. B **28**, 6358 (1983).
10. J. Canisius and J. L. van Hemmen, J. Phys. C **18**, 4873 (1985).
11. M. I. Vasilevskiy, O. V. Baranova, and S. V. Stroganova, Comput. Phys. Commun. **97**, 199 (1996).
12. G. Dolling and R. A. Cowley, Proc. Phys. Soc. **88**, 463 (1996).
13. W. Weber, Phys. Rev. B **15**, 4789 (1977).
14. M. I. Vasilevskiy, A. G. Rolo, M. J. M. Gomes, *et al.*, J. Phys.: Condens. Matter **13**, 3491 (2001).
15. J. H. Wilkinson and C. Reinsch, *Linear Algebra* (Springer, Berlin, 1971; Mashinostroenie, Moscow, 1976).
16. J. M. Ziman, *Models of Disorder: The Theoretical Physics of Homogeneously Disordered Systems* (Cambridge Univ. Press, Cambridge, 1979; Mir, Moscow, 1982).
17. I. M. Lifshits, S. A. Gredeskul, and L. A. Pastur, *Introduction to the Theory of Disordered Systems* (Nauka, Moscow, 1982; Wiley, New York, 1988).
18. D. W. Taylor, *Optical Properties of Mixed Crystals*, Ed. by R. J. Elliott and I. P. Ipatova (North-Holland, Amsterdam, 1988), p. 35.

Translated by A. Kazantsev

Mechanism of the D'yakonov–Perel' Spin Relaxation in Frequent Electron–Electron Collisions in a Quantum Well with a Finite Width

M. M. Glazov

Ioffe Physicotechnical Institute, Russian Academy of Sciences, Politekhnicheskaya ul. 26, St. Petersburg, 194021 Russia
e-mail: glazov@coherent.ioffe.rssi.ru
Received October 15, 2002

Abstract—A precession mechanism of spin relaxation of conduction electrons in a square quantum well is analyzed. The dependence of the spin relaxation time on the width of a quantum well and the height of its barriers is calculated under the assumption that the electron–electron collisions dominate over other processes of carrier scattering. © 2003 MAIK "Nauka/Interperiodica".

1. INTRODUCTION

In recent years, spin relaxation processes have attracted the particular attention of researchers due to the possible use of spin relaxation in the field of spintronics. One of the most efficient mechanisms of spin relaxation of conduction electrons in a quantum well over a wide range of temperatures is the D'yakonov–Perel' (precession) mechanism [1, 2], which is associated with the splitting of spin branches in the dispersion relation for electrons in systems without an inversion center. This splitting can be treated as a manifestation of an effective magnetic field with the Larmor precession frequency $\mathbf{\Omega_k}$, which is dependent on the magnitude and direction of the electron wave vector $\mathbf{k}$. The spin relaxation time can be estimated as $\tau_s^{-1} \propto \langle \mathbf{\Omega_k^2} \rangle \tau$, where the angle brackets indicate averaging over the electron energy distribution and τ is the microscopic relaxation time. In a quantum well, the Larmor frequency $\mathbf{\Omega_k}$ is a linear function of the electron wave vector $\mathbf{k}$; in this case, it is common practice to assume that τ is the time of momentum relaxation of electrons [2–4]. However, recent investigations have demonstrated that the contribution to the reciprocal of the relaxation time τ is additively made not only by different mechanisms of momentum relaxation but also by electron–electron collisions [5, 6]. Actually, the electron–electron collisions bring about random changes in the wave vector $\mathbf{k}$ and, hence, in the Larmor frequency $\mathbf{\Omega_k}$. Therefore, the spin relaxation occurring through the precession mechanism is controlled by electron–electron collisions as well as by other scattering processes. In our previous work [5], we calculated the time of spin relaxation for a two-dimensional electron gas under the condition that the electron–electron collisions are predominant. However, in contrast with the case considered in [5], it is of interest to take into account that, in a

real quantum well, the wave function for an electron proves to be quasi-two-dimensional due to its delocalization inside the quantum well and the penetration of tunneling tails of this function into regions under the barriers. In this respect, the aim of the present work was to calculate the dependence of the relaxation time τ on the width of a quantum well and the height of its barriers.

2. THEORETICAL BACKGROUND

Let us consider square quantum wells grown from materials with a zinc blende lattice in the [001] direction. In the parabolic approximation, the effective Hamiltonian for an electron located in the lowest conduction subband can be represented in the form

$$\mathcal{H} = \frac{\hbar^2 k^2}{2m} + \beta_{ln}\sigma_l k_n, \qquad (1)$$

where m is the effective electron mass, σ_l stands for the Pauli matrices, and k_n are the components of the electron wave vector in the plane of the quantum well. For a quantum well with symmetric interfaces, the term linear with respect to the electron wave vector $\mathbf{k}$ is associated with the absence of an inversion center in the bulk material and can be written in the form [2]

$$\beta_1(\sigma_y k_y - \sigma_x k_x). \qquad (2)$$

Here, the x and y axes are chosen parallel to the [100] and [010] crystallographic directions, respectively; $\beta_1 \propto \langle k_z^2 \rangle$ is a constant; and the angle brackets indicate the quantum-mechanical average. For an asymmetric quantum well, the effective Hamiltonian, in addition to term (2), contains the following spin-dependent contribution to the terms linear in $\mathbf{k}$ [7]:

$$\beta_2(\sigma_x k_y - \sigma_y k_x), \qquad (3)$$

where β_2 is a constant.

Now, we introduce the Cartesian coordinates x' ∥ [110], y' ∥ [110], z' ∥ [001], in which the part of the Hamiltonian that is linear with respect to the wave vector can be written as

$$\mathcal{H}_{c1} = \frac{\hbar}{2}(\mathbf{\Omega_k}\mathbf{\sigma}). \tag{4}$$

In relationship (4), we introduced the effective Larmor frequency with components $\mathbf{\Omega}_{kx'} = \beta_- k_{y'}$, $\mathbf{\Omega}_{ky'} = \beta_+ k_{x'}$, and $\mathbf{\Omega}_{kz} = 0$ and the coefficients $\beta_{\pm} = 2(\beta_2 \pm \beta_1)$.

The electron distributions over the wave vector and over the spin will be described by the spin density matrix, which, in turn, can be conveniently represented as a linear combination of 2×2 basic matrices:

$$\hat{\rho}_\mathbf{k} = f_\mathbf{k} + \mathbf{s_k}\mathbf{\sigma},$$

where $f_\mathbf{k} = \mathrm{Sp}(\hat{\rho}_\mathbf{k}/2)$ is the spin-averaged electron distribution function, $\mathbf{s_k} = \mathrm{Sp}[\hat{\rho}_\mathbf{k}(\mathbf{\sigma}/2)]$ is the average spin vector for an electron at the point $\mathbf{k}$, and the identity matrix is omitted. In the case when the splitting of spin states is disregarded, the spin-polarized nondegenerate electron gas with an equilibrium energy distribution can be described by the density matrix $\hat{\rho}_\mathbf{k}^0 = f_\mathbf{k}^0 (1 + 2\mathbf{S}_0\mathbf{\sigma})$, where $f_\mathbf{k}^0 = \exp[(\mu - E_\mathbf{k})/k_BT]$ is the Boltzmann distribution function, $E_\mathbf{k} = \hbar^2 k^2/2m$, μ is the chemical potential, and $\mathbf{S}_0$ is the spin per electron. If the spin splitting is small compared to $\hbar/\tau$, the distribution function remains unchanged, whereas the spin vector acquires the nonzero correction $\delta\mathbf{s_k} = \mathbf{s_k} - 2f_\mathbf{k}^0\mathbf{S}_0$, which is proportional to the spin splitting. Hence, the density matrix can be represented in the following form:

$$\hat{\rho}_\mathbf{k} = \hat{\rho}_\mathbf{k}^0 + \delta\mathbf{s_k}\mathbf{\sigma}. \tag{5}$$

By ignoring the spin flip in electron–electron collisions, the kinetic equation for $\mathbf{s_k}$ can be written in a standard form:

$$\frac{d\mathbf{s_k}}{dt} + \mathbf{\Omega_k} \times \mathbf{s_k} + \mathbf{Q_k}\{\mathbf{s}, f^0\} = 0. \tag{6}$$

Here, $\mathbf{Q_k}\{\mathbf{s}, f^0\}$ is the electron–electron collision integral, which accounts for the mixing of the spins in the $\mathbf{k}$ space; other processes of electron scattering are ignored; and the electron distribution function $f_\mathbf{k}$ is assumed to be an equilibrium function. If the exchange interaction is ignored, the electron–electron collision integral takes the form [5]

$$\mathbf{Q_k}\{\mathbf{s}, f^0\} = \frac{2\pi}{\hbar}\sum_{\mathbf{k'pp'}} \delta_{\mathbf{k+k', p+p'}}\delta(E_k + E_{k'} - E_p - E_{p'}) \tag{7}$$
$$\times 2V_{\mathbf{k-p}}^2(\mathbf{s_k}f_k^0 - \mathbf{s_p}f_p^0).$$

Here, $V_\mathbf{q}$ is the Fourier transform of the effective potential of the electron–electron interaction in the quantum well, which can be obtained by averaging the three-dimensional Coulomb potential energy; that is,

$$V(\rho) = \frac{e^2}{\kappa}\int\int \frac{\varphi_{e1}^2(z)\varphi_{e1}^2(z')}{\sqrt{\rho^2 + (z-z')^2}}dzdz',$$

where e is the elementary charge, κ is the permittivity, ρ is the separation between the electrons in the plane of the interface, and φ_{e1} is the envelope of the electron wave function describing the quantum confinement along the growth direction. After the Fourier transformation, we obtain the relationship [8]

$$V_\mathbf{q} = \frac{2\pi e^2}{\Sigma\kappa q}H(q), \tag{8}$$

where Σ is the surface area of the sample in the plane of the interfaces and $H(q) = \int\int \exp(-q|z - z'|)\varphi_{e1}^2(z)\varphi_{e1}^2(z')dzdz' \le 1$ is the form factor characterizing the delocalization of the electron wave function in the quantum well. The inclusion of the form factor in the calculation of the spin relaxation time is the main objective of the present work. The form factor $H(q)$ suggests a weakening of the electron–electron interaction as compared to the limiting case of a two-dimensional electron gas when $H(q) \equiv 1$. In the special case of infinitely high potential barriers, the envelope of the electron wave function for a quantum well of width a has the simple form $\varphi_{e1}(z) = \sqrt{2/a}\cos(\pi z/a)$ and the form factor is given by the relationship

$$H(q)$$
$$= \frac{-32\pi^4 + 32\pi^4 e^{-qa} + 3(qa)^5 + 20(qa)^3\pi^2 + 32\pi^4 qa}{[(qa)^2 + 4\pi^2]^2(qa)^2}.$$

In the limiting case where the separation between electrons is large ($qa \ll 1$), we obtain the form factor $H(q) \cong 1$ and the interaction between the electrons becomes strictly two-dimensional. In the opposite limiting case, the form factor $H(q)$ is inversely proportional to q; consequently, we have $V_\mathbf{q} \propto q^{-2}$, as is the case with a three-dimensional electron gas.

The state of an electron in a quantum well with barriers of finite height V can be described by the envelope

$$\varphi(z) = C\begin{cases} \cos kz, & |z| \le a/2 \\ \cos(ka/2)\exp[-\kappa(|z| - a/2)], & |z| > a/2, \end{cases} \tag{9}$$

where C is the normalization constant, $k = (2mE/\hbar^2)^{1/2}$, and $k = [2m(V - E)/\hbar^2]^{1/2}$. In this case, the difference between the electron masses in the materials of the quantum well and barriers is ignored. The boundary conditions of continuity of the functions φ and $d\varphi/dz$

can be reduced to the matching condition $\cos\xi = \gamma\xi$, where $\xi = ka/2$ and $\gamma = \hbar/a(2/mV)^{1/2}$ is the dimensionless parameter characterizing the well depth. For the square quantum well under investigation, the form factor $H(q)$ depends on two parameters of the well, namely, the quantum well width a and the barrier height V.

After the summation of expression (6) over the wave vector, we obtain an equation describing slow relaxation of the average spin:

$$dS_{0\alpha}/dt + \tau_{s,\alpha\beta}^{-1}S_{0\beta} = 0.$$

Here, the tensor of the inverse spin relaxation times is determined from the equation

$$\tau_{s,\alpha\beta}^{-1}S_{0\beta} = \frac{1}{N}\sum_{\mathbf{k}}[\mathbf{\Omega_k}\times\delta\mathbf{s_k}]_{\alpha}, \qquad (10)$$

where N is the electron concentration in the quantum well.

Let us assume that $\mathbf{\Phi_k}$ is the angle between the electron wave vector $\mathbf{k}$ and the axis $x'\parallel[110]$. In order to derive an appropriate equation for the correction $\delta\mathbf{s}$ to the spin distribution function, we retain the terms proportional to $\cos\mathbf{\Phi_k}$ and $\sin\mathbf{\Phi_k}$ in the kinetic equation:

$$\mathbf{\Omega_k}\times(2f_{\mathbf{k}}^0\mathbf{S}_0) + Q_{\mathbf{k}}\{\delta\mathbf{s}, f^0\} = 0. \qquad (11)$$

3. SOLUTION OF THE EQUATIONS AND DISCUSSION

When solving Eqs. (10) and (11), the projection of the vector product $\mathbf{\Omega_k}\times\mathbf{S}_0$ is conveniently represented in the form $\Lambda_{\alpha\beta\gamma}k_\beta S_{0\gamma}$. Here, we introduce the third-rank tensor Λ with four nonzero components, namely, $\Lambda_{xxz} = -\Lambda_{zxx} = \beta_+/\hbar$ and $\Lambda_{yyz} = -\Lambda_{zyy} = -\beta_-/\hbar$. Since the operator $Q_{\mathbf{k}}\{\delta s_\alpha, f^0\}$ conserves the angular distribution of the spin in the $\mathbf{k}$ space, the function $(1/k_\beta)Q_{\mathbf{k}}\{k_\beta F_k, f^0\}$ is independent of the azimuthal angle $\mathbf{\Phi_k}$, provided the arbitrary function F_k depends solely on the magnitude of the wave vector $\mathbf{k}$. Equation (11) can be conveniently represented in dimensionless units. For this purpose, we write the solution in the form

$$\delta s_\alpha(\mathbf{k}) = -\Lambda_{\alpha\beta\gamma}\frac{k_\beta}{k}S_{0\gamma}k_T\tau_{ee}^*e^{\mu/k_BT}v(K), \qquad (12)$$

where $v(K)$ satisfies the integral equation

$$Ke^{-K^2} = \int d^2K'\int d^2P\,W_{\mathbf{PP',KK'}}$$

$$\times[v(K)e^{-K^2} - \cos\Theta\,v(P)e^{-P^2}]. \qquad (13)$$

Here, we used the following designations: $\mathbf{K} = \mathbf{k}/k_T$, $k_T = (2mk_BT/\hbar^2)^{1/2}$, Θ is the angle between the vectors $\mathbf{K}$ and $\mathbf{P}$, $\mathbf{P'} = \mathbf{K} + \mathbf{K'} - \mathbf{P}$,

$$\tau_{ee}^* = \frac{\hbar k_B T\kappa^2}{e^4 N},$$

$$W_{\mathbf{PP',KK'}}$$

$$= \frac{1}{|\mathbf{K}-\mathbf{P}|^2}H(k_T|\mathbf{K}-\mathbf{P}|)\delta(K^2 + K'^2 - P^2 - P'^2).$$

By substituting $\delta\mathbf{s_k}$ in the form of expression (12) into Eq. (10) and summing over $\mathbf{k}$, we obtain the principal values of the tensor of the inverse spin relaxation times:

$$\frac{1}{\tau_{x'x'}^s} = \left(\frac{\beta_+ k_T}{\hbar}\right)^2\tau, \quad \frac{1}{\tau_{y'y'}^s} = \left(\frac{\beta_- k_T}{\hbar}\right)^2\tau,$$

$$\frac{1}{\tau_{zz}^s} = \frac{1}{\tau_{x'x'}^s} + \frac{1}{\tau_{y'y'}^s}, \qquad (14)$$

Here, the parameter τ, which characterizes the spin relaxation occurring through the D'yakonov–Perel' mechanism, is defined as

$$\tau = \tau_{ee}^*I, \quad I = \frac{1}{2}\int_0^\infty v(K)K^2\,dK. \qquad (15)$$

In relationship (13), the inhomogeneous term and the function $v(K)$ were expanded in series using the basis set $l_n(\varepsilon) = \sqrt{2}\exp(-\varepsilon)L_n(2\varepsilon)$, where $L_n(x)$ are the Laguerre polynomials and $\varepsilon = K^2$. Upon substituting the series expansions into relationship (13) and performing Monte Carlo summation over the dimensionless wave vectors, we obtain a system of linear inhomogeneous equations for the expansion coefficients of the function $v(K)$. The coefficient I involved in expression (15) was calculated as a function of the dimensionless parameters α and γ in the same manner.

The calculated dependence of the coefficient I on the barrier height V ($V > 200$ meV) at a constant width of the quantum well ($a = 42$ Å) can be approximately described by the following formula: $I \approx 0.032 + 1.2$ meV/V. A decrease in the barrier height leads to a decrease in the coefficient I and the time τ controlling the spin relaxation, because the electron wave function is distributed on a larger scale and the electron–electron interaction weakens.

The figure shows the calculated dependence of the coefficient I on the quantum well width. For a quantum well with infinitely high barriers, the coefficient I increases monotonically with an increase in the quantum well width. For a quantum well with a zero width, we obtained $I \approx 0.027$, as is the case with a two-dimensional electron gas in the absence of exchange interactions [5]. The dependence $I(\alpha)$ can be approximated by a linear function: $I(\alpha) \approx 0.027 + 0.009\alpha$. In the case when the quantum well width increases to $a \sim \pi/k_T$, the relative change in the coefficient I becomes of the order of unity, because the quantum-confinement energy is
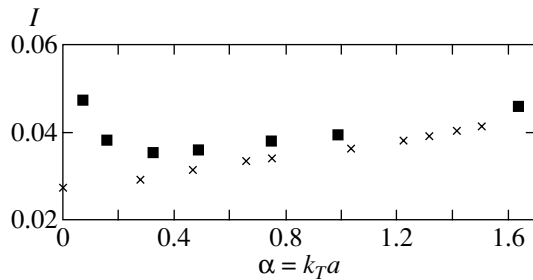
Dependence of the coefficient I determining the spin relaxation time [according to relationships (14) and (15)] on the quantum well width. Squares indicate the calculated dependence of the coefficient I on the dimensionless parameter $\alpha = k_T a$ for the barrier height $V = 300$ meV. For comparison, crosses show the calculated values of I for a quantum well with infinitely high barriers.

comparable to the energy of thermal motion of the electron.

For a quantum well with barriers of a finite height, the characteristic time of electron–electron collisions τ changes nonmonotonically with variations in the quantum well width and passes through a minimum $a = a_m \sim 2\hbar(2mV)^{1/2}$ when the electron wave function is subject to a minimum delocalization in the quantum well. As the quantum well width increases (or decreases) as compared to a_m, the integral I and, therefore, the time $\tau = \tau_{ee}^* I$ increase monotonically.

4. CONCLUSIONS

Thus, the precession mechanism of spin relaxation in a quantum well with barriers of a finite height was investigated theoretically. The characteristic time τ of electron–electron collisions responsible for spin relaxation was examined as a function of the width of a quantum well and the height of its barriers. It was demonstrated that the dependence of the relaxation time τ on the quantum well width exhibits a nonmonotonic behavior. In this case, the minimum of the parameter τ is determined by the maximum localization of the electron density in the quantum well. It can be clearly seen from the figure that, in the situation where the values of $k_T a$ fall in the range from 0.2 to 1.8, the time τ differs

from that for a two-dimensional electron gas by no more than 50%.

It should also be noted that the parameter τ is involved in the expressions for the tensor of the inverse spin relaxation times with factors $\beta_{\pm}^2$ [see relationships (14)], which can strongly depend on the quantum well width. In particular, for a quantum well with symmetric interfaces (when $\beta_2 = 0$), in the limiting case of infinitely high barriers, the factor β_1^2 decreases as a^{-4} with an increase in the quantum well width.

REFERENCES

1. M. I. D'yakonov and V. I. Perel', Fiz. Tverd. Tela (Leningrad) **13** (12), 3581 (1971) [Sov. Phys. Solid State **13**, 3023 (1971)].
2. M. I. D'yakonov and V. Yu. Kachorovskiĭ, Fiz. Tekh. Poluprovodn. (Leningrad) **20** (1), 178 (1986) [Sov. Phys. Semicond. **20**, 110 (1986)].
3. E. L. Ivchenko, P. S. Kop'ev, V. P. Kochereshko, *et al.*, Pis'ma Zh. Éksp. Teor. Fiz. **47** (8), 407 (1988) [JETP Lett. **47**, 486 (1988)].
4. Y. Ohno, R. Terauchi, T. Adachi, *et al.*, Phys. Rev. Lett. **83** (20), 4196 (1999).
5. M. M. Glazov and E. L. Ivchenko, Pis'ma Zh. Éksp. Teor. Fiz. **75** (8), 476 (2002) [JETP Lett. **75**, 403 (2002)].
6. R. T. Harley, M. A. Brand, A. Malinowski, *et al.*, in *Proceedings of the International Conference on Superlattices Nanostructures and Nanodevices, Toulouse, France* (2002).
7. Yu. L. Bychkov and É. I. Rashba, Pis'ma Zh. Éksp. Teor. Fiz. **39** (2), 66 (1984) [JETP Lett. **39**, 78 (1984)].
8. V. V. Afonin, V. L. Gurevich, and R. Laiho, Phys. Rev. B **62** (23), 15913 (2000).

Translated by O. Borovik-Romanova

LOW-DIMENSIONAL SYSTEMS
AND SURFACE PHYSICS

Grain-Boundary Diffusion in Nanocrystals with a Time-Dependent Diffusion Coefficient

A. A. Nazarov

Institute of Problems of Metal Superplasticity, Russian Academy of Sciences,
ul. Khalturina 39, Ufa, 450001 Bashkortostan, Russia
e-mail: Nazarov@anrb.ru
Received October 15, 2002

Abstract—A solution to the equation of grain-boundary diffusion is obtained under conditions where migration of the diffusant from the boundaries into the grains is absent and the diffusion coefficient decreases with time from an increased value to a value characteristic of equilibrium grain boundaries. The specific features of the grain-boundary diffusion in nanocrystals are qualitatively analyzed in terms of this solution. © *2003 MAIK "Nauka/Interperiodica".*

1. INTRODUCTION

Direct measurements of the coefficient of grain-boundary diffusion D_b in nanocrystalline materials lead to contradictory results. The first investigations demonstrated that, for nanocrystals prepared through condensation in a gas with subsequent compaction of the powder, the diffusion coefficient D_b is many orders of magnitude greater than the coefficient of grain-boundary diffusion in the materials with a standard grain size [1]. As a result, even the averaged diffusion coefficient for nanocrystals turns out to be larger than the coefficient D_b for usual materials. The activation energy of grain-boundary diffusion in nanocrystals, as a rule, is approximately equal to half the activation energy in coarse-grain materials and is close to the activation energy of surface diffusion [1]. More recent studies revealed that this effect is most likely associated with the porosity of nanocrystalline samples, which was found to be equal to 10% and greater [2]. For nanocrystals with a density close to that of the crystal, the diffusion coefficient at nanocrystal boundaries proved to be equal or somewhat greater than the diffusion coefficient at usual grain boundaries [2, 3]. However, in submicrocrystalline nickel with a grain size of about 300 nm and a density approximately equal to that of the crystal, the coefficient of copper grain-boundary diffusion in the temperature range 398–448 K is four or five orders of magnitude larger than the diffusion coefficient determined from extrapolating the data for coarse-grain nickel in the high-temperature range [4]. Preliminary annealing of submicrocrystalline nickel at a temperature of 623 K leads to the complete disappearance of the effect of an increase in the diffusion coefficient.

From the aforesaid, it follows that the coefficient of grain-boundary diffusion in nanocrystals depends primarily not on the grain size but on the structure of the grain boundaries that exist in a nonequilibrium state in the as-prepared samples. In particular, nonequilibrium grain boundaries involve free volumes, which is confirmed by positron annihilation spectroscopy [2] and dilatometry [5]. Consequently, the diffusion coefficient for nonequilibrium grain boundaries can exceed the diffusion coefficient for equilibrium grain boundaries. Possible mechanisms leading to this effect have been discussed recently (see, for example, [6, 7]). Direct experimental measurements of the diffusion coefficient, as a rule, are carried out at sufficiently high temperatures in order to provide appreciable penetration of the diffusant into the studied material. Under these conditions, the nonequilibrium structure of the grain boundaries undergoes relaxation due to grain-boundary diffusion [8]. The relaxation is accompanied by a gradual decrease in the grain-boundary diffusion coefficient. Thus, the actual diffusion experiment with nanocrystals is necessarily accomplished with a time-dependent diffusion coefficient. This can substantially affect the experimentally measured diffusion coefficient.

The purpose of this paper is to analyze the available experimental data on the coefficient of grain-boundary diffusion in nanocrystals in terms of the solution to the diffusion equation with a time-dependent coefficient.

2. SOLUTION OF THE DIFFUSION EQUATION WITH A VARIABLE COEFFICIENT

In order to estimate the diffusion coefficient at nonequilibrium grain boundaries characteristic of the structure of as-prepared nanocrystals, we use the Borisov relationship [9]

$$D_b^{\text{ne}} = D_b^{\text{eq}} \exp\left(\frac{\Delta E}{kT}\right), \qquad (1)$$

where D_b^{ne} and D_b^{eq} are the diffusion coefficients at non-equilibrium and equilibrium grain boundaries, respectively, and ΔE is the excess energy of nonequilibrium grain boundaries per atom.

Investigations into the recovery kinetics of nonequilibrium grain boundaries have demonstrated that relaxation of the excess energy of these boundaries occurs according to the exponential law [8]:

$$\Delta E = \Delta E_0 \exp\left(-\frac{t}{t_0}\right). \qquad (2)$$

Here, the time t_0 is equal to half the characteristic time of decreasing the density of extrinsic grain-boundary dislocations, because the excess energy is proportional to the square of the dislocation density; that is,

$$t_0 \approx \frac{d^3 kT}{200 \delta D_{bs}^{eq} G V_a}. \qquad (3)$$

Here, d is the grain size, δD_{bs}^{eq} is the product of the grain-boundary self-diffusion coefficient by the diffusion breadth for equilibrium grain boundaries, G is the shear modulus, and V_a is the atomic volume.

It is assumed that the gradient of the diffusant concentration is directed along the x axis lying in the plane of the grain boundary. Taking into account relationships (1)–(3), the diffusion equation can be represented in the form

$$\frac{\partial c}{\partial t} = D_b^{eq} \exp\left(\frac{\Delta E_0}{kT} e^{-t/t_0}\right) \frac{\partial^2 c}{\partial x^2}. \qquad (4)$$

This equation can be solved by changing the variables:

$$\tau = \int_0^t \exp\left(\frac{\Delta E_0}{kT} e^{-t/t_0}\right) dt = t_0 \int_0^{t/t_0} \exp\left(\frac{\Delta E_0}{kT} e^{-z}\right) dz. \qquad (5)$$

As a result, we obtain a standard diffusion equation,

$$\frac{\partial c}{\partial \tau} = D_b^{eq} \frac{\partial^2 c}{\partial x^2}. \qquad (6)$$

For diffusion in mode C, which is characterized by the absence of migration of the diffusant from the boundaries into the grains and is most commonly used to measure the grain-boundary diffusion coefficient in nanocrystals [1–4], the solution to Eq. (6) takes the form

$$c(x, \tau) = c_0 \operatorname{erfc}\left(\frac{x}{\sqrt{4 D_b^{eq} \tau}}\right). \qquad (7)$$

With due regard for expression (5), this solution can be transformed into a function of the coordinate x and time t.
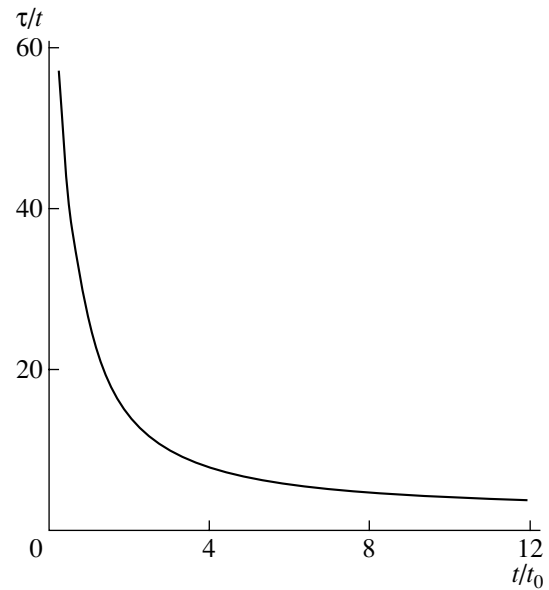
Fig. 1. Time dependence of the ratio τ/t characterizing the relative increase in the diffusion coefficient.

3. ANALYSIS OF THE SPECIFIC FEATURES OF DIFFUSION IN NANOCRYSTALS

As a rule, the experimental diffusion coefficient can be determined from constructed concentration profiles, i.e., dependences of the diffusant concentration on the diffusion depth at the instant of time corresponding to the time of diffusion annealing. It follows from relationship (7) that, upon changing over from the variable τ to the variable t, the dependence of the concentration on the depth remains unchanged. Consequently, the time dependence of the diffusion coefficient does not affect the functional form of the concentration profiles. However, from the analysis of the experimental profiles constructed in the c–t coordinates, we can determine the effective diffusion coefficient satisfying the condition $D_b^{eq} \tau = D_{ef} t$; that is,

$$D_{ef}/D_b^{eq} = \tau(t)/t. \qquad (8)$$

The dependence of the ratio $\tau(t)/t$ on t is shown in Fig. 1. As an example, the ratio D_b^{ne}/D_b^{eq} at the initial instant of time is chosen equal to 100.

Let us now consider two limiting cases. In the first case, the diffusion experiment is performed under the condition that the time of annealing is considerably longer than the time of relaxation ($t \gg t_0$). This becomes possible at a sufficiently high temperature of annealing. Hence, we have $\tau \approx t$ and the measured diffusion coefficient coincides with the diffusion coefficient at the equilibrium grain boundaries: $D_{ef} \approx D_b^{eq}$. In the second case ($t \ll t_0$), we obtain $\tau \approx \exp(\Delta E_0/kT)t \gg t$. This situation can occur in short-time annealing at low temperatures. Under these conditions, the effective diffusion

Characteristic relaxation times of nonequilibrium grain boundaries in comparison with the annealing times in measurements of the diffusion coefficient of nanocrystals

Metal	d, nm	T, K	D_b, m^2/s	t_0, h	t_d, h
Pd	100	430	2×10^{-21}	15	240
		577	1×10^{-18}	0.04	48
Ni	300	398	6×10^{-21}	80	3
		448	3×10^{-19}	1.8	3
Fe	25	450	1×10^{-22}	3	386
		500	1×10^{-20}	0.03	1.5–69

coefficient exceeds the diffusion coefficient at the equilibrium grain boundaries by several orders of magnitude. In the range between the limiting cases, the time of annealing is of the same order of magnitude as the time of relaxation and an increase in the temperature (or in the time of diffusion annealing) leads to a gradual decrease in the ratio $D_b^{\mathrm{ne}}/D_b^{\mathrm{eq}}$.

It can be seen from Fig. 1 that, at $D_b^{\mathrm{ne}}/D_b^{\mathrm{eq}} = 100$, the effective diffusion coefficient exceeds the value of D_b^{eq} by approximately one order of magnitude even after a lapse of time $t \approx 3t_0$. Therefore, the measured diffusion coefficient substantially depends on the time of diffusion annealing; i.e., the shorter the time of diffusion annealing, the larger the effective diffusion coefficient. In order to determine the diffusion coefficient D_b^{eq}, it is necessary to perform the diffusion annealing for a time considerably longer than t_0.

The above behavior of the diffusion coefficient is confirmed by the experimental data. For example, the measured coefficient of grain-boundary self-diffusion in nanocrystalline iron with a grain size $d = 19–38$ nm
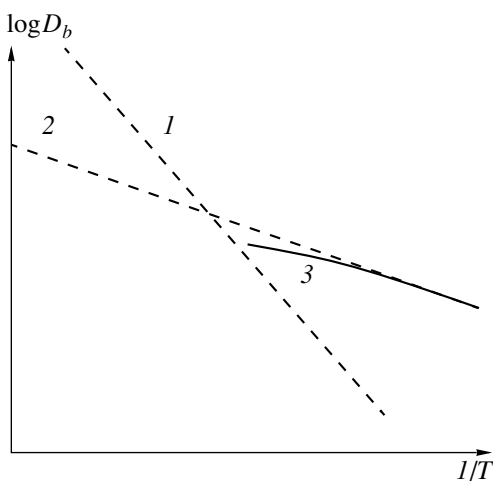
Fig. 2. Temperature dependences of the diffusion coefficient for (*1*) equilibrium grain boundaries at high temperatures, (*2*) nonequilibrium grain boundaries at low temperatures, and (*3*) nonequilibrium grain boundaries at intermediate temperatures.

decreases by one order of magnitude in the case when the time of diffusion annealing at the same temperature (473 K) increases from 1.5 h to 3 days [10]. In submicrocrystalline nickel, the copper diffusion coefficient decreases by three orders of magnitude after annealing at a temperature of 523 K [4].

The disagreement between the available experimental data can be explained to some extent in terms of the time dependence of the effective diffusion coefficient considered above. The table presents the calculated relaxation times t_0 for the nonequilibrium structure of the grain boundaries in comparison with the times of diffusion annealing used in the experiments. It is evident from the table that, in the measurements performed with nanocrystalline palladium and iron, the diffusion annealing over the entire temperature range covered was carried out during a period of time considerably longer than the time of relaxation. Under these conditions, the effective diffusion coefficient is close to the coefficient D_b^{eq}, which is observed in the experiment. On the other hand, three-hour annealing is obviously not sufficient for relaxation of grain boundaries in nickel and the effective diffusion coefficient in submicrocrystalline nickel substantially exceeds the diffusion coefficient D_b^{eq}.

The processes of relaxation proceeding during the diffusion experiment cause another significant effect, namely, a drastic decrease in the apparent activation energy of diffusion. According to relationship (1), the activation energy of diffusion decreases by ΔE; consequently, the activation energy of diffusion at the grain boundaries appears to be $E_b - \Delta E$. Figure 2 depicts the dependences $\log D_b(1/T)$ with activation energies E_b (straight line *1*) and $E_b - \Delta E$ (straight line *2*). As the temperature increases, the temperature dependence of the diffusion coefficient is represented first by branch *2* and then (after the complete relaxation of the grain boundaries) by branch *1*. At intermediate temperatures and times of annealing, the relaxation decreases the diffusion coefficient at nonequilibrium grain boundaries as compared to that represented by branch *2* and the actual dependence deviates downward along curve *3*. The slope of this branch is less than that of branch *2*. Therefore, the diffusion activation energy measured in

the experiment should be less than the value of $E_b - \Delta E$. This can explain the fact that the measured activation energy of grain-boundary diffusion in nanocrystals is approximately half that for usual polycrystals [4].

In the case when the time of diffusion annealing is chosen without regard for the relaxation time t_0 and is identical for all the temperatures studied above, we cannot rule out the possibility that the diffusion coefficient exhibits an anomalous behavior when portion *3* in Fig. 2 has a negative slope, i.e., when the apparent activation energy of diffusion is negative.

ACKNOWLEDGMENTS

REFERENCES

1. H. Gleiter, Phys. Status Solidi B **172** (1), 41 (1992).
2. R. Würschum, U. Brossmann, and H.-E. Schaefer, in *Nanostructured Materials: Processing, Properties, and Potential Applications*, Ed. by C. C. Koch *et al.* (William Andrew, New York, 1998), Chap. 7.
3. R. Würschum, K. Reimann, S. Qruß, *et al.*, Philos. Mag. B **76** (4), 401 (1997).
4. Yu. R. Kolobov, G. P. Grabovetskaya, M. B. Ivanov, *et al.*, Scr. Mater. **44**, 873 (2001).
5. R. Sh. Musalimov and R. Z. Valiev, Fiz. Met. Metalloved., No. 9, 95 (1992).
6. A. A. Nazarov, Philos. Mag. Lett. **80** (4), 221 (2000).
7. I. A. Ovid'ko and A. B. Reǐzis, Fiz. Tverd. Tela (St. Petersburg) **43** (1), 35 (2001) [Phys. Solid State **43**, 35 (2001)].
8. A. A. Nazarov, Interface Sci. **8** (4), 315 (2000).
9. V. T. Borisov, V. M. Golikov, and G. V. Shcherbedinskiǐ, Fiz. Met. Metalloved., No. 17, 881 (1964).
10. S. Herth, T. Michel, H. Tanimoto, *et al.*, Defect Diffus. Forum **194–199**, 1199 (2001).

Translated by O. Moskalev

Morphology and Optical Spectra of Metal Iodate Microcrystals in Porous Matrices

V. F. Agekyan*, I. Akai**, and T. Karasawa**

*Fock Institute of Physics, St. Petersburg State University, Petrodvorets, St. Petersburg, 198504 Russia
e-mail: avf@VA4678.spb.edu
**Department of Physics, Osaka City University, Sugimoto, Osaka, 558 Japan
Received October 31, 2002

Abstract—Microcrystals of iodates of mercury, lead, thallium, and bismuth were grown in pores of glass and polymer matrices from solutions or through sublimation in vacuum. Images of these microcrystals embedded in matrices were obtained with an electron microscope. Exciton absorption and luminescence spectra of the microcrystals revealed a strong difference in the temperature regions of stability of the various structural modifications between bulk crystals and microcrystals of some iodates. The absorption and luminescence spectra are broadened inhomogeneously because of considerable size dispersion of the microcrystals and exhibit quantum confinement effects. The exciton emission spectra show that exciton interaction in microcrystals becomes significant at very low optical pumping levels because of efficient excitation transfer from the matrix. © 2003 MAIK "Nauka/Interperiodica".

1. INTRODUCTION

The past decade has witnessed increased interest in the properties of metal halide microcrystals embedded in zeolites and other porous host matrices. The optical spectra of metal halides exhibit strongly pronounced excitonic effects, which makes the spectra sensitive to variations in the parameters of porous matrices and the conditions in which the microcrystals were loaded, as well as to transformations occurring in the course of sample ageing. Metal halides possess the characteristic property of being soluble in some liquids and having a low sublimation temperature, thus offering the possibility of microcrystal growth in matrices with low melting temperatures. Among the factors responsible for the difference between the optical spectra of microcrystals embedded in matrices and the optical spectra obtained from bulk crystals are quantum confinement, size dispersion, and the strong effect of near-surface regions, as well as a relation between the restrictions on microcrystal growth and the stability of some crystal modifications.

The present communication reports on a study of microcrystals of iodates of thallium, mercury, lead, and bismuth grown in a polymer and a glass porous matrix; presents micrographs of these systems; and compares the spectra of microcrystals with those of bulk crystals. The micrographs were obtained with a JSM-5600 scanning electron microscope having a resolution of 10 nm. Since the systems studied have a low electrical conductivity, the surface of the samples was coated with a gold film a few nanometers thick to make electron microscope measurements possible.

2. MERCURY IODATE

Mercury iodate emits bright luminescence, whose structure was studied comprehensively with a high resolution in [1]. Crystalline HgI_2 consists of heavy elements and is therefore used for the detection of ionizing radiation [2], and attempts are under way to employ, for these purposes, not only bulk crystals but also heterostructures containing layers of HgI_2-based solid solutions [3]. This makes investigation of thin films and microcrystals of mercury iodate an urgent problem. Bulk HgI_2 crystals crystallize usually in the tetragonal red modification (RM); however, the orthorhombic orange modification (OM), which transforms eventually to the RM, has been found to be stable in microcrystals grown in porous glasses with pore diameters of up to 50 nm and in porous polymer materials [4, 5]. Copper iodate has recently been shown to have the same property; indeed, CuI microcrystals embedded in a polyethylene methacrylate matrix are predominantly hexagonal, whereas bulk crystals have tetragonal symmetry [6]. The present study dealt with structural properties of HgI_2 microcrystals and their optical spectra obtained at different excitation levels, as well as with variation of these properties with time for a range of temperatures. The microcrystals were grown from saturated solutions of mercury iodate in acetone in (and partially, on the surface of) a porous polymer matrix. The pores are produced in the matrix by ion bombardment, and their diameters are, on the average, about one micrometer.

The two exciton luminescence peaks near 2.32 and 2.45 eV are due to the RM and OM of mercury iodate

(Fig. 1a). The spectra of an as-prepared sample practically do not have any indication of the presence of the RM. While the RM luminescence in the sample stored for a week at room temperature is already significantly stronger than the OM emission, the transformation of the OM in to the RM is not completed. The transition to the RM involves diffusion of material and growth of crystals in size, and we believe the residual OM to be due to the OM microcrystals, which were originally fairly large and, therefore, more stable. The importance of thermally activated diffusion of the material for a structural transition is also supported by the observation that, in a sample stored at 77 K, no OM-to-RM transformation is seen to occur and the sample does not change color. An increase in the concentration of the material in the matrix favors the formation of RM crystals, so that after several cycles of loading of a saturated solution with its subsequent evaporation, it is the RM that originally predominates in the sample. This observation stresses the relation between the crystal size and stability of a specific lattice modification.

In addition to an intensity redistribution between the OM and RM emission bands with time, the peaks of both exciton bands exhibit a long-wavelength shift (Fig. 1a). HgI_2 microcrystals in as-prepared samples have substantial size dispersion; for this reason, the quantum confinement effect, typical of microcrystals, contributes noticeably to the inhomogeneous broadening of the emission bands. Because sample ageing favors growth of RM microcrystals in size and it is the comparatively large OM microcrystals that persist the longest, the luminescence bands weaken in the high-energy regions. This scenario correlates with the time evolution of the spectra, where the increase in the RM contribution and the low-energy shifts of the maxima of both exciton bands (by 0.015 eV for the RM and by 0.025 eV for the OM) are accompanied by broadening of the maxima. The low-energy shift of the lowest exciton level can be treated with the well-known expression for the case of weak size quantization, $\Delta E = h^2\pi^2/2MR^2$, where M is the exciton translational mass and R is the microcrystal radius. The average radii of mercury iodate microcrystals in an as-prepared sample are estimated as 5 nm for the RM and 3 nm for the OM. As seen from photomicrographs, the comparatively large OM microcrystals present in an as-prepared sample are surrounded by clouds of small microcrystals (Fig. 2a), whereas the sample stored for several days at room temperature contains large RM microcrystals (Fig. 2b). Thus, the photomicrographs of the system support the idea of the transformation of its luminescence and absorption spectra with sample ageing.

Let us turn now to the dependence of the emission spectra on the excitation level by a pulsed molecular nitrogen laser (photon energy 3.68 eV) at $T = 2$ K (Fig. 1b). The ratio of the integrated RM to OM band intensities in the sample where the RM predominates
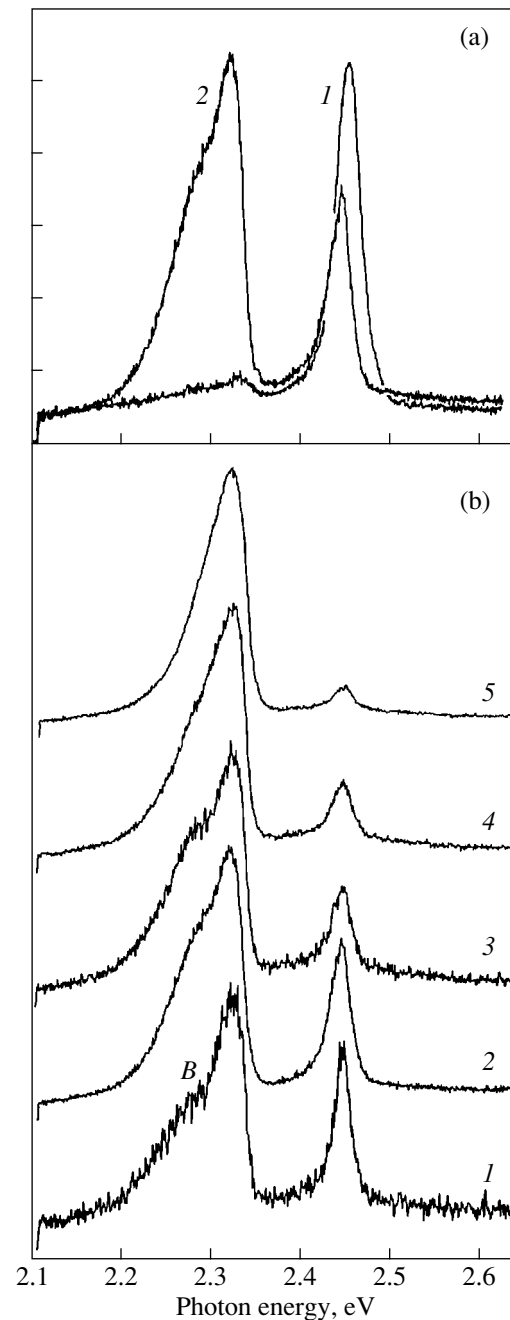
Fig. 1. Exciton luminescence spectra of HgI_2 microcrystals grown in porous polymer matrices. The bands at 2.32 and 2.45 eV correspond to the red and orange modifications, $T = 4$ K. (a) Ageing-induced transformation of the spectrum: (*1*) as-prepared sample and (*2*) sample stored at room temperature for a week. (b) Spectra of the aged sample obtained at different levels W_0 of pulsed nitrogen laser excitation (pump photon energy, 3.68 eV). W_0 increases from (*1*) 10^{-1} to (*5*) 10^2 W/cm^2. B is the band originating from exciton–exciton interaction.

varies by a few times as the pump level W_0 increases from 10^{-1} to 10^2 W/cm^2. As the excitation level increases, the RM and OM emission band maxima shift toward lower energies by 0.015 and 0.010 eV, respec-
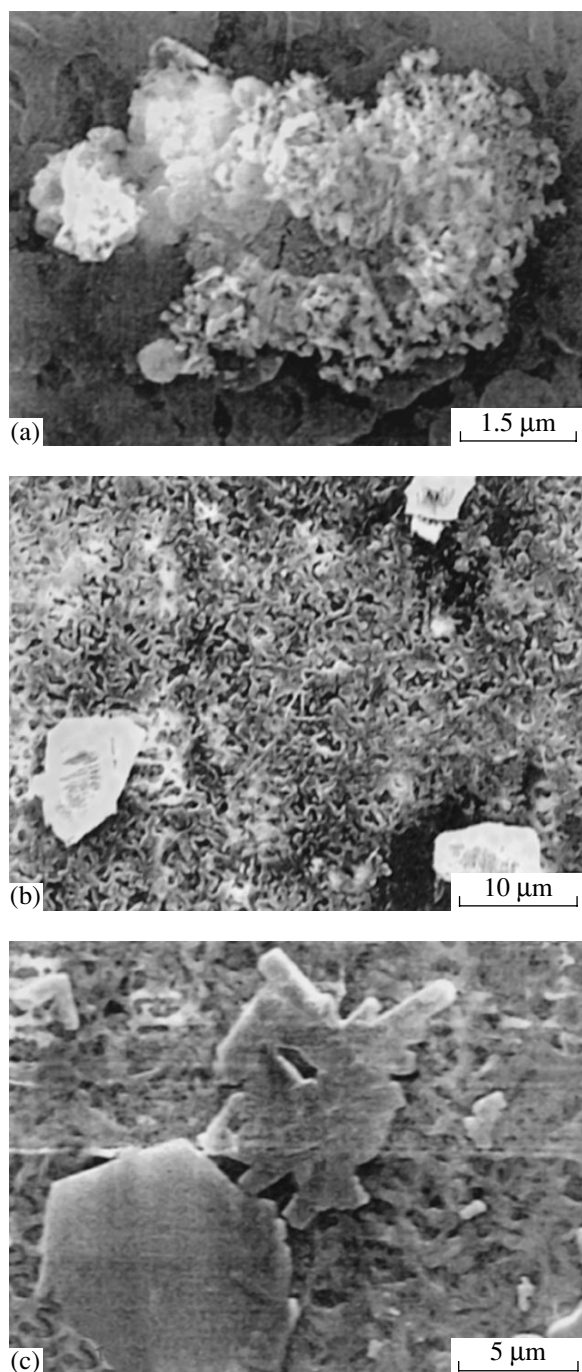
Fig. 2. Micrographs of a porous polymer matrix containing HgI$_2$ and PbI$_2$ microcrystals. (a) As-prepared sample with mercury iodate (clouds of small microcrystals of the orange modification), (b) the same sample stored for a week at room temperature (large microcrystals of the red modification), and (c) sample with platelets of hexagonal lead iodate.

tively. These features can be assigned to the saturation of emission from small microcrystals of both modifications and emission saturation of all OM microcrystals. The luminescence characteristics of HgI$_2$ microcrystals

become nonlinear at W_0 levels that are several orders of magnitude lower than those quoted for bulk crystals [7]. This difference is determined by efficient excitation transfer from the matrix to HgI$_2$ microcrystals, a conjecture supported by the luminescence of the matrix becoming weaker with increasing concentration of the mercury iodate in it. Already at $W_0 = 10^{-1}$ W/cm^2, band *B* produced by exciton interaction (biexcitons, inelastic exciton–exciton and carrier–exciton scattering) appears on the low-energy wing of the RM exciton band. We assign the much stronger manifestation of nonlinearity in the emission of the RM compared to OM microcrystals to the existence of local levels in the matrix, which lie above the RM electron band extrema in energy but below the extrema of the OM bands. It is via such levels that carriers can transfer from the matrix to the RM microcrystals.

3. LEAD IODATE

There is a wealth of publications on optical spectra of lead iodate microcrystals embedded in various matrices and of lead-iodate-based metal-organic nanostructures (see, e.g., [8–12]). Since PbI$_2$ is a layered crystal, its microcrystals should be modeled by microdisks, in which case the quantum confinement energy level shift is determined primarily by the thickness of the microcrystal rather than by its comparatively large lateral dimensions. In microcrystals grown in alkali borosilicate glass with an average pore size of 6 nm from a water solution saturated at 60°C, the high-energy shift of the lowest exciton level with respect to its bulk crystal position varies from 0.06 to 0.08 eV for various samples, which corresponds to a characteristic geometric size of the nanocrystals of about 2 nm. Assuming this dimension to be in the direction perpendicular to the crystal layers, the microdisk thickness should be 6–8 PbI$_2$ elementary layers. This estimate was made under the assumption of the microcrystals belonging to the 2*H* polytype characteristic of bulk crystals. However, because of the crystal growth being spatially confined, the layer packet stacking order may change. If PbI$_2$ microcrystals in porous matrices grow in the 4*H* structure, the exciton level shift will be governed, at least partially, by the difference between the band gap widths, which in the 4*H* polytype is slightly larger. While the luminescence spectrum of an as-prepared sample exhibits only free-exciton emission, repeat measurement shows the exciton to have completely relaxed to the bound state (Fig. 3). This is due to the photoinduced formation or recharging of defects.

While PbI$_2$ crystallized from a water solution in a porous polymer matrix does not exhibit a noticeable quantum confinement shift of the exciton luminescence maximum, the spectrum contains a high-energy tail, which corresponds to emission exceeding the band gap of the bulk 2*H* polytype in energy. A the photomicro-

graph of this system shows that the lateral dimensions of the microcrystals greatly exceed their thickness (Fig. 2c).

4. THALLIUM IODATE

A remarkable property of the thallium halides is their very large low-frequency dielectric permittivity. In standard conditions, thallium iodate has orthorhombic structure, which transforms into CsCl-type cubic at 170°C and atmospheric pressure (at room temperature, this structural transition requires a pressure of about 5 kbar to take place).

We grew microcrystals of thallium iodate in porous alkali borosilicate glass through immersion of the matrix in a TlI water solution saturated at 60°C, which was followed by its dehydration, a procedure repeated several times. At the sites where pores emerge onto the matrix surface, microcrystals with a size in excess of the pore diameter form. The exciton peak of the direct interband transition in the absorption spectrum of the orthorhombic TlI lies at 2.867 eV at $T = 2$ K [13], and the indirect edge starts 0.1 eV below it [14]. The sharp direct absorption edge of the system studied by us lies near 2.85 eV at $T = 77$ K (Fig. 4), thus implying orthorhombic symmetry of the microcrystals, because the direct exciton peak energy in the cubic TlI is 2.7 eV. The orthorhombic symmetry of TlI is corroborated by the shape of the microcrystals forming on the matrix surface (Fig. 5a).

The luminescence band peak of the TlI microcrystals is shifted by 0.1 eV relative to the direct edge, so that this peak lies in the region of the indirect absorption edge. Note that, because of the direct and indirect edges being very closely located, the oscillator strength of the indirect transition in the orthorhombic TlI is comparatively large. At high energies, the TlI emission band overlaps with the matrix luminescence band (Fig. 4), thus complicating analysis of its shape; it is obvious, however, that the microcrystal emission tail lies considerably higher in energy than the exciton peak in the bulk crystal spectrum. Thus, this system also exhibits the emission of small microcrystals, whose energy levels are shifted toward higher energies by quantum confinement. Our estimates place the exciton radius in TlI at 5–6 nm, which allows one to conclude that there are microcrystals a few nanometers in size in the matrix. Significantly, heating the samples to nearly the melting point of TlI (440°C) does not transfer the microcrystals to the cubic phase, whereas in bulk crystals, this structural transition occurs at a much lower temperature. This indicates a broadening of the stability region for the low-symmetry modification of the microcrystals, which is also characteristic of mercury and copper iodates.
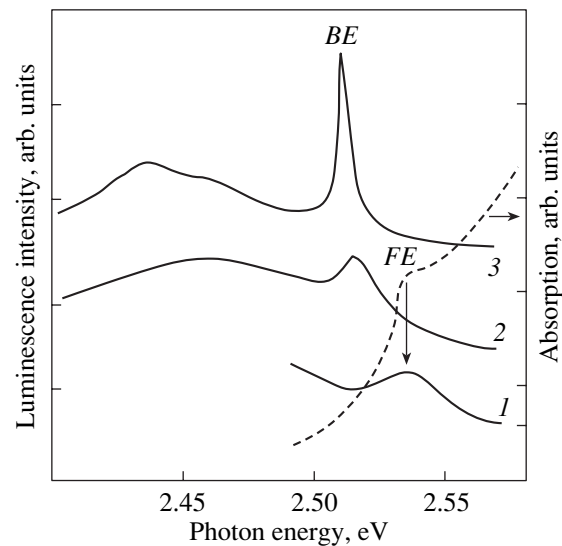

Fig. 3. Luminescence (solid lines) and absorption (dashed line) of PbI$_2$ microcrystals in a porous glass matrix. (*1*) As-prepared sample at $T = 77$ K and (*2, 3*) spectra of the same sample after relaxation at $T = 77$ and 4 K, respectively. *FE* stands for free exciton, and *BE*, for bound exciton.
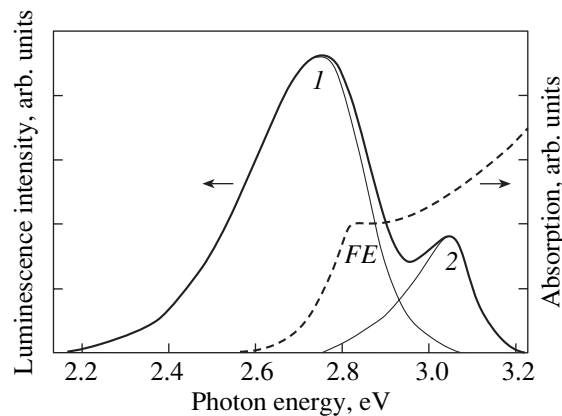
Fig. 4. Absorption (dashed line) and luminescence (solid line) spectra of a polymer matrix containing TlI microcrystals at $T = 77$ K. (*1*) Emission of TlI microcrystals and (*2*) emission of the matrix.

5. BISMUTH IODATE

Porous-glass platelets and BiI$_3$ single crystals were placed in an evacuated ampoule and heated to 300–400°C, a process in which microcrystals grew under sublimation in the pores (Fig. 5b). After termination of the growth, the matrices with the microcrystals were cooled either gradually or abruptly. In the latter case, the spectra were more diffuse because of large strains. The growth on the glass matrix surface starts primarily at the pore entrances, near which a dendritic microcrystalline structure forms (Fig. 5c). One can also grow BiI$_3$

(a) 2 μm

(b) 0.2 μm

(c) 1 μm
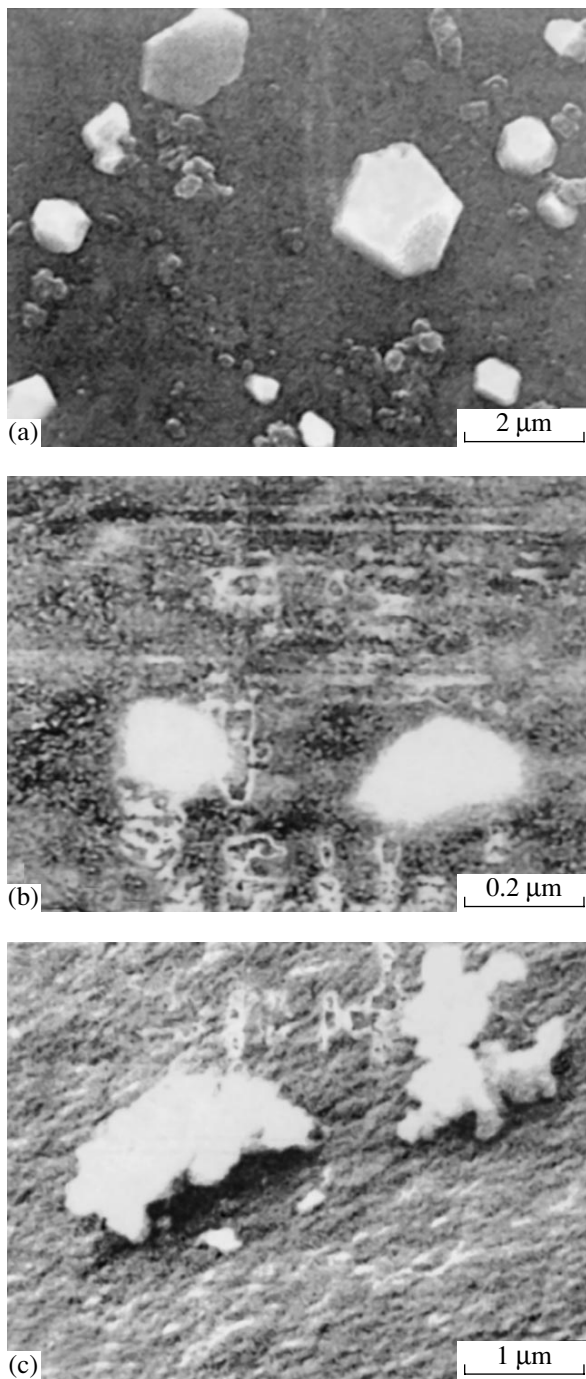
Fig. 5. Micrographs of a porous glass matrix containing TlI and BiI₃ microcrystals. (a) Microcrystals of thallium iodate, (b) microcrystals of bismuth iodate embedded in the matrix, and (c) dendritic structure of bismuth iodate on the matrix surface.

microcrystals in a polymer matrix from a solution of bismuth iodate in hydrochloric acid.

In glasses with large pores, the absorption spectrum of microcrystals is close to that of bulk BiI₃ in the position of the direct-exciton maximum and of the indirect-exciton phonon replicas. Matrices with pore dimensions of 6 nm exhibit a short-wavelength shift of the exciton absorption maximum by 20 to 50 meV as compared with bulk BiI₃ (Fig. 6a) [14]. Assuming the shift to be determined primarily by the thickness of the layered microcrystal, one can estimate the bismuth iodate microcrystal thicknesses in the weak size quantization approximation from known exciton parameters as seven to three layer packets. In matrices with a low BiI₃ microcrystal concentration, the absorption spectrum contains, in addition to a structure close in energy to the bulk-crystal absorption edge, bands observed earlier in spectra of small BiI₃ clusters [8].

Let us briefly compare the luminescence spectrum of relatively large BiI₃ microcrystals grown in pores of the glass matrix and on its surface with that of bulk crystals (Fig. 6b). The size-quantized shift of the exciton band center for such microcrystals does not exceed 10 meV. The microcrystal emission band X_2 lies in the region 1.91–1.93 eV, where bulk BiI₃ (C_{3i}^2 symmetry) exhibits a sharp structure due to excitons imprisoned in mesoscopic domains; these domains can be modeled by quantum disks one, two, and three layer packets thick. The exciton light emission from such domains consists of groups of narrow lines, denoted by W_1, W_2, and W_3 in the spectra presented in [14–16]. The BiI₃ lattice in these domains has D_{3d} symmetry; therefore, the energy of emission from the domains is determined by the band gap of bulk BiI₃ with D_{3d} symmetry (which is considerably less than the band gap of the conventional BiI₃ crystal of C_{3i}^2 symmetry) and by the size-quantized shift of energy levels in domains of different thickness. As in bulk crystals with domains, the emission of microcrystals in the range 1.91–1.93 eV varies from one sample to another, depending on the actual concentration of the mesoscopic domains and their size distribution. The maximum of the other band, X_1, varies in position in different microcrystalline samples from 1.97 to 2.02 eV, which overlaps the region of the narrow T, S, and R lines of excitons bound to stacking faults. These lines are seen in absorption (Fig. 6a) and luminescence of bulk BiI₃ crystals [16, 17]. We believe that the strong microcrystal emission band X_1 of a complex structure contains contributions from both excitons bound to stacking faults and W_1-type domain excitons. The spectra of strongly strained BiI₃ microcrystals are dominated by low-energy components of this band. The position of the weak X_2 band can be identified with the W_2 and W_3 domain excitons, which have a lower energy than W_1 and belong to comparatively large mesoscopic domains. Mesoscopic domains (disks) in microcrystals should be, first, dominated by thin disks (exciton W_1) and, second, confined in lateral disk dimensions, which should shift the groups of the W_1, W_2, and W_3 narrow
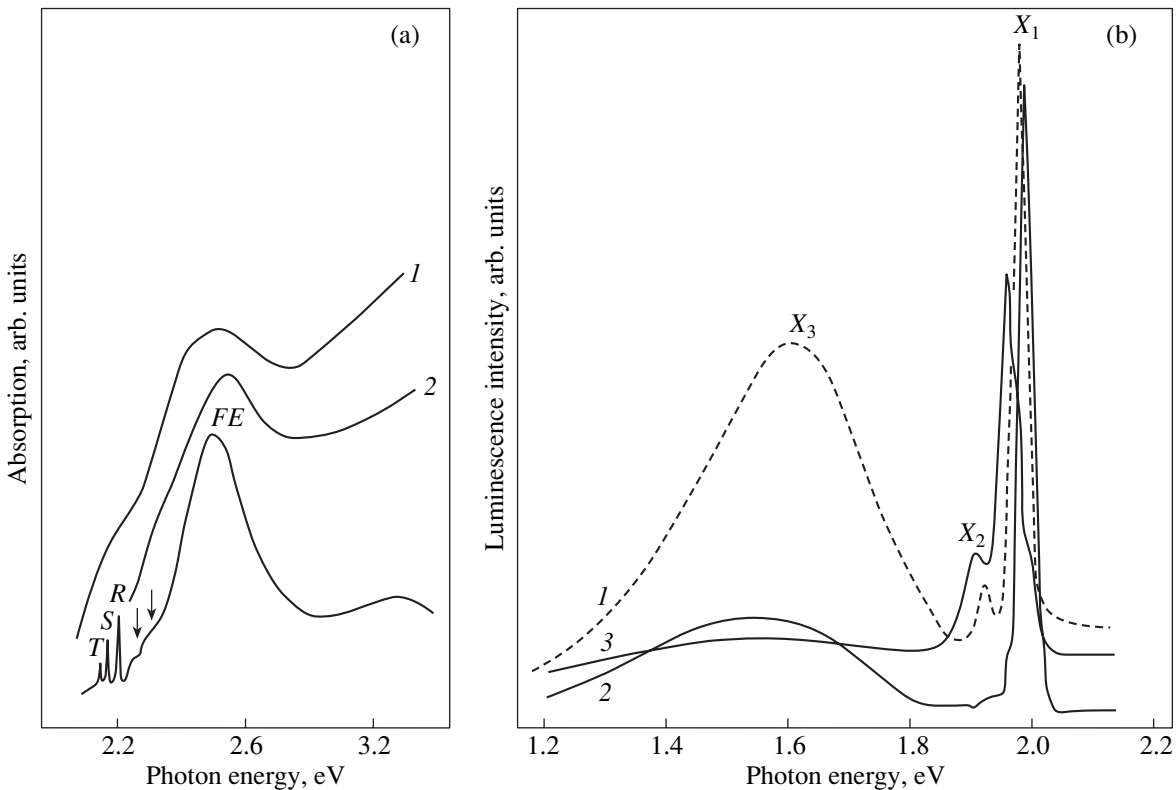
Fig. 6. Spectra of BiI_3 microcrystals grown in porous glass matrices, $T = 4$ K. (a) Absorption spectra of matrices with (*1*) high and (*2*) low bismuth iodate concentrations; shown below for comparison is a spectrum of a 500-nm-thick BiI_3 single crystal (*T*, *S*, *R* are the lines of stacking-fault-bound excitons; *FE* stands for free exciton; arrows identify the indirect-exciton edge steps). (b) Luminescence spectra of matrices with (*1*) low and (*2*) high microcrystal concentration and (*3*) spectrum of a sample with strongly strained microcrystals. Bands X_1 and X_2 are due to the emission of comparatively large microcrystals, and band X_3 relates to small microcrystals.

lines to even higher energies. The broad band peaking at 1.6 eV is the strongest in samples with a low BiI_3 microcrystal concentration. It originates most likely from an emission of small microcrystals characterized by large Stokes losses [14], which determine the position of the luminescence band in the low-energy spectral region. This band weakens with increasing quantity of BiI_3 in the matrix, an observation that can reasonably be assigned to a decrease in the volume fraction of small microcrystals.

Thus, for metal iodates having several structural modifications, the temperature region of modification stability changes radically in going from large crystals to microcrystals. The optical spectra of layered iodate microcrystals are governed primarily by the number of layer packets, which increases with an increasing the loading of matrix pores by the material under study.

REFERENCES

1. X. J. Bao, T. E. Schlesinger, R. B. James, *et al.*, J. Appl. Phys. **68**, 2951 (1990).
2. R. Farell, F. Olschner, K. Shah, and M. R. Squillante, Nucl. Instrum. Methods Phys. Res. A **387**, 194 (1997).
3. N. V. Sochinskii, V. Munos, J. M. Perez, *et al.*, Appl. Phys. Lett. **72**, 2023 (1998).
4. I. Kh. Akopyan, O. N. Volkova, B. V. Novikov, and B. I. Venzel', Fiz. Tverd. Tela (St. Petersburg) **39**, 468 (1997) [Phys. Solid State **39**, 407 (1997)].
5. V. F. Agekyan, A. Yu. Serov, and Yu. A. Stepanov, Fiz. Tverd. Tela (St. Petersburg) **42**, 1786 (2000) [Phys. Solid State **42**, 1832 (2000)].
6. I. Akai, T. Sato, A. Tanji, *et al.*, J. Lumin. **87–89**, 516 (2000).
7. I. Kh. Akopyan, B. V. Novikov, M. M. Pimonenko, and B. S. Razbirin, Pis'ma Zh. Éksp. Teor. Fiz. **17** (3), 419 (1973) [JETP Lett. **17**, 299 (1973)].
8. Z. K. Tang, Y. Nozue, and T. Goto, J. Phys. Soc. Jpn. **60**, 2090 (1991).
9. V. F. Agekyan and A. Yu. Serov, Fiz. Tverd. Tela (St. Petersburg) **38**, 122 (1996) [Phys. Solid State **38**, 65 (1996)].

10. A. Yamamoto, H. Nakahara, M. Yoshihara, and T. Goto, J. Phys. Soc. Jpn. **67**, 2120 (1998).

11. A. Nagai, K. Okamura, and T. Ishihara, Physica B (Amsterdam) **227**, 346 (1996).

12. N. Ohno, K. Nakamura, and Y. Nakai, J. Phys. Soc. Jpn. **55**, 3659 (1986).

13. N. Ohno and M. Itoh, J. Phys. Soc. Jpn. **62**, 2966 (1993).

14. T. Komatsu, D. Kim, T. Kobayashi, *et al.*, Surf. Rev. Lett. **3**, 1127 (1996).

15. T. Komatsu, T. Iida, K. Mirayama, *et al.*, Mol. Cryst. Liq. Cryst. **37**, 218 (1992).

16. T. Komatsu, T. Karasawa, I. Akai, and T. Iida, J. Lumin. **70**, 448 (1996).

17. T. Komatsu, T. Iida, I. Akai, and V. F. Agekyan, Fiz. Tverd. Tela (St. Petersburg) **37**, 2433 (1995) [Phys. Solid State **37**, 1332 (1995)].

Translated by G. Skrebtsov

<hr>

LOW-DIMENSIONAL SYSTEMS
AND SURFACE PHYSICS

<hr>

Structure and Physical-Mechanical Properties of Nanostructured Thin Films

D. V. Shtanskiĭ*, S. A. Kulinich**, E. A. Levashov*, and J. J. Moore***

* Moscow Institute of Steel and Alloys, Leninskiĭ pr. 4, Moscow, 119991 Russia
e-mail: shtansky@shs.misis.ru
** National Institute for Materials Science, Sakura 3-13, Tsukuba, 305-0003 Japan
*** Colorado School of Mines, Golden, Colorado, 80401-1887 USA
Received October 8, 2002; in final form, November 19, 2002

Abstract—The structure and mechanical properties of nanostructured thin films based on carbides, nitrides, and borides of transition metals are described. The mechanisms of localized deformation of the films during indentation are compared. It is shown that the tendency of a material to form shear bands during deformation can be predicted using the parameter H^3/E^2, which describes the resistance of the material to plastic deformation. The columnar structure of the films is found to play an important role during deformation, which proceeds via slipping of columnar structural elements along the direction of an applied load. © 2003 MAIK "Nauka/Interperiodica".

1. INTRODUCTION

The structures of nanomaterials differ from those of ordinary materials, which thus leads to the discovery of new physical phenomena as a result of the unique structure and properties of nanomaterials. Surface engineering has currently reached the nanometer scale. However, significant problems were encountered regarding both fundamental understanding of the behavior of nanosystems and quantitative measurements and interpretation of their properties, and this has hampered the development and application of nanotechnologies [1, 2].

Tribological coatings should have low abrasive wear, high fatigue strength, and high resistance to deformation and fracture. According to the classical theory of wear, low abrasive wear is ordinarily related to high hardness (which has been repeatedly borne out for films [3, 4]) and high fatigue strength corresponds to high values of the Young's modulus. In real practice, the hardness H of a material is usually measured; however, this quantity is a dependent characteristic and is connected with the elastic and plastic properties of the material. The hardness of nanostructured films can be as high as 50–70 GPa [3] and even exceed that of polycrystalline diamond [5]. Most bulk materials with high hardness exhibit high values of the modulus of elasticity E, which makes them brittle. To estimate the resistance of materials to elastic strain to failure, the ratio of the hardness to the elastic modulus H/E, which is also called the plasticity index, is used. To estimate the resistance of materials to plastic strain, the parameter H^3/E^2 is applied [6]. Whence it follows that, in order to possess an increased resistance to elastic breaking strain and a decreased plastic strain, a material should have high hardness and a low modulus of elasticity. One of

the methods for producing materials with a high H/E ratio is the deposition of nanostructured coatings.

An interesting feature of hard, superhard ($H \geq 40$ GPa), and ultrahard ($H \geq 70$ GPa) nanostructured films is that, apart from high hardness, they also have high strength and elastic recovery W_e (up to 90%) [7, 8]. Thus, we deal with a new class of materials that have high hardness and elasticity and allow intentional variation of the values of H, E, and W_e. The elastic behavior of nanostructured films can be caused by an absence of internal sources of dislocations in nanocrystals of sizes below a certain critical value [9]. In this case, the mechanism limiting the deformation of nanostructured films is diffusion mass transfer and/or grain-boundary slip, whereas dislocation motion is hindered because of small crystallite size and the presence of intergrain amorphous layers. The strength of the interface, whose volume fraction can be as high as 50%, becomes one of the key factors determining the deformation of nanomaterials. Moreover, the critical crack size in nanomaterials coincides with the size of crystallites and is only a few nanometers. Therefore, it was assumed that nanostructured materials cannot deform plastically. Vepřek and Reiprich [10] believe that multiple nanocracks, which cannot grow above a critical size specified by crystallite size, appear during deformation of nanostructured films. Upon unloading, these nanocracks become closed, thus leading to the partial or complete recovery of deformed regions. This hypothesis is in conflict with a number of experimental results. For example, the authors of [9, 11–13] showed that the deformation of nanostructured films can be both homogeneous and inhomogeneous (localized, with the formation of shear bands). Plastic deformation in localized

Table 1. Basic deposition parameters and film structures

Film composition	Deposition parameters			Film structure		
	temperature, °C	bias voltage V, V	nitrogen partial pressure (N_2/Ar)	crystal structure	grain size, nm	film morphology
Ti–B–N (1)	250	–250	0	NaCl	10–40	Equiaxed grains
Ti–B–N (2)	400	0	0	NaCl	4–10	"
Ti–Cr–B–N	250	0	0.15	NaCl	2–7	"
Ti–Si–N	250	0	0.15	NaCl	10–30	Columnar grains
Cr–B	250	–250	0	AlB_2	1000*	"

* Each columnar grain consists of grains and subgrains 20-–40 nm in size.

Table 2. Mechanical properties and roughness of films

Film composition	Hardness H, GPa (Si substrate)	Elastic modulus E, GPa	H/E	H^3/E^2, GPa	R_{rms}, nm	Elastic recovery W_e, %
Ti–B–N (1)	34	250	0.136	0.63	1.15	81
Ti–B–N (2)	42	300	0.140	0.82	4.5	77
Ti–Cr–B–N	27	240	0.112	0.34	0.3	73
Ti–Si–N	24	210	0.114	0.31	1.3	76
Cr–B	33	276	0.119	0.47	1.0	73

regions is typical for amorphous materials and was also observed in some nanostructured and ceramic materials. Although there are various models for the deformation of materials via the formation of shear bands [14], this phenomenon has not been properly explained.

The microstructure of single-phase films is usually well described by the model of structural zones [15, 16]. According to this model, films prepared under the conditions of low mobility of adsorbed atoms have a strongly anisotropic columnar structure. This structure often appears in films grown through physical deposition and causes undesirable stresses parallel to the surface of the substrate. Localized strain in films with a pronounced columnar structure is assumed to develop homogeneously, whereas the formation of shear bands is typical of films with an equiaxed-grain structure [9, 11–13].
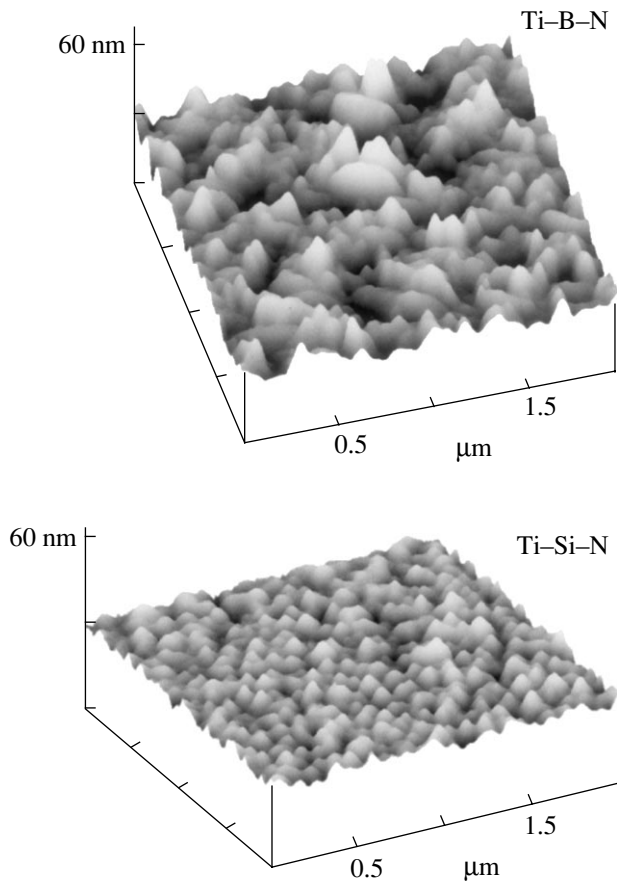
The purpose of this work is to describe the behavior of nanostructured films based on carbides, nitrides, and borides of transition metals under localized deformation and to reveal an interrelation between their structure and physical-mechanical properties.

Composite targets to be sputtered were fabricated through the process of force SHS compacting (self-propagating high temperature synthesis) from exothermic blends of different powders [17]. Thin films were deposited through magnetron sputtering of the composite targets in an argon atmosphere or a gaseous mixture of argon and nitrogen. The temperature and bias voltage were varied (Table 1). For substrates, we used (001) silicon single crystals, nickel, stainless steel, and a VK-type hard alloy. The structure of coatings was studied using a Hitachi S-4200 scanning and a Hitachi-9000NAR transmission electron microscope. Foils for a high-resolution electron microscopic study of transverse sections were prepared following the standard technique [1]. A Geigerflex diffractometer was used for x-ray diffraction analysis. Depth profile analysis of the film composition was performed using Auger electron spectroscopy on an LHS-10 SAM apparatus. The hardness, modulus of elasticity, and elastic recovery were measured on a TriboScope device (Hysitron, Inc., USA) and a nanohardness tester (CSM Instruments, Switzerland) by following the Oliver and Pharr technique [18]. Localized deformation in films was initiated with a tetrahedral Vickers pyramid under loads of 10, 25, and 50 g. Film surface topography before and after indentation was studied using NanoScope III (Digital Instruments, US) and NanoScan (Russia) atomic-force microscopes (AFMs).
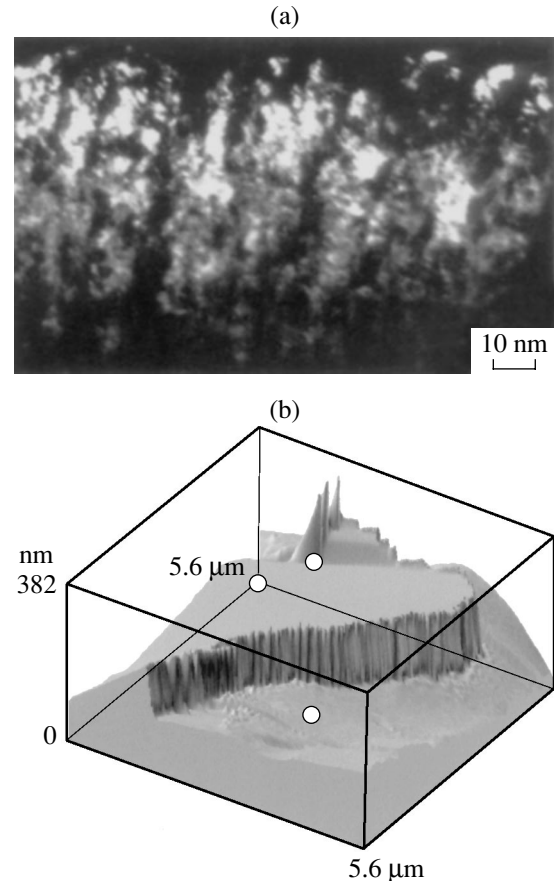
2. FILM STRUCTURES

Table 2 gives the root-mean-square values of the surface roughness R_{rms} of films measured using AFM with an accuracy of 5%. The film roughness is seen to depend on both the chemical composition and parameters of the physical deposition. The smoothest surface was detected in the Ti–Cr–B–N films, which inherited the roughness (0.2 nm) of the silicon substrate after ion etching. When a bias voltage is applied, the outer layers of a film are sputtered by ions of a working gas and then deposited, which smoothens the film surface. However,

Fig. 1. Surface topography of Ti–B–N (2) and Ti–Si–N films.

Fig. 2. Films with a columnar structure: (a) electron microscopic dark-field image of the cross section of a Ti–Si–N film and (b) fractograph of the fracture surface of a CrB_2 film.

in the case of multicomponent films, a perfect surface can be prepared without applying a bias voltage. With increasing substrate temperature, the film surface roughness increases because of the increased mobility of deposited atoms and their diffusion to islands formed earlier. AFM images (Fig. 1) show that the film surfaces are covered with three-dimensional hillocks 40–50 nm (Ti–Cr–B–N), 60–70 nm (Ti–Si–N), 80–100 nm (Ti–B–N (1)), 130–140 nm (CrB_2), and 170–190 nm (Ti–B–N (2)) in size. The nature of these hillocks is usually connected with the film growth mechanism, i.e., with the formation of separate islands on the substrate surface (the Volmer–Weber mechanism) and their growth and coalescence, which result in the formation of intergrain cavities due to the shielding effect.

The results of the structural analysis are given in Table 1. The structures and morphology of the films are seen to differ significantly. The Cr–B and Ti–Si–N films have a pronounced columnar structure with columns 10–30 nm and 0.1 μm in diameter, respectively (Fig. 2). Columnar grains in the latter films, however, contain many equiaxed grains and subgrains, which means that the actual size of crystallites in them
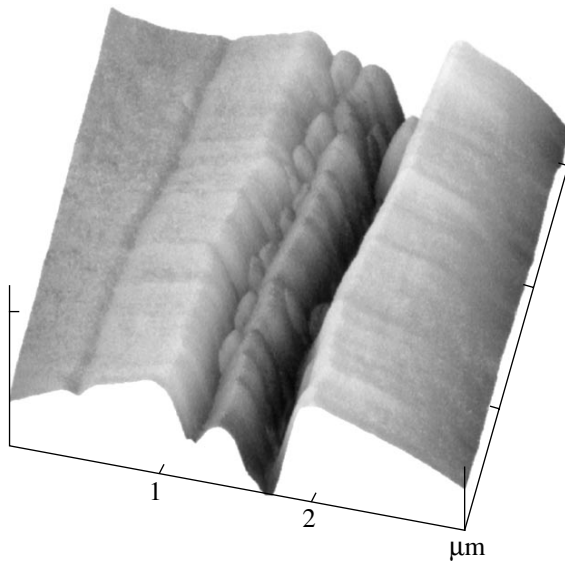
(20–40 nm) turns out to be substantially smaller than the width of columnar macrograins. Note that a columnar structure with many crystallites inside its elements was observed earlier in [19]. The cross-sectional electron microscopic study of the Ti–B–N and Ti–Cr–B–N films showed the absence of a columnar structure (Figs. 3a, 3b). A dark-field image of the structure of the Ti–Cr–B–N film demonstrates crystallites 2–7 nm in size (Fig. 3c). The corresponding electron diffraction pattern shows that they have a cubic NaCl-type structure. Note that the film grows along the image plane, which indicates the absence of a columnar structure. Instead, TiN-based equiaxed grains and intergrain amorphous regions are formed. Figure 3d shows a high-resolution micrograph of a Ti–Cr–B–N film with a separate TiN nanocrystallite 3–4 nm in size oriented along the $\langle 001 \rangle$ zone axis.

It is interesting that Ti–Si–N and Ti–Cr–B–N films deposited under identical conditions ($T = 250°C$, $V = 0$, $N_2/Ar = 0.15$) have different morphology, namely, a columnar grain structure in the former case and an equiaxed-grain structure in the latter. The formation of a strongly anisotropic columnar structure is ordinarily

Ti–B–N (1)

0.1 μm

(a)

Ti–Cr–B–N

0.2 μm

(b)

Ti–Cr–B–N

220
200
111

10 nm

(c)

Ti–Cr–B–N

(100)

(010)

2 nm

(d)
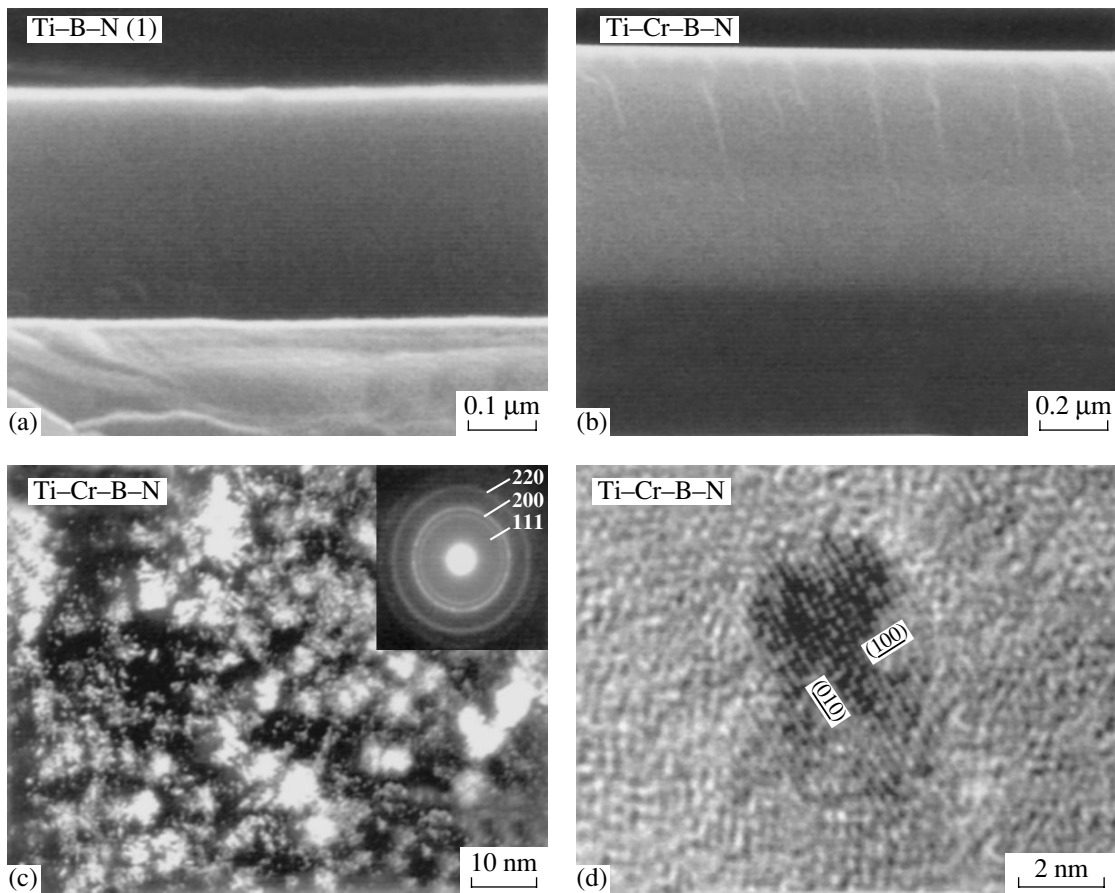
Fig. 3. Electron microscopic images of films with an equiaxed-grain structure: (a, b) scanning, (c) dark-field, and (d) high-resolution images.

related to segregation of impurities along grain boundaries when the mobility of adsorbed atoms is low [15, 16]. Our results indicate that the structure of a multicomponent film cannot be unambiguously predicted using the model of structural zones, which performed

1

2

μm

Fig. 4. Fractograph of the fracture surface of a Ti–Cr–B–N film after scratching its surface with a diamond pyramid.

0.2 μm
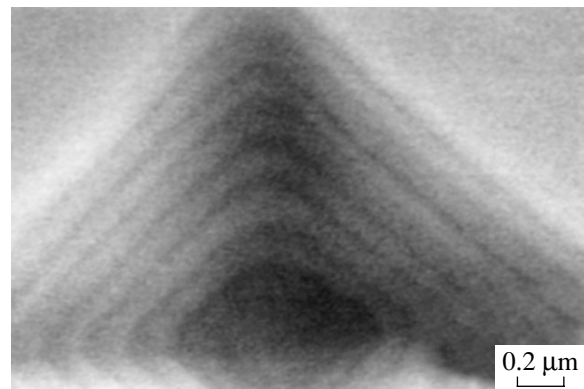
Fig. 5. Electron microscopic image of an indentation made by a Vickers pyramid in a Ti–Cr–B–N film at a load of 25 g.

Table 3. Deformation types of nanostructured thin films (published data)

Composition	Crystal structure	Morphology	References
	Homogeneous deformation		
TiN	NaCl	Columnar	[9]
(Ti, Al)N	NaCl	"	[11–13]
Ti(B, N)	AlB$_2$	"	[11–13]
	Inhomogeneous deformation		
TiB$_2$	AlB$_2$	Partially columnar or lumplike	[9]
AlN	ZnS	"	[11–13]

well for single-phase films. For a multiphase system, it seems to be difficult even to establish the basic parameter T/T_m (T_m is the melting point), which specifies the surface mobility of deposited particles of a material. The introduction of additional elements into the composition of coatings can hinder the growth of a columnar structure and stimulate the nucleation of new grains, thus leading to an equiaxed-grain structure at various temperatures.

Three-dimensional islands on the surface of the films with a columnar structure are the places where the ends of individual grains come to the surface. The characteristic scale of the surface relief for the films with an equiaxed-grain structure (80–100 nm for Ti–B–N (1),

180 nm for Ti–B–N (2), and 40–50 nm for Ti–Cr–B–N) exceeds the size of crystallites in these films (10–40, 4–10, and 2–7 nm, respectively) by an order of magnitude. When films are deposited onto a surface, hollows and grooves form, decreasing the total surface energy [20]. These regions have a low density because of the high volume fraction of pores, defects, and incoherent interfaces. The formation of such interfaces results in a latent columnar structure. Although this structure cannot be revealed when cross-sectional fracture surfaces of films are examined with a scanning electron microscope, it plays a decisive role in deformation. Figure 4 shows a fracture micrograph for a Ti–Cr–B–N film after scratching its surface with a diamond indenter. A pronounced columnar structure is visible after deformation, and its geometry correlates with the film surface topography. It is seen that, in the process of deformation, individual columns or columnar structural elements (CSEs) consisting of many crystallites slip with respect to each other.

3. LOCALIZED DEFORMATION IN THIN FILMS

For fractography analysis, we chose films differing in crystal structure, grain size, and grain morphology (Table 1), according to data on the deformation types of nanostructured films obtained earlier (Table 3).

Figure 5 shows an electron microscopic image of an indentation made with a Vickers pyramid at a load of 25 g in a Ti–Cr–B–N film deposited onto a silicon substrate. The applied load is seen to cause shear bands

Table 4. Formation of shear bands and particles rejected outside (PROs) in regions of localized deformation

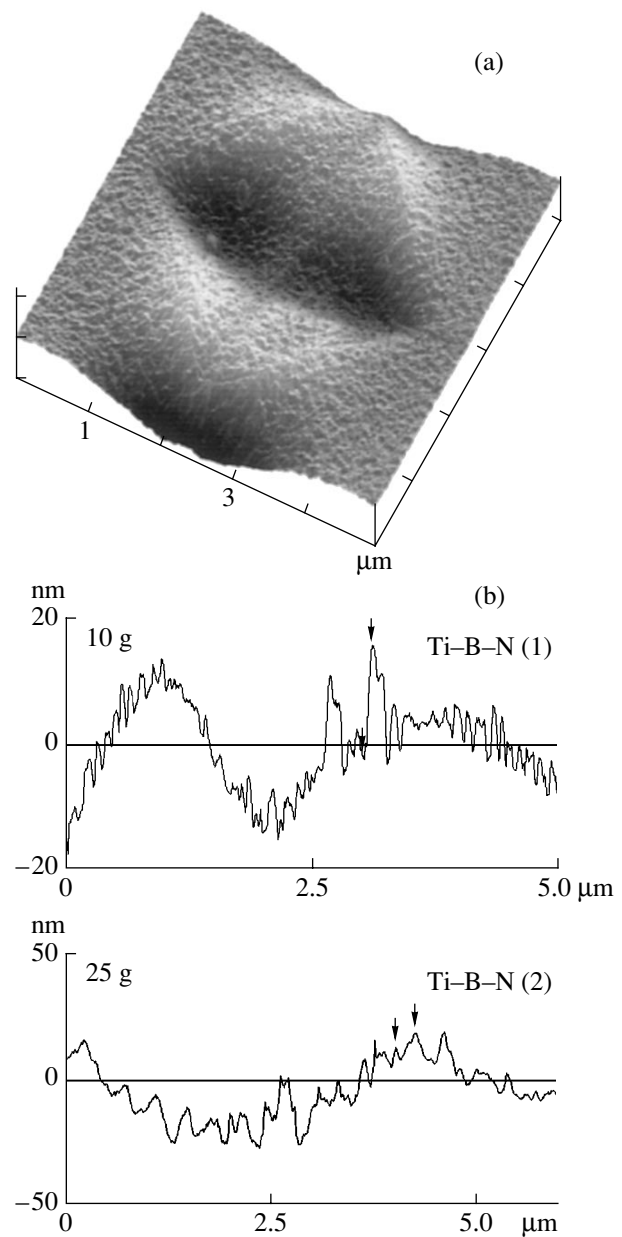| Film composition	10 g		25 g		50 g	
	shear bands	PROs	shear bands	PROs	shear bands	PROs
Ti–B–N (1)	–	+	–	+		
Ti–B–N (2)	–	–	–	–	–	–
Ti–Cr–B–N	+	+	+	+	+	+
Ti–Si–N	–	–	+	–	+	+
Cr–B	–	–	–	–	+	+

Table 5. Comparison of the values of hardness, elastic modulus, and elastic recovery obtained in this work for multicomponent films with published data

Film composition	Hardness H, GPa	Elastic modulus E, GPa	Elastic recovery W_e, %	H^3/E^2, GPa	References
Ti–Si–N	42.3	273	78	1.02	
Ti–Zr–C–O	41.9	289	77	0.88	
Ti–B–N	42.0	300	77	0.82	
Ti–Ca–C–O	41.4	325	68	0.67	
Ti–Al–N	41.9	397	74	0.46	[24]
Ti–Mo–N	43.0	442	68	0.41	[25]
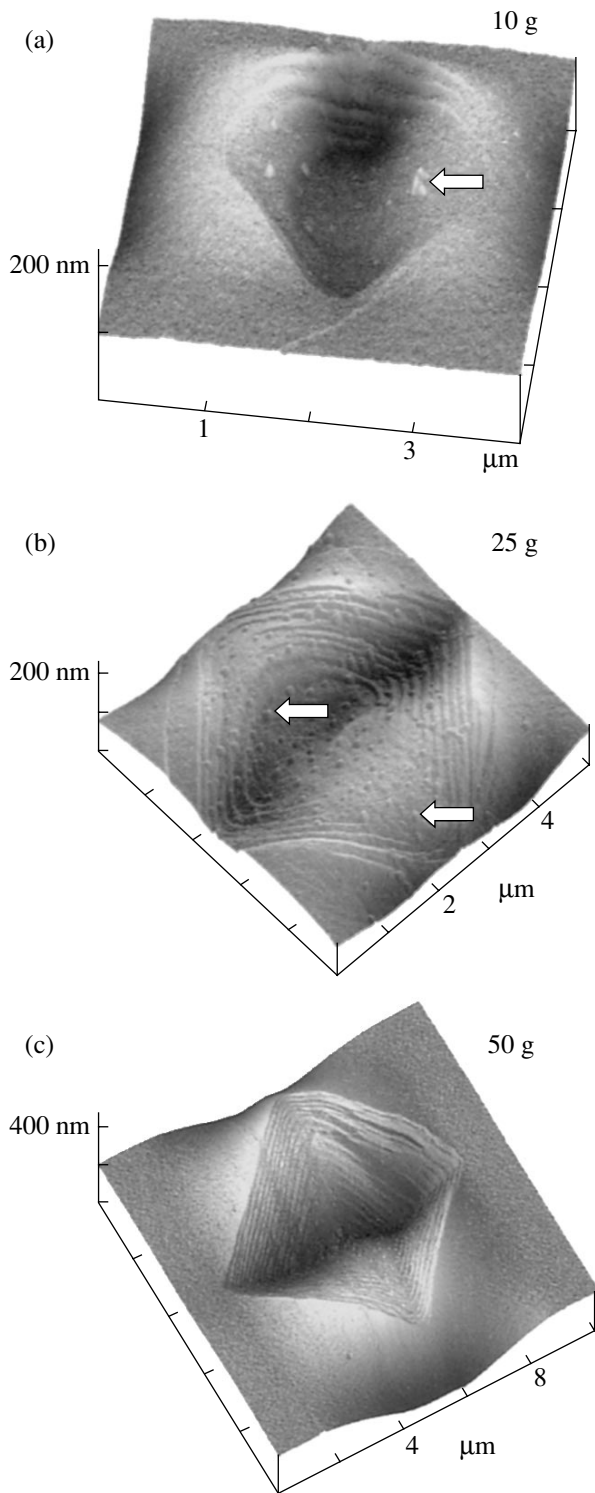
Fig. 6. AFM images of regions with localized deformation in a Ti–Cr–B–N film indented with a Vickers pyramid at a load of (a) 10, (b) 25, and (c) 50 g. Particles rejected outside are shown by arrows.

Fig. 7. (a) AFM image and (b) line scans of regions with localized deformation in Ti–B–N films indented with a Vickers pyramid at a load of (a) 50 and (b) 10 and 25 g.

along the faces of the indenter pyramid. Table 4 gives the critical applied loads for the formation of shear bands. The topography of the Ti–Cr–B–N film surface

in the regions of localized deformation at loads of 10, 25, and 50 g is shown in Fig. 6. The height and width of the plastic-strain steps are 5–15 and 100–200 nm, respectively (irrespective of the applied load). As the load increases, the number of steps increases but the spacing between them remains unchanged.

Figure 7a shows an image of an indentation made with the Vickers pyramid at a load of 50 g in the Ti–B–N (2) film; the image was taken with an atomic-force scanning microscope. In the Ti–B–N system, no shear bands or radial cracks were observed over the whole range of applied loads, which indicates the homoge-

neous character of the film deformation. From line scans taken from vertical sections of indentations (Fig. 7b), it follows that the film surface relief in a deformed region and the roughness of the initial film surface have virtually the same scale. This is evidence that localized deformation develops via slipping of CSEs along the direction of an applied load. This conclusion is illustrated by an AFM image of an indentation made with the Vickers pyramid (Fig. 8). The cooperative motion of columnar grains along the applied load is seen to occur, with the width of each step being 1–3 columns. The shape of the ends of columns remains unchanged during deformation, and the film surface topography in the indentation is identical to that of the film surface.

The appearance of ejected particles on the terraces of steps is noteworthy. This phenomenon was also observed in [12], but no explanation was provided for it. The size of the particles (100–200 nm) agrees well with the size of individual islands on the surface of the initial films observed in topographic examination. It follows that some CSEs are ejected outside in the course of unloading. Thus, the ejected particles on the terraces of steps are likely to be the apices of individual CSEs (columnar grains or portions of the material).

It was assumed in [9, 11, 12] that homogeneous deformation could occur only in films with a columnar structure. However, the results of this work do not support this assumption. We failed to detect periodic regions of plastic deformation in the form of steps in the fractographs of an indentation made by the Vickers pyramid in Ti–B–N films without a pronounced columnar structure. Analysis of the results (Tables 1, 2) shows that none of the structural parameters or mechanical properties, taken separately, characterizes the deformation mechanism. However, it was found that the quantity H^3/E^2, which characterizes the resistance of the material to plastic deformation [6, 21], allows one to predict the formation of shear bands in the process of localized deformation: steps were formed only at low values of the parameter H^3/E^2. This follows from the theoretical analysis performed by Johnson [22], where it was shown that the load P required for the beginning of plastic deformation in the case where an undeformable ball of radius r is indented into a semi-infinite solid is given by the expression $P = 0.78r^2(H^3/E^2)$. Note that the plastic component in the case of inhomogeneously deformed coatings is larger than in the case of the Ti–B–N coatings deformed without step bands (see parameter W_e in Table 2). Thus, a comparison of the film surface topography before deformation and the film surface relief in the region of an indentation made by a Vickers pyramid, on the one hand, with the size of particles ejected after unloading, on the other, shows that both deformation mechanisms proceed through slipping of CSEs (separate grains or multigrain portions of the material) along the applied load. The results obtained indicate that grain-boundary slip is the main
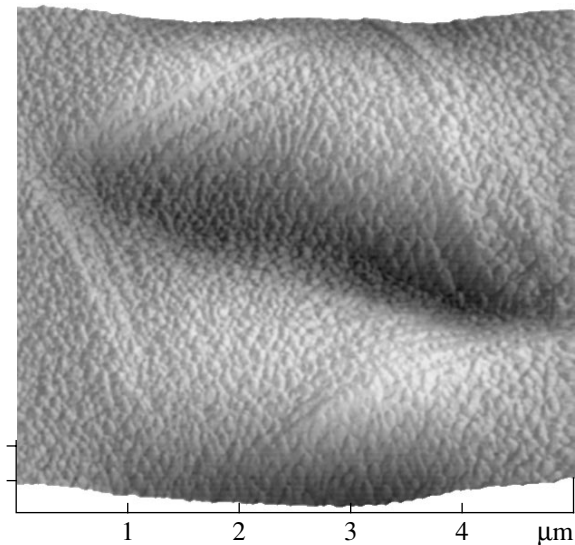

Fig. 8. Fractograph of the fracture surface of a Ti–Si–N film indented with a Vickers pyramid at a load of 25 g.

mechanism of deformation in both cases. In the case of inhomogeneous deformation, cooperative motion of the CSEs takes place because of the larger binding energy between columns. Deformation proceeds at a constant volume and is accompanied by the rejection of an amount of deformed material outside (the formation of hillocks) and/or by elastic compression. Upon unloading, individual CSEs can be rejected outside due to the elastic-stress relaxation or the reverse plasticity, which causes the appearance of ejected particles (visible in Figs. 6, 7a).

4. PHYSICAL-MECHANICAL PROPERTIES

The values of the hardness, modulus of elasticity, and elastic recovery of films are given in Table 2. The depth of indentation for all loads was smaller than 15% of the film thicknesses. The Ti–B–N (2) film had the maximum hardness (42 GPa). Young's modulus for coatings of this system varied in the range 250–300 GPa, which is significantly lower than that for bulk TiN and TiB$_2$ compounds [23]. The Ti–B–N films also had the maximum value of elastic recovery (77–81%) and the minimum plastic deformation (23–19%). Note that shear bands formed only in the films with large plastic deformation.

An important advantage of multicomponent nanostructured films is that one can fabricate superhard materials with identical hardness and different values of the Young's modulus (Table 5). This means that thin films with identical hardness can differ in their elastic strain to failure (H/E) and the resistance to plastic deformation (H^3/E^2). Their elastic properties can also be significantly different. A combination of high hardness and elastic recovery characterizes multicomponent nanostructured films as new unique hard and, at the same time, elastic materials. It is also important that

different materials can have virtually the same mechanical properties (e.g., Ti–Zr–C–O and Ti–B–N films, see Table 5). Thus, superhard coatings can be produced with different combinations of elastic and plastic properties, which provides a wide choice of coatings for various specific tasks.

Additional studies should be made to determine the E and W_e values required for high wear resistance of a material. One of the indubitable advantages of films with a low modulus of elasticity is that such films better fit steel substrates (E = 205 GPa), which minimizes the elastic stresses at the coating/substrate interface and the internal residual stresses in the system, thereby significantly decreasing the wear [6].

5. CONCLUSIONS

Thus, we have found that multicomponent nanostructured films deposited through magnetron sputtering have either a pronounced or a latent columnar structure; such a structure plays a significant role and manifests itself in deformation. Localized deformation in nanostructured thin films can develop both homogeneously and inhomogeneously (with the formation of shear bands). To predict the formation of shear bands in a material subjected to deformation, we can use the parameter H^3/E^2, which describes the resistance of the material to plastic deformation. Both deformation mechanisms involve slipping of CSEs (individual grains or multigrain portions of the material) along the direction of the applied load. In the case of a weak chemical bond between neighboring grains, individual CSEs can be rejected outside as a result of relaxation of elastic stresses upon unloading. The inhomogeneous deformation mechanism is associated with cooperative motion of CSEs due to the large binding energy between grains.

ACKNOWLEDGMENTS

REFERENCES

1. D. V. Shtansky, K. Kaneko, Y. Ikuhara, and E. A. Levashov, Surf. Coat. Technol. **148** (2–3), 204 (2001).

2. D. V. Shtanskiĭ and E. A. Levashov, Izv. Vyssh. Uchebn. Zaved., Tsvetn. Metall. **3**, 52 (2001).

3. D. V. Shtansky, E. A. Levashov, A. N. Sheveiko, and J. J. Moore, J. Mater. Synth. Process. **7** (3), 187 (1999).

4. D. V. Shtansky, E. A. Levashov, A. N. Sheveiko, and J. J. Moore, J. Mater. Synth. Process. **6** (1), 61 (1998).

5. A. Niederhofer, P. Nesládek, H.-D. Männling, *et al.*, Surf. Coat. Technol. **120–121**, 173 (1999).

6. A. Leyland and A. Matthews, Wear **246** (1–2), 1 (2000).

7. S. Veprěk, J. Vac. Sci. Technol. A **17** (5), 2401 (1999).

8. J. Musil, Surf. Coat. Technol. **125** (1–3), 322 (2000).

9. R. A. Andrievskiĭ, G. V. Kalinnikov, and D. V. Shtanskiĭ, Fiz. Tverd. Tela (St. Petersburg) **42** (4), 741 (2000) [Phys. Solid State **42**, 760 (2000)].

10. S. Veprěk and S. Reiprich, Thin Solid Films **268** (1–2), 64 (1995).

11. R. A. Andrievski, G. V. Kalinnikov, and D. V. Shtansky, Mater. Res. Soc. Symp. Proc. **581**, 583 (2000).

12. R. A. Andrievski, G. V. Kalinnikov, J. Jauberteau, and J. Bates, J. Mater. Sci. **35** (11), 2799 (2000).

13. R. A. Andrievsky and G. V. Kalinnikov, Surf. Coat. Technol. **142–144**, 573 (2001).

14. D. V. Shtansky, S. A. Kulinich, E. A. Levashov, *et al.*, Thin Solid Films **420–421**, 330 (2002).

15. V. A. Movchan and A. V. Demchishin, Fiz. Met. Metalloved. **83**, 83 (1969).

16. J. A. Thornton, J. Vac. Sci. Technol. **11** (4), 666 (1974).

17. E. A. Levashov, A. S. Rogachev, V. I. Yukhvid, and I. P. Borovinskaya, *Physicochemical and Technological Fundamentals of Self-Propagating High-Temperature Synthesis* (BINOM, Moscow, 1999).

18. W. C. Oliver and G. M. Pharr, J. Mater. Res. **7** (6), 1564 (1992).

19. H. Ljungcrantz, C. Engstrom, L. Hultman, *et al.*, J. Vac. Sci. Technol. A **16** (5), 3104 (1998).

20. V. I. Trofimov and V. A. Osadchenko, Sov. J. Technol. **60** (8), 540 (1993).

21. T. Y. Tsui, G. M. Pharr, W. C. Oliver, *et al.*, Mater. Res. Soc. Symp. Proc. **383**, 447 (1995).

22. K. L. Johnson, *Contact Mechanics*, 1st ed. (Cambridge Univ. Press, Cambridge, 1985), p. 155.

23. R. A. Andrievskiĭ, G. V. Kalinnikov, N. P. Kobelev, *et al.*, Fiz. Tverd. Tela (St. Petersburg) **39** (10), 1859 (1997) [Phys. Solid State **39**, 1661 (1997)].

24. J. Musil and H. Hrubý, Thin Solid Films **365** (1), 104 (2000).

25. J. Musil, F. Kunc, H. Zeman, and H. Poláková, Surf. Coat. Technol. **154** (2–3), 304 (2002).

Translated by K. Shakhlevich

POLYMERS
AND LIQUID CRYSTALS

Deformation of Solid Polymers in a Constant Magnetic Field

N. N. Peschanskaya and P. N. Yakushev

Ioffe Physicotechnical Institute, Russian Academy of Sciences, Politekhnicheskaya ul. 26, St. Petersburg, 194021 Russia
e-mail: yak@pav.ioffe.ru

Received July 8, 2002; in final form, October 7, 2002

Abstract—The effect of a constant magnetic field on the creep rate is investigated for poly(vinyl butyral), styrene–methacrylic acid copolymer [poly(styrene) + 16 wt % methacrylic acid], poly(methylene oxide), and other polymers. It is demonstrated that the constant magnetic field can variously affect different polymers and that the effect of the magnetic field is enhanced in a particular range of strain rates. © 2003 MAIK "Nauka/Interperiodica".

1. INTRODUCTION

The influence of constant magnetic fields on the structure and properties of polymers has been intensively studied in liquid-crystal and molten states [1–8]. The mechanism of interaction of constant magnetic fields with diamagnets (including polymers) on different structural levels has been investigated both theoretically and experimentally with the use of IR spectroscopy, x-ray diffractometry, and birefringence [5, 9–11]. It has been established that the effect of constant magnetic fields on molecules is reduced to their orientation due to high diamagnetic susceptibility anisotropy of long polymer chains [9, 11].

In many cases, the magnetic treatment of materials makes it possible to order the structure of polymers and to increase their strength considerably [4, 5]. According to the data available in the literature, magnetic effects depend on many factors (for example, on the magnetic field strength, the time of magnetic treatment, and the chemical structure of the molecules). In recent years, it has been proved that constant and pulsed magnetic fields affect the mechanical properties of solid polymers [16] and other diamagnets [15, 17]. It is assumed that the interaction of constant magnetic fields with solid and liquid polymers proceeds through the same mechanism. However, in the case of solid polymers, the orientation of chain fragments capable of affecting the mechanical properties, for example, the strain rate, calls for prolonged magnetic treatment ($10–10^5$ s). In our earlier work [13], the orientation of poly(methyl methacrylate) molecules at 290 K upon prolonged exposure to a constant magnetic field was revealed from the change in the birefringence. However, orientational effects were observed only under certain conditions. In this respect, some doubts have often been cast on the effect of constant magnetic fields on diamagnets. As follows from the results obtained in [12], the strain rate of poly(methyl methacrylate) substantially increases only after exposure to a constant magnetic field (with the induction $B = 0.2$ T) for approximately
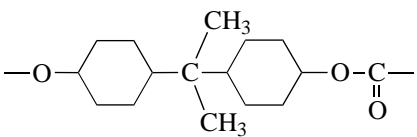
five days. In [18], it was found that, in LiF and NaNO diamagnetic crystals, the change in the creep in response to a constant magnetic field is observed only when the strain rate varies in a particular range. Thus, both experiment [12–19] and theory [5, 9, 10] indicate that different properties of any diamagnet can change in constant magnetic fields under specific conditions. Unfortunately, only a few materials, particularly polymers, have been studied to date and the inference made are ambiguous.

In this work, we analyzed the changes in the creep of amorphous and amorphous–crystalline polymers after preliminary treatment in a constant magnetic field and also under exposure to this field in the course of deformation. Moreover, we determined the conditions corresponding to the minimum and maximum effects of the constant magnetic field on the creep characteristics of the polymers under investigation.

2. SAMPLES AND EXPERIMENTAL TECHNIQUE

Under conditions of uniaxial compression at a constant load and a temperature of 200 K, we studied the creep rate of solid polymers, such as poly(vinyl butyral), poly(methyl methacrylate), styrene–methacrylic acid copolymer [poly(styrene) + 16 wt % methacrylic acid], poly(methylene oxide), polycarbonate, poly(vinyl chloride), and high-density poly(ethylene) (see table). The creep curves (the dependences of the strain ε on the time t) were compared for the initial samples and samples treated in constant magnetic fields ($B = 0.2$ T). An unloaded sample was placed in a setup between the magnet poles. The sample axis was perpendicular to the magnetic vector, and the polymer structure involved no preferred directions. After treatment in a magnetic field, the sample was loaded and the strain was measured for several minutes. For substantial magnetic effects, the time dependence of the strain was measured accurate to within 0.1% with a pointer instrument. In cases when the magnetic field was

Correlation between the diamagnetic susceptibility and creep characteristics

Polymer	χ_3, χ_3', 10^{-6} mg^3/mol		$h^* = h_O/h_H$	$k = \dot{\varepsilon}_H/\dot{\varepsilon}_O$
	x_3	x_3'		
	monomer unit	main chain		
Poly(ethylene) –CH$_2$–CH$_2$–	−11.5	−11.5	~1.07	~1.05
Poly(methylene oxide) –O–CH$_2$–	−16	−16	~1.08	~1.22
Poly(vinyl chloride) —CH$_2$—CH— | Cl	−22	−20	–	~1.40–1.15
Poly(methyl methacrylate) CH$_3$ —CH$_2$—C— COOCH$_3$	−56.6	−22	~1.1	~1.35–1.17
Poly(vinyl butyral) —CH$_2$—CH—CH$_2$—CH— O O CH CH$_2$ CH$_2$ CH$_3$	−120	−52	~2.3	~1.6
Poly(styrene) —CH$_2$—CH— C CH CH CH CH CH	−130	−33	~1.0–0.7	~1.40–1.25
Polycarbonate CH$_3$ —O— C —O–C— CH$_3$ O	−164	−135	~3	~2.00–1.65

applied for a short time during the creep, the process was recorded using a laser interferometer [12, 13]. The strain rate prior to and after application of the magnetic field was calculated from the interferogram with the use of the formula $\dot{\varepsilon} = \lambda\nu/2l_O$, where $\lambda = 0.63$ µm, ν is the beat frequency in the interferogram, and l_O is the sample height. The creep rate was measured accurate to within 1% at small deformation increments (0.3 µm).

Precision measurements of the creep rate made it possible to reveal weak variations in the creep that did not manifest themselves in the conventional ε–t curve. For the short-term action of the constant magnetic field, we calculated the rate ratios inside and outside the magnet: $k = \dot{\varepsilon}_H/\dot{\varepsilon}_O$.

In the present work, we also investigated how the constant magnetic field affects the stepwise creep on the micrometer level [12, 20–22]. In this case, we compared the ratios of the maximum to minimum creep rates $h = \dot{\varepsilon}_{max}/\dot{\varepsilon}_{min}$, which were determined in the magnetic field (h_H) and in the absence of the magnetic field (h_O).

3. RESULTS AND DISCUSSION

Figure 1 depicts the creep curves for two samples. It can be seen that, at the same instants of time, the strains of the polymer exposed to a constant magnetic field are considerably lager than those in the absence of the mag-

netic field. As is known, the mechanical orientation of polymer chains initially leads to disordering of the structure [23]. The same situation should be expected for the magnetic action. We assume that, in the case of a weakly pronounced orientation, the magnetic field suppresses intermolecular nonchemical interactions hindering the deformation and leads to acceleration of the creep (Figs. 1, 2). The kinetic approach also provides support for our view on the possibility of accelerating the creep under exposure to a magnetic field. The creep rate is usually described by the exponential relationship

$$\dot{\varepsilon} = A \exp\{-(Q_0 - \alpha\sigma)/kT\},$$

where Q_0 is the activation barrier associated with the intermolecular interaction and the quantity $\alpha\sigma$ allows for the action of the mechanical stress lowering the potential barrier. According to Rodin [5], the orientational effect of the magnetic field can be described in terms of the Boltzmann factor $\exp(-\beta)$, where $\beta = \Delta\chi H^2/2kT$. Here, $\Delta\chi$ is the diamagnetic susceptibility anisotropy, H is the magnetic field strength, and T is the temperature. The term $\Delta\chi H^2$ determining the magnetic energy can be introduced into the exponent, which results in a decrease in the barrier Q_0 and an increase in the rate $\dot{\varepsilon}$.

Let us now consider situations illustrating a more complex behavior of the strain characteristics under the action of a constant magnetic field.

The creep curves measured for the same poly(methylene oxide) sample at identical loads are depicted in Fig. 2. The second loading of the initial sample does not lead to a change in the strain rate (curve *1*). However, the exposure to the magnetic field results in an increase in the creep rate (the strain at the same instant of time). It can be seen from Fig. 2 that the treatment of the sample in the magnetic field is accompanied by an increase in the strain rate, even though this effect decreases gradually (see curves *3*, *4* in Fig. 2). The saturation can be caused by a decrease in the number of activation barriers that are overcome in the course of deformation in given force and magnetic fields. Curve *3* was measured after prolonged exposure to a constant magnetic field and relaxation for one day. As is known, the birefringence in unloaded polymers decreases after removal of a constant magnetic field, which implies a disorientation in the structure. In our case (curve *3* in Fig. 2), the strained sample upon holding without a magnetic field does not regain its original state. This means that either the strain stabilizes the effect of the constant magnetic field or the relaxation of the orientation induced by the magnetic field occurs in local regions and large-sized molecular fragments retain the ability to undergo deformation shears. Note that the largest response to the constant magnetic field is observed for the polymers with a high diamagnetic susceptibility χ. The constant magnetic field only slightly affects the creep of poly(ethylene), which is characterized by a small value of χ.
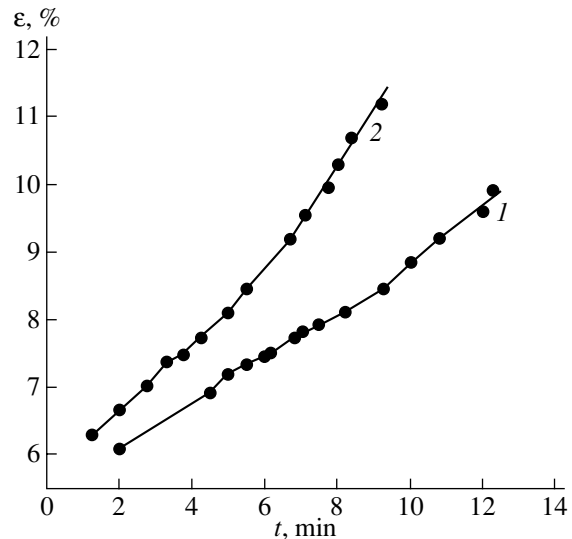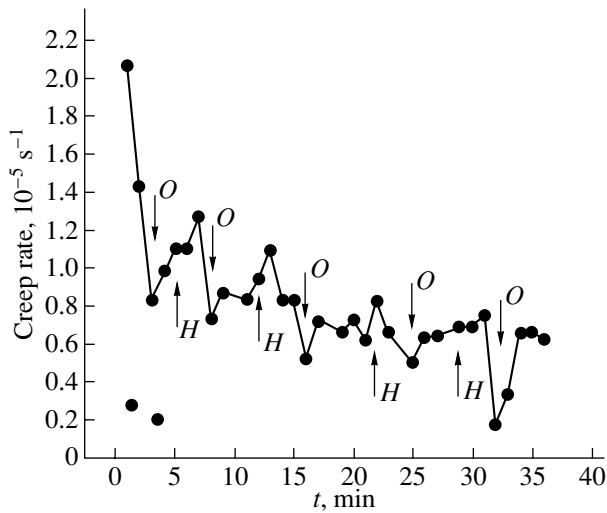
Fig. 1. Time dependences of the strain for the styrene–methacrylic acid copolymer [poly(styrene) + 16 wt % methacrylic acid] at $T = 290$ K, $\sigma = 84$ MPa, and $B =$ (*1*) 0 and (*2*) 0.2 T.
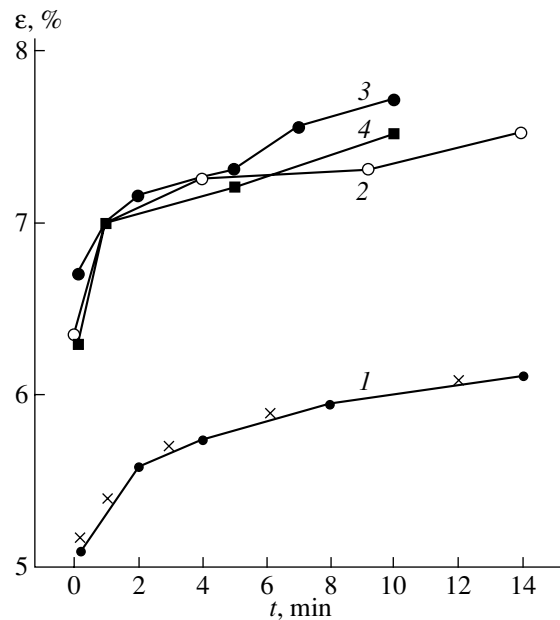
Fig. 2. Time dependences of the strain for poly(methylene oxide). $\sigma = 70$ MPa. The measurements are performed with the same sample (*1*) unexposed and (*2–4*) exposed to a constant magnetic field with $B = 0.2$ T. Curve *1* shows the results obtained for two sequential loadings. Experimental conditions: (*2*) magnetic treatment for 15 days, (*3*) additional magnetic treatment for 15 days and holding without a magnetic field for 1 day, and (*4*) additional magnetic treatment for 40 days.

Now, we dwell on other effects that are observed upon exposure of polymers to a constant magnetic field in the course of creep. Figure 3 shows the time dependence of the strain rate for the styrene–methacrylic acid

Fig. 3. Time dependence of the creep rate for the styrene–methacrylic acid copolymer [poly(styrene) + 16 wt % methacrylic acid] at $\sigma = 60$ MPa and $B = 0.2$ T. Points H and O indicate the instants of time of application and removal of the constant magnetic field, respectively.


Fig. 4. The ratios $k = \dot{\varepsilon}_H/\dot{\varepsilon}_O$ of the creep rates in the filed ($\dot{\varepsilon}_H$) and in the absence of a field ($\dot{\varepsilon}_O$) as a function of the creep rate $\dot{\varepsilon}_O$ for poly(vinyl butyral) at $\sigma = 27$ MPa and $\varepsilon = 12\%$.

copolymer upon application (points H) and removal (points O) of the constant magnetic field during the creep. Each point corresponds to a deformation increment of 0.3 μm. As can be seen from Fig. 3, the application of the constant magnetic field results in an increase in the creep rate, whereas the removal of the field leads to a decrease in this rate. The change in the creep rate under short-term exposure to the constant magnetic field indicates the occurrence of deformation and magnetic orientation events with short relaxation times (seconds and minutes). The ratio $k = \dot{\varepsilon}_H/\dot{\varepsilon}_O$ can serve as a measure of the magnetic field effect. The dependences of these ratios determined from dependences similar to those plotted in Fig. 3 are represented in Figs. 4 and 5. It can be seen from these figures that an increase in the rate in the presence of the magnetic field ($k > 1$) is observed only when the rate varies in a certain range. At higher and lower rates, the constant magnetic field either does not affect or even retards the creep ($k < 1$). For different polymers, the rate ranges in which the magnetic field accelerates the creep can differ significantly.

In our earlier works [20–22], we examined the stepwise creep on the micrometer level. It is believed that the stepwise strain (rate) is associated with the irregularity in the arrangement and interaction of polymer molecular fragments. The strongest local bonds play the role of stoppers (nodes) in elementary shear acts and are responsible for the lower rate in a step. The breaking of a strong bond leads to a sharp increase in the rate. The ratio $h = \dot{\varepsilon}_{max}/\dot{\varepsilon}_{min}$ varies differently upon exposure of different polymers to the same constant magnetic field [12, 13]. Most frequently, the constant magnetic field brings about a decrease in the ratio h
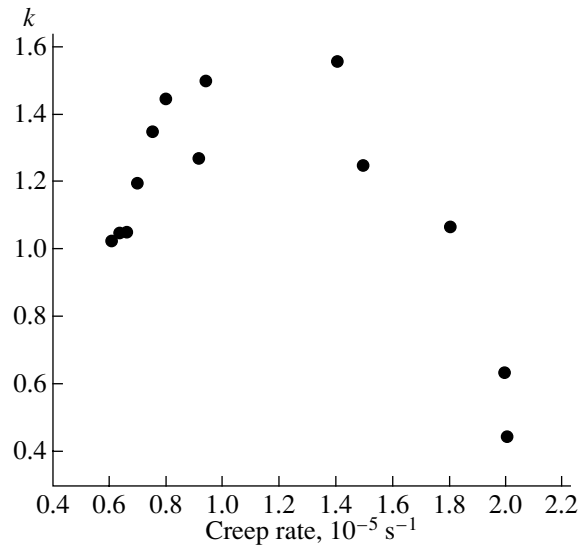
(Fig. 6). It is assumed that the decrease in the ratio h in the magnetic field is caused by the decrease in the bonding force just in nodes and the smoothing of the potential along the shear plane. The ratios h^* of the rate-step steepnesses in the absence of the magnetic field h_O and in the field h_H are presented in the table. Among the studied polymers, the most pronounced effect is observed for poly(vinyl butyral) and polycarbonate, in which groups of adjacent molecules can form strong bonds. Since the response to the constant
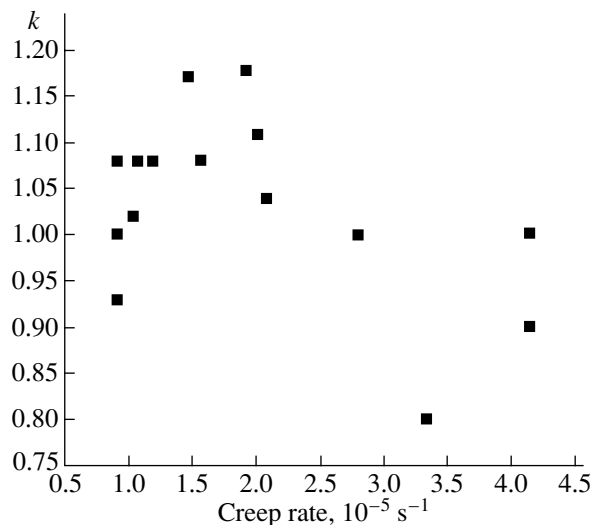
Fig. 5. The ratios $k = \dot{\varepsilon}_H/\dot{\varepsilon}_O$ as a function of the creep rate $\dot{\varepsilon}_O$ for the styrene–methacrylic acid copolymer [poly(styrene) + 16 wt % methacrylic acid] at $\sigma = 80$ MPa and $\varepsilon = 10\%$.

magnetic field can depend on both the chemical structure and the molecular mobility, the magnetic field should variously affect the creep in different temperature relaxation regions.

Upon application of the magnetic field in the course of creep, we obtained the largest ratios $k = \dot{\varepsilon}_H/\dot{\varepsilon}_O$ for different polymers (Figs. 4, 5).

Let us compare our data on the influence of the constant magnetic field on the creep rate and the data available in the literature on the magnetic susceptibility for monomer units of polymers (see table).

The diamagnetic susceptibilities of particular molecules and bonds are given in [5, 9–11]. For nonaromatic molecules, the susceptibility along the molecular axis can be derived using the Pascal additive system: $\chi_3 = \Sigma\chi_i + \lambda$, where χ_3 is the magnetic susceptibility tensor along the axis, $[\chi_i]$ is the magnetic susceptibility of a particular chemical bond, and λ is the term associated with the structure factor (in approximate calculations, the term λ is taken equal to zero). The table lists the susceptibilities χ_3 for monomer units (taken from [5, 9]). In poly(styrene), the benzene ring in the side group is responsible for the anomalously strong diamagnetism. Possibly, poly(styrene) does not obey the observed correlation between χ_3 and h (χ_3 and k), because the susceptibility χ_3 is predominantly determined by the magnetic susceptibility of the side group, whereas fragments of the main chain are involved in deformation displacements. In this work, the approximate diamagnetic susceptibilities χ_3' were calculated from the above formula for χ_3 only for bonds of the main chain. Note that the presence of methacrylic acid molecules in the styrene–methacrylic acid copolymer was disregarded. As can be seen from the table, a reasonable correlation between the quantities χ_3' and k (χ_3' and h) is observed for the polymers under consideration. It should be noted that small variations in the rate ($k = 1.1$) are reliably determined owing to the sensitive technique used for the rate measurement. The parameter k depends on the strain rate, and the largest parameters obtained at different points in the experimental creep curves are given in the table.

The selective effect of the constant magnetic field on the strain rate can be explained by the difference in the magnetic and mechanical relaxation times at different stages of the creep. It should be taken into account that not only the external magnetic field can change the molecular mobility (creep rate), but also an increase in the mobility and orientation of molecules in response to mechanical forces can affect the direction of dipole magnetic moments and the magnetic polarizability anisotropy which determine the magnetic anisotropy [5, 10].

A constant magnetic field can have a profound effect on the creep in the case when the relaxation time and the direction of deformation events coincide with those of the magnetic orientation events.
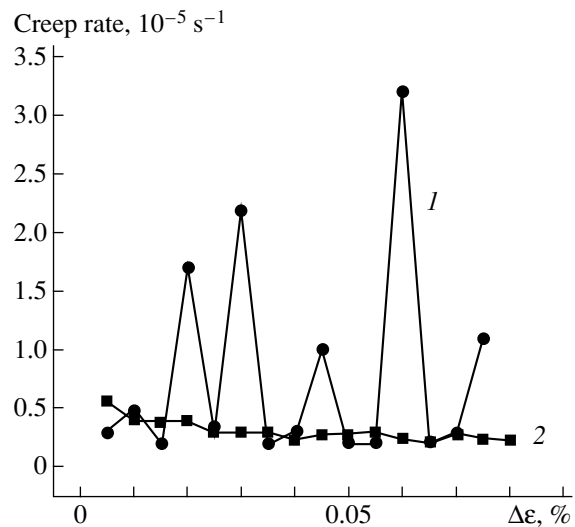
Creep rate, 10^{-5} s^{-1}

Fig. 6. Dependence of the stepwise creep rate on the strain increment for poly(vinyl butyral) at $\sigma = 45$ MPa, $\varepsilon = 2.5\%$, and $B = (1)$ 0 and (2) 0.2 T. Upper points correspond to $\dot{\varepsilon}_{max}$, and lower points indicate $\dot{\varepsilon}_{min}$.

4. CONCLUSIONS

Thus, despite an ambiguity, the results obtained allow us to make the following inferences.

(1) In solid polymers, short- and long-term processes affecting the strain rate proceed under the effect of constant magnetic fields.

(2) The effect of a constant magnetic field (at $B = 0.2$ T) manifests itself under specific conditions (in our case, over a narrow range of creep rates).

(3) The effect of a constant magnetic field on the steepness of creep rate steps suggests that the internal magnetic fields are localized in regions of strong nonchemical interactions between molecular groups of the adjacent polymer chains.

REFERENCES

1. Yu. M. Molchanov, E. R. Kisis, and Yu. P. Rodin, Mekh. Polim. **4**, 737 (1973).
2. Sridhar C. Guha, W. A. Hines, and E. T. Samulski, J. Chem. Phys. **61**, 947 (1974).
3. C. Noel, L. Monnerie, M. F. Achard, *et al.*, Polymer **22**, 578 (1981).
4. Yu. P. Rodin and Yu. M. Molchanov, Mekh. Kompoz. Mater., No. 6, 1056 (1982).
5. Yu. P. Rodin, Mekh. Kompoz. Mater., No. 3, 490 (1991).
6. A. Answer and A. H. Windle, Polymer **32**, 103 (1991).
7. A. Answer and A. H. Windle, Polymer **34**, 3347 (1993).
8. H. E. Assender and A. H. Windle, Polymer **37**, 371 (1996).
9. Ya. G. Dorfman, *Diamagnetism and the Chemical Bond* (Fizmatgiz, Moscow, 1961; Elsevier, New York, 1965).
10. S. V. Vonsovskiǐ, *Magnetism* (Nauka, Moscow, 1971; Wiley, New York, 1974).

11. V. S. Zapasskiĭ, *Physical Encyclopedia* (BRE, Moscow, 1990), Vol. 2, p. 482.

12. N. N. Peschanskaya, V. Yu. Surovova, and P. N. Yakushev, Fiz. Tverd. Tela (St. Petersburg) **34** (7), 2111 (1992) [Sov. Phys. Solid State **34**, 1127 (1992)].

13. N. N. Peschanskaya and P. N. Yakushev, Fiz. Tverd. Tela (St. Petersburg) **39** (9), 1690 (1997) [Phys. Solid State **39**, 1509 (1997)].

14. Yu. I. Golovin, R. B. Morgunov, and S. Yu. Liksutin, Vysokomol. Soedin., Ser. A **42** (2), 1 (2000).

15. Yu. I. Golovin and R. B. Morgunov, Materialovedenie, Nos. 3–6, 2 (1997).

16. Yu. I. Golovin, R. B. Morgunov, and S. Yu. Liksutin, Vysokomol. Soedin., Ser. B **40** (2), 373 (1998).

17. Yu. A. Osip'yan, Yu. I. Golovin, R. B. Morgunov, *et al.*, Fiz. Tverd. Tela (St. Petersburg) **43** (7), 1333 (2001) [Phys. Solid State **43**, 1389 (2001)].

18. B. I. Smirnov, N. N. Peschanskaya, and V. I. Nikolaev, Fiz. Tverd. Tela (St. Petersburg) **43** (12), 2154 (2001) [Phys. Solid State **43**, 2250 (2001)].

19. V. I. Borisenko and G. S. Zhdanov, Khim. Vys. Energ. **27** (5), 69 (1993).

20. N. N. Peschanskaya and P. N. Yakushev, Fiz. Tverd. Tela (Leningrad) **30** (7), 2196 (1988) [Sov. Phys. Solid State **30**, 1264 (1988)].

21. N. N. Peschanskaya, Ju. Hristova, and P. N. Yakushev, Polymer **42**, 7101 (2001).

22. N. N. Peschanskaya, Fiz. Tverd. Tela (St. Petersburg) **43** (8), 1418 (2001) [Phys. Solid State **43**, 1478 (2001)].

23. V. V. Kochervinskiĭ, Vysokomol. Soedin., Ser. A **33** (10), 2106 (1991).

Translated by O. Borovik-Romanova

POLYMERS
AND LIQUID CRYSTALS

Shear Flow of a Nematic Liquid Crystal near a Charged Surface

A. V. Zakharov and A. A. Vakulenko

Institute for Problems of Mechanical Engineering, Russian Academy of Sciences, Bol'shoĭ pr. 61,
Vasil'evskiĭ ostrov, St. Petersburg, 199178 Russia

Abstract—The maximum alignment angle θ_{eff} and the effective rotational viscosity coefficient γ_i^{eff} of polar liquid crystals, such as 4-*n*-octyloxy-4'-cyanobiphenyl (8OCB), are investigated in the vicinity of charged bounding surfaces. The quantities θ_{eff} and γ_1^{eff} are calculated in the framework of the Ericksen–Leslie theory. The results of calculations demonstrate that, for a homeotropic alignment of molecules on charged indium tin oxide surfaces, the effective rotational viscosity coefficient γ_i^{eff} can increase by 7.8% as compared to the bulk rotational viscosity coefficient γ_1. © *2003 MAIK "Nauka/Interperiodica"*.

1. INTRODUCTION

In a shear laminar flow of a nematic liquid crystal between two bounding surfaces, the flow field $\mathbf{v}(\mathbf{r})$ is one of the main factors affecting the director field $\mathbf{n}(\mathbf{r})$. In the bulk of a nematic liquid crystal, the influence of bounding surfaces can be ignored and the hydrodynamic properties can be described in terms of the classical Ericksen–Leslie theory allowing for the interaction of the fields $\mathbf{n}(\mathbf{r})$ and $\mathbf{v}(\mathbf{r})$. For a Couette flow between two plane-parallel surfaces when one (lower) surface is stationary and the other (upper) surface moves with a constant velocity $\mathbf{v}$, the flow field takes the form $\mathbf{v}(\mathbf{r}) = v(y)i$. Here, the x axis is aligned with the unit vector $\mathbf{i}$ oriented parallel to the bounding surfaces and the y axis is directed along the unit vector $\mathbf{j}$ perpendicular to the bounding surfaces. At high flow rates, the equilibrium angle θ_{bulk} between the vectors $\mathbf{n}$ and $\mathbf{v}$ can be determined from the condition that the hydrodynamic torques acting on an elementary volume of the nematic liquid crystal $T_{vis} = (1/2)(\gamma_1 + \gamma_2 \cos\theta_{bulk})\dot{\gamma}$ are equal to zero [1, 2]. As a result, we have

$$\theta_{bulk} = \frac{1}{2}\cos^{-1}(1/\lambda), \qquad (1)$$

where $\lambda = -\gamma_2/\gamma_1$, γ_1, and γ_2 are the rotational viscosity coefficients of the nematic liquid crystal and $\dot{\gamma} = \partial v(y)/\partial y$ is the strain rate. However, in the vicinity of charged bounding surfaces, the hydrodynamic description of anisotropic systems such as liquid crystals should take into account the effect of elastic and surface forces acting on the material over a depth ξ. Since these forces make an additional contribution to the balance of the torques acting on the elementary volume of the nematic liquid crystal, they also affect the angle θ_{bulk} and the rotational viscosity coefficients γ_i ($i = 1, 2$). In this case, the surface forces are responsible for the coupling of nematic liquid-crystal molecules with the surface and the surface coupling energy can be written in the form [3]

$$f_0 = -\frac{1}{2}\omega_0(\mathbf{n}_s \cdot \mathbf{n}_0)^2 = -\frac{1}{2}\omega_0\cos^2(\theta_s - \theta_0), \qquad (2)$$

where ω_0 is the coupling constant having the dimension of the surface energy density, θ_s is the angle between the vectors $\mathbf{n}_s$ and $\mathbf{n}_0$, and θ_0 is the angle between the vectors $\mathbf{n}_s$ and $\mathbf{v}$. Here, $\mathbf{n}_s$ stands for the director $\mathbf{n}$ on the bounding surface and $\mathbf{n}_0$ is the unit vector aligned along the easy orientation axis [3] and characterizing the surface anisotropy. The surface energy f_0 is localized in a narrow surface layer of depth $\lambda_s \sim 10$–100 nm [4]. In this range, the order parameter of the nematic liquid crystal varies from the surface to bulk value. When the solid bounding surface is in contact with the nematic liquid crystal, the surface selectively interacts with ions involved in the nematic phase. For example, a negatively charged surface with the charge density σ attracts positive ions and repels negative ions. If the number N_+ of positive ions is equal to the number N_- of negative ions, the depth of penetration of the electric field $\mathbf{E}(y)$ induced by the surface charge density σ is equal to the Debye length λ_D [5] (the case of a weak electrolyte). The spatial dependence of this electric field for the bulk screening can be represented in the following form:

$$\mathbf{E}(y) = E_0\exp(-y/\lambda_D)\mathbf{j}, \qquad (3)$$

where $E_0 = \sigma/\epsilon_0\bar{\epsilon}$ is the electric field strength of the charged surface, ϵ_0 is the permittivity of free space, $\bar{\epsilon} = (\epsilon_\parallel + 2\epsilon_\perp)/3$ is the mean permittivity, and $\epsilon_\parallel$ and $\epsilon_\perp$ are the permittivities parallel and perpendicular to the director $\mathbf{n}$, respectively.

In the present work, we applied the Ericksen–Leslie theory [1, 2] to analyze how the surface charge density σ affects the angle $\theta_{eff}(y)$ and the rotational viscosity coefficient γ_1^{eff} at distances of the order of ξ. Since experimenters have encountered considerable difficulties in measuring these parameters in the vicinity of bounding surfaces [6], theoretical data on $\theta_{eff}(y)$ and γ_1^{eff} are undeniably of particular importance. This paper is organized as follows. The basic equations of the hydrodynamic theory for nematic liquid crystals in the vicinity of charged bounding surfaces are presented in Section 2. The results of numerical calculations of the angles $\theta_{eff}(y)$ and the rotational viscosity coefficients γ_1^{eff} are summarized in Section 3.

2. BASIC EQUATIONS OF THE HYDRODYNAMIC THEORY FOR NEMATIC LIQUID CRYSTALS NEAR A CHARGED SURFACE

Within the classical Ericksen–Leslie approach to considering the viscosity of nematic liquid crystals, a preferential orientation of molecules in the vicinity of points $\mathbf{r}$ is described by the director vector field $\mathbf{n}(\mathbf{r}, t)$. This orientation can vary from point to point. In the incompressible-fluid approximation ($\nabla \cdot \mathbf{v} = 0$), the balances of momentum and torques acting on an elementary volume are represented by the relationships [1, 2]

$$\rho\frac{d\mathbf{v}}{dt} = \nabla \cdot \bar{\sigma}, \tag{4}$$

$$\mathbf{T}_{vis} + \mathbf{T}_{el} + \mathbf{T}_{elast} = 0. \tag{5}$$

Here, $\rho = N/V$ is the particle number density and $\bar{\sigma}$ is the stress tensor with the components defined by the expressions [2]

$$\bar{\sigma}_{ij} = \alpha_1 n_l n_m M_{lm} n_i n_j + \alpha_2 n_i N_j + \alpha_3 N_i n_j$$
$$+ \alpha_4 M_{ij} + \alpha_5 n_i n_l M_{lj} + \alpha_6 M_{im} n_m n_j, \tag{6}$$

where

$$N_m = \frac{dn_m}{dt} + \frac{1}{2}(v_{m,k} - v_{k,m})n_k,$$

$$M_{ij} = \frac{1}{2}(v_{i,j} + v_{j,i}). \tag{7}$$

In relationships (7), $M_{i,j}$ are the components of the symmetric part of the Euler tensor. The formula describing the director kinetics includes the antisymmetric part W of this tensor (the components of the vector $\mathbf{N}$) in the

form of the convolution $W \cdot \mathbf{n}$, which is the vector with components $(1/2)(v_{m,k} - v_{k,m})n_k$ ($m = 1, 2, 3$). The material derivatives of the components of the vector $\mathbf{n}$ can be written as $\dfrac{dn_m}{dt} = \dfrac{\partial n_m}{\partial t} + v_l n_{m,l}$.

The Leslie coefficients α_i ($i = 1, 2, …, 6$) satisfy the Onsager–Parodi relation $\alpha_2 + \alpha_3 = \alpha_6 - \alpha_5$, and, hence, only five out of six coefficients α_i are independent. The rotational viscosity coefficients γ_i ($i = 1, 2$) and the Leslie coefficients α_i are related by the expressions $\gamma_1 = \alpha_3 - \alpha_2$ and $\gamma_2 = \alpha_6 - \alpha_5$. The torque with respect to the director due to the hydrodynamic forces has the form

$$\mathbf{T}_{vis} = -\mathbf{n} \times (\gamma_1 \mathbf{N} + \gamma_2 \mathbf{M} \cdot \mathbf{n}), \tag{8}$$

the torque associated with the electric forces is given by the relationship

$$\mathbf{T}_{el} = (\epsilon_a/\epsilon_0)\mathbf{n} \times \mathbf{E}(\mathbf{E} \cdot \mathbf{n}), \tag{9}$$

and the torque caused by the elastic forces is defined as

$$\mathbf{T}_{elast} = \mathbf{n} \times \mathbf{h}. \tag{10}$$

Here, the components of the vector $\mathbf{N}$ are determined by relationships (7) and $M \cdot \mathbf{n}$ is the convolution of the symmetric part M of the Euler tensor with the vector $\mathbf{n}$. This convolution represents the vector with components $(v_{i,j} + v_{j,i})n_j/2$ ($i = 1, 2, 3$). The molecular field associated with the gradients of the director $\mathbf{n}$ [3] in the strained nematic liquid crystal is specified by the vector $\mathbf{h} = \mathbf{h}_s + \mathbf{h}_t + \mathbf{h}_b$, where $\mathbf{h}_s = K_1\nabla(\nabla \cdot \mathbf{n})$, $\mathbf{h}_t = -K_2[(\mathbf{n} \cdot \mathbf{l})\mathbf{l} + \nabla \times (\mathbf{n} \cdot \mathbf{l})\mathbf{n}]$, $\mathbf{h}_b = K_3[\mathbf{n} \times \mathbf{l} \times \mathbf{l} + \nabla \times (\mathbf{n} \times (\mathbf{n} \times \mathbf{l}))]$, and $\mathbf{l} = \nabla \times \mathbf{n}$. Here, the Frank elastic constants K_i ($i = 1, 2, 3$) describe three types of strains in the nematic liquid crystal, namely, the lateral bending, torsional, and buckling strains, respectively, and $\epsilon_a = \epsilon_\parallel - \epsilon_\perp$ is the dielectric anisotropy of the nematic liquid crystal.

In the case of a Couette flow with a planar geometry, the vectors $\mathbf{v}(\mathbf{r})$ and $\mathbf{n}(\mathbf{r})$ are represented by the expressions $\mathbf{v} = (v(y), 0, 0)$ and $\mathbf{n} = (\cos\theta_{eff}, \sin\theta_{eff}, 0)$. Making allowance for the sole nonzero component of the flow field gradient $\dot{\gamma} = \partial v(y)/\partial y$, expression (5) can be transformed into the form [6]

$$\frac{\partial\theta_{eff}}{\partial\tau} + \frac{1}{2}[1 + (\gamma_2/\gamma_1)\cos 2\theta_{eff}] - \frac{1}{2}\sin 2\theta_{eff}\bar{B}^2$$
$$- h(\theta_{eff})\frac{\partial^2\theta_{eff}}{\partial\bar{y}^2} - \frac{1}{2}h'(\theta_{eff})\left(\frac{\partial\theta_{eff}}{\partial\bar{y}}\right)^2 = 0, \tag{11}$$

where $\bar{B}^2 = B^2/\gamma_1\dot{\gamma} = \epsilon_a\sigma^2/(\bar{\epsilon}^2\epsilon_0^3\gamma_1\dot{\gamma})\exp(-2\bar{y})$, $\bar{y} = y/\lambda_D$ is the dimensionless coordinate, $\tau = t\dot{\gamma}$ is the dimensionless time, $h(\theta_{eff}) = (K_1\cos^2\theta_{eff} + K_3\sin^2\theta_{eff})/(\gamma_1\dot{\gamma}\lambda_D^2)$, and $h'(\theta_{eff})$ is the derivative of the function $h(\theta_{eff})$ with respect to θ_{eff}. At high strain rates, the director orientation is determined by the balance of

only the hydrodynamic forces and the electric forces affect the material over a depth $0 \le \xi \le 3 \ \mu m$ [6]. In particular, for 4-*n*-octyloxy-4'-cyanobiphenyl (8OCB) at $\dot{\gamma} = 800 \ s^{-1}$ and $\sigma = 10^{-3} \ C/m^2$, we obtain $|T_{elast}| \sim 0.5$ N/m^2, $|T_{vis}| \sim 4.0 \ N/m^2$, $|T_{el}(y = 0.1 \ \mu m)| \sim 212 \ N/m^2$, and $|T_{el}(y = 1 \ \mu m)| \sim 0.2 \ N/m^2$. Taking into consideration that $\Delta = |T_{elast}|/|T_{vis}| \sim 0.125$, the contribution of the elastic forces to the momentum balance can be disregarded at strain rates $\dot{\gamma} \ge 800 \ s^{-1}$.

Therefore, Eq. (11) can be rewritten in the following form:

$$\frac{\partial \theta_{eff}}{\partial \tau} + \frac{1}{2}[1 + (\gamma_2/\gamma_1)\cos 2\theta_{eff}] - \frac{1}{2}\sin 2\theta_{eff} \bar{B}^2 = 0. \quad (12)$$

For a stationary Couette shear flow and arbitrary strain rates $\dot{\gamma}$, Eq. (11) can be represented in the form

$$\frac{\partial^2 \theta_{eff}(\bar{y})}{\partial \bar{y}^2} - A\exp(-2\bar{y})\theta_{eff}(\bar{y}) + D = 0, \quad (13)$$

where $A = \epsilon_a \sigma^2 \lambda_D^2 / \bar{\epsilon}^2 K_1$ and $D = (\gamma_1 + \gamma_2)\dot{\gamma}\lambda_D^2/2K_1$.

Equation (13) was written with due regard for the fact that the last term in Eq. (11) can be ignored in comparison with the other terms, because we have $\theta_{eff} \le 14°$ ($|\theta_{eff}| < 0.18$) for all liquid crystals [3, 6] and $\theta''_{eff}(\bar{y}) \approx 0.01$. The boundary conditions for Eq. (13) are as follows: $\theta_{eff}(\bar{y}) = 0$ and $\theta'_{eff}(\bar{y}) = 0$ at $\bar{y} = \bar{y}_a = \lambda_s/\lambda_D$ and $\theta_{eff}(\bar{y}) = \theta_{bulk}$ and $\theta'_{eff}(\bar{y}) = 0$ at $\bar{y} = \bar{y}_b$. Below, we will demonstrate that $\sigma = 10^{-3} \ C/m^2$ and $\lambda_D = 0.545 \ \mu m$ for the homeotropic orientation of the 8OCB molecules of the nematic liquid crystal on the indium tin oxide bounding surface at a temperature of 340 K and $\sigma = 10^{-3} \ C/m^2$. The theoretical calculations performed in terms of the statistical–mechanical theory [4] indicate that it is reasonable to choose $\lambda_s \sim 0.1 \ \mu m$ for 8OCB molecules in the vicinity of the indium tin oxide surfaces. On this basis, the interval boundaries are determined to be $\bar{y}_a = 0.18$ and $\bar{y}_b = 5.5$. At $|A| \gg 1$, Eq. (13) without the last term D possesses the asymptotic solution [7]

$$\theta_{eff}(\bar{y}) = q^{1/4}\exp\left(\pm i\delta \int_0^{\bar{y}} q^{1/2}d\bar{y}\right)[1 + O(\delta^{-1})], \quad (14)$$

where $q = \exp(-2\bar{y})$ and $\delta = i\sqrt{A}$. For the 8OCB nematic liquid crystal, we find $A \simeq 37.71$ at $\sigma = 10^{-3} \ C/m^2$. Since $D \simeq 0.004$, the last term in Eq. (13) can be ignored. Then, the asymptotic solution of Eq. (13) with

allowance made for the boundary conditions takes the form

$$\theta_{eff}(\bar{y}) = C_1\exp[\bar{y}/2 + \sqrt{A}(\exp(-\bar{y})) - 1]$$
$$+ C_2\exp[\bar{y}/2 - \sqrt{A}(\exp(-\bar{y}) - 1)], \quad (15)$$

where $C_i = \theta_{bulk}\beta_i/\beta$ ($i = 1, 2$), $\beta = \beta_2\beta_3 - \beta_1\beta_4$, $\beta_1 = \exp\{\bar{y}_a/2 - \sqrt{A}[\exp(-\bar{y}_a) - 1]\}$, $\beta_2 = \exp\{\bar{y}_a/2 + \sqrt{A}[\exp(-\bar{y}_a) - 1]\}$, $\beta_3 = \exp\{\bar{y}_b/2 - \sqrt{A}[\exp(-\bar{y}_b) - 1]\}$, and $\beta_4 = \exp\{\bar{y}_b/2 + \sqrt{A}[\exp(-\bar{y}_b) - 1]\}$.

At high strain rates ($\dot{\gamma} \ge 800 \ s^{-1}$), Eq. (11) in the vicinity of the charged bounding surface has the form

$$\dot{\gamma}[\gamma_1 + \gamma_2\cos 2\theta_{eff}] = B^2\sin 2\theta_{eff} \quad (16)$$

and the equation for θ_{eff} can be written as follows:

$$\theta_{eff} = \frac{1}{2}\cos^{-1}(1/\lambda_{eff}) = \frac{1}{2}\cos^{-1}C, \quad (17)$$

where $C = \lambda_{eff}^{-1} = \alpha_0\kappa[1 + (1 + (\bar{B}^4 - 1)\kappa^{-1})^{1/2}]$, $\alpha_0 = \lambda^{-1} = -\gamma_1/\gamma_2$, and $\kappa = 1 + \alpha_0^2\bar{B}^4$.

According to the theory proposed by Kuzuu and Doi [8], the rotational viscosity coefficient can be represented in the form

$$\gamma_1 = (2f/\lambda)\bar{P}_2. \quad (18)$$

Here, $\bar{P}_2$ is the order parameter of the nematic liquid crystal (the second-degree Legendre polynomial averaged over molecular orientations [8]), $f = \rho k_B T p/D_\perp$, $D_\perp$ is the coefficient of rotational diffusion with respect to the short axes of the molecules of the nematic liquid crystal, k_B is the Boltzmann constant, $p = (a^2 - 1)/(a^2 + 1)$, and $a = \sigma_\parallel/\sigma_\perp$ is a geometric parameter equal to the length-to-width ratio of molecules forming the nematic liquid crystal. It should be noted that the bounding surface affects the order parameter $\bar{P}_2$ only in a very thin layer (~10–100 nm [4]). Moreover, the broadband dielectric spectroscopic data obtained by Rozanski *et al.* [9] indicate that the relaxation time τ_{00}^1 of molecular rotation about the short axes for cyanobiphenyls (including 8OCB) in pores with a diameter of up to $0.2 \ \mu m$ is virtually identical to that in the bulk of samples. Since the relaxation time τ_{00}^1 and the rotational diffusion coefficient $D_\perp$ are related through the expression

$$\tau_{00}^1 = \left[D_\perp\frac{2 - 2\bar{P}_2}{1 - 2\bar{P}_2}\right]^{-1},$$

there are strong grounds to believe that the quantities $\bar{P}_2$ and $D_\perp$ depend only on the temperature. Therefore, the ratio of the rotational viscosity coefficients in the

Magnitudes of the rotational viscosity coefficients γ_1 and γ_2 in the bulk of the nematic phase of 8OCB according to the data taken from [10]

T, K	340	345	350
γ_1, kgm/s	0.046	0.033	0.021
$-\gamma_2$, kgm/s	0.049	0.035	0.023

vicinity of the charged bounding surface γ_1^{eff} and in the bulk of the sample has the form

$$\gamma_1^{\text{eff}}/\gamma_1 = \lambda/\lambda_{\text{eff}} = -(\gamma_1/\gamma_2)\cos 2\theta_{\text{eff}}(\bar{y}). \qquad (19)$$

Knowing the rotational viscosity coefficients in the bulk of the nematic liquid crystal, for example, 8OCB [10] (see table), we can calculate the effective rotational viscosity coefficients γ_1^{eff} and the angle $\theta_{\text{eff}}(\bar{y})$. In the case of high strain rates ($\dot{\gamma} \geq 800$ s^{-1}), the above ratio of the rotational viscosity coefficients can be written as follows [11]:

$$\gamma_1^{\text{eff}}/\gamma_1 = \lambda/\lambda_{\text{eff}} = \kappa[1 + (1 + (\bar{B}^4 - 1)\kappa^{-1})^{1/2}]. \quad (20)$$
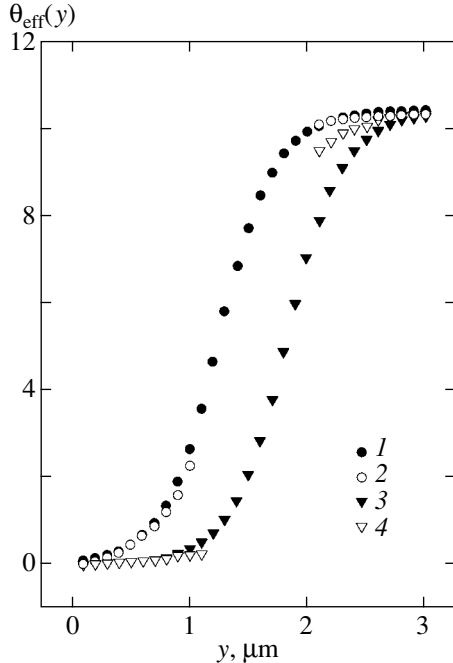
Fig. 1. Spatial dependences of the angle θ_{eff} in a shear flow of the 8OCB nematic liquid crystal at a temperature of 340 K for a homeotropic alignment of molecules ($\theta_s = 0$) on a charged bounding surface ($\sigma = 10^{-3}$ C/m^2). Strain rates: (*1, 2*) 80 and (*3, 4*) 100 s^{-1}. Calculations are performed according to relationships (*1, 4*) (15) and (*2, 3*) (17).

3. RESULTS OF NUMERICAL CALCULATIONS AND DISCUSSION

The derived relationships allow us to calculate the profiles $\theta_{\text{eff}}(\bar{y})$ and the dependence of the ratio $\gamma_1^{\text{eff}}/\gamma_1$ of the rotational viscosity coefficients on the distance to the charged bounding surface. Hereafter, we will analyze the shear flow of the anisotropic system formed by 8OCB molecules near the indium tin oxide surface in the temperature range from 340 to 350 K corresponding to the nematic phase [6]. Taking into account that the bulk concentration of ions in the liquid-crystal phase is given by $n_{\text{bulk}} = N_+/V = N_-/V \simeq 5 \times 10^{20}$ m^{-3} [6, 12], the Debye screening length can be calculated from the formula [5, 13]
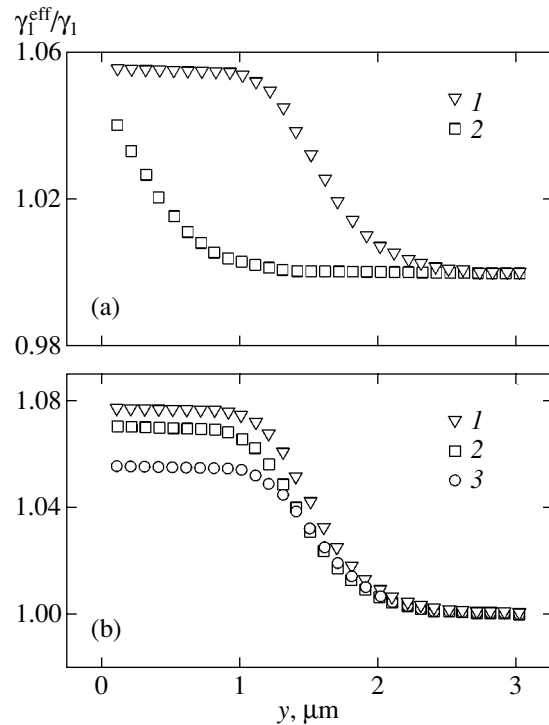
$$\lambda_D = \left(\frac{\epsilon_0 \epsilon k_B T}{2e^2 n_{\text{bulk}}}\right)^{1/2},$$

where $e = 1.602 \times 10^{-19}$ C is the proton charge and $\epsilon = \epsilon_0(\epsilon_\parallel \cos^2\theta_s + \epsilon_\perp \sin^2\theta_s)$. The Debye screening length was determined to be $\lambda_d = 0.55$ μm for the homeotropic orientation of the director on the bounding surface ($\theta_s = 0$) and $\lambda_D = 0.28$ μm for the planar alignment of the director ($\theta_s = \pi/2$). In our calculations, the surface charge density was chosen to be $\sigma = 10^{-3}$ C/m^2. This surface charge density $\sigma = en_{\text{surf}}$ corresponds to the surface concentration of charge carriers $n_{\text{surf}} = 10^{16}$ m^{-2} and agrees well with the experimental data $n \sim 10^{15}$–10^{16} m^{-2} [5, 14]. The strain rate in our calculations varied from 10 to 800 s^{-1}. Figure 1 depicts the dependences $\theta_{\text{eff}}(y)$ calculated from formulas (15) and (17) for the homeotropic orientation of the director on the bounding surface ($\theta_s = 0$) at the surface charge density $\sigma = 10^{-3}$ C/m^2 and a temperature of 340 K. At this temperature, the equilibrium angle $\theta_{\text{eff}}(y)$ monotonically increases to the bulk value $\theta_{\text{eff}}(y \sim 3\ \mu\text{m}) = \theta_{\text{bulk}} = 10.35°$ with an increase in the distance to the bounding surface. It was found that, for flows at high strain rates $\dot{\gamma} \geq 800$ s^{-1}, the angles $\theta_{\text{eff}}(y)$ calculated from relationship (15) (Fig. 1, curve *1*), which takes into account the contributions of the hydrodynamic, elastic, and electric forces to the momentum balance, are almost identical to those calculated with expression (17) (Fig. 1, curve *2*) allowing only for the contribution of the hydrodynamic forces. As the strain rate γ decreases, the contribution of the elastic forces increases; as a result, the dependence $\theta_{\text{eff}}(y)$ calculated from relationship (17) (Fig. 1, curve *3*) is shifted with respect to the dependence $\theta_{\text{eff}}(y)$ calculated using relationship (15) (Fig. 1, curve *4*). Therefore, shear flows of nematic liquid crystals in charged channels at strain rates $\dot{\gamma} \simeq 800$ s^{-1} and lower should be calculated with allowance made for the elastic forces.

The spatial dependences of the ratio $\gamma_1^{\text{eff}}/\gamma_1$ for the homeotropic orientation of 8OCB molecules on the indium tin oxide bounding surface ($\theta_s = 0$) at two sur-
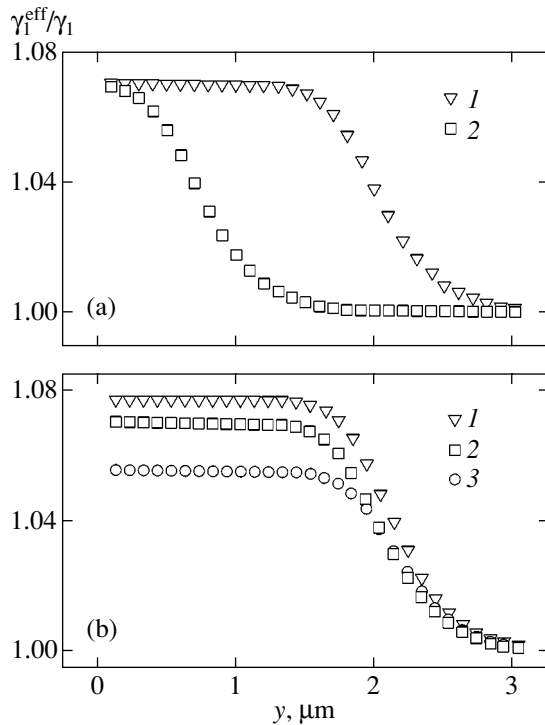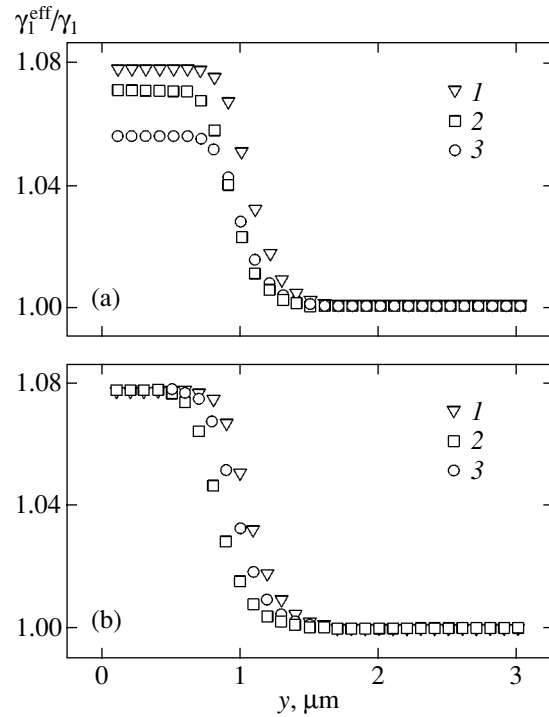
Fig. 2. Dependences of the ratio $\gamma_1^{\text{eff}}/\gamma_1$ of the rotational viscosity coefficients on the distance y to the bounding surface for the 8OCB nematic liquid crystal at the homeotropic alignment of the director ($\theta_s = 0$) for the strain rate $\dot{\gamma} = 100$ s^{-1} (a) at two surface charge densities (1) 10^{-3} and (2) 10^{-4} C/m^2 and the temperature $T = 340$ K and (b) at three temperatures $T = $ (1) 340, (2) 345, and (3) 350 K. Calculations are performed according to relationship (19).

face charge densities $\sigma = 10^{-3}$ C/m^2 (curves 1) and $\sigma = 10^{-4}$ C/m^2 (curves 2), a temperature of 340 K, and strain rates $\dot{\gamma} = 100$ and 800 s^{-1} are displayed in Figs. 2a and 3a, respectively. The behavior of the dependences of the ratio $\gamma_1^{\text{eff}}/\gamma_1$ suggests that the electric forces are involved in the bulk of the shear flow over a depth of ~3 μm. As the surface is approached, the effective rotational viscosity coefficient γ_1^{eff} increases by 7.8% as compared to the bulk coefficient γ_1. The surface charge density affects the depth of penetration of the electric forces. For shear flows at the strain rate $\dot{\gamma} = 100$ s^{-1}, an increase in σ by an order of magnitude from 10^{-4} to 10^{-3} C/m^2 results in an increase in the depth of penetration of the electric field by ~1.5 μm. The calculated ratios $\gamma_1^{\text{eff}}/\gamma_1$ for the homeotropic orientation of the director on the bounding surface at three temperatures $T = 340$ K (curves 1), 345 K (curves 2), and 350 K (curves 3) and the strain rates $\dot{\gamma} = 100$ and 800 s^{-1} are presented in Figs. 2b and 3b, respectively. It can be seen that, in both cases, an increase in the temperature is

Fig. 3. The same as in Fig. 2 at the strain rate $\dot{\gamma} = 800$ s^{-1}.

Fig. 4. Dependences of the ratio $\gamma_1^{\text{eff}}/\gamma_1$ of the rotational viscosity coefficients on the distance y to the bounding surface for the 8OCB nematic liquid crystal at the planar alignment of the director ($\theta_s = \pi/2$) for the surface charge density $\sigma = 10^{-3}$ C/m^2 (a) at three temperatures $T = $ (1) 340, (2) 345, and (3) 350 K and the strain rate $\dot{\gamma} = 100$ s^{-1} and (b) at three strain rates $\dot{\gamma} = $ (1) 100, (2) 200, (3) 300 s^{-1} and the temperature $T = 340$ K.

accompanied by a decrease in the effective rotational viscosity coefficient γ_1^{eff}.

An analysis of the results presented in Figs. 2a and 3a demonstrates that the depth of penetration of the electric field into the shear flow increases with a decrease in the strain rate. In turn, this leads to an increase in the effective rotational viscosity coefficient γ_1^{eff}.

The spatial dependences of the ratio $\gamma_1^{\text{eff}}/\gamma_1$ calculated for the planar alignment of the director on the bounding surface ($\theta_s = \pi/2$) are plotted in Fig. 4. The dependences at three temperatures ($T = 340$, 345, and 350 K), the surface charge density $\sigma = 10^{-3}$ C/m^2, and the strain rate $\dot{\gamma} = 100$ s^{-1} are depicted in Fig. 4a. Figure 4b shows the dependences at the temperature $T = 340$ K, the surface charge density $\sigma = 10^{-3}$ C/m^2, and three strain rates ($\dot{\gamma} = 100$, 200, 300 s^{-1}). In all cases, the depth of penetration of the electric field into the bulk of the shear flow is approximately equal to 1.5 μm, which is half as large as the depth for the homeotropic orientation. Knowing the magnitudes of the bulk coefficients γ_i ($i = 1, 2$) calculated recently in [10] for the nematic phase of 8OCB (see table), it is easy to obtain the magnitudes of the coefficients γ_1^{eff}. It should be noted that, according to relationship (20), an infinite increase in the surface potential density σ results in $\lim_{\sigma \to \infty} \gamma_1^{\text{eff}}/\gamma_1 = -\gamma_2/\gamma_1$ and an infinite increase in the depth of penetration of the electric field into the bulk of the sample. Therefore, the maximum increment in the coefficient γ_1^{eff} with respect to the coefficient γ_1 is approximately equal to 6–8% [10, 15]. In the other limiting case $\sigma \longrightarrow 0$, we have $\lim_{\sigma \to \infty} \gamma_1^{\text{eff}}/\gamma_1 = 1$.

4. CONCLUSIONS

Thus, the influence of the charged bounding surface on the rotational viscosity in the shear flow of the nematic liquid crystal was investigated in the framework of the Ericksen–Leslie theory. The contribution of the long-range electric forces to the rotational viscosity coefficient and the maximum alignment angle between the direction of the Couette shear flow and the director was analyzed. For this purpose, the terms associated with the hydrodynamic, elastic, and electric forces were included in the equation for the balance of the torques acting on the elementary volume. It was established that the effective rotational viscosity coefficient increases as the surface is approached. In the case of the 8OCB nematic liquid crystal, this coefficient can increase by 7.8% as compared to the bulk rotational viscosity coefficient γ_1. It was found that the contribution of the elastic forces to the torque balance can be ignored for shear flows at strain rates $\dot{\gamma} \geq 800$ s^{-1}.

REFERENCES

1. J. L. Ericksen, Arch. Ration. Mech. Anal. **4**, 231 (1960).
2. F. M. Leslie, Arch. Ration. Mech. Anal. **28**, 265 (1968).
3. P. G. de Gennes and J. Prost, *The Physics of Liquid Crystals*, 2nd ed. (Oxford Univ. Press, Oxford, 1995; Mir, Moscow, 1982), p. 360.
4. A. V. Zakharov, Phys. Rev. E **51**, 5880 (1995).
5. J. N. Israelachvili, *Intermolecular and Surface Forces*, 2nd ed. (Academic, London, 1992).
6. A. V. Zakharov and R. Y. Dong, J. Chem. Phys. **116**, 6348 (2002).
7. V. F. Zaĭtsev and A. D. Polyanin, *A Handbook on Ordinary Differential Equations* (Fiz.–Mat. Lit., Moscow, 2001), p. 576.
8. N. Kuzuu and M. Doi, J. Phys. Soc. Jpn. **52**, 3486 (1983).
9. S. A. Rozanski, R. Stunnarius, H. Groothues, and F. Kremer, Liq. Cryst. **20**, 59 (1996).
10. A. V. Zakharov and R. Dong, Phys. Rev. E **63**, 011704 (2001).
11. A. V. Zakharov and R. Dong, Eur. Phys. J. E **7**, 267 (2002).
12. S. Ponti, P. Ziherl, C. Ferrero, and S. Zumer, Liq. Cryst. **26**, 1171 (1999).
13. R. N. Thurston, J. Cheng, R. B. Meyer, and G. D. Boyd, J. Appl. Phys. **56**, 263 (1984).
14. S. Ponti, P. Ziherl, C. Ferrero, and S. Zumer, Liq. Cryst. **26**, 1171 (1999).
15. A. G. Chmielewski, Mol. Cryst. Liq. Cryst. **132**, 319 (1986).

Translated by O. Borovik-Romanova

FULLERENES
AND ATOMIC CLUSTERS

Electrophysical Studies of Nanoporous Carbon Materials Prepared of Silicon Carbide Powders

A. I. Veĭnger*, B. D. Shanina***, A. M. Danishevskiĭ*,
V. V. Popov*, S. K. Gordeev**, and A. V. Grechinskaya**

*Ioffe Physicotechnical Institute, Russian Academy of Sciences, Politekhnicheskaya ul. 26, St. Petersburg, 194021 Russia
e-mail: Alex.D@pop.ioffe.rssi.ru
**Central Research Institute of Materials, St. Petersburg, 191014 Russia
***Institute of Semiconductor Physics, National Academy of Ukraine, Kiev, 03028 Ukraine
Received April 4, 2002; in final form, December 2, 2002

Abstract—Measurements of the electrophysical properties of nanoporous carbon (NPC) samples (conductivity and Hall effect), as well as studies of the same samples using electron spin resonance (ESR), are summarized. Free holes are shown to play the major part in charge transport in such materials, thus permitting identification of the ESR signal with free holes. An analysis of the shape of the resonance lines, as well as of their dependence on temperature and the technology employed in sample preparation, established the ESR signals to consist of two superimposed resonance lines associated with carriers, free or localized to various extents, whose magnetic susceptibility obeys Pauli and Curie–Weiss laws, respectively. The temperature dependences of the ESR signal parameters were studied, and the experimental relations were compared with theory to determine the model-parameters. An analysis of the temperature behavior of these parameters suggests the conclusion that NPC samples are heterophase porous systems whose properties are dominated by structural characteristics. © 2003 MAIK "Nauka/Interperiodica".

1. INTRODUCTION

Carbon nanocluster structures have been recently attracting considerable interest because of their great diversity and the possibility of modifying their properties. Activated nanoporous carbon systems (activated carbon) have been employed for a long time as adsorbers, filters, etc. An essentially new class of such materials possessing a high nanoporosity has been prepared recently. These materials exhibit an extremely large specific surface area (~1300 m²/g), and, as such, can be employed, besides in the traditional applications, as electrodes in electrolytical double-layer capacitors and rechargeable lithium batteries. One of the methods used for their preparation consists in the chemical removal of non-carbon carbide-forming atoms from various crystalline (polycrystalline) carbide materials to form nanoporous (cluster) carbon [1–3]. Methods permitting preparation of bulk solid-state nanoporous carbon (NPC) elements with a total porosity over 70% and a nanoporosity of up to 50% were later developed [4–7]. The carbon nanoclusters bridging the pores in such elements approach in dimension nanopores themselves. X-ray [8–10] and Raman [11] studies show the carbon skeleton in these materials to be made up of small graphene sheets, which are, as a rule, arranged arbitrarily between the pores to form a quasi-amorphous network. The most probable size of small nanoparticles was established to vary from 0.8 to 2.0 nm, depending on the actual type of the original carbide [8, 10]. There

are, however, larger nanoclusters with a more regular structure in small amounts.

The electrophysical properties of NPC materials, which play a dominant role in their applications, are determined by the distribution and concentration of carriers and trapping centers, as well as by the character of current conduction in the system of nanoclusters, with potential barriers forming apparently at their boundaries. The very large specific area of the material, as well as the presence of adsorbates on it, suggests that carrier capture by surface traps should play a prominent part in conduction. This confers a particular scientific and practical importance to studies of the electrophysical properties of NPC materials.

In this communication, we report on measurements of the conductivity and Hall effect in NPC, as well as on studies of the same samples by using electron spin resonance (ESR).

The existence of ESR in the graphitic form of carbon has been known for a long time [12–14]. It was established that the ESR signal in single-crystal graphite is determined primarily by the characteristics of free carriers, which persist in graphite down to very low temperatures because this material is a semimetal. The magnitude of the g factor and its anisotropy in graphite depend on the position of the Fermi level. The recent discovery of new carbon forms (fullerenes, nanotubes, nanohorns, etc.), featuring primarily graphite sp^2 hybridization, spurred new interest in the magnetic
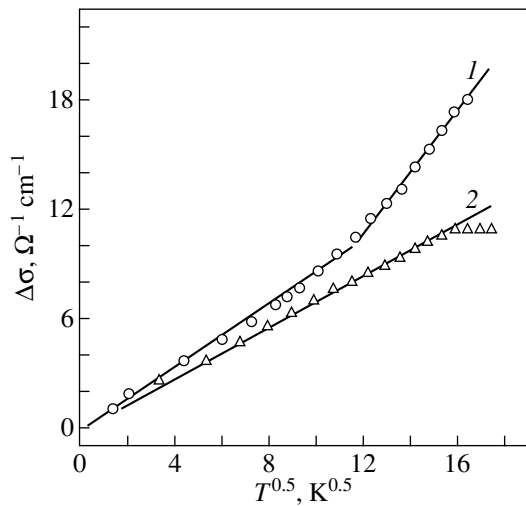
Fig. 1. Temperature dependences of the conductivity of NPC samples studied using ESR: (*1*) C(SiC)*A*, $\sigma(0 \text{ K}) = 25 \ \Omega^{-1} \text{ cm}^{-1}$ and (*2*) C(SiC)*B*, $\sigma(0 \text{ K}) = 31 \ \Omega^{-1} \text{ cm}^{-1}$.
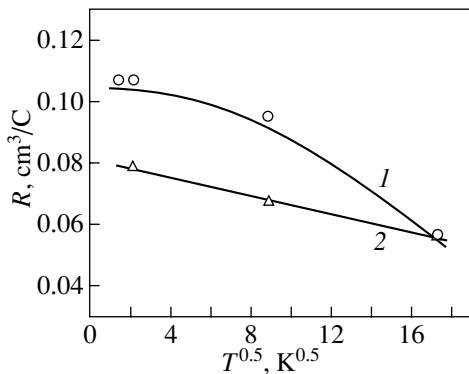
Fig. 2. Temperature dependences of the Hall constant in samples studied by ESR: (*1*) C(SiC)*A* and (*2*) C(SiC)*B*.

properties of such structures (see, e.g., [15, 16]). While the ESR in such structures was found to be also due to graphite bonding, the behavior of the *g* factor and of the ESR line width and amplitude are observed to have features associated with the variation of the concentration of carriers and of their interaction with temperature.

2. SAMPLE PREPARATION

The nanocluster carbon materials discussed in this communication were prepared of polycrystalline carbide powder, SiC. Bulk samples were obtained from powders with grains 40 and 2–5 μm in size (70 and 30 wt %, respectively); powder with a binder was pressed in a disk 20 mm in diameter, and pyrocarbon was synthesized in macropores to bind the carbide grains, after which the sample was chlorinated at a high temperature (~900°C) to all atoms remove other than carbon, a process culminating in the formation of a high-porosity carbon system. This was followed by placing the samples in an argon flow to remove chlorine. The NPC samples thus prepared are denoted by *B*; they contain a fraction (9–10 wt %) of nonporous but chlorination-modified pyrocarbon. While the porosity of such samples was, as a rule, in excess of 65%, the nanopore volume in the type-*B* material did not exceed 35% of the total sample volume.

Part of the samples was subjected, before chlorination, to additional silicification to transform the pyrocarbon inclusions to SiC grains, after which one could remove the silicon by reacting it with chlorine (from both the original SiC grains and the newly formed ones) and obtain in this way carbon with a higher nanoporosity (46–47 vol %). The NPC samples thus prepared are denoted subsequently by *A*. Note that the yield of pyrocarbon precipitation in the preliminary stage of sample-*A* preparation was higher (18–20 wt %) than that for type-*B* samples; the macropore volume in the final NPC material for type-*A* samples was substantially smaller than that in samples of type *B*.

3. STUDIES OF THE CONDUCTIVITY AND HALL EFFECT

Figure 1 plots the electrical conductivity $\Delta\sigma$ vs. $T^{0.5}$ [$\Delta\sigma = \sigma(T) - \sigma(0)$], and Fig. 2, the Hall coefficient *R* vs. $T^{0.5}$, for two NPC samples of the *A* and *B* types, which were also used in the ESR studies. The *R(T)* relation follows the same pattern in both samples; namely, the Hall coefficient increases slightly with decreasing temperature. The sign of *R* is that for hole conduction. The sign of the Seebeck coefficient also corresponds to the hole mechanism and coincides, in this sense, with the sign of the Hall coefficient. The Hall voltage depends linearly on magnetic field for most of the samples up to $H = 30$ kOe. One may thus assume the conduction to have primarily a one-band character. In the case of one-band conduction, the hole concentration n_h in various samples of the above type lies in the range $n_h = 1/eR \sim 5 \times 10^{19}$–$10^{21}$ cm^{-3} [17]. The corresponding Hall mobility μ ($T = 77$ K) calculated from the relation $\mu = R/\rho$ (ρ is the electrical resistivity) is of the order of 1–3 cm^2/V s. This quantity decreases in approximately linearly with increasing temperature.

Band overlap in pure single-crystal graphite is known to result in electron–hole anisotropic conduction with a high carrier mobility. In microcrystalline graphite, the Fermi level shifts to the *p* band. The growth of hole concentration with decreasing grain size is usually related to the increase in the number of surface states at the boundaries, which act as electron trapping centers [18]. Thus, the high hole concentration in nanoporous carbon can be due to the strongly developed free surface and, accordingly, to a high concentration of acceptor states. The low hole mobility is apparently caused by band structure distortion at the boundaries of nanoclusters and by the mean free path being limited by the nanocluster dimensions.

The existence of a linear section in the $\Delta\sigma$ vs. $T^{0.5}$ curves at low temperatures indicates the temperature dependence of the conductivity to be determined by quantum corrections associated with electron–electron scattering [19]. The decrease in the mobility with temperature suggests that the conduction exhibits quasi-metallic behavior. The effect of this decrease on the temperature dependence of conductivity at sufficiently high temperatures is counterbalanced by thermal activation of carriers from fluctuation potential wells.

4. ESR STUDIES OF NANOPOROUS CARBON

4.1. Experiment

The ESR signals were studied on samples measuring $4.5 \times 2 \times 1$ mm^3. We analyzed the temperature-induced variations of the ESR parameters, more specifically, of the amplitude, width, and shape of the resonance lines. Conclusions were drawn concerning the character of interaction of carriers and their magnetic properties in the samples studied.

The ESR spectra were measured with an E-112 ESR spectrometer (Varian) equipped with an ESR-9 cryostat (Oxford Instruments), which made it possible to record spectra in the temperature range 3.2–300 K. ESR spectra were measured at fixed temperatures in a heating run performed after the sample cooling. After a type-A sample was heated to 300 K, the temperature was again lowered to 25 K and the measurements were repeated. The samples were maintained in a gaseous helium environment at all times.

Figure 3 displays ESR spectra of a type-A sample obtained at various temperatures in the range 3–150 K. At all temperatures, the signals are seen to have an asymmetric shape characteristic of free carriers [20, 21]. This appears only natural, because the samples had an electrical resistivity $\rho \approx (2–4) \times 10^{-2}$ Ω cm, i.e., a skin depth $\delta \approx 5 \times 10^{-2}$ mm, which is substantially less than the sample dimensions. The sample resistivity decreased by a factor of no more than 1.5 as the temperature was increased from liquid-helium to room temperature.

Note also that the signals in Fig. 3 are actually a superposition of at least two lines with different resonance fields and widths. Because the temperature dependence of the skin depth is proportional to $\rho^{1/2}$, one can readily take into account the variation of this quantity when analyzing the shape of the ESR spectrum.

The recorded spectra were deconvolved into constituents with a "true" spin resonance (SR) shape. This deconvolution was achieved by fitting the experimental spectrum with the theoretical signal shape function $F(x) = \Sigma_j a_j f(x_j)$, where $x_j = g(H - H_{res, j})T_{2j}, f(x_j)$ is the theoretical SR signal shape (see, e.g., [19]), and a_j is the weighting factor of the jth signal. The fitting was done using a FORTRAN code to compute the resonance signal and the PeakFit program to choose the parameters
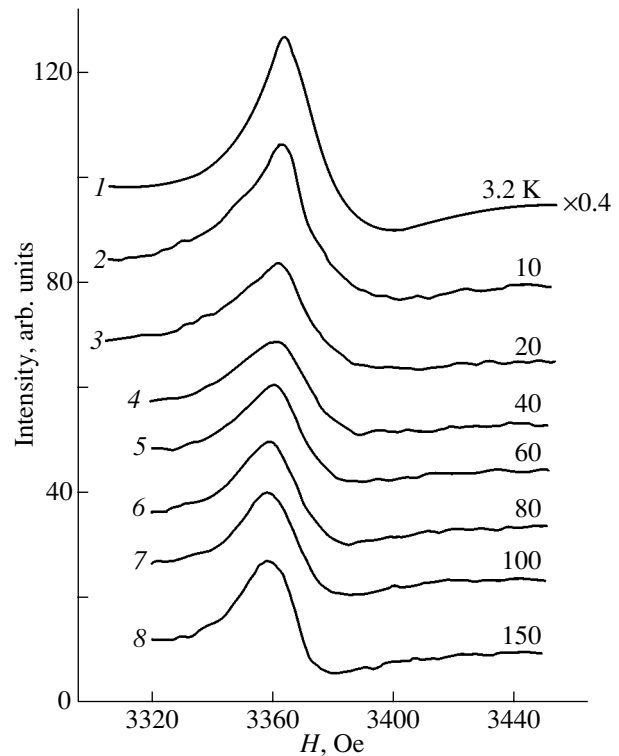

Fig. 3. ESR signals of an NPC sample, type A_1, measured at various temperatures.

of the signals making up the spectrum. The fitting yielded the amplitudes, resonance fields, widths of the spectral components, and the values of T_{2j}^{-1} for the jth spin subsystem. Note that $T_2 = h(g\beta\Delta H)^{-1}$; therefore, we omit subsequently all constants in this relation and write $T_2^{-1} = \Delta H$.

The concentration was estimated by integrating the absorption curves corresponding to the spectral components thus found and by comparing then with the absorption of a Varian reference sample reduced to the same experimental conditions (microwave power, gain, etc.).

4.2. General Characteristics of the Signals

All samples produce ESR signals consisting of two resonance signals with strongly varying g factors and linewidths. We denote the original sample A by A_1 and the same sample heated to 300 K and cooled subsequently to 25 K by A_2. The ESR signals from A_1 and A_2 differ in the magnitude of the g factor and its temperature behavior (see Table 1). This difference may be due to the fact that the extremely developed surface of nanoporous carbon always has adsorbed oxygen (paramagnetic center) and the changes that occur in sample A_2 are probably connected with the diffusion of oxygen atoms and the associated rearrangement of atomic bonding. The strong effect of oxygen on the ESR signal

Table 1. Parameters of ESR signals in samples A_1, A_2, and B

Sample	g_1	ΔH_1, G	g_2	ΔH_2, G
A_1	2.0085–2.0128	12–22	2.0180–2.0240	12–25
A_2	2.0085–2.0078	30–20	2.0268–2.0078	38–150
B	2.0018–2.0032	4–9	2.0024–2.0048	16–26

parameters and their temperature behavior in a system of porous carbon with nanohorns was studied in [16].

4.3. Integrated Intensities

The experimental ESR signals were fitted against theoretical ESR signals of carriers calculated for different values of the ratio of the skin depth to the diffusion length through the skin depth $R_1 = d/d_D$ (the theoretical signals were obtained for R_1 from 0.1 to 50). The first estimate of R_1 was made from the amplitude ratio of the derivative of the absorption signal at its maximum and minimum (line shape asymmetry parameter), after which this ratio was varied because the signal was a combination of two lines. After deconvolution of the
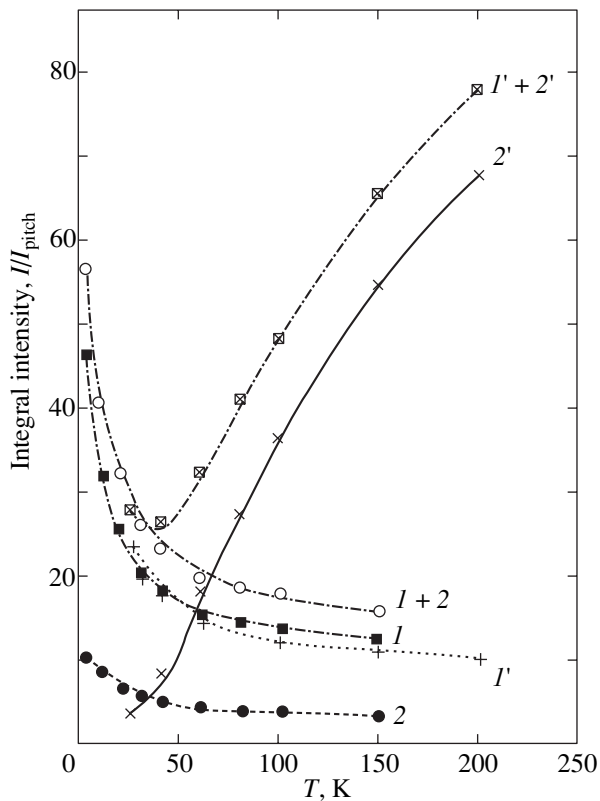
Fig. 4. Temperature dependences of integrated intensities of the total ESR signal and of its constituents for samples A_1 and A_2. (*1, 2*) Data for lines *1* and *2* obtained in the original (A_1) measurement, (*1', 2'*) data for lines *1* and *2* obtained in a repeated measurement, (*1 + 2*) total signal from A_1, and (*1' + 2'*) total signal from A_2. The lines represent calculation.

signal into its constituent parts and their theoretical description, the integrated intensities were found; they are displayed in Figs. 4 (for A_1, A_2) and 5 (for B). The integrated intensities of total signals are, with rare exceptions, sums of two contributions, namely, of the contribution from the subsystem with a Curie–Weiss paramagnetic susceptibility χ''_{C-W} and of that from the subsystem with a Pauli susceptibility χ''_P, which does not depend on temperature. Sample A_2 and, to a lesser extent, sample B also exhibit a contribution due to the carriers released in the ionization of shallow centers. Thus, the integrated intensity $I(T)$ [expressed in units of integrated intensity of the reference sample (pitch) with a paramagnetic center concentration 2.58×10^{15} cm^{-3} measured under the same experimental conditions] can be written as

$$I(T) = I_P + C/(T + \theta_p) + I_{\text{ion}}\exp(-E_i/kT), \quad (1)$$

where I_P is the contribution due to the subsystem of degenerate carriers, C is the Curie constant in relative units, θ_p is the paramagnetic temperature in the Curie–Weiss relation (which characterizes the sign and magnitude of exchange interaction between localized spins), and E_i is the ionization energy. Table 2 lists the values of the constants entering Eq. (1) for the integrated intensities of the total signal and its components.

These integrated intensities were used to derive the concentrations (Table 3) of the localized centers N_{loc} responsible for the Curie–Weiss susceptibility, of the degenerate carriers n_c contributing to the Pauli susceptibility, and of the shallow carrier traps N_{ion} providing a contribution to the ionization term in the integrated intensity.

As seen from Table 2, localized centers in samples A_1 and B interact antiferromagnetically with one another ($\theta_p > 0$) and only the centers producing resonance line *1* in sample B are ferromagnetically coupled, although their concentration is low and their interaction is weak. Since the concentration of the localized centers is low, their exchange interaction is actually a hole-mediated indirect exchange interaction.[1]

4.4. g Factors

Figures 6a and 7a display the temperature dependences of the *g* factors for the two lines responsible for the ESR signal in samples A_1, A_2, and B. Prior to dis-

---

[1] Note that although free-hole ESR in widely studied semiconductors is not observed because of the short spin-lattice relaxation time, in graphite, whose minimum band gap is not located at a high-symmetry point in the Brillouin zone center, there is no band degeneracy and the spin relaxation times of the electrons and holes can be of the same order of magnitude. Because the signs of the Hall effect and of the Seebeck coefficient indicate the transport effects in these materials to be associated with the hole component, it may be safely conjectured that the observed ESR characteristics are also dominated by free or weakly bound holes.

Table 2. Relative contributions to integrated ESR signal intensities due to the Pauli, Curie–Weiss, and ionization subsystems

Sample	ESR signal	I_P, arb. units	C, K	θ_p, K	I_{ion}, arb. units	E_i, K
A_1	1	10.15	383.7	7.5	–	–
	2	1.98	210	23.82	–	–
	Total	12.1	632	11	–	–
A_2	1	8.42	383.7	0	–	–
	2	0.31	61.9	0	127	127.7
	Total	8.7	445.6	0	127	127.7
B	1	0.03	14.38	–2.39	4.7	197
	2	18.8	1282	22	–	–
	Total	18.8	967.3	11.43	4.7	197

cussing the temperature behavior of the g factors, we note that an analysis of the integrated intensities of the deconvolved ESR lines suggests that the localized and free spin subsystems are tightly coupled. Another point is that the signals always have the line shape of free-carrier spin resonance. This argues for a strong interaction of carriers with localized states and the existence of a phonon bottleneck, which makes the cross-relaxation between the subsystems considerably faster than the spin–lattice relaxation or the relaxation mediated by spin–orbit coupling. In the phonon bottleneck conditions, the magnetic moments of both subsystems precess together, so that the resonance signal amplitude contains contributions due to the susceptibilities χ″ of both subsystems (see, e.g., [22]). Now, if the localized spins and carriers have different g factors, the resonance field and its temperature dependence for the resultant resonance line can be described by the following expression, first proposed in [23]:

$$H^{res} = (\chi_P'' H_{c,\,res} + \chi_{C-W}'' H_{1,\,res})/(\chi_P'' + \chi_{C-W}''). \quad (2)$$

Equation (2) readily yields an expression for the g factors,

$$g = (1 + \chi_{C-W}''/\chi_P'')[g_c^{-1} + g_{loc}^{-1}(\chi_{C-W}''/\chi_P'')]^{-1}. \quad (3)$$

Note that the temperature dependence of the g factor in Eq. (3) is determined not only by the temperature factor in the Curie–Weiss relation but also by the change in the free carrier concentration resulting from the ionization occurring in samples B and A_2. The phonon bottleneck conditions play a considerable role in the behavior of g(T) for both resonance lines, 1 and 2, in samples A_1 and B, as well as for line 2 in sample A_2. No phonon-bottleneck conditions were observed for line 1 in sample A_2; therefore, the g factor is determined here only by the free-carrier g factor, slightly corrected for the exchange coupling with local spins [22]:

$$g_{1A_2} = g_c/(1 + \alpha\chi_{C-W}''), \quad \alpha = -4.2 \times 10^{-4}, \quad (4)$$

where α is the dimensionless exchange interaction constant, with α < 0 relating to ferromagnetic coupling. By fitting Eqs. (3) and (4) to the experimental curves in Figs. 6a and 7a, we found the values of g_{loc} and g_c for the local centers and carriers, respectively. These values are given in Table 4.

The χ_{C-W}''/χ_P'' ratio in Eq. (3) can be written as

$$\chi_{C-W}''/\chi_P'' = (C/T)[I_P + I_i\exp(-E_i/T)]^{-1} \quad (5)$$

and it would seem that the constants for each ESR line in Eq. (5) should coincide with those in Table 2. However, as follows from curve fitting of the theory to the experimental data obtained on samples A_1 and A_2, the constants calculated for lines 1 do indeed fit to lines 1, whereas for lines 2, one should substitute the parameters of the total intensities. For sample B, the system with C = 1282 K and θ_p = 22 K from Table 2 plays in both cases the part of a localized system, while the carriers thermally activated from the density-of-states tails (with an activation energy E_i = 197 K) act as exchange-coupled carriers.

4.5. Signal Width

In the phonon bottleneck conditions, the ESR signal width is given by an expression similar to Eq. (2) [22],

$$\Delta H_{eff} = (\chi_P''\Delta H_c + \chi_{C-W}''\Delta H_{loc})/(\chi_P''^* + \chi_{C-W}''^*). \quad (6)$$

Here, ΔH_c is the carrier ESR linewidth, ΔH_{loc} is the local-center ESR linewidth, and $\chi_P''^*$ and $\chi_{C-W}''^*$ are the values of the corresponding susceptibilities with inclu-

Table 3. Spin concentration in samples

Sample	A_1	A_2	B
N_{loc}, cm^{-3}	5.2×10^{15}	3.8×10^{15}	8×10^{15}
n_c, cm^{-3}	1.3×10^{19}	10^{19}	2.1×10^{19}
N_{ion}, cm^{-3}	0	0.95×10^{20}	0.27×10^{19}
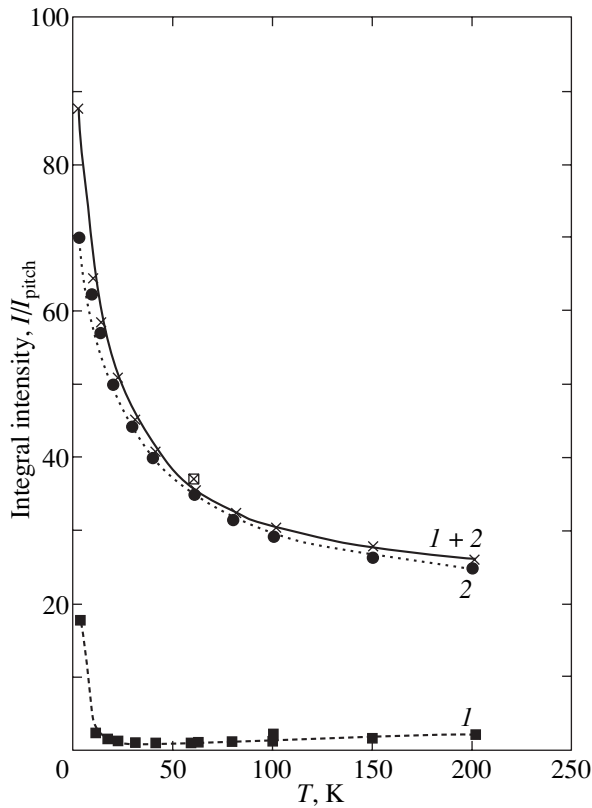
Fig. 5. Temperature dependences of integrated intensities of the total ESR signal and of its constituents for sample *B*. (*1*) First signal component, (*2*) second signal component, and (*1* + *2*) total intensity. The lines represent calculation.

sion of the exchange interaction between the two subsystems,

$$\chi_P''^* = \chi_P''(1 + \alpha\chi_{C-W}''), \quad \chi_{C-W}''^* = \chi_{C-W}''(1 + \alpha\chi_P''). \quad (7)$$

For low concentrations of local centers, we have $T_{2c}^{-1} = \Delta H_c \gg \Delta H_{loc}$. In this case, the signal linewidth is determined primarily by the inverse carrier spin lifetime, i.e., by the rate of carrier scattering from defects in a disordered medium, so that, in view of Eq. (7), the signal linewidth can be presented in the form

$$\Delta H_{eff} = \Delta H_c/(1 + \alpha\chi_{C-W}'') + \Delta H_c'(T). \quad (8)$$

The second term in Eq. (8) accounts for changes in the properties of the subsystems, e.g., carrier generation in

Table 4. *g* Factors for the paramagnetic subsystems contributing to resonance absorption

Sample	A_1		A_2		B	
Line	*1*	*2*	*1*	*2*	*1*	*2*
g_c	2.0141	2.0232	2.0080	2.0070	2.0037	2.0114
g_{loc}	2.0088	2.0171	–	2.0280	2.0018	2.0024

sample A_2 at higher temperatures. In view of this, the linewidths for samples A_2 (line *2*) and *B* in Figs. 6b and 7b are described by the following theoretical relations. For sample A_2, line *2*,

$$\Delta H_{A22} = (152 + 32C_{A22}T^{-1}\delta\chi_i'')/(1 + CT^{-1}\delta\chi_i''^{-1}),$$

where C_{A22} and $\delta\chi_i'' = I_{ion}\exp(-E_i/T)$ are taken from Table 2 for line *2* of sample A_2.

For sample *B*, line *1*:

$$\Delta H_{B1} = 1.6/(1 + \alpha_{B1}C_{B1}/(T - 2.3)) + 2 + 12\exp(-197/T),$$
$$\alpha_{B1} = -0.75,$$

and line *2*:

$$\Delta H_{B2} = 5 + 24/(1 + \alpha_{B2}C_{B2}/(T + 22)), \quad \alpha_{B2} = 0.58.$$

One readily sees that line *2* in sample A_2 broadens in accordance with Eq. (6) under the phonon bottleneck conditions. By contrast, while local centers in sample *B* do not contribute to the linewidth, exchange interaction between carriers and local centers dominates the temperature dependence and reduces the linewidth in the case of ferromagnetic coupling (line *1*) or increases it in the case of antiferromagnetic coupling (line *2*). In addition, line *1* is broadened exponentially in the temperature region $T > 80$ K by carrier concentration fluctuations when the carriers are activated from the density-of-states tails.
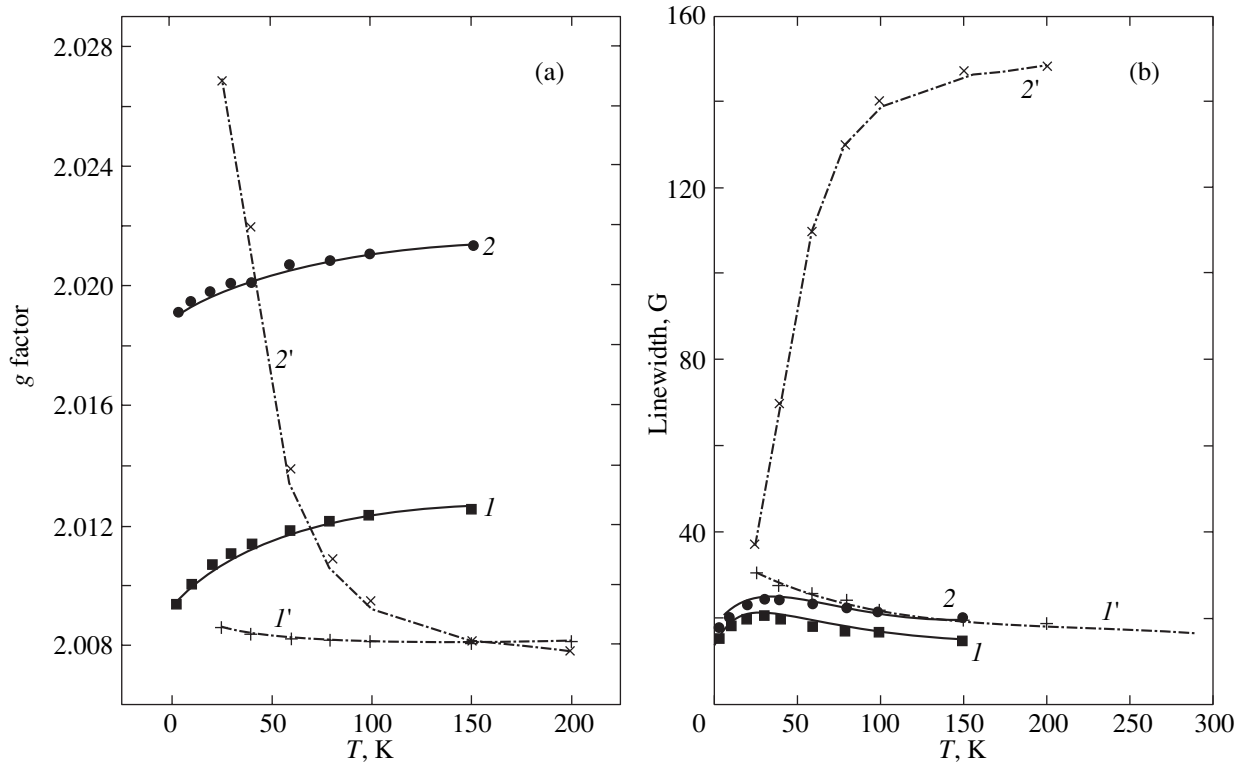
The temperature dependence of the widths of lines *1* and *2* in sample A_1 and of line *1* in sample A_2 follows a different pattern (the latter line remained practically constant after the cooling–heating cycle). The width is dominated here by carrier scattering. As the temperature increases, the low-temperature scattering rate grows slightly because of the increase in the carrier thermal velocity, but after that, the line narrows, probably as a result of variable-range hole hopping between neighboring regions separated by a potential barrier. For these three lines, the experimental data can be described by the following relation

$$\Delta H = (\Delta H_c^{(0)} + s\sqrt{T})$$
$$\times [1 + (w/\Delta H_c^{(0)})^2\exp(-2(T_0/T)^{1/4})]^{-1}. \quad (9)$$

Here, w is the hopping probability between neighboring acceptor states, T_0 is the hopping activation energy, s is a coefficient accounting for the thermal enhancement of carrier scattering, and $\Delta H_c^{(0)}$ is the original carrier spin relaxation rate. The numerical parameters of the fit are given in Table 5.

4.6. Line Asymmetry

The degree of resonance line asymmetry is another parameter that provides valuable information on conducting samples. The asymmetry of a Dyson-shaped ESR line is known [20] to be determined by the ratio of

Fig. 6. Temperature dependences of the g factor and ESR linewidth for samples A_1 and A_2. (a) (1, 2) Data for signal components obtained in the original (A_1) measurement, ($1'$, $2'$) data obtained in the second (A_2) measurement, (b) (1, 2) data for lines 1 and 2 (A_1), and ($1'$, $2'$) data for lines 1 and 2 (A_2). The lines represent calculation.

the free-electron diffusion time through the skin depth, T_D, to the spin–lattice relaxation time T_2. This distortion is expressed through the ratio of the amplitude of the weak-field positive wing in the derivative of the absorption line, a, to that of the strong-field negative wing, b. For $T_D/T_2 \gg 1$, $a/b = 2.7$. This is valid for metals where the Fermi level is located far above the conduction band bottom. Studies of weakly degenerate Ge [24] have shown, however, that free spins located near the conduction band bottom interact with fluctuations of the conduction band bottom potential, producing an additional ac electric field. The characteristic frequency of this field is inversely proportional to the time taken by a carrier to travel a distance on the order of the potential fluctuation correlation length. Therefore, the expression relating T_D to T_2 contains, in place of the time needed for a carrier to cross the skin depth, the time it takes for a carrier to travel this correlation length. As the temperature increases, this length can also increase, provided the potential fluctuations are small enough. In these conditions, the carrier no longer experiences these fluctuations at a high temperature. In a nanoporous system, however, potential fluctuations may be far larger than kT. This may be, for instance, the case with pore boundaries. In this case, the frequency of the internal field acting on a moving carrier will grow with temperature as a result of the increase in the carrier thermal velocity.

Because the signal fitting procedure yields both the quantity $R_1 = T_D/T_2$ and T_2^{-1}, one can readily obtain the temperature dependence of T_D. Figure 8 displays the temperature variation of the carrier diffusion rate. In the original sample A_1, the diffusion rate at high temperatures is seen to be two orders of magnitude greater than in A_2 and B and it grows very smoothly with temperature. This is possible if the potential fluctuations greatly exceed kT, because the carrier velocity naturally increases with temperature.

In sample B (for the system described by line 1) and in sample A_2, a sharp decrease in T_D^{-1} is observed for $T > 80$ K; this decrease should be assigned to the generation of additional carriers (see Table 2). In sample B (for line 1), the decrease in the diffusion rate is apparently accounted for by large inhomogeneities in the

Table 5. Parameters determining $\Delta H(T)$ for lines 1 and 2 in sample A_1 and line 1 in sample A_2

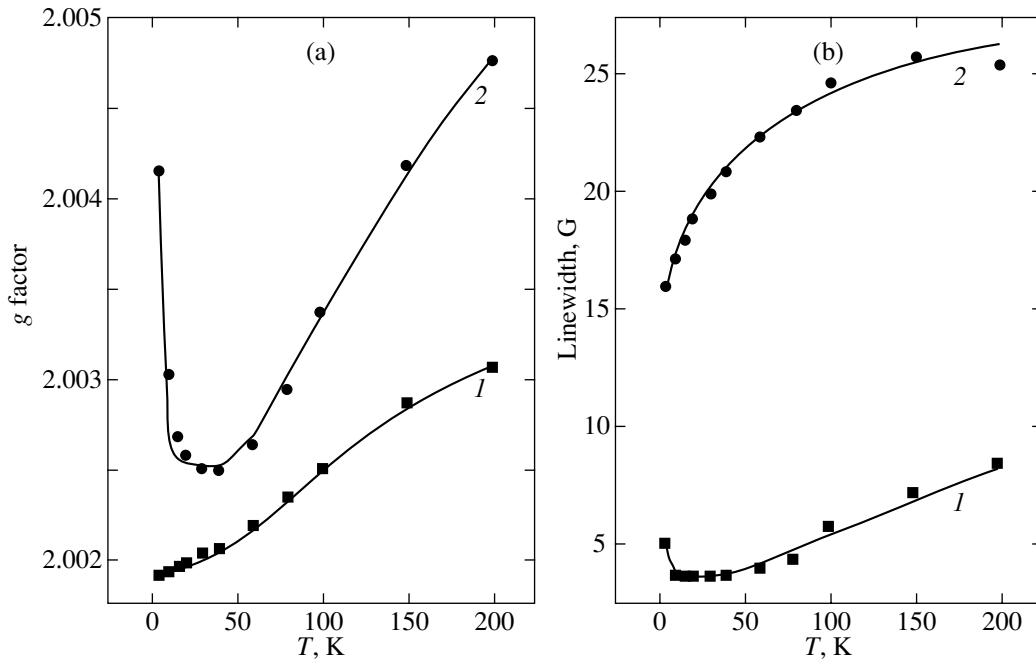| Sample	Line	$\Delta H_c^{(0)}$, G	s, G K$^{-1/2}$	w, 10^9 s^{-1}	T_0, K
A_1	1	9.14	3.28	2.10	3309
A_1	2	8.46	4.11	1.83	3309
A_2	1	33	0	2.63	1430

Fig. 7. Temperature dependences of the *g* factor and ESR linewidth for sample *B*. Notation same as in Fig. 6.

sample structure, and in sample A_2, by the part played by oxygen atoms which are released under thermal cycling.

At higher temperatures, the decrease in T_D^{-1} in sample *B* and, partially, in A_2 slows down substantially. This finds explanation if the potential fluctuations are assumed to be distributed in amplitude such that carriers gradually cease interacting with some of the fluctuation as the temperature increases. The carriers will interact with progressively larger fluctuations. Under these conditions, the effective dimensions of a spatial inhomogeneity increase with temperature, with the carrier needing increasingly longer times to cross such a fluctuation.

5. DISCUSSION

Both components of the signal of sample *A* obtained in the first measurement (A_1) are spin resonance signals of free carriers which are strongly exchange-coupled with local centers. The contribution of the Pauli susceptibility is comparable to that of the Curie–Weiss susceptibility even at 40 K. This indicates a higher concentration of free carriers compared to that of localized centers. The widths of both signals exhibit the same temperature dependence and are similar in magnitude. For temperatures $T < 40$ K, these widths grow with temperature; i.e., the carrier relaxation times decrease because of the increasing thermal velocity, which scales with temperature as $T^{0.5}$. For $T > 40$ K, the lines narrow because of the decreasing cross section of interaction of free spins with relaxation centers.

An analysis of the temperature dependence of integrated intensity suggests that the local centers contributing to lines *1* and *2* are located in different regions of the sample. The paramagnetic temperature for centers of one type is 7.5 K, and that for the other type, 23.8 K. This means that indirect exchange interaction between centers of the first type is considerably weaker than that between centers of the second type. The latter centers reside apparently in a more porous medium; i.e., they are separated by wider potential barriers.

The second measurement revealed considerable changes in the structure of sample *A*, but not in all of its volume, because the *g* factor, the linewidth, and the integrated intensity of line *1* behave in the same way as those of lines *1* and *2* in sample A_1. As for the second line, all of its parameters change dramatically with increasing temperature. An analysis showed this behavior to be associated with an increase in the density of states in the tails near the Fermi level and with thermal ionization with a characteristic energy of 11 meV. The carrier concentration increases by an order of magnitude at $T = 300$ K. Another remarkable change consists in the vanishing of the paramagnetic temperature, $\theta_p = 0$; in other words, there is no longer any indirect exchange between localized paramagnetic centers. As already mentioned, one may assume that these processes involve oxygen diffusion initiated by the variation of the oxygen partial pressure under variation of temperature. An analysis of the ESR signals shows sample *B* to be highly inhomogeneous. The temperature dependence of integrated intensity of line *1* is contributed by free spins interacting with localized spins, which are characterized by a very large fraction of

localized states and a pronounced antiferromagnetic coupling (line *2*). At the same time, there are ferromagnetically coupled (θ_p = 2.39 K) local centers (line *1*). The fraction of these centers is two orders of magnitude smaller than the relative concentration of type-*2* centers. This behavior of the paramagnetic susceptibility, as well as the behavior of the spin–lattice relaxation time, implies heterogeneity of the spin system.

The signal due directly to degenerate free carriers in sample *A* is not observed because of strong exchange binding of free and bound carriers. The observed ESR lines are due to such mixed systems. This shows that the difference in carrier concentration between various parts of the heterogeneous system is considerably smaller than that in sample *B*.

A comparison of the temperature dependences $\chi''(T)$ of these two samples suggests that samples prepared by following technology *A* have a more uniform free-carrier concentration than do samples synthesized using technology *B*.

As follows from high-resolution electron microscope images [25], a sizable part of the carbon framework in NPC samples is made up of small graphene sheets. There are also larger aggregates, most of them representing carbon "onions" or "quasi-onions." They were found in much larger numbers in type-*B* samples with pyrocarbon inclusions. It is possible that the fairly loose and not well-ordered pyrocarbon in type-*B* samples transforms during the high-temperature chlorination to form onion like and arbitrarily bent quasi-graphitic structures in various amounts. These structures are 30–50 nm in size, which exceeds by far the size of graphene sheets (1–2 nm). Therefore, it is these two types of elements of the skeleton in NPC samples that one should most likely associate with the two spin systems derived from the ESR data. Because the onions and quasi-graphitic inclusions have a more perfect structure, one may expect the free-carrier concentration in them to be lower than that in the disordered graphene sheet network. This conjecture is borne out by data obtained in a study of carrier transport in a system of practically pure onions [26]. It was found that the conductivity of those samples was substantially lower than that in NPC samples even at high temperatures and decreased exponentially with decreasing temperature [26]. In view of the fact that carrier conductivity over sheets within an onion or quasi-graphitic cluster should be substantially higher than 1–3 cm^2/V s (this value is derived from conductivity and Hall effect measurements on NPC samples), one may expect the concentration of mobile carriers in onions to be orders of magnitude less than the value extracted from the Hall effect data available for these samples.

In this case, the observed ESR signals with a smaller *g* factor should possibly be assigned to the onion part of NPC samples and those with *g* > 2.01, to the skeleton of disordered graphene sheets.
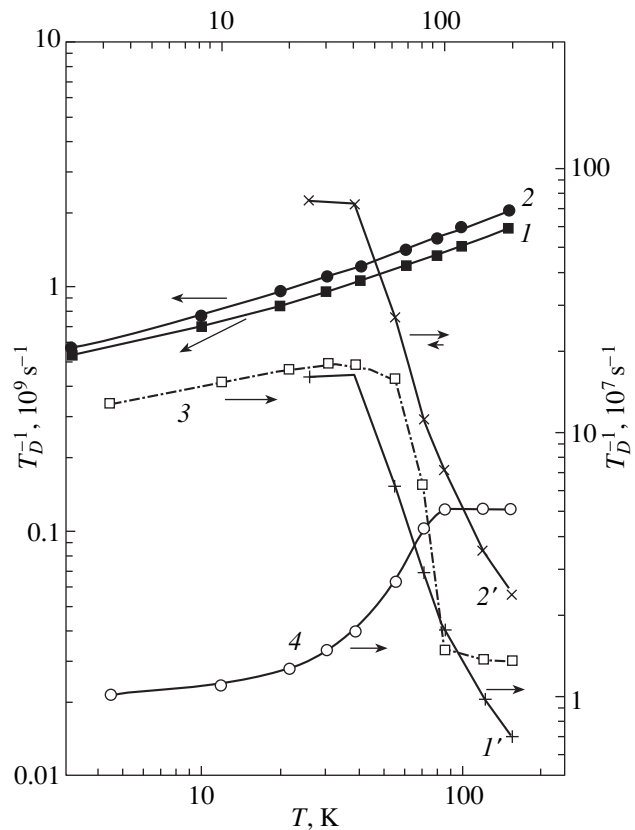
Fig. 8. Temperature dependences of carrier diffusion rates. (*1*, *2*) Data for lines *1* and *2* (A_1), (*1'*, *2'*) data for lines *1* and *2* (A_2), and (*3*, *4*) data for lines *1* and *2* of sample *B*.

6. CONCLUSIONS

Thus, an analysis of experimental data on ESR line parameters obtained for NPC samples prepared by following technologies *A* and *B* suggests certain conclusions as to the magnetic properties of free carriers and the microstructure of the samples themselves.

(1) NPC has a heterophase structure. Experimentally, one observes at least two phases differing in free-hole spin behavior, as well as in the concentration of localized centers (dangling bonds, apparently).

(2) The phases differ in the temperature behavior of the paramagnetic susceptibility, spin–lattice relaxation time, and the magnitude of exchange interaction between the localized paramagnetic centers. The properties of the phases depend on the technology employed in NPC preparation.

(2a) At low temperatures, a type-*B* sample reveals, against the background of the large contribution from localized paramagnetic centers, a phase with a lower concentration of free spins with χ'' varying with temperature according to the Pauli law and of local ferromagnetically coupled centers. The spin–lattice relaxation rate in this phase is weakly temperature-dependent. This phase is tentatively associated with the onionlike and bent quasi-graphitic fragments observed

[25] to exist in samples of type *B*. In type-*A* samples, the two phases do not differ so strongly from each other. This suggests that the two types of structural elements of the carbon framework differ little from each other both in size and in the degree of ordering.

(2b) At sufficiently high temperatures, the temperature behavior of χ'' in samples of both types *A* and *B* obeys the Pauli law, because the susceptibility of localized centers decreases with temperature fairly rapidly in accordance with the Curie–Weiss law. The spin–lattice relaxation in *A* and *B* samples is dominated by exchange interaction with the relaxation centers.

The phase providing a high-temperature contribution to ESR signals is possibly related to the quasi-amorphous network of graphene sheets arranged arbitrarily between the graphene sheet pores. In samples *B* and A_2, which was prepared from A_1 through heating and cooling, additional carriers appear at $T > 80$ K; these carriers are thermally activated from density-of-states tails with ionization energies of 11 meV in sample A_2 and 16.9 meV in sample *B*.

(2c) The *g* factor was found to behave substantially differently with temperature in samples prepared using different technologies. The main reason for this difference lies in the magnitude of exchange interaction between the free and bound carriers. In sample *A*, this interaction is considerably stronger, which suggests that two-dimensional fragments dominate in the carbon framework of these NPC samples.

(3) Summing up, ESR data suggest that the structure of the NPC framework in samples *A* has more elements that are uniform in carrier concentration than does that in samples *B*.

ACKNOWLEDGMENTS

REFERENCES

1. U.S. Patent No. 3,066,099 (1962); FRG Patent No. 1,185,163 (1966).
2. N. F. Fedorov, G. K. Ivakhnyuk, V. V. Tetenov, and G. V. Matyukhin, Zh. Prikl. Khim. (Leningrad) **54** (7), 1464 (1981); N. F. Fedorov, G. K. Ivakhnyuk, and D. N. Gavrilov, Zh. Prikl. Khim. (Leningrad) **55** (1), 46 (1981); N. F. Fedorov, G. K. Ivakhnyuk, and D. N. Gavrilov, Zh. Prikl. Khim. (Leningrad) **55** (1), 272 (1981).
3. N. F. Fedorov, G. K. Ivakhnyuk, D. N. Gavrilov, *et al.*, Carbonic Adsorbents from Inorganic Carbon Compounds, in *Carbonic Adsorbents and Their Application in Industry* (Moscow, 1983), p. 20.
4. S. K. Gordeev and A. V. Vartanova, Zh. Prikl. Khim. (Leningrad) **63** (6), 1178 (1991).
5. S. K. Gordeev and A. V. Vartanova, Zh. Prikl. Khim. (St. Petersburg) **66** (8), 1375 (1994).
6. S. K. Gordeev and A. V. Vartanova, Zh. Prikl. Khim. (St. Petersburg) **66** (7), 1080 (1994).
7. S. K. Gordeev, A. V. Vartanova, S. G. Zhukov, *et al.*, RF Patent No. 2,026,735 (1995), Byull. No. 2; R. G. Avarbé, S. K. Gordeev, A. V. Vartanova, *et al.*, RF Patent No. 2,084,036 (1997), Byull. No. 19.
8. R. N. Kyutt, É. A. Smorgonskaya, S. K. Gordeev, *et al.*, Fiz. Tverd. Tela (St. Petersburg) **41**, 891 (1999) [Phys. Solid State **41**, 808 (1999)].
9. R. N. Kyutt, É. A. Smorgonskaya, S. K. Gordeev, *et al.*, Fiz. Tverd. Tela (St. Petersburg) **41**, 1484 (1999) [Phys. Solid State **41**, 1359 (1999)].
10. É. A. Smorgonskaya, R. N. Kyutt, S. K. Gordeev, *et al.*, Fiz. Tverd. Tela (St. Petersburg) **42**, 1141 (2000) [Phys. Solid State **42**, 1176 (2000)].
11. A. M. Danishevskiĭ, É. A. Smorgonskaya, S. K. Gordeev, and A. V. Grechinskaya, Fiz. Tverd. Tela (St. Petersburg) **43**, 132 (2001) [Phys. Solid State **43**, 137 (2001)].
12. J. G. Castle, Phys. Rev. **92**, 1063 (1953).
13. G. R. Henning, B. Smaller, and E. L. Yasaitis, Phys. Rev. **95**, 1088 (1954).
14. G. Wagoner, Phys. Rev. **118**, 647 (1960).
15. A. S. Kosotonov and D. V. Shilo, Carbon **36**, 1649 (1998).
16. S. Garaj, L. Thien-Nga, R. Gaal, *et al.*, Phys. Rev. B **62**, 17115 (2000).
17. V. V. Popov, S. K. Gordeev, A. V. Grechinskaya, and A. M. Danishevskiĭ, Fiz. Tverd. Tela (St. Petersburg) **44**, 758 (2002) [Phys. Solid State **44**, 789 (2002)].
18. M. S. Dresselhaus, Phys. Rev. B **15**, 3180 (1977).
19. T. A. Polyanskaya and Yu. V. Shmartsev, Fiz. Tekh. Poluprovodn. (Leningrad) **23**, 3 (1989) [Sov. Phys. Semicond. **23**, 1 (1989)].
20. F. G. Dyson, Phys. Rev. **98**, 349 (1955).
21. C. P. Poole, *Electron Spin Resonance* (Wiley, New York, 1967).
22. J. H. Pifer and R. T. Longo, Phys. Rev. B **4**, 3797 (1971).
23. S. Schultz, M. R. Shanaberger, and P. M. Platzman, Phys. Rev. Lett. **19**, 749 (1967).
24. A. I. Veĭnger, A. G. Zabrodskiĭ, and T. V. Tisnek, Fiz. Tekh. Poluprovodn. (St. Petersburg) **34**, 46 (2000) [Semiconductors **34**, 45 (2000)].
25. E. A. Smorgonskaya, A. M. Danishevskii, R. N. Kyutt, *et al.*, J. Non-Cryst. Solids **299–302**, 810 (2002).
26. V. L. Kuznetsov, Yu. V. Butenko, A. L. Chuvilin, *et al.*, Chem. Phys. Lett. **336**, 397 (2001).

Translated by G. Skrebtsov